# Advances and applications of artificial intelligence and numerical simulation in risk emergency management and treatment

**Edited by**
Yunhui Zhang, Chengyi Pu, Zou Quanle, Yihuai Zhang and Lei-Lei Liu

**Coordinated by**
Meiben Gao

## About Frontiers

Frontiers is more than just an open access publisher of scholarly articles: it is a pioneering approach to the world of academia, radically improving the way scholarly research is managed. The grand vision of Frontiers is a world where all people have an equal opportunity to seek, share and generate knowledge. Frontiers provides immediate and permanent online open access to all its publications, but this alone is not enough to realize our grand goals.

## Frontiers journal series

The Frontiers journal series is a multi-tier and interdisciplinary set of open-access, online journals, promising a paradigm shift from the current review, selection and dissemination processes in academic publishing. All Frontiers journals are driven by researchers for researchers; therefore, they constitute a service to the scholarly community. At the same time, the *Frontiers journal series* operates on a revolutionary invention, the tiered publishing system, initially addressing specific communities of scholars, and gradually climbing up to broader public understanding, thus serving the interests of the lay society, too.

## Dedication to quality

Each Frontiers article is a landmark of the highest quality, thanks to genuinely collaborative interactions between authors and review editors, who include some of the world's best academicians. Research must be certified by peers before entering a stream of knowledge that may eventually reach the public - and shape society; therefore, Frontiers only applies the most rigorous and unbiased reviews. Frontiers revolutionizes research publishing by freely delivering the most outstanding research, evaluated with no bias from both the academic and social point of view. By applying the most advanced information technologies, Frontiers is catapulting scholarly publishing into a new generation.

## What are Frontiers Research Topics?

Frontiers Research Topics are very popular trademarks of the *Frontiers journals series*: they are collections of at least ten articles, all centered on a particular subject. With their unique mix of varied contributions from Original Research to Review Articles, Frontiers Research Topics unify the most influential researchers, the latest key findings and historical advances in a hot research area.

Find out more on how to host your own Frontiers Research Topic or contribute to one as an author by contacting the Frontiers editorial office: frontiersin.org/about/contact

# Advances and applications of artificial intelligence and numerical simulation in risk emergency management and treatment

**Topic editors**

Yunhui Zhang — Southwest Jiaotong University, China
Chengyi Pu — Central University of Finance and Economics, China
Zou Quanle — Chongqing University, China
Yihuai Zhang — University of Glasgow, United Kingdom
Lei-Lei Liu — Central South University, China

**Topic Coordinator**

Meiben Gao — Xihua University, China

# Table of contents

# Editorial: Advances and applications of artificial intelligence and numerical simulation in risk emergency management and treatment

Yunhui Zhang[1]*, Quanle Zou[2], Yihuai Zhang[3], Leilei Liu[4] and Chengyi Pu[5]

[1]Faculty of Geosciences and Environmental Engineering, Southwest Jiaotong University, Chengdu, China, [2]State Key Laboratory of Coal Mine Disaster Dynamics and Control, College of Resources and Environmental Science, Chongqing University, Chongqing, China, [3]James Watt School of Engineering, University of Glasgow, Glasgow, United Kingdom, [4]School of Geoscience and Info-Physics, Central South University, Changsha, China, [5]School of Insurance, Central University of Finance and Economics, Beijing, China

Editorial on the Research Topic
Advances and applications of artificial intelligence and numerical simulation in risk emergency management and treatment

There are various types of risks in the world, with geological, environmental, and ecological risks, such as karst desertification, water inrush, rock burst, debris flow, and landslides, existing in natural and engineering situations (Liu et al., 2019; Luo et al., 2020; Xue et al., 2020; Zhang et al., 2021; Huang et al., 2022). These risks pose significant safety threats to human survival. Therefore, risk emergency management and treatment have become important topics of the national governance system and governance capacity. They take on the crucial responsibility of preventing and resolving significant security risks, timely responding to all kinds of disasters and accidents, the significant mission of protecting people's lives and property, and maintaining social stability. To better study risk emergency management and treatment, interdisciplinary risk science was formed, which includes environmental science, earth science, engineering science, safety science, and information science.

Our Research Topic focused on novel research in risk emergency management and treatment. A total of 21 research papers on this Research Topic present the *Advances and applications of artificial intelligence and numerical simulation in risk emergency management and treatment*.

Artificial intelligence and numerical simulation are feasible in the prevention of geohazards, such as landslides, karst desertification, etc. Ma et al., Wei et al., and Wang

et al. investigated the regional characteristics of landslides and evaluated the susceptibility by machine learning methods. Cai et al., Yang et al., and Yan and Xiao analyzed the mechanical mechanisms and treatment measures of local rock slopes by numerical simulation.

A geophysical exploration is an efficient approach to detecting blind geological problems. Chen et al. used a 3D vertical seismic profile (VSP) survey to indicate an offshore subsurface characterization. Jia et al. applied the high-density resistivity method to detect a mined-out area of a quarry in Xiangtan City. Li et al. found a new way to efficiently calculate seismic wave travel time. Zheng et al. introduced a very new technology to explain unmanned aerial vehicle remote-sensing images based on a fully convolutional neural network.

Advances and applications of artificial intelligence and numerical simulation were applied to tunnel engineering. Chen et al., Li et al., Lu et al., and Zeng et al. used numerical simulations to investigate engineering problems and their mechanisms. Gao et al., Li et al., Zhang et al., and Zhang et al. used artificial intelligence and numerical simulation to seek advanced and efficient methods to address engineering.

This Research Topic also brings some novel research related to the ecological environment. Qin et al. revealed the karst water circulation of eastern Sichuan in southwestern China based on the GIS and environmental isotope methods. Xu et al. conducted a comprehensive evaluation of the Ruoergai Prairie ecosystem upstream of the Yellow River.

So far, brilliant achievements have been obtained in the field of artificial intelligence and numerical simulation in risk emergency management and treatment. However, more related research is expected to be carried out, helping to construct a safer world.

## Author contributions

All authors listed have made a substantial, direct, and intellectual contribution to the work and approved it for publication.

## Acknowledgments

## Conflict of interest

The authors declare that the research was conducted in the absence of any commercial or financial relationships that could be construed as a potential conflict of interest.

## Publisher's note

All claims expressed in this article are solely those of the authors and do not necessarily represent those of their affiliated organizations, or those of the publisher, the editors and the reviewers. Any product that may be evaluated in this article, or claim that may be made by its manufacturer, is not guaranteed or endorsed by the publisher.

## References

Huang, F., Yan, J., Fan, X., Yao, C., Huang, J., Chen, W., et al. (2022). Uncertainty pattern in landslide susceptibility prediction modelling: Effects of different landslide boundaries and spatial shape expressions. *Geosci. Front.* 13 (2), 101317. doi:10.1016/j.gsf.2021.101317

Liu, Y., Feng, Y., Xu, M., Zhang, Y., Long, H., and Zhu, H. (2019). Effect of an incremental change in external water pressure on tunnel lining: A case study from the tongxi karst tunnel. *Nat. Hazards* 98 (2), 343–377. doi:10.1007/s11069-019-03692-3

Luo, Y., Fan, X., Huang, R., Wang, Y., Yunus, A. P., and Havenith, H. (2020). Topographic and near-surface stratigraphic amplification of the seismic response of a mountain slope revealed by field monitoring and numerical simulations. *Eng. Geol.* 271, 105607. doi:10.1016/j.enggeo.2020.105607

Xue, Y., Kong, F., Qiu, D., Su, M., Zhao, Y., and Zhang, K. (2020). The classifications of water and mud/rock inrush hazard: A review and update. *Bull. Eng. Geol. Environ.* 80 (3), 1907–1925. doi:10.1007/s10064-020-02012-5

Zhang, Y., Dai, Y., Wang, Y., Huang, X., Xiao, Y., and Pei, Q. (2021). Hydrochemistry, quality and potential health risk appraisal of nitrate enriched groundwater in the Nanchong area, southwestern China. *Sci. Total Environ.* 784, 147186. doi:10.1016/j.scitotenv.2021.147186

# Fast iterative method for seismic wave travel time calculation under undulating surface conditions

Meng Li[1,2], Jian Zhang[1,2]*, Hui Sun[1], Fuliu Gao[1], Chenglang Wang[1], Ruoge Xu[1], Xiaoyan Zhao[2] and Jun Zhou[3]

[1]Faculty of Geosciences and Environmental Engineering, Southwest Jiaotong University, Chengdu, China, [2]MOE Key Laboratory of High-speed Railway Engineering, Southwest Jiaotong University, Chengdu, China, [3]School of Resources and Environment, University of Electronic Science and Technology of China, Chengdu, China

Seismic wave travel time is an important seismic attribute information and is widely used in various seismic forward and inversion methods, including seismic migration imaging, seismic tomography, seismic wave forward modeling and other core seismic data processing methods. The accuracy and efficiency of the travel time algorithm are important for the above methods. In the practical application of seismic exploration, it is often carried out under the condition of undulating surface, which has a significant impact on the travel time calculation. Therefore, it is of great significance to study an efficient and high-precision travel time calculation method that can adapt to undulating surface condition. In this paper, Fast iterative method (FIM) is modified to a topography travel time calculation method. The method employs an iterative method to solve the equation of function to obtain seismic wave travel time by maintaining a narrow band called the active list, and the algorithm can update all grid nodes in the active list at a time. We will verify the travel time computing power of the FIM method through several different velocity models.

## 1 Introduction

Seismic exploration has played an important role in the fields of petroleum and mineral resource exploration, geological disaster investigation, hydrological investigation, and engineering quality inspection. Travel time is an important attribute in seismic exploration, and is widely used in data processing technologies such as migration and tomography (Jetschny et al., 2011; Song et al., 2019; Wang et al., 2020; Lu et al., 2022). The travel time calculation method also determines the accuracy and efficiency of the above methods. Since imaging processing often includes models of complex surfaces and strong velocity changes, the ability of travel time calculation methods to adapt to complex models is particularly important (Aki et al., 1977; Hole, 1992; Sun, 2000; Sun, 2004). Therefore, it

is of great significance for the theoretical research and practical application of seismic processing methods to study high-efficiency and high-precision seismic wave travel time algorithms that can adapt to complex models (Thurber, 1983; Zelt and Smith, 1992; Eberhart-Phillips and Michael, 1993; Graeber et al., 2002).

Since the finite difference method for travel time calculation was first proposed by Vidale, many scholars have paid enough attention to the method (Vidale, 1988). This method solves the eikonal equation based on the finite difference method, and calculates the travel time of the entire grid area recursively. Van Trier et al. introduced the windward finite difference method to solve the equation of function and then obtained the viscous solution of the equation of function (van Trier and Symes, 1991), which greatly improved the stability of the difference scheme. Based on the Vidale method (Podvin and Lecomte, 1991), Podvin systematically analyzes the different wave propagation forms that may appear at each calculation grid point, and finally determines the wavefront expansion method, which improves the accuracy of the method. Based on the idea of Dijkstra's algorithm, Qin performs expansion calculation from the actual wave front, and expands the wave front by finding the minimum travel time point, which improves the adaptability of the finite difference method to complex models and the stability of the algorithm (Dijkstra, 1959; Qin et al., 1992). FMM was first proposed by Sethian. This is the most widely used wavefront expansion method (Sethian, 1996; Sethian, 1999). FMM relies on the data structure of the heap to realize the wavefront expansion that meets the narrowband technology, and the algorithm complexity is $O(Nlog_2N)$. The performance of the algorithm depends on the size and data structure of the input data. Since the algorithm keeps the data updated by inserting and deleting each element in the heap, the cost of maintaining the heap data structure will be relatively high in the face of large grid computing big. Based on the standard FMM algorithm, Kim proposed a group update method GMM (Group Marching Method) which is based on global boundaries and does not use a sorted data structure. The algorithm complexity is $O(N)$ (Kim and Folie, 2000; Kim, 2001). GMM improves the performance of Computational efficiency. GMM needs to obtain the slowness information of the minimum travel time point in the narrow band to determine the expansion group. If the speed information of the calculation grid point changes greatly, the algorithm may need to perform a large number of iterative calculations, which will reduce the performance of the algorithm. Jeong proposed a new calculation method FIM (Jeong and Whitaker, 2008; Hong and Jeong, 2016), which can effectively solve functional equations on a parallel architecture. FIM manages the active list through an iterative method, and performs grid node insertion and deletion based on convergence metrics. The algorithm does not require active list management. It maintains a special data structure and can update the

calculation at multiple points at the same time, thereby effectively improving the calculation efficiency.

The problem of complex undulating surface model is the key problem faced by seismic exploration at present, and the research on forward modeling and imaging method of complex undulating surface is an important geophysical problem. In the study of travel time calculation methods for complex undulating ground, Sun Z et al. studied the calculation of seismic wave travel time under complex surface conditions (Sun et al., 2009), as well as the unequal interval difference method, and compared and analyzed the stepped grid difference method (Sun et al., 2012b), the unequal interval grid finite difference method and the hybrid method. Performance of linear grid interpolation in travel time calculations for complex surface models (Sun et al., 2012a). In the past 50 years, the application scope of geophysical exploration has been expanded rapidly, and the seismic exploration method has been widely used in the monitoring, forecasting and prevention of geological disasters due to its high efficiency and high resolution. Stucchi et al. used seismic survey methods to survey the extension of historical landslides, and the resulting superimposed profiles revealed the deep geometry of the main landslide body and indicated the existence of a potential separation surface at the location of the toe of the landslide (Stucchi and Mazzotti, 2009). Hu G et al. proposed a coal seam seismic exploration technology for predicting coal mine disasters. This method is based on the different propagation velocity of channel waves in the roof and floor of surrounding rock and coal seam, and has dispersion phenomenon, so it can be used to detect geological structures such as voids and faults in coal seams. And achieved good results in practical applications (HU et al., 2013). Maraio et al. used a high-resolution active source seismic exploration method to explore a valley in eastern Italy where a large debris flow occurred, and performed high-precision migration imaging for the measurement results. The processing results reflected the accumulation of sediments behind the debris flow alluvial fan. Characteristics and stratigraphic structure at the top of the bedrock, as well as a quantitative estimate of the total thickness of the valley sediment deposits (Maraio et al., 2018). Feng et al. proposed a modeling method for random noise in seismic exploration in weakly inhomogeneous media, and quantitatively compared the proposed random noise model with the actual random noise. The results show that the proposed noise model is more reliable, The proposed method is successfully applied to construct a complete denoising training set of convolutional neural network to prove the application value of random noise model (Feng et al., 2020). Lei et al. successfully applied the seismic survey method of reflected wave and environmental noise to the survey of urban active faults, and made measurements near actual faults. The research of the combination of the two methods shows that the environmental noise seismic exploration method is feasible for

the detection of urban active faults, especially suitable for large-scale regional exploration (Lei et al., 2020). Liu et al. proposed a body wave separation method based on the frequency-domain signal-to-noise ratio, and successfully applied it to the surface wave body wave imaging of passive seismic exploration in actual shallow coverage areas, and the imaging profile was consistent with the active seismic results better (Liu et al., 2021). Fu et al. proposed a seismic prediction and evaluation method for hot dry rock exploration and development, which is based on seismic exploration and combined with other geophysical methods, and can realize nonlinear quantitative prediction and evaluation of hot dry rock reservoirs (Fu et al., 2022). Zhan et al. proposed a 3D structural modeling method for seismic exploration based on knowledge graph, aiming at the problem of image quality degradation in 3D structural modeling in seismic exploration. And under the guidance of the knowledge map, the surface is reconstructed and closed geological bodies are generated. Finally, the effectiveness and feasibility of the method are proved by the field model (Zhan et al., 2022).

In this paper, the FIM algorithm is introduced to solve the seismic wave travel time. Firstly, the basic principle, difference format and algorithm implementation scheme of FIM algorithm are expounded, and then the calculation accuracy and calculation efficiency of FIM algorithm are verified. Finally, the stability of FIM algorithm is verified by different complex models. This method can not only obtain high-precision seismic wave travel time, but also greatly shorten the calculation time, laying a foundation for the accuracy of research results such as tomography and seismic wave inversion.

# 2 Algorithm principles and implementations

## 2.1 Principles of fast iterative method algorithm

FIM is a highly efficient numerical algorithm that satisfies the iterative scheme and the narrowband technique, and satisfies the 2D eikonal equations,

$$|\nabla t(x,z)| = s(x,z), \qquad (1)$$

Where $t(x,z)$ is the time-travel function, $s(x,z)$ which is the model medium slowness function.

FIM uses the time-travel gradient term of the discrete equation of the Godun Windward Differential Formula to obtain the time-traveling time of the seismic waves.

$$max\left(D_{ij}^{-x}, D_{ij}^{+x}, 0\right)^2 + max\left(D_{ij}^{-z}, D_{ij}^{+z}, 0\right)^2 = s_{ij}^2, \qquad (2)$$

Where the $D_{ij}^{-x}t, D_{ij}^{+x}t, D_{ij}^{-z}t, D_{ij}^{+z}t$ $x$ and $z$ direction forward and backward difference operators are respectively, taking the first-order difference format as an example, there are

$$D_{ij}^{-x}t = \frac{t_{i,j} - t_{i-1,j}}{\Delta x}, D_{ij}^{+x}t = \frac{t_{i+1,j} - t_{i,j}}{\Delta x}, \qquad (3)$$

$$D_{ij}^{-z}t = \frac{t_{i,j} - t_{i,j-1}}{\Delta z}, D_{ij}^{+z}t = \frac{t_{i,j+1} - t_{i,j}}{\Delta z}. \qquad (4)$$

The main idea of FIM is to selectively solve the equation function equations across all mesh nodes, without the need to maintain a fixed data structure. The wavefront extended narrowband employed by FIM is called the active list, which is used to store the grid node information that is being updated, rather than using a special data structure to track the causal relationship between the grid nodes, FIM keep the relationship loose and update all nodes in the active list at the same time. During each update iteration, all neighboring points of the current calculation point are likely to participate in the update calculation of that point. When the compute node's solution is up-to-date relative to its proximity (that is, the compute node has converged), the node is removed from the active list and can be reattached to the active list when the value of any windward neighbor node is updated, so FIM is an algorithm that takes a simple data structure and allows each mesh node to be updated multiple times.

Figure 1 shows a 2D schematic of the FIM wavefront expansion. The grid node in the upper left corner is the source point, the black node is the fixed node, that is, the node whose travel time has been calculated, the gray node is the active node, that is, the node that is about to be updated and calculated, the diagonal rectangle containing the active node is the active list, and the black node is the active node. The arrows indicate the forward direction of the narrow band, and the white nodes are the far away points, that is, the nodes that have not yet been calculated when traveling. Figure 1A is the initial stage, the source is initialized, and the initial activity list is constructed; Figure 1B is after the first update step, the wavefront propagates forward, and all neighboring points around the activity list are included for calculation, and the calculation is completed. Nodes of are removed from the active list; Figure 1C is after the second update step, and the wavefront continues to propagate forward until all grid nodes complete the computation. Since grey nodes only depend on their neighbors (black nodes), all grey nodes in the active list can be updated at the same time. If the feature path does not change direction, then all updated gray nodes can be fixed and their white neighbors will form a new narrow band.

## 2.2 Undulating surface fast iterative method implementation scheme

The implementation scheme of FIM is similar to FMM and is mainly divided into two parts: initialization and active list update:

Initialization process:

Definition: X represents all grid nodes in the calculation area, x represents a grid node in the calculation area, L represents the
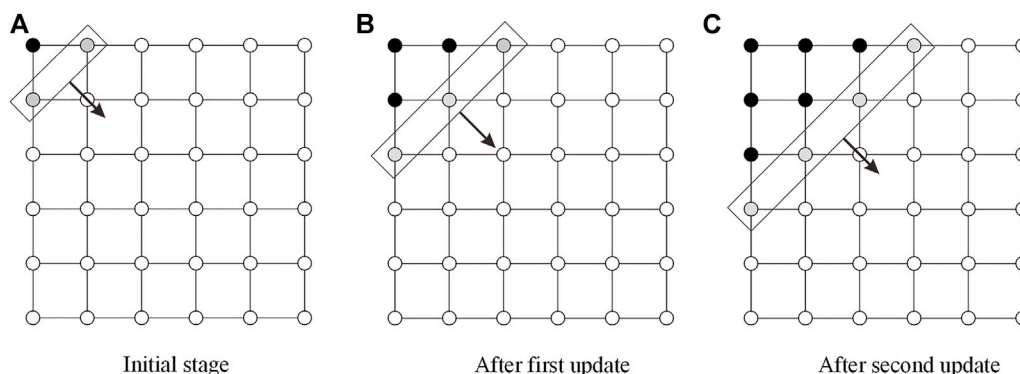
**FIGURE 1**
Schematic 2D example of FIM wavefront propagation, **(A)** Initial stage; **(B)** After first update; **(C)** After second update.

list of activities, and U(x) represents the timeout value of the calculated point x.

(A1) For all computed grid points, set the time-travel value of the source point to 0, the time-travel value U(x) of the remaining grid nodes to maximum, and the program to set U(x). = 1.0e5;

(A2) Move all adjacent points of the source into L to form an initial list of activities;

Extended update for the list of activities

(B1) For all mesh nodes $x_i$ in the active list L, do as follows

1) First, get its time value $U(x_i)$, denoted as $p_i$;
2) Use Eq. 1 to get the tick value of $x_i$ point, note it as $q_i$, and assign the $q_i$ value to $U(x_i)$.

(B2) The following judgment is made if $p_i$, $q_i$ meets the $|pi-qi|$ <$k$, then

1) The node information of each neighboring point xj of the compute point xi is judged
2) If xj does not belong to the active list, record the travel time value U (xj) of xj as pj;
3) Use solving Eq. 1 to obtain the travel time value of $x_j$ points, denoted as $q_j$;
4) If U ($x_j$)>$q_j$, assign $q_j$ to U ($x_j$), otherwise move $x_j$ to the active list L;
5) Move the calculation point $x_i$ out of the active list.

(B3) Determine whether the active list L is empty, otherwise, return B1 to continue the calculation.

FIM is an iterative calculation method, which means that the nodes are continuously updated until convergence. But for general computational models, most nodes only need one update to converge. When the angle between the direction of the feature path and the direction of advance of the narrowband is less than 45°, an accurate solution at the nodes of the computational mesh can be obtained with

only one update. If the angle is greater than 45°, nodes at locations where the eigenpath changes direction will have initial values computed with the wrong upwind neighbors, and they will be replaced in successive iterations as neighbors refine their values renew. So it will continue to update the travel time value of these nodes, instead of removing them from the active list, until the correct result is finally calculated. Unlike FMM, where the wavefront propagates at a point where the wavefront is closed, FIM causes the thicker band to split up where the characteristic path changes direction. Additionally, the wavefront can be moved to a mesh node that has converged and moved back into the active list to update the travel time value when the next mesh node is calculated. In addition, the FIM algorithm is similar to the FMM algorithm in the seismic wave travel time calculation scheme, and the travel time results are obtained by solving the functional equation using the upwind difference scheme, so the results of the FIM algorithm should be similar to the FMM algorithm. The advantage of the FIM algorithm is that it can update the travel time value of all grid nodes in the calculation activity list at the same time. The FMM algorithm can only update the travel time value of one grid node in the narrowband list at a time. Therefore, FIM can obtain close to FMM accuracy on the premise. FIM algorithm program flow chart is shown in Figure 2. Greatly improve computing efficiency. The next section will demonstrate the computational power of the FIM algorithm with numerical examples.

# 3 Algorithm accuracy and efficiency analysis

In order to verify the accuracy and efficiency of the algorithm used in this paper, we designed a uniform velocity model with a horizontal width of 4 km, a longitudinal width of 4km, and a seismic wave velocity of
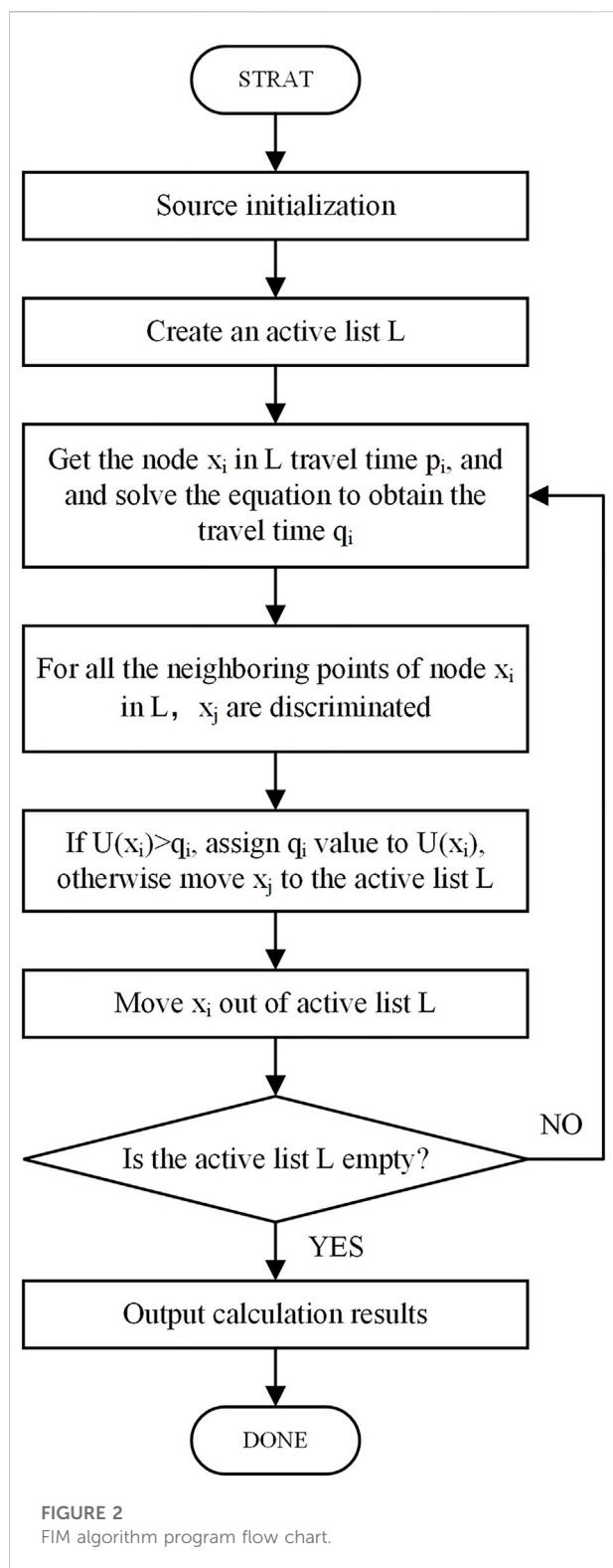
**FIGURE 2**
FIM algorithm program flow chart.

each grid node by FMM, GMM and FIM at the same time, and compare the calculation results with the analytical values. The accuracy index uses the average relative error (L (%)), and the efficiency index uses the calculation time (CPU time consumption(s)), and the results are as shown in Table 1 as shown.

Table 1 lists the five grid spacings of 0.5m, 1m, 2m, 5m, and 10 m The calculation accuracy and calculation time of the three methods of FMM, GMM and FIM. The law of the change of the average relative error data in the analysis table shows that under different velocity models, the average relative error of the three methods tends to be consistent, and as the grid spacing becomes smaller, the relative error gradually becomes smaller. Overall, all three algorithms have high computational accuracy, and even in the case of a large distance dispersion between meshes of 10 m, the average relative error of all three algorithms is on the order of 0.72%.

The calculation results shown in Figure 3 are calculated on a uniform model with a grid size of 2001×2001, a grid spacing of 2 m×2 m, and a wave speed of 1000 m/s. Since the calculation results of the three methods are similar, only one result graph of each method is shown here. By analyzing the error distribution of these two algorithms, it can be found that the errors of the three algorithms of FMM, GMM, and FIM are concentrated in the diagonal direction, which is due to three The method uses the windward difference scheme to solve the equation function equation to obtain the seismic wave travel time, and only the four neighbors of the calculation point above, down, left and right are included in the calculation when updating the calculation, and the influence of the diagonal neighbors on the overall calculation accuracy is ignored.

In order to further verify the computing power of the FIM algorithm, we designed three complex models of different degrees and used three methods for trial calculation. Model 1 is a slope velocity model, model 2 is a velocity model with undulating terrain, and model 3 is a high-speed model. The velocity model of the body, the medium velocity distribution range of model 1 and model 2 is 2000 m/s-5000 m/s, the velocity of model 3 is 2000m/s in the low-velocity layer, and the velocity in the high-velocity layer is 5000 m/s. Since the calculation results of the three methods are similar, only the calculation results of one method of each model are shown here. The calculation results are shown in Figure 4. In addition, the calculation efficiency of FIM is about 30% higher than that of GMM, and about 3 times higher than that of FMM algorithm. The calculated results are in good agreement with the above numerical test results.

Table 1 also lists the calculation time of FMM, GMM and FIM under different calculation grids, and the data in the analysis table shows that the calculation efficiency of FIM is the highest, higher than that of GMM algorithm, which is about the same about 4 times the FMM algorithm. Theoretically,

1000 m/s, and placed the epicenter at the center of the model. We use five kinds of distance scattering velocity models between grids and calculate the initial wave travel time of

TABLE 1 Analysis of the accuracy and efficiency of the time-travel calculation of the three algorithms.

| Grid spacing | 10 m | | 5 m | | 2 m | | 1 m | | 0.5 m | |
|---|---|---|---|---|---|---|---|---|---|---|
| Grid size | 400×400 | | 800×800 | | 2000×2000 | | 4,000×4,000 | | 8,000×8,000 | |
| Format | L | CPU | L | CPU | L | CPU | L | CPU | L | CPU |
| FMM | 0.72 | 0.08 | 0.40 | 0.21 | 0.25 | 5.23 | 0.11 | 32.88 | 0.08 | 269.22 |
| GMM | 0.72 | 0.05 | 0.40 | 0.12 | 0.25 | 2.17 | 0.11 | 12.26 | 0.08 | 92.37 |
| FIM | 0.72 | 0.03 | 0.40 | 0.07 | 0.25 | 1.67 | 0.11 | 9.58 | 0.08 | 71.16 |
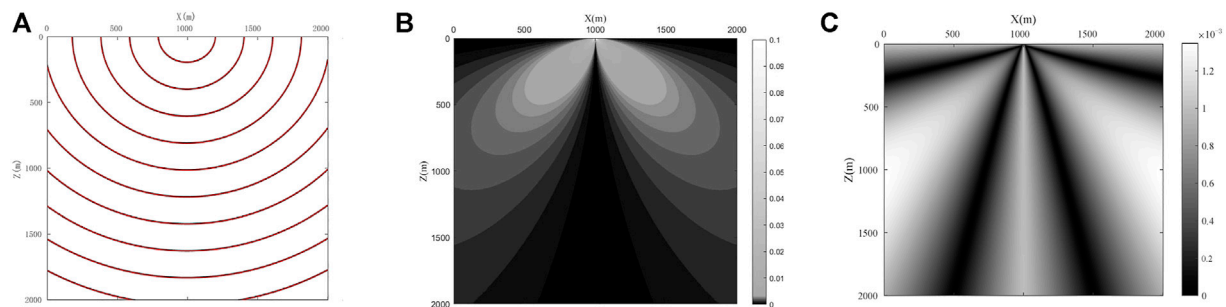


FIGURE 3
Schematic diagram of trial calculation results for homogeneous media, **(A)** Schematic diagram of FIM travel time contour (calculated value of red line, theoretical value of black line); **(B)** schematic diagram of relative error of FMM; **(C)** schematic diagram of absolute error of GMM.
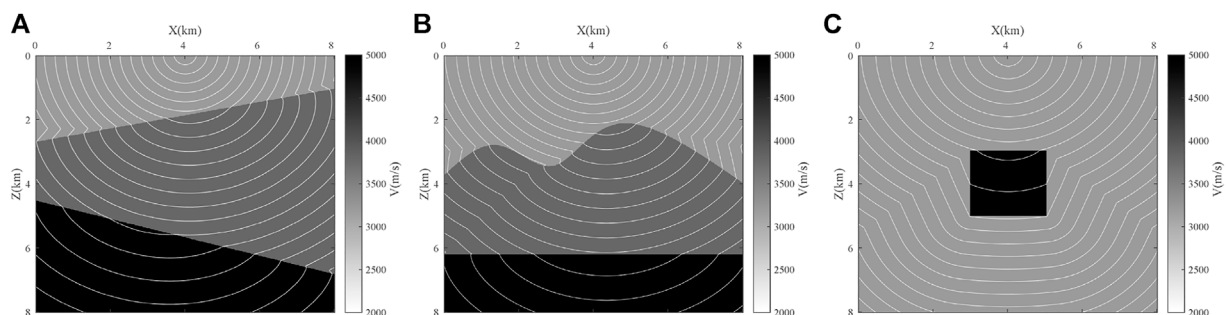


FIGURE 4
Travel time contour maps of the three algorithms, **(A)** FIM contour; **(B)** FMM contour; **(C)** GMM contour.

FMM and GMM have similar algorithmic structures, both of which are extended in front of the wave through Dijstra algorithm ideas. The biggest difference between the two is narrowband expansion, FMM through the priority queue to achieve the narrowband mesh point removal and insertion operation, the use of heap sorting method for narrowband minimum time point selection, so the FMM time complexity is $O(Nlog_2N)$ (N is the total number of calculated grid points). The GMM algorithm performs time-out calculations by traversing the selected group G within a narrow band, so the GMM time complexity is $O(N)$, so GMM The computational efficiency is higher than FMM, but when FIM expands the active list, it incorporates all the neighboring points of the calculation points into the calculation, and updates all the nodes in the active list, so this is also the root cause of the calculation efficiency of the FIM algorithm being higher than the above two algorithms and as the computational model increases, This advantage will be even more pronounced.
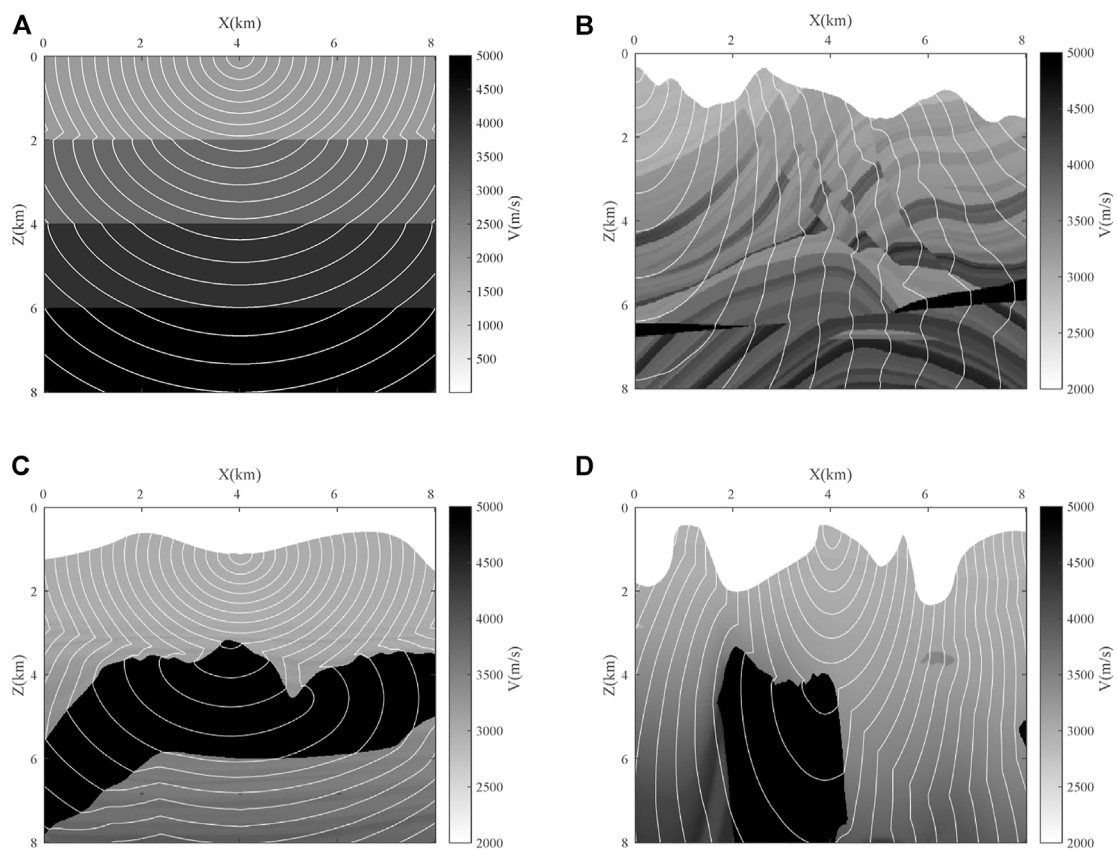
**FIGURE 5**
Contour maps of different models, **(A)** 4-layer gradient model, **(B)** Marmousi (part) model, **(C)** Sigsbee (part) model,**(D)** BP (part) model.

# 4 Examples

The above content mainly focuses on the principle, calculation accuracy and calculation efficiency of the FIM travel time algorithm. The purpose of studying these content is to make the algorithm introduced in this paper suitable for complex surface models. The following will verify the stability and practicability of the FIM algorithm through several complex calculation examples.

Figure 5A is an isochrone diagram of the 4-layer media model, the grid size is 801×801, the grid spacing is 5 m×5 m, and the speed of the three layers from top to bottom is 2000 m/s, 3000 m/s, 4000 m/s, 5000 m/s. Figure 5B shows the Marmousi model, the media velocity distribution range is 2000 m/s-5000 m/s, Figure Figure5C For the Sigsbee model, Figure 5D is the BP model. The above two velocity models are complex models containing high-speed layers, where the low-speed layer speed ranges from 2000 m/s to 3000 m/s and the high-speed layer speed ranges from 6000 m/s to 7,000 m/s. It should be pointed out that in order to make the size of the graphs of the calculation results uniform, we take part of the graphs in the Marmousi model, the

Sigsbee model and the BP model. The analysis and calculation results show that the model in Figure 5A is a three-layer homogeneous model, and the contour lines are distributed in each layer of medium when the seismic waves travel, and as the speed of the medium increases, the contour spacing also becomes larger. Figure 5B is a complex surface model with large speed changes, in the face of complex geological structures such as anticline and fault in the model, the time line of seismic waves bends and the distribution gradually becomes sparse, which is due to the rapid propagation speed of seismic waves between high-speed thin layers, so the time contours are more sparse, and the distribution of time lines is denser in areas with smaller speeds. Figures 5C, 4D are time-travel lines of seismic waves containing high-speed bodies, and the time-travel line diagram clearly reflects the propagation law of seismic waves spreading rapidly in the high-speed layer and spreading out slowly in the low-speed layer. Moreover, the time line is still distributed continuously at the boundary between the high-speed layer and the low-speed layer, which shows that the FIM algorithm has good adaptability to the strong speed change model. The comprehensive calculation results show that the distribution of

seismic wave time lines conforms to the propagation law of seismic waves in underground media, which further verifies the adaptability of FIM algorithm to complex models.

# 5 Conclusion

In order to efficiently obtain high-quality seismic wave travel time under complex undulating surface conditions, the FIM algorithm in the finite difference algorithm is introduced. The FIM algorithm combines FMM narrowband technology and iterative strategy to update all nodes in the active list at once in the seismic wavefront expansion calculation, and obtain the seismic wavefront time value through multiple iteration calculations. In this paper, the implementation scheme of FIM algorithm to calculate seismic wave travel under undulating surface conditions is given, and the algorithm is compared with FMM algorithm and GMM algorithm. The results show that FIM effectively improves the computational efficiency while maintaining high precision. Finally, through numerical analysis and calculation examples, the FIM algorithm has the following characteristics: 1) The algorithm increases the calculation efficiency by about 4 times compared with the FMM algorithm while taking into account the accuracy of the time-of-action calculation; 2) The algorithm has good stability and adaptability to complex near-surface models and strong velocity change models. The experimental results show that the FIM method can be used as a high-precision and higher-efficiency seismic wave timing calculation method, and has a good application prospect under complex terrain conditions.

# Data availability statement

The original contributions presented in the study are included in the article/Supplementary Material, further inquiries can be directed to the corresponding author.

# Author contributions

ML: designed and implemented the algorithm, and initially wrote the manuscript. JiZ: contributed to the data analysis and helped write the manuscript. HS and FG: contributed to model construction. CW: contributed to data calculation. RX and XZ: helped polish the manuscript. All authors have read and agreed to the published version of the manuscript.

# Conflict of interest

The authors declare that the research was conducted in the absence of any commercial or financial relationships that could be construed as a potential conflict of interest.

# Publisher's note

All claims expressed in this article are solely those of the authors and do not necessarily represent those of their affiliated organizations, or those of the publisher, the editors and the reviewers. Any product that may be evaluated in this article, or claim that may be made by its manufacturer, is not guaranteed or endorsed by the publisher.

# References

Aki, K., Christoffersson, A., and Husebye, E. S. (1977). Determination of the three-dimensional seismic structure of the lithosphere. *J. Geophys. Res.* 82 (2), 277–296. doi:10.1029/JB082i002p00277

Dijkstra, E. W. (1959). A note on two problems in connexion with graphs. *Numer. Math. (Heidelb).* 1 (1), 269–271. doi:10.1007/bf01386390

Eberhart-Phillips, D., and Michael, A. J. (1993). Three-dimensional velocity structure, seismicity, and fault structure in the Parkfield Region, central California. *J. Geophys. Res.* 98 (B9), 15737–15758. doi:10.1029/93jb01029

Feng, Q., Li, Y., and Yang, B. (2020). Modeling land seismic exploration random noise in a weakly heterogeneous medium and the application to the training set. *IEEE Geosci. Remote Sens. Lett.* 17 (4), 701–705. doi:10.1109/lgrs.2019.2926756

Fu, G. Q., Peng, S. P., Wang, R. Z., Zhao, J. T., Yan, F., Xie, J. Y., et al. (2022). Seismic prediction and evaluation techniques for hot dry rock

exploration and development. *J. Geophys Eng.* 19 (4), 694–705. doi:10.1093/jge/gxac042

Graeber, F. M., Houseman, G. A., and Greenhalgh, S. A. (2002). Regional teleseismic tomography of the Western lachlan orogen and the newer volcanic province, southeast Australia. *Geophys. J. Int.* 149 (2), 249–266. doi:10.1046/j.1365-246X.2002.01598.x

Hole, J. A. (1992). Nonlinear high-resolution three-dimensional seismic travel time tomography. *J. Geophys. Res.* 97 (B5), 6553–6562. doi:10.1029/92jb00235

Hong, S., and Jeong, W.-K. (2016). A group-ordered fast iterative method for eikonal equations. *IEEE Trans. Parallel Distrib. Syst.* 28 (2), 1. doi:10.1109/tpds.2016.2567397

Hu, G.-z., Teng, J.-w., Pi, J.-l., and Wang, W. (2013). In-seam seismic exploration techniques——A geophsical method predictting coal-mine disaster. *Geophysics* 28 (1), 439–451. doi:10.6038/pg20130150

Jeong, W.-K., and Whitaker, R. T. (2008). A fast iterative method for eikonal equations. *SIAM J. Sci. Comput.* 30 (5), 2512–2534. doi:10.1137/060670298

Jetschny, S., Bohlen, T., and Kurzmann, A. (2011). Seismic prediction of geological structures ahead of the tunnel using tunnel surface waves. *Geophys. Prospect.* 59 (5), 934–946. doi:10.1111/j.1365-2478.2011.00958.x

Kim, S. (2001). An $\cal O(N)$ level set method for eikonal equations. *SIAM J. Sci. Comput.* 22 (6), 2178–2193. doi:10.1137/s1064827500367130

Kim, S., and Folie, D. (2000). "The group marching method: An 裂 (N) level set eikonal solver," in *SEG technical program expanded abstracts 2000 (society of exploration geophysicists)*, Houstone TX USA, 2297–2300. doi:10.1190/1.1815917

Lei, X. Q., Zhang, J., Jin, W. Y., Han, C., and Xu, X. W. (2020). The application of ambient noise and reflection seismic exploration in an urban active fault survey. *Interpretation* 8 (4), SU1–SU10. doi:10.1190/Int-2020-0085.1

Liu, G. F., Liu, Y., Meng, X. H., Liu, L. B., Su, W. J., Wang, Y. Z., et al. (2021). Surface wave and body wave imaging of passive seismic exploration in shallow coverage area application of Inner Mongolia. *Chin. J. Geophysics-Chinese Ed.* 64 (3), 937–948. doi:10.6038/cjg2021O0064

Lu, X. L., Hu, X. Q., Xu, Z. Y., Liao, X., Liu, L. H., and Fu, Z. H. (2022). Tunnel concealed karst cave joint detection by tunnel seismic and transient electromagnetic. *Lithosphere-Us* 2022 (1). 2827582, doi:10.2113/2022/2827582

Maraio, S., Bruno, P. P. G., Picotti, V., Mair, V., and Brardinoni, F. (2018). High-resolution seismic imaging of debris-flow fans, alluvial valley fills and hosting bedrock geometry in Vinschgau/Val Venosta, Eastern Italian Alps. *J. Appl. Geophy.* 157, 61–72. doi:10.1016/j.jappgeo.2018.07.001

Podvin, P., and Lecomte, I. (1991). Finite difference computation of traveltimes in very contrasted velocity models: A massively parallel approach and its associated tools. *Geophys. J. Int.* 105 (1), 271–284. doi:10.1111/j.1365-246X.1991.tb03461.x

Qin, F., Luo, Y., Olsen, K. B., Cai, W., and Schuster, G. T. (1992). Finite-difference solution of the eikonal equation along expanding wavefronts. *Geophysics* 57 (3), 478–487. doi:10.1190/1.1443263

Sethian, J. A. (1996). A fast marching level set method for monotonically advancing fronts. *Proc. Natl. Acad. Sci. U. S. A.* 93 (4), 1591–1595. doi:10.1073/pnas.93.4.1591

Sethian, J. A. (1999). Fast marching methods. *SIAM Rev. Soc. Ind. Appl. Math.* 41 (2), 199–235. doi:10.1137/s0036144598347059

Song, A., Song, B., and Qian, R. Y. (2019). Experiment of 3D seismic reflection technique for forward probing on TBM tunnel face. *J. Environ. Eng. Geophys.* 24 (4), 609–619. doi:10.2113/Jeeg24.4.609

Stucchi, E., and Mazzotti, A. (2009). 2D seismic exploration of the Ancona landslide (Adriatic Coast, Italy). *Geophysics* 74 (5), B139–B151. doi:10.1190/1.3157461

Sun, J. (2000). Limited-aperture migration. *Geophysics* 65 (2), 584–595. doi:10.1190/1.1444754

Sun, J. (2004). True-amplitude weight functions in 3D limited-aperture migration revisited. *Geophysics* 69 (4), 1025–1036. doi:10.1190/1.1778245

Sun, Z., Sun, J., and Han, F. (2009). Calculation of seismic wave travel time based on linear interpolation and narrowband technique under complex surface conditions. *Chin. J. Geophys-Ch* 52 (11), 2846–2853. doi:10.3969/j.issn.0001-5733.2009.11.019

Sun, Z., Sun, J., and Han, F. (2012a). Three kinds of seismic wave travel time algorithms for complex terrain and their comparison. *Chin. J. Geophys-Ch* 55 (2), 560–568. doi:10.6038/j.issn.0001-5733.2012.02.018

Sun, Z., Sun, J., and Han, F. (2012b). Unequal distance upwind difference method for calculating seismic wave travel time under three-dimensional undulating surface conditions. *Chin. J. Geophys-Ch* 55 (7), 2441–2449. doi:10.6038/j.issn.0001-5733.2012.07.028

Thurber, C. H. (1983). Earthquake locations and three-dimensional crustal structure in the Coyote Lake Area, central California. *J. Geophys. Res.* 88 (B10), 8226–8236. doi:10.1029/JB088iB10p08226

van Trier, J., and Symes, W. W. (1991). Upwind finite-difference calculation of traveltimes. *Geophysics* 56 (6), 812–821. doi:10.1190/1.1443099

Vidale, J. (1988). Finite-difference calculation of travel times. *Bull. Seismol. Soc. Am.* 78 (6), 2062–2076. doi:10.1785/BSSA0780062062

Wang, J., Liu, J. P., Cheng, F., Yang, H. J., and Huang, Y. F. (2020). Reverse time migration imaging of tunnels via the finite element method using an unstructured mesh. *Appl. Geophys.* 17 (2), 267–276. doi:10.1007/s11770-020-0814-x

Zelt, C. A., and Smith, R. B. (1992). Seismic traveltime inversion for 2-D crustal velocity structure. *Geophys. J. Int.* 108 (1), 16–34. doi:10.1111/j.1365-246X.1992.tb00836.x

Zhan, X. L., Lu, C., and Hu, G. M. (2022). 3D structural modeling for seismic exploration based on knowledge graphs. *Geophysics* 87 (3), Im81–Im100. doi:10.1190/Geo2020-0924.1

# Calculation of surface settlement and pile foundation deformation caused by shield machine tunnelling along curve section

Feng Zeng[1,2,3,4]*, Yang Gao[1,2,3,4], Fujiang Chen[1,2,3,4], Qingqing He[1] and Zhihao He[1]*

[1]School of Emergency Management, Xihua University, Chengdu, China, [2]Key Laboratory of Geohazard Prevention of Hilly Mountains, Ministry of Natural Resources, Fuzhou, China, [3]Fujian Key Laboratory of Geohazard Prevention, Fuzhou, China, [4]State Key Laboratory of Geohazard Prevention and Geoenvironment Protection, Chengdu University of Technology, Chengdu, China

The shield machine tunnelling along the curve section causes more disturbance to the surrounding environment than the straight section. Pile foundation is the most commonly used foundation form in high-rise buildings, and high-rise buildings have extremely high requirements for controlling non-uniform deformation. Therefore, it is necessary to study the surface settlement and the deformation law of pile foundations caused by shield machine tunnelling along the curve section. Considering the shield machine tunnelling factors along the curve section and the coupling effect of piles and soil, the analytical calculation formula of the ground settlement and the pile foundation deformation caused by the shield machine tunnelling along the curve section is deduced. According to the actual project situation, a finite difference model (FDM) is constructed, and the correctness of the FDM and analytical prediction formula is verified by comparing the on-site monitoring data. The research shows that the error among the FDM results, the analytical prediction results, and the on-site monitoring data are small, and the surface settlement and pile foundation deformation meet the construction control standards. The friction resistance of the shield shell, the integrative gap at the shield tail (IGST), and the over-cutting gap (OG) are the main factors leading to the surface settlement. However, the shield shell friction and OG are the main reasons leading to the inner settlement of the curve section being more prominent than the outer side. The difference in the pile foundation settlement on both sides of the curve section is slight, the

maximum settlement difference rate is 1.8%, and the maximum horizontal deformation rate of the pile foundation on the inner and outer sides is 9.2%, which shows that the horizontal deformation of the pile foundation is more sensitive to the asymmetrically distributed construction factors.

## Introduction

The shield method has the characteristics of less disturbance of excavation and high construction efficiency. Underground lines such as urban subways and municipal pile lines are usually constructed by the shield method (Xie and Tang, 2017; Chen et al., 2018). The extremely limited underground space in the city makes the construction environment of the shield tunnel very complicated. Living pile lines, hidden buildings and building foundations are intricately distributed. Shield tunnelling will disturb these existing structures, resulting in settlement, deformation and even cracking of existing structures, posing a significant threat to the safe use of existing structures (Li et al., 2019; Huang et al., 2020; Lin et al., 2020; Liu et al., 2020; Miao et al., 2020).

The pile foundation is the most commonly used foundation for high-rise buildings. Compared with other types of foundations, the shield machine is more likely to disturb the soil around the pile foundation, and cause the settlement of the pile foundation, resulting in quicksand and piping in the foundation pit, thus affecting the surrounding environment. Numerous scholars have studied the pile foundation settlement caused by shield tunnelling through analytical analysis, laboratory tests and numerical simulations. Hu et al. (2021) proposed a simplified calculation method to analyse the impact of shield excavation on adjacent pile foundations. A two-stage method of modified Peck formula and Winkler elastic foundation model was used to investigate the additional displacement and internal force of pile; Basile (2014) proposed an efficient analysis method is presented for estimating the effects induced by tunnelling on existing pile foundations; Lee and Jacobsz (2006) studied the effects of tunnelling on an existing pile constructed in weathered

residual soil and rock by carrying out three-dimensional parametric elasto-plastic numerical analyses. Franza et al. (2017) present an elastic study of tunnel-pile-structure interaction through Winkler-based Two-Stage Analysis Methods (TSAMs), focussing on structural displacements resulting from tunnel excavation beneath piled frames or simple equivalent beams; Jongpradist et al. (2013) investigate the influences of tunnel excavation on existing loaded piles by three-dimensional elasto-plastic numerical analyses; Mroueh and Shahrour (2002) used an elastoplastic three-dimensional finite element modelling to analysis of the impact of the construction of urban tunnels on adjacent pile foundations. He et al. (2013) used the Φ520 mm earth pressure balance (EPB) model shield machine to investigate the impact of shield tunnelling on the existing pile foundation deformation and internal forces; Min et al. (2011) used a three-dimensional finite element simulation and centrifuge test to investigate the effects of tunnel construction on nearby pile foundation. Miao et al. (2022) used a geotechnical centrifugal test to reveal the failure mode and deformation mechanism under the action of water level fluctuation and rainfall. Zhang et al. (2021) have analysed the relationship between groundwater quality and human health risks. Soomro et al. (2021) used an advanced hypoplastic soil model to investigate the response of an existing vertically loaded 2 × 2 pile group in a lateral direction due to the advancement of twin stacked tunnels in dry sand. However, few studies focus on shield machine tunnelling along the curve section. In actual construction, it is more common for the shield machine tunnelling along the curve section than the straight section. According to Deng's research (Deng et al., 2022), the construction factors of shield machine tunnelling along the curve section are more complicated than that of the straight section, which will cause more disturbance to the surrounding environment. Therefore, it is necessary to study the deformation law of pile foundations caused by shield machine tunnelling along the curve section and to propose the analytical calculation formula of pile foundation settlement.

The main contents of this study include: In section "Soil deformation caused by tunnelling construction factor," the analytical calculation formula of soil deformation caused

**FIGURE 1**
Load distribution of shield machine tunnelling.



**FIGURE 2**
Distribution of ground loss in the curve section.

by the additional thrust, the shield shell friction and the additional grouting pressure are derived. Then, the analytical calculation formula of soil deformation caused by OG and IGST is derived based on the mirror image method and the Loganathan formula, respectively. In section "Calculation of pile foundation deformation," the pile foundation is regarded as a Euler-Bernoulli beam placed on the elastic foundation beam. The calculation formula of the pile deformation is deduced considering the coupling effect of the pile-soil displacement. In section "Numerical calculation model," based on actual engineering cases, a finite difference model (FDM) calculation model is constructed; then, the analytical formula prediction results, FDM calculation results, and on-site monitoring data

are compared to verify the rationality of the analytical calculation formula and FDM. This study can provide an analytical prediction formula for similar projects and predict the construction risk of shield tunnelling in advance.

## Soil deformation caused by tunnelling construction factor

Existing studies have pointed out that the additional thrust, the shield shell friction, the additional grouting pressure, and the ground loss are the main factors that disturb the surrounding soil during the shield machine tunnelling process. Different

excavation parameters need to be set for the units on the inner and outer sides of the curve section to realise the deflection of the excavation axis when the shield machine tunnelling along the curve section field (Liang et al., 2018; Li and Li, 2021). The thrust of the inner cylinder will be smaller than that of the outer cylinder, and due to the extrusion of the inner soil, the friction of the inner shield will be greater than that of the outer shield. According to the above analysis, this study assumes that the applied load satisfies the following assumptions (Deng et al., 2021): (1) The soil is an isotropic homogeneous body, the calculation area is a linear elastic semi-infinite space, and the effect of soil drainage and consolidation during construction is not considered; (2) $q_1$ and $q_2$ is the additional inner thrust and additional outer thrust, respectively, generally speaking, $q_2 > q_1$, that is, the additional thrust on the outside is greater than the additional thrust on the inside. (3) $f_1$ and $f_2$ are the friction of the inner shield shell and outer shield shell, respectively. During the turning process, the inner shield shell receives more soil extrusion, which leads to the additional thrust on the outside being more significant than the additional thrust on the inside. (4) The influence range of the shield tail grouting is the width of the three-ring segment behind the shield tail. According to the above analysis, the load distribution of the shield machine when driving along the curved section is shown in **Figure 1**.

The shield machine is squeezed by asymmetric distribution on the inside and outside of the curve section, which will make the shield machine challenging to excavate and reduce its service life of the shield machine. Therefore, given the circumstance that the shield machine is tunnelling along the curved section, the turning of the shield machine is generally realised by setting the asymmetric distribution of the thrust of the oil cylinders on both sides in the weak stratum. In the hard stratum, according to the actual construction situation, it is also necessary to over-cutting of the inner soil. When the shield machine excavates in the straight section, the ground loss mainly comes from the gap caused by the shield tail void. Although the technology of synchronous grouting is becoming increasingly mature, the ground loss caused by the shield tail void is still unavoidable. This part of the formation loss is known as the integrative gap at the shield tail (IGST). In the hard soil layer, the over-cutting of the inner soil will also cause ground loss, and this part of the formation loss is called the over-cutting gap (OG). **Figure 2** shows the distribution of ground loss.

## Computational theory

Mindlin (1936) takes the elastic semi-infinite space body as the research area and derives the settlement calculation formula of any point $(x, y, z)$ in the space caused by the horizontal and vertical loads at a certain point $(x_0, y_0, z_0)$.

The point $(x_0, y_0, z_0)$ under the action of the horizontal load $P_h$ to cause another point of vertical deformation $W_{z1}$ and horizontal deformation $W_{x1}$, $W_{y1}$ calculation formula:

$$W_{z1} = \frac{P_h(x - x_0)}{16\pi G(1 - \mu)}\left[\frac{z - z_0}{R_1^3} + \frac{(3 - 4\mu)(z - z_0)}{R_2^3}\right.$$
$$\left. - \frac{6zz_0(z + z_0)}{R_2^5} + \frac{4(1 - \mu)(1 - 2\mu)}{R_2(R_2 + z + z_0)}\right] \quad (1)$$

$$W_{x1} = \frac{P_h}{16\pi G(1 - \mu)}\left[\frac{1 - 4\mu}{R_1} + \frac{1}{R_2} + \frac{(x - x_0)^2}{R_1^3}\right.$$
$$+ \frac{(3 - 4\mu)(x - x_0)^2}{R_2^3} + \frac{2zz_0}{R_2^3}\left(1 - \frac{3(x - x_0)^2}{R_2^2}\right)$$
$$\left. + \frac{4(1 - \mu)(1 - 2\mu)}{R_2 + z + z_0}\left(1 - \frac{(x - x_0)^2}{R_2(R_2 + z + z_0)}\right)\right] \quad (2)$$

$$W_{y1} = \frac{P_h(x - x_0)(y - y_0)}{16\pi G(1 - \mu)}\left[\frac{1}{R_1^3} + \frac{(3 - 4\mu)}{R_2^3} - \frac{6zz_0}{R_2^5}\right.$$
$$\left. - \frac{4(1 - \mu)(1 - 2\mu)}{R_2(R_2 + z + z_0)^2}\right] \quad (3)$$

The point $(x_0, y_0, z_0)$ under the action of the vertical load $P_v$ to cause another point of vertical deformation $W_{v2}$ and horizontal deformation $W_{h2}$ calculation formula:

$$W_{z2} = \frac{P_v}{16\pi G(1 - \mu)}\left[\frac{3 - 4\mu}{R_1} + \frac{8(1 - \mu)^2 - (3 - 4\mu)}{R_2}\right.$$
$$+ \frac{(z - z_0)^2}{R_1^3} + \frac{(3 - 4\mu)(z - z_0)^2 - 2zz_0}{R_2^3}$$
$$\left. + \frac{6zz_0(z + z_0)^2}{R_2^5}\right] \quad (4)$$

$$W_{x2} = W_{y2} = \frac{P_v((x - x_0)^2 + (y - y_0)^2)^{1/2}}{16\pi G(1 - \mu)}\left[\frac{z - z_0}{R_1^3}\right.$$
$$+ \frac{(3 - 4\mu)(z - z_0)}{R_2^3} + \frac{4(1 - \mu)(1 - 2\mu)}{R_2(R_2 + z + z_0)}$$
$$\left. + \frac{6zz_0(z + z_0)^2}{R_2^5}\right] \quad (5)$$

Where: $G$ is the shear modulus of the soil; $\mu$ is the Poisson's ratio of soil; $R_1 = [(x-x_0)^2+(y-y_0)^2+(z-z_0)^2]^{1/2}$; $R_2 = [(x-x_0)^2+(y-y_0)^2+(z+z_0)^2]^{1/2}$.

In order to simplify the expression of the calculation formula, the formula is simplified as: $W_{z1} = W_{z1}(x,y,z,x_0,y_0,z_0,P_h)$, $W_{x1} = W_{x1}(x,y,z,x_0,y_0,z_0,P_h)$, $W_{y1} = W_{y1}(x,y,z,x_0,y_0,z_0,P_h)$, $W_{z2} = W_{z2}(x,y,z,x_0,y_0,z_0,P_v)$, $W_{x2}(x,y,z,x_0,y_0,z_0,P_v)$, $W_{y2}(x,y,z,x_0,y_0,z_0,P_v)$.

## Frontal additional thrust

The additional frontal thrust acting on the cutter head can be approximated as a horizontal load. According to the distribution

in **Figure 1**, the coordinates of the centre point of the cutter head are $(0, 0, H)$. Assuming that the additional thrust is evenly distributed on the cutter head, the additional thrust per unit area is $dP_h = qdA = rqdrd\theta$. The coordinates of a point $(x_0, y_0, z_0)$ on the cutter head can be expressed as:

$$\begin{cases} x_0 = 0 \\ y_0 = r\cos\theta \\ z_0 = H - r\sin\theta \end{cases} \quad (6)$$

Substituting the above formula into Eqs 1–3, the calculation formula of the formation deformation caused by the additional thrust per unit area is:

$$dW_{qx} = W_{x1}(x, y, z, x_0, r\cos\theta, H - r\sin\theta, rqdrd\theta) \quad (7)$$

$$dW_{qy} = W_{y1}(x, y, z, x_0, r\cos\theta, H - r\sin\theta, rqdrd\theta) \quad (8)$$

$$dW_{qz} = W_{z1}(x, y, z, x_0, r\cos\theta, H - r\sin\theta, rqdrd\theta) \quad (9)$$

The above equation has two integral variables, $r$ and $\theta$, respectively. The integral range of r is $0{\sim}R$. The inner and outer sides of the cutter head are integrated, and the calculation formula of the formation deformation caused by the additional thrust of the cutter head is calculated as follows:

$$W_{qx} = \int_{-pi/2}^{pi/2}\int_0^R W_{x1}(x, y, z, x_0, r\cos\theta, H - r\sin\theta, rq_1drd\theta)drd\theta +$$

$$\int_{pi/2}^{-pi/2}\int_0^R W_{x1}(x, y, z, x_0, r\cos\theta, H - r\sin\theta, rq2drd\theta)drd\theta \quad (10)$$

$$W_{qy} = \int_{-pi/2}^{pi/2}\int_0^R W_{y1}(x, y, z, x_0, r\cos\theta, H - r\sin\theta, rq_1drd\theta)drd\theta +$$

$$\int_{pi/2}^{-pi/2}\int_0^R W_{y1}(x, y, z, x_0, r\cos\theta, H - r\sin\theta, rq2drd\theta)drd\theta \quad (11)$$

$$W_{qz} = \int_{-pi/2}^{pi/2}\int_0^R W_{z1}(x, y, z, x_0, r\cos\theta, H - r\sin\theta, rq_1drd\theta)drd\theta +$$

$$\int_{pi/2}^{-pi/2}\int_0^R W_{z1}(x, y, z, x_0, r\cos\theta, H - r\sin\theta, rq2drd\theta)drd\theta \quad (12)$$

## Shield friction

The action range of the shield shell friction is from the cutter head to the shield tail, assuming that the shield shell friction is evenly distributed on the shield shell. The shield friction can also be regarded as a horizontal acting load. The friction $dP_h = fRd\beta ds$ on the shield shell per unit area, the coordinates of any point on the shield shell can be expressed as:

$$\begin{cases} x_0 = -s \\ y_0 = R\cos\theta \\ z_0 = H - R\sin\theta \end{cases} \quad (13)$$

Substituting the above formula into Eqs 1–3, the calculation formula of the formation deformation caused by the shield shell friction per unit area is:

$$dW_{fx} = W_{x1}(x, y, z, -s, R\cos\theta, H - R\sin\theta, fRd\beta ds) \quad (14)$$

$$dW_{fy} = W_{y1}(x, y, z, -s, R\cos\theta, H - R\sin\theta, fRd\beta ds) \quad (15)$$

$$dW_{fz} = W_{z1}(x, y, z, -s, R\cos\theta, H - R\sin\theta, fRd\beta ds) \quad (16)$$

There are two integral variables in the above formula: s and β. The integral interval of s is $0{\sim}L$. By integrating both sides of the shield shell, the calculation formula of the formation deformation caused by the friction resistance of the shield shell can be calculated as follows:

$$W_{fx} = \int_{-pi/2}^{pi/2}\int_0^L W_{x1}(x, y, z, -s, R\cos\theta, H - R\sin\theta, f_1Rd\beta ds)d\beta ds +$$

$$\int_{pi/2}^{-pi/2}\int_0^R W_{x1}(x, y, z, -s, R\cos\theta, H - R\sin\theta, f_2Rd\beta ds)d\beta ds \quad (17)$$

$$W_{fy} = \int_{-pi/2}^{pi/2}\int_0^L W_{y1}(x, y, z, -s, R\cos\theta, H - R\sin\theta, f_1Rd\beta ds)d\beta ds +$$

$$\int_{pi/2}^{-pi/2}\int_0^R W_{y1}(x, y, z, -s, R\cos\theta, H - R\sin\theta, f_2Rd\beta ds)d\beta ds \quad (18)$$

$$W_{fz} = \int_{-pi/2}^{pi/2}\int_0^L W_{z1}(x, y, z, -s, R\cos\theta, H - R\sin\theta, f_1Rd\beta ds)d\beta ds +$$

$$\int_{pi/2}^{-pi/2}\int_0^R W_{z1}(x, y, z, -s, R\cos\theta, H - R\sin\theta, f_2Rd\beta ds)d\beta ds \quad (19)$$

## Additional grouting pressure

The action range of the additional grouting pressure is the length of the three-ring segment behind the shield tail, and the action direction is the normal outer direction of the segment. The grouting pressure can be decomposed into horizontal action load and vertical action load. The value of the additional grouting pressure per unit area of the segment is $dp = pRd\beta da$, the value of the horizontal load is $dP_h = pR\cos\beta d\beta da$, and the value of the vertical load is $dP_v = pR\sin\beta d\beta da$. The coordinates of any point on the segment can be expressed as:

$$\begin{cases} x_0 = -L - a \\ y_0 = R\cos\beta \\ z_0 = H - R\sin\theta \end{cases} \quad (20)$$

Substituting the above formula into Eqs 1–6, the calculation formula of the formation deformation caused by the additional grouting pressure per unit area is:

$$dW_{px} = W_{x1}(x, y, z, -L - s, R\cos\theta, H - R\sin\theta, pR\cos\beta d\beta da)$$
$$+ W_{y2}(x, y, z, -L - s, R\cos\theta, H$$
$$- R\sin\theta, pR\sin\beta d\beta da) \quad (21)$$

$$dW_{py} = W_{y1}(x, y, z, -L - s, Rcos\theta, H - Rsin\theta, pRcos\beta d\beta da)$$
$$+ W_{z2}(x, y, z, -L - s, Rcos\theta, H$$
$$- Rsin\theta, pRsin\beta d\beta da) \tag{22}$$

$$dW_{pz} = W_{z1}(x, y, z, -L - s, Rcos\theta, H - Rsin\theta, pRcos\beta d\beta da)$$
$$+ W_{x2}(x, y, z, -L - s, Rcos\theta, H$$
$$- Rsin\theta, pRsin\beta d\beta da) \tag{23}$$

Two integral variables in the above formula, a and β, are integrated over the entire action area. The integral interval of a is 0∼3$l$, and the integral interval of β is 0∼2π .

## Ground loss

### Integrative gap at the shield tail

According to the model proposed by Loganathan (1998) and Lee et al. (1992) deduces the calculation formula of the soil settlement $w_{igstz}$ and horizontal deformation $w_{igstx}$ caused by the clearance of the shield tail.

$$w_{igstz} = R^2 \left\{ -\frac{z - H}{x^2 + (z - H)^2} + (3 - 4\nu)\frac{z + H}{x^2 + (z + H)^2} \right.$$
$$\left. - \frac{2z\left[x^2 - (z + H)^2\right]}{\left[x^2 + (z + H)^2\right]^2} \right\} \frac{4Rg + g^2}{4R^2}$$
$$\exp \left\{ -\left[\frac{1.38x^2}{(H + R)^2} + \frac{0.69z^2}{H^2}\right] \right\} \tag{24}$$

$$w_{igstx} = -R^2 x \left[ \frac{1}{x^2 + (H - z)^2} + \frac{3 - 4\nu}{x^2 + (H + z)^2} \right.$$
$$\left. - \frac{4z(z + H)}{\left(x^2 + (H + z)^2\right)^2} \right] \cdot \frac{4gR + g^2}{4R^2}$$
$$\exp \left\{ -\left[\frac{1.38x^2}{(H + R)^2} + \frac{0.69z^2}{H^2}\right] \right\} \tag{25}$$

Where: ($x$, $y$, z) is the calculated point coordinate; ($x_0$, $y_0$, $H$) is the coordinate of the centre point of the cutter head; $g$ is the ground loss parameter, (m).

### Over-cutting gap

Festa et al. (2012) proposed the calculation formula of the over-cutting gap amount δ:

$$\delta = \frac{\sqrt{(2R_0 + 2R)^2 + L^2} - (2R_0 + 2R)}{2} \tag{26}$$

Sagaseta (1987) deduced that the settlement change amount of the calculated point is the settlement used by the shear stress and the settlement caused by the volume change. The formation deformation caused by shear stress can be ignored, and only the formation deformation caused by the volume change needs to

be considered. The calculation formulas of vertical deformation $w_{zog}$ and horizontal deformation $w_{xog}$ are:

$$w_{zog} = -\frac{1}{4\pi}\left(\frac{z - z_0}{r_1^3} - \frac{z + z_0}{r_2^3}\right) \tag{27}$$

$$w_{xog} = -\frac{1}{4\pi}\left(\frac{x - x_0}{r_1^3} - \frac{x - x_0}{r_2^3}\right) \tag{28}$$

Where: ($x_1$, $y_1$, $z_1$) are the void point coordinates; $r_1 = [(x-x_0)^2+(y-y_0)^2+(z-z_0)^2]^{1/2}$; $r_2 = [(x-x_0)^2+(y-y_0)^2+(z+z_0)^2]^{1/2}$.

The ground loss caused by OG is mainly located in the inner side of the curve section, and this part of the ground loss always exists before the cutter head passes, so the distribution range of the ground loss caused by OG is from the cutter head to the shield tail. The coordinates of the void point can be expressed as:

$$\begin{cases} x_0 = x - s \\ y_0 = r\cos\theta \\ z_0 = H - r\sin\theta \end{cases} \tag{29}$$

According to Eqs 27, 28, integrating the over-excavation area, the calculation formula of the formation deformation caused by the OG can be obtained as follows:

$$W_{zog} = \int_{-\pi/2}^{\pi/2} \int_R^{R+\delta} \int_0^L w_{zog} d\theta dr ds \tag{30}$$

$$W_{xog} = \int_{-\pi/2}^{\pi/2} \int_R^{R+\delta} \int_0^L w_{xog} d\theta dr ds \tag{31}$$

To sum up, the calculation formula of formation deformation caused by shield tunnelling along the curve section is:

$$W(x) = W_{qx} + W_{fx} + W_{px} + W_{igstx} + W_{xog} \tag{32}$$

$$W(y) = W_{qy} + W_{fy} + W_{py} + W_{igsty} + W_{yog} \tag{33}$$

$$W(z) = W_{qz} + W_{fz} + W_{pz} + W_{igstz} + W_{zog} \tag{34}$$

## Calculation of pile foundation deformation

Commonly used elastic foundation beam models include Winkler's foundation model, Pasternak's foundation model and Vlasov's foundation model (Zheng et al., 2021). The two-parameter Pasternak's foundation model considers the shearing effect of soil based on Winkler's foundation model foundation beam and contains only two parameters. Therefore, it is often used to calculate the deformation of underground structures.

The governing differential equations of Pasternak's foundation model can be expressed as:

$$EI\frac{\partial^4 w(i)}{\partial y^4} - G_c\frac{\partial^2 w(i)}{\partial y^2} + Kw(i) = KDw(i) \tag{35}$$

where $w(i)$ is the deformation of the pile; $K$ is the foundation reaction modulus; $G_c$ is the stiffness of the shear layer; $i$ represents three coordinate directions. The values of $K$ and $G_c$ are shown in Eqs 36, 37.

$$K = 0.65(\frac{E_s D^4}{EI})^{\frac{1}{12}} \frac{E_s}{D(1 - \mu^2)} \quad (36)$$

$$G_c = \frac{E_s t}{6(1 + \mu)} \quad (37)$$

where $Es$ is the elastic modulus of soil; $D$ is the diameter of the pile; $EI$ is the bending stiffness of the pile; $t$ is the thickness of a shear layer, $t$ is typically considered to be 2.5 times equal to the pile diameter.

## Pile-soil coupling equation

Equation 34 is a high-order differential equation. It is difficult to obtain accurate results by conventional calculation methods and the calculation is challenging (Liang et al., 2018; Zhang et al., 2018; Ma et al., 2020). The finite difference method is one of the essential means of solving the high-order differential equation. The pile body is discretised into 2N+5 units and each unit have a length of $t$, including 2N+1 units within the calculation range and two virtual units on both sides of the calculation range. The pile foundation after discretisation is shown in **Figure 3**.

According to the central difference rule, higher-order differential equations can be converted to regular equations by the following equation.

$$\begin{cases} \frac{\partial^4 w_N(i)}{\partial y^4} = \frac{6w_N(i) - 4(w_{N+1}(i) + w_{N-1}(i)) + (w_{N+2}(i) + w_{N-2}(i))}{t^4} \\ \frac{\partial^2 w_N(i)}{\partial y^2} = \frac{w_{N+1}(i) - 2w_N(i) + w_{N-1}(i)}{t^2} \end{cases} \quad (38)$$

Equation 35 is then converted to:

$$w_{n-2}(i) - \left(4 + \frac{G_c D t^2}{EI}\right) w_{n-1}(i) + \left(6 + 2\frac{G_c D t^2}{EI} + \frac{KG_c t^4}{EI}\right)$$

$$w_n(i) - \left(4 + \frac{G_c D t^2}{EI}\right) w_{n+1}(i) + w_{n+2}(i) = \frac{KD t^4}{EI} W(i) \quad (39)$$

Assuming that the top of the pile foundation and the bottom of the pile end are both free ends, then the bending moment and shear force at both ends of the pile foundation are 0, and the nodes outside the calculation range satisfy:

$$\begin{cases} w_{-1} = 4w_0 - 4w_1 + w_2 \\ w_{-2} = 2w_{-1} - w_0 \\ w_{2N+1} = 2w_{2N} - w_{2N-1} \\ w_{2N+2} = 4w_{2N} - 4w_{2N-1} + w_{2N-2} \end{cases} \quad (40)$$

Convert the corresponding system of equations to a matrix-vector:

$$[q(i)]_{(2N+1)(2N+1)} = \{[k]_{(2N+1)(2N+1)} - [G]_{(2N+1)(2N+1)}$$

$$+ [K]_{(2N+1)(2N+1)}) [w_G(z)]_{(2N+1)(2N+1)} \quad (41)$$



**FIGURE 3**
Pile foundation discrete diagram.
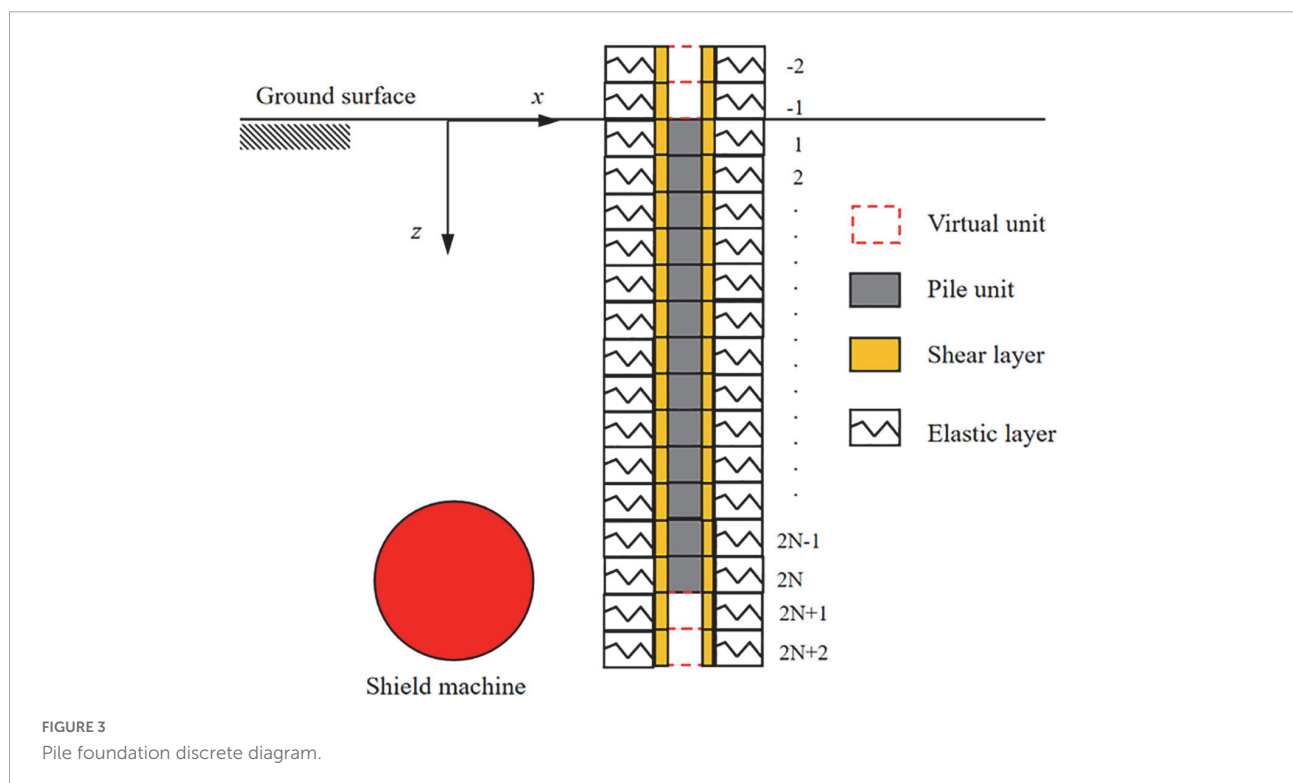
Where: $[q(z)]_{2N+1}$ is the additional load matrix; $[k]_{2N+1}$ is the soil subgrade coefficient matrix; $[G]_{2N+1}$ is the shear layer stiffness matrix; $[K]_{2N+1}$ is the stiffness matrix of the pile body; $[w_G(z)]_{2N+1}$ is the deformation matrix of the pile body.

## Deformation formula

According to the above analysis, it is only necessary to determine the stiffness matrix in Eq. 41 and the deformation matrix of the calculation point in the tunnelling process of the shield machine. Then the deformation of the pile can be calculated.

For the deformation stiffness matrices in the $x$ and $y$ directions of the pile foundation:

$$[w(x)] = [K_x]^{-1} [k_x] [W(x)] \tag{42}$$

$$[K_x] = \begin{Bmatrix} k_{x,-2} & & & & \\ & k_{x,1} & & & \\ & & \ddots & & \\ & & & k_{x,2N+1} & \\ & & & & k_{x,2N+2} \end{Bmatrix}_{(2N+1)(2N+1)} \tag{43}$$

$[k_x]$

$$= \begin{Bmatrix} 2\alpha+\beta+4 & -4 & 2 & & & & \\ \alpha+2 & \beta-1 & \alpha & 1 & & & \\ 1 & \alpha & \beta & \alpha & 1 & & \\ & \ddots & \ddots & \ddots & \ddots & \ddots & \\ & & 1 & \alpha & \beta & \alpha & 1 \\ & & & 1 & \alpha & \beta-1 & \alpha+2 \\ & & & & 2 & -4 & 2\alpha+\beta+4 \end{Bmatrix}_{(2N+1)(2N+1)} \tag{44}$$

where $k_{x,i} = KDt^4/EI$, $(-2 \le i \le 2N+2)$, $\alpha = -(4+G_cDt^2/EI)$, $\beta = 6+2G_cDt^2/EI+KDt^4/EI$.

For the stiffness matrix in the $z$ direction:

$$[K_x] = \begin{Bmatrix} k_{z,-2} & & & & \\ & k_{z,1} & & & \\ & & \ddots & & \\ & & & k_{z,2N+1} & \\ & & & & k_{z,2N+2} \end{Bmatrix}_{(2N+1)(2N+1)} \tag{45}$$

$$[K_z] = \begin{Bmatrix} A+2 & & & & & \\ 1 & A & 1 & & & \\ & 1 & A & 1 & & \\ & & \ddots & \ddots & \ddots & \\ & & & 1 & A & 1 \\ & & & & & A+2 \end{Bmatrix}_{(2N+1)(2N+1)} \tag{46}$$

where $k_{z,i} = -Kt^2/G_c$, $(-2 \le i \le 2N+2)$, $A = -(2+Kt^2/G_c)$.

# Numerical calculation model

Based on constitutive models and failure mechanism of geotechnical materials (Chen et al., 2022; Gao et al., 2022), the numerical method has developed rapidly. It is an attractive tool been widely used in civil engineering. In this paper, finite difference software is used. Based on the solid engineering background, a FDM is constructed to verify the correctness of the theoretical calculation formula.

## Research background

The subway project of Line 5 in Changsha City, Hunan Province, China, adopts the shield tunnelling method. The left and right lines of the section are two single-track tunnels. In a specific section of the line, the plane curve radius of the left line is 350 m, and the plane curve radius of the right line is 1800 m. The radius of the tunnel is 6.2 m, and the length of the shield shell is 6.5 m. The tunnel is assembled with C30 segments, and the width of the single ring segment is 1.5 m. The distribution of surrounding buildings is complicated. A high-rise hotel (25 floors, pile foundation, depth 15 m, pile diameter 2.0 m) is only 6 m away from the left subway section. According to the on-site exploration results, the mechanical parameters are shown in **Table 1**.

## Model introduction

The shield machine has the most significant risk of disturbance to the high-rise hotel during the tunnelling process of the curve section. At the same time, the distance between the left line and the pile foundation is the closest, and the distance between the right line and the pile foundation exceeds six times the hole diameter. Therefore, only the left line alone is considered in the model. In order to eliminate the influence of boundary conditions (Nematollahi and Dias, 2019), the size of the model is taken as $100 \times 100 \times 33$ m, and the overall numerical calculation model constructed is shown in **Figure 4A**. The influence of the distance from the pile group to the tunnel on the pile foundation settlement, the positional relationship between the tunnel and the pile group, and the distribution of the pile group can be analysed as shown in **Figure 4B**.

For the shield tunnels, the structures that need to be simulated include solidified slurry, unsolidified slurry, segment, cutter head, shield shell, IGST, and OG. Since the shield machine is in the process of tunnelling in the curved section, the cutter head and shield shell on the inner and outer sides of the curve section need to exert different forces, so it is necessary to divide the cutter head and the shield shell into two parts. The constructed shield tunnel model is shown in **Figure 5**.

TABLE 1 Mechanical parameters of soil layer.

| | The soil materials | $\gamma$ (kN/m³) | $\varphi$ (kPa) | $c$ (°) | $E_s$ (MPa) | $\mu$ |
|---|---|---|---|---|---|---|
| < 1–1 > | Miscellaneous fill | 17.8 | 7 | 12 | 3 | 0.33 |
| < 4–1 > | Silty clay | 18.2 | 32 | 12 | 7 | 0.32 |
| < 4–4 > | Sand | 18.0 | 5 | 27 | 20 | 0.28 |
| < 4–6 > | Sand cobble | 18.7 | 5 | 40 | 38 | 0.25 |
| < 7–1 > | Mudstone | 19.2 | 45 | 20 | 79 | 0.23 |



FIGURE 4
Model diagram. **(A)** Overall model and **(B)** spatial location of tunnel and pile group.



FIGURE 5
Shield tunnel model.
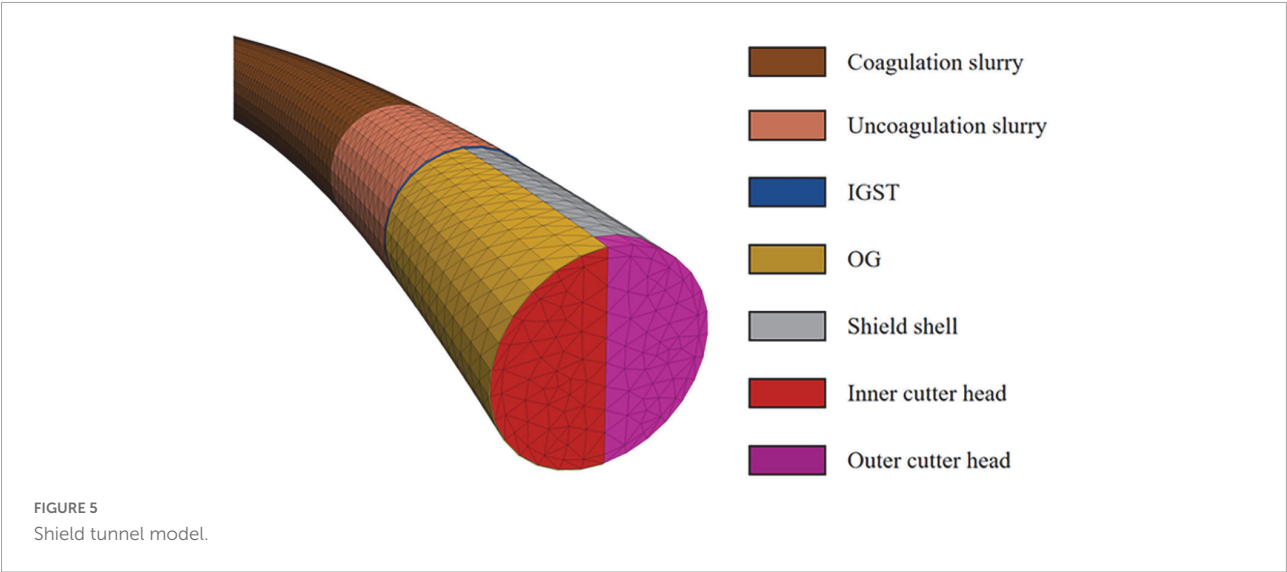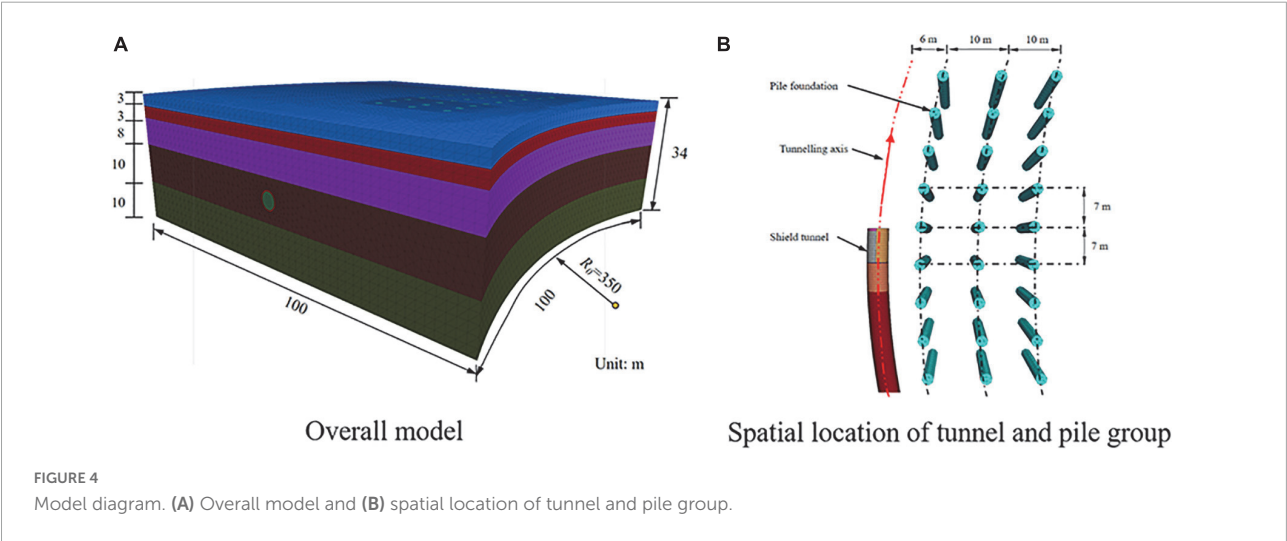
## Material parameters

The soil is selected as an elastic-plastic solid element, and the Mohr–Coulomb constitutive is adopted. The material parameters of each soil layer are shown in Table 1. Segments, shield shells, cutter heads, grouting slurry, and piles are simulated by elastic solid elements. The strength of the unsolidified slurry is about 1/10 of the strength of the solidified slurry (Oggeri et al., 2021). The material parameters are shown in Table 2.

## Acting loads

To simulate the tunnelling process of the shield machine, the force of the shield machine during the tunnelling needs to

TABLE 2  Simulation unit parameters.

| Material | $\gamma$ (kN/m$^3$) | $E$(GPa) | $\mu$ |
|---|---|---|---|
| Segment (C30) | 25 | 30 | 0.3 |
| Shield shell | 27 | 200 | 0.2 |
| Cutter head | 27 | 200 | 0.2 |
| Pile | 25 | 30 | 0.3 |
| Unsolidified area of the slurry | 23 | 0.04 | 0.3 |
| Solidification area of the slurry | 23 | 0.4 | 0.3 |

be considered in the numerical calculation model. The research points out that the front thrust of the shield machine, the shield shell friction and the grouting pressure are the main forces in the excavation process of the shield machine. The frontal thrust is about 1.2 times the static earth pressure of the excavation surface. During the excavation in the curve section, the frontal thrust exerted by the inner cutter head is smaller than that of the outer cutter head. According to the test excavation data, the ratio of the two is about 1.5 when the inner over-excavation measures are taken, and the ratio of the two is about 2.5 when the over-excavation measures are not taken. The shield shell friction is about 0.1 times that of the static earth pressure. Although the over-cutting of the inner soil is taken, it is still unavoidable that the inner shield will be squeezed by the soil more than the outer shield. The friction resistance ratio can be taken as 1.5–2.5. When no over-cutting measures are taken, the inner shield shell will be more severely squeezed by the soil, and the asymmetric distribution of the friction resistance distribution of the shield shell will be higher. According to the construction experience, no over-excavation is adopted. When taking measures, the friction ratio of the inner and outer shield

shells is 3–5. According to the distribution of soil layers and the design scheme of the project, it is calculated that the frontal thrust exerted by the inner cutter head is 194 kPa, the frontal thrust exerted by the outer cutter head is 292 kPa, and the friction exerted on the inner shield shell is 37.5 kPa. The friction applied to the outer shield shell is 16.1 kPa, the additional grouting pressure is 200 kPa, and the action range of additional grouting pressure is the unsolidified slurry area.

The upper surface of the model is set as a free boundary condition, the bottom and sides are subjected to normal constraints, and the influence of groundwater seepage on the results is not considered in the calculation process. The calculation process is divided into three steps. First, the in-situ stress is balanced, then the displacement after the initial in-situ stress balance is zeroed, and the initial in-situ stress on-site is retained. Then, the elastic material is given to the pile, and a vertical uniform load of 1200 kPa is applied to the top of the pile. Simulate the force of the superstructure, and submit the calculation to obtain the stress on-site after the pile action. Finally, the displacement on-site after the pile action is reset to zero, and the properties of the shield machine and tunnel reserved element are changed to complete the tunnelling simulation of the shield machine.

## Discussion

### Surface subsidence

Figure 6 is the cloud map of surface subsidence. The surface in front of the cutter head is slightly uplifted, while the surface subsides near and behind the cutter head. From the cloud
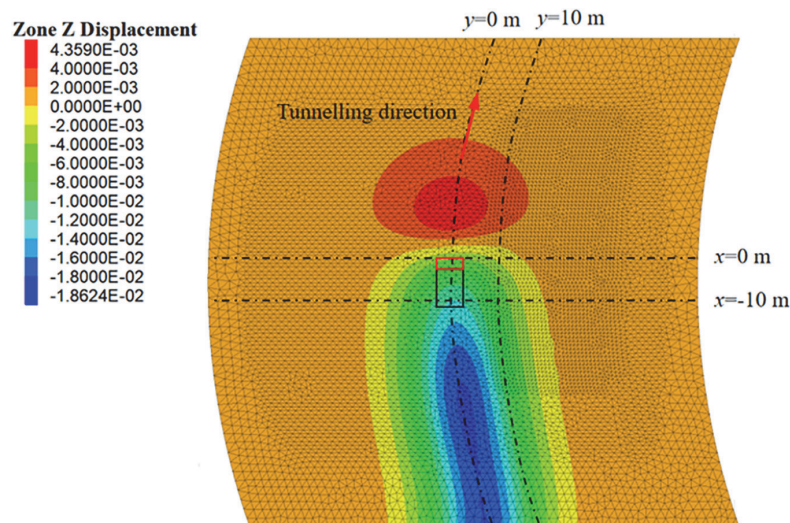


FIGURE 6
Surface subsidence cloud map.

map, the maximum surface subsidence is 18.6 mm, which meets the construction control standard (maximum surface subsidence < 30 mm). To compare the FDM calculation results, analytical results and on-site monitoring values, the lateral surface subsidence ($x = 0$ m, $x = -10$ m) and the surface longitudinal subsidence curve ($y = 0$ m, $y = 10$ m) were extracted. The comparison of surface subsidence values is shown in **Figure 7**.

As you can see from **Figure 7**:

(1) The distribution of lateral subsidence of the surface is a "V"-shaped distribution, but the surface subsidence is not symmetrically distributed. The maximum lateral subsidence point of the surface is not located on the central axis. Still, it appears inside the curve section, which is different from the law of surface subsidence of the straight section. The additional frontal thrust, the shield shell friction and the asymmetric distribution of the over-cutting gap may be the reasons for the asymmetric distribution of the surface subsidence;

(2) The lateral subsidence of the surface at $x = -10$ m is significantly more significant than that at $x = 0$ m, because the closer the monitoring section is to the IGST, the greater the subsidence value;

(3) The longitudinal subsidence distribution of the ground surface is an "S"-shaped distribution, and the numerical results are consistent with those shown in the cloud map. A slight uplift occurs on the surface in front of the cutter head, while subsidence occurs at the cutter head and behind the cutter head. The position of the maximum surface subsidence appears behind the shield tail;

(4) The longitudinal subsidence of the ground surface with $y = 0$ m is significantly larger than that with $y = -10$ m,

and the closer to the tunnelling axis, the greater the longitudinal subsidence of the ground surface;

(5) From the comparison of lateral settlement and longitudinal settlement, it can be seen that the error of the maximum surface settlement value calculated by the three methods of analytical analysis results from the on-site monitoring data and numerical simulation data is small, which verifies the correctness of the analytical analysis formula and numerical calculation model. However, FDM and on-site monitoring data show that the surface subsidence remains unchanged behind the shield tail. This is because the soil is regarded as an elastic space in the analytical calculation, and the plastic deformation caused by excavation is ignored. In contrast, the plastic deformation of the soil usually causes stable surface subsidence after excavation disturbance.

**Figure 8** shows the surface subsidence curves caused by various factors considered in this study; it can be seen that:

(1) **Figure 8A** shows that the additional frontal thrust, shield friction, IGST, and OG will cause surface subsidence, and the contribution of the frontal thrust to the surface subsidence can be ignored. Shield Shell friction, IGST, and OG are the main factors leading to the surface subsidence, the surface deformation caused by the additional frontal thrust can be ignored, and the reasonable additional grouting pressure can control the surface subsidence. Therefore, when the shield machine tunnelling along the curve section, the shield friction, and OG are the main factors that cause the surface subsidence to be asymmetric. The additional grouting pressure will cause the surface



FIGURE 7
Surface subsidence curve. **(A)** Lateral surface subsidence curve and **(B)** surface vertical subsidence curve.
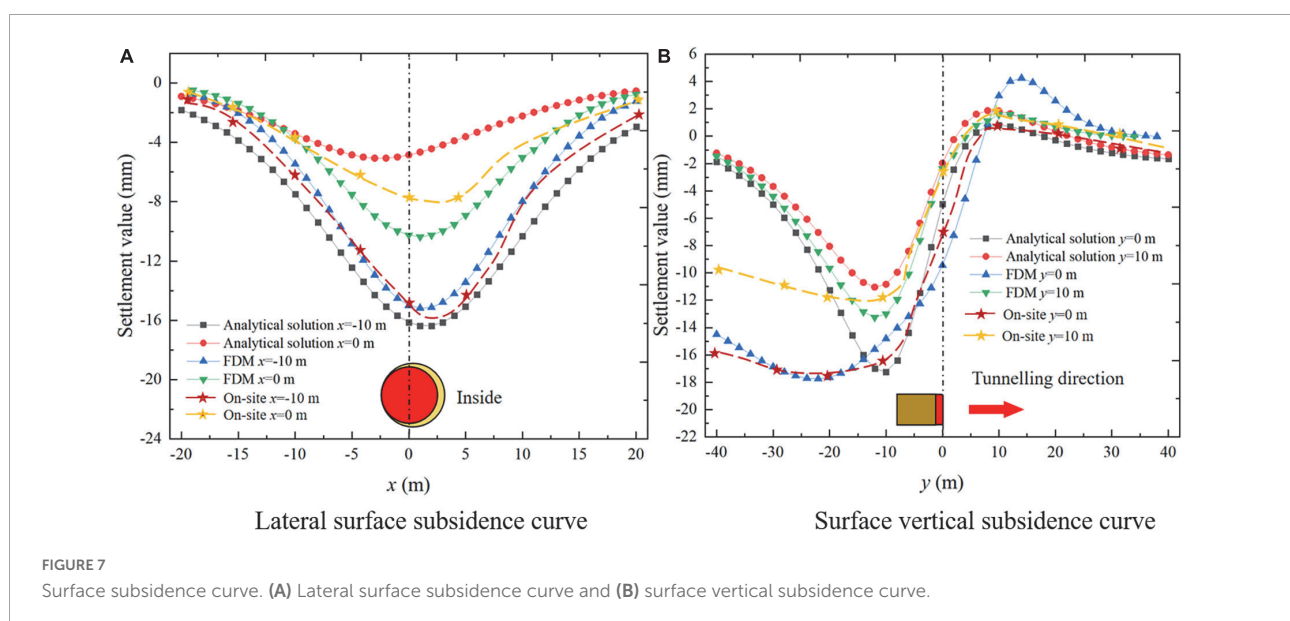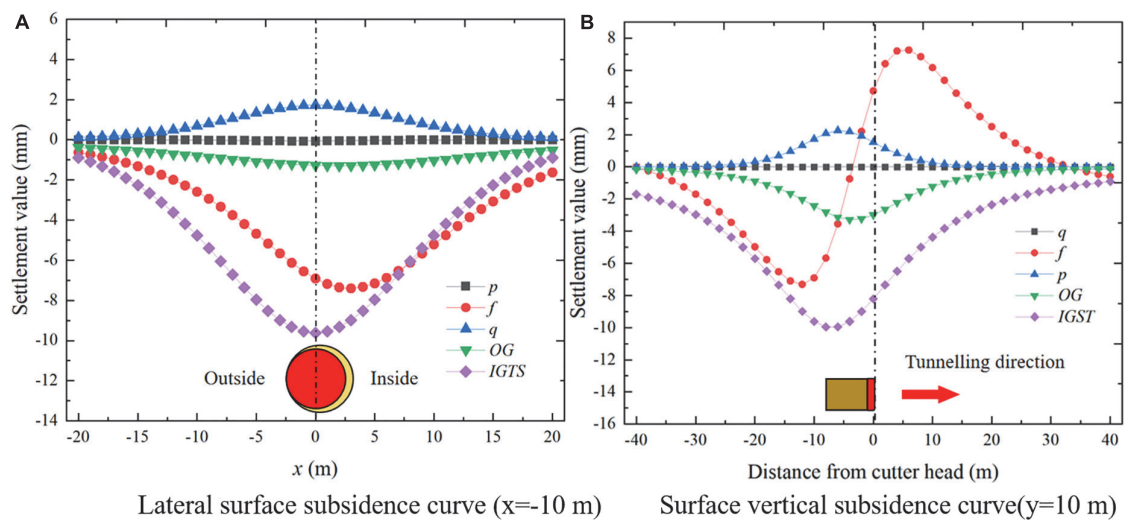
**FIGURE 8**
Surface settlement curve caused by construction factors. **(A)** Lateral surface subsidence curve ($x = -10$ m) and **(B)** surface vertical subsidence curve ($y = 10$ m).

uplift, so the surface settlement can be controlled by applying a moderate additional grouting pressure.

(2) **Figure 8B** shows that in front of the middle of the shield shell, the shield shell friction will cause the surface to uplift, and behind the middle of the shield shell, the shield shell friction will cause the surface to subside. The additional grouting pressure will cause the surface to bulge, and the maximum bulge is located behind the shield tail. Both OG and IGST cause surface subsidence and the maximum subsidence positions are located at the midpoint of the shield shell and the shield tail, respectively.

## Analysis of pile foundation deformation

### Analysis of pile foundation settlement

**Figure 9** shows the settlement cloud diagram of the pile. It can be seen that the settlement law of the pile foundation is the same as that of the surface settlement. The pile foundation in front of the cutter head will bulge slightly, while the pile foundation behind the cutter head will settle. It can be seen from the pile foundation settlement cloud diagram that the pile foundation settlement reaches the maximum value at the position of $x = -28$ m, the maximum settlement value is 9.2 mm, and the maximum differential settlement rate is 0.045%. The above indicators are lower than the construction control standard (maximum settlement value < 20 mm, maximum differential sedimentation rate < 0.45%). Surface deformation and adjacent pile foundation deformation meet the construction control requirements. To compare the results of the three methods, the pile foundation settlement curve behind the cutter

head ($x = 0$ m, $x = -7$ m, $x = -14$ m) was extracted, as shown in **Figure 10**.

It can be seen that the error between the on-site monitoring value and the FDM calculation results and the analytical analysis results is small, which verifies the correctness of the model and the analytical analysis results. The analytical analysis results are consistent with the pile foundation settlement law obtained by the FDM numerical calculation results. The settlement decreases along the depth direction and reaches the maximum at the top of the pile, which is also proved by the study of Loganathan et al. (2001).



**FIGURE 9**
Pile foundation settlement cloud map.
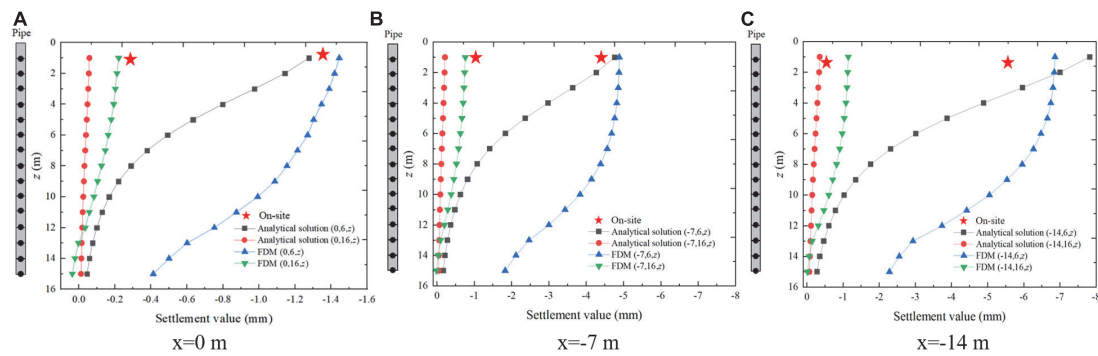
FIGURE 10
Pile foundation settlement curve. **(A)** x = 0 m, **(B)** x =−7 m, and **(C)** x =−14 m.
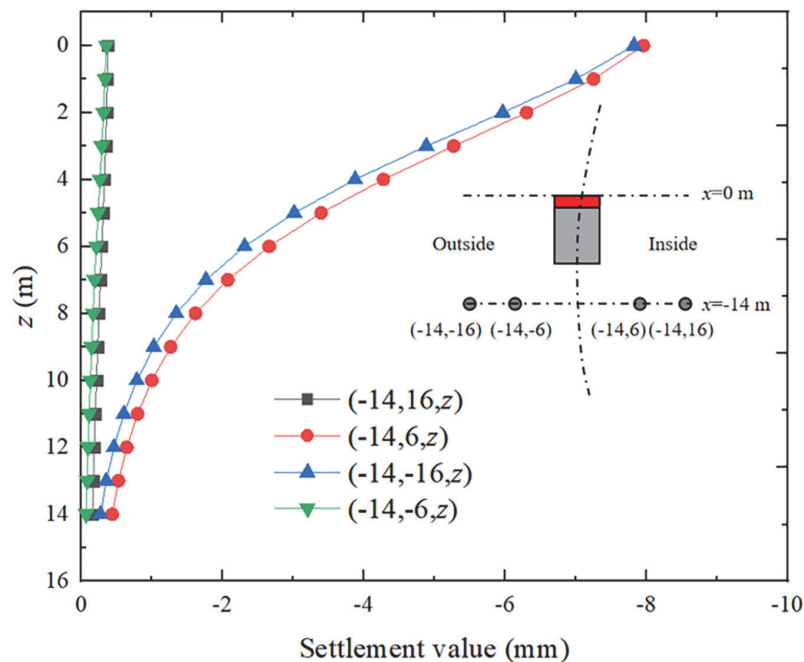


FIGURE 11
Comparison of settlement curves of pile foundations on both sides of inner and outer sides.

For the pile foundation with the same ordinate, the settlement value of the pile foundation closer to the tunnel excavation axis is larger. The settlement of the pile foundation behind the shield tail is larger than the pile foundation with the same abscissa. Since the numerical calculation model and the actual construction situation on the site did not include the pile foundation on the outside of the curve, the settlement of the pile foundation on the inside and outside of the curve section at x =−14 m was calculated through the analytical solution, as shown in **Figure 11**.

It can be seen that the settlement of the pile foundation located on the inside of the curve section is larger than the curve section, which is similar to the law of surface settlement.

The maximum settlement of the pile foundation inside the curve section is 1.8% higher than outside. Due to the pile-soil coupling effect and the stiffness of the pile itself, the asymmetric settlement of the pile foundation on the inner and outer sides caused by the excavation of the curved section can be ignored.

## Analysis of horizontal deformation of pile foundation

Similarly, it can be seen that the horizontal deformation of the pile foundation reaches the maximum at the top of the pile. At the position of the cutter head and in front of the cutter head, the horizontal deformation of the pile body is a positive deformation along the x-axis. After the shield machine
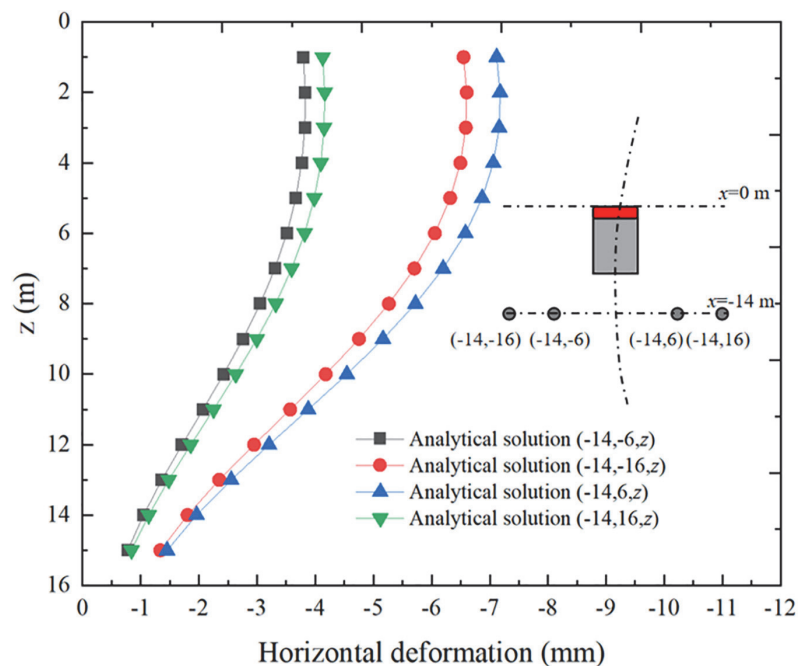
**FIGURE 12**
Horizontal deformation curve of pile foundation.

passes through, the horizontal deformation of the pile is the negative deformation along the *x*-axis. **Figure 12** shows the curve of the horizontal deformation of the pile foundation on the inside and outside of the curved section. It can be seen that it is consistent with the settlement law. The horizontal deformation of the pile foundation on the inside of the curved section is significantly larger than that on the outside of the curved section. The maximum horizontal deformation of the pile foundation on the inside and outside of the curved section The deformations are 7.1 and 6.5 mm, respectively, and the horizontal deformation of the piles located on the inner side of the curve segment is 9.2% larger than that on the outer side. The horizontal deformation of the pile foundation is more sensitive to the asymmetric distribution of the tunnelling factors.

## Conclusion

In this study, considering the tunnelling of the shield machine along the curve section, the analytical calculation formulas of adjacent pile foundation deformation and surface settlement caused by the additional thrust, the shield shell friction, the additional grouting pressure and the ground subsidence were deduced. The analytical prediction results are verified by an FDM and on-site monitoring data. The results show that:

(1) The errors among the on-site monitoring data, the FDM calculation results and the analytical calculation results are small, which verifies the correctness of the FDM and analytical calculation formula. The maximum settlement value of the ground surface is 18.2 mm, and the adjacent pile foundation's maximum settlement value and horizontal deformation value are 9.2 and 9.4 mm, respectively. All of them meet the construction control requirements;

(2) The shield shell friction, IGST, and OG are the main factors leading to the surface subsidence, the surface deformation caused by the additional frontal thrust can be ignored, and the reasonable additional grouting pressure can control the surface subsidence;

(3) The surface settlement inside the curve section is larger than the outside of the curve section, and the surface settlement grooves are asymmetrically distributed. The pile foundation settlement and deformation inside the curve section are larger than those outside of the curve section. The asymmetrically distributed shield friction and OG are the main reasons that caused the settlement of the inside curve section to be larger than the outer side of the curve section;

(4) The deformation of the pile foundation located on the inner side of the curve segment is larger than that of the pile foundation outside the curve segment. The maximum difference is 9.2%, and the horizontal deformation of the pile foundation is more sensitive to the asymmetric distribution of shield tunnelling factors;

(5) The analytical formula derived from this paper can predict the disturbance risk of the shield machine to the surrounding environment during the tunnelling process

to determine whether corresponding control measures need to be taken.

## Data availability statement

The original contributions presented in the study are included in the article/supplementary material, further inquiries can be directed to the corresponding author.

## Author contributions

FZ and YG were responsible for the writing. QH and ZH were responsible for the numerical simulation and data analyzing. FC was responsible for review and proofreading. All authors contributed to the article and approved the submitted version.

## Funding

## Conflict of interest

The authors declare that the research was conducted in the absence of any commercial or financial relationships that could be construed as a potential conflict of interest.

## Publisher's note

All claims expressed in this article are solely those of the authors and do not necessarily represent those of their affiliated organizations, or those of the publisher, the editors and the reviewers. Any product that may be evaluated in this article, or claim that may be made by its manufacturer, is not guaranteed or endorsed by the publisher.

## References

Basile, F. (2014). Effects of tunnelling on pile foundations. *Soils Found.* 54, 280–295.

Chen, W. C., Song, Z. P., Tian, W., and Wang, Z.-F. (2018). Shield tunnel uplift and deformation characterisation: A case study from Zhengzhou metro. *Tunn. Undergr. Space Technol.* 79, 83–95. doi: 10.1016/j.tust.2018.05.002

Chen, Z. Q., Ma, C. C., Li, T. B., and He, C. (2022). Experimental investigation of the failure mechanism of deep granite under high seepage water pressure and strong unloading effect. *Acta Geotech.* 193, 1–22. doi: 10.1007/s11440-022-01665-8

Deng, H., Fu, H., Shi, Y., Zhen, H., and Huang, Q. (2021). Analysis of asymmetrical deformation of surface and oblique pipeline caused by shield tunneling along curved section. *Symmetry* 13:2396. doi: 10.3390/sym13122396

Deng, H.-S., Fu, H.-L., Yue, S., Huang, Z., and Zhao, Y.-Y. (2022). Ground loss model for analyzing shield tunneling-induced surface settlement along curve sections. *Tunn. Undergr. Space Technol.* 119:104250. doi: 10.1016/j.tust.2021.104250

Festa, D., Broere, W., and Bosch, J. W. (2012). "Tunnel-boring in soft soil: A study on the driving forces applied to a slurry-shield TBM," in *Proceedings of the WTC 2012, tunneling and underground space for a global society*, 18–24 May 2012, Bangkok.

Franza, A., Marshalla, A. M., Haji, T., Abdelatif, A. O., Carbonari, S., and Morici, M. (2017). A simplified elastic analysis of tunnel-piled structure interaction. *Tunn. Undergr. Space Technol.* 61, 104–121. doi: 10.1016/j.tust.2016.09.008

Gao, M. B., Cui, S. H., Li, T., Ma, C., Wu, Z., and Zhang, Y. (2022). Investigation on the expression ability of a developed constitutive model for rocks based on statistical damage theory. *Lithosphere* 2022:9874408. doi: 10.2113/2022/9874408

He, C., Jiang, Y., Yong, F., Kun, F., and Jun, W. (2013). Impact of shield tunneling on adjacent pile foundation in sandy cobble strata. *Adv. Struct. Eng.* 16, 1457–1468. doi: 10.1260/1369-4332.16.8.1457

Hu, H., Zhu, Y., Zhang, G., and Tu, P. (2021). The environmental effects induced by a metro shield tunnel side-crossing on adjacent pile foundations and its impact partition. *Adv. Civ. Eng.* 2021:8216724. doi: 10.1155/2021/8216724

Huang, Z., Zhang, H., Fu, H., Ma, S., and Liu, Y. (2020). Deformation response induced by surcharge loading above shallow shield tunnels in soft soil. *KSCE J. Civ. Eng.* 24, 2533–2545. doi: 10.1007/s12205-020-0404-8

Jongpradist, P., Kaewsri, T., Sawatparnich, A., Suwansawat, S., Youwai, S., Kongkitkul, W., et al. (2013). Development of tunneling influence zones for adjacent pile foundations by numerical analyses. *Tunn. Undergr. Space Technol.* 34, 96–109.

Lee, C. J., and Jacobsz, S. W. (2006). The influence of tunnelling on adjacent piled foundations. *Tunn. Undergr. Space Technol.* 21:430. doi: 10.1016/j.tust.2005.12.072

Lee, K. M., Rowe, R. K., and Lo, K. Y. (1992). Subsidence owing to tunnelling. I. Estimating the gap parameter. *Can. Geotech. J.* 29, 929–940. doi: 10.1139/t92-104

Li, S.-H., and Li, P.-F. (2021). Analytical solutions to ground settlement induced by ground loss and construction loadings during curved shield tunneling. *J. Zhejiang Univ. Sci. A.* 22, 296–313. doi: 10.1631/jzus.A2000120

Li, X., Zhou, X., Hong, B., and Zhu, H. (2019). Experimental and analytical study on longitudinal bending behavior of shield tunnel subjected to longitudinal axial forces. *Tunn. Undergr. Space Technol.* 86, 128–137. doi: 10.1016/j.tust.2019.01.011

Liang, R., Wu, W., Yu, F., Jiang, G., and Liu, J. (2018). Simplified method for evaluating shield tunnel deformation due to adjacent excavation. *Tunn. Undergr. Space Technol.* 71, 94–105. doi: 10.1016/j.tust.2017.08.010

Lin, C., Huang, M., Nadim, F., and Liu, Z. (2020). Embankment responses to shield tunnelling considering soil-structure interaction: case studies in Hangzhou soft ground. *Tunn. Undergr. Space Technol.* 96:103230. doi: 10.1016/j.tust.2019.103230

Liu, B., Yu, Z., Han, Y., Wang, Z., Zhang, R., and Wang, S. (2020). Analytical solution for the response of an existing tunnel induced by above-crossing shield tunneling. *Comput. Geotech.* 124:103624. doi: 10.1016/j.compgeo.2020.103624

Loganathan, N. (1998). Analytical prediction for tunneling-induced ground movements in clays. *J. Geotech. Geoenviron. Eng.* 124, 846–856. doi: 10.1061/(ASCE)1090-02411998124:9(846)

Loganathan, N., Poulos, H. G., and Xu, K. J. (2001). Ground and pile-group responses due to tunnelling. *Soils Found.* 41, 57–67. doi: 10.3208/sandf.41.57

Ma, B. H., Hu, Z. Y., Li, Z., Cai, K., Zhao, M.-H., He, C.-B., et al. (2020). Finite difference method for the one-dimensional non-linear consolidation of soft ground under uniform load. *Front. Earth Sci.* 8:111. doi: 10.3389/feart.2020.00111

Miao, F., Wu, Y., Török, Á, Li, L., and Xue, Y. (2022). Centrifugal model test on a riverine landslide in the three gorges reservoir 1 induced by rainfall and water level fluctuation. *Geosci. Front.* 13:101378. doi: 10.1016/j.gsf.2022.101378

Miao, Y., He, H., Yang, Q., and Yang, S. (2020). Analytical solution considering the tangential effect for an infinite beam on a viscoelastic Pasternak foundation. *Appl. Math. Model.* 85, 231–243. doi: 10.1016/j.apm.2020.03.031

Min, Y., Sun, Q., Li, W. C., and Ma, K. (2011). Three-dimensional finite element analysis on effects of tunnel construction on nearby pile foundation. *J. Cent. South Univ. Technol.* 18, 909–916. doi: 10.1007/s11771-011-0780-9

Mindlin, R. D. (1936). Force at a point in the interior of a semi-infinite solid. *Physics* 7, 195–202. doi: 10.1063/1.1745385

Mroueh, H., and Shahrour, I. (2002). Three-dimensional finite element analysis of the interaction between tunneling and pile foundations. *Int. J. Numer. Anal. Methods Geomech.* 26, 217–230.

Nematollahi, M., and Dias, D. (2019). Three-dimensional numerical simulation of pile-twin tunnels interaction – case of the shiraz subway line. *Tunn. Undergr. Space Technol.* 86, 75–88. doi: 10.1016/j.tust.2018.12.002

Oggeri, C., Oreste, P., and Spagnoli, G. (2021). The influence of the two-component grout on the behaviour of a segmental lining in tunnelling. *Tunn. Undergr. Space Technol.* 103750:109. doi: 10.1016/j.tust.2020.103750

Sagaseta, C. (1987). Analysis of undraind soil deformation due to ground loss. *Geotechnique* 37, 301–320. doi: 10.1680/geot.1987.37.3.301

Soomro, M. A., Mangi, N., Mangnejo, D. A., and Noor Ahmed, M. (2021). 3D centrifuge and numerical modelling of lateral responses of a vertical loaded pile group to twin stacked tunnels. *Eur. J. Environ. Civ. Eng.* 26, 5517–5544. doi: 10.1080/19648189.2021.1907227

Xie, X., and Tang, G. (2017). Effects of curved shield tunnelling adjacent to existing tunnel. *Eur. J. Environ. Civ. Eng.* 22, s164–s178. doi: 10.1080/19648189.2017.1419882

Zhang, Y. H., Dai, Y. S., Ying, W., Huang, X., Xiao, Y., and Pei, Q. M. (2021). Hydrochemistry, quality and potential health risk appraisal of nitrate enriched groundwater in the Nanchong area, southwestern China. *Sci. Total Environ.* 784:147186. doi: 10.1016/j.scitotenv.2021.147186

Zhang, Z., Huang, M., Xu, C., Jiang, Y., Wang, W. (2018). Simplified solution for tunnel-soil-pile interaction in Pasternak's foundation model. *Tunn. Undergr. Space Technol.* 78, 146–158. doi: 10.1016/j.tust.2018.04.025

Zheng, J., He, S., Li, Y., He, J., and He, J. (2021). Longitudinal deformation of deep shield tunnels caused by upper load reduction. *Materials* 14:3629. doi: 10.3390/ma14133629

# Application of the high-density resistivity method in detecting a mined-out area of a quarry in Xiangtan City, Hunan Province

Xie Jia[1], Liu Yang[1]*, Lu Yulong[1] and Zhang Lianzhi[2]

[1]School of Earth Sciences and Spatial Information Engineering, Hunan University of Science and Technology, Xiangtan, Hunan, China, [2]Second Team of Hunan Nonferrous Metals Geological Exploration Bureau, Xiangtan, Hunan, China

Goaf ground collapse has great constraints on people's lives, property safety, and social development within the influence scope because of its concealment and suddenly happening characteristics. The high-density resistivity method is used to explore the goaf of a quarry in Xiangtan City, Hunan Province. The surface subsidence of the goaf is analyzed using the apparent resistivity inversion section diagram and the comprehensive analysis results. The filling water or sediment in the goaf is reflected as a low-resistivity abnormal body, with a resistivity change that is significantly different from the resistivity change of the surrounding bedrock and the contour fluctuation. The morphological characteristics and geological conditions of the underground abnormal body in the goaf are deduced. Based on the geophysical prospecting method, geological disasters such as goaf ground collapse can be explored. From the combined analysis and processing of inversion data, the geological structure and stratum information of goaf can be inferred, which provides a theoretical basis for further disaster prevention.

## Introduction

Karst ground collapse is the collapse of bedrock and overlying soils and the formation of collapse pits in the ground in areas where carbonate rocks are found, due to sufficient natural hydrological interaction and human factors (Wang and He, 2006). One of the main causes of geological hazards is the formation of subsurface cavities—underground cavities formed by human-induced destruction of ore layers on the bedrock surface (Shen et al., 2001; Zhang et al., 2015; Gong and Li, 2018). With the development of economic construction, China has become a major source of geological disasters; most of the damages caused by mining and karst collapse in China have become increasingly serious, with over 778 karst collapses and more than 30,000 collapse pits in 23 provinces, mainly in Hunan, Yunnan, Guizhou, Jiangxi, and Sichuan (Xie et al., 2021). Karst collapse is characterized by suddenness in time and

concealment in space and is usually accompanied by secondary disasters such as foundation instability and building tilting and fracturing, causing significant economic losses and seriously endangering people's lives and property. Hence, preventing and reducing the occurrence of karst collapse disasters, and therefore the occurrence of mining collapse disasters, have become a matter of close concern (Luo and Cheng, 2016; Li et al., 2017; Yan et al., 2021). The study area is located on the southwest border of Xiangtan City, which is a typical area with frequent occurrence of karst and ground collapse disasters. The mining area is rich in mineral resources such as mineral water, limestone, and gypsum, and has three basic conditions: soluble carbonate rocks, mainly chert; water with dissolution capacity; and good water circulation (Li et al., 2014; Jia et al., 2021). The ground collapse disaster site is located in the eastern part of the quarry. Due to the large scale and high frequency of mining activities prior to the collapse, there is a certain range of underground quarry area. Ground collapse disaster causes a certain degree of damage to the local ecological environment, and its potential danger has a serious impact on the safety of people's property and economic development in the area. Therefore, it is crucial to investigate the underground space situation and analyze the potential hazards (Zeng and Zheng, 2007; Lei et al., 2009). At present, geophysical exploration is the main method to detect the geological situation of the underground mining area and karst ground collapse. Seismic exploration is based on seismic wave exploration of the stratigraphic structure, using refraction and reflection wave characteristics to determine the existence of collapse, while the geological radar method uses electromagnetic wave propagation in the stratigraphic medium. If there is an unknown geological body or anomaly, the electromagnetic wave will produce reflection and refraction, and the phase, amplitude, and frequency will change. These methods have the advantages of high efficiency, low cost, use of lighter instruments and tools, and more accurate interpretation of results (Zheng et al., 2017; Huang et al., 2019). Compared with other physical exploration methods such as the traditional resistivity method, the high-density resistivity method is used to identify geological formations and subsurface anomalies by comparing the differences in resistivity between rocks and soils through observation and analysis. The method has the advantages of fast data collection, high efficiency, rich information, and convenient interpretation, all of which can significantly improve the exploration capability (Wang et al., 2011; Jin and Liu, 2014; Li et al., 2019). In this study, the high-density resistivity method is used to conduct a rapid and effective hazard analysis of a mining area in the lower part of a township in Xiangtan City, Hunan Province, to detect and invert the geology of its subsurface space and provide a theoretical basis for further comprehensive disaster prevention and control.

# Overview of the goaf

## Geology

The mining area is located in a town in Xiangtan City, Hunan Province, which is mainly a hilly mountainous landscape and belongs to the Xianggan hilly area in South China, with concentrated rainfall; small differences in the spatial distribution of light, temperature, and water; more disastrous weather; and obvious continental climatic characteristics. According to the site investigation and regional information, the stratigraphy of the disaster area is divided from top to bottom into the Quaternary Holocene strata, Cretaceous red strata, and Middle Devonian Qiziqiao Group limestone, among which the Cretaceous and Devonian strata are in unconformity and have the basic conditions for karst collapse. The geological structure can be divided into a fault-fold structural zone, a basin structural zone, and a neotectonic movement zone.

## Geological hazards

The ground collapse disaster site directly threatens the safety of four surrounding houses and affects the surrounding environment such as ponds and roads. The resulting collapse pit is water-filled and the inside of the pit has an irregular round shape, approximately 35 m in diameter and 20.5 m in depth. The ground collapse disaster is accompanied by secondary hazards such as sliding slopes, depleted water levels in surrounding wells, and fallen trees, and the site remains in an unstable state (Figure 1).

The collapse occurred with secondary disasters such as house breakage. At present, the foundation and wall at the upper right corner of house No. 3 have collapsed, and the collapse pit has a clear tendency to increase in size. Tensile cracks are found at the entrance of the garage of house No. 3 with the occurrence of the collapse (Figure 2), and the whole house is tilted toward the collapse pit (Figure 3). House No. 1 is only 7.5 m away from the collapse pit and house No. 3 is 15 m away from house No. 1, and there are obvious tension cracks on the right side of the front lawn and new cracks in the house. Houses No. 2 and No. 4 are not obviously affected by the collapse, and no new cracks have been seen in the surrounding ground and houses for the time being. In recent years, small cracks have appeared in the house, but no obvious intensification of the phenomenon has occurred. The recent collapse is in a less stable state, and the loose soil above the slope collapses at times.

**FIGURE 1**
Panorama of disaster scope and affected houses.



**FIGURE 2**
Tensile cracks in the garage of house No. 3.



**FIGURE 3**
Tensile cracks in house No. 3.

## Exploration method in the goaf

### Principle of the high-density resistivity method

The high-density resistivity method is based on the difference in the electrical conductivity of rocks. The traditional resistivity method can realize mineral resources exploration or be used to resolve other related geological problems by observing and studying the distribution law of the artificially established stable current field in the medium. The high-density resistivity method differs from the traditional resistivity method in that the high-density resistivity method requires a large number of high-density measurement points to be set up during installation and observation. In the field, all the electrodes should be placed at once on the measurement points at certain intervals according to the required arrangement before starting the instrument for observation. After processing and analyzing the reflected apparent resistivity profile, the information on stratigraphic distribution can be obtained, which in turn can be used to delineate strata, circle anomalous areas, and determine the location of hazards (Di QingyunShi et al., 2001; Lv et al.,
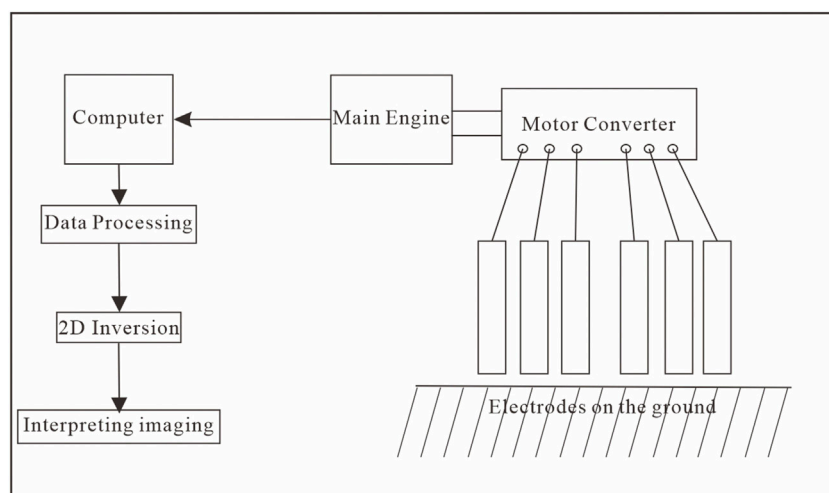
**FIGURE 4**
Working block diagram of the high-density resistivity method.
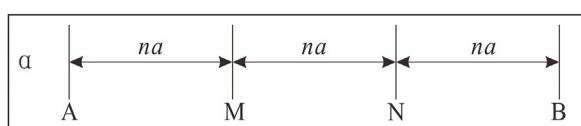


**FIGURE 5**
α-Array signal diagram of the high-density resistivity method.
A, B, supply electrode; M, N, measurement electrode; a, electrode
distance; n, measurement factor.

2005; Ge et al., 2008). The high-density resistivity method uses large-scale integrated circuits in a computer system, and automatic control theory is applied to establish the operation and processing system. Since this operating system can control a large number of electrodes at the same time and can control the connection of different electrodes for free combination, it can save a lot of time, improve the efficiency of observation, collect more information about the underground electric field, and be more intelligent (Figure 4) (Yang et al., 2012; Zhu and Wang, 2012; Han, 2020).

At present, the main ways to carry out high-density resistivity measurements include α, β, and γ arrangements; all three arrangements evolved from symmetric quadruple, monopole–monopole, *etc*. The β and γ arrangements are measured point by point when the electrode distance is the same, then double the electrode distance, and so on; the different points are mainly the difference between A and B positions. The α arrangement is commonly used at present, based on the basic

arrangement of symmetric quadruple, setting the control electrode at the same distance from the measuring electrode, AM = MN = NB, to achieve the measurement of the proposed section of the underground space (Figure 5) (Dong and Wang, 2003).

According to the regional geological overview and the list of rock electrical parameters (Table 1), the strata within the working area of the high-density electrical method in the goaf mainly include the Quaternary Holocene till and silty sand with low resistivity, the common value of which is 30 Ω m. The local water content is relatively small, which may present local high-resistance characteristics and uneven bodies of mass; the resistivity values of bedrocks such as silty mudstone, Devonian limestone, and dolomitic limestone vary considerably. The common resistivity value of argillaceous limestone is 400 Ω m, while the resistivity of the limestone is 1500–1800 Ω m, and its resistivity contours fluctuate widely. The resistivity is used as the basis for the collection and evaluation of parameters of the high-density electrical method and is based on the electrical differences between the goaf and the surrounding rocks. When there is an underground extraction area, the air or water filling generally appears as local high resistance or local low resistance, but when there are hidden karst and fissure development caused by tectonics such as faults and folds, the development zone is filled with water or sediment and other filling materials, and the area usually shows medium resistance or low resistance compared to the surrounding rocks, and the anomalies are often characterized by a resistivity of only a few hundred Ω·m.

**TABLE 1 List of rock electrical parameters.**

| Lithology | Measurement method | Range of resistivity values ($\Omega \cdot m$) | Common resistivity value ($\Omega \cdot m$) |
|---|---|---|---|
| Clay | — | $1–10^2$ | 30 |
| Limestone | Mini-four-electrode array on outcrops | $60–5 \times 10^3$ | 1500 |

Note: Filled air in goaf often exhibits locally high or very high resistance.



**FIGURE 6**
Goaf survey line layout and geological survey map. 1, Quaternary Holocene; 2, Middle Devonian; 3, road; 4, line position and number for the high-density resistivity method; 5, house; 6, collapsed pit; 7, quarry; 8, pond; 9, inferred scope of goaf; 10, inferred scope of karst.
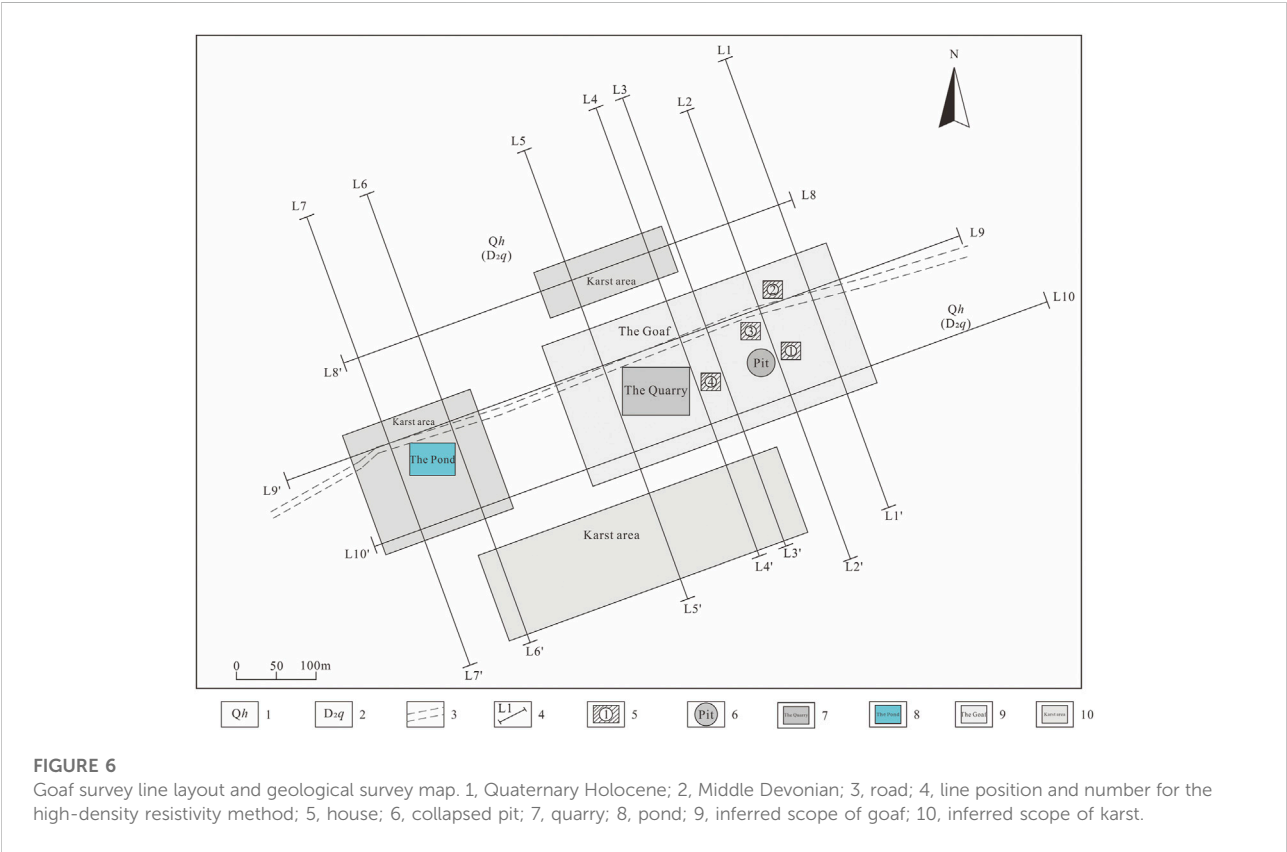
## Field work methods

According to the geological conditions and geophysical characteristics of the area, a total of 10 survey lines were laid in the goaf and its impact area, of which seven were in the north–south direction, named as L1, L2, L3, L4, L5, L6, and L7 from east to west, and three in the east–west direction, named as L8, L9, and L10 from north to south. The length of the measured profiles in the north–south direction was 600 m, and the length of the east–west profiles L9 and L10 was 900 m and that of L8 was 600 m. Survey line L1 was laid on the eastern periphery of house No. 2 in the goaf, with the profile direction near the north–south, to control the peripheral area affected by the collapse; survey line L2 is roughly parallel to the L1 line, laid on the eastern side of the collapse pit and passing

through houses No. 1, 2, and 3, to control the investigation of the dangerous house disaster area; survey line L3 is roughly parallel to L1 and L2, laid on the west side of the collapse pit, located on the east side of house No. 4. Survey line L4 is basically parallel to L3 and is located on the west side of house No. 4; survey line L5 is basically parallel to L4 and is located on the west side of the quarry, about 100 m away from L4; survey line L6 is located on the east side of the pond; and survey line L7 is located on the west side of L6, in order to identify the karst collapse channels on the east and west sides of the pond. The east–west survey lines L8, L9, and L10 cross the area: measuring line L8 is placed to the north of the road to detect the karst development area existing in the shallow part of the collapse periphery, and measuring lines L9 and L10 pass through the dangerous house area, quarry, and pond to identify the underground anomaly information in

the affected area. The main purpose of the three survey lines is to verify the stratigraphic information of the goaf and karst ground collapse area inferred from the north–south survey lines and to improve the detection accuracy. The 10 survey lines cover the quarrying area and its impact area, and can be used to effectively detect the geological conditions and resistivity anomalies, and therefore infer the ground collapse anomalies caused by quarrying and karst through the inverse map of the physical survey profile, providing a theoretical basis for further verification and disaster prevention and control (Figure 6).

The WDJD-3 multi-functional digital DC exciter and WDZJ-3 multiplex electrode converter were selected as the main control machine for this high-density resistivity method exploration. An electrode distance of 5 m was selected for the high-density resistivity method, 60 electrodes were arranged as one arrangement, one section was rolled 58 times, and the number of profiles was 19 layers in total. The location of the measurement points was determined by a hand-held GPS device, supplemented by compass orientation and measuring distance with a leather tape. The electrodes were arranged in an α arrangement (Winner device AMNB). In the survey process, first of all, AM = NB = MN was set as one electrode spacing; A, M, N, and B were moved from one end of the survey line to the other end one point at a time; and the first profile was measured in turn. Second, AM, MN, and NB were increased to two electrode spacing and were moved from one end of the survey line to the other end one point at a time. Subsequently, the electrode distance was measured in an increasing order to finally form an inverted trapezoidal section.

## Data processing

High-density electrochemical data processing consists of two parts: the first consists of data pre-processing, pre-editing the apparent resistivity values, eliminating distorted data such as abrupt points or noise from the resistivity profiles, and then stitching multiple measurement sections into a complete and uniform profile. For profiles with significant differences in data and large topographic relief, subsequent inversion processing is required to analyze their characteristics (Gao et al., 2015; Fu et al., 2019). By converting the actual field survey data into a depth–resistivity relationship, the resistivity profile characteristics of the strata are obtained, and the influence of anomalous interference on the interpretation of the electro-magnetic data is eliminated to the maximum extent possible to ensure clarity and reliability of the inversion interpretation (Xiao et al., 2008; He, 2016). Second, the inversion calculation analysis is carried out, and the initial two-dimensional geoelectric model is established by the least squares method based on the denoised subsurface spatial information data, which are converted into a depth–apparent resistivity relationship to obtain a physical inversion cross-sectional map showing the

characteristic changes in apparent resistivity at the mining area and ground collapse site (Guo et al., 2004; Luo et al., 2020).

## Anomalous features and explanations

### High-density resistivity method anomaly characteristics

From the basic geological data of the goaf, combined with the analysis of the geophysical inversion section map, it is inferred that the surface layer from the top to bottom is Quaternary clay and cultivated soil layer, which is about 1–8 m thick, and the contour change is not uniform due to the influence of surface hydrological conditions and human activities, and the overall low resistance form. The relative resistivity of the underlying bedrock layer is larger, and with the increase in the detection depth, the overall resistivity trend increases, and the contour change is more uniform. In the area of ground collapse caused by mining and karst, the low resistivity resistance is mainly due to water or sediment filling, and the contour changes are obvious and appear as low-resistance clumps; in the area of fractures or fissures, the originally uniform resistivity appears to be broken, and the contour lines extend in a certain direction.

### Interpretation of data inferred from anomalous areas

The high-density resistivity method of physical prospecting is used to lay three lines of measurement in the east–west and seven lines of measurement in the north–south vertical direction in the goaf, covering the mining void and karst ground collapse and their impact areas, to detect and analyze the distribution of strata and the size of cavities, and to infer the morphological characteristics and location of underground anomalies. Based on the resistivity changes in the inversion map of the geophysical prospecting, the overall low-resistance anomaly and the area where the contour lines are closed into clumps are inferred to be a mining hole or a karst collapse: line L1 detects a strip of low resistance underneath the area between measurement points 200 and 290, which is laterally sloping to the north and extends for nearly 70 m, inferred to be caused by the development of fissures in the mining hole and karst, filled with low-resistance water or sediment, with uneven contour distribution. The range of anomalies is extremely large, which is a more serious area of potential ground collapse disaster (Figure 7A); measurement line L2 detects a large-scale anomalous pit-like collapse that is elliptical in shape between measurement points 250 and 330, with a depth of about 30 m from the surface, which is inferred to be a continuous anomalous zone belonging to line L1 and located in the influence area of anomalous collapse in the goaf (Figure 7B); and measurement
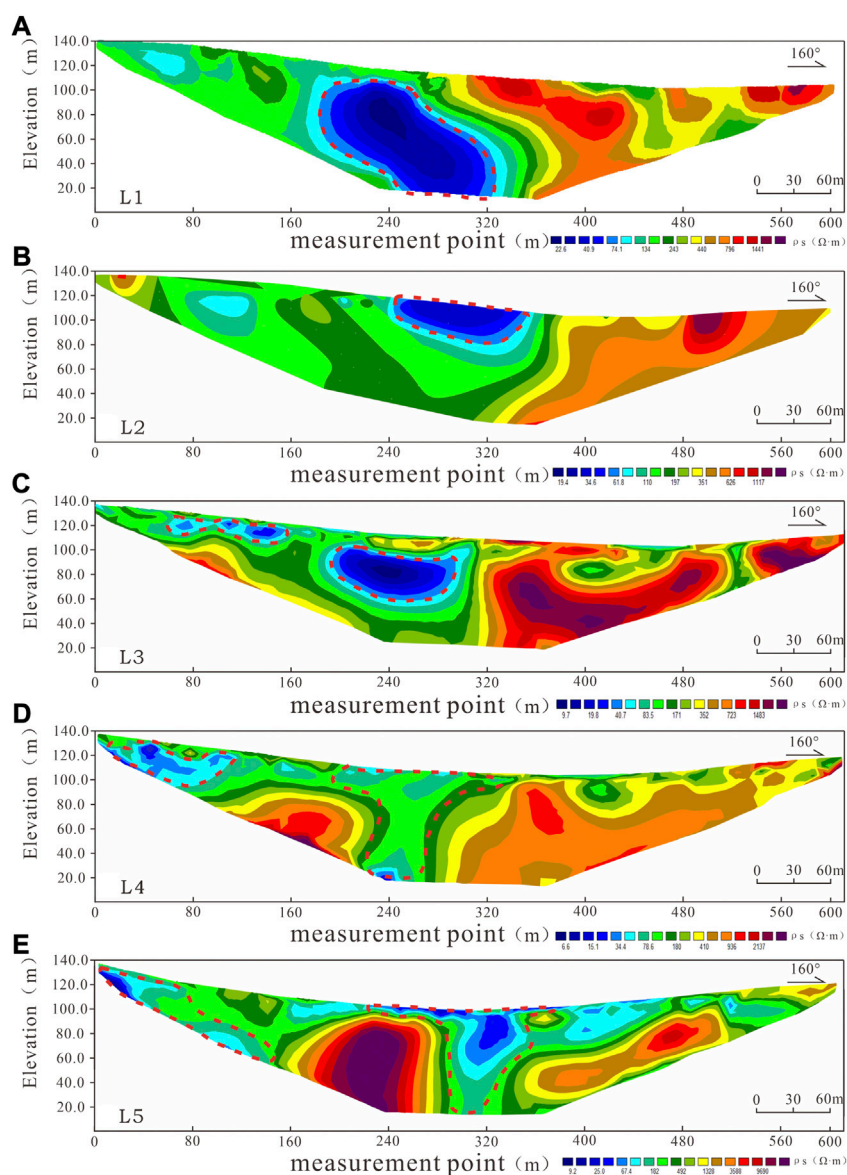
**FIGURE 7**
Geophysical inversion section (lines L1–L5, **A–E**) of the high-density resistivity method. 1, inferred scope of collapse.

line L3, with measurement point 300 as the center of the station, detects an anomalous pit-like collapse near the station. The anomalous zone in the south is located at measurement points 70–150, at an altitude of 110–130 m, while the anomalous zone in the middle is located at measurement points 200–270, at an altitude of 95–110 m, and is a zone prone to mining collapse (Figure 7C). The anomalous pattern revealed by measurement line L4 is obviously different, at measurement points 30–110 in the south, at an altitude of 90–120 m, and is inferred to be caused by the filling of low-resistance sediment in the goaf, while the anomalous zone between measurement points 230 and 290, which extends to the bottom in depth, is inferred to be a

mining area anomaly with a resistivity of about $100 \, \Omega \, m$, where ground collapse disaster has not occurred yet, and the high-resistance bodies on either side of it are presumed to be the safety pillars, which refer to the part of the ore body that is not mined to protect the safety of the surrounding environment (Figure 7D). Measurement line L5 infers that the anomalous zone between measurement points 30 and 140 and at an elevation of 80–110 m is continuous with L4 and L3, while the anomalous zone between measurement points 280 and 330 extending to the bottom is presumed to be an anomalous area of collapse formed under the joint influence of mining and karst, and the high-resistance areas to the south and north of it are presumed to be
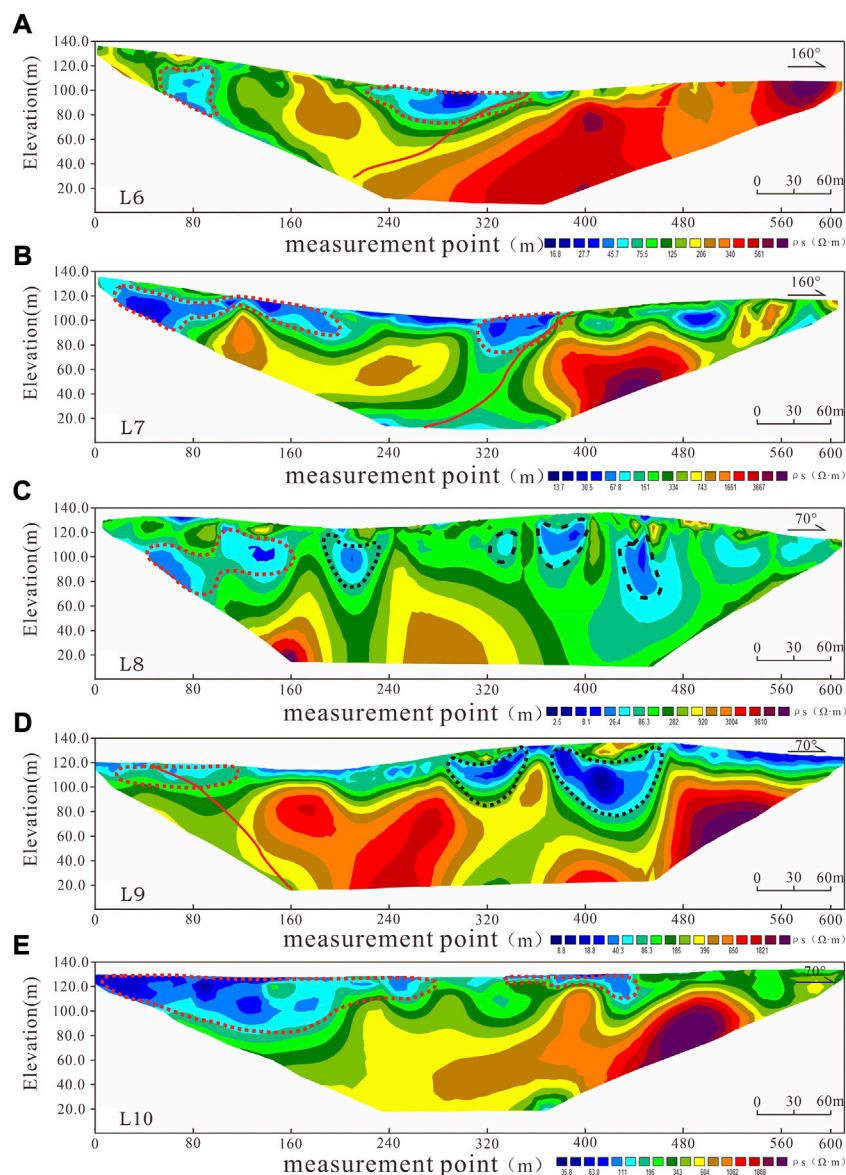
**FIGURE 8**
Geophysical inversion section (lines L6–L10, **A–E**) of the high-density resistivity method. 1, inferred scope of karst; 2, inferred scope of collapse; 3, inferred line of fracture.

the safety pillars (Figure 7E). The karst development zone revealed by the southern measurement point of measurement line L6 is distributed between measurement points 70 and 90 and at an elevation of 80–1,120 m. Another anomaly exists between measurement points 250 and 320, and at measurement point 300 in the center of the line, there is an extension of the contour to the southeast, with an obvious discontinuity with the surrounding bedrock resistivity, inferring the existence of a fracture dipping to the southeast (Figure 8A); the karst development zone in the south-central part of line L7 continues to extend and becomes wider, with another karst

development zone at point 320, with the lower contour extending to the southeast and a resistivity misconnection, inferring the existence of a fracture dipping to the southeast (Figure 8B).

Three measurement lines were laid in the near east–west profile: L8, L9, and L10. The anomalous area and geological structure distribution revealed by the seven longitudinal lines and three transversal lines are integrated, and it is inferred that line L8 is located at measurement points 50–130, with a karst development zone between 70 and 110 m in depth and an irregular elliptical shape overall. Between measurement points 290 and 320, 470 and 490, 520 and 580, and 610 and 660, the

anomalous area is in the shape of small blocks or clusters. The anomaly is located between measuring points 290 and 320, 470 and 490, 520 and 580, and 610 and 660, and between 60 and 100 m above sea level, and the anomalous area is in the shape of small blocks or clusters, which may be filled with shallow water bodies and have low resistivity (Figure 8C). According to the resistivity variation of measurement line L9, there is a resistivity discontinuity in the area extending from south to north between measurement points 100 and 170, and the contour variation is uneven, presumably due to the existence of fractures; between measurement points 430 and 480 and between 540 and 660, the contour circle between 40 and 90 m above sea level is depressed, presumably a mining collapse anomaly (Figure 8D). The shallow surface above 80 m elevation was identified as a large karst anomaly with an irregular elongated shape, mainly due to the erosion of carbonate rocks by water bodies (Figure 8E).

The goaf is filled with water and sediment due to mining activities, and the geophysical inversion section shows a low-resistance irregular shape. The strong hydrological exchange in the carbonate area can easily trigger geological disasters such as cave collapse pits. Geophysical exploration of the area was carried out using the high-density resistivity method and the seven north–south lines and the three east–west lines, which run through the anomalous area of mining and karst ground collapse and its influence range, to verify the anomalous area detected by the seven north–south lines, so as to obtain the overall distribution of mining ground collapse in the area and its morphological characteristics and to detect the possible occurrence and influence range of ground collapse caused by both mining and karst. In this study, the ground collapse caused by both mining and karst and its influence range are detected, and the location of underground anomalies and the distribution pattern of stratigraphy in the area are identified, indicating that the high-density resistivity method can effectively detect the location of similar geological hazards such as ground collapse caused by mining and karst.

## Conclusion

(1) The study area is located in a carbonate rock region, where there are many mining activities and human engineering activities, a certain range of underground mining areas, and good conditions for alternating water circulation. The integrity and strength of bedrocks are greatly affected by the karst ground collapse and other geological hazards and hidden dangers, together with the complex geological formations in the mining areas. This in turn greatly affects the safety of life and property of the residents. The high-density resistivity method was used to investigate the mining ground collapse in the study area by laying seven longitudinal lines and three transversal lines, and the mining

ground collapse and geological structures revealed by the longitudinal lines were all revealed by the transversal lines. The cross-sectional and longitudinal profiles were mutually verified, and the revealed geohazard development areas were found to have a high degree of overlap.

(2) The high-density resistivity method is suitable for application in karst and mining collapse areas and can effectively identify the distribution of strata and the morphological characteristics of the anomalous areas. It can be used to detect and analyze ground collapse and other geological hazards caused by mining and karst. It can provide an important basis for the selection of hole placement for later drilling work and provide a theoretical basis for the detection and identification of similar geological hazards.

## Data availability statement

The original contributions presented in the study are included in the article/Supplementary Material; further inquiries can be directed to the corresponding author.

## Author contributions

XJ wrote the manuscript, generated the plots, and analyzed the data; LY provided guidance for data processing and result interpretation; LYL provided guidance for methods selection and the field work; and ZL provided guidance for the field work

## Funding

## Conflict of interest

The authors declare that the research was conducted in the absence of any commercial or financial relationships that could be construed as a potential conflict of interest.

## Publisher's note

All claims expressed in this article are solely those of the authors and do not necessarily represent those of their affiliated organizations, or those of the publisher, the editors, and the reviewers. Any product that may be evaluated in this article, or claim that may be made by its manufacturer, is not guaranteed or endorsed by the publisher.

# References

Di, Q., Shi, K., Wang, M., et al. (2001). Water resources exploration with CSAMT and high-density electric resistivity method. *Prog. Geophys.* 16 (03), 53–57+127.

Dong, H., and Wang, C. (2003). Development and application of 2D resistivity imaging surveys. *Earth Sci. Front.* 10(01), 171–176.

Fu, G., Huang, J., Liu, Y., Li, X., Chen, G., and Huang, Y., (2019). Multi-electrode resistivity method and CSAMT method in geothermal exploration of Babei area in Huichang County, Jiangxi Province. *Geol. China* 46 (04), 927–936.

Gao, M., Yu, S., Zheng, J., Xu, C., Zhang, K., and Hui, L., (2015). Application of PSBP method in high-density two-dimensional resistivity inversion. *J. Jilin Univ. Technol. Ed.* 45 (06), 2026–2033.

Ge, S., Li, X., Shao, C., Chen, J., and Chen, X., (2008). Application of seismic refraction and resistivity for exploration of reservoir dam site. *Prog. Geophys.* 23(04), 1299–1303.

Gong, P., and Li, W. (2018). Application of transient electromagnetic method in collapse hazard of goaf:take the investigation of the goaf in Shendong coal mine as an example. *J. Geomechanics* 24 (03), 416–423.

Guo, X., Jia, Y., Huang, X., and Niu, J. (2004). Application of multi-electrodes electricalmethod to detection of slide-face position. *Chin. J. Rock Mech. Eng.* 23 (10), 1662–1669.

Han, P. (2020). Forward modeling and inversion of the high-density resistivity method in detecting karst caves of different filling types. *Geol. Explor.* 56 (06), 1219–1225.

He, G. (2016). The application high-density resistivity method to karst detection. *Chin. J. Eng. Geophys.* 13 (02), 175–178.

Huang, G., Zhao, J., Li, C., and Li, S. (2019). Detection of underground karst caves by comprehensive geophysical exploration in karst area: Taking yongan dahu basin in fujian province as example. *Prog. Geophys.* 34 (03), 1184–1191.

Jia, X., Liu, Y., Li, X., et al. (2021). The application of Opposing Coils Transient Electromagnetics in the detection of karst subsidence area. *Coal Geol. Explor.* 49 (03), 212–218.

Jin, C., and Liu, J. (2014). Two-dimensional numerical simulation and application of the high-density resistivity method. *Geol. Explor.* 50 (05), 984–990.

Lei, J., Yang, J., Xiao, W., and Liu, C. (2009). Analysis of forming conditionsand maininfluential factors of karst collapse in Guanzhou. *Geol. Explor.* 45 (04), 488–492.

Li, H., Xu, H., Zheng, L., and He, Y. (2019). *In situ* experimental study on resistivity-magnetic resonance sounding coupling imaging diagnosis method for an embankment dam with seepage defects. *Prog. Geophys.* 34 (04), 1627–1634.

Li, J., Nie, Q., Liu, Q., and Jia, X. (2017). Logistic regression model for stability assessment of karst ground collapse of Tangshan city. *Rock Soil Mech.* 38 (S2), 250–256.

Li, W., Zhang, Y., Zhang, B., Li, J., Wang, J., and Ma, X. (2014). Origin, characteristics and significance of collapsed-paleocave systems in Sinian to Permian carbonate strata in Central Sichuan Basin, SW China. *Petroleum Explor. Dev.* 41 (05), 563–573. doi:10.1016/s1876-3804(14)60067-7

Luo, X., and Cheng, L. (2016). Comprehensive geological prediction and risk assessment of covered karst ground collapse. *Carsologica Sin.* 35 (01), 51–59.

Luo, Z., Liu, W., Cao, P., et al. (2020). Application of the high-density resistivity method in detecting a mined-out area in the Xiaozhuohe iron deposit of Laizhou City, Shandong Province. *Geol. Explor.* 56 (01), 0113–0122.

Lv, H., liu, S., and liu, B. (2005). Application of resistivity tomography survey method in detecting ground subsidence. *Prog. Geophys.* 20 (02), 381–386.

Shen, N., Yang, J., and Zheng, X. (2001). Prediction of mining collapse based on neural network. *Coal Geol. Explor.* 29(03), 42–44.

Wang, B., and He, K. (2006). Study on limit equilibrium height expression of critical soil cave of karst collapse. *Rock Soil Mech.* 27 (03), 458–462.

Wang, S., Xianguo, T., Li, H., et al. (2011). The application of radon measurement method and high-density electrical method in the exploration of the fault location. *Earth Sci. Front.* 18 (02), 315–320.

Xiao, H., Wan, L., and Sun, X. (2008). The anomaly characteristics of the high-density resistivity method used in landslide investigation. *J. Catastrophology* 23 (03), 27–31.

Xie, J., Tan, F., Jiao, Y., Zuo, J., and Mao, J., (2021). Prediction of karst ground collapse based on factor analysis-GA-ELM model. *J. Eng. Geol.* 29 (2), 536–544.

Yan, Q., Yang, y., Li, S., et al. (2021). Application of the high-density resistivity method in karst site investigation of a waste incineration environmental protection power station. *Geol. Explor.* 57 (05), 1107–1116.

Yang, Z., Yan, J., Liu, Y., et al. (2012). Research progresses of the high-density resistivity method. *Geol. Explor.* 48 (05), 969–978.

Zeng, Y., and Zheng, X. (2007). Fuzzy evaluation method for karst collapse risks. *J. Eng. Geol.* 15 (01), 62–65.

Zhang, G., Yang, B., Zhang, Z., et al. (2015). Susceptibility prediction of underground mining collapse based on GIS and BP neural network. *Trop. Geogr.* 35 (05), 770–776.

Zheng, Z., Zeng, J., Gan, F., et al. (2017). Application of high-density electrical resistivity imaging to karst collapse investigation at the Taiyangcun town, Liuzhou. *Geol. Exoloration* 53 (01), 124–132.

Zhu, Y., and Wang, Y. (2012). The application high-density resistivity and the method to underground karst detection. *Chin. J. Eng. Geophys.* 9 (06), 738–742.

**frontiers** | Frontiers in Earth Science

# Construction risk control technology of a large tunnel complex in urban area

Xinqiang Gao[1], Chao Kong[2]*, Daifeng Wu[3], Feng Lu[4]*,
Maoyi Liu[3], Haiyan Wang[5] and Songbo Ren[2]

[1]State Key Laboratory of Mechanical Behavior and System Safety of Traffic Engineering Structures,
Shijiazhuang Tiedao University, Shijiazhuang, China, [2]School of Civil Engineering and Architecture,
Southwest University of Science and Technology, Mianyang, China, [3]Chongqing Urban Construction
Investment (Group) Co., Ltd., Chongqing, China, [4]School of Emergency Management, Xihua
University, Chengdu, Sichuan, China, [5]College of Transportation Engineering, Nanjing Tech University,
Nanjing, China

The stability of the surrounding rock analysis and evaluation during tunnel construction is the basis of tunnel construction risk control. In this paper, we focus on the stability of a large-scale transportation tunnel complex during its construction in a densely-populated urban area. The tunnel complex includes seven shallow-buried tunnels with large cross-sections. In order to gain insight into the excavation influence of the different tunnels, stability analyses were first carried out using FLAC$^{3D}$ numerical simulation. Results showed that the tunnels were subjected to heave and crown settlement induced by adjacent excavation. Also, stress concentrated in the rock blocks connecting different tunnels. Subsequently, a bench-scale model test was performed to understand the failure of the rock blocks and to examine the accuracy of the numerical simulation. The test results agreed well with the numerical simulation. Based on the numerical and test results, the mechanism of the rock blocks failure was explained and construction risk control technology to stabilize the rock blocks was proposed. The construction risk analyses revealed: 1) tunnels are subjected to significant heave due to the excavation of tunnels located above; 2) the stability of the rock blocks is the paramount determinant for stabilizing the whole tunnel complex; 3) ensuring rock blocks to be in a state of triaxial stress is conducive to its stability and hence the stability of multiple tunnels.

KEYWORDS

construction risk, tunnel complex, stability, rock blocks, laboratory model test, numerical simulation

## 1 Introduction

The analysis and evaluation of tunnel stability is the basis of tunnel construction risk control (Liu et al., 2018; Xu et al., 2021). The stability of the rock mass during underground construction is the highest priority for engineers and scholars in the field of underground engineering because it is closely related to people's lives and property safety. Previous experience has shown that rock mass failure in underground

works induces heavy casualties and property loss, especially in densely-populated urban areas. For example, the collapse of a large-scale metro tunnel support system in Singapore claimed four victims and caused subsidence of the nearby Nicoll Highway (COI, 2005; Whittle, 2006). Another serious accident during the metro construction in Sao Paulo (Barton, 2008), seven lives were lost. The risk of tunnel construction is primarily assessed by the geological environment, surrounding rock stability, liner deformation, surrounding rock stress, and so on (Yu et al., 2017; Li et al., 2019).

The construction stability of large tunnel complex is related to the degree of fracture and shear strength of the rock. The correct selection of rock strength is the premise of tunnel stability calculation. Many scholars have made a lot of research on the accurate measurement of rock strength. To better understand the shear behavior of infilled rock joints with standard joint roughness coefficient (JRC) profiles, Zhao (Zhao et al., 2020) used the direct shear method to experiment on sand-filled joints by replicating standard JRC profiles on rock-like materials and placing fill material within the joints. Due to the discrete nature of rock strength, a new natural rock formation strength model was developed based on the shear-related roughness classification of fuzzy integrated evaluation (Zhao et al., 2021a). And other rock strength measurement methods are also available (Zhao et al., 2019; Cao et al., 2016). In fact, the importance of rock mass stability has long been recognized and a great deal of research in recent years has focused on this issue for the underground engineering safety (Liu et al., 2011; Feng et al., 2012; Qian and Lin, 2016; Liang and Liu, 2022). Unfortunately, due to the complexity of geotechnical engineering, stability analysis of rock mass still heavily relies on empiricism even though a few failure criteria (e.g., the Mohr-Coulomb criterion) has been proposed (John, et al., 2007). Zheng et al. (2006, 2008) formulated a strength reduction finite element method (SRFEM) to deal with this problem. Athough still in research phase, the SRFEM has gradually been recognized in engineering practice in China (Zhang, et al., 2007; Pan et al., 2021; Wang et al., 2022).

On the other hand, limited space on the ground has stimulated the development of underground space. For example, in recent years there has been significant construction of underground infrastructure in urban areas with the emergence of adjacent transport tunnel projects (Kim, 1996; Liu et al., 2009; Kong et al., 2016; Hu et al., 2021; Zhao et al., 2021b), even the projects of tunnel complex (multiple tunnels) (Zheng, et al., 2009; Duan and Li, 2012; Zhang et al., 2018; Zheng et al., 2021; Zheng et al., 2022). It is clear that the trend of urban underground excavations is becoming increasingly complex, which makes the complicated stability analysis of rock mass an even more critical issue. And the risks of construction are significantly increased. For tunnel
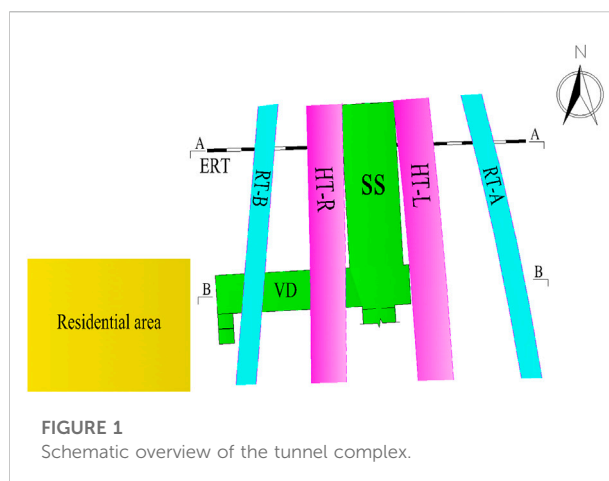


FIGURE 1
Schematic overview of the tunnel complex.

construction risk control measures, different construction situations require targeted analysis. Safety risk control mainly includes pre-construction risk identification and risk warning in construction (Li et al., 2018). During the risk identification phase, a number of challenges need to be overcome. First, traditional methods require a lot of human resources, materials and time. The second problem is the shortage of experienced risk identification experts. Limited by time and space, timely sharing of knowledge becomes unrealistic. Finally, the tunnel construction team will be disbanded at the end of the construction. Therefore, the accumulation of security risk knowledge is completely blank. On the other hand, the quality of risk warning depends on the monitoring data during construction. However, the formulation of control standards based on monitoring data is not reasonable (Zhou et al., 2015).

This paper, based on an unprecedented tunnel complex that contains seven parallel or intersecting tunnels with shallow depths and large cross sections, investigates the stability of the rock mass using FLAC$^{3D}$ numerical models. Stress distribution, crown displacement and the development of plastic zones induced by excavations of multiple tunnels were analyzed. Results showed that the stability of the rock blocks connecting different tunnels was the primary determinant of the overall stability of the multiple tunnels. Furthermore, in order to examine the accuracy of the above analyses, a scaled model test was performed in the laboratory. The test results confirmed the accuracy of the numerical simulation in terms of the potential failure zones and the stress distribution in the rock mass. Subsequently, the mechanism of the stability of the rock blocks was discussed on the basis of the Mohr-Coulomb criterion. According to the analysis, a practical reinforcement scheme strengthening the rock blocks was proposed to reduce the construction risk of the entire tunnel complex project.

TABLE 1 Geological profile of the ground.

| Depth (m) | | Description | General properties |
|---|---|---|---|
| **A-A** | **B-B** | | |
| 0–16.8 | 0–21.4 | Gray and brown miscellaneous fill | Heterogeneity and low strength |
| 16.8–28.8 | 21.4–34.8 | Fuchsia and brown argillaceous sandstone | Moderately weathered, high strength and water-sensitive |
| 28.8–34.8 | 34.8–47.6 | Gray sandstone | Slightly weathered and high strength |
| 34.8~ | 47.6~ | Brown argillaceous sandstone | Slightly weathered, high strength and water-sensitive |

# 2 Engineering background

The large-scale tunnel complex, consisting of seven shallow-buried tunnels with large cross-sections, is located in the Hongyan Village in Chongqing, China. Specifically, the seven tunnels are as follows (Figure 1): a subway station (SS); a ventilation duct (VD) intersecting with the subway station; two parallel double-lane highway tunnels (HT-L and HT-R); two ramp tunnels (RT-A and RT-B) that are in close proximity to the highway tunnels; an existing railway tunnel (ERT) which was built in the 1970s and now is out of service. Additionally, it is worth mentioning that the minimum distance between the SS and the ERT is only 1.2 m and the minimum distance between the SS and the HT-L is only 2.0 m. The south and west sides of the project are adjacent to populated residential areas with densely built buildings.

A detailed field study revealed that the vertical geological profile of the tunnel complex: the sandstone and argillaceous sandstone strata are overlaid by miscellaneous fill material with a thickness of approximately 20 m, as can be seen in Table 1.

# 3 Numerical simulation

Clearly, due to the complexity of the multiple tunnels, a two-dimensional (2D) model based on the plane strain assumption is incapable of meeting the accuracy requirements of stability analysis. Consequently, in accordance with the actual terrain and engineering design parameters, 3D numerical simulations were performed utilizing finite difference analysis software FLAC$^{3D}$ (Itasca, 2012), which is widely applied in the field of geotechnical engineering.

## 3.1 Three-dimensional numerical model

The numerical simulation makes the following basic assumptions.

1) The tunnel is located in a semi-infinite horizontal laminated medium, with each layer made up of thin layers that extend infinitely in the horizontal direction.

2) Each layer is an isotropic homogeneous medium, and the conditions for coordination of displacements between layers and between subsurface structures and rock layers are satisfied, with no relative slippage or detachment between them.

3) The influence of pore water pressure and sand liquefaction is ignored, and only ground stress under gravity's action is considered.

In order to minimize the boundary effect, the model dimensions were selected to be 60 m (length)*160 m (width) *50 m (depth). In terms of boundary conditions, the displacements were set to be zero in all three directions with no horizontal and vertical movements allowed at the bottom of the model. The movements in two horizontal directions were restrained, and only vertical movement was permitted on the four side boundaries.

Shotcrete and lining were modeled using shell elements and elastic solid elements respectively. In addition, the rock mass was modeled utilizing elastic-perfectly plastic constitutive elements (based on the Mohr-Coulomb failure criterion) without joint consideration.

The total number of hexahedral elements used for the rock mass was 13, 1642 eight-noded, while 2, 1001 structural elements were used for shotcrete and cladding (Figure 2).

## 3.2 Excavation simulation

The Z-axis is the tunneling direction, with excavation starting from −Z toward +Z direction. The simulation was carried out in the following excavation sequence:

1) Firstly, the ERT was excavated using bench cut method with its proper lining.

2) Secondly, the SS was excavated using double-wall poilt method followed by the excavation of the VD using bench cut method, and the lining was constructed as soon as the excavations were completed.
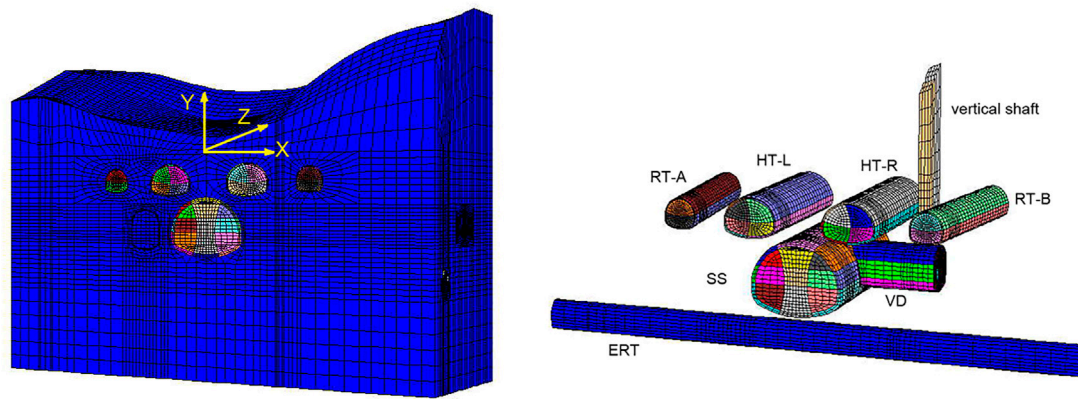
**FIGURE 2**
Three-dimensional numerical model and positional relationship of the tunnels.

TABLE 2 Calculation parameters of rock mass.

| Name | $\gamma$ (N/m³) | E (MPa) | $\mu$ | c (kPa) | $\varphi$ (°) | $S_t$ (kPa) |
|---|---|---|---|---|---|---|
| Miscellaneous fill | 21000 | 30 | 0.45 | 50 | 8.9 | — |
| Argillaceous sandstone | 25900 | 1420 | 0.35 | 100 | 26.0 | 115 |
| Sandstone | 25200 | 6892 | 0.30 | 700 | 42.0 | 302 |

Notes: $\gamma$ is the unit weight; E is Young's modulus; $\mu$ is Poisson's ratio; c and $\varphi$ are the cohesion and the friction angle; $S_t$ is the tensile strength.

TABLE 3 Calculation parameters of shotcrete and lining.

| Tunnel name | Shotcrete | | | | Lining | | | |
|---|---|---|---|---|---|---|---|---|
| | t (cm) | $\gamma$ (N/m³) | E (GPa) | $\mu$ | t (cm) | $\gamma$ (N/m³) | E (GPa) | $\mu$ |
| ERT[a] | — | — | — | — | 30 | 23000 | 20 | 0.3 |
| SS | 33 | 25000 | 23 | 0.25 | 100 | 25000 | 35 | 0.25 |
| VD | 27 | 25000 | 23 | 0.25 | 70 | 25000 | 35 | 0.25 |
| HT-L | 27 | 25000 | 23 | 0.25 | 60 | 25000 | 35 | 0.25 |
| HT-R | 27 | 25000 | 23 | 0.25 | 70 | 25000 | 35 | 0.25 |
| RT-A and RT-B | 24 | 25000 | 23 | 0.25 | 50 | 25000 | 35 | 0.25 |

Note: t is the thickness of structures; $\gamma$ is the unit weight; E is Young's modulus; $\mu$ is Poisson's ratio.
[a]The lining of ERT, is built by masonry (without metal bars inside) material.

3) Thirdly, after the lining strength of the SS and the VD reached the design strength, the HT-L and the HT-R were excavated respectively using bench cut method followed by lining construction.
4) Finally, the RT-A and the RT-B were excavated simultaneously utilizing bench cut method.

For more details regarding these excavation methods can be found in Wang et al. (2010).

## 3.3 Parameters of numerical model

To determine the geological conditions, a comprehensive site investigation was carried out by Survey and Design Institute of Chongqing, the major contractor of the project. According to the Code for Design on Highway Tunnel (JTG D70-2004, 2004), the rock mass was classified as Grade IV. The survey also found that the tunnel complex was built at an elevation of 65 m above the water table and that pore water and joint water were both in short

FIGURE 3
The distribution of surrounding mass stress before excavation (negatives indicate compressive stress whereas positives indicate tensile stress). **(A)** Distribution diagram of the maximum principal stress of A-A cross-section before the excavation of the tunnel complex. **(B)** Distribution diagram of the minimum principal stress of A-A cross-section before the excavation of the tunnel complex. **(C)** Distribution diagram of the deviatoric stress of A-A cross-section before the excavation of the tunnel complex.



FIGURE 4
The distribution of surrounding mass stress (A-A). **(A)** Distribution diagram of the maximum principal stress of A-A cross-section. **(B)** Distribution diagram of the minimum principal stress of A-A cross-section. **(C)** Distribution diagram of the deviatoric stress of A-A cross-section.

supply. Therefore, the influence of water on the rock mass is insignificant. Based on the geotechnical drilling, *in situ* data and laboratory testing, together with previous experience (Qiu et al., 2010) in the Chongqing region, the relevant calculation parameters of the rock mass, shotcrete and liner design parameters used in this study are given in

Table 2. The shotcrete and liner design parameters are listed in Table 3.

## 4 Results analyses

### 4.1 Stress analyses of rock mass

1) Stress regime before the excavation of the tunnel complex.

Figure 3A,B shows the distribution of maximum and minimum principal stress while Figure 3C provides plots of the deviatoric stress before the tunnel complex is built.

**FIGURE 5**
The distribution of surrounding mass stress (B-B). **(A)** Distribution diagram of the maximum principal stress of B-B cross-section. **(B)** Distribution diagram of the minimum principal stress of B-B cross-section. **(C)** Distribution diagram of the deviatoric stress of B-B cross-section.



**FIGURE 6**
Crown displacement of the tunnels. **(A)** Crown displacement of the ERT along its axial direction. **(B)** Crown displacement of the SS along its axial direction. **(C)** Crown displacement of the HT-L and the HT-R along their axial direction.

Negatives indicate compressive stress whereas positives indicate tensile stress Due to the disturbance induced by excavation of ERT. The influence range of surrounding rock is from ERT vault to 6 m above the vault.

Cross-section A-A

Figure 4A and Figure 4B illustrate that the rock mass mainly bears compressive stress and Figure 4C shows the plots of deviatoric stress. Tensile stress zones mainly localize the periphery of individual tunnels. The maximum tensile stress is 0.73 Mpa, occurring near the crown of the SS. This tensile stress far exceeds the tensile strength of rock mass (see Table 2), which will bring to cracking and even small-scale collapse of the rock. Figure 4A clearly shows that stress concentrates in two zones after the

excavation of multiple tunnels: 1) the rock blocks connecting the SS and the HT-L; 2) the rock blocks connecting the SS and the HT-R. The maximum value in the stress concentration zone is 2.1 MPa.

Cross-section B-B.

As shown in Figure 5A,B, the rock mass primarily bears compressive stress and the deviatoric stress plots are shown in Figure 5C. Tensile stress zones only localize the periphery of

**FIGURE 7**
The distribution diagram of the plastic zones of the tunnels.
**(A)** The 3D distribution diagram of the plastic zones (tunnel support structures are not shown). **(B)** The distribution diagram of the plastic zones of the A–A cross-section. **(C)** The distribution diagram of the plastic zones of the B–B cross-section.
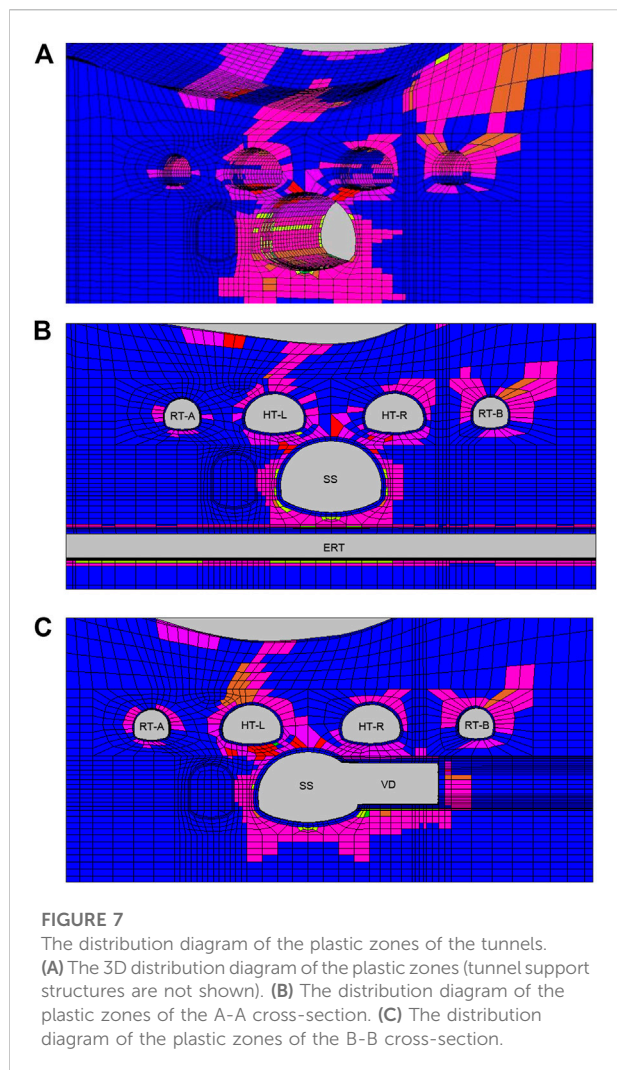
individual tunnels. The maximum tensile stress is 0.97 Mpa, occurring at the toe of the SS's left sidewall. This tensile stress far exceeds the tensile strength of rock mass (see Table 2), which will bring to cracking and even small-scale collapse of the rock. Obviously, stress concentrates in the rock blocks connecting the SS and the HT-L after the excavation of multiple tunnels. The maximum value in the stress concentration zone is 2.4 MPa.

In summary, during the construction of the multiple tunnels, stress concentrates in the rock blocks. This is likely to decrease the strength of the rock mass due to the propagation of discontinuities (such as joints) and ultimately threaten the stability of the tunnel complex. It also should be noted that although the tensile stress exceeds the tensile strength in limited areas and therefore brings cracking of the rock, the area of tensile stress zones is so limited that this would not cause failure of multiple tunnels.

## 4.2 Displacement analyses of linings

1) As can be seen in Figure 6A, the excavation of the SS and other multiple tunnels located above the ERT results in a significant heave displacement of the ERT. In particular, the scope of -20–20 m is subjected to strong influence and the maximum heave is 11.2 mm (curve ②). This heave is triggered by the load release effect induced by the excavation. In addition, it is worth noting that the heave caused by the excavation of the SS is over 10 mm (curve ①), accounting for 89.3% of the final heave displacement (curve ②). Because the lining of the ERT was constructed using masonry (without metal bars inside) whose tensile strength is low, the heave poses a great threat to the stability of the ERT.

2) According to Figure 6B, the weight of the overlying rock mass causes the crown settlement of the SS after its excavation with the maximum value of 13.3 mm occurring at the coordinate of 28 m along its axial direction (curve ①). Despite the ERT is located directly below the 0–20 m scope of the SS, curve 1 shows that the crown settlement of the SS in the 20–60 m scope is slightly larger than that of the 0–20 m scope (the difference is only 0.7 mm), which indicates that the weight of the overlying rock mass exerts a stronger influence on the crown settlement of the SS compared with the presence of the ERT.

Curve ② proves that the load release effect induced by the excavation of the multiple tunnels located over the SS leads to a small uplift of the SS (the maximum value is only 0.6 mm). This small heave probably results from the fact that the multiple tunnels are not excavated directly above the SS. Also, the overlying rock mass of the SS is sandstone with high strength, which may contribute to the small heave of the SS.

3) According to Figure 6C, for both the HT-L and the HT-R, the overall crown settlement gradually increases with increasing buried depth along the tunnel axial direction. The maximum settlement values of the HT-L and the HT-R are 13.0mm and 13.8 mm respectively.

Since the VD is excavated directly below the HT-R whereas no excavation is done directly below the HT-L, more remarkable settlements occur in the middle section along the axial direction of the HT-R.

## 4.3 Plastic zone analyses

As shown in Figure 7A–C, plastic zones of the rock mass mainly localize in three areas: 1) the rock blocks connecting the SS and the ERT; 2) the rock blocks connecting the SS and the HT-L; 3) the rock blocks connecting the SS and the HT-R. Also, plastic zones near the crown of the HT-L have been developed on the ground surface.

**FIGURE 8**
Dimensions of the test model. (unit: mm).
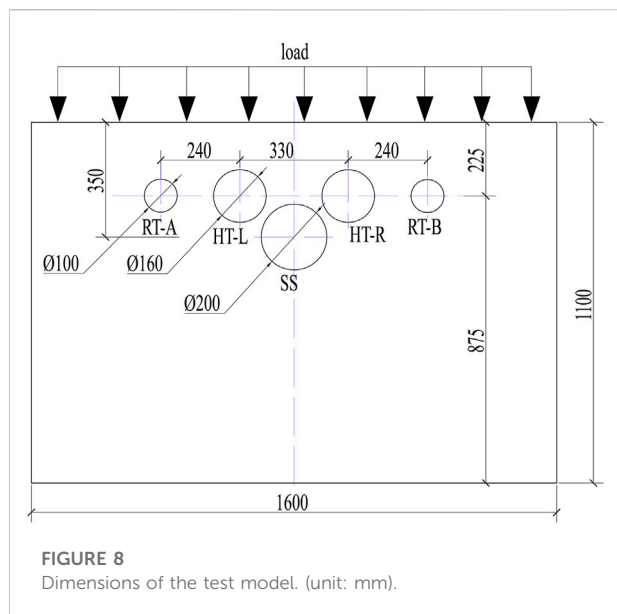
Due to the residual strength, being in plastic states does not necessarily mean strength failure of the rock blocks. Nevertheless, numerical simulation clearly proves that the stability of the rock blocks is the paramount factor for stabilizing the entire tunnel complex.

# 5 Discussions

## 5.1 Stability of the ERT

The three-dimensional numerical simulation shows that the ERT is subjected to significant heave induced by the excavation of multiple tunnels located above it. On the other hand, because the ERT was constructed in the 1970s (now it is out of service) and its lining was built of masonry (without metal bars inside) material with low tensile strength, the heave may cause instability of the ERT. Clearly, this would threaten the stability of the whole tunnel complex. Therefore, given the fact that the ERT is no longer in operation, it is recommended that the affected section of the ERT (−40m–40 m along its axial coordinate) should be sealed up by concrete filling before the excavation of multiple tunnels for the sake of the overall stability. The timing of the seal operation is crucially important. It must allow enough time for the hardening process of concrete.

## 5.2 Stability test of rock blocks

It has been widely accepted that it is important to make good use of the bearing capacity of the rock mass during tunnel construction. However, in terms of the construction of the tunnel complex, the bearing capacity of the rock mass is severely undermined by multiple openings in the rock mass and hence causing stress concentration in the rock blocks and the shotcrete and lining. As a result, the stability of the rock blocks emerges as the most critical factor for stabilizing of the entire tunnel complex.

In order to gain insight into the failure process of the rock mass and verify the accuracy of the numerical simulation, a scaled model test was conducted in the laboratory.

### 5.2.1 Overview of the test

The test model was made according to the A-A cross-section. For the purpose of simplifying the problem, the test was on the basis of the plane strain assumption and the actual terrain was not considered. Moreover, the influence of the ERT was negligible due to the proposal mentioned earlier (the ERT should be sealed up). Figure 8 shows the test model and cross-sectional dimensions.

The test apparatuses consist of a scaled model (including lining models and the simulated rock mass), a set of loading equipment and micro geotechnical pressure cells.

During the test, the ground load level was gradually increased by a step of 20 kN until the failure of the model. Simultaneously, the failure modes and behavior of the rock mass were carefully observed. Micro geotechnical pressure cells were used to measure the stress on the liner.

### 5.2.2 Test materials and similarity rules

The lining models were made of low-pressure polyethylene. A homogeneous material was used to simulate the actual rock mass (argillaceous sandstone), and the stratum characteristic of the actual rock mass was not considered because of the complexity of the simulation test. The simulated rock mass was made of cement, fly ash, gypsum, river sand and water (25.0%, 13.2%, 6.5%, 5.3%, and 50%, by mass percentage).

Material parameters of the prototype were adopted from actual engineering data and their model counterparts are listed in Table 4. During the laboratory test, five groups of parameters were simulated and the similarity ratios (Physical variables with subscript p refer to the prototype, and physical variables with subscript m refer to the model) are: $C_l = l_p/l_m$ =100; $C_E = E_p/E_m$ =100; $C_\rho = \rho_p/\rho_m$ =1.2; $C_c = C_p/C_m$ =1.7; $C_\phi = \phi_p/\phi_m$ =1.2. Under the premise of ensuring the reliability of the test results, the similarity ratio is determined mainly based on the size of the test setup, the tunnel prototype and the loading capacity of the test chamber.

### 5.2.3 Test results and analyses
1) Failure modes

The failure process of the rock mass is shown in Figure 9: initially, the destruction occurred at the spring line of the SS 1)

TABLE 4 Rock mass and lining parameters of the prototype and model.

| Name | c (kPa) | φ (°) | E (MPa) | ρ (g/cm³) | μ | t (cm) |
|------|---------|-------|---------|-----------|---|--------|
| Rock mass prototype | 252 | 33.5 | 4000 | 24.5 | 0.35 | — |
| Simulated rock mass | 352 | 30.0 | 41.5 | 20.0 | 0.30 | — |
| Lining prototype | — | — | 20 | 2.55 | 0.2 | 30 |
| Lining model | — | — | 0.15 | 0.94 | 0.2 | 0.3 |

Notes: c and φ are the cohesion and the friction angle; E is Young's modulus; ρ is the density; μ is Poisson's ratio, t is thickness.
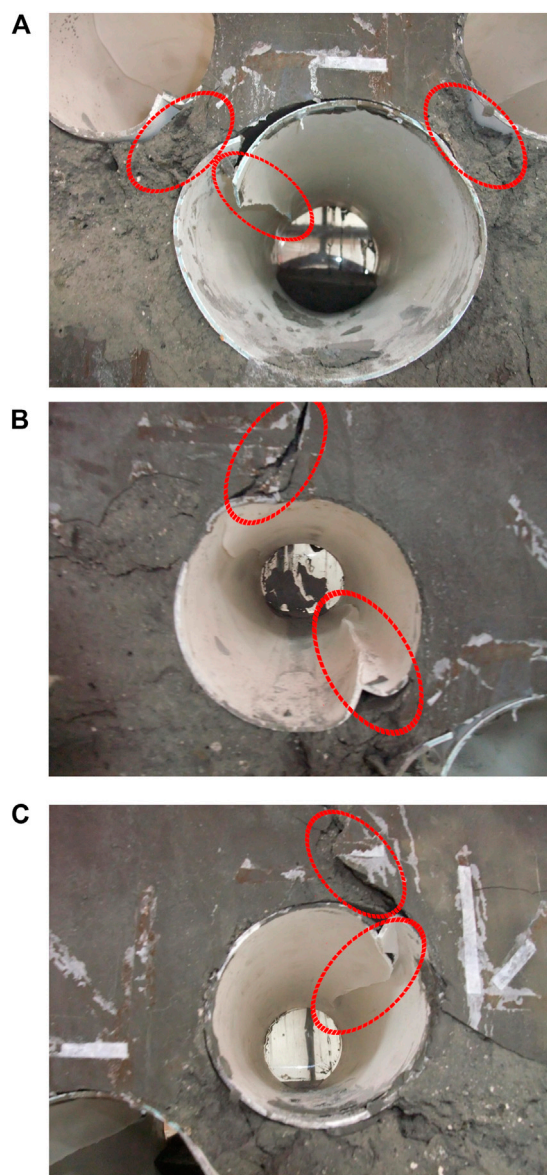


**FIGURE 9**
Detailed failure modes in the test. **(A)** Failure modes around the SS. **(B)** Failure modes around the HT-L. **(C)** Failure modes around the HT-R.

and then the toe of sidewall of the HT-L 2): next, the rock blocks connecting the SS and the HT-L broke; subsequently, the rock blocks connecting the SS and the HT-R damaged 3); eventually, cracks occurred in the area of d and e and they spread into the ground surface. Model failure occurred when the load level reached 200 kN (Figure 11). A detailed description of the failure modes is shown in Figure 10.

2) Stress distribution on the lining

The failure zones observed in the test were in fairly good agreement with the theoretical failure zones calculated by the strength reduction finite element method (SRFEM), as can be seen from Figure 10A and Figure 10B. The numerical model used in SRFEM is a 2D model and its dimensions and boundary conditions are the same as the 3D model. The parameters of the rock mass are listed in Table 4. Details about the SRFEM can be found in Zheng et al. (2006, 2007).

In terms of the stability of the rock blocks, only the rock blocks connecting the SS and the HT-L (the left rock blocks) damaged in the SRFEM numerical simulation (2D). However, apart from that, the rock blocks connecting the SS and the HT-R (the right rock blocks) also damaged during the test. This discrepancy may be due to the fact that the actual terrain was considered in the SRFEM numerical simulation whereas it was not considered in the model test: the slope of the terrain produced asymmetric rock mass pressure to tunnels whereas the load in the test was nearly symmetric.

Nevertheless, both the test and the SRFEM numerical results showed that the damage of the left rock blocks was more severe compared to the right rock blocks. This is mainly due to the greater thickness of the right rock blocks and hence the greater bearing capacity compared with the left rock blocks.

The pressure exerted on the linings when the rock mass failed can be seen in Figure 10C. Data from the pressure cells SS-2 and SS-4 are 788.74 kPa and 783.33 kPa respectively, which were much greater compared with other pressure cells. This indicates that stress concentrates in the left rock blocks and the right rock

FIGURE 10
Failure zones comparison and Stress distribution on the lining. **(A)** Failure zones in the test. **(B)** Failure zones in SRFEM numerical simulation. **(C)** Pressure distribution on the lining when the rock mass failed. (unit: kPa).



FIGURE 11
Mechanical model and analysis. **(A)** Rock blocks stress analysis. **(B)** Rock blocks principal stress analysis using Mohr's circle.

## 5.3 Mechanism of the rock blocks failure

As an example, consider the left-hand rock blocks (Figure 11A) to explain the failure mechanism of the rock blocks. During the whole process, the Mohr circle at the rock blocks underwent five changes: the first time, after the excavation of the SS, the tangential stress at the rock blocks was released significantly due to stress relief, and the Mohr circle was cut with the strength envelope; the second time, after the completion of the SS construction, the Mohr circle diameter decreased, and it gradually moved away from the strength envelope; the third time, a large concentration of tangential stresses occurred during the excavation of the HT-L, and the diameter of the molar circle increased until it was tangential to the strength envelope; the fourth time, after the support was set in HT-L, the radial stress increased and the diameter of the molar circle became smaller and gradually moved away from the strength envelope; the fifth time, after the excavation of the tunnel complex was completed, the molar circle again gradually moved away from the strength envelope.

Clearly, the tangential stress ($\sigma_\tau$) concentration leads to the radial expansion of the rock blocks due to the Poisson

blocks. This test result agrees well with the stress distribution in the 3D numerical simulation.

The failure zones of rock blocks damage in the test is basically consistent with the zones of surrounding rock stress concentration in the numerical simulation, and the lining damage pattern is also basically consistent with the lining stress distribution in the numerical simulation, which indicates that the test and numerical simulation results have certain correlation and can provide support for the conclusion.

effect. Meanwhile, the tunnel lining provides radial stress ($\sigma_r$), turning the rock blocks into a state of biaxial stress. As the degree of stress concentration increases, the tangential stress increases to a certain level when the lining becomes incapable to provide sufficient radial stress (lining is buckled) to sustain the biaxial stress state. Subsequently, the radial expansion increases sharply as a consequence of the end of biaxial stress state. The state of uniaxial stress produces shear failure of the rock blocks, which ultimately leads to the failure of the multiple tunnels.

## 5.4 Reinforcement for rock blocks

The above analyses suggest that providing sufficient radial stress is vitally important for stabilizing rock blocks. This can be demonstrated by plotting the Mohr's circle diagrams of the principal stresses of the rock blocks.

Based on the plane strain assumption together with ignoring the effect of the ERT and the VD, two cases were calculated using FLAC³D: 1) tunnels without support structures; 2) tunnels with support structures. The principal stress analysis of the left rock blocks is shown in Figure 11B.

Before the excavation of the SS, the Mohr's circle is below the failure envelope and the rock blocks are stable. At this stage the rock mass has not been disturbed by excavation.

Under the condition of tunnels without lining, the Mohr's circle is above the failure envelope after the excavation of the SS, which indicates the beginning of rock blocks failure. When the excavation of the HT-L is completed, the radius of the Mohr's circle increases and hence the Mohr's circle is above the failure envelope due to the tangential stress concentration. At this stage the rock blocks fail.

As for the tunnels with lining, the Mohr's circle is on the failure envelope after the excavation of the SS, indicating the state of equilibrium. When the excavation of the HT-L is completed, the radius of the Mohr's circle increases but the Mohr's circle moves to the right due to the radial stress provided by lining. Therefore, it is still below the failure envelope: the rock blocks remain stable.

In engineering practice, auxiliary stabilization measures that can provide radial stress (e.g., rock bolts and pre-stressed anchor cables) can improve the stress state of the rock blocks, ensuring the rock blocks are in a state of triaxial stress. It should be noted, however, the number of these measures must be limited in order to avoid excessively weakening the integrity of rock blocks.

## 6 Conclusion

This paper presents stability analyses of a large-scale tunnel complex based on a case study in Chongqing, China. The analyses were performed using FLAC3D and compared with a scaled model test in the laboratory. The following conclusions can be drawn from the study:

1) The stability of the surrounding rock analysis and evaluation during tunnel construction is the basis of tunnel construction risk control. For tunnel construction risk control measures, different construction situations require targeted analysis.
2) During the excavation of the multiple tunnels, stress concentrates in the rock blocks and the plastic zones localize in the rock blocks. Because the rock blocks function as the main bearing body and connect the lining of different tunnels to form a bearing system, the stability of the rock blocks is the paramount determinant for stabilizing the entire tunnel complex.
3) The ERT and the SS are subjected to heave displacement due to the excavation of the tunnels located above. Particularly, the ERT is strongly influenced. In order to stabilize the multiple tunnels, it is proposed to seal up the ERT by concrete filling given it is no longer in operation.
4) The stability of rock blocks is the key to control construction risk. Ensuring the rock blocks to be in a state of triaxial stress is conducive to its stability. This can be achieved by applying rock bolts and pre-stressed anchor cables in engineering practice. Radial stress provided by these measures can turn the rock blocks into a state of triaxial stress, thereby enhancing its bearing capacity.
5) Multiple tunnel failure modes were obtained in the scaled model experiments. Despite some limitations in the study, the conclusions still provide important technical guidance to the construction of this tunnel complex. And it can reduce construction risk.

## Data availability statement

The original contributions presented in the study are included in the article/Supplementary Material, further inquiries can be directed to the corresponding authors.

## Author contributions

XG: contributed to conceptualization, methodology, analysis, and writing; CK, DW, and FL: contributed to validation, resources, and funding acquisition; CK and HW: contributed to experiment design, and data collection; FL, ML, and SR: contributed to investigation, supervision, and review editing. All authors have read and agreed to the published version of the manuscript.

## Conflict of interest

Authors DW and ML were employed by the company of Chongqing urban construction investment (group) Co., Ltd.

The remaining authors declare that the research was conducted in the absence of any commercial or financial relationships that could be construed as a potential conflict of interest.

## Publisher's note

All claims expressed in this article are solely those of the authors and do not necessarily represent those of their affiliated organizations, or those of the publisher, the editors and the reviewers. Any product that may be evaluated in this article, or claim that may be made by its manufacturer, is not guaranteed or endorsed by the publisher.

## References

Barton, Nick (2008). *International workshop (TC41) geotechnical infrastructure for mega cities and new capitals.* Brazil: Buzios.The main causes of the Pinheiros cavern collapse.

Cao, R. H., Cao, P., Fan, X., Xiong, X., and Lin, H. (2016). An experimental and numerical study on mechanical behavior of ubiquitous-joint brittle rock-like specimens under uniaxial compression. *Rock Mech. Rock Eng.* 49 (11), 4319–4338. doi:10.1007/s00603-016-1029-6

COI (2005). *Report of the Committee of Inquiry into the incident at the MRT circle line worksite that led to collapse of Nicoll Highway on 20 April 2004.* Singapore: Ministry of Manpower.

Duan, B. F., and Li, L. (2012). Study of construction technology for subsurface excavation of metro tunnel group in complex environment. *Chin. J. Rock Mech. Eng.* 31, 2776–2782.

Feng, W. K., Huang, R. Q., and Li, T. (2012). Deformation analysis of a soft-hard rock contact zone surrounding a tunnel. *Tunn. Undergr. Space Technol.* 32, 190–197. doi:10.1016/j.tust.2012.06.011

Hu, Z., Shen, J., Wang, Y., Guo, T., Liu, Z., and Gao, X. (2021). Cracking characteristics and mechanism of entrance section in asymmetrically-load tunnel with bedded rock mass: A case study of a highway tunnel in southwest China. *Eng. Fail. Anal.* 122, 105221. doi:10.1016/j.engfailanal.2021.105221

Itasca (2012). *User's guide for FLAC3D, version 3.0.*

John, A. H., and John, P. H. (2007). *Engineering rock mechanics.* first ed. Amsterdam: Elsevier, 106–107.

JTG D70-2004 (2004). *Code for design on highway tunnel.* Beijing, China: The Professional Standards Compilation Group of People's Republic of China.

Kim, S. H. (1996). *Model testing and analysis of interactions between tunnels in clay.* United States: Department of Engineering Science, University of Oxford.

Kong, C., Gao, X., Cao, L., and Liu, K. (2016). Analysis of the failure of primary support of a deep-buried railway tunnel in silty clay. *Eng. Fail. Anal.* 66, 259–273. doi:10.1016/j.engfailanal.2016.04.008

Li, M., Yu, H., Jin, H., and Liu, P. (2018). Methodologies of safety risk control for China's metro construction based on BIM. *Saf. Sci.* 110, 418–426. doi:10.1016/j.ssci.2018.03.026

Li, T., He, Y., and Fu, X. (2019). Dynamic risk assessment method and application of large deformation of high ground stress tunnel during construction period. *J. Eng. Geol.* 27 (1), 29–37.

Liang, Y., and Liu, Q. (2022). Early warning and real-time control of construction safety risk of underground engineering based on building information modeling and internet of things. *Neural Comput. Applic.* 34 (5), 3433–3442. doi:10.1007/s00521-021-05755-8

Liu, H. L., Li, P., and Liu, J. Y. (2011). Numerical investigation of underlying tunnel heave during a new tunnel construction. *Tunn. Undergr. Space Technol.* 26, 276–283. doi:10.1016/j.tust.2010.10.002

Liu, H. Y., Small, J. C., Carter, J. P., and Williams, D. J. (2009). Effects of tunnelling on existing support systems of perpendicularly crossing tunnels. *Comput. Geotechnics* 36, 880–894. doi:10.1016/j.compgeo.2009.01.013

Liu, W., Zhao, T., Zhou, W., and Tang, J. (2018). Safety risk factors of metro tunnel construction in China: An integrated study with EFA and SEM. *Saf. Sci.* 105, 98–113. doi:10.1016/j.ssci.2018.01.009

Pan, Y., Liu, Y., Tyagi, A., Lee, F. H., and Li, D. Q. (2021). Model-independent strength-reduction factor for effect of spatial variability on tunnel with improved soil surrounds. *Géotechnique* 71 (5), 406–422. doi:10.1680/jgeot.19.p.056

Qian, Q., and Lin, P. (2016). Safety risk management of underground engineering in China: Progress, challenges and strategies. *J. Rock Mech. Geotechnical Eng.* 8 (4), 423–442. doi:10.1016/j.jrmge.2016.04.001

Qiu, C. Y., Zheng, Y. R., Song, Y. K., Ge, S. M., and Yuan, Y. (2010). Failure pattern study and security analysis of tunnel affected by pile load. *Chin. J. Rock Mech. Eng.* 29, 3132–3143.

Wang, M. S. (2010). *Tunnelling and underground engineering technology in China.* Beijing: China Communication Press, 72–97.

Wang, W., Zhang, J., and Li, A. (2022). The application of the strength reduction shortest path method to the stability analysis of shallow buried tunnel. *Geotech. Geol. Eng.* 40 (3), 1091–1101. doi:10.1007/s10706-021-01944-3

Whittle, A. J. (2006). "Nicoll highway collapse: Evaluation of geotechnical factors affecting design of excavation support system," in International Conference on Deep Excavation, Singapore, June 28-30.

Xu, Z., Cai, N., Li, X., Xian, M., and Dong, T. (2021). Risk assessment of loess tunnel collapse during construction based on an attribute recognition model. *Bull. Eng. Geol. Environ.* 80 (8), 6205–6220. doi:10.1007/s10064-021-02300-8

Yu, J., Zhong, D., Ren, B., Tong, D., and Hong, K. (2017). Probabilistic risk analysis of diversion tunnel construction simulation. *Computer-Aided Civ. Infrastructure Eng.* 32 (9), 748–771. doi:10.1111/mice.12276

Zhang, H., Chen, L., Chen, S., Sun, J., and Yang, J. (2018). The spatiotemporal distribution law of micro seismic events and rockburst characteristics of the deeply buried tunnel group. *Energies* 11 (12), 3257. doi:10.3390/en11123257

Zhang, L. M., Zheng, Y. R., Wang, Z. Q., and Wang, J. X. (2007). Application of strength reduction finite element method to road tunnels. *Rock Soil Mech.* 28, 97–101.

Zhao, Y., Shi, Y., and Yang, J. (2021a). Study of the concrete lining cracking affected by adjacent tunnel and oblique bedded rock mass. *Iran. J. Sci. Technol. Trans. Civ. Eng.* 45 (4), 2853–2860. doi:10.1007/s40996-021-00710-y

Zhao, Y., Wang, Y., Wang, W., Tang, L., Liu, Q., and Cheng, G. (2019). Modeling of rheological fracture behavior of rock cracks subjected to hydraulic pressure and far field stresses. *Theor. Appl. Fract. Mech.* 101, 59–66. doi:10.1016/j.tafmec.2019.01.026

Zhao, Y., Zhang, C., Wang, Y., and Lin, H. (2021b). Shear-related roughness classification and strength model of natural rock joint based on fuzzy comprehensive evaluation. *Int. J. Rock Mech. Min. Sci.* 137, 104550. doi:10.1016/j.ijrmms.2020.104550

Zhao, Y., Zhang, L., Wang, W., Liu, Q., Tang, L., and Cheng, G. (2020). Experimental study on shear behavior and a revised shear strength model for infilled rock joints. *Int. J. Geomech.* 20 (9), 04020141. doi:10.1061/(asce)gm.1943-5622.0001781

Zheng, B. C., Cheng, W. B., and Hu, G. W. (2009). Analysis and monitoring of ground subsidence caused by excavation of adjacent and crossing metro tunnel with shallow-depth and subsurface excavation method. *J. Railw. Eng. Soc.* 124, 72–76.

Zheng, H., Li, P., and Ma, G. (2021). Stability analysis of the middle soil pillar for asymmetric parallel tunnels by using model testing and numerical simulations. *Tunn. Undergr. Space Technol.* 108, 103686. doi:10.1016/j.tust.2020.103686

Zheng, H., Li, P., Ma, G., and Zhang, Q. (2022). Experimental investigation of mechanical characteristics for linings of twins tunnels with asymmetric cross-section. *Tunn. Undergr. Space Technol.* 119, 104209. doi:10.1016/j.tust.2021.104209

Zheng, Y. R., Deng, C. J., and Zhao, S. Y. (2007). Development of finite element limiting analysis method and its applications in geotechnical engineering. *Eng. Sci.* 5, 10–36.

Zheng, Y. R., Qiu, C. Y., Zhang, H., and Wang, Q. Y. (2008). Exploration of stability analysis method for surrounding rocks of soil tunnel. *Chin. J. Rock Mech. Eng.* 27, 1968–1980.

Zheng, Y. R., Zhao, S. Y., Deng, C. J., Liu, M. W., Tang, X. S., and Zhang, L. M. (2006). Development of finite element limit analysis method and its applications to geotechnical engineering. *Eng. Sci.* 12, 39–61.

Zhou, Z., Goh, Y. M., and Li, Q. (2015). Overview and analysis of safety management studies in the construction industry. *Saf. Sci.* 72, 337–350. doi:10.1016/j.ssci.2014.10.006

# Key predisposing factors and susceptibility assessment of landslides along the Yunnan–Tibet traffic corridor, Tibetan plateau: Comparison with the LR, RF, NB, and MLP techniques

Sen Wang[1], Sixiang Ling[1,2]*, Xiyong Wu[1,2], Hong Wen[1,3], Junpeng Huang[1], Feng Wang[4] and Chunwei Sun[1]

[1]Faculty of Geosciences and Environmental Engineering, Southwest Jiaotong University, Chengdu, China, [2]MOE Key Laboratory of High-Speed Railway Engineering, Southwest Jiaotong University, Chengdu, China, [3]School of Architecture and Civil Engineering, Xihua University, Chengdu, China, [4]School of Information Technology, University of Sydney, Sydney, NSW, Australia

The Yunnan–Tibet traffic corridor runs through the Three Rivers Region, southeastern Tibetan Plateau, which is characterized by high-relief topography and active tectonics, with favourable conditions for landslides. It is of great significance to identify the key predisposing factors of landslides and to reveal the landslide susceptibility in this area. A total of 2,308 landslides were identified as learning samples through remote sensing interpretation and detailed field surveys, and four machine learning algorithms involving logistic regression (LR), random forest (RF), naïve Bayes (NB) and multilayer perceptron (MLP) were compared to model the landslide susceptibility. Through the multicollinearity test, 13 influential factors were selected as conditioning factors. The area under the curve (AUC) values of LR, RF, NB and MLP models are .788, .918, .785 and .836 respectively, indicating that the four models have good or very good prediction accuracy in landslide susceptibility assessment along the Yunnan–Tibet traffic corridor. In addition, the elevation, slope, rainfall, distance to rivers, and aspect play a major role in landslide development in the study area. The susceptibility zoning map based on the best RF model shows that the areas with high susceptibility and very high susceptibility account for 12.24% and 6.72%, respectively, and are mainly distributed along the Jinsha River, the Lancang River and the G214 highway.

## 1 Introduction

The Yunnan–Tibet traffic corridor is located in the Three Rivers Region in the southeastern part of the Qinghai–Tibet Plateau, and the corridor mainly involves the G214 National Highway and the planned corridor. The Jinsha River, Lancang River, and Nujiang River flow southward parallel to the Three Rivers Region. The geological environment is fragile due to steep terrain, substantial river incision, active tectonic activity, weak lithology, and frequent earthquakes (Zhang et al., 2000; Zhang et al., 2016). These internal and external dynamics of geological processes provide favourable conditions for the occurrence of geological hazards,

especially landslides (Li et al., 2019; Ling et al., 2021; Zhao et al., 2019; Yan et al., 2022). Landslides are the most critical type of geological disaster and have the characteristics of a wide distribution area, high frequency of occurrence, fast movement speed, and severe losses. Because of the uplift of the Qinghai–Tibet Plateau, the internal and external dynamic geological processes are enormously intertwined, and creating complex geological conditions and intense dynamic valley processes; these processes bring more uncertainty to the occurrence of landslides in the Yunnan–Tibet traffic corridor (Peng et al., 2004; Peng et al., 2020). Frequent landslides not only cause heavy casualties and property losses but also seriously affect the construction and safe operation of Yunnan–Tibet highways and planned corridors and restrict the development of the regional economy. However, landslide investigations in the study area are limited due to factors such as high elevations, and poor traffic conditions. Therefore, it is of great significance to integrate the existing survey data, analyse the key predisposing factors, and predict the potential landslide-prone zones in the area.

Landslide susceptibility evaluation is based on existing landslide investigations and evaluates the possibility of landslide occurrence under a combination of conditioning factors (Niu et al., 2012; Wen et al., 2022). The common methods for landslide susceptibility evaluation include deterministic and non-deterministic methods (Kavzoglu et al., 2019). The deterministic method is mainly based on the quantitative calculation of slope stability. Non-deterministic methods mainly include mathematical analytical methods, such as the analytic hierarchy process, fuzzy comprehensive evaluation, information method, probability ratio, logistic regression, neural network, support vector machine, etc. (Yao et al., 2008; Youssef et al., 2016; Kavzoglu et al., 2019; Huang et al., 2020; Ling et al., 2022). These methods have achieved good application results in evaluating regional landslide susceptibility. In recent years, with the rapid development of artificial intelligence, machine learning algorithms have been applied by many researchers in the fields of earthquake prediction, groundwater storage change prediction, precipitation data correction, and landslide susceptibility mapping (Yao et al., 2008; Youssef et al., 2016; Kavzoglu et al., 2019; Huang et al., 2020; Ling et al., 2022). These frequently used algorithms mainly include regression algorithms, instance-based learning, neural network (NN) algorithms, Bayesian algorithms, kernel-based learning algorithms and decision tree (DT) algorithms (Huang et al., 2022b). However, different algorithm models have their unique characteristics, and the performance of each model varies according to the input data, model structure, and accuracy (Nachappa et al., 2020). Therefore, it is not reliable to use only one algorithm model for landslide susceptibility assessment in a region, and it requires comparative evaluation of multiple models.

Logistic regression (LR) algorithm is a kind of regression algorithms. LR, which is a multivariable analysis model, and can be used to predict the presence or absence of characteristics or results according to the values of a group of prediction variables. The advantages of LR are fast training speed, easy to use and explain. However, LR cannot be used to solve non-linear problems, because the decision surface of logical regression is linear, and it is more sensitive to multicollinearity data (Ayalew and Yamagishi, 2005; Pradhan and Lee 2010). Pham et al. (2017a) evaluated and compared prediction capability of Bagging Ensemble Based Alternating Decision Trees (BADT), LR, and J48 Decision Trees (J48DT) for landslide susceptibility mapping at part of the Uttarakhand State (India),

and the three landslide models all performed well. Among them, BADT model has the highest prediction ability in the validation data set, followed by LR model and J48DT model. Random forest (RF) algorithm is a kind of DT algorithms, which is an ensemble of separately trained binary decision trees (Ravì et al., 2016). RF model can handle a large number of input variables without deleting variables, and return a very small classification set to maintain high prediction accuracy (Zhang et al., 2017). In addition, RF models have no prior assumptions about model dependency and can handle classified data and continuous data. However, when more trees are added, the RF model will not over fit, but will produce a small generalization error (Peters et al., 2007; Ließ et al., 2012). Chen et al. (2018) used the best-first decision tree, random forest, and naïve Bayes tree to evaluate the landslide susceptibility in the Longhai area of China. Comparing the evaluation results of the three models, the RF has the best performance. Naïve Bayes (NB) algorithm is a kind of Bayesian algorithms, which is an independent feature model with simple probability classification. Due to its simplicity of construction of no requirement of complex iterative parameter estimation scheme, it has stable classification efficiency and performs well for small-scale data (Sikorska and Seibert, 2018). However, its shortcomings are also obvious, because the assumption that the attributes of the NB model are independent of each other is often untenable in practical applications. When the number of attributes is large or the correlation between attributes is good, the classification effect is poor (Lee et al., 2020). Lee et al. (2020) used NB and Bayesian network models to draw landslide susceptibility map in Umyeonsan, Korea. Both of the two models have relatively high accuracy, and the performance of NB model is slightly better than that of Bayesian network model. Multilayer perceptron (MLP) algorithm is a kind of NN algorithms. It is defined as a biological excitation feed-forward network composed of multiple layers, each layer containing multiple artificial neuron units (Yan et al., 2006). Multilayer structure and non-linear activation function enable MLP to identify non-linearly separable data with high accuracy. However, the neural unit is prone to death, leading to data diversification and loss (Kavzoglu et al., 2019). Hong et al. (2019) applied four models, NB, MLP, kernel logistic regression (KLR), and J48 bagging, to evaluate the susceptibility of landslides in Youfang area, China. It is found that the MLP model is the most stable and reasonable.

In this paper, we identified landslides by remote sensing interpretation and field geological survey verification and constructed conditioning factor combinations. Then, four machine learning methods, namely, logistic regression, multilayer perceptron, random forest, and naïve Bayes, were used to draw landslide susceptibility index maps. Finally, these results were compared and evaluated with mathematical methods and knowledge from field surveys. This study can provide a reference for the planning and construction of roads, railways, and hydropower projects in the region.

# 2 Geological settings

This paper selects the river basin along the G214 National Highway from Shangri-La County to Bangda town as the study area, with a total area of 23,858.54 km$^2$. The study area is the 35 km buffer zone on both sides of the highway and the intersection of the area within the first watershed (Figure 1).
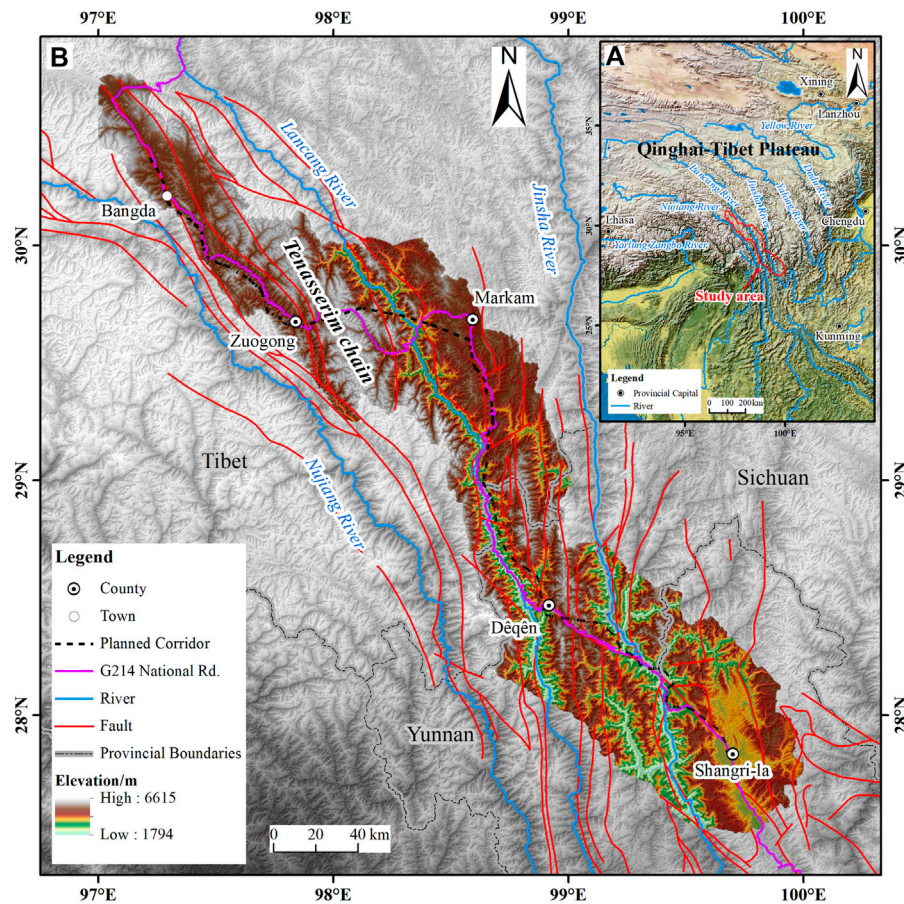
**FIGURE 1**
Location and tectonic map of the study area. **(A)** Study area location index map. **(B)** Regional topographic and tectonic map.

The study area is located at the southeastern edge of the collisional extrusion zone between the Eurasian and Indian plates, and the regional tectonic line is spreading north–south under solid extrusion. In addition, the neotectonic movements are intense (Peng et al., 2004). The active fault zones mainly include the Dêqên–Zhongdian fault zone, the Batang fault zone, the Jinsha fault zone, the Lancang fault zone, and the Nujiang fault zone (Chai et al., 2021). The stratigraphy of the region is well distributed and involves almost all eras, and a wide variety of rocks is present. Mesozoic terrestrial lacustrine, fluvial mudstone, and muddy sandstone strata are widely exposed, with significant thicknesses, complex lithologies, and rapid phase changes, and they are mostly soft rocks. Some areas contain slate, schist, micrite, and other metamorphic rocks. Magmatism is active, and the magmatic bodies are enormous. In addition, sedimentary rocks and early granites are generally subject to varying degrees of low-temperature and high-pressure powerful metamorphism.

Regarding geomorphological units, the area is located on the southeastern edge of the Tibetan Plateau in the middle and northern sections of the Hengduan Mountains. The area is characterized by high mountain and valley landscapes, with intermontane basins and lakes of varying sizes, juxtaposed peaks and valleys, and consistent spreading directions. The mountains are steep, most are above 4,000 m in absolute height, and the peaks are above 5,000 m, some of which reach 6,000 m or more; the peaks have year-round snow and modern glaciers. Due to the increased downcutting force of the river, the high mountain valley terrain is very well developed, with relative height differences reaching 1,000 to 1,500 m. In the north–central part, away from the gorge, the plateau surface is at altitudes of 4,200 to 4,300 m, representing a well-preserved level of ravines, and the tributaries of the three rivers have slower drops. The whole region is mainly influenced by the warm and humid air currents of both the Southeast Pacific Ocean and Southwest Indian Ocean. The distribution of the annual precipitation in the study area shows an overall trend of decreasing from southwest to northeast. At the same time, the seasonal distribution of precipitation is highly uneven, with distinct rainy and dry seasons. The rainy season is between June and September and accounts for more than 80% of the year.

# 3 Data and methodology

The entire landslide susceptibility assessment process includes the following five steps (Figure 2): 1) preparing a landslide inventory; 2) selecting and assessing the landslide conditioning factors; 3) modeling process using the LR, MLP, RF, and NB models; 4) validating and
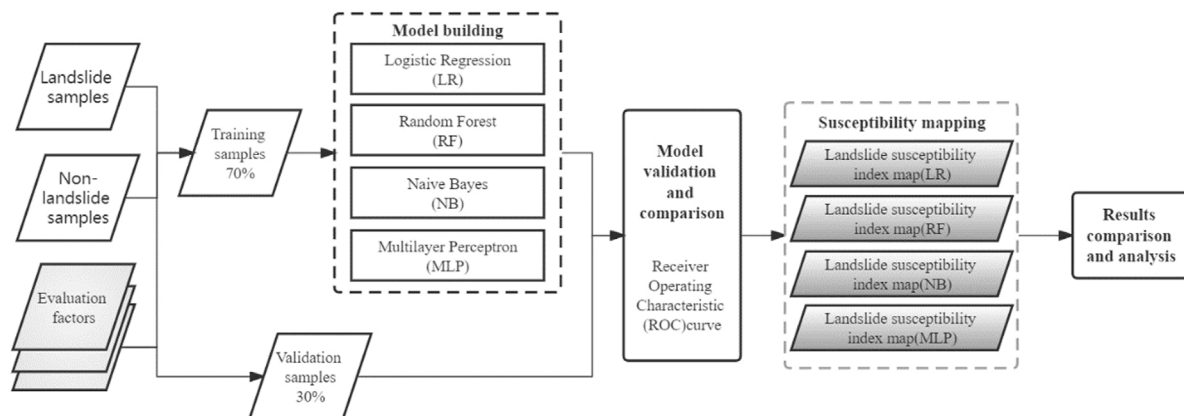
**FIGURE 2**
Flow chart of landslide susceptibility evaluation.
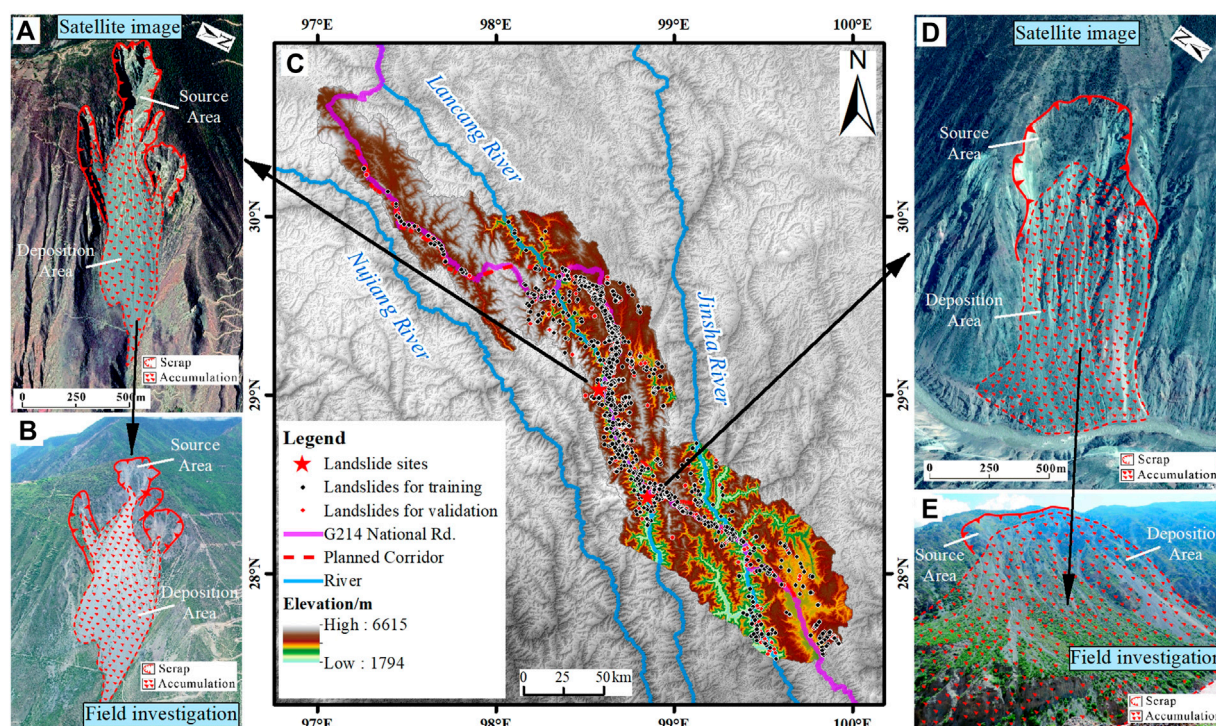


**FIGURE 3**
Landslide inventory map with interpretation and field validation examples. **(A,D)** Landslide interpretation from remote sensing images. **(B,E)** Field validation photographs corresponding to **(A,D)**, respectively. **(C)** Landslide inventory map.

comparing the susceptibility models; and 5) producing landslide susceptibility maps.

## 3.1 Landslide inventory map

Landslide inventory is an essential input data for landslide modeling, and accurate landslide location is an important guarantee for reliable landslide susceptibility assessment.

Remote sensing interpretation can be carried out according to landslide image features (e.g., rock exposure and vegetation damage) on satellite images and landslide geomorphological features (e.g., crown, headscarp, abnormal benches and landslide acceleration mass) on digital elevation model (DEM). Then, field surveys were carried out to confirm the landslide characteristics such as the headscarf, tension cracks, grab ends, undrained depressions, bulges, and lobes.

TABLE 1 Conditioning factors and data sources.

| Type | Evaluate factors | Data sources |
|---|---|---|
| Topography and geomorphology | Elevation, slope, aspect, plan curvature, profile curvature, and TWI | Advanced Land Observing Satellite World 3D– 30 m (AW3D30) (30 m resolution) |
| | | https://www.eorc.jaxa.jp/ALOS/en/index_e.htm |
| Geological structure and lithology | Engineering rock groups, fault | 1:200,000-scale regional geological map |
| | | http://www.ngac.org.cn/ |
| Meteorology and hydrology | Mean annual rainfall | Statistical interpolation of meteorological data in the study area and surrounding stations from 1981 to 2010 |
| | | http://data.cma.cn/ |
| | River | 1:250,000 public geographic data of China Geographic Information Resource Directory Service System |
| | | https://www.webmap.cn/ |
| Human activity | Road | 1:250,000 public geographic data of China Geographic Information Resource Directory Service System |
| | | https://www.webmap.cn/ |
| Surface coverage | NDVI | Landsat-8 remote sensing data |
| | | https://earthexplorer.usgs.gov |
| | Landcover | 30 m Land Cover Data of China Geographic Information Resource Directory Service System |
| | | https://www.webmap.cn/ |

Through remote sensing interpretation of satellite images in the study area, we identified 2,308 landslide hazard points and verified 80% of landslides through two-month-long field surveys in August 2017 and August 2020. These landslide samples (Figure 3) are mainly distributed in the Jinsha River valley, Lancang River valley, and along the G214 highway. ArcGIS software was used to randomly generate the same number of random points for the landslide samples as the non-landslide samples (2,308), forming a total data set of 4,616 samples. Of these, 3,232 (70%) samples were randomly selected for machine learning modelling. The remaining 1,384 (30%) samples were used for model testing, with the same number of landslide and non-landslide samples in the training and testing samples.

## 3.2 Landslide conditioning factors

### 3.2.1 Preparation of landslide condition factor data

Reviewing the previous literature and combining the geological characteristics of the region, the following 13 quantifiable extraction factors were selected: elevation, slope angle, slope aspect, plan curvature, profile curvature, engineering rock group, distance to faults, distance to rivers, topographic wetness index (TWI), mean annual rainfall, normalized difference vegetation index (NDVI), land cover, and distance to roads (Table 1) (Reichenbach et al., 2018; Yao et al., 2020). Among them, the basic topographic and geomorphic factors, such as elevation, slope, aspect, plan curvature, profile curvature, and TWI, were calculated from the Advanced Land Observing Satellite (ALOS) World 3D– 30 m (AW3D30) (30 m × 30 m resolution) data that are freely disclosed by the geographic data cloud; the engineering rock group and fault data are from the 1:

200,000-scale regional geological map; the NDVI data are calculated from Landsat-8 remote sensing data (2021.04.23-2021.05.08); and the data on rivers, roads, rainfall, and land cover are all from online public data. Considering the actual situation of the study area, a grid unit of 90 m × 90 m was finally selected, with a total of 2,942,534 grids.

Through ArcGIS software, the distribution map of each conditioning factor was drawn (Figure 4). Among all factors, specific values cannot be given for engineering rock groups and land cover types. The data were divided into 6 engineering rock groups according to the degree of softness and hardness of the main lithology of the stratum (Yao et al., 2020). Group 1 includes bulk structure and is mainly composed of Pleistocene and Holocene strata; Group 2 includes soft and weak rock layers that are mainly composed of conglomerate, mudstone, and shale; Group 3 contains softer rock layers that are mainly composed of slate, sandstone, and muddy tuff; Group 4 contains harder rock layers that are mainly composed of tuff and dolomite; Group 5 includes hard rock layers that are mainly composed of ejecta; and Group 6 contains tough rock layers that are mainly composed of intrusive rocks (Figure 4F). The range of NDVI values is -1 to 1. When the NDVI is less than 0, the surface is a water system, glaciers, or snow, and when the NDVI is 0, the surface is rock or bare soil. When the NDVI is greater than 0, the surface is vegetation, and when the NDVI is larger, the vegetation is lusher (Figure 4K).

### 3.2.2 Multicollinearity test for landslide conditioning factors

Multicollinearity among evaluation factors should be considered in screening susceptibility factors (Tamura et al., 2019). Multicollinearity refers to the fact that the explanatory variables in the model are not objective and accurate because of the precise or high

**FIGURE 4**
(Continued).
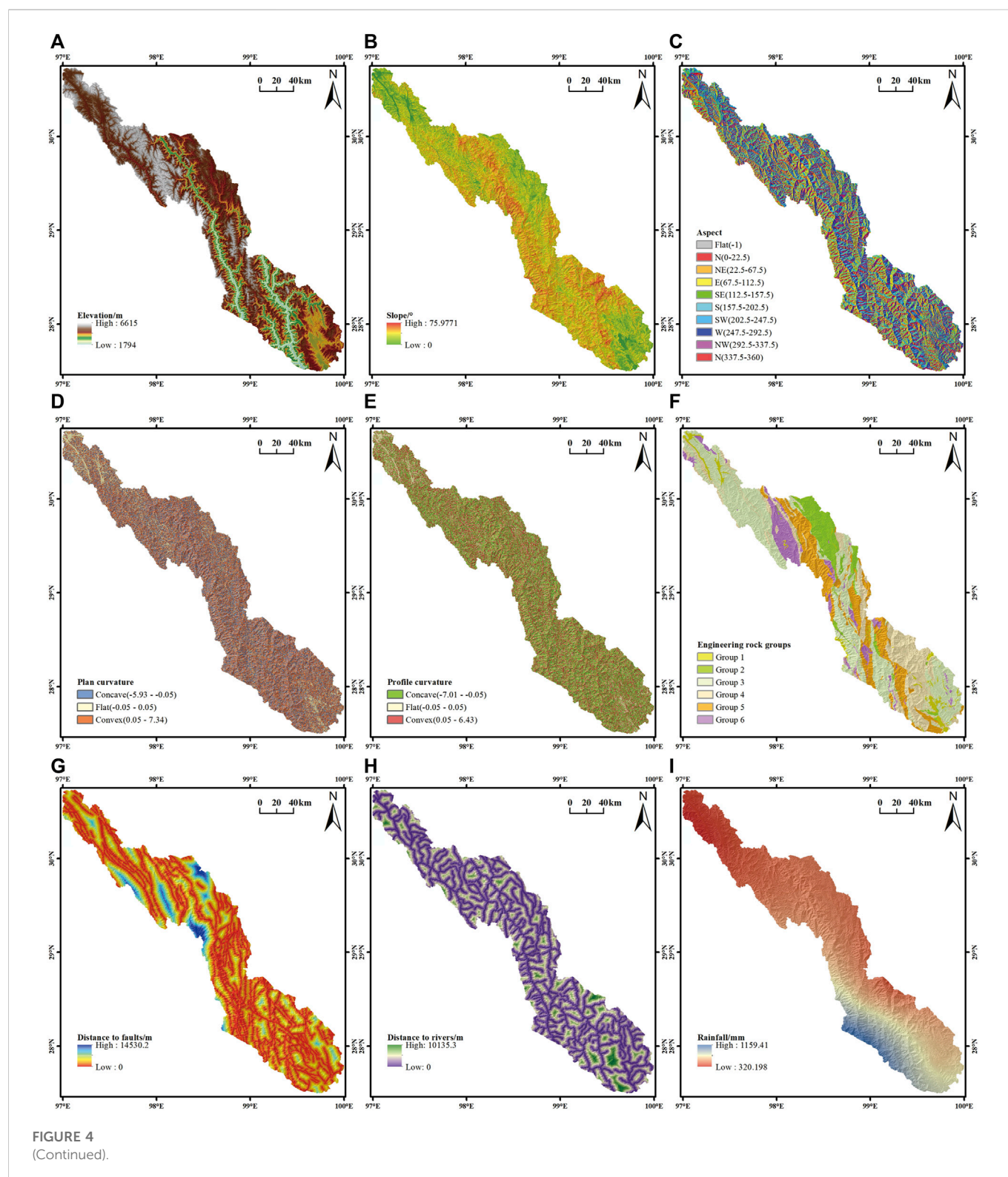
correlation (Thompson et al., 2017). This paper tested multicollinearity by applying the variance inflation factor (VIF) and tolerance. The *VIF* is reciprocal to the tolerance values, which are calculated using Equations 1, 2:

$$Tolerance = 1 - R_J^2 \qquad (1)$$

$$VIF = \left[\frac{1}{Tolerance}\right] \qquad (2)$$

where $R_J^2$ is the coefficient of determination of a regression of explanator $j$ on all the other explanators. The threshold value of tolerance and the *VIF* is greater than .1. The closer the *VIF* value is to 1,
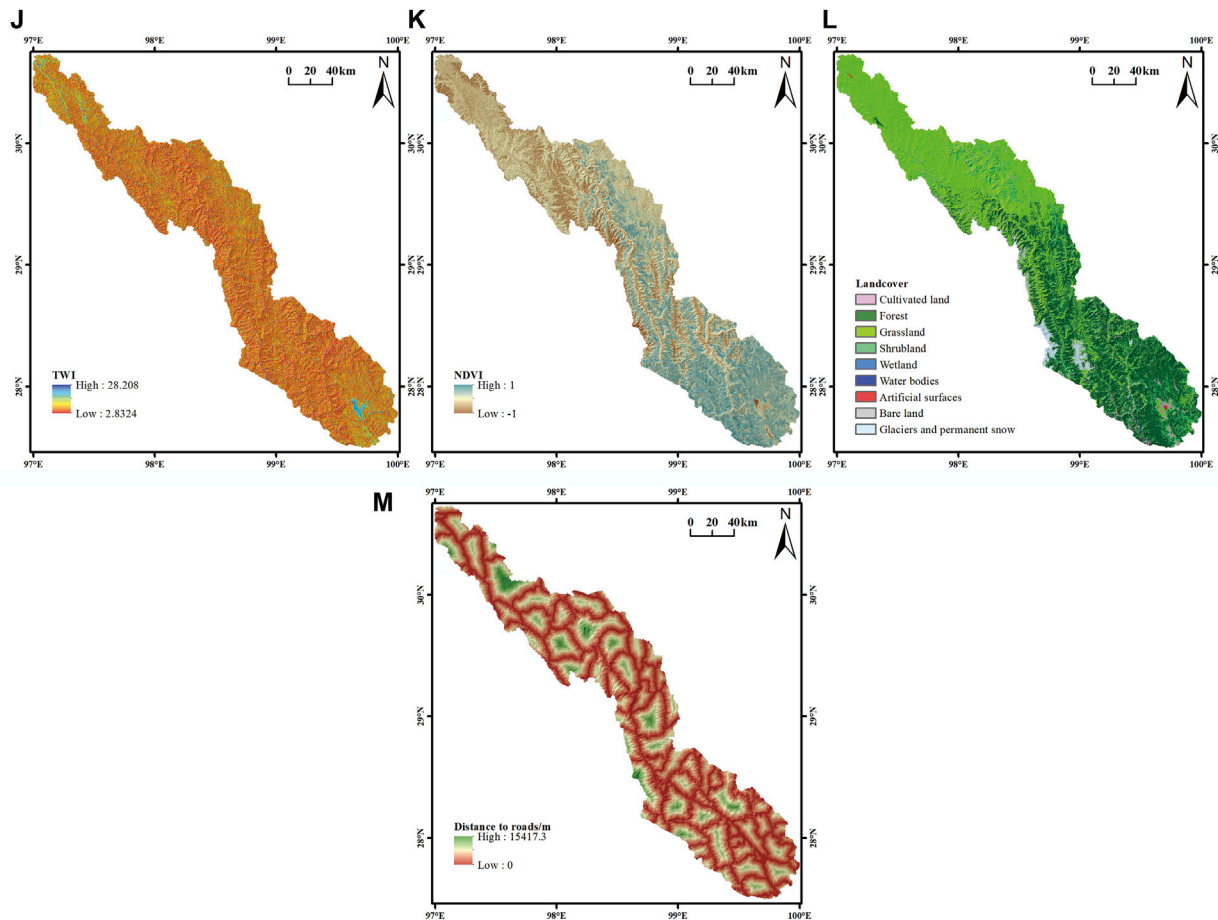
**FIGURE 4**
Conditioning factor distribution. **(A)** elevation; **(B)** slope; **(C)** aspect; **(D)** plan curvature; **(E)** profile curvature; **(F)** engineering rock groups; **(G)** distance to faults; **(H)** distance to rivers; **(I)** rainfall; **(J)** TWI; **(K)** NDVI; **(L)** land cover, and **(M)** distance to roads.

the lighter the multicollinearity is, and *vice versa* (Thompson et al., 2017). Generally, 10 is used as the judgement boundary. When the $VIF < 10$, there is no multicollinearity; when $10 \leq VIF <100$, there is strong multicollinearity; and when the $VIF \geq 100$, there is severe multicollinearity. Arabameri et al. (2019) used multicollinearity analysis to test the topographical, geomorphological, and environmental factors for landslide susceptibility mapping. In the current research, the multicollinearity of the thirteen landslide conditioning factors (LCFs) was tested using SPSS software.

## 3.3 Landslide susceptibility models

### 3.3.1 Logistic regression (LR)

The LR is a generalized linear regression analysis model that can better solve the problem of binary variables in the vulnerability assessment of geological disasters (Ozdemir and Altural, 2013). In the current situation, the dependent variable is a binary variable representing presence or absence of landslide. Where the dependent variable is binary, the logistic link function is applicable (Atkinson and Massari, 1998). When the probability of an event is $P$, the range of $P$ values is 0–1, and the probability of the event not occurring is $1- P$. When the probability value $P$ is close to 0 or 1, it is difficult to determine the value of $P$, so it is necessary to transform the

value of $P$ and take the natural logarithm of $P/(1- P)$, which is called the Logit transform, that is, Logit $P =z$, so $P$ is:

$$P = \frac{1}{1 + e^{-z}} \tag{3}$$

$$z = \beta_0 + \beta_1 x_1 + \beta_2 x_2 + \cdots +\beta_n x_n \tag{4}$$

where $x_1, x_2, \cdots, x_n$ is the landslide impact factor; $\beta_0$ is the constant term; and $\beta_1, \beta_2, \cdots, \beta_n$ are the regression coefficients.

### 3.3.2 Multilayer perceptron (MLP)

MLP is a feed-forward artificial neural network model that maps multiple input data sets to a single output data set (Ramchoun et al., 2016). A single-layer perceptron can learn only linear functions, while MLP can also learn non-linear functions, which is suitable for non-linear problems, such as landslide susceptibility evaluation. The parameters of MLP mainly include the number of neurons in the hidden layer and the type of activation function. The role of the activation function is to introduce non-linearity into the neuron's output (Lin et al., 2008; Bui et al., 2016). MLP can use any form of activation function, but to learn efficiently using the backpropagation algorithm, the activation function must be restricted to be differentiable. Commonly used activation functions include sigmoid, tanh, and ReLU. In the landslide susceptibility mapping, input layer is the landslide conditioning factors, output layer is the

**TABLE 2 Inspection table for the VIF values of the landslide evaluation factor.**

| Conditioning factor | VIF | Conditioning factor | VIF | Conditioning factor | VIF |
|---|---|---|---|---|---|
| Elevation | 2.25 | Engineering rock groups | 1.16 | Landcover | 1.16 |
| Slope | 1.91 | Distance to faults | 1.21 | NDVI | 1.27 |
| Aspect | 1.03 | Distance to rivers | 1.23 | Distance to roads | 1.39 |
| Plan curvature | 1.65 | TWI | 2.01 | — | — |
| Profile curvature | 1.44 | Rainfall | 1.60 | — | — |
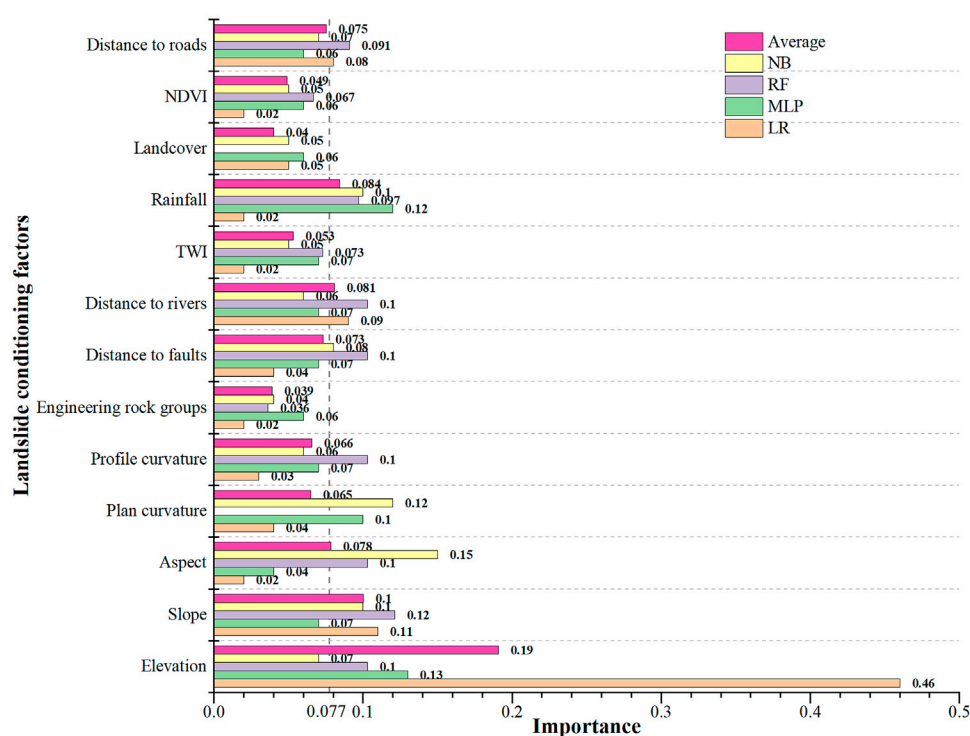


**FIGURE 5**
Relative importance of landslide conditioning factors.

result (1 or 0) class, and the hidden layer is the classifying tool (Ermini et al., 2005; Zare et al., 2013). In this paper, let $x = x_i$, $i = 1, 2, \ldots 13$ be the vector of the 13 landslide induced factors, y = 1 or 0. The formula of MLP for classification is

$$y = f(x) \tag{5}$$

where $f(x)$ is an hidden function (Pham et al., 2017b).

### 3.3.3 Random forest (RF)

RF mainly obtains the optimal classification result through the voting results of each tree in multiple decision trees (Youssef et al., 2016). Each decision tree has more comprehensive variable input information due to the method of replacement and the data set obtained by randomly obtaining data features. The model's robustness can be improved by integrating multiple decision trees, which can prevent model overfitting (Ravì et al., 2016). The main feature of the RF model is that it can give the Gini index of the corresponding input variable, that is,

the importance order of each input variable. In the RF tree, impurity is used to measure the optimal segmentation, and the importance of the basic environmental factor is calculated by the reduction value $D_{Gk}$ of the Gini index of environmental factor $k$ when the node is divided (Masetic and Subasi, 2016). It involves calculating the percentage of the average Gini reduction in the sum of the average Gini reductions of all basic environmental factors, as follows:

$$P_k = \frac{\sum_{h=1}^{n} \sum_{j=1}^{t} D_{Gkhj}}{\sum_{k=1}^{m} \sum_{h=1}^{n} \sum_{j=1}^{t} D_{Gkhj}} \tag{6}$$

where $m$, $n$, and $t$ are the total numbers of basic environmental factors, the number of classification trees and the number of nodes in a single tree, respectively; $D_{Gkhj}$ is the reduction value of the Gini index of the $k$th factor on the $j$th node of the $h$th tree; and $P_k$ is the $k$th factor in the severity of the underlying environmental factors.
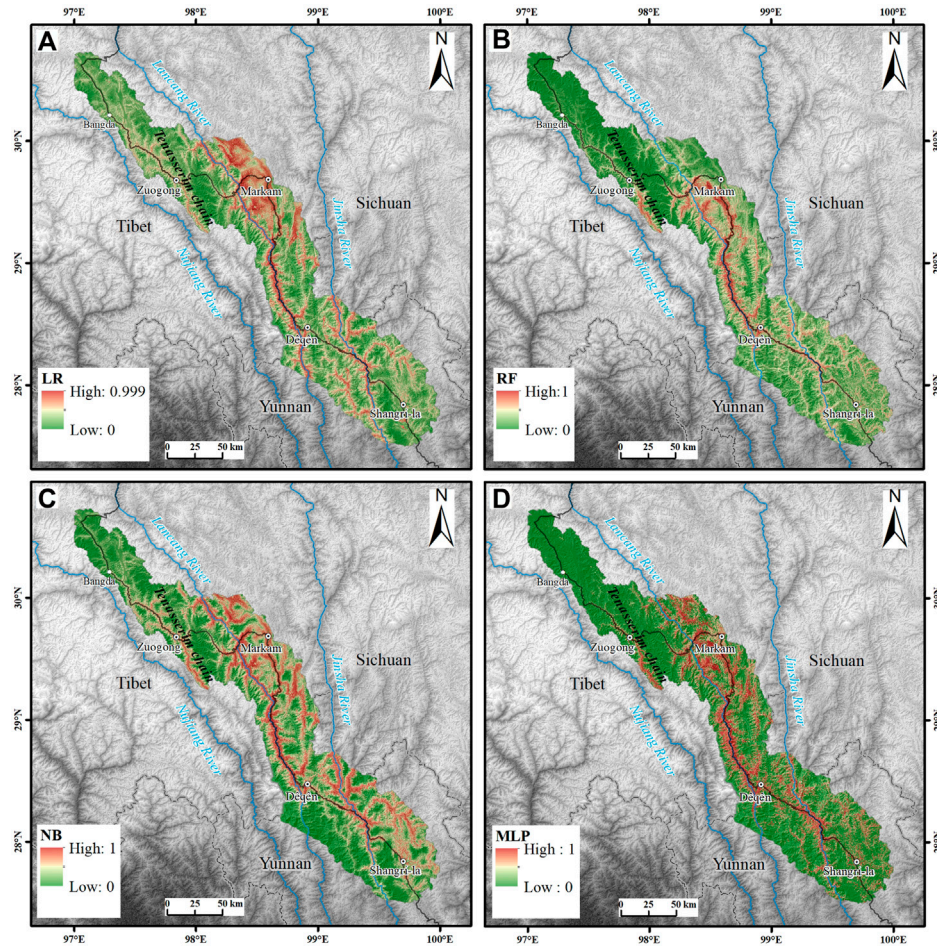
**FIGURE 6**
Landslide susceptibility index maps. **(A)** LR model **(B)** RF model **(C)** NB model **(D)** MLP model.

**TABLE 3 Statistical index results of different models.**

| Parameters | LR | RF | NB | MLP |
|---|---|---|---|---|
| True postive | 494 | 599 | 520 | 531 |
| Ture negitive | 509 | 551 | 469 | 513 |
| False positive | 183 | 141 | 223 | 179 |
| False negative | 198 | 93 | 172 | 161 |
| PPR/% | 72.97 | 80.95 | 69.99 | 74.79 |
| NPR/% | 71.99 | 85.56 | 73.17 | 76.11 |
| Sensitivity/% | 71.39 | 86.56 | 75.14 | 76.73 |
| Specificity/% | 73.55 | 79.62 | 67.77 | 74.13 |
| ACC/% | 72.47 | 83.09 | 71.46 | 75.43 |
| $F_1$ | .72 | .84 | .72 | .76 |
| $k$ | .45 | .66 | .43 | .51 |

## 3.3.4 Naïve bayes (NB)

NB is a method based on Bayes' theorem and assumes that feature conditions are independent of each other (Kavzoglu et al., 2019). First,

through the given training set, with the assumption that the feature words are independent of each other, the joint probability distribution is learned from input to output, and then based on the learned model, $X$ is input to find the output $Y$ that maximizes the posterior probability (Bhargavi and Jyothi, 2009).

There is a sample data set $D = \{d_1, d_2, \cdots, d_n\}$, and the feature attribute set corresponding to the sample data is $X = \{x_1, x_2, \cdots, x_d\}$. The class variable is $Y = \{y_1, y_2, \cdots, y_m\}$, that is, $D$ can be divided into $y_m$ categories. $X = \{x_1, x_2, \cdots, x_d\}$ is independent and random; then, the prior probability of $Y$ is $P_{prior} = P(Y)$, and the posterior probability of $Y$ is $P_{post} = P(Y|X)$. The posterior probability obtained by the NB algorithm can be calculated from the prior probability $P_{post} = P(Y|X)$, the evidence $P(X)$, and the class conditional probability $P(X|Y)$:

$$P(Y|X) = \frac{P(Y)P(X|Y)}{P(X)} \tag{7}$$

NB is based on the independence of each feature. In the case of a given category $y$, the above formula can be further expressed as follows:

$$P(X|Y = y) = \prod_{i=1}^{d} P(x_i|Y = y) \tag{8}$$

**FIGURE 7**
ROC curve of the prediction rate for the RF, MLP, NB, and LR
models with the validation data set.
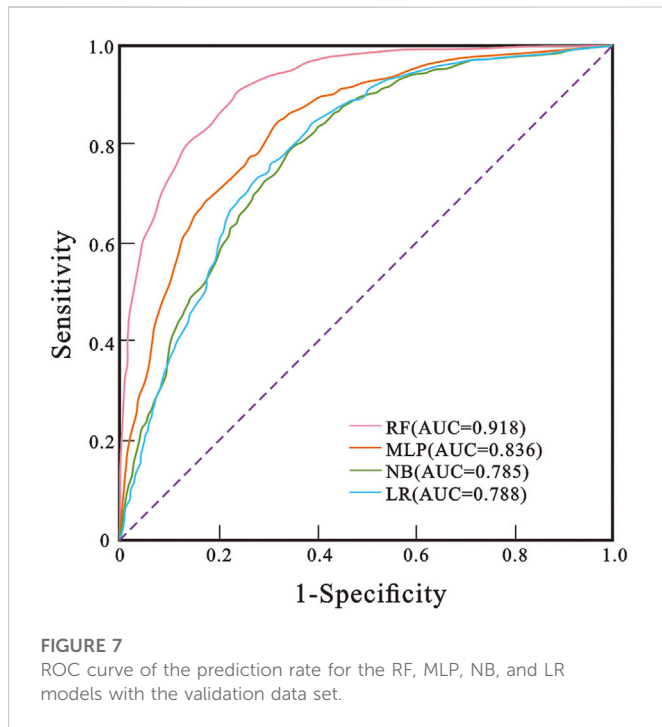
From the above two equations, the posterior probability can be
calculated as follows:

$$P_{post} = P(Y|X) = \frac{P(Y)\prod_{i=1}^{d}P(x_i|Y)}{P(X)} \quad (9)$$

Since the number of $P(X)$ is fixed, only the numerator part of the
above formula needs to be compared when comparing the posterior
probability. Therefore, a NB calculation in which the sample data
belong to category $y_i$ can be obtained:

$$P(y_i|x_1, x_2, \cdots, x_d) = \frac{P(y_i)\prod_{j=1}^{d}P(x_j|y_i)}{\prod_{j=1}^{d}P(x_j)} \quad (10)$$

## 3.4 Model validation

Positive predictive rate (*PPR*), negative predictive rate (*NPR*),
*sensitivity*, *specificity*, accuracy (*ACC*), F-measure (*F₁*), and
Cohen's kappa (*k*) coefficient are seven statistical indicators
that are widely used to define the performance of spatial
models (Pham et al., 2020). The highest value of the statistical
index is 1. The higher the value, the better the model performance
(Chen et al., 2018). The performance of the four models is
evaluated by calculating the above seven statistical index values
of LR, MLP, RF and NB model validation data sets. The formula is
calculated as follows (Huang et al., 2020):

$$PPR = \frac{TP}{TP + FP} \quad (11)$$

$$NPR = \frac{TN}{TN + FN} \quad (12)$$

$$Sensitivity = \frac{TP}{TP + FN} \quad (13)$$

$$Specificity = \frac{TN}{FP + TN} \quad (14)$$

$$ACC = \frac{TP + TN}{TP + FP + TN + PN} \quad (15)$$

$$F_1 = \frac{2 \times Sensitivity \times PPR}{Sensitivity + PPR} \quad (16)$$

$$k = \frac{ACC - ACC_{exp}}{1 - ACC_{exp}} \quad (17)$$

$$ACC_{exp} = \frac{(TP + FN)(TP + FP) + (FP + TN)(TN + FN)}{(TP + TN + FP + FN)^2} \quad (18)$$

where *TP* (true positive) and *TN* (true negative) are the numbers of
pixels that are correctly classified as landslides. *FP* (false positive) and
*FN* (false negative) are the numbers of pixels that are incorrectly
classified. $ACC_{exp}$ is the expected accuracy.

The receiver operating characteristic (ROC) curve reflects the
relationship between sensitivity and specificity (Mandrekar, 2010).
It is a graph generated at different thresholds from the false positive
rate (1-*specificity*) on the *x*-axis and the true positive rate (*sensitivity*)
on the *y*-axis. *Sensitivity* and *specificity* represent the probability that
the model correctly judges landslides and non-landslides. However,
these two indicators cannot show the overall accuracy of the model
performance, so the area under the curve (AUC) value is generally
used to test the model accuracy. The *AUC* value refers to the area
enclosed by the ROC curve and the coordinate axis and is an
evaluation index for calculating the performance of the binary
classifier. The *AUC* value ranges from 0 to 1, and the closer the
*AUC* value is to 1, the higher the prediction accuracy of the model
(Mandrekar, 2010; Shahabi et al., 2019).

# 4 Results

## 4.1 Assessment and comparison of landslide conditioning factors

By extracting the training data set and performing collinearity
diagnosis on the values of all evaluation factors of each sample, Table 2
is obtained. The results show that the *VIF* values of all landslide
conditioning factors are lower than the threshold value of 10, of which
the maximum value is only 2.25 and the minimum value is 1.03. There
is no multicollinearity problem among the factors influencing the
landslides in the study area, and all proposed landslide conditioning
factors are suitable for use in the study area.

In the process of landslide modelling through a machine learning
algorithm, the importance of each conditioning factor can be obtained
by analysing the characteristics of variables. The importance obtained
by different algorithms is inconsistent, as shown in Figure 5. If the
importance of each conditional factor is equal, the importance of the
conditional factor is 1/13, equal to .077. We believe that the condition
factor with importance greater than .077 is the main factor controlling
the landslide development. In the LR model, elevation, slope, distance
to rivers and distance to roads are the main factors; in the MLP model,
elevation, rainfall and plan curvature are the main factors; in the RF
model, elevation, slope, distance to rivers, profile curvature, aspect,
rainfall and distance to roads are the main factors; in the NB model,
aspect, plan curvature, slope, rainfall and distance to faults are the
main factors. Among the four models, the elevation, slope and rainfall
importance of three models are the main factors; the distance to rivers,
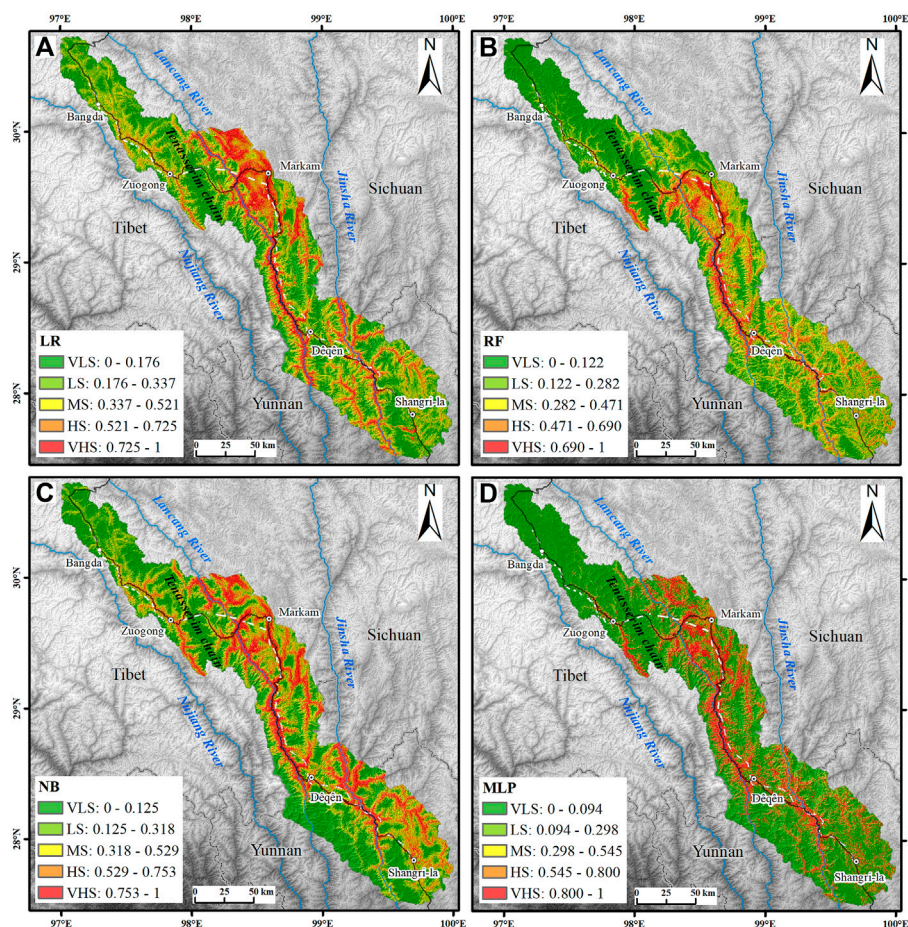
**FIGURE 8**
Landslide-prone zoning using the **(A)** LR method, **(B)** RF method, **(C)** NB method, and **(D)** MLP method. VLS, very low susceptibility; LS, low susceptibility; MS, moderate susceptibility; HS, high susceptibility; VHS, very high susceptibility.
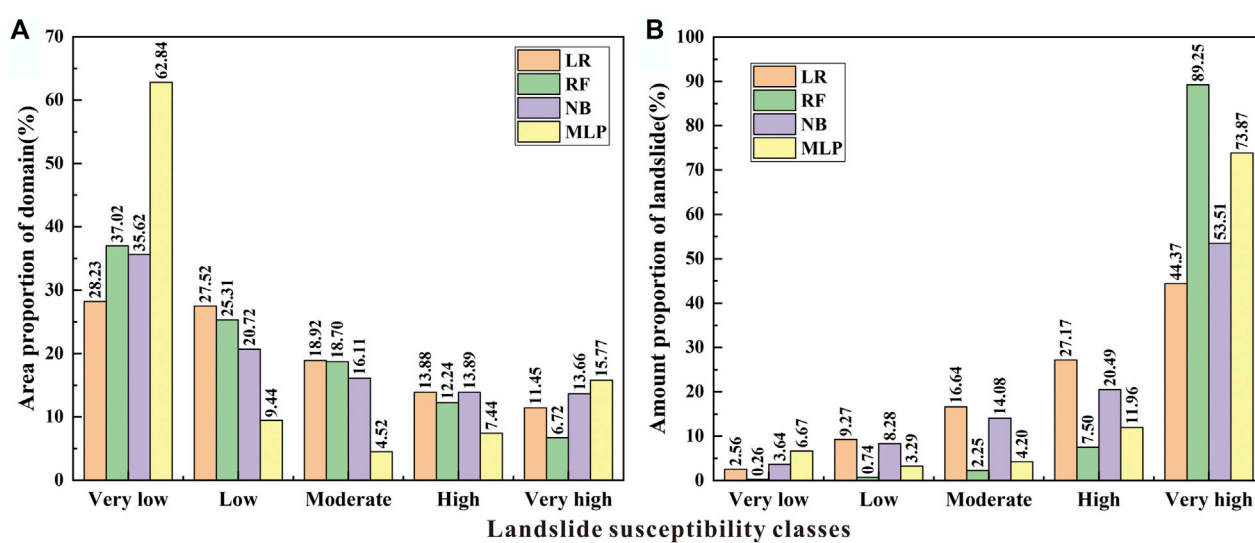


**FIGURE 9**
Quantitative analysis of the landslide susceptibility maps. **(A)** Area proportion of the domain in each susceptibility class. **(B)** Proportion of landslides in each susceptibility class.

aspect, distance to roads, distance to faults and plan curvature importance of two models are the main factors; the profile curvature importance of one model is the main factor; and the TWI, NDVI, landcover and engineering rock groups importance of none model are the main factors. It can be found that topographic factors (elevation, slope, aspect, plan curvature, and profile curvature), meteorological and hydrological factors (rainfall and distance to rivers), human activity factor (distance to roads) and tectonic factor (distance to faults) are of higher importance.

## 4.2 Generating landslide susceptibility maps

The probability distributions of landslide occurrence predicted by the four models, LR, RF, NB, and MLP, are shown in Figure 6. The landslide-prone locations in the four distribution maps are roughly the same, and they are all distributed along rivers, trunk faults, and highways, which is also consistent with the results obtained from field surveys and theoretical analysis. However, the four distribution maps have their characteristics and shortcomings. In the distribution map of the LR model, the area surrounding Markam County is displayed in red, indicating that the landslide susceptibility in this area is generally high. However, in addition to the river valley and the area along the highway, it includes many mountains. Compared with other model distribution maps, the area is too large, and the distribution is unreasonable. In the MLP model, the distribution of high-susceptibility regions is more reasonable. However, the probability of landslide occurrence is concentrated at both ends of 0 and 1, which causes a steep change in the evaluation result from low susceptibility to high susceptibility. This result does not match the actual situation. The RF and NB model distribution maps show relatively clear and coherent evaluation results. The distribution of high-risk areas also follows the characteristics of distribution along river valleys and highways, which are more reasonable.

## 4.3 Validation of the models

The performance of the applied models was assessed and compared using statistical indices (Table 3). For the performance of the landslide testing data set, the RF model (*PPR* = 80.95%, *NPR* = 85.56%, *sensitivity* = 86.56%, *specificity* = 79.62%, *ACC* = 83.09%, $F_1$ = .84, and $k$ = .66) performs the best, followed by MLP (*PPR* = 74.79%, *NPR* = 76.11%, *sensitivity* = 76.73%, *specificity* = 74.13%, *ACC* = 75.43%, $F_1$ = .76, and $k$ = .51), LR (*PPR* = 72.97%, *NPR* = 71.99%, *sensitivity* = 71.39%, *specificity* = 73.55%, *ACC* = 72.47%, $F_1$ = .72, and $k$ = .45), and NB (*PPR* = 69.99%, *NPR* = 73.17%, *sensitivity* = 75.14%, *specificity* = 67.77%, *ACC* = 71.46%, $F_1$ = .72, and $k$ = .43).

The ROC curves of LR, RF, NB and MLP models were drawn by extracting the landslide susceptibility probability values of the test sample points in each model, combined with the actual value of landslide occurrence at the test sample points (Figure 7). The *AUC* values of the LR, RF, NB, and MLP models are .788, .918, .785, and .836, respectively, all of which are greater than .7. When the *AUC* value ≤.5, the result has no predictive value; when .5 < *AUC* value ≤.7, the model accuracy is low; when .7 < *AUC* value ≤.9, the model accuracy is high; when .9 < *AUC* value ≤1, the model has very high accuracy (Chen et al., 2017). The *AUC* accuracy of the four models is high or very high, indicating that the susceptibility partitions of the

four models can better predict the regional landslide susceptibility. Among them, the *AUC* value of the RF model is greater than .9, and the evaluation results are excellent. The order of accuracy of the four models is RF > MLP > LR > NB.

# 5 Discussion

## 5.1 Key predisposing factor analysis

Calculate the average value of the importance of each model landslide conditioning factor in Figure 5, and the factors according to their importance are in the following order: elevation, slope, rainfall, distance to rivers, aspect, distance to roads, distance to faults, profile curvature, plan curvature, TWI, NDVI, land cover, and engineering rock group. Since the average importance is greater than .077, elevation, slope, rainfall, distance to rivers and aspect are the main factors controlling landslide development in the study area. The elevation indicates the potential energy of the slope and controls the stability of the slope to a large extent (Hong et al., 2020). It affects not only the water content and stress in the slope but also the strength of human engineering activities and the vegetation distribution on the slope surface. The slope reflects the steepness and gentleness of the surface and controls the stability of the slope body to a certain extent. As the slope increases, there is a strong stress concentration at the foot of the slope, which easily causes landslides under the induction of other factors (Kavzoglu et al., 2019). Rainfall has always been considered as the main inducement of landslide. Rainfall infiltration can increase the weight of the slope, enhance the pore water pressure, and reduce the shear strength of the slope forming materials, leading to the loss of slope stability (Yan et al., 2019). The river has cut and eroded the bank of the slope for a long time, especially in the flood season, which has greatly increased the free face of the front edge of the slope, creating natural conditions for the occurrence of geological disasters, mainly in the spatial distribution of landslides (Zhao et al., 2019). The slope aspect shows the inclination direction of the slope, which has a certain control over the formation and distribution of landslides in the study area. In particular, many aspects show significant differences between sunny and shady slopes. In the study area, the south-facing slope is exposed to the sun for a longer time, with stronger radiation, more luxuriant vegetation and a higher weathering degree. Therefore, the rock and soil mass characteristics in different slope directions are different, and the geological disasters developed on them are different spatially (Hong et al., 2017).

## 5.2 Model performance and comparison

The LR model is more inclined to solve linear problems (Pradhan and Lee, 2010). For the non-linear susceptibility evaluation with 13 evaluation factors, the adaptability of the LR model is relatively poor, and the accuracy of the evaluation results is relatively low. The specific performance indicates that the probability distribution of landslide occurrence is unreasonable, and the *AUC* value is almost at the bottom of the four models. The processing power of RF models for high-dimensional data sets is excellent (Zhang et al., 2017). It can process thousands of input variables and determine the essential variables. In addition, it has the advantages of anti-interference and

high-accuracy (Merghadi et al., 2020). In landslide susceptibility evaluation research, its performance has always been relatively stable and the performance is the best in this study. The NB model is less sensitive to missing data, and the algorithm is relatively simple (Sikorska and Seibert, 2018). When the NB model has a given output category and a large number of attributes, the classification effect is not good (Lee et al., 2020). This result leads to the lowest *AUC* value of this model. The MLP model has outstanding adaptability to the fitting of non-linear problems (Kavzoglu et al., 2019). The MLP model has a remarkable property: if enough neurons and layers are present, it is theoretically possible to learn arbitrary input–output functions (Yan et al., 2006). Therefore, it performed well in this study. In conclusion, the study shows that the RF model is more suitable for landslide susceptibility evaluation in this area than the MLP, LR, and NB models.

## 5.3 Landslide-prone zoning

The landslide susceptibility index values were normalized and classified into five susceptibility classes (very low, low, moderate, high, and very high) using the natural break method by LR, RF, NB, and MLP (Figure 8). Compared with the classification methods such as defined intervals, equal intervals, quantiles, and standard deviations, the natural break method depends on the intrinsic features of the dataset and has no subjective opinions (Chen and Zhang, 2021), so it was adopted in this study. The area and landslide proportion in each landslide susceptibility class are shown in Figure 9.

In general, the area proportions of domains as very low, low, moderate, high and very high susceptibility classes of each model that decrease sequentially (Figure 9A). The area proportions of LR, RF and NB are similar, while the very low susceptibility class of MLP accounts for 62.84%, which is the majority. Overall, the proportion of landslides in the very low, low, moderate, high and very high susceptibility classes of each model increases sequentially (Figure 9B). Among them, the proportion of landslides in the very high susceptibility class of the RF model is the highest, reaching 89.25%, presenting the most efficient model for landslide prediction, followed by the MLP model (73.87%), while the proportion of landslides in the NB and LR models is the lowest. This finding is consistent with the ROC curve verification results.

In the RF model with the most reasonable prediction, very high, high, moderate, low and very low susceptibility zones accounted for 6.72%, 12.24%, 18.70%, 25.31% and 37.02% of the total area, respectively (Figure 9A). Among them, the total area of very low and low prone areas is close to 2/3, and these areas are mainly distributed in the gentle plateau area to the west of the Tenasserim chain and the peak area of alpine valleys. The total area of high and very high prone areas is close to 1/5, and these areas are mainly distributed in the Jinsha River and its tributaries, the Lancang River and its tributaries, and the steep canyon areas along the G214 highway (Figure 8B). These areas overlap greatly with human activities and pose significant security risks. The development of landslide hazards is affected by plate movement. The continuous uplift of the Qinghai–Tibet Plateau has created deep and steep river valley landforms, and the river valleys are often distributed along faults, resulting in the fragmentation of the bank slope rock mass and the development of fissures (Peng et al., 2004). In addition, the runoff on the bank slope surface is large. Therefore, the infiltration of rainfall

and ice and snow melt water increases the water content of the bank slope, thereby increasing the pore water pressure inside the rock and soil mass; the freeze–thaw cycle causes the joints and fissures to expand and penetrate. The cutting slope at the foot of the slope or the scouring of the river makes the front edge of the slope form a void and weakens the supporting force (Zhao et al., 2019). Under the superposition of these factors, the slope body cracks and slips under the action of gravity, forming a failure process of local sliding at the leading edge to creeping, pulling, and cracking, and then to overall sliding. For example, as shown in Figure 3D, the slope toe of Jianwangtong landslide was unstable due to long-term scouring by the river, resulting in traction sliding as a whole.

## 5.4 Limitations

Some limitations and uncertainty should be noted in this study. First, due to the large area of the study area and the limitation of computer computing ability, the grid size of 90 m * 90 m is selected in this paper. This grid is so large that multiple landslides may be included in the same grid. These landslides may be on both banks of the river and at different elevations of the same slope, but they are all given the same parameters, resulting in a certain degree of distortion of the input data of the condition factors. Different algorithm models have their unique characteristics, and the performance of each model variables according to the input data (Nachappa et al., 2020). This will eventually lead to the deviation of landslide susceptibility assessment results. Second, the spatial resolution of some condition factors is inconsistent (such as elevation, engineering rock group and distance to rivers). Although it is difficult to accurately define the uncertainty caused by the inconsistent spatial resolution (Rahman et al., 2021), the interpolation and extraction made in the process of unifying the condition factor data into 90 m resolution will also affect the assessment results of each model, Especially the model with high sensitivity to input data.

# 6 Conclusion

Based on the results of this study, the following can be concluded:

1) This paper obtained 2,308 landslide sample data points and established a relatively complete landslide catalogue database. The elevation, slope, aspect, plan curvature, profile curvature, topographic wetness index, distance to rivers, mean annual rainfall, engineering rock group, distance to faults, normalized difference vegetation index, land cover, and distance to roads were selected as conditioning factors. By calculating the influential factor importance, it was found that the elevation, slope, rainfall, distance to rivers, and aspect play a significant role.

2) Four susceptibility index distribution maps were obtained using the LR, RF, NB, and MLP machine learning algorithms to train the model. *AUC* values of LR, RF, NB and MLP model test samples were .788, .918, .785, and .836, respectively. The results show that these four models have good prediction accuracy and are suitable for landslide susceptibility evaluation of the Yunnan–Tibet traffic corridor in the Three Rivers Region. Based on the distribution of the *AUC* values and susceptibility index, it was found that the

evaluation result of the RF model is the most reasonable in this area.

3) Using the natural break method, the landslide susceptibility index values of the RF model were divided into five susceptibility classes: very high, high, moderate, low, and very low, with area ratios of 6.72%, 12.24%, 18.70%, 25.31% and 37.02%, respectively. The zones of high and very high landslide susceptibility are mainly distributed in the Jinsha River and its tributaries, the Lancang River and its tributaries, and the steep canyons along the G214 highway. The very low and low susceptibility zones are distributed in the gentle plateau area to the west of the Tenasserim chain and the peak areas of the alpine valleys. Affected by plate movement, the mountains in this area are towering and constantly rising, and the accompanying active faults break the rock mass and develop fissures, which makes the rivers strongly undercut and sidecut, thereby forming a steep river valley with unloading belts. Affected by topography, traffic engineering should be constructed along river valleys and face the threat of severe landslides and other geological slope disasters. The results can provide a scientific basis and reference for landslide disaster prevention and mitigation work in the major construction of traffic corridor in the three parallel river areas.

## Data availability statement

The original contributions presented in the study are included in the article/Supplementary Material, further inquiries can be directed to the corresponding author.

## Author contributions

Conceptualization, SW, SL, and JH; Data curation, XW and SL; Formal analysis, SW, HW, and CS; Funding acquisition, SL; Investigation, SW, SL, and HW; Project administration, SL; Software, SW, HW, and JH; Supervision, XW; Validation, SL, CS, and JH; Visualization, SW, CS, and XW; Writing-original draft, SW and FW; Writing-Review and editing, SL, HW, and CS. All authors have read and agreed to the published version of the manuscript.

## Funding

## Acknowledgments

## Conflict of interest

The authors declare that the research was conducted in the absence of any commercial or financial relationships that could be construed as a potential conflict of interest.

## Publisher's note

All claims expressed in this article are solely those of the authors and do not necessarily represent those of their affiliated organizations, or those of the publisher, the editors and the reviewers. Any product that may be evaluated in this article, or claim that may be made by its manufacturer, is not guaranteed or endorsed by the publisher.

## References

Arabameri, A., Pradhan, B., Rezaei, K., Sohrabi, M., and Kalantari, Z. (2019). GIS-based landslide susceptibility mapping using numerical risk factor bivariate model and its ensemble with linear multivariate regression and boosted regression tree algorithms. *J. Mt. Sci.* 16, 595–618. doi:10.1007/s11629-018-5168-y

Atkinson, P. M., and Massari, R. (1998). Generalized linear modeling of susceptibility to landsliding in the central Apennines. *Italy Comput. Geosci.* 24, 373–385. doi:10.1016/s0098-3004(97)00117-9

Ayalew, L., and Yamagishi, H. (2005). The application of GIS-based logistic regression for landslide susceptibility mapping in the Kakuda–Yahiko Mountains Central Japan. *Geomorphology* 65, 15–31. doi:10.1016/j.geomorph.2004.06.010

Bhargavi, P., and Jyothi, S. (2009). Applying naive bayes data mining technique for classification of agricultural land soils. *Int. J. Comput. Sci. Netw. Secur.* 9, 117–122.

Bui, D. T., Tuan, T. A., Klempe, H., Pradhan, B., and Revhaug, I. (2016). Spatial prediction models for shallow landslide hazards: A comparative assessment of the efficacy of support vector machines, artificial neural networks, kernel logistic regression, and logistic model tree. *Landslides* 13, 361–378. doi:10.1007/s10346-015-0557-6

Cama, M., Conoscenti, C., Lombardo, L., and Rotigliano, E. (2016). Exploring relationships between grid cell size and accuracy for debris-flow susceptibility models: A test in the giampilieri catchment (sicily, Italy). *Environ. Earth Sci.* 75, 238. doi:10.1007/s12665-015-5047-6

Chai, C. Y., Ling, S. X., Wu, X. Y., Hu, T., and Su, D. (2021). Characteristics of the *in situ* stress field and engineering effect along the lijiang to Shangri-La railway on

the southeastern Tibetan plateau, China. *Adv. Civ. Eng.* 2021, 1–11. doi:10.1155/2021/6652790

Chen, W. W., and Zhang, S. (2021). GIS-based comparative study of Bayes network, Hoeffding tree and logistic model tree for landslide susceptibility modeling. *Catena* 203, 105344. doi:10.1016/j.catena.2021.105344

Chen, W., Xie, X., Wang, J., Pradhan, B., Hong, H., Bui, D. T., et al. (2017). A comparative study of logistic model tree, random forest, and classification and regression tree models for spatial prediction of landslide susceptibility. *Catena* 151, 147–160. doi:10.1016/j.catena.2016.11.032

Chen, W., Zhang, S., Li, R. W., and Shahabi, H. (2018). Performance evaluation of the GIS-based data mining techniques of best-first decision tree, random forest, and naive Bayes tree for landslide susceptibility modeling. *Sci. Total Environ.* 644, 1006–1018. doi:10.1016/j.scitotenv.2018.06.389

Choubin, B., Mosavi, A., Alamdarloo, E. H., Hosseini, F. S., Shamshirband, S., Dashtekian, K., et al. (2019). Earth fissure hazard prediction using machine learning models. *Environ. Res.* 179, 108770. doi:10.1016/j.envres.2019.108770

Ermini, L., Catani, F., and Casagli, N. (2005). Artificial neural networks applied to landslide susceptibility assessment. *Geomorphology* 66, 327–343. doi:10.1016/j.geomorph.2004.09.025

Hong, H. Y., Liu, J. Z., and Zhu, A. X. (2019). Landslide susceptibility evaluating using artificial intelligence method in the Youfang district (China). *Environ. Earth Sci.* 78, 488–520. doi:10.1007/s12665-019-8415-9

Hong, H. Y., Liu, J. Z., and Zhu, A. X. (2020). Modeling landslide susceptibility using LogitBoost alternating decision trees and forest by penalizing attributes with the bagging ensemble. *Sci. total Environ.* 718, 137231. doi:10.1016/j.scitotenv.2020.137231

Hong, H. Y., Pradhan, B., Sameen, M. I., Chen, W., and Xu, C. (2017). Spatial prediction of rotational landslide using geographically weighted regression, logistic regression, and support vector machine models in Xing Guo area (China). *Geomatics, Nat. Hazards Risk* 8, 1997–2022. doi:10.1080/19475705.2017.1403974

Huang, F. M., Cao, Z. S., Guo, J. F., Jiang, S. H., Li, S., and Guo, Z. Z. (2020). Comparisons of heuristic, general statistical and machine learning models for landslide susceptibility prediction and mapping. *Catena* 191, 104580. doi:10.1016/j.catena.2020.104580

Huang, J. P., Ling, S. X., Wu, X. Y., and Deng, R. (2022a). GIS-Based comparative study of the bayesian network, decision table, radial basis function network and stochastic gradient descent for the spatial prediction of landslide susceptibility. *Land* 11, 436. doi:10.3390/land11030436

Huang, J. P., Ma, N., Ling, S. X., and Wu, X. Y. (2022b). Comparing the prediction performance of logistic model tree with different ensemble techniques in susceptibility assessments of different landslide types. *Geocarto Int.*, 1–31. doi:10.1080/10106049.2022.2087751

Kavzoglu, T., Colkesen, I., and Sahin, E. K. (2019). "Machine learning techniques in landslide susceptibility mapping: A survey and a case study," in *Landslides: Theory, practice and modelling* (Berlin, Germany: Springer), 283–301. doi:10.1007/978-3-319-77377-3_13

Lee, S., Lee, M. J., Jung, H. S., and Lee, S. (2020). Landslide susceptibility mapping using naive bayes and bayesian network models in umyeonsan, korea. *Geocarto Int.* 35, 1665–1679. doi:10.1080/10106049.2019.1585482

Li, X. N., Ling, S. X., Sun, C. W., Xu, J. X., and Huang, T. (2019). Integrated rockfall hazard and risk assessment along highways: An example for Jiuzhaigou area after the 2017 Ms 7.0 Jiuzhaigou earthquake, China. *J. Mt. Sci.* 16, 1318–1335. doi:10.1007/s11629-018-5355-x

Ließ, M., Glaser, B., and Huwe, B. (2012). Uncertainty in the spatial prediction of soil texture: Comparison of regression tree and random forest models. *Geoderma* 170, 70–79. doi:10.1016/j.geoderma.2011.10.010

Lin, W. T., Chou, W. C., and Lin, C. Y. (2008). Earthquake-induced landslide hazard and vegetation recovery assessment using remotely sensed data and a neural network-based classifier: A case study in central taiwan. *Nat. hazards* 47, 331–347. doi:10.1007/s11069-008-9222-x

Ling, S. X., Sun, C. W., Li, X. N., Ren, Y., Xu, J. X., and Huang, T. (2021). Characterizing the distribution pattern and geologic and geomorphic controls on earthquake-triggered landslide occurrence during the 2017 Ms 7.0 Jiuzhaigou earthquake, Sichuan, China. *Landslides* 18, 1275–1291. doi:10.1007/s10346-020-01549-6

Ling, S. X., Zhao, S. Y., Huang, J. P., and Zhang, X. T. (2022). Landslide susceptibility assessment using statistical and machine learning techniques: A case study in the upper reaches of the minjiang river, southwestern China. *Front. Earth Sci.* 10, 986172. doi:10.3389/feart.2022.986172

Mandrekar, J. N. (2010). Receiver operating characteristic curve in diagnostic test assessment. *J. Thorac. Oncol.* 5, 1315–1316. doi:10.1097/JTO.0b013e3181ec173d

Masetic, Z., and Subasi, A. (2016). Congestive heart failure detection using random forest classifier. *Comput. Methods Programs Biomed.* 130, 54–64. doi:10.1016/j.cmpb.2016.03.020

Merghadi, A., Yunus, A. P., Dou, J., Whiteley, J., ThaiPham, B., Bui, D. T., et al. (2020). Machine learning methods for landslide susceptibility studies: A comparative overview of algorithm performance. *Earth-Science Rev.* 207, 103225. doi:10.1016/j.earscirev.2020.103225

Nachappa, T. G., Ghorbanzadeh, O., Gholamnia, K., and Blaschke, T. (2020). Multi-hazard exposure mapping using machine learning for the state of salzburg, Austria. *Remote Sens.* 12, 2757. doi:10.3390/rs12172757

Niu, R. Q., Peng, L., Ye, R. Q., and Wu, X. L. (2012). Landslide susceptibility assessment based on rough sets and support vector machine. *J. Jilin Univ. Sci. Ed.* 42, 430–439. (In Chinese with English abstract). doi:10.13278/j.cnki.jjuese.2012.02.015

Ozdemir, A., and Altural, T. (2013). A comparative study of frequency ratio, weights of evidence and logistic regression methods for landslide susceptibility mapping: Sultan Mountains, SW Turkey. *J. Asian Earth Sci.* 64, 180–197. doi:10.1016/j.jseaes.2012.12.014

Peng, J. B., Cui, P., and Zhuang, J. Q. (2020). Challenges to engineering geology of Sichuan-Tibet railway. *Chin. J. Rock Mech. Eng.* 39, 2377–2389. (In Chinese with English abstract). doi:10.13722/j.cnki.jrme.2020.0446

Peng, J. B., Ma, R. Y., Lu, Q. Z., Li, X. A., and Shao, T. Q. (2004). Geological hazards effects of uplift of Qinghai-Tibet Plateau. *Adv. Earth Sci.* 19, 457–466. (In Chinese with English abstract). doi:10.3321/j.issn:1001-8166.2004.03.018

Peters, J., Baets, B. D., Verhoest, N. E. C., Samson, R., Degroeve, S., Becker, P. D., et al. (2007). Random forests as a tool for ecohydrological distribution modelling. *Ecol. Model.* 207, 304–318. doi:10.1016/j.ecolmodel.2007.05.011

Pham, B. T., Bui, D. T., Prakash, I., and Dholakia, M. B. (2017b). Hybrid integration of Multilayer Perceptron Neural Networks and machine learning ensembles for landslide susceptibility assessment at Himalayan area (India) using GIS. *CATENA* 149, 52–63. doi:10.1016/j.catena.2016.09.007

Pham, B. T., Bui, D. T., and Prakash, I. (2017a). Landslide susceptibility assessment using bagging ensemble based alternating decision trees, logistic regression and J48 decision trees methods: A comparative study. *Geotechnical Geol. Eng.* 35, 2597–2611. doi:10.1007/s10706-017-0264-2

Pham, B. T., Trung, N. T., Qi, C. C., Phong, T. V., Dou, J., Ho, L. S., et al. (2020). Coupling RBF neural network with ensemble learning techniques for landslide susceptibility mapping. *Catena* 195, 104805. doi:10.1016/j.catena.2020.104805

Pradhan, B., and Lee, S. (2010). Delineation of landslide hazard areas on Penang Island, Malaysia, by using frequency ratio, logistic regression, and artificial neural network models. *Environ. Earth Sci.* 60, 1037–1054. doi:10.1007/s12665-009-0245-8

Rahman, M., Chen, N. S., Elbeltagi, A., Islam, M. M., Alam, M., Pourghasemi, H. R., et al. (2021). Application of stacking hybrid machine learning algorithms in delineating multi-type flooding in Bangladesh. *J. Environ. Manag.* 295, 113086. doi:10.1016/j.jenvman.2021.113086

Ramchoun, H., Janati Idrissi, M. A., Ghanou, Y., and Ettaouil, M. (2016). Multilayer perceptron: Architecture optimization and training. *Int. J. Interact. Multimedia Artif. Intell.* 4, 26–30. doi:10.9781/ijimai.2016.415

Ravì, D., Bober, M., Farinella, G. M., Guarnera, M., and Battiato, S. (2016). Semantic segmentation of images exploiting DCT based features and random forest. *Pattern Recognit.* 52, 260–273. doi:10.1016/j.patcog.2015.10.021

Reichenbach, P., Rossi, M., Malamud, B. D., Mihir, M., and Guzzetti, F. (2018). A review of statistically-based landslide susceptibility models. *Earth-science Rev.* 180, 60–91. doi:10.1016/j.earscirev.2018.03.001

Shahabi, H., Jarihani, B., TavakkoliPiralilou, S., Chittleborough, D., Avand, M., and Ghorbanzadeh, O. (2019). A semi-automated object-based gully networks detection using different machine learning models: A case study of bowen catchment, queensland, Australia. *Sensors* 19, 4893. doi:10.3390/s19224893

Sikorska, A. E., and Seibert, J. (2018). Value of different precipitation data for flood prediction in an alpine catchment: A bayesian approach. *J. hydrology* 556, 961–971. doi:10.1016/j.jhydrol.2016.06.031

Tamura, R., Kobayashi, K., Takano, Y., Miyashiro, R., Nakata, K., and Matsui, T. (2019). Mixed integer quadratic optimization formulations for eliminating multicollinearity based on variance inflation factor. *J. Glob. Optim.* 73, 431–446. doi:10.1007/s10898-018-0713-3

Thompson, C. G., Kim, R. S., Aloe, A. M., and Becker, B. J. (2017). Extracting the variance inflation factor and other multicollinearity diagnostics from typical regression results. *Basic Appl. Soc. Psychol.* 39, 81–90. doi:10.1080/01973533.2016.1277529

Wen, H., Wu, X. Y., Ling, S. X., Sun, C. W., Liu, Q., and Zhou, G. Y. (2022). Characteristics and susceptibility assessment of the earthquake-triggered landslides in moderate-minor earthquake prone areas at southern margin of Sichuan Basin, China. *Bull. Eng. Geol. Environ.* 81, 346. doi:10.1007/s10064-022-02821-w

Xiong, P., Tong, L., Zhang, K., Shen, X. H., Battiston, R., Ouzounov, D., et al. (2021). Towards advancing the earthquake forecasting by machine learning of satellite data. *Sci. Total Environ.* 771, 145256. doi:10.1016/j.scitotenv.2021.145256

Yan, F., Zhang, Q. W., Ye, S., and Ren, B. (2019). A novel hybrid approach for landslide susceptibility mapping integrating analytical hierarchy process and normalized frequency ratio methods with the cloud model. *Geomorphology* 327, 170–187. doi:10.1016/j.geomorph.2018.10.024

Yan, H. M., Jiang, Y. T., Zheng, J., Peng, C. L., and Li, Q. H. (2006). A multilayer perceptron-based medical decision support system for heart disease diagnosis. *Expert Syst. Appl.* 30, 272–281. doi:10.1016/j.eswa.2005.07.022

Yan, Y., Cui, Y. F., Huang, X. H., Zhou, J. J., Zhang, W. G., Yin, S. Y., et al. (2022). Combining seismic signal dynamic inversion and numerical modeling improves landslide process reconstruction. *Earth Surf. Dynam.* 10, 1233–1252. doi:10.5194/esurf-10-1233-2022

Yao, X., Deng, J. H., Liu, X. H., Zhou, Z. K., Yao, J. M., Dai, F. C., et al. (2020). Primary recognition of active landslides and development rule analysis for pan Three-river-parallel Territory of Tibet Plateau. *Adv. Eng. Sci.* 52, 16–37. (In Chinese with English abstract). doi:10.15961/j.jsuese.202000529

Yao, X., Tham, L. G., and Dai, F. C. (2008). Landslide susceptibility mapping based on support vector machine: A case study on natural slopes of Hong Kong, China. *Geomorphology* 101, 572–582. doi:10.1016/j.geomorph.2008.02.011

Youssef, A. M., Pourghasemi, H. R., Pourtaghi, Z. S., and Al-Katheeri, M. M. (2016). Landslide susceptibility mapping using random forest, boosted regression tree, classification and regression tree, and general linear models and comparison of their performance at Wadi Tayyah Basin, Asir Region, Saudi Arabia. *Landslides* 13, 839–856. doi:10.1007/s10346-015-0614-1

Zare, M., Pourghasemi, H. R., Vafakhah, M., and Pradhan, B. (2013). Landslide susceptibility mapping at vaz watershed (Iran) using an artificial neural network model: A comparison between multilayer perceptron (MLP) and radial basic function (RBF) algorithms. *Arabian J. Geosciences* 6, 2873–2888. doi:10.1007/s12517-012-0610-x

Zhang, D. F., Fengquan, L., and Jianmin, L. (2000). Eco-environmental effects of the qinghai-tibet plateau uplift during the quaternary in China. *Environ. Geol.* 39, 1352–1358. doi:10.1007/s002540000174

Zhang, K. X., Wu, X. L., Niu, R. Q., Yang, K., and Zhao, L. R. (2017). The assessment of landslide susceptibility mapping using random forest and decision tree methods in the Three Gorges Reservoir area, China. *Environ. Earth Sci.* 76, 405. doi:10.1007/s12665-017-6731-5

Zhang, Y. S., Guo, C. B., Yao, X., Yang, Z. H., Wu, R. A., and Du, G. L. (2016). Research on the geohazard effect of active fault on the eastern margin of the Tibetan Plateau. *Acta Geosci. Sin.* 37, 277–286. (In Chinese with English abstract). doi:10.3975/cagsb.2016.03.03

Zhao, S. Y., Chigira, M., and Wu, X. Y. (2019). Gigantic rockslides induced by fluvial incision in the Diexi area along the eastern margin of the Tibetan Plateau. *Geomorphology* 338, 27–42. doi:10.1016/j.geomorph.2019.04.008

# Comprehensive evaluation of the Ruoergai Prairie ecosystem upstream of the Yellow River

Xiangning Xu[1], Qingwen Yang[2]*, Guoping Xiang[1]*, Tao Liu[1], Mengjie Yang[2], Xi Xiong[1] and Tao Jiang[2]

[1]Sichuan Bureau of Geology and Mineral Exploration and Development, Chengdu, China, [2]State Key Laboratory of Geohazard Prevention and Geoenvironment Protection, Chengdu University of Technology, Chengdu, China

With complex and diverse ecosystem types and complete ecological elements such as mountains, rivers, forests, farmlands, lakes, grasslands, sand, and glaciers, the Ruoergai Prairie upstream of the Yellow River is an integral part of the Qinghai-Tibet Ecological barrier and a critical area for ensuring the ecological security of China. In the Ruoergai Prairie, climate change and human activities have led to grassland degradation, water and soil loss, and a shrinking forest area, which has highlighted the need for ecological restoration. Therefore, a comprehensive ecosystem evaluation is of great significance for ecosystem restoration. This study evaluated the ecosystem quality, ecosystem service function importance, ecological vulnerability, ecological protection importance, ecological resilience, and ecological landscape patterns of prairies, wetlands, and forests. The ecosystem quality of the study area was medium to good. The ecosystem service function of the study area with weak ecosystem resilience is important. However, the ecological landscape in the study area has been heavily degraded. Therefore, the protection and restoration of mountains, waters, forests, farmlands, lakes, grasslands, sand, and glaciers are needed.

KEYWORDS

Ruoergai Prairie, grassland degradation, water and soil erosion, ecosystem evaluation, reduction in forest area

## 1. Introduction

As a transitional part of the Chinese terrain from the first to the second tier, the Ruoergai Prairie is the watershed of the Yellow and Yangtze rivers and their source. The Ruoergai Prairie is the largest plateau peat swamp wetland and an important water conservation area for China's plateau ecological maintenance, as well as the world's most important wildlife habitat and rare plant spreading area (Shen et al., 2016; Cui et al., 2022). However, it is located in a high-altitude and cold area east of the Tibetan Plateau with a vulnerable ecosystem. Due to the effects of global climate change and human activities, including grassland degradation, wetland water loss, soil loss, and forest area reduction, ecological restoration has become necessary.

Comprehensive ecosystem assessment is used to identify ecosystem health, analyze ecosystem service functions and the economy, and evaluate future development trends. Several studies have been conducted on ecological monitoring and evaluation.

For example, in 2003, the United Nations proposed a conceptual framework-based ecosystem service function qualitative evaluation plan (Shao et al., 2016). The U.S. evaluated ecosystem conditions (O'Malley, 2008) using many key indices, including ecosystem distribution, chemical and physical features, products and services, landscape patterns, and species. It started the construction of the "National Ecosystem Observation Network" in 2011 (Committee on the National Ecological Observatory

Network, 2004). Moreover, in China, Huang (1989) published an initial evaluation report on desert ecosystems in 1989. Many evaluations of the service value, ecological quality, and ecological landscape pattern of the singular ecosystem of the Ruoergai grassland have been conducted. Subsequently, studies have used field surveys, remote sensing, and GIS technology to assess the study area's ecosystem quality, vulnerability, and risk (De Lange et al., 2010; Jiang et al., 2017; Hou et al.,
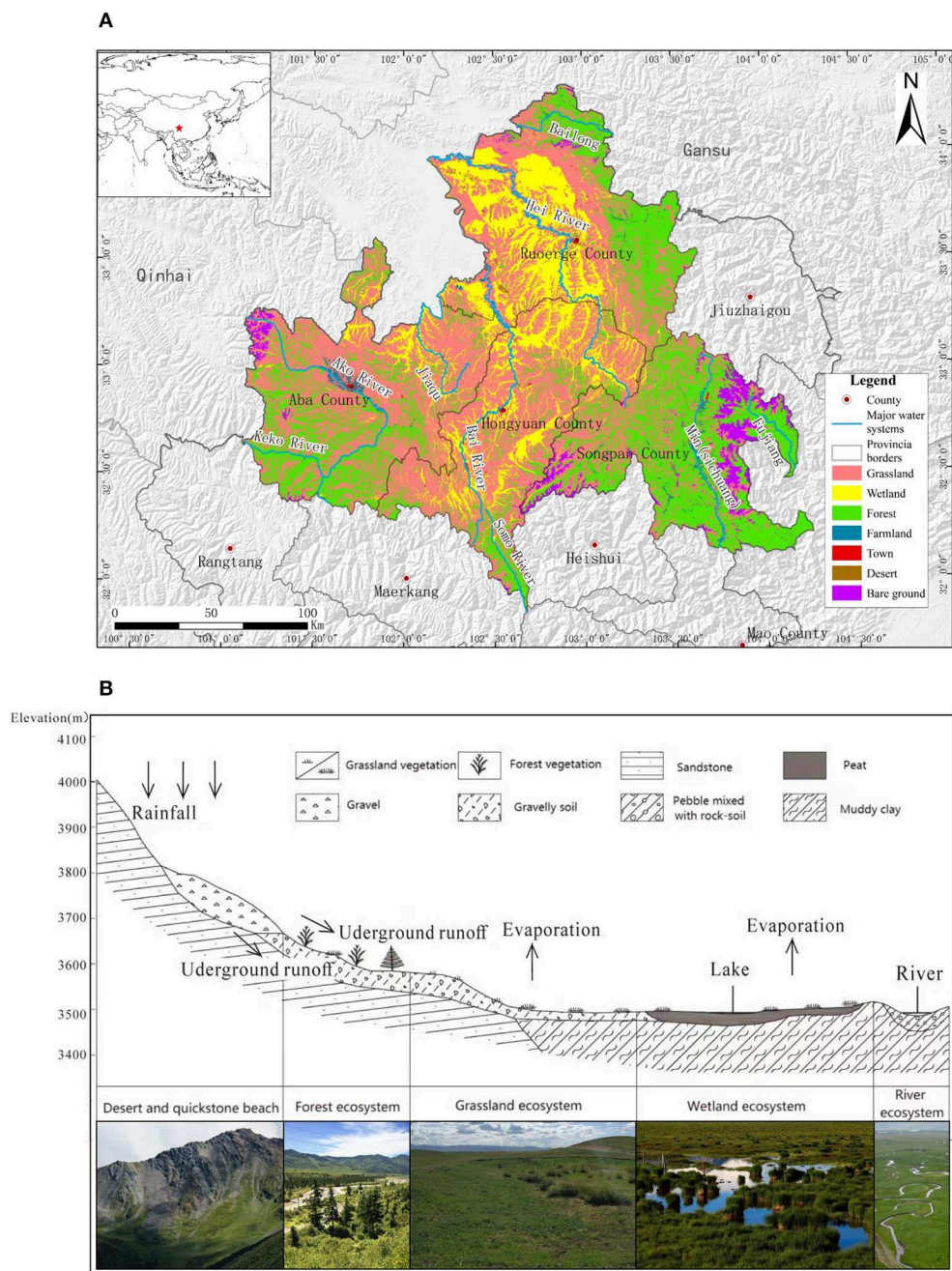


FIGURE 1
Ecosystem distribution in the study area. **(A)** Ecosystem types. **(B)** Ecosystem section.

2020). The evolution of an ecosystem has been studied through multi-phase remote sensing data (Bai et al., 2008; Shen et al., 2019). The factors driving ecosystem degradation, such as nature, humanity, and biological species, have been studied (Zhang et al., 2007; Pang et al., 2010; Hu et al., 2012; Wang et al., 2019). Wan et al. (2011) and Peng et al. (2022) studied the water conservation service function, and Bai (2013) verified the changes in biodiversity, water conservation, soil carbon sink, and other service functions through field investigations. Changes in ecosystem service values were calculated using remote sensing data (Li et al., 2010; Pang, 2019). In addition, some studies have conducted ecosystem health assessments (Wu et al., 2018) and ecological restoration effect assessments (Hu, 2019).

Previous studies performed various ecological assessments in the study area. However, comprehensive evaluations and studies on multiple ecosystems are limited. Therefore, the Ruoergai Prairie was used in this study to evaluate ecosystem quality, ecosystem service function importance, ecological vulnerability, ecological protection importance, ecological resilience, and ecological landscape patterns.

## 2. Study area

The Ruoergai Prairie (102° 08′-103° 39′ E, 32° 56′-34° 19′ N) is subordinate to Sichuan Province and is located on the northeast edge of the Qinghai-Tibet Plateau. The southeastern Ruoergai Prairie is close to Jiuzhaigou, Songpan, Hongyuan, and Aba counties. The eastern and northern parts are adjacent to the Diebu, Zhuoni, Luqu, and Maqu counties of Gansu Province. The study area, with its complex terrain, can be divided into two geographical units by the watersheds of the Yellow and Yangtze rivers. The mountainous area, with steep terrain and an altitude range of 2,410–4,490 m, is situated to the east. The plateau, which accounts for more than 69% of the county's area, developed on the western side.

The study area, with an average elevation of 3,500 m, is influenced by the humid monsoon climate in the cold temperate zone, and the average annual temperature is 0.6–1.1°C. The vegetation growing season in Ruoergai County is from May to July annually, and rainfall is concentrated during this period. The annual rainfall is 500–600 mm, the annual relative humidity
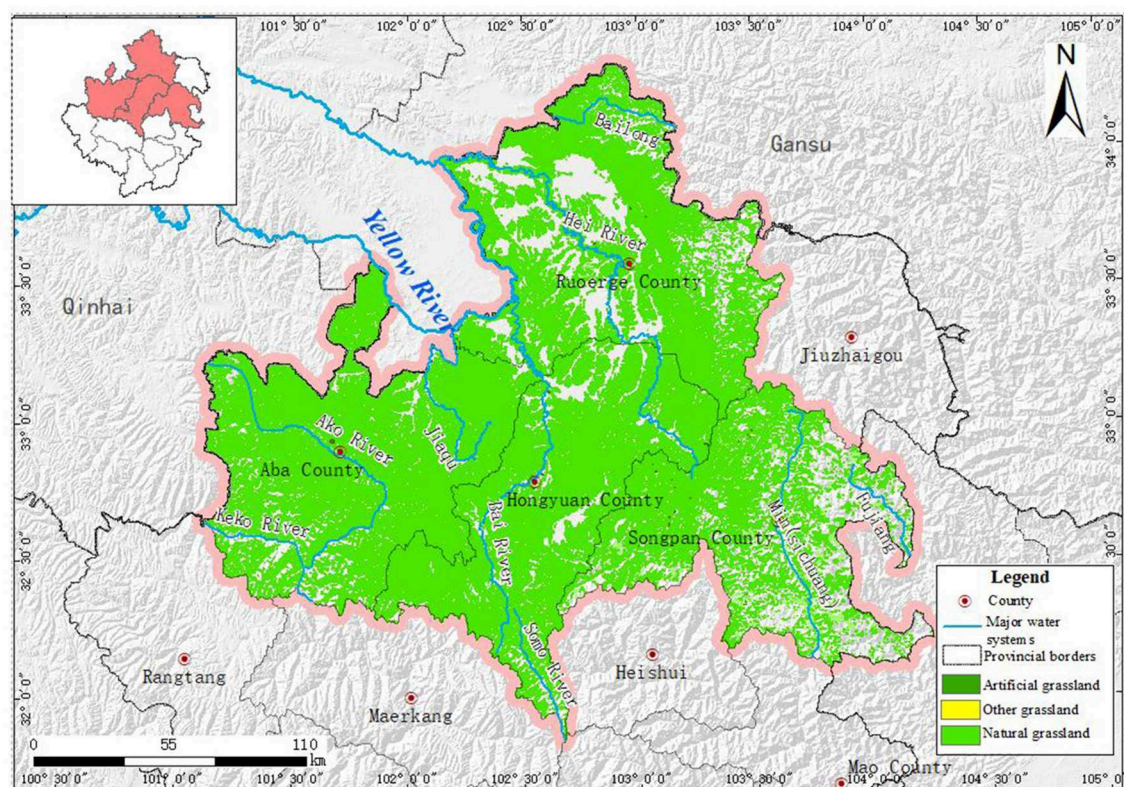


FIGURE 2
Grassland resource distribution in the study area.
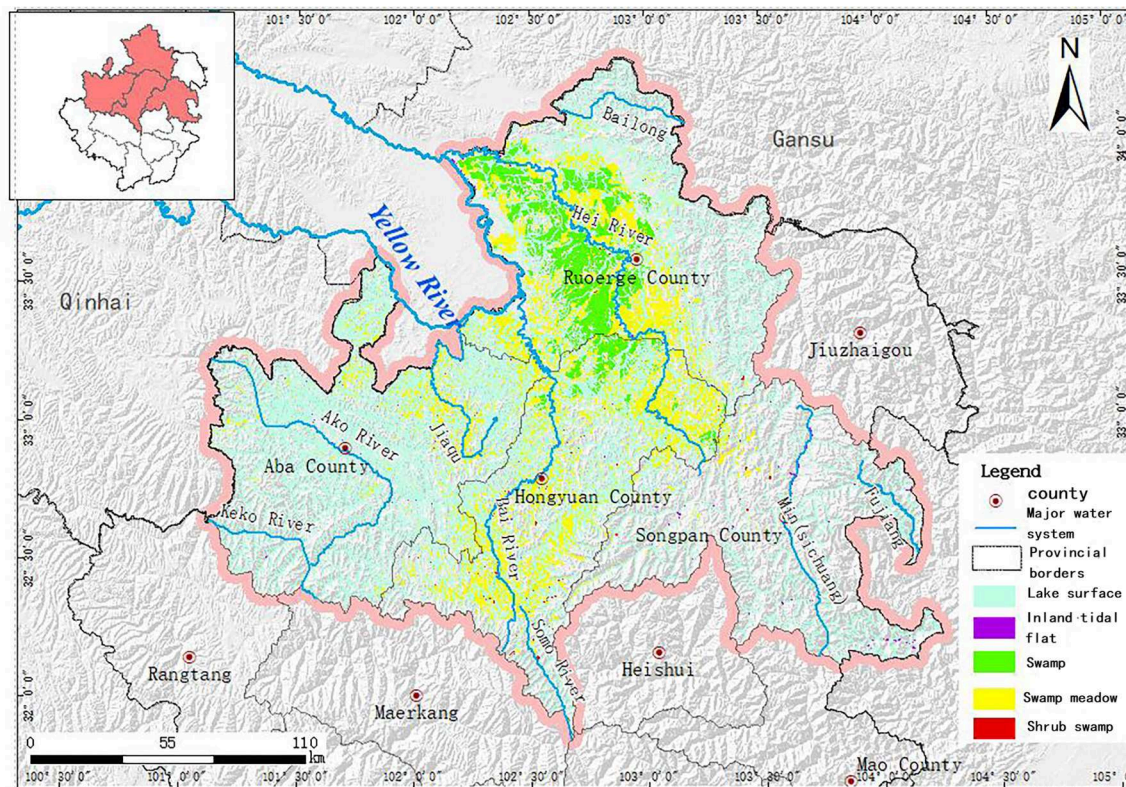
**FIGURE 3**
Wetland resource distribution in the study area.

is 69%, and the annual evaporation is 1,232 mm. Ruoergai County is rich in water. The main rivers are the Bailong, Baozuo, and Brazil rivers and Gaqu, Moqu, and Requ rivers, which flow into the Yellow River from south to north. Human disturbance activities in the Ruoergai area include overgrazing, excavations, and mining.

The ecosystem of the study area is mainly composed of grassland, wetland, forest, farmland, urban, desert, and bare land (Figure 1).

## 2.1. Grassland ecosystem

Ruoergai Prairie is the second-largest prairie in China and is classified as the Qinghai-Tibetan Steppe Region. With a total area of 18,227.14 km$^2$, the grassland ecosystem is the major ecosystem type in the study area (Figure 2) and is widely distributed in Ruoergai, Abay, and Hongyuan counties. The grassland in the study area, one of the four major pastoral areas in China, is divided into seven types: alpine meadow, subalpine meadow, alpine marsh meadow, alpine marsh grassland, subalpine forest edge meadow, alpine shrub grassland, and mountain shrub grassland.

## 2.2. Wetland ecosystem

The Ruoergai wetland is essential to maintaining the Himalayan fauna, flora, and biodiversity. The wetland in the study area covers an area of 6,153.21 km$^2$. It is mainly distributed to the west of Ruoergai, the north of Hongyuan County, the northeast of Aba County, upstream of the Heihe, Baiher, Jiaqu, and Dadu rivers, as well as coastal regions (Figure 3). Over the past 30 years, the Ruoergai alpine peat swamp wetland has degraded into a desert in the northwest (Ruoergai County) and a meadow in the southeast (Hongyuan, Aba, and Songpan counties) (Xiong et al., 2011).

## 2.3. Forest ecosystem

The northeastern, southern, and eastern parts of the study area, mainly covered by forest, belong to the Yangtze River system, where several terrestrial wild fauna and flora protection areas are also important biodiversity aggregation and water source conservation areas upstream of the Yangtze River. In addition, the northwest, west, and middle parts of the Yellow River system are important water source conservation areas
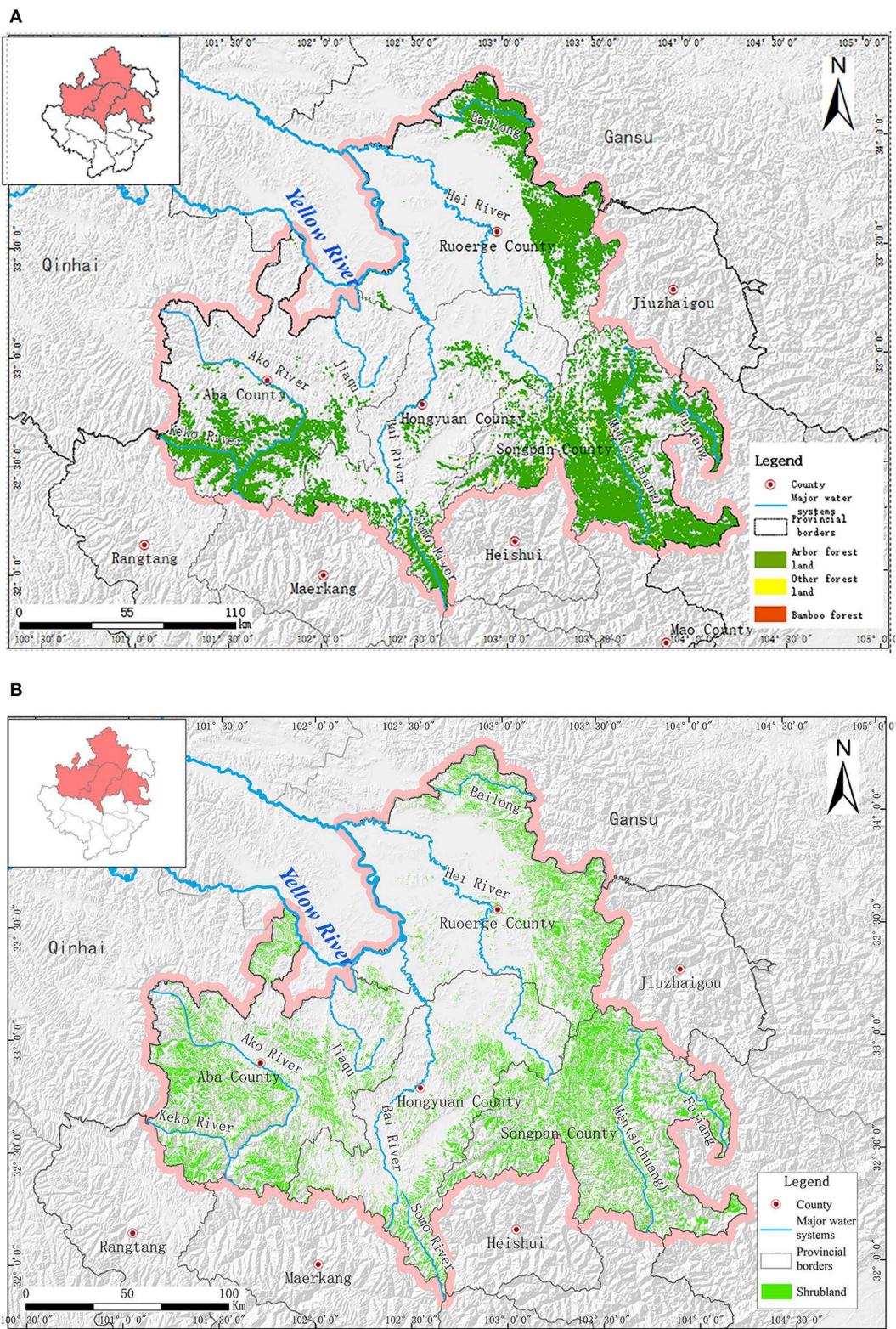
**FIGURE 4**
Forest ecosystem distribution in the study area. **(A)** Arbor forest distribution. **(B)** Bushwood distribution.
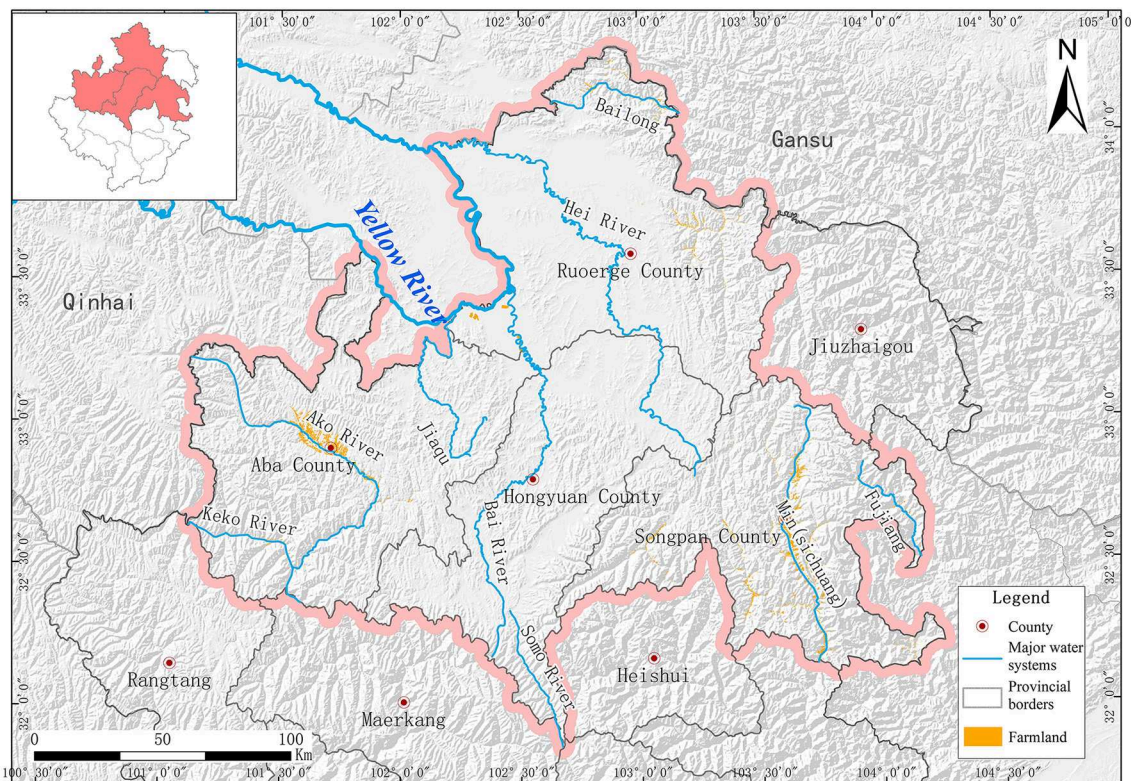
**FIGURE 5**
Farmland ecosystem distribution in the study area.

in the Ruoergai Prairie wetland. In the study area, the forest ecosystem is mainly composed of arbor forest and brushwood (Figure 4), with an area of 11,068.88 km$^2$ accounting for 29.81%.

In the study area, arbor forests are mainly distributed in the Minjiang River Basin bordering Songpan County, the Minshan Mountain Range to the east of Ruoergai County, the Keke River Basin to the south of Aba County, and the southwest of Hongyuan County. Bushwood is usually found in the northern part of Songpan County, west of Aba County, the north and east parts of Ruoergai County, and southeast of Hongyuan County. In the Yangtze River Basin, bushwood is mainly distributed in the Bailong, Minjiang, and Dadu river basins. Although it plays a crucial role in maintaining the regional ecological balance, it is also an important water source conservation area upstream of the Yangtze River. The coverage of bushwood is relatively smaller in the Yellow River Basin, only along the edge of the Ruoergai Basin and the middle and upper parts of the hilly plateau area.

## 2.4. Farmland ecosystem

With an aggregate area of 289.53 km$^2$, the farmland ecosystem of the study area is located in Songpan, Aba, and Ruoergai counties (Figure 5). It is mainly composed of cultivated land and garden plots.

## 2.5. Urban ecosystem

The urban ecosystem, with a total area of 187.31 km$^2$, accounts for 0.50% of the study area and is scattered around counties and within the borders of towns (Figure 6).

## 2.6. Desert ecosystem

The desert ecosystem covers an area of 49.42 km$^2$, accounting for 0.13% of the study area. Sandy land was mainly distributed in the western region of Ruoergai County (Figure 7). Intra-regional sandy land is largely pasture, mainly caused by land desertification.

## 2.7. Bare land ecosystem

Bare land and rock-gravel land constitute the central part of the bare land ecosystem in the study area (Figure 8). It is

**FIGURE 6**
Urban ecosystem distribution in the study area.
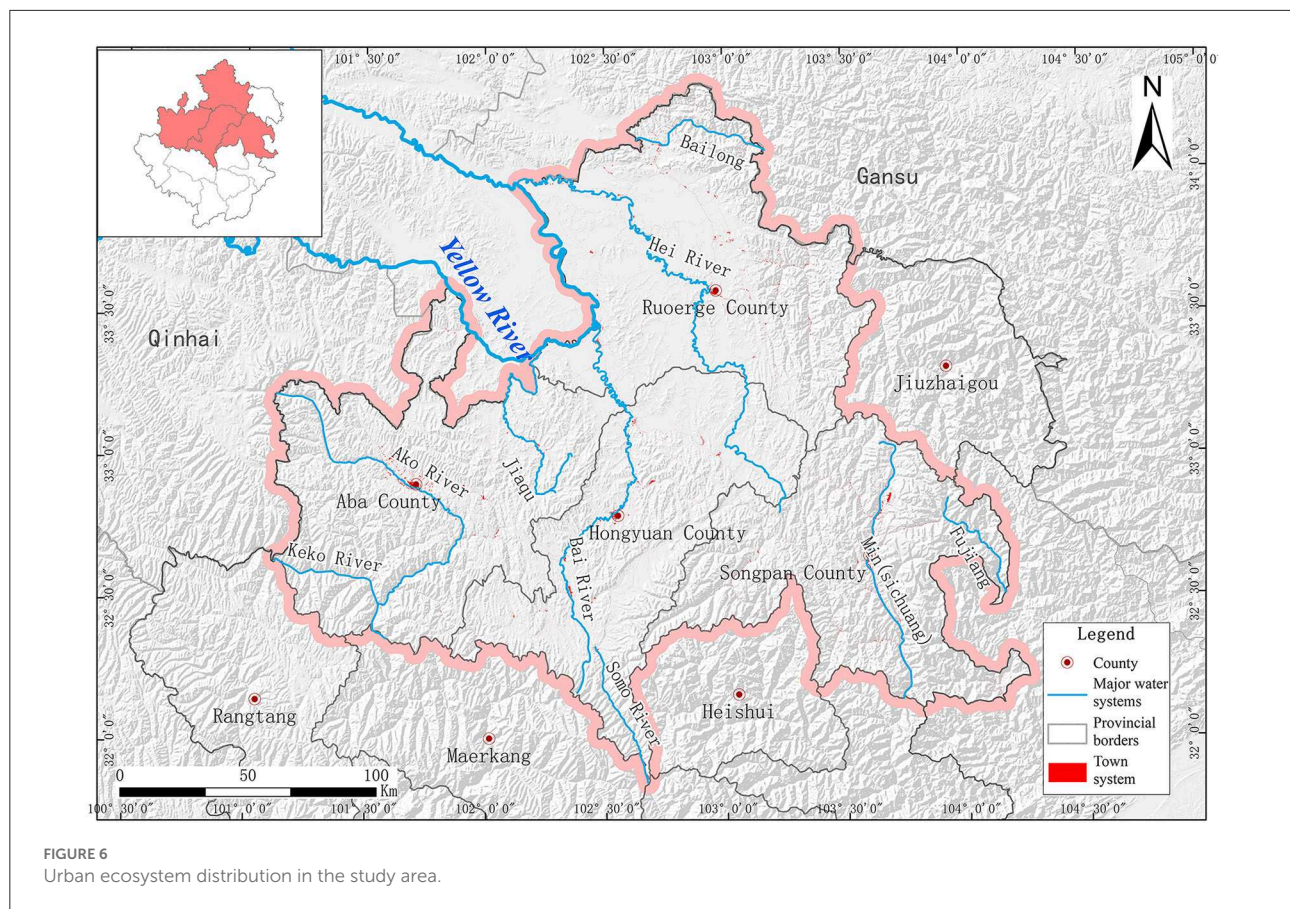
mainly distributed on the tops of many huge mountains, such as Yakexia Snow Mountain, the western slope of Zhegushan Snow Mountain, Lianbaoyeze in Aba County, and Xuebaoding-Gonggangling in Songpan County, where glacier, snow, and permafrost usually exist. Besides the gross area of 1,160.19 $km^2$, there are also 0.43 $km^2$ of scattered bare and idle lands. Bare land is indispensable to maintaining the study area's river hydrological ecology.

# 3. Methods

The administrative regions of the Ruoergai Prairie include Ruoergai, Hongyuan, Aba, and Songpan counties in Sichuan Province, Maqu and Luqu counties in Gansu Province, and Jiuzhi County in Qinghai Province. This study used the Ruoergai Prairie as the research area and ArcGIS software to pre-process digital elevation model (DEM) data with a spatial resolution of 30 m (including Ruoergai, Hongyuan, Aba, Songpan, and other administrative areas), such as splicing and projection. The data projection was unified using UTM/WGS84 to obtain DEM data within the study area.

Regarding issues related to the protection and restoration of the main degraded ecosystems, including grasslands, wetlands,

and forests, the evaluation methods for ecological system quality, ecosystem service function importance, ecological vulnerability, ecological protection importance, ecological resilience, and ecological landscape pattern were proposed in this study (Figure 9).

## 3.1. Ecosystem quality evaluation method

Remote sensing ecological index (RSEI) (forest vegetation coverage (FVC), leaf area index (LAI), and general primary production (GPP) were used as indicators to identify the existing quality problems of the ecosystem by evaluating food chain integrity, biodiversity, and structural function stability based on the practical situation of the study area. Considering the maximum values of the ecological indices of the four types of ecosystems, including forest, brushwood, grassland, and farmland, as reference values, the ratios between the ecological indices and reference values of all four ecosystem types individually were used to obtain the relative density of the corresponding ecological index. If the ratio was closer to 1, the ecological index of the ecosystem was closer to the reference value, and the ecosystem quality was better in this area.

**FIGURE 7**
Desert ecosystem distribution in the study area.
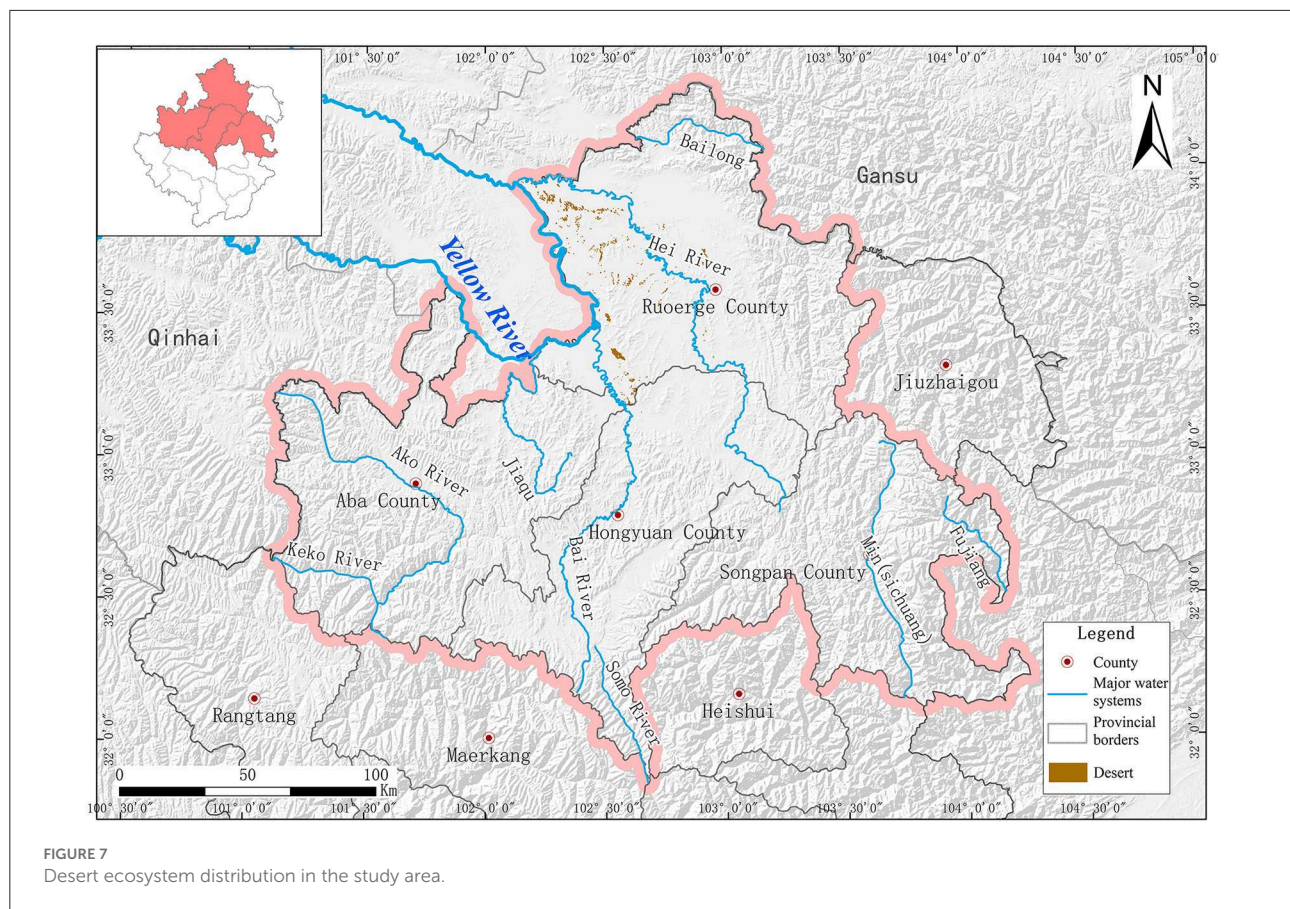
Then, the ecosystem quality index (EQI) was calculated after the numerical normalization of the data. The ecosystem quality index (EQI) was ranked into different levels according to the Technical Specifications for Ecological Conditions Investigation and Assessment-Ecosystem Quality Assessment to obtain the ecosystem quality level of the study area.

## 3.2. Importance of ecosystem service function evaluation

The ecosystem service function evaluation mainly includes evaluating the importance of ecological service functions such as water conservation, biodiversity maintenance, grassland and wetland preservation, wind prevention, and sand fixation. The service values of different types of ecosystems were obtained through evaluation. Following the Guides for Ecological Protection Red Line Delineation, the corresponding values of cumulative service value at 50 and 80% of the total ecosystem service value were used as the points for ecosystem service function grading. The importance of ecosystem service functions was divided into three levels. Levels I, II, and III represent "extremely important," "important," and "generally

important" levels, respectively. Further details are shown in Figure 9.

The relative importance of ecosystem water conservation can be evaluated using water conservation, which is calculated by subtracting evapotranspiration and surface runoff from precipitation. Ecosystem types in arid and semi-arid lands, the number of days in windy weather, vegetation coverage, and soil sand content are the basis for ecosystem wind prevention and sand fixation importance evaluations. Using ecosystem wind prevention and sand fixation serviceability as evaluation indicators and wind prevention and sand fixation amount (the difference between potential and actual wind erosion) as evaluation parameters, it is possible to determine the regional wind prevention and sand fixation amount through the revised wind erosion equation, based on remote sensing statistics, digital elevation, meteorological and soil data, and data from the MODIS snow cover product of China.

Because ecosystems, species, and genetic resources reflect the importance of the biodiversity maintenance function, evaluation of the importance of biodiversity maintenance functions could be performed from these three aspects. The plant net primary productivity (NPP) and meteorological and elevation data were used to obtain the regional biodiversity maintenance indices. Biodiversity maintenance serviceability

**FIGURE 8**
Bare land ecosystem distribution in the study area.
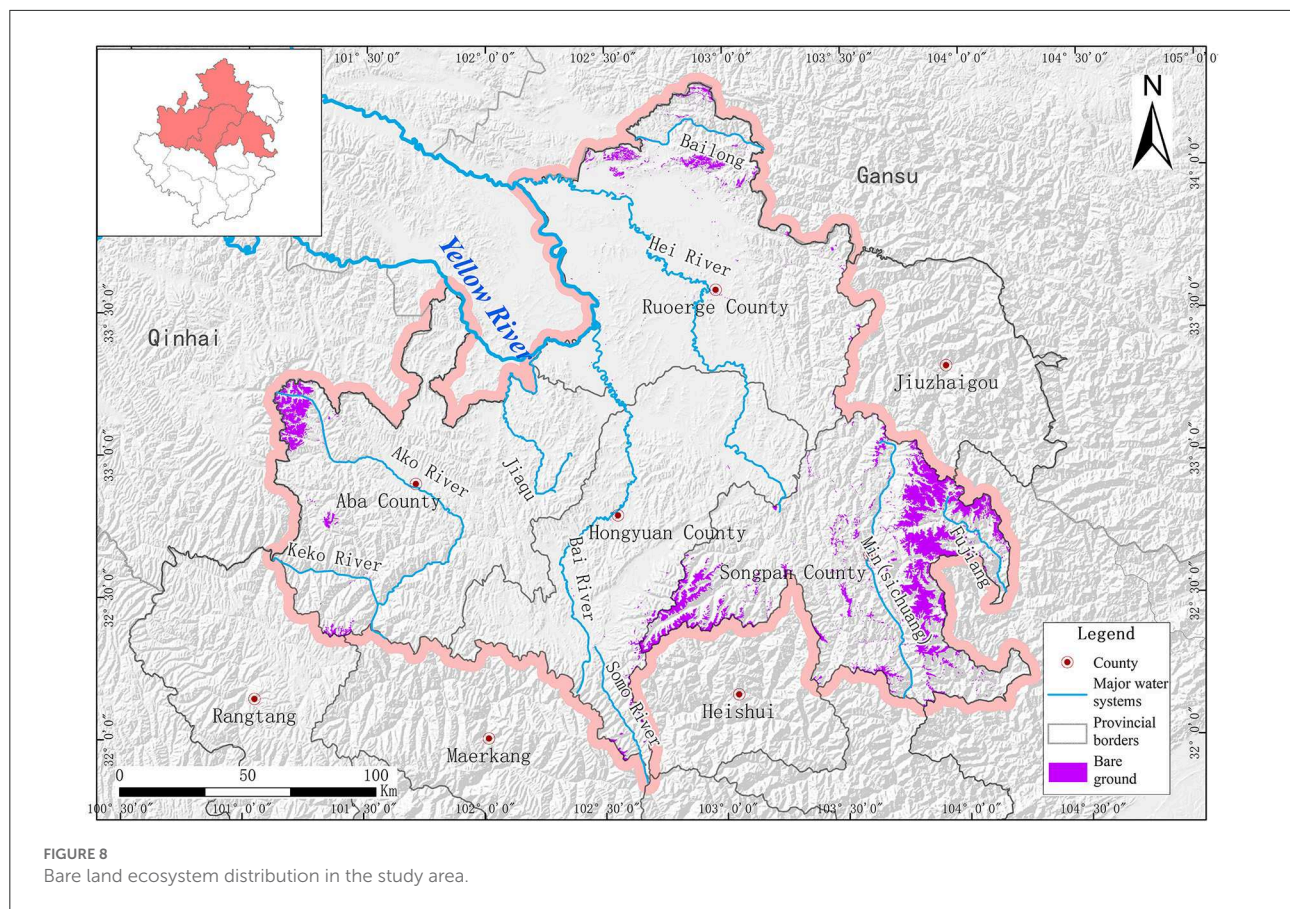
was used as the evaluation index. Ecosystem authenticity and integrity, species conservation value, and important genetic resources were combined.

The relative importance of ecosystem soil conservation function was evaluated based on ecosystem types, vegetation coverage, and differences in topographic features. Water and soil conservation functions were mainly determined by climate, soil, topography, and vegetation. Considering ecosystem water and soil conservation indicators as evaluation indices and water and soil conservation amount (the difference between potential and actual soil erosion) as the evaluation parameters, we expected to obtain the regional water and soil conservation amount using the revised water and soil loss equation (RUSLE). Water and soil conservation can be divided into three grades: "general," "important," and "extremely important."

## 3.3. Methods for ecological vulnerability evaluation

Ecological vulnerability, which reflects the possibility of ecological problems in a certain area, is used to demonstrate the possible ecological consequences of

human activities (Li et al., 2018). Water and soil loss vulnerability and desertification vulnerability are two major forms of ecological vulnerability, which were used together to obtain the ecological vulnerability of the study area after analysis based on the soil erosion and desertification monitoring data. Ecological vulnerability is categorized into five degrees: general, miner, moderate, heavy, and extreme.

## 3.4. Methods for ecological protection: importance

The importance of ecological protection is obtained based on a comprehensive evaluation of the importance of ecosystem service function and ecological vulnerability, which is divided into three degrees: "extremely important," "important," and "generally important." Ecosystem services include biodiversity maintenance, water conservation, water and soil preservation, wind prevention, and sand fixation. The more important the ecosystem service functions are, the greater the importance of ecological protection.
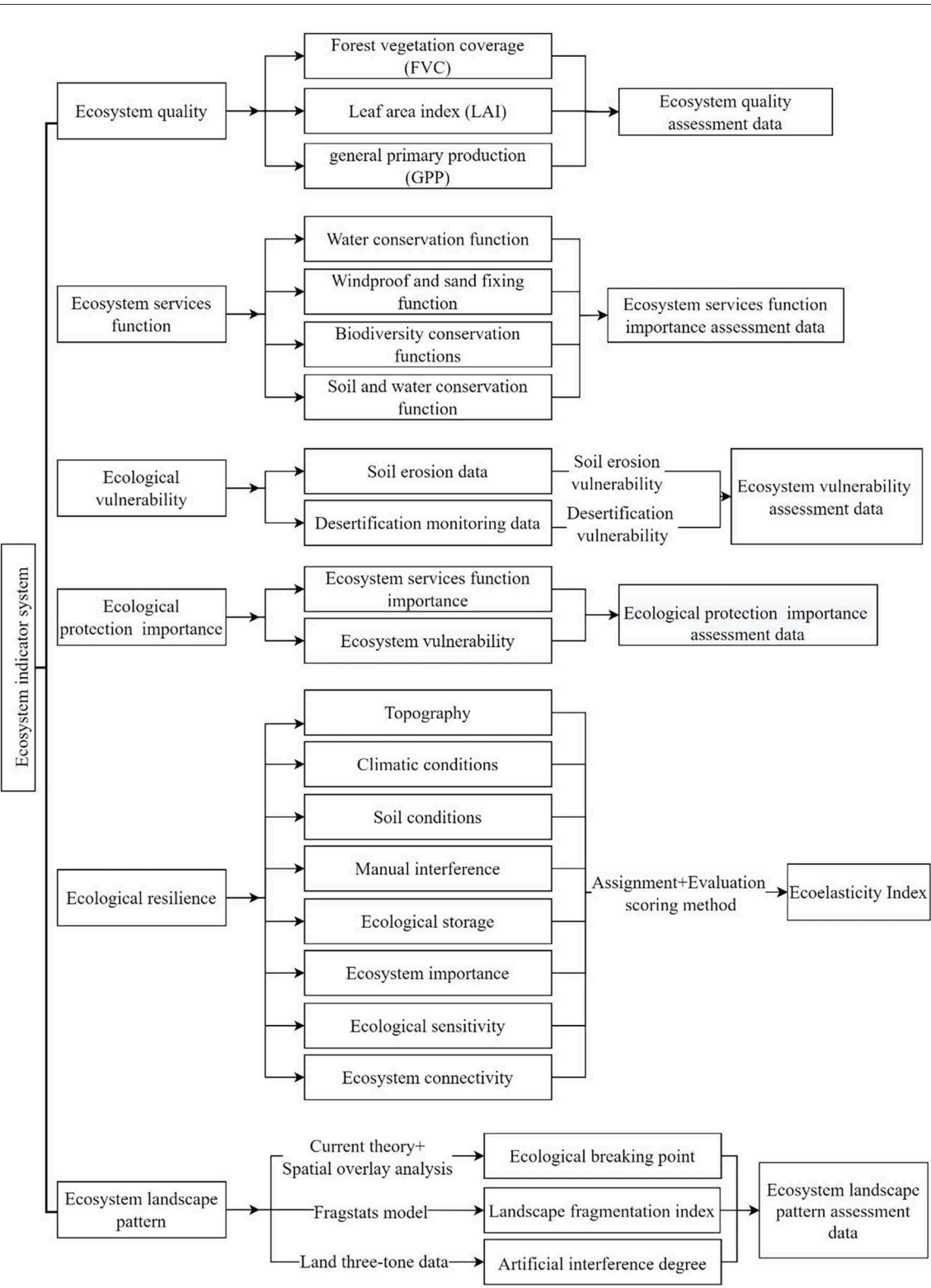
FIGURE 9
Method of comprehensive ecosystem assessment.
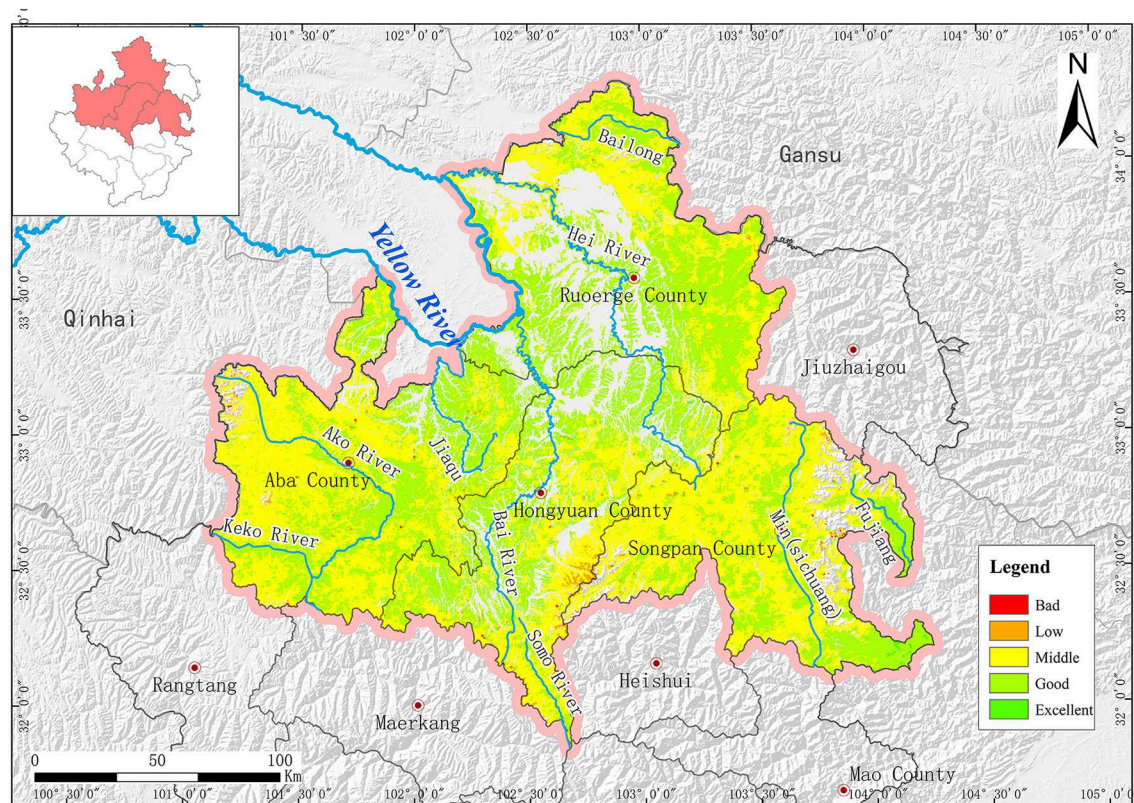
**FIGURE 10**
Ecosystem quality assessment.

## 3.5. Methods for ecological restoration evaluation

The ecosystem restoration ability was calculated using the limit coefficient method. According to the field investigation and analysis results, evaluation scoring assigned values to relevant indices such as topography, climatic conditions, soil conditions, artificial interference, ecological storage, ecosystem importance, ecological sensitivity, and ecosystem connectivity. All data were normalized to obtain a raster plot of the ecological resilience index for the study area. Thus, ecosystem resilience after interference is shown in quantity or space by the resilience index model.

## 3.6. Methods for ecological landscape pattern evaluation

Habitat patch (relatively homogeneous non-linear region different from surroundings) islanding refers to the ecological environment showing a discontinuity for a breach of integrity.

It becomes very different from the surrounding environment (Zhang et al., 2021). This phenomenon would greatly weaken the operation and control efforts of the ecosystem and cause problems with biogenic migration, which could directly affect regional ecosystem functions and threaten the sustainable development of the regional ecosystem. Based on current theory and spatial overlaying, namely the uniform spatial reference system, this study aimed to identify the ecological source, ecological corridors, ecological pinch points, barriers, and existing corridors (including river and road corridors) in the study area and constitute the ecological safety pattern of Ruoergai, Hongyuan, Aba, and Songpan counties by performing set pre-computations for a series of data. The landscape surface was regarded as a conductive surface. Considering the advantage of the random flow property of electrons in the circuit, it can be used to predict the spreading and migration rules of species, identify more alternative paths in a certain width of the landscape, and confirm the relative importance of habitat patches and corridors based on the inter-source current strength by simulating the migration and spread of individual species or genes in the landscape with electrons on a conductive surface (McRae, 2006; McRae and Beier, 2007; McRae et al., 2008).
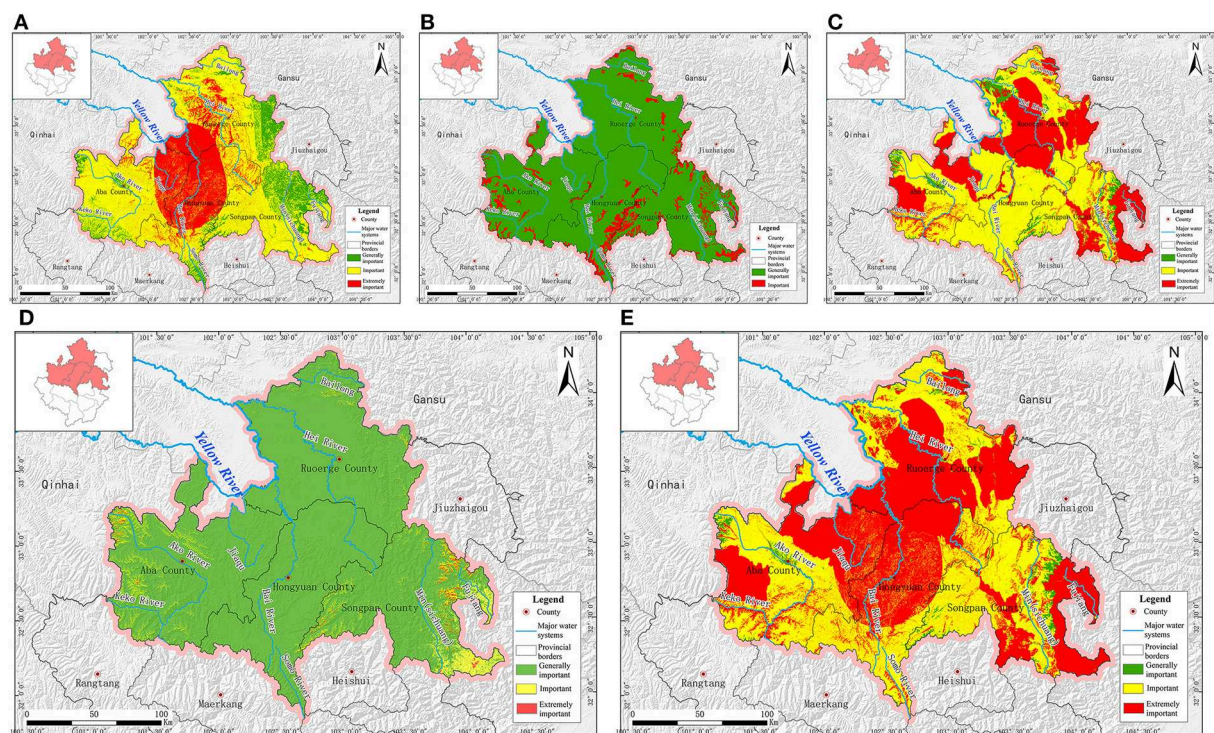
**FIGURE 11**
Importance assessment. **(A)** Water conservation function. **(B)** Windbreak and sand fixation function. **(C)** Biodiversity maintenance function. **(D)** Water and soil conservation function. **(E)** Ecosystem service function.

The growth of population pressure, cultivated land reclamation, urban construction, and many other human activities have sped up landscape fragmentation in the study area, which directly affects ecological features and processes, including biodiversity, energy flow, and mass circulation in the landscape. Therefore, landscape fragmentation was regarded as the leading cause of wetland ecosystem degradation, weakening, and even loss of biodiversity maintenance. Based on the ecosystem-type data, the Fragstats model was used to simulate the landscape fragmentation indices in the study area. The fragmentation was divided into four degrees: high, relatively high, medium, and low.

A land-cover classification-based human interference grading system was established in accordance with the data of the third national land survey in China. Then, a human activity interference diagram was drawn using the area weight-based comprehensive human interference index model. A quantitative analysis and evaluation of the degree of human interference with land cover in the study area and its dynamic changes from the aspects of boundaries, grids, and the main functional area scale were conducted. The describing factors mainly included frequency (the number of interferences within a certain time), strength (the degree of influence of interference on pattern and process or ecosystem structure and functions), area (the area of landscape suffering from interference within a certain time after interference),

and influence (the influence of interference on organisms, communities, or ecosystems).

## 4. Results

### 4.1. Ecosystem quality

The high ecosystem quality area, with an area of 48.71 km$^2$ (Figure 10), is mainly scattered around the upstream source areas of the Baihe, Heihe, and Dadu rivers, as well as the Giant Panda National Park (Songpan Area). In contrast, areas of relatively low and poor ecosystem quality are distributed in the Baihe, Heihe, Minjiang, and Dadu river basins at scattered points, with an area of 291.72 and 17.52 km$^2$, respectively. The medium ecosystem quality area accounts for 56.78%, and the good ecosystem quality area accounts for 42.01% of the study area are widely distributed in forests, brushwood, cultivated land, and grass fields.

### 4.2. Importance of ecosystem service function

The amount of water conserved was calculated using the water balance equation. The importance of the water
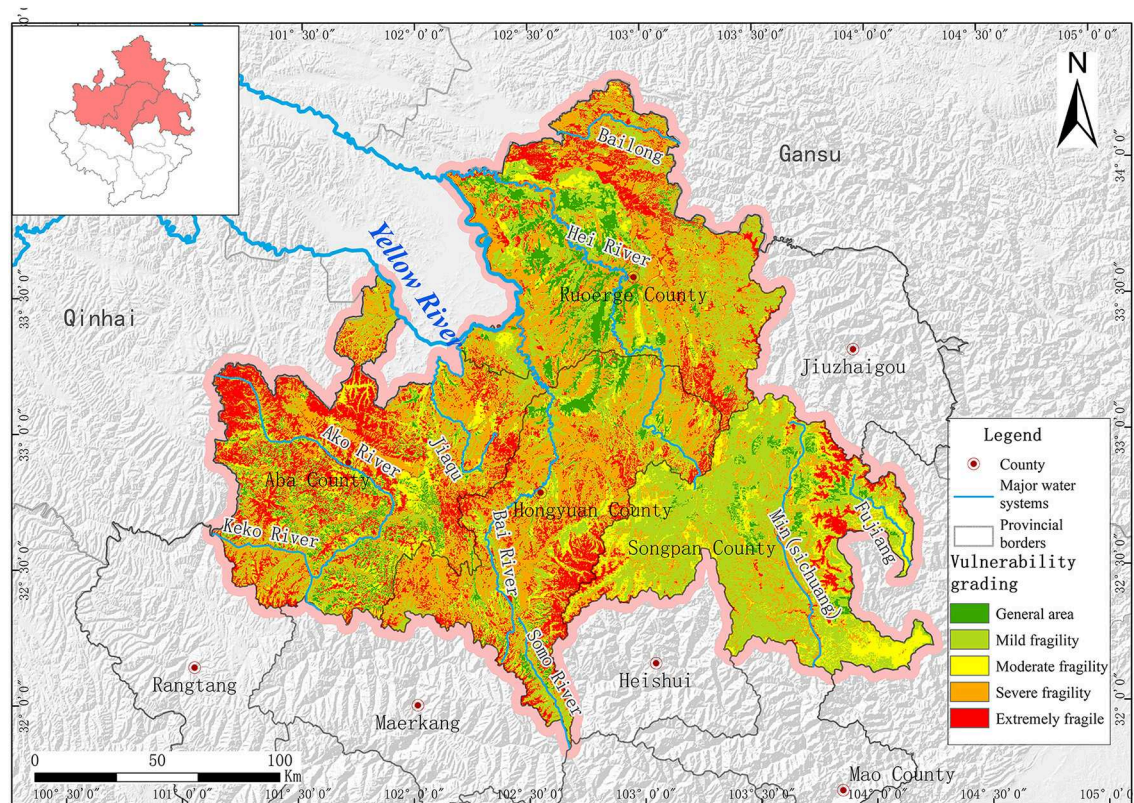
**FIGURE 12**
Ecological vulnerability assessment.

conservation function was evaluated according to the ecosystem type, meteorological, and evapotranspiration data. The existing and expected areas for implementing the water conservation function were identified (Figure 11).

The entire study area can be divided into three parts: the "generally important," "important," and "extremely important" parts, accounting for 13.48, 63.09, and 23.43%, respectively. The generally important part was composed mainly of residential land, and mountains are distributed in Songpan County and east of Ruoergai County. The important part was mainly distributed in Aba County, the middle of Ruoergai County, and the west of Songpan County. The extremely important part dominated by the wetland ecosystem was clustered at the junction of the four counties: Aba, Hongyuan, Songpan, and Ruoergai.

The wind prevention and sand fixation results are shown in Figure 11B. They can be graded as a "generally important degree" or an "important degree." The general important degree area accounted for 90.09%, and the important degree area accounted for only 9.91% and was mainly distributed in Ruoergai County.

The results of the calculation of the biodiversity maintenance ability index for the study area are shown in Figure 11C. Of the study area, 37.53% plays an essential role in biodiversity

maintenance and is mainly composed of the Ruoergai wetland, Giant Panda National Park (Songpan), Tiebu, Baozuo, Lianbaoyeze Natural Protection Area, and Sichuan Rewugou Forest Park. Of these, 57.41% were important areas, with the majority distributed in Hongyuan County. The remaining small part of only 5.06% of the study area was generally important for biodiversity maintenance and was mainly covered by residential and bare land.

The results of the important evaluation of the water and soil conservation functions are shown in Figure 11D. The most important area is 97.70%. An important degree area of 2.27% was mainly distributed around and on both sides of the rivers in the study area. The extremely important area, accounting for only 0.03%, was scattered at the source of the Ake River and the eastern part of the Minjiang River.

Based on the analysis of the four major ecological service functions (Figure 11E), the generally important area accounted for 2.10% with an area of 780.31 km$^2$ was mainly covered by a residential area, an important area of 17,108.69 km$^2$ accounting for 46.07% was mainly distributed in the south of Hongyuan County, east of Aba County and west of Songpan County, and the extremely important area of 19,247.10 km$^2$ accounted for 51.83% was distributed in Ruoergai wetland, Baihe River

**FIGURE 13**
Ecological protection assessment.
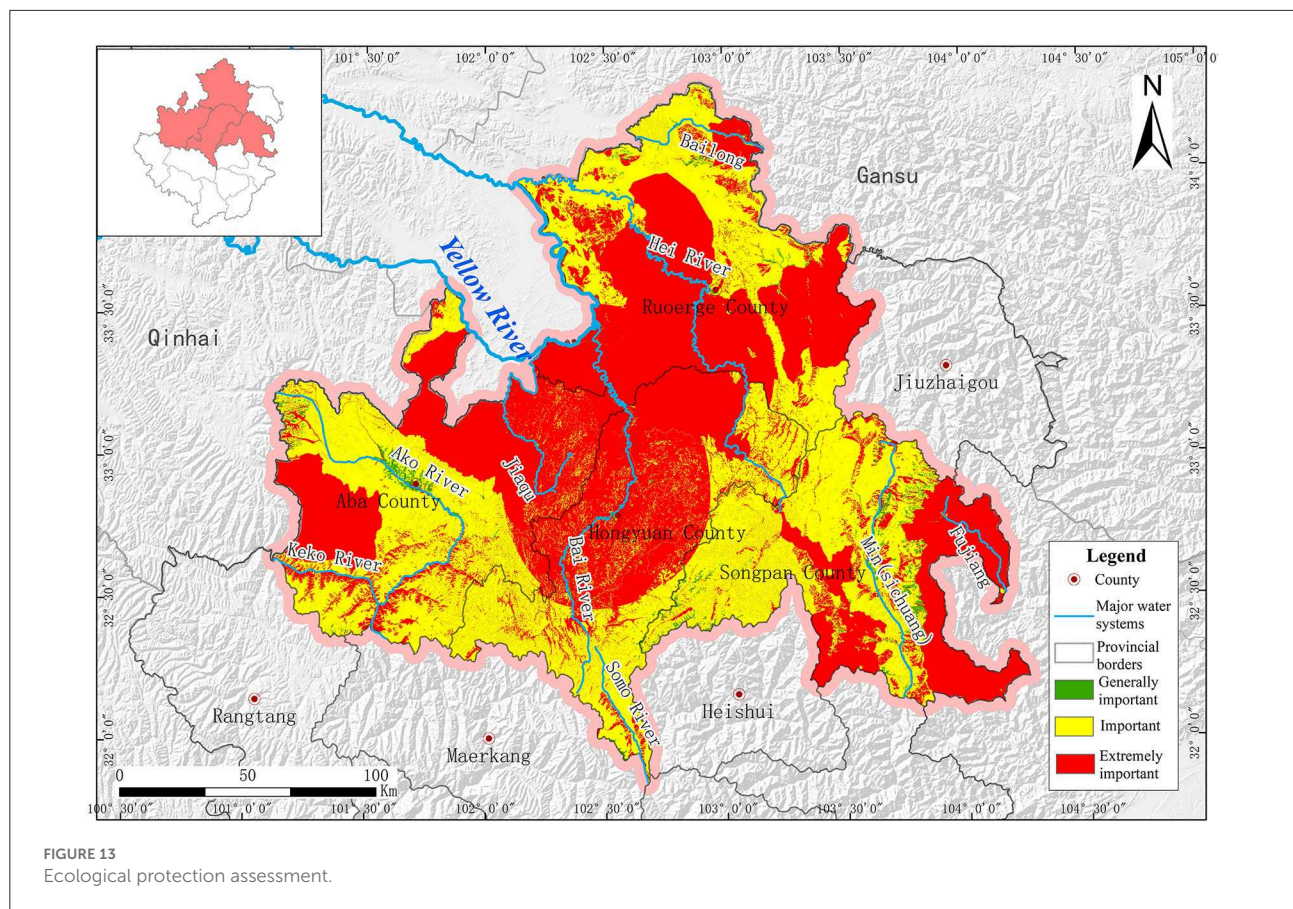
Basin, Giant Panda National Park (Songpan), Tiebu, Baozuo, and Lianbaoyeze Nature Protection Area and Sichuan Rewugou Forest Park.

## 4.3. Ecological vulnerability

According to the study area ecological vulnerability evaluation results in Figure 12, 6.36% of the study area was generally weak, with an area of 2,361.01 km$^2$, 29.23% was slightly weak, covering 10,854.41 km$^2$, and 15.6% was moderately weak, covering 5,794.25 km$^2$. The heavy weak mainly distributed in Keke River, Baihe River, and Minjiang River Basin with an area of 30.79%. The extremely weak (18.02%) is mainly distributed in the south of Hongyuan County and north of Aba County with an area of 6,693.12 km$^2$, significantly overlapping with the land desertification, water, and soil loss area.

## 4.4. Ecological protection importance

The ecological protection evaluation results for the study area are shown in Figure 13. The extremely important area for

ecological protection in the study area is 19,246.85 km$^2$, which accounts for 51.83%, and is mainly distributed in Ruoergai wetland, Baihe Basin, Giant Panda National Park (Songpan), Baozuo, Lianbaoyeze Nature Protection Area, Sichuan Rewugou Forest Park, the lower section of Keke, and Suomo river basins. Furthermore, the important area for ecological protection is 17,354.54 km$^2$, which accounts for 46.73% of the total and is mainly distributed in the Dadu, Bailong, and Minjiang river basins. The generally important area for ecological protection is only 534.71 km$^2$, accounting for 1.44% of the total area, and is mainly distributed in the Gougu Urban Area.

## 4.5. Ecological resilience

According to the ecological resilience evaluation results (Figure 14), 7.70% of the study area has weak ecological resilience and is mainly distributed in the west and south of Aba County, the south of Hongyuan County, the Ruoergai wetland, the Bailong River Basin, the Minjiang River Basin, and the Middle East of Songpan County. Ecological resilience (87.64%) was widely distributed in the study area. Only 4.66% was strong
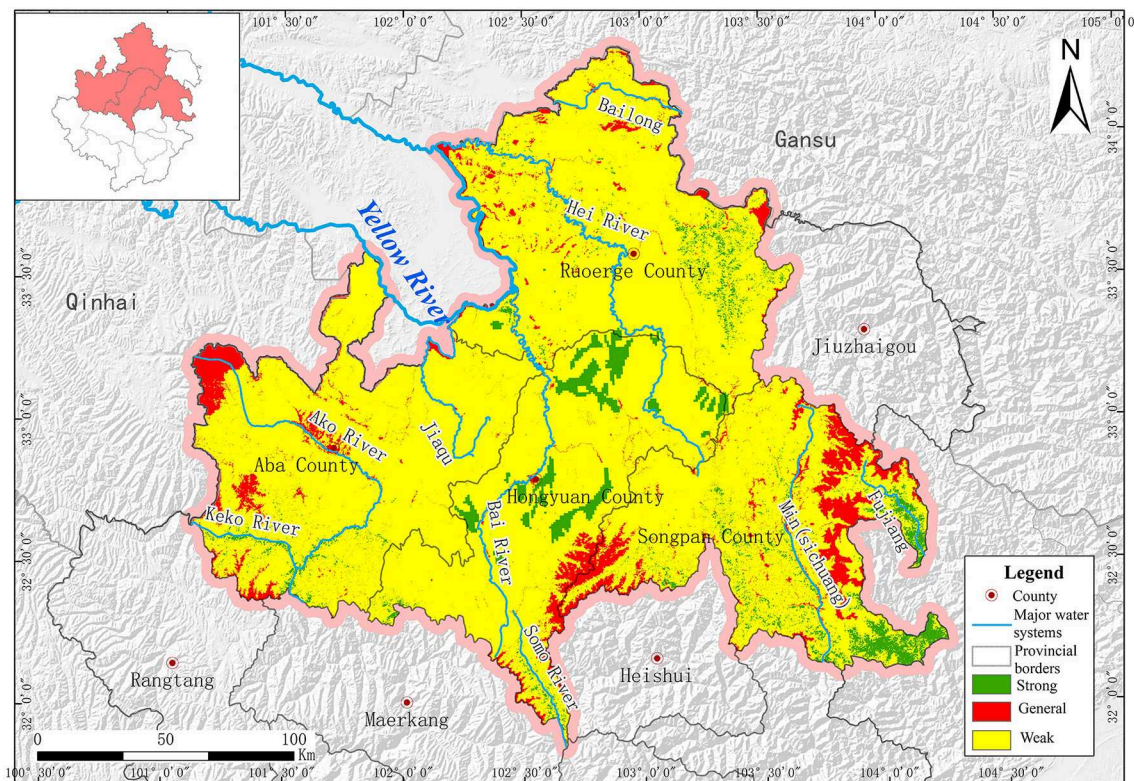
**FIGURE 14**
Ecological restoration capacity assessment.

in ecological resilience, mainly distributed in Ruoergai, Songpan, and Hongyuan counties.

The ecological environment in the study area is difficult to restore after damage, mainly because the study area stretches across the alpine valley region of Hengduan County and the alpine area of the Qinghai-Tibet Plateau, where the ecological environment is relatively weak with low biological protection potential. Moreover, areas with fragile ecological environments in the study area, such as the Lianbaoyeze rocky mountain area in Aba County, the desertification area in Ruoergai wetland, and high mountainous areas with vegetation in the Minjiang and Bailong river basins, show low ecosystem resilience potential.

## 5. Discussion

A comprehensive evaluation of the Ruoergai Prairie ecosystem was conducted in this study. Landscape ecosystem problems include increasingly severe landscape fragmentation, human activity interference, overall ecological environment quality, and coercion on land resources. Three ecological breaking points exist in the study area, located in the giant panda migrating corridor in the Peijiang River Basin, the wildlife migrating corridor in the Ake River Basin, and the wildlife

migrating corridor in the Lianbaoyeze Nature Protection Area (Figure 15A). The cause of the Ake River's breaking point area can be attributed to ecosystem degradation, ecological and environmental damage, roads, water systems, and other linear engineering constructions in valleys that have hindered wildlife migration between ecological sources on both sides of the valley. The Lianbaoyeze breaking point area is caused by geological disasters, including debris flows, landslides, and collapses, which have destroyed wildlife migrating corridors in the Lianbaoyeze Nature Protection Area. The breaking of the giant panda migration corridor upstream of the Peijiang River Basin threatens biodiversity. Although the study area has developed with a wide range of nature protection areas, high vegetation coverage, and a large number of natural ecological corridors, the expansion of urban and rural construction and the development of modern transportation networks exacerbate ecological patch fragmentation, obstruct ecological space communication, considerably reduce the effective connection between ecological patches, break ecosystem stability, and seriously affect the communication of rare animals such as giant pandas.

Based on the ecosystem type data, the landscape fragmentation indices of the study area were graded into four levels (Figure 15B) by the Fragstats simulation. Areas
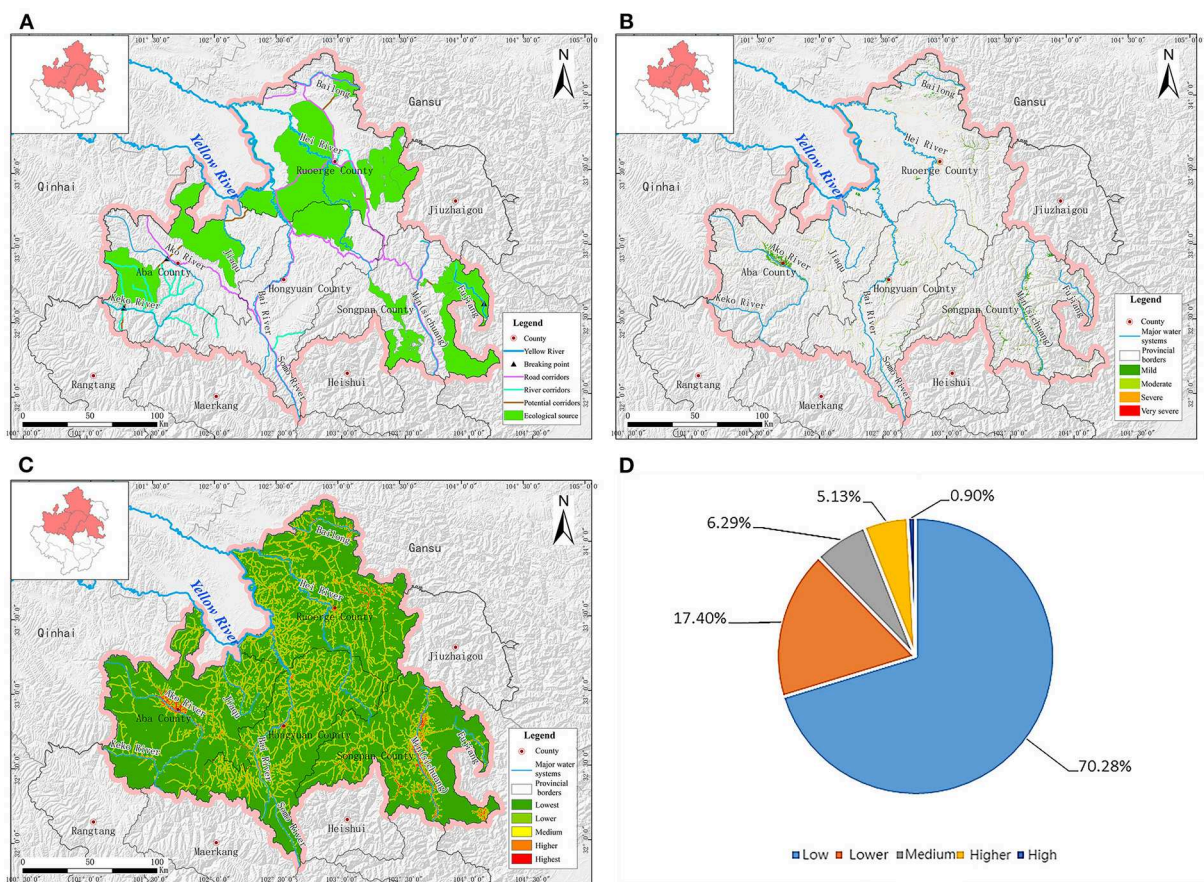
**FIGURE 15**
Ecological and environmental problems. **(A)** Ecological corridors. **(B)** Landscape fragmentation. **(C)** Human activity interference degree diagram. **(D)** Statistic of human activity interference degree.

of high and relatively high fragmentation were distributed in Ruoergai and Hongyuan counties. Moderate fragmentation areas are scattered in Aba, Hongyuan, and Ruoergai counties. The area of relatively low fragmentation mainly covers Aba and Ruoergai counties, and the area of low fragmentation covers the entire study area extensively.

A ground-based artificial interference evaluation model was established according to the third national land survey data to obtain the degree of human activity interference diagram (Figure 15C). Under the effects of large-scale human construction activities, the prominent ecological problems caused by human activities include river basin ecosystem damage due to extensive agricultural and forestry utilization, the negative influence of cascade river development on the river basin ecological environment, river basin ecological environment degradation caused by disordered industrial construction, and the occupation of fertile land and wetlands caused by unreasonable use of urban land. This has seriously impeded the local river basin region's overall social and economic development.

Figure 15D shows the human interference statistics. The degree of human interference is densely distributed within the scope of the study area. Relatively high human interference areas are mainly distributed in construction land-centered areas, including urban and road areas. Urban areas suffer the greatest amount of human interference. High mountainous areas to the south of the study area show relatively low human interference and density.

Because the ecosystem of the study area is diverse and complex, and ecological environment change is a long-term process, studies on ecosystem changes and assessment need to be considered from multiple disciplines. In this study, the Ruoergai Prairie was considered a case study, and a comprehensive assessment of multiple ecosystems was conducted. The data obtained in this study can be used as a reference for local ecological restoration. This study has some limitations. Although many influencing factors are involved in the ecosystem, only important indicators were selected for this study. In addition, some environmental factors were not independent. The elimination of the

correlation between elements is also worth considering. Some assessments have still not been considered, such as those on ecosystem risk, ecosystem sensitivity, and ecological health.

## 6. Conclusion

According to the comprehensive analysis, evaluation, and statistical results on ecosystem quality, ecosystem service function importance, ecological vulnerability, ecological protection importance, and ecological resilience, 98.79% of the study area was identified and evaluated at fine and good levels in ecosystem quality, 97.90% at important and extremely important levels in ecosystem services, 64.41% with a weak ecological environment, 98.56% at important and extremely important levels in ecological protection, and 87.64% with neither good nor bad ecological resilience. The ecological landscape in the study area has difficulties in breaking points, a high fragmentation degree, and severe coercion on land resources, which require integrated protection and restoration over mountains, waters, forests, farmlands, lakes, grasslands, sand, and glaciers.

## Data availability statement

The original contributions presented in the study are included in the article/supplementary material, further inquiries can be directed to the corresponding author.

## Author contributions

XX: funding acquisition, supervision, and project administration. QY: conceptualization and writing-original draft. GX: writing-review and editing. TL and XX: data curation. MY and TJ: formal analysis and investigation. All authors contributed to the article and approved the submitted version.

## Conflict of interest

The authors declare that the research was conducted in the absence of any commercial or financial relationships that could be construed as a potential conflict of interest.

## Publisher's note

All claims expressed in this article are solely those of the authors and do not necessarily represent those of their affiliated organizations, or those of the publisher, the editors and the reviewers. Any product that may be evaluated in this article, or claim that may be made by its manufacturer, is not guaranteed or endorsed by the publisher.

## References

Bai, J. H., Ouyang, H., and Cui, B. S. (2008). Landscape pattern change of Zoige plateau alpine wetland during the past 40 years. *Acta Ecol. Sin.* 28, 2245–2252. doi: 10.1016/S1872-2032(08)60046-3

Bai, J. P. (2013). *Study on Ecological Restoration Process and Ecosystem Service Function in Zoige Alpine Grassland Desertification Control Area.* Yaan: Sichuan Agricultural University.

Committee on the National Ecological Observatory Network. *NEON-Addressing the Nation's Environmental Challenges.* Washington, DC: The National Academy Press (2004).

Cui, S. H., Wu, H., Pei, X. J., Yang, Q. W., Huang, R. Q., and Guo, B. (2022). Characterizing the spatial distribution, frequency, geomorphological and geological controls on landslides triggered by the 1933 Mw 7.3 Diexi Earthquake, Sichuan, China. *Geomorphology* 403, 108177. doi: 10.1016/j.geomorph.2022.108177

De Lange, H. J., Sala, S., Vighi, M., and Faber, J. H. (2010). Ecological vulnerability in risk assessment: a review and perspectives. *Sci. Total Environ.* 408, 3871–3879. doi: 10.1016/j.scitotenv.2009.11.009

Hou, M., Ge, J., Gao, J., Meng, B., Li, Y., Yin, J., et al. (2020). Ecological risk assessment and impact factor analysis of alpine wetland ecosystem based on LUCC and boosted regression tree on the Zoige Plateau, China. *Remote Sens.* 12, 368. doi: 10.3390/rs12030368

Hu, G. Y., Dong, Z., Lu, J., and Yan, C. (2012). Driving forces of land use and land cover change (LUCC) in the Zoige Wetland, Qinghai-Tibetan Plateau. *Sci. Cold Arid Reg.* 4, 422–430. doi: 10.3724/SP.J.1226.2012.00422

Hu, S. J. (2019). *Evaluation of the Ecological Conservation Effect.* Yaan: Sichuan Agricultural University.

Huang, P. Y. (1989). Preliminary evaluation on the development of Mosuo Bay and the influence on desert ecosystem. *Arid Land Geogr.* 2, 1–7.

Jiang, W., Lv, J., Wang, C., Chen, Z., and Liu, Y. (2017). Marsh wetland degradation risk assessment and change analysis: a case study in the Zoige Plateau, China. *Ecol. Indicat.* 82, 316–326. doi: 10.1016/j.ecolind.2017.06.059

Li, G. M., Guo, B., Gan, Q., and Li, S. (2018). Remote sensing monitoring and evaluation of ecosystem vulnerability in Ruoergai County. *Surv. Map. Geogr. Inform.* 43, 11–14. doi: 10.14188/j.2095-6045.2016166

Li, J., Wang, W., Hu, G., and Wei, Z. (2010). Changes in ecosystem service values in Zoige Plateau, China. *Agric. Ecosyst. Environ.* 139, 766–770. doi: 10.1016/j.agee.2010.10.019

McRae, B. H. (2006). Isolation by resistance. *Evolution* 60, 1551–1561. doi: 10.1111/j.0014-3820.2006.tb00500.x

McRae, B. H., and Beier, P. (2007). Circuit theory predicts gene flow in plant and animal populations. *Proc. Natl. Acad. Sci. U. S. A.* 104, 19885–19890. doi: 10.1073/pnas.0706568104

McRae, B. H., Dickson, B. G., Keitt, T. H., and Shah, V. B. (2008). Using circuit theory to model connectivity in ecology, evolution, and conservation. *Ecology* 89, 2712–2724. doi: 10.1890/07-1861.1

O'Malley, R. (2008). The State of the Nation's ecosystems 2008: measuring the lands, waters, and living resources of the United States. *Fut. Surv.* 28, 215–224.

Pang, A., Li, C., Wang, X., and Hu, J. (2010). Land use/cover change in response to driving forces of Zoige County, China. *Proc. Environ. Sci.* 2, 1074–1082. doi: 10.1016/j.proenv.2010.10.119

Pang, Y. J. (2019). *Evaluation and Monitoring of the Zoige Plateau Wetland Ecosystem Based on Remote Sensing Technology*. Wuhan: Wuhan University.

Peng, H., Zhai, J., Jin, D. D., Zhou, Y., Chen, Y., and Gao, H. F. (2022). Assessment of changes in key ecosystem factors and water conservation with remote sensing in the Zoige. *Diversity* 14, 552. doi: 10.3390/d14070552

Shao, Q. Q., Fan, J. W., Liu, J. Y., Huang, L., Cao, W., Xu, X., et al. (2016). Evaluation on ecological effects of sanjiangyuan ecological protection and construction phase I project. *Acta Geogr. Sin.* 71, 3–20. doi: 10.11821/dlxb201601001

Shen, G., Xu, B., Jin, Y. X., Yang, X., and Zhou, Q. (2016). Research progress of Ruoergai Plateau Wetland. *Geogr. Geogr. Inform. Sci.* 32, 76–82. doi: 10.3969/j.issn.1672-0504.2016.04.013

Shen, G., Yang, X. C., Jin, Y. X., Xu, B., and Zhou, Q. (2019). Remote sensing and evaluation of the wetland ecological degradation process of the Zoige Plateau Wetland in China. *Ecolo. Indicat.* 104, 48–58. doi: 10.1016/j.ecolind.2019.04.063

Wan, P., Wang, Q. A., Li, Z. Y., Yan, S., Liu, M., Hu, L. X., et al. (2011). Water conservation function of Ruoergay according to soil water storage capacity. *Sichuan Environ.* 30, 121–123. doi: 10.3969/j.issn.1001-3644.2011.05.026

Wang, Y. Y., He, Y. X., Ju, P. J., Zhu, Q. A., Liu, J. L., and Chen, H. (2019). Application of hierarchical analysis in the study of Joergai wetland degradation. *J. Appl. Environ. Biol.* 25, 46–52. doi: 10.19675/j.cnki.1006-687x.2018.03042

Wu, C., Chen, W., Cao, C., Tian, R., Liu, D., and Bao, D. (2018). Diagnosis of wetland ecosystem health in the Zoige Wetland, Sichuan of China. *Wetlands* 38, 469–484. doi: 10.1007/s13157-018-0992-y

Xiong, Y. Q., Wu, P. F., and Zhang, H. Z. (2011). Soil water conservation function during the degradation of Ruoergai Wetland. *J. Ecol.* 31, 5780–5788.

Zhang, Q. S., Li, F. X., and Wang, D. W. (2021). Research on the change of ecological spatial connectivity in Jiangsu Province based on ecological network. *J. Ecol.* 41, 3007–3020. doi: 10.5846/stxb202005181264

Zhang, S. Q., Guo, H. Y., and Luo, Y. (2007). Evaluation of the driving force of Zoige grassland desertification by climate change and livestock load. Chin. *Grassland J.* 5, 64–71. doi: 10.3969/j.issn.1673-5021.2007.05.011

Check for updates

# The effect of CRD method and auxiliary construction on surface settlement in shallow-buried tunnels

Lin Zhang[1], Yuangui Pan[2]*, Kezhu Chen[3]*, Guoqiang Zheng[3], Yang Gao[4], Peng Chen[1], Guoxiang Zhong[1], Panfeng Chen[1], Fengshou Xu[1], Yong Zhang[1], Guangyu Nan[1], Haobo Xue[1], Tingshuai Wang[1], Peng Zhao[1] and Feng Lu[4]

[1]The 5th Engineering Co., Ltd., of China Railway Construction Bridge Engineering Bureau Group, Chengdu, Sichuan, China, [2]Sichuan Huadi Construction Engineering Co., Ltd., Chengdu, Sichuan, China, [3]Sichuan Communication Surveying and Design Institute Co., Ltd., Chengdu, Sichuan, China, [4]School of Emergency Management, Xihua University, Chengdu, Sichuan, China

Several engineering practices have shown that the excavation of shallow-buried tunnels beneath major roads, as well as the selection of appropriate engineering measures and construction methods, has a significant impact on road surface settlement. Therefore, field monitoring and numerical simulation are adopted in this study to analyze the effect of the cross diaphragm (CRD) excavation method on surface settlement for the under-construction Yüan 1 railroad tunnel. The findings show that during the excavation of the four divisions of the CRD excavation method for shallow-buried tunnels, the amount of surface settlement caused by the excavation of part 1 accounts for 40% of the total surface settlement, followed by the excavation of part 3, accounting for 30% of the total surface settlement, and the difference between the excavation of parts 2 and 4 is insignificant, with part 2 slightly larger than part 4. The main influence of the CRD method on surface settlement for shallow-buried tunnels is 0.64−0.86 times the cavity diameter from the tunnel median, within which the final surface settlement caused by excavation is within the same horizontal range, and beyond which the surface settlement is prone to dramatically decline. By applying advanced grouting and adjusting the construction method of CRD based on the monitoring data, the effect of the CRD excavation method on surface settlement can be controlled.

KEYWORDS

shallow-buried tunnel, ground surface settlement, CRD, on-site supervision, over-grouting

# 1 Introduction

With the continuous development of China's urban infrastructure transportation business, the focus of infrastructure has gradually shifted from the surface to the underground, and the proportion of tunnel projects is gradually increasing. However, many adverse geological conditions are frequently encountered during tunnel construction, such as shallow-buried bias sections or soft ground, where the settlement needs to be strictly controlled for therein lying important structures on the surface. The shallow tunneling method is used for excavating underground spaces in shallow-buried soft ground for urban railways, mountain tunnel portals, and similar spaces for other uses (Li, 2008). According to a previous study, when tunnels are excavated in fragile rocks, the tunnel roofs are prone to collapse. The study demonstrated that folds can exert a significant influence on the strength and stability of fragile rocks, and the use of pre-support measures can effectively protect tunnel roofs from collapsing (Ebrahim et al., 2017). The additional longitudinal stress in an existing tunnel is the main cause of tunnel lining seepage and structural damage; the key influencing factors of existing tunnel settlement such as spatial location, support pressure, and tunnel stiffness have been discussed, and an empirical formula for existing tunnel settlement caused by the excavation of a new shield tunnel has been proposed (Jin et al., 2018). The settlement of the immersed tunnel is affected by various factors. The main influencing factors are tidal loading, siltation and dredging disturbance, and groundwater-level drop, and the analysis of the mechanisms and change laws of these influencing factors can help control tunnel surface settlement (Gang et al., 2012; Liu et al., 2021). New excavation will affect the stress distribution and settlement behavior of existing tunnels, and the second underpass construction will cause more upper tunnel settlement than the first underpass due to the interaction of the new excavation (Wang, 2012). Soil stresses caused by group piles in high-rise buildings and the settlement of adjacent tunnels are analyzed on the basis of the effects of group piles on adjacent subway tunnels (Javad et al., 2015). A combination of analytical, numerical, and experimental methods is used to investigate the subway tunnel settlement station at the Imam Campus of the University of Ali. A parallel gray neural network model (PGNN) is used to predict the settlement displacement of a tunnel monitoring point in the Nanjing subway, and the prediction accuracy of the PGNN is significantly higher than that of a single gray neural network prediction method (Zhu et al., 2015). Tunnel settlement in soft ground is primarily caused by ground settlement beneath the tunnel and is unrelated to the compression of the upper soil layer (Wu et al., 2017; Lai et al., 2020). Based on monitoring data and finite difference method numerical simulation, the settlement characteristics of existing tunnels are investigated. The deformation of existing tunnels caused by shield underpassing is dominated by vertical

settlement accompanied by torsional deformation; these existing tunnels experience the maximum settlement and torsional deformation in the crossover area. The impact area of ground settlement caused by the metro construction is 200 m, and the maximum ground settlement rate is 23.2 mm $yr^{-1}$ (Li et al., 2020). Installing grouting rings on existing tunnels can effectively reduce the amount of tunnel settlement, and increasing the length and thickness of grouting rings can protect existing tunnels (Qi et al., 2021). Similarly, the change laws of the surrounding rock stress, strain, and displacement fields are analyzed, and the characteristics of the support force state of different excavation methods and step-arch tunnels are investigated (Li et al., 2014). The applicability of the cross diaphragm (CRD) method to the type of surrounding rock is analyzed, and the reinforcement measures for the tunnel vault based on the analysis results are proposed (Duan et al., 2019). Controlling the critical construction steps of the CRD method plays a critical role in ensuring efficient construction and safety (Wang et al., 2020). Based on the analysis and study of the ground settlement deformation laws of large-span shallow-buried concealed stations, the excavation of guide holes on both sides will cause longitudinal ground settlement (Yan et al., 2022). The problem of pavement settlement caused by underground works is not limited to tunnel works, for example, coal mining causes large subsidence above the mining area (Shang et al., 2022). The settlement of loess increases nonlinearly with the peak acceleration during earthquakes (Wang et al., 2022). The stability of a rocky slope is controlled by the rock bridge, which is a key intrinsic factor of the rockslide (Tang et al., 2020; Tang et al., 2021). In tunnel excavation, the soil strength and tunnel lining method control the amount of tunnel settlement, so the soil strength becomes an intrinsic factor of tunnel settlement, whereas the lining method becomes an extrinsic factor of tunnel settlement. Fattah et al. (2015) investigated the effectiveness of transfer boundaries in the dynamic analysis of soil–structure interactions in tunnels. Soil surface settlement from tunnel construction is caused by stress release and settlement resulting from the movement of upholders during excavation (Fattah et al., 2013). By analyzing the soil with the elastic–plastic and modified clay models in finite elements (Fattah et al., 2011a), the study found that, due to the effect of additional loads, the maximum surface settlement is exhibited on both sides of the lined tunnel rather than above its center (Fattah et al., 2012). Al-Damluji et al. (2011) found that the main factors influencing the stresses and deformations around tunnels and underground excavations are shapes, sizes, depths of openings below the surface, the distance between openings, and types of upholders. In addition, a study showed that when the upper step length of a tunnel is taken to be 1–2 times the tunnel span, the deformation and stress of the initial upholders will be more reasonable (Zhang et al., 2019).

In summary, the analysis of the CRD excavation method for tunnels under single rocky stratigraphic conditions has been

**FIGURE 1**
Groundwater level line.
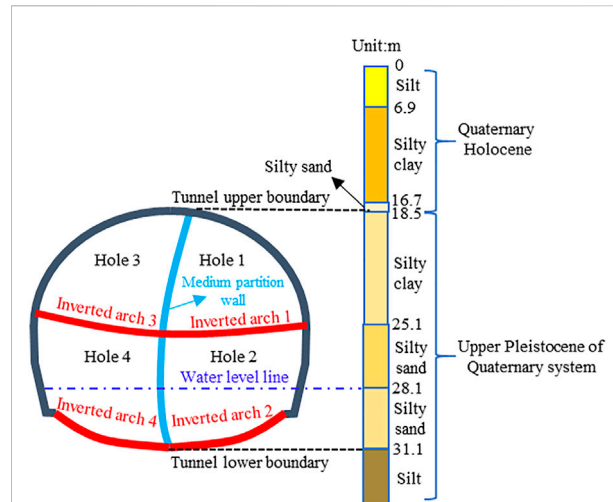


**FIGURE 2**
Location of the tunnel in relation to the strata.

investigated at home and abroad, and research on the deformation of tunnels has been conducted in terms of scale and results, but the understanding of the CRD excavation method under complex stratigraphic and soft surrounding rock conditions and the control of displacement and settlement of the ground under the synergistic effect of auxiliary construction is still lacking. Therefore, this study relies on the Yüan 1 railroad tunnel project and existing monitoring data for data analysis, numerical simulation analysis, and program planning for subsequent construction operations. The numerical simulation serves as direct guidance for the project under construction and provides some reference for subsequent tunnel construction under similar engineering conditions. Soil surface settlement caused by tunnel construction is due to stress release and settlement caused by the movement of supports during excavation (Fattah et al., 2011b).

## 2 Project overview

The tunnel is located on the northern edge of the North China Plain, an alluvial plain with flat and open topography, and the terrain dips gently from northwest to southeast. The tunnel is beneath the roadbed section of the Jingtai Expressway. The tunnel under the highway concealed excavation section mileage DK33+175–DK33+315 with the total length of 140 m, small mileage concealed excavation work shaft DK33+166–DK33+175 with the length of 9 m, and large mileage concealed excavation work shaft DK33+315–DK33+324 with the length of 9 m. The tunnel is designed according to the principle of the Neo–Aofa method, with the CRD method for shallow-buried concealed excavation
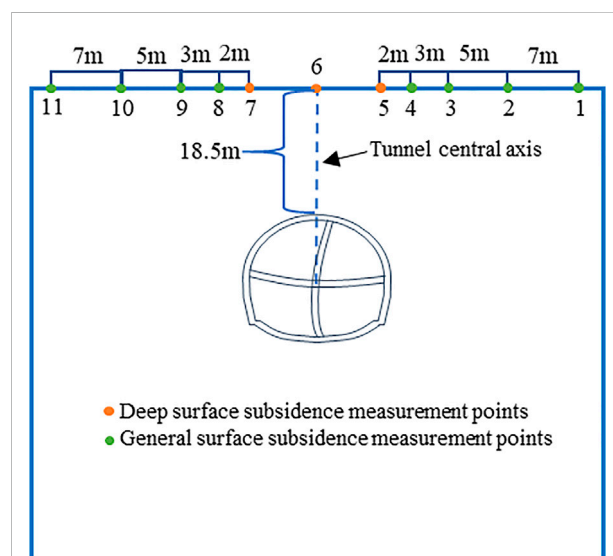


**FIGURE 3**
Monitoring point layout diagram.

construction, the lining structure to curve sidewall arch composite type, shotcrete, reinforcement mesh, and steel frame as the initial support, large pipe shed and pipe curtain pile as the over-support, and molded reinforced concrete as a secondary and tertiary lining.

The tunnel is concealed and excavated more than 30 m into the ground at the small mileage end, and the ground survey data show that the stratum in this section is primarily $Q_4^{al}$ (chalky clay, soil, and sand) and $Q_3^{al}$ (chalky clay, soil, and sand), and the water table line detected by excavation is 1.2 m–3 m above the bottom of the arch.

**FIGURE 4**
DK+201 surface measurement point subsidence temporal curve.
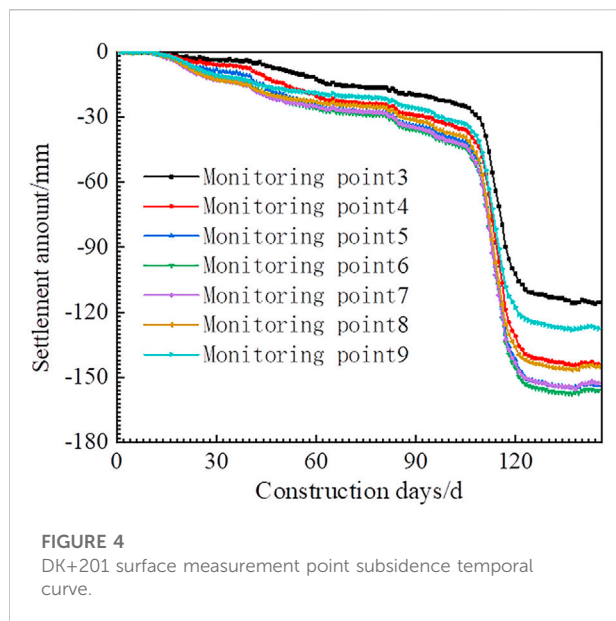
The water table line in the tunnel is depicted in Figure 1. The stratigraphic distribution, excavation sequence, water table line, and the relative position of the tunnel are shown in Figure 2.

CRD is an excavating method that divides a section up and down and left and right, with the next door and elevated arch.

Based on the existing large-span tunnel construction status and construction experience, the main construction methods are as follows: center diaphragm, CRD, double-side heading, full-section excavation, and bench methods.

# 3 Analysis of monitoring data

To monitor the surface deformation information in real time, 11 surface subsidence observation points were set up in the DK33+201 mileage section. The location of the monitoring points above the tunnel is depicted in Figure 3.

Monitoring points 1, 2, 10, and 11 are far away from the tunnel median, and the amount of surface settlement is relatively small. Therefore, the surface deep settlement monitoring point 6 at the tunnel median/surface junction, as well as the remaining two deep settlement monitoring points 5 and 7, and four general settlement monitoring points 3, 4, 8, and 9 near the deep settlement monitoring points, were chosen. Figure 4 depicts the monitored surface settlement data from the beginning of construction to the current progress at the seven monitoring sites.

As shown in Figure 4, the time of the steep increase in the settlement at surface monitoring points 3–9 of the DK33+201 section is consistent with the time of tunnel boring 1–4 to this section, and the settlement increases approximately linearly with the time when the four excavated parts are dug to

this section, respectively. The excavation of Hole 1 has the greatest impact on surface settlement, and its contribution to surface settlement can reach 41.67%, followed by the excavation of Hole 3, with its contribution to surface settlement reaching 27.48%; whereas the excavation of holes 2 and 4 contributes 18.23% and 12.62% to surface settlement, respectively. After tunnel boring, each measurement point reflects that the surface settlement gradually stabilizes, with the curves cut between the excavation of Hole 1 and Hole 4 excavation to calculate the relative deviations of the slope of the seven curves and the slope of the cut line at the measurement point 6.

The average increment in surface settlement is illustrated in Table 1. Table 1 shows that the closer the ground surface is to the tunnel's centerline, the greater the average settlement is during tunnel excavation. The corresponding average increase in surface settlement within the area, where only the tunnel cross-section is located, has a minor difference. The greater the distance from the tunnel's centerline, the less the excavation affects ground settlement and the smaller the average surface increment.

# 4 Numerical simulation analysis

## 4.1 Computational model

The influence range of a circular tunnel on the stress redistribution in the surrounding rock is approximately one time the diameter of the tunnel (Xiao et al., 1987), and the entire span of the tunnel is 14 m, the height is 12.6 m, and the vault is buried 18.5 m from the surface, so the stratigraphic model is constructed by extending the stratigraphic model from the outer contour of the tunnel twice the length of the tunnel span to the left, right, and lower sides, respectively. The numerical simulation calculation model is depicted in Figure 5. The PLANE42 element in ANSYS software is used as the model soil element and the BEAM3 element as the supporting one, with the displacement on both the left and right sides of the model fixed to the $x$-direction and that on its lower side fixed to the $y$-direction as the boundary conditions.

According to the geological survey report, the calculated parameters of each stratum are listed in Table 2, and the intensity of the stratum below the water table line is discounted to 70% of the original parameters (Zhang et al., 2003).

## 4.2 Analysis of surface settlement results

The simulated excavation process is divided into four steps, with a numbering sequence of holes 1–4, all of which use full-section excavation and apply initial support after excavation, which is consistent with the excavation sequence and process on site. The evolution of settlement deformation during the simulated tunnel excavation process is illustrated in Figure 6.

TABLE 1 Average increment of surface subsidence.

| Curve number | Measurement point number | Slope (mm/d) | Relative deviation |
|---|---|---|---|
| 1 | 3 | 5.325 | 24.49% |
| 2 | 4 | 6.612 | 6.24% |
| 3 | 5 | 6.986 | 0.94% |
| 4 | 6 | 7.052 | 0 |
| 5 | 7 | 6.968 | 1.20% |
| 6 | 8 | 6.706 | 4.90% |
| 7 | 9 | 5.847 | 17.09% |



FIGURE 5
Calculation model diagram.
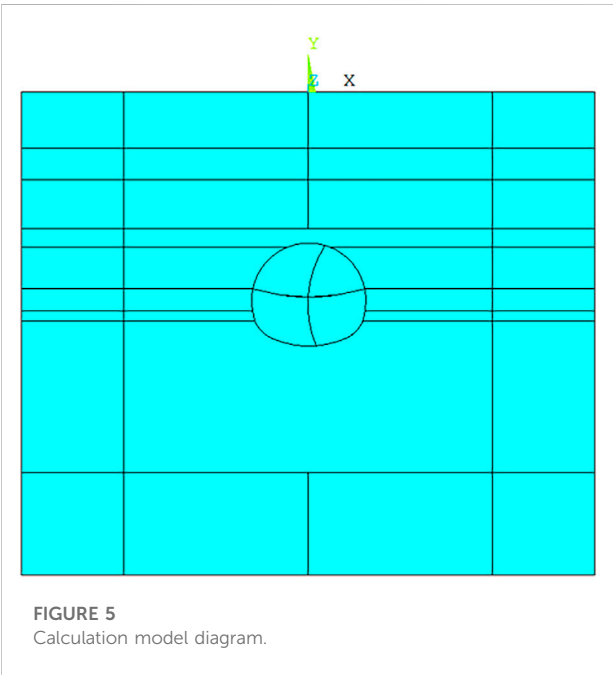
The amount of surface settlement increases with increasing tunnel excavation. After the termination of tunnel excavation, the main influence area of surface settlement gradually shrinks, forming a radial area with the centerline of the tunnel as the reference line toward the surface (the area represented by dark blue in Figure 6D), which has the same distribution trend as the field-monitoring point response. The numerical simulation results of the surface settlement and field-monitoring data were compared and analyzed, and the results of the comparative analysis are shown in Figure 7. The relative errors of the final settlement of field monitoring and those of the numerical simulation are shown in Table 3.

The proportion of the excavation of Hole 1 accounts for 35.71% of the total surface settlement, followed by the excavation of Hole 3, which accounts for 33.15%, and holes 2 and 4 accounting for 16.16% and 14.98%, respectively. Comparing the numerical simulation results with the measured value, the proportion of Hole 1 decreases by 5.96%, that of Hole 3 increases by 5.67%, and those of holes 2 and 4 do not change significantly: the proportion of Hole 2 decreases by 2.07% and that of Hole 4 decreases by 2.36%. The

TABLE 2 Numerical simulation parameter values table.

| Stratigraphic age | Surrounding rock/ support type | Modulus of elasticity (E)/Mpa | Poisson's ratio (u) | Angle of internal friction $(\varphi)/°$ | Cohesion (c)/KPa | Unit weight/ (kN/m3) | Depth range/m |
|---|---|---|---|---|---|---|---|
| Q4 | Silt | 14.4 | 0.30 | 24.2 | 5.2 | 20.00 | 0–6.9 |
| | Silty clay | 13.1 | 0.30 | 20.7 | 15.1 | 18.50 | 6.9–16.7 |
| | Silty sand | 12.3 | 0.25 | 34.3 | 3.3 | 19.50 | 16.7–18.5 |
| Q3 | Silty clay | 6.5 | 0.31 | 18.9 | 13.5 | 18.50 | 18.5–25.1 |
| | Silty sand | 11.8 | 0.25 | 37.2 | 2.9 | 19.50 | 25.1–28.1 |
| Q3 (below water level) | Silty sand | 11.8 | 0.25 | 26.0 | 2.0 | 9.50 | 28.1–31.1 |
| | Silt | 12.5 | 0.30 | 16.5 | 3.5 | 10.00 | 31.1- |
| – | Reinforcement ring | 35 | 0.32 | 35 | 15.0 | 22.00 | 15.5–34.1 |
| – | Initial support structure | 27,500 | 0.2 | – | – | 25.00 | – |
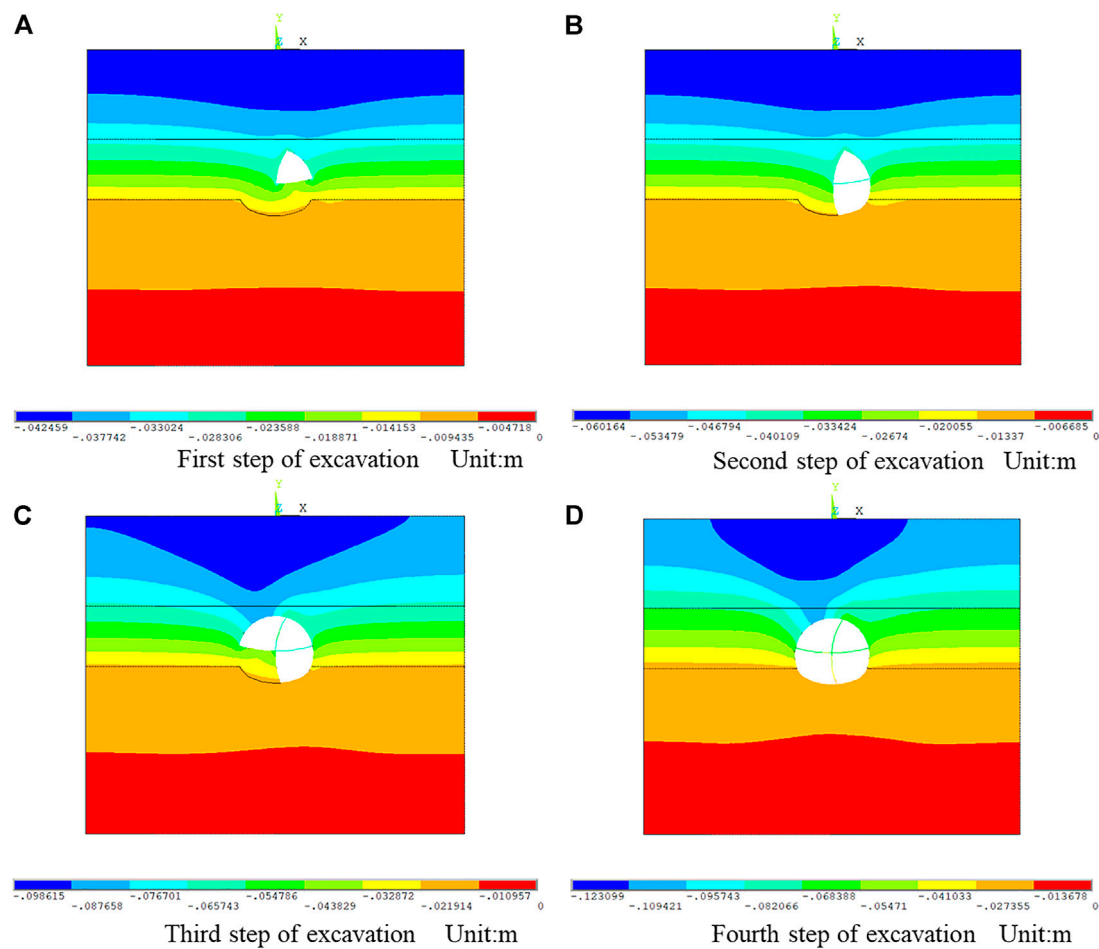
**FIGURE 6**
Y-direction displacement cloud. **(A)** First step of excavation, unit: m. **(B)** Second step of excavation, unit: m. **(C)** Third step of excavation, unit: m.
**(D)** Fourth step of excavation, unit: m.

measured value of the surface settlement is maintained at the same level within 9 m from the tunnel's centerline, with an average value of 108.5 mm, and there is a significant decreasing trend in the surface settlement caused by the tunnel excavation above 9 m from the tunnel's centerline. The relative error between the results of the numerical simulation within 9 m from the tunnel's centerline and the measured value is not greater than 15.97%, and the relative error between the results of the surface settlement simulation more than 9 m from the tunnel's centerline and the measured value is approximately 30%. The aforementioned data show that the numerical simulation of the surface of a certain range can reflect real surface settlement changes, the range of which is 0.64–0.86 times the tunnel's centerline. The differences between numerical simulation and field monitoring may be because of the complex stratigraphic distribution of the site, the fact that the stratigraphic model used in the simulation is determined by the part excavated and explored with the

DK+201 section distribution, or that the distribution of a layer is assumed uniform in depth in the numerical simulation; the assumed position of the water table line in the numerical simulation is the highest water table line; for the physical and mechanical parameters of the strata below the water table line, only gravity reduction and strength discounting are considered.

# 5 Ancillary construction synergy analysis

## 5.1 Analysis of surface settlement results

To further control surface settlement, full-section overburden grouting is proposed in the subsequent excavation to pre-reinforce the strata; the excavation method of reserving the core soil is adopted for holes 1 and 3, and the step method is
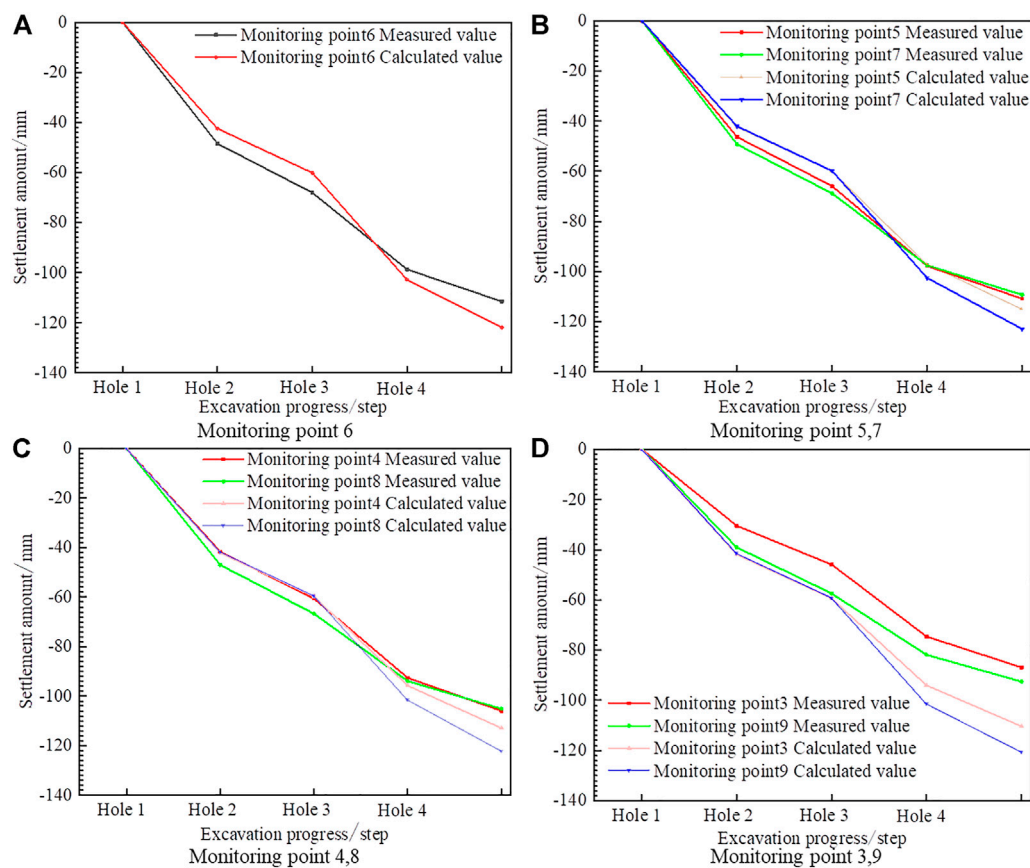
**FIGURE 7**
Comparison of measured and calculated values of surface settlement at different measurement points. **(A)** Monitoring point 6. **(B)** Monitoring points 5 and 7. **(C)** Monitoring points 4 and 8. **(D)** Monitoring points 3 and 9.

**TABLE 3** Relative error between measured and calculated values of final ground settlement.

| Monitoring point number | Measured settlement value/mm | Calculated settlement value/mm | Relative error (%) | Distance from the centerline of the tunnel/m |
|---|---|---|---|---|
| 3 | −86.89 | −110.35 | 27.00 | 12 |
| 4 | −105.9 | −112.87 | 6.58 | 9 |
| 5 | −110.86 | −115.00 | 3.73 | 7 |
| 6 | −111.50 | −122.83 | 10.16 | 0 |
| 7 | −109.29 | −122.36 | 11.96 | 7 |
| 8 | −105.08 | −121.86 | 15.87 | 9 |
| 9 | −92.53 | −120.83 | 30.58 | 12 |

(Note: the "-" sign indicates sinking).

adopted for holes 2 and 4 to reduce the critical surface of one excavation. The auxiliary construction collaborative excavation process is depicted in Figure 8.

Figure 9 shows the calculated model with the displacement cloud in the *y*-direction after excavation. Figures 6D, 9B show

that after grouting and using the pre-core soil with the step method excavation process, the displacement around the shallow-buried tunnel is well controlled, the favorable effect of reinforcement radiates to the surface, and the maximum settlement of the surface is 103.94 mm.

**FIGURE 8**
Schematic diagram of the new excavation process.
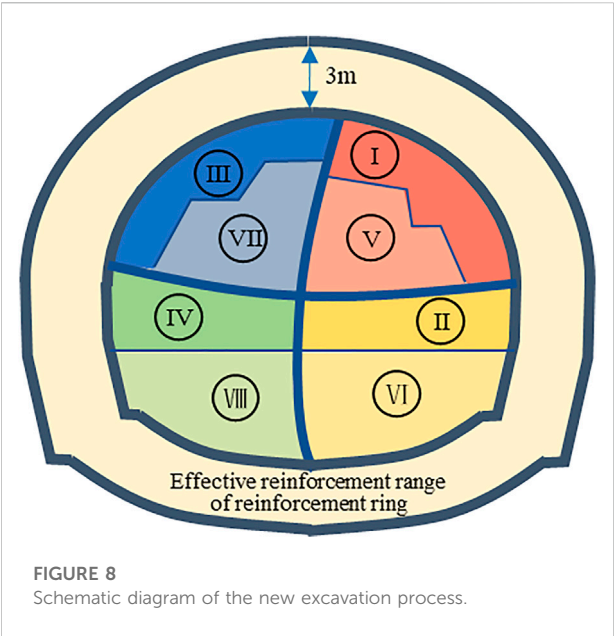
Table 4 compares the calculated values of surface settlement for the new and old excavation methods. Comparing the surface settlement displacements at monitoring point 6, the results show that the surface settlement caused by the new method in the corresponding excavation stage is generally reduced by approximately 15% compared with that caused by the original method. The new process plays a certain role in controlling surface settlement. On this basis, the surface settlement rate can be controlled by increasing the strength of the initial support and the strength of the second lining support so that the accumulated settlement of important buildings on the surface is within the control value.

## 5.2 Discussion

The material point method combines the advantages of the Lagrangian and Eulerian methods and has advantages in modeling significant deformation (Dong et al., 2021). By studying the transient impact process of a submarine landslide



**FIGURE 9**
Calculation model and calculation results. **(A)** Computational model. **(B)** Y-direction displacement cloud, unit: m.
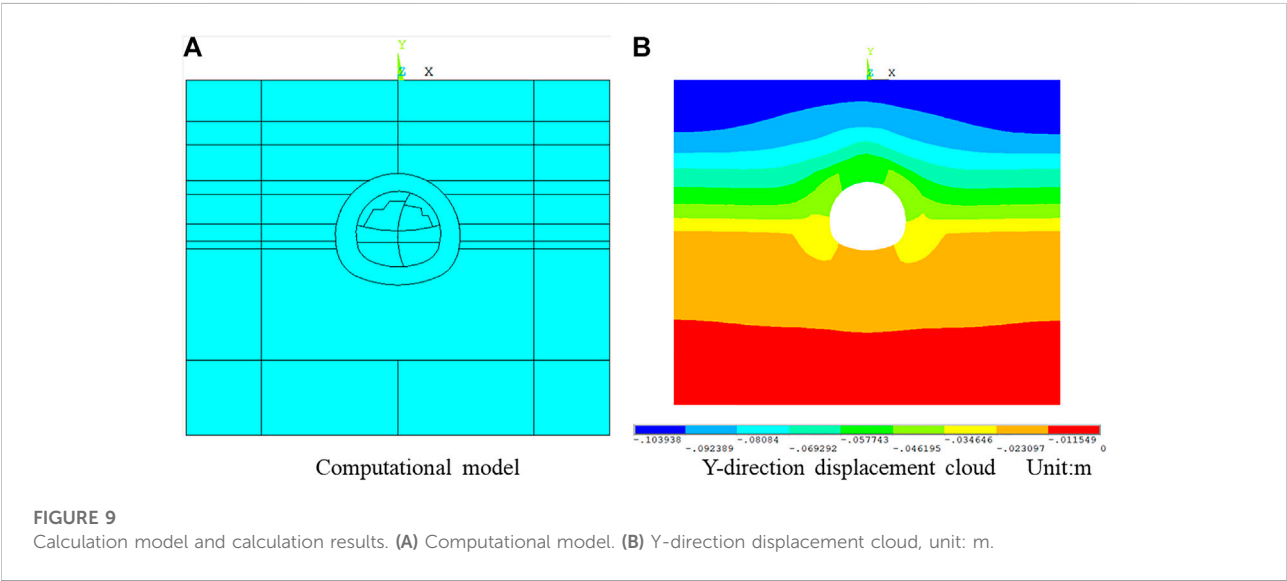
**TABLE 4 Comparison of the calculated values of surface settlement between the new method and the old method.**

| Excavation stage | Settling volume/mm (before reinforcement) | Settling volume/mm (after reinforcement) | Decrease percentage (%) |
|---|---|---|---|
| 1 | −42.41 | −36.24 | 14.54 |
| 2 | −60.15 | −49.91 | 17.02 |
| 3 | −102.85 | −86.49 | 15.91 |
| 4 | −121.86 | −103.84 | 14.79 |

on pipelines and the effect on the parameters with regard to the landslide quality, Fan et al. (2022) elucidated the formation mechanism of the transient impact force based on the characteristic analysis of flow velocity and acceleration fields around the pipeline during the slide–pipeline interaction. Wang et al. (2021) proposed a general framework for analyzing the spatial and temporal evolution of multistage riparian landslides that applied a three-dimensional geological model to integrate a large amount of data from surface surveys, subsurface exploration, *in situ* monitoring, and geological mapping and to predict landslide triggers based on these data.

The top of a shallow-buried tunnel is typically buried within 20 m of the surface. Because of the tunnel's shallow depth, excavation construction will disturb the ground surface and upper buildings, which may lead to the collapse of the ground surface and the tunnel without notice, causing unnecessary safety accidents. The common full-section excavation method should not be used in tunneling shallow-buried tunnels because it can cause uncontrolled displacement and even lead to tunnel collapse resulting from excessive one-time excavation and excessive soil deformation. In this study, the CRD method was adopted for the initial excavation to ensure that the construction proceeded as scheduled without operational accidents, and the field-monitoring data were combined with numerical simulation tools to investigate the effect of the CRD method on surface deformation characteristics in shallow-buried tunnels. Overall, the findings show that after applying the CRD method, the surface settlement caused by the upper cavern excavation (holes 1 and 3) accounts for the majority of the total surface settlement, approximately 70%, with the excavation sequence and the spatial relative position of the caves being presumed as the main influencing factors. Hole 1 was excavated first, which is equivalent to directly removing a part of the originally complete plane, and the stress change caused by it can be transferred to the ground surface through the surrounding rocks in the upper part of the hole, so the surface settlement caused by it is the largest among the four steps. After that, Hole 2 is excavated, whose spatial location is directly below Hole 1. Because the body of Hole 1 has been excavated, there is no medium to transmit the change in stress distribution caused by the excavation of the body of Hole 2; thus, the stress change caused therein is transmitted from the surrounding rock bodies on the left and right sides of the Hole 2 body to the surroundings and then to the surface, so the amount of surface settlement caused by the excavation of Hole 2 is smaller than that of Hole 1, i.e., only approximately 15–18%. The surface settlement caused by the excavation of Hole 3 is the second largest, only 2.5% smaller than that of Hole 1, based on the calculated average of each measurement point. Because the distance from these two holes to the surface is the same, the transfer processes of stress changes caused therein to the surface are similar. The surface settlement caused by the excavation of Hole 4 accounts for 12–15%, with its effect consistent with that of Hole 2.

With the CRD method, outstanding tunnels will not be excavated unless and until their surrounding rocks are reinforced by applying the full-section overburden grouting method to further control the surface settlement, after which the mechanical strength (including cohesion, internal friction angle, and elastic modulus) of the surrounding rocks will increase, and the displacement of these rocks caused by the stress during tunneling is smaller than that of the unreinforced rocks, which in turn causes less surface settlement. On this basis, the core soil is reserved during excavation as soil strength support. Reserving the core soil while applying the bench tunneling method is to reduce soil deformation by further reducing the earthwork volume of one excavation and the area of the free face. The adoption of the new method can further reduce the amount of surface settlement. In areas with complex ground strata, the deformation characteristics and deformation rates of tunnels can be found in time by monitoring using this method, and the excavation method, supporting method, and soil strength can be dynamically adjusted to protect important buildings on the ground.

# 6 Conclusion

In this study, data were analyzed by monitoring on-site surface settlement in a section of an under-construction railroad tunnel beneath a highway. Finite element software was used to analyze the surface settlement pattern caused by the concealed excavation under weak surrounding rocks using the shallow-buried tunnel CRD method, and the research results were compared with the actual settlement on site, and suggestions for adjusting subsequent excavation plans were made as follows:

(1) For the construction of a shallow-buried tunnel using the CRD method, the amount of surface settlement caused by the excavation of Hole 1 can account for 40% of the total amount, followed by the excavation of Hole 3, accounting for 30% of the total amount of surface settlement, and the difference between the amount of surface settlement caused by the excavation of holes 2 and 4 is insignificant. In the subsequent excavation process, the excavation plans of holes 1 and 3 should mainly be adjusted.

(2) The distance from the centerline of the tunnel to 0.64–0.86 times the diameter of the tunnel has the greatest influence on surface settlement in shallow-buried tunnels using the CRD method. The farther the distance from the tunnel's centerline, the less the ground settlement is affected. The finite element numerical simulation prediction for surface settlement within the main influence range is credible.

(3) The calculated value of surface settlement is slightly larger than the measured value of the surface settlement, and its relative error is in the range of 3.73–30.58%; the distance of the monitoring point from the center of the tunnel decreases, and its error exhibits a decreasing trend.

(4) In the CRD excavation method, the auxiliary construction can effectively reduce the amount of surface settlement by approximately 15%. On this basis, the strength of the subsequent support can be enhanced, and the excavation process can be flexibly adjusted to control the amount of surface settlement.

## Data availability statement

The original contributions presented in the study are included in the article/Supplementary Material; further inquiries can be directed to the corresponding authors.

## Author contributions

LZ, KC, and YP were responsible for writing. GZ, PC, GZ, PC, and YG provided engineering data and performed geophysical analysis. FX, YZ, and GN were responsible for numerical simulation analysis. HX, TW, and PZ were responsible for the ancillary construction synergy analysis. YP was responsible for review and proofreading. FL was responsible for producing pictures.

## Funding

## Conflict of interest

The authors LZ, PeC, GZ, PaC, FX, YZ, GN, HX, TW and PZ were employed by The 5th Engineering Co., Ltd. of China Railway Construction Bridge Engineering Bureau Group. The author YP was employed by Sichuan Huadi Construction Engineering Co., Ltd. The authors KC and GZ were employed by Sichuan Communication Surveying and Design Institute Co., Ltd.

The remaining authors declare that the research was conducted in the absence of any commercial or financial relationships that could be construed as a potential conflict of interest.

## Publisher's note

All claims expressed in this article are solely those of the authors and do not necessarily represent those of their affiliated organizations, or those of the publisher, the editors, and the reviewers. Any product that may be evaluated in this article, or claim that may be made by its manufacturer, is not guaranteed or endorsed by the publisher.

## References

Al–Damluji, O. F. S., Fattah, M. Y., and Al-Adthami, R. A. J. (2011). Analysis of soil media containing cavities or tunnels by the boundary element method. *J. Alhosn Univ. J. Eng. Appl. Sci.* 3 (2), 27–49.

Dong, Y. K., Cui, L., and Zhang, X. (2022). Multiple-GPU parallelization of three-dimensional material point method based on single-root complex. *Int. J. Numer. Methods Eng.* 123 (2), 1481–1504. doi:10.1002/nme.6906

Duan, J., Huang, C. R., Cui, X. Y., Li, K., and Guo, H. Y. (2019). Evaluation of a tunnel in Yunnan using CRD construction method. *E3S Web Conf.* 136 (3), 04020. doi:10.1051/e3sconf/201913604020

Ebrahim, F. S., Majidreza, N., and Anna, G. (2017). A numerical investigation of sinkhole subsidence development over shallow excavations in tectonised weak rocks: The dolaei tunnel's excavation case. *Geotech. Geol. Eng. (Dordr).* 35 (4), 1685–1716. doi:10.1007/s10706-017-0202-3

Fan, N., Jiang, J. X., Dong, Y. K., Guo, L., and Song, L. F. (2022). Approach for evaluating instantaneous impact forces during submarine slide-pipeline interaction considering the inertial action. *Ocean. Eng.* 245 (6), 110466. doi:10.1016/j.oceaneng.2021.110466

Fattah, M. Y., Hamood, M. J., and Dawood, S. H. (2015). Dynamic response of a lined tunnel with transmitting boundaries. *Earthquakes Struct.* 8 (1), 275–304. doi:10.12989/EAS.2015.8.1.275

Fattah, M. Y., Shlash, K. T., and al-Soud, M. S. (2012). Boundary element analysis of a lined tunnel problem. *ije.* 25 (2), 89–97. doi:10.5829/idosi.ije.2012.25.02b.02

Fattah, M. Y., Shlash, K. T., and Salim, N. M. (2011a). Effect of reduced zone on time-dependent analysis of tunnels. *Adv. Civ. Eng.* 12 (4), 1. doi:10.1155/2011/963502

Fattah, M. Y., Shlash, K. T., and Salim, N. M. (2013). Prediction of settlement trough induced by tunneling in cohesive ground. *Acta Geotech.* 8, 167–179. doi:10.1007/s11440-012-0169-4

Fattah, M. Y., Shlash, K. T., and Salim, N. M. (2011b). Settlement trough due to tunneling in cohesive ground. *J. Indian Geotechnical J.* 41 (2), 64–75.

Gang, W., Hui, J. Q., and Xin, J. W. (2012). Analysis of settlement reasons and mechanism in immersed tunnel. *J. Appl. Mech. Mater.* 238, 803–807. doi:10.4028/www.scientific.net/amm.238.803

Javad, S., and Hadi, H. S. (2015). Tehran subway tunnel settlement analysis by using analytical, experimental and numerical methods (case study: Station of Imam Ali university). *J. Int. J. Sci. Eng. Technol.* 4 (5), 325–328. doi:10.17950/ijset/v4s5/513

Jin, D. L., Yuan, D. J., Li, X. G., and Zheng, H. T. (2018). Analysis of the settlement of an existing tunnel induced by shield tunneling underneath. *Tunn. Undergr. Space Technol.* 81, 209–220. doi:10.1016/j.tust.2018.06.035

Lai, H. P., Zheng, H. W., Chen, R., Kang, Z., and Liu, Y. (2020). Settlement behaviors of existing tunnel caused by obliquely under-crossing shield tunneling in close proximity with small intersection angle. *Tunn. Undergr. Space Technol.* 97, 103258. doi:10.1016/j.tust.2019.103258

Li, F. K., Gong, H. L., Chen, B. B., Gao, M. L., and Zhou, C. F. (2020). Subsidence monitoring with TerraSAR-X data in beijing central business district and subway tunnelings, China. *Proc. IAHS.* 382, 125–130. doi:10.5194/piahs-382-125-2020

Li, J., Wang, Z. L., and Zhong, J. F. (2014). Force state of country rock and supporting structure in multi-arch tunnel under central hole + CRD method. *J. Appl. Mech. Mater.* 580-583, 1192–1196. doi:10.4028/www.scientific.net/amm.580-583.1192net/AMM.580-583.1192

Li, W. (2008). *ANSYS example analysis of tunnel and underground engineering.* Yichang, China; Water&Power Press.

Liu, Z. Y., Xue, J. F., Ye, J. Z., and Qian, J. G. (2021). A simplified two-stage method to estimate the settlement and bending moment of upper tunnel

considering the interaction of undercrossing twin tunnels. *Transp. Geotech.* 29 (9), 100558. doi:10.1016/j.trgeo.2021.100558

Qi, Y. J., Wei, G., Xie, Y., and Wang, Q. (2021). Effect of grouting reinforcement on settlement of existing tunnels: Case study of a new crossing underpass. *Symmetry (Basel).* 13 (3), 482. doi:10.3390/sym13030482

Shang, H., Zhan, H. Z., Ni, W. K., Liu, Y., Gan, Z. H., and Liu, S. H. (2022). Surface environmental evolution monitoring in coal mining subsidence area based on multi-source Remote sensing data. *Front. Earth Sci. (Lausanne).* 10. doi:10.3389/feart.2022.790737

Tang, P., Chen, G. Q., Huang, R. Q., and Wang, D. (2021). Effect of the number of coplanar rock bridges on the shear strength and stability of slopes with the same discontinuity persistence. *Bull. Eng. Geol. Environ.* 80 (5), 3675–3691. doi:10.1007/s10064-021-02180-y

Tang, P., Chen, G. Q., Huang, R. Q., and Zhu, J. (2020). Brittle failure of rockslides linked to the rock bridge length effect. *Landslides* 17 (4), 793–803. doi:10.1007/s10346-019-01323-3

Wang, J., Schweizer, D., Liu, Q., Su, A., Hu, X., and Blum, P. (2021). Three-dimensional landslide evolution model at the Yangtze River. *Eng. Geol.* 292 (1), 106275. doi:10.1016/j.enggeo.2021.106275

Wang, K. (2012). Theoretical calculation and parametric analysis of tunnel settlements due to neighboring over-length pile groups. *J. Appl. Mech. Mater.* 238, 769–772. doi:10.4028/www.scientific.net/amm.238.769net/AMM.238.769

Wang, P., Xu, S. Y., Shao, S. J., Wang, H. J., Li, X. D., and Qian, Z. L. (2022). Mesoscopic characteristics and performance evaluation of loess treated by different

anti-seismic subsidence technologies. *Front. Earth Sci. (Lausanne).* 9. doi:10.3389/feart.2021.762508

Wang, Z. W., Yang, R. H., Guo, H. Y., and Li, K. (2020). Study on key construction procedures of CRD method for Re shuitang No.3 tunnel. *IOP Conf. Ser. Mat. Sci. Eng.* 711 (1), 012074. doi:10.1088/1757-899X/711/1/012074

Wu, H. N., Shen, S. L., and Yang, J. (2017). Identification of tunnel settlement caused by land subsidence in soft deposit of shanghai. *J. Perform. Constr. Facil.* 31 (6). doi:10.1061/(ASCE)CF.1943-5509.0001082

Xiao, S. F., and Yang, S. B. (1987). *Rock Mechanics*. M. Geological Publishing House Co., Ltd., Beijing, China, 211.

Yan, N., Jing, D. S., Sang, S. K., Bai, X. Y., Liu, X. Y., et al. (2022). An investigation on longitudinal surface subsidence deformation of large-span undercut metro tunnel. *Front. Earth Sci. (Lausanne).* 10, 839242. doi:10.3389/feart.2022.839242

Zhang, F. Z., Chen, X. P., and WuHuang, H. F. G. Y. (2003). The characteristic of residual strength of soft clayey rocks of the east river-shenzhen water supply project. *J. J. Eng. Geol.* 11 (01), 54–57.

Zhang, N., Zhang, G. W., Liu, R. H., Gao, H. J., and Gong, H. X. (2019). Optimization analysis of step length in tunnel construction by bench method. *J. Highw.* 64 (10), 299–303.

Zhu, L., Huang, T., Shen, Y. Q., and Zeng, X. M. (2015). Study on tunnel settlement prediction method based on parallel grey neural network model. *J. Proc. Spie–The Int. Soc. Opt. Eng.* 9808, 98082B–98082B7. doi:10.1117/12.2207838

# Comparison of time-dependent viscosity slurry and cement-clay slurry for anti-seepage grouting on faults

Jiaxing Zhang[1], Xiangjun Pei[1]*, Zhihao He[1,2], Zuan Pei[1] and Guoxun Zheng[3]

[1]State Key Laboratory of Geohazard Prevention and Geoenvironment Protection, Chengdu University of Technology, Chengdu, China, [2]School of Emergency Managment, Xihua University, Chengdu, China, [3]Changchun Institute of Technology, Changchun, China

The complex rock mass structure in fault fracture zone weakens the permeability of strata. This has led to curtain grouting being used to improve the anti-seepage properties of fault zones. This study evaluates the groutability and impermeability of a time-dependent viscosity slurry and a cement-clay slurry in a shattered fault zone. Rheology, setting time, mechanism, and permeability were tested to evaluate the groutability, and Lugeon and grouting field tests were carried out to evaluate the anti-seepage grouting characteristics of a fault zone. The results show that the time-dependent viscosity slurry had higher initial fluidity, a shorter and more controllable setting time, and higher strength than cement-clay slurry, better ensuring the slurry diffusion radius, pores filling rate, and bearing capacity and durability of the consolidated body. The permeability coefficient of the two grouts was less than $1 \times 10^{-7}$ cm/s, and the blocking rate of heavy metal ions was more than 98%, sufficient to effectively control the leakage of sewage. The P~Q curve of the Lugeon test showed that the original strata were of the washout type (>200 Lu), and the rock mass quality grade was the D grade (Poor). Under the same grouting depth, the amount of time-dependent viscosity slurry required was 72.6% of that of cement-clay slurry, and the permeability decreased to 10 Lu, far lower than the 50 Lu of the cement-clay slurry. The time-dependent viscosity slurry improved the quality of the rock mass from D to B-C grade, while the cement-clay slurry test area is remained C-D grade. In general, the time-dependent viscosity slurry performed better than cement-clay slurry in the water-bearing fault zone.

KEYWORDS

permeation grouting, cement-clay slurry, time-dependent viscosity, water pressure, penetrability

## Introduction

Water resources are the basis of human survival and socio-economic development, but environmental pollution has become a growing threat to those resources (Zhang et al., 2021b; Yao et al., 2022). Mineral resource exploitation is a fundamental element of the Chinese economy, but generates a large number of waste tailings. Under the leaching effect of precipitation and surface water infiltration, large quantities of heavy metal ions are released from the tailings and diffuse to the environment with groundwater seepage (Adamovic et al., 2022; Esteller et al., 2015; Raghavendra and Deka, 2015; Zhang et al., 2021a; Zhang et al., 2022). Researchers have studied the dissolution laws of various metal ions and proposed pollutant migration and diffusion models (Huang et al., 2014; Hussein et al., 2021). Landfill is another source of environmental pollution caused by the leakage of leachate containing organic matter and heavy metal ions (Xaypanya et al., 2018; Westlake, 2014; Gworek et al., 2016). Such pollution is characterized by difficulty in discovery, a lag of pollution, and difficulty in remediation. Seepage prevention usually involves the construction of a vertical impermeable curtain, such as concrete or clay-cement plastic impermeable walls and geotechnical impermeable blankets. However, these methods are of limited use when the seepage occurs in cracks or dissolution channels. In this situation, curtain grouting can play a significant role.

Grouting is a method to inject the grouting materials into the joints, fractures and voids of the rock mass and soil formation, which is used to improve the ground conditions. The main function of grouting is to both improve the strength and reduce the deformation of the rock mass or formation under the structures and to reduce hydraulic conductivity. Grouting is one of the most effective geotechnical methods in hydraulic engineering, geotechnical engineering, and tunneling engineering for treating rock formations and controlling seepage (Foster et al., 2000; Azadi et al., 2017; Lee et al., 2017). Curtain grouting and consolidation grouting are both types of permeation grouting, which means that the grouting materials are designed to penetrate the cracks and thus spread into the rock mass or formation. The spreading of grout and the result of grouting depend on the properties of the grout and the rock formation (Mortazavi and Maadikhah, 2016). Relevant grout properties include penetrability and rheology, which are determined by the types of composition of the cementitious grout materials employed (Eklund and Stille, 2008; Carter et al., 2012). Relevant ground properties include aperture size and number, the roughness and irregularity of the crack surface, and the fill condition of the joints.

Due to the strong tectonic action, the fault zone has the characteristics of rock mass fragmentation, fracture development, large difference in filling rate and good permeability, which is a natural to water conduction and storage structure. At the same time, it is also the key part of all kinds of anti-seepage projects. Historically, the understanding and designing of grouting were based mainly on empirical knowledge. As a deeper understanding of the grouting and grout diffusion mechanism in rock fractures and soil formations, the grouting method and grouting materials have also been improved (Stille et al., 2012), such as "real-time grouting control method", which is defined as governing the grouting process through calculating the grouting penetration and applying active control method (Stille et al., 2009). However, there is no targeted grouting method for anti-seepage grouting of fault zones, especially those with dynamic water. On the other hand, grouting materials have also been developed from the clay slurry, cement clay (bentonite) slurry, pure cement paste to the use of complex geological conditions of the new cement based slurry (Xu and Yang, 2006; Zhang et al., 2018; Liu and Chen, 2019; Jiang and Qiu, 2021). Researchers have observed that water can spread into the fractures under lower pressure, but a higher grouting pressure should be used for grout displacement (Ewert, 1998; Fransson, 2001). This demonstrates that the rheological properties of the fluid directly affect its diffusion characteristics under pressure. High-viscosity and low-viscosity slurry adopts to different geological conditions (Stare et al., 2013). Low-viscosity materials are suitable for smaller voids and fractures, but larger fractures and dynamic water environment require the use of high-viscosity and low-dispersion materials. Which grout is suitable for water-bearing fault zones needs further validation. Therefore, the development of efficient grouting method and high flow, low dispersion grouting material is the key technology for solving the water-bearing fault zone seepage control grouting.

In this study, the anti-seepage treatment of the fault zone of the coal chemical plant was taken as the engineering background. The influence of the grouting method and materials on the penetration of a fault were investigated. The Lugeon values and secondary permeability index (SPI) of the fault under test before and after grouting were calculated using a water pressure test, and the quality of the treatment were judged by SPI. In the field grouting test, two kinds of cementitious grout materials were used, namely, a time-dependent viscosity slurry and a cement-clay slurry. The suitability of the chosen grouting materials for use with the fault under test could also be judged from the grouting pressure and grout uptake during the injection.

## Background

### Project overview

The study area is a large excavation and fill area site intended for use in the future as a coal-chemical industrial district and located from $105°45'$ to $105°48'$E and $26°52'$ to $26°55'$N in Guizhou Province, China. The site is 25 km north of the village of Zhijin and 150 km northwest of Guiyang city and

FIGURE 1
Location of the study area.
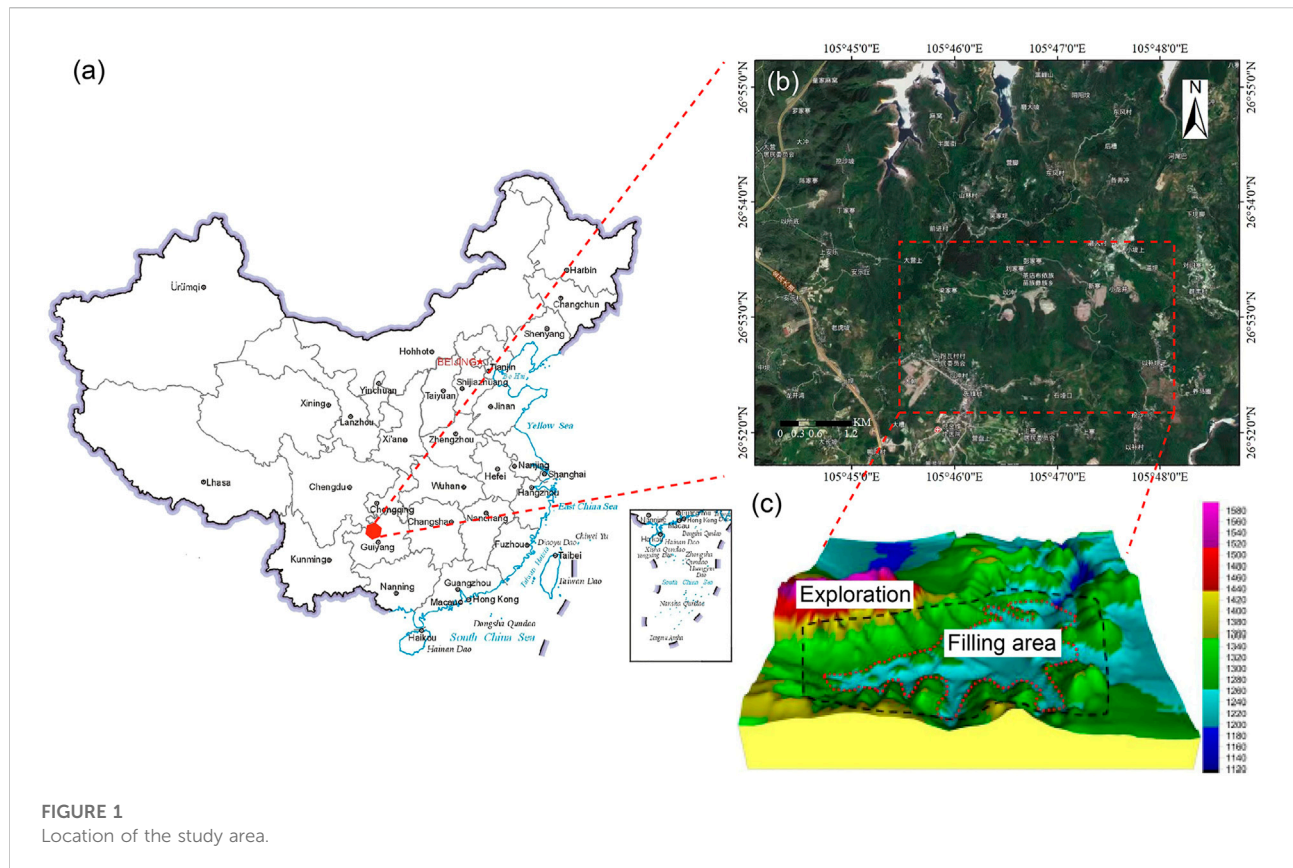
the total area is 415 hectares. This area has unique topographic and geomorphic conditions and complicated geology and hydrology. The total amount of excavation and fill is about 11 million m³, and the maximum excavation depth and maximum filling thickness are 98 m and 45 m, respectively. The excavation and fill process causes lots of rock falls, faults are exposed, and the penetration of formation is increased. Therefore, the use of anti-seepage grouting should be considered to reduce the risk of underground pollution. The location and topography of the study are shown in Figure 1.

# Geological overview

## Lithology

The strata in the study area are mainly composed of shallow water carbonates. The sediment strata are thicker and have abundant biological fossils, such as bivalves and planktonic ammonite. The lithology can be classified as Upper Triassic Xujiahe formation ($T_3x$), which consists of sandstone and shale, and is mainly composed of cross-bedding and oblique bedding, and Middle Triassic Falang ($T_2f$) and Guanling ($T_2g$) formations, which are dominantly composed of argillaceous

limestone, siliceous limestone, sandy shale, and calcareous siltstone and dolomite. The geological map is shown in Figure 2.

## Tectonic characteristics

The study area is in the Central Guizhou Uplift, which is an EW uplift of Ordovician and Silurian distributed in Zunyi, Guizhou province. There are seven faults in the study area (Figure 2).

# Hydrological setting

## Surface water

The site is a low-middle mountain erosion, denudation and dissolution landform. The Yichong river flows through the whole site and then flows into the Liugui river in the Hongjiadu Power Station reservoir. There are several mountain streams in the upper reaches of the Yichong River, and the catchment area of the whole field is about 12.5 km². The upper reach of the Yichong River is about 2 m wide, while the widest part of the lower reaches is 8m, and the maximum cutting depth is 3 m. The riverbed
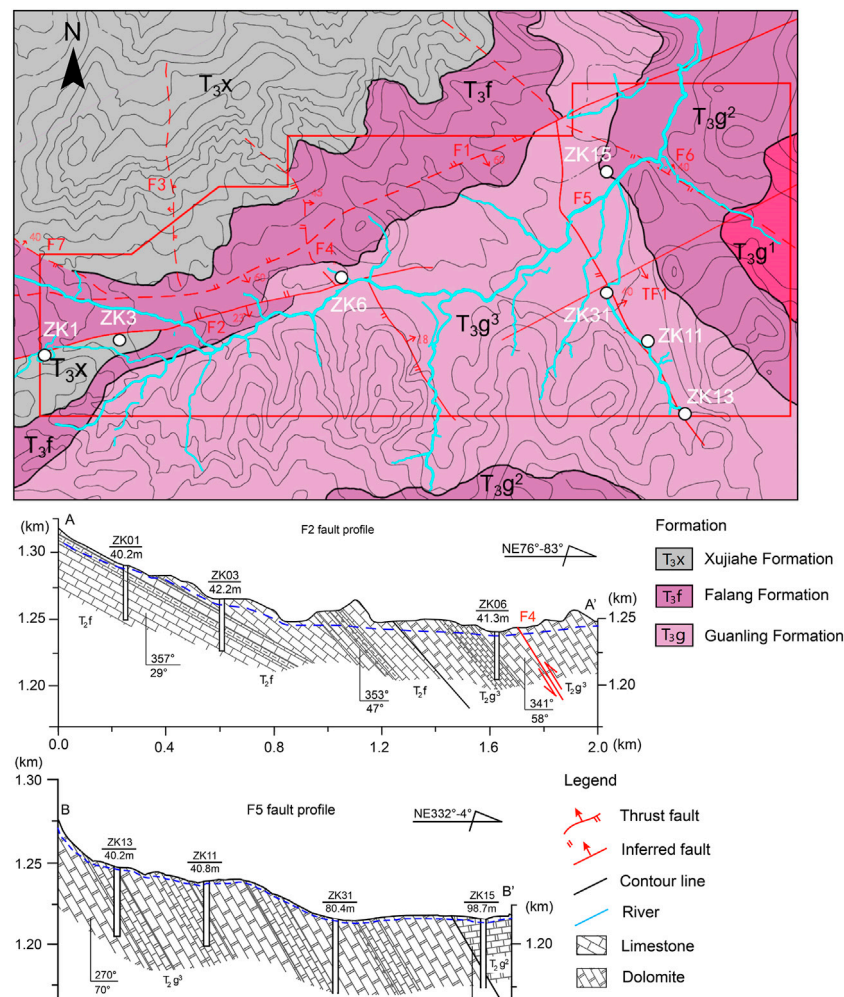
**FIGURE 2**
Regional lithology and geological structure of the study area.

elevation in the study area is 1247 m and 1207 m in the upper and lower reaches, respectively. The water level varies greatly under the influence of atmospheric rainfall, with a general range of 0–1.5 m and a maximum of 3.0 m. The annual average discharge is 0.9 m³/s, and, in general, surface water drainage conditions are good.

## Groundwater

The groundwater in the area is of three types: quaternary pore water, clastic rock fissure water and carbonate karst fissure water. The quaternary pore water is mainly supplied by atmospheric precipitation, and its buried depth is controlled by the topography, with maximum and minimum buried depths of 10 m and 1m, respectively. The fracture water mainly occurs in the sandstone fissures and is mainly supplied by atmospheric

precipitation and upper quaternary pore water, with a flow rate of 0.5–22 m³/d. The karst fissure water is mainly found in the limestone and dolomitic limestone areas. Especially in the middle section of $T_2g$, grey karst crevasse is relatively developed, there are local large karst caves, and underground rivers with large water volumes have formed, such as Dalongjing river with a flow of 500–3000 m³/d. Rainfall can be up to $2 \times 10^4$ m³/d.

The main aquifers in the site are distributed in limestone, dolomitic limestone, calcinous dolomite, and argillaceous limestone of the Middle Triassic Guanling Formation ($T_2g$), and calcinous dolomite of the Lower Triassic Yongningzhen Formation ($T_1yn$). The dip angle of rock strata is generally low (20°–45°), and the adjacent water-bearing rock groups form independent recharge, runoff and drainage systems, mainly in the form of karst fissure water and karst pipe water, which have poor uniformity and a degree of zonation. In the field

TABLE 1 The chemical constituents of the Portland cement and bentonite.

| Constituents | SiO2 | Fe2O3 | TiO2 | CaO | MgO | SO3 | Al2O3 | Na2O | K2O | Loss on ignition |
|---|---|---|---|---|---|---|---|---|---|---|
| Cement content (%) | 20.9 | 2.7 | 0.5 | 63.1 | 2.1 | 2.8 | 6.6 | — | — | 1.27 |
| Bentonite Content (%) | 75.9 | 2.2 | 0.3 | 2.4 | 2.4 | — | 13.1 | 2.2 | 0.2 | 15.7 |

TABLE 2 Composition of the grouts.

| No. | W/C | Clay (%) | XJY-2 (%) | 1# (%) | 2# (%) | 3# (%) |
|---|---|---|---|---|---|---|
| 1 | 0.6 | 3 | 0.8 | — | — | — |
| 2 | 0.6 | 4 | 1.3 | — | — | — |
| 3 | 0.6 | 5 | 1.8 | — | — | — |
| 4 | 0.7 | 4 | 1.8 | — | — | — |
| 5 | 0.7 | 5 | 0.8 | — | — | — |
| 6 | 0.7 | 3 | 1.3 | — | — | — |
| 7 | 0.6 | — | — | 0.33 | 2.2 | 0.3 |
| 8 | 0.6 | — | — | 0.33 | 2.2 | 0.5 |
| 9 | 0.6 | — | — | 0.33 | 2.2 | 0.7 |
| 10 | 0.6 | — | — | 0.33 | 2.2 | 1.0 |

test area, two groups of faults (NE trending F1 and NW trending F2, F1 and F4 are dislocated by F2) have developed compression-torsional dense fracture zones on both sides, creating conditions for groundwater migration in the hard rock of limestone and dolomite, so that the fault fracture zone is highly water-rich and highly permeable. In the soft rocks of marl and mudstone, the fault fracture zone is mylonized and has strong water isolation.

## Materials and methods

### Grouting materials

Cement and cement-based materials are commonly used in the anti-seepage grouting of dam sites and other reservoir structures. Cement pastes are suitable for many geological conditions as its rheology can be adjusted from Newtonian fluid to Bingham fluid simply by changing the water/cement (w/c) ratio. The rheology of base-cement slurry can also be transformed by using different additives, such as accelerator, fluid-loss additives, or extender. In this study, cement-clay (bentonite) slurry and time-dependent viscosity grouting material have been used for anti-seepage grouting in the test area rock mass. Using bentonite to replace cement can adjust the slurry rheology, improve stability, and reduce the permeability, which can reduce the dispersion of slurry under water and increase the filling rate of fracture (Azadi et al., 2017;

Benyounes and Benmounah, 2014; Mesboua et al., 2018). On the other hand, Bentonite as a clay mineral can effectively adsorb pollution substances in sewage such as heavy metal ions and organic (Tiller et al., 1984; Khan and Khan, 1995). The addition of bentonite can effectively modify the adsorption characteristics of cement grout to pollutants and improve the durability of anti-seepage body (Calvanese et al., 2002; Cioffi et al., 2001). The time-dependent viscosity grouting material is composed of cement and a variety of admixtures, which has the characteristics of large initial fluidity, fast viscosity change and controllable setting time. The rheology, pumping time, setting time and strength can be adjusted by changing the dosage of admixtures. The slurry with high viscosity and short setting time is suitable for steep-wide cracks and dynamic water environment, and on the contrary is suitable for long and narrow fractures (Zhang et al., 2017).

### Cement

The cement used in this study is P.O 42.5R Portland cement (LAFARGE GROUP). The cement was sieved through an 80 μm square-hole sieve so that large particles do not exceed 2.4%, and its properties of setting time and strength meet the standard requirements of common Portland cement (GB175–2007). The main chemical constituents of the cement are listed in Table 1.
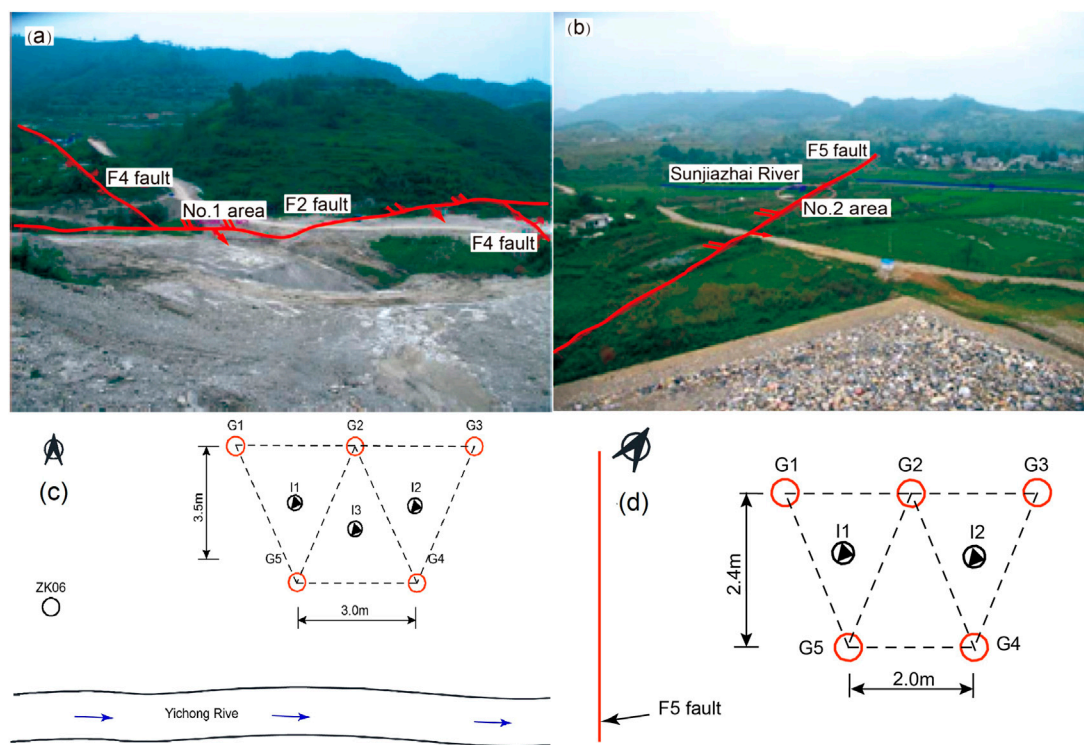
**FIGURE 3**
The location of the two test areas and grouting hole arrangement in **(A)** No. 1 test area, **(B)** No. 2 test area, **(C)** arrangement in No. 1 test area, and **(D)** arrangement in No. 2 test area.

## Clay

The clay used in the test was sodium bentonite mined in Weifang, Shandong province, China. The average particle size of the bentonite was 44μm, and the main chemical component was montmorillonite, as shown in Table 1.

## Additives

Superplasticizer: To improve the pumpability and fluidity of the cement-clay slurry with a low w/c ratio, a polycarboxylate plasticizer (XJY-2) was used as an additive in this test.

Time-dependent viscosity grouting material: includes modified fiber (1#), calcium-silicon early strength agent (2#) and acylamide derivatives (3#). The modified fiber (1#) consists mainly of a mixture of organic fibers, while the calcium-silicon early strength agent (2#) consists mainly of inorganic salts, which can provide an alkaline environment for the cement paste and stimulate the hydration of the cement. The setting time can be adjusted by control of the acylamide derivatives (3#) content (Zhang et al., 2017). This grouting material has high initial fluidity, good groutability, and a short setting time. Its

rheological and mechanical properties can be adjusted by changing the w/c ratio and the dosage of each additive.

The shattered fault zone anti-seepage grouting needs both to satisfy the requirement of filling ratio and also need to prevent the infinite diffusion of the grouting material. Therefore, the grouting material should have good flowability and suitable pumpable and setting times, and the grouting solidified body should have high strength and low permeability. Based on previous studies, the cement-clay slurry and time-dependent viscosity slurry are used as the grouting materials to compare their suitability for fault fracture zones with flowing water. The composition of grouting materials is shown in Table 2.

## Grouting method

### Grouting hole arrangement

Two compression-torsion fault zones were selected for the grouting test (Figure 3A). Test area No.1 is located at the intersection of the F2 and F4 faults, 5 m from the Yichong River. The test area is 3.3–5.5 m of weathered limestone with a broken rock mass structure. Below 5.5 m, there is middle weathered limestone with fractures that are fragmentary to
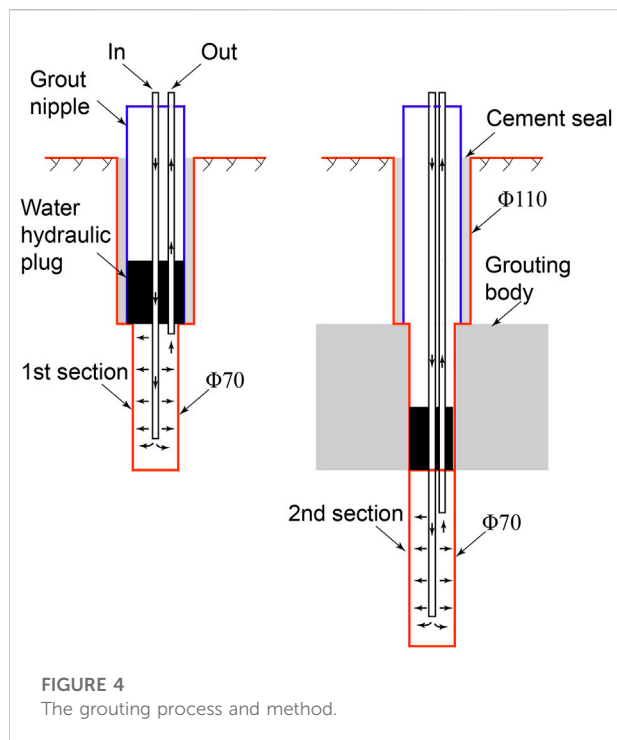
**FIGURE 4**
The grouting process and method.

massive and filled with sand. A total of five grouting holes were arranged in a triangle with a spacing of 3 m and a row spacing of 3.4 m. The three holes in sequence one are G1, G3 and G5, and the two holes in sequence two are G2 and G4, as shown in Figure 3C. Test area No.2 is located on the upper section of the F5 fault and 50 m away from Sunjiazhai River (Figure 3B). The test area below 2.0 m is middle weathered limestone with fractures, which are fragmentary to massive and filled with sand. A total of five grouting holes were arranged in a triangle with a spacing of 2 m and a row spacing of 2.4 m, this was used for grouting with cement-clay slurry. The three holes in sequence one are G1, G3, and G5, and two holes in

sequence two are G2 and G4 (Figure 3D). The I1 and I2 are the inspection holes.

## Grouting process

In this paper, a new grouting technique consisting of closed local circulating grouting from top to bottom is proposed for use with formations with a loose and broken structure. A schematic diagram of the new grouting process is shown in Figure 4. A water pressure plug is used to separate the grouting section from the non-grouting section. Before grouting, the borehole should be cleaned, and the water should be pressed into borehole from the top of water pressure plug, and then returned from the return pipe. When the returned water is clear without sediment, the hole washing operation can be terminated. During grouting, the slurry is sent to the bottom of the grouting section from the injection pipe and then returned to the return pipe. Through control of the returned volume, the flow rate of grout and grouting can be controlled. Thus, local circulation grouting in the hole under different pressure can be realized. The grouting pressure of the first and second sections is 0.1–0.2 MPa and 0.4–0.8 MPa, respectively. When the grouting pressure of first and second section exceeds 0.3 MPa and 1.0 MPa or the injection rate is less than 1L/min, the grouting can be finished by continuing for a further 15–30 min. When the first grouting section is completed, the first section of the next borehole is constructed. After the first hole section is solidified for 3 days, the drilling and grouting of the next hole section are carried out.

## Verification method

The water pressure test, also known as the Lugeon test, is the most common approach to detecting rock cracks and permeability in geotechnical engineering (Azimian and Ajalloeian, 2015). The permeability parameters of a curtain

**TABLE 3 The properties of grouts with different composition.**

| No. | Initial fluidity (cm) | Pumping time (min) | Bleeding rate (%) | Viscosity (s) | Initial setting time (min) |
|-----|-----------------------|--------------------|--------------------|----------------|----------------------------|
| 1 | 17.8 | 208 | 7.8 | 53.7 | 424 |
| 2 | 16.3 | 81 | 0.9 | 61.2 | 392 |
| 3 | 15.4 | 48 | 0.5 | 67.5 | 324 |
| 4 | 23.2 | 487 | 2.0 | 35.8 | 501 |
| 5 | 19.2 | 245 | 1.0 | 48.3 | 445 |
| 6 | 25.1 | 314 | 3.1 | 27.7 | 504 |
| 7 | 23.2 | 18 | 0.5 | 64.7 | 212 |
| 8 | 23.6 | 27 | 0.5 | 51.2 | 255 |
| 9 | 24.8 | 39 | 0.7 | 47.8 | 269 |
| 10 | 24.9 | 67 | 1.7 | 45.2 | 314 |

**FIGURE 5**
The variation of fluidity and viscosity with time for the cement-clay slurry and the time-dependent viscosity slurry.
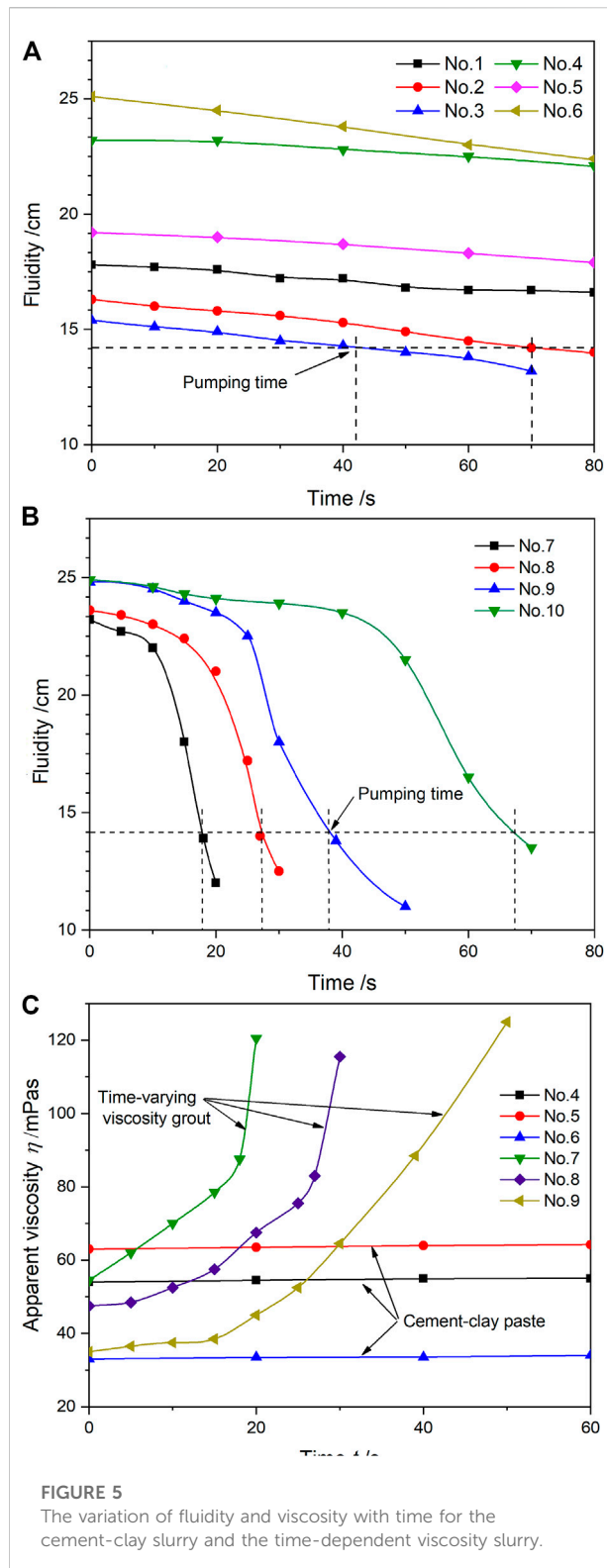
structure and test section are determined by this method, providing basic data for evaluating the hydraulic characteristics of a rock mass controlled by discontinuities,

water absorption capacity, compactness, and effectiveness of grouting, and also explaining some geomechanical behaviors. In this study, water pressure tests were conducted before and after grouting using a five-step water pressure loading and unloading (Foyo et al., 2005; Lisa et al., 2013) process that generated five sets of water pressure (P) and water discharge (Q) values, one for each of the five steps that are presented as P–Q diagrams for each interval. The final permeability value can be determined from the maximum stress stage (Stage 3).

The calculation of the permeability of the test section from the water pressure tests is shown in Eq. 1:

$$q = \frac{Q}{PL} \tag{1}$$

where $q$ is the permeability of the test section, Lu. $Q$ is the water discharge values, L/min. $P$ is the effective pressure acting on the test section, MPa. $L$ is the length of the test section, m.

To judge the quality change of rock mass before and after grouting, the secondary permeability index (SPI) were used. The SPI is calculated as shown in Eq. 2:

$$\text{SPI} = C \frac{\ln\left(\frac{2l_e}{r} + 1\right)}{2\pi l_e} \frac{Q}{Ht} \tag{2}$$

where SPI is the secondary permeability index, l/s per m² of the borehole test surface. $C$ is a constant depending upon viscosity for an assumed temperature of rock at 10°C, 1.49×10⁻¹⁰. $l_e$ is the test section length, m $t$ is the test time, s. $H$ is the total pressure expressed as a water column, m.

## Results and discussion

### Properties of the grouting materials

The rheological and setting properties of the grouts are shown in Table 3, and the apparent viscosity and fluidity are shown in Figure 5. The fluidity of the cement-clay slurry decreases slowly with time and increases with increasing w/c and decreasing clay content. Compared with the cement-clay slurry, the time-dependent viscosity slurry has high initial fluidity under the same w/c ratio, which can be maintained for some time and then rapidly decreases into pumpable time. The fluidity can be controlled by the amount of the three# admixture. As Figure 5C shows, under the condition of similar initial fluidity, the apparent viscosity of time-dependent viscosity slurry increases approximately exponentially with time, while that of the cement-clay slurry remains almost constant. The grouting diffusion radius can be affected directly by grout viscosity and pressure. High fluidity increases the grouting diffusion distance but makes it difficult to increase the grouting pressure to the design value. In addition, groundwater will cause erosion and dilution of the grout, and the lower the viscosity after perfusion, the more serious the

TABLE 4 The strength properties of the grout.

| No. | 1 day (MPa) | 3 days (MPa) | 7 days (MPa) | 28 days (MPa) |
|-----|-------------|--------------|--------------|---------------|
| 1 | 7.1 | 16.5 | 24.0 | 31.3 |
| 2 | 6.2 | 15.7 | 22.3 | 28.9 |
| 3 | 5.4 | 15.0 | 20.3 | 24.6 |
| 4 | 6.2 | 13.9 | 17.3 | 26.3 |
| 5 | 5.6 | 13.3 | 17.2 | 24.8 |
| 6 | 5.8 | 13.6 | 17.0 | 26.4 |
| 7 | 8.5 | 14.2 | 24.0 | 33.4 |
| 8 | 8.9 | 14.7 | 24.7 | 34.5 |
| 9 | 8.0 | 14 | 23.8 | 32.5 |
| 10 | 7.8 | 13.2 | 22.5 | 30.2 |

erosion. Therefore, in the grouting of water-rich broken rock mass, the grout should ideally have high initial fluidity, a controllable pumping time and a shorter initial setting time.

The anti-seepage capacity is affected by the compressive strength and permeability of the stone body of grout. The unconfined compressive strength of the two grouts is shown in Table 4. The pre and post compressive strength of time-dependent viscosity slurry are both higher than those of the cement-clay slurry. The 28 days strength is greater than 20 MPa, which meets the requirements of curtain grouting. The strength of the cement-clay slurry increases with time and decreases with increasing w/c ratio and clay content. The strength of time-dependent viscosity slurry decreases with the increase of admixture.

Figure 6 shows the evolution of permeability and contaminant retardancy with time. The permeability coefficients of the grouts increase with time and are affected by their composition. The permeability coefficient of the cement-clay slurry decreases with increasing clay content, while that of the time-dependent viscosity slurry is not affected by the amount of admixture. The arrest rates of Hg, As, Pb and Cd were more than 99%. The heavy metal arrest rate of cement clay slurry is affected by the clay content. When the clay content is 4%, the arrest rate is the highest.

The difference of rheological-hardening characteristics of the two kinds of grout is mainly caused by cement hydration. Due to the high water absorption of bentonite, the free water in the system decreases with the increase of dosage, and a large amount of free water is closed in the network space composed of cement and clay particles, which leads to the decrease of slurry fluidity, the increase of viscosity and the improvement of stability. However, the mutual adsorption of bentonite and cement reduces the hydration rate of cement. So the setting time of the slurry is extended. On the contrary, the time-depending viscosity additives increase the hydration rate and products by adjusting the early hydration of cement to change the viscosity and setting time.

## Analysis of grout take

Figure 7 and Table 5 show the total and unit grout take, respectively, of formations with different degrees of weathering in the two test areas. Figure 7A shows that the grout takes of the strongly weathered limestone is between 750 and 1640 L, while that of the medium weathered formation is between 460 and 687 L. Figure 7B shows that the grouting volume of the upper middle weathered formation is between 520 L and 750 L, while that of the lower formation is between 980 L and 3150 L. The unit grout takes of strongly weathered formation with time-varying grout is the same as that of the two test areas with cement-clay grout, but it is 31% in the medium weathered formation.

This result indicates that the grout take is controlled both by formation conditions and grout rheology. The two kinds of grout have the same initial rheological parameters, which ensures the diffusion of grout through the formation. With the extension of grouting time, the viscosity of time-dependent slurry suddenly increases, which increases the shear stress required for its flow in the formation pores, slowing down the diffusion speed and reducing the grouting take. While the yield stress of the cement-clay slurry remains constant, a large amount of slurry is needed to achieve mechanical equilibrium in the grouting process. Hence, the grouting quantity difference under the same formation conditions.

## Analysis of permeability coefficient before and after grouting

The P-Q diagram types (hydromechanical behavior) of the rock mass before and after grouting were identified using the five-stage water pressure tests (WPTs) and statistically analyzed. Typical P-Q diagrams are shown in Figure 8 and Figure 9 in the form of a straight line, which includes both the strongly and medium weathered formation before and after grouting in the
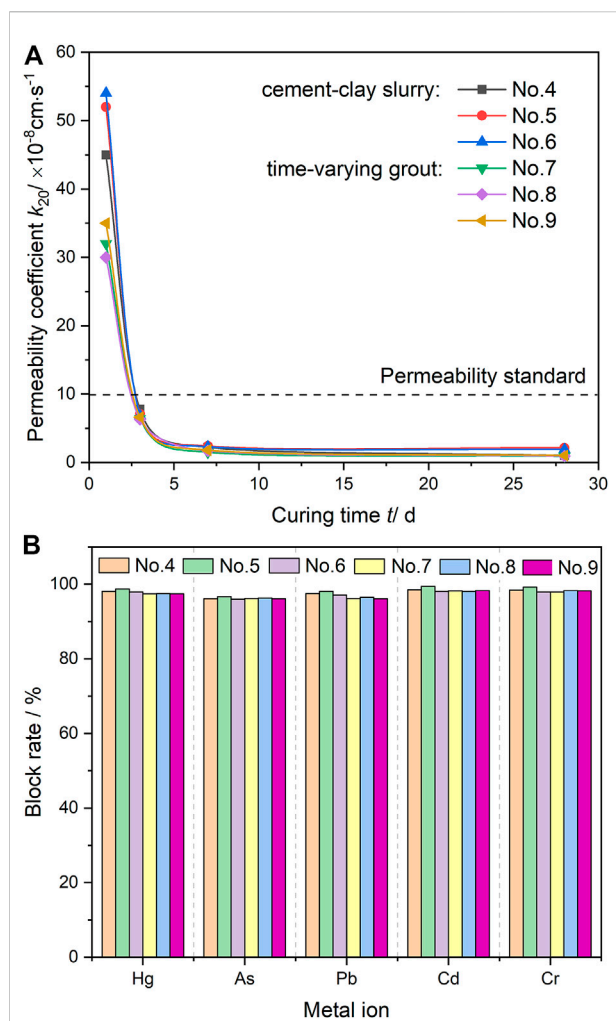
**FIGURE 6**
Relationship between permeability coefficient and curing time for the two slurries, and blocking rate for heavy metal ions.



**FIGURE 7**
Grout take and depth relationship for the No. 1 and No. 2 test areas.

two test areas. Based on the complete hydromechanical behavior model for the fault, the following points are obtained.

With respect to the behavior of the two test areas, the strongly weathered formation is washout, while the medium weathered formation can be divided into dilation and washout (Figure 8). The results of the WPTs of No.1 test area indicate washout to be the dominant behavior in depths of 3.3 m–5.5 m. The Lugeon values of the five pressure stages are 212.5 Lu, 274.7 Lu, 322.7 Lu, 362.3 Lu, and 395.4 Lu, respectively (Figure 8A). In the process of the water pressure, the water erodes and carries the filling materials between the pores and cracks of formation, and causes plastic deformation of the rock mass. Therefore, the permeability increases significantly during the low pressure stages 4 and 5. In depths of 5.5 m–10 m, the dominant behavior is dilation, the Lugeon values of stages 4 and 5 are bigger than stages 1 and

2 (Figure 8B). This result indicate that the joints experience elastic widening or slight erosion under the effect of pressure. In the No.2 test area, the hydromechanical behaviors are dilation from 4.5 m to 7 m and washout from 7 m to 10.2 m, with permeabilities of 58.1 Lu and 307.6 Lu, respectively (Figure 8C,D). The reason for this phenomenon may be that the deep rock mass is more affected by the fault structure than the shallow. The fragmentation degree of deep rock mass is greater than that of shallow rock mass, and the fissure filling material is obviously eroded by groundwater. Overall, the degree of rock fragmentation in No. One test area is greater than that in No. Two test area.

The WPTs results for the two inspection boreholes in No.1 test area indicate that the hydromechanical behavior changes from washout and dilation to laminar flow after time-dependent viscosity slurry grouting (Figure 9A,B). The path of water flow changes is consistent during the pressure rise and fall phases, which suggest that the water channel is no longer deformed under pressure. The permeability coefficient of the

**TABLE 5 The average grout take of 1-m depth in the different weathered formations.**

| Test area no. | Sequence | Strongly weathered (L) | Medium Weathered (L) | |
|---|---|---|---|---|
| 1 | 1 | 524.1 | 151.5 | |
| | 2 | 465.9 | 139.5 | |
| 2 | 1 | 0 | 326.7 | 627.8 |
| | 2 | 0 | 254 | 505 |
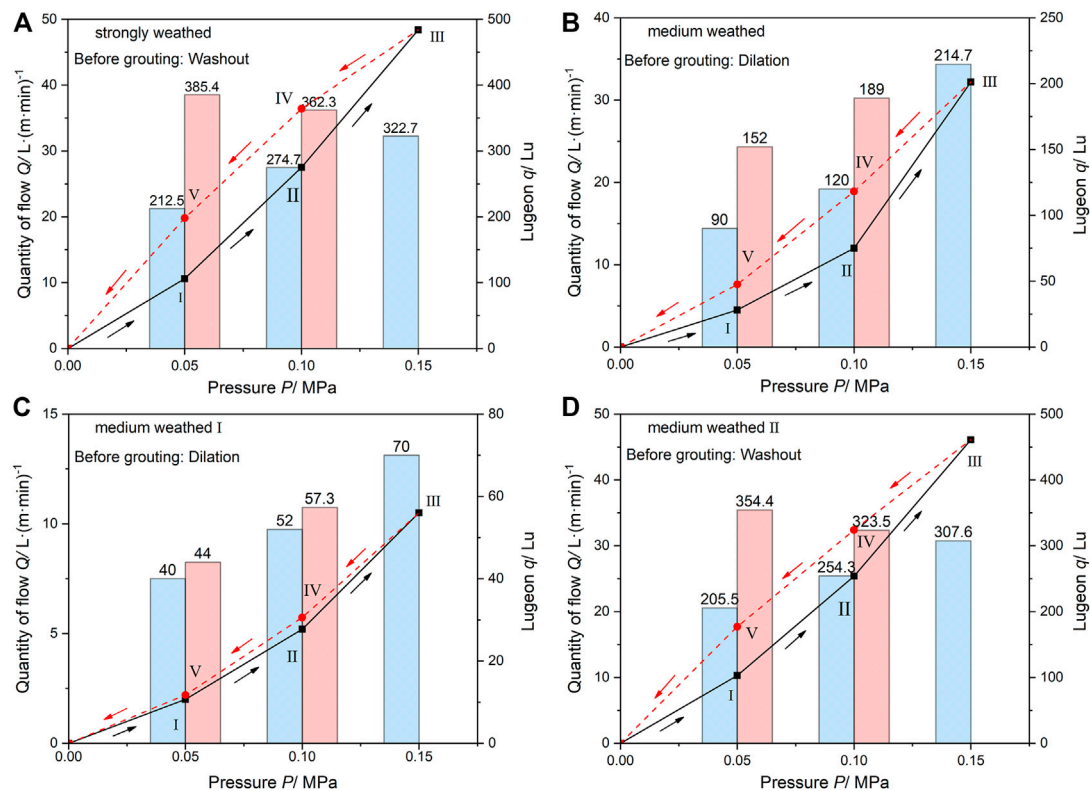


**FIGURE 8**
Formation permeability before grouting **(A)** strongly weathered formation of No. 1 test area, **(B)** medium weathered formation of No. 1 test area, **(C,D)** the upper and lower weathered formations of No. 2 test area.

two grouting sections decreases by 90% and 95%, respectively, and is roughly the same (10 Lu). Therefore, it can be concluded that the quality of rock mass in time-dependent viscosity slurry grouting area tend to be consistent, and the cracks normally tend to closed and a small section are not completely filled. In No.2 test area, the hydromechanical behavior of first grouting section changes from dilation to laminar, but the pressure rise and fall curves still exist gap (Figure 9C), which indicates that the grouting consolidation body still has some deformation under the action of pressure. The second section changes from washout to dilation (Figure 9D), which shows that the joint structure is

partially or mostly still open. The permeability of the two grouting sections decreases by 50.9% and 81.9%, but there is still a big difference. It indicates that the grouting quality of cement-clay slurry is quite different.

The permeability level is calculated by SPI, and this is used to classify the rock mass of the test areas. The SPI classes are given in Table 6. The SPI values for the formation before grouting show that 100% of the tested intervals fall within the D (>80 Lu, very poor), this means the formation needs to be grouted. After grouting, the SPI values of No.1 test area fall to $1.22 \times 10^{-13}$–$9.81 \times 10^{-14}$, which can be classified as B-C (Good-fair to Poor). Similarly, the SPI values of the No.2 test area reduce
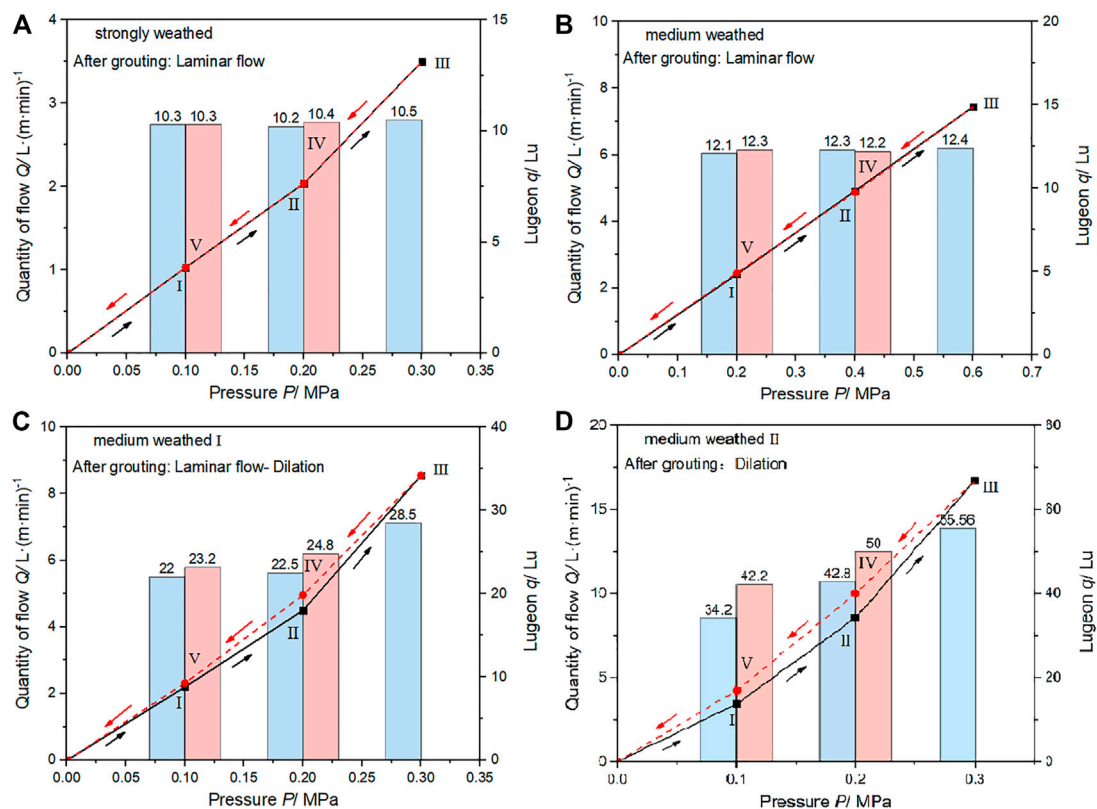
**FIGURE 9**
Formation permeability after grouting **(A)** strongly weathered formation of No. 1 test area, **(B)** medium weathered formation of No.1 test area, **(C,D)** the upper and lower weathered formation of No. 2 test area.

**TABLE 6 Rock mass classification in the two areas after grouting.**

| Test area no. | Classification | | | |
|---|---|---|---|---|
| | A-great | B-good fair | C-poor (%) | D-very poor |
| 1 | 0 | 85% | 15 | 0 |
| 2 | 0 | 0 | 70 | 30% |

to $2.37 \times 10^{-13}$–$9.78 \times 10^{-13}$, which can be classified as C to D (Poor to Very Poor).

Based on the grout take and permeability analysis, the consumption of time-dependent viscosity slurry is 27.4% less than cement-clay slurry under the same engineering and hydrogeological conditions and can significantly reduce the degree of fracture (or pore) in the fault zone, reduce the permeability, and improve the quality grade of the rock mass. The different arises due to the following factors. The good initial fluidity and low viscosity of the time-dependent viscosity slurry ensure a good diffusion distance in the formation. With the extension of grouting time, the rheology of the front grout changes abruptly from fluid to plastic paste, thus, blocking the flow of the subsequent grout, thereby increasing of grouting pressure and the filling rate and compactness of the pores by the slurry are significantly increased under the action of this additional pressure. In contrast, the fluidity of the cement-clay slurry changes slowly, resulting in its continuous diffusion to the periphery under the action of grouting pressure, making it difficult for grout to compact and fill the pores. In addition, the cement-clay slurry with high dispersion is easily eroded by groundwater, while the high viscosity and quick setting of time-dependent viscosity slurry can effectively resist the dispersion of groundwater and ensure the filling rate of pores. The cement-clay slurry has poor stability, and its water absorption rate is four times that of time-dependent slurry. During the process of setting, the volume contraction causes the filled cracks to open again, which is also a reason for the poor quality of cement-clay grouting. Therefore, it can be concluded that the rheology-setting characteristics of slurry and the grouting pressure have great influence on the seepage prevention of fault fracture zone.

# Conclusion

Curtain grouting is an important element of seepage control design in landfill, chemical plant and water conservation, and hydropower projects. Based on the experimental analysis of the rheology-setting properties for a time-dependent viscosity slurry and a cement-clay slurry, this study focuses on anti-seepage treatment in a water-bearing fault fracture zone, analyzing the permeability before and after grouting by different approaches. From the results, the following conclusions can be drawn:

1) Under the condition of the same initial fluidity, the pumping time of time-dependent viscosity slurry is 3.7%–21.3% that of the cement-clay slurry and can be adjusted within 18–67 min. The water bleeding of the cement-clay slurry is 1.8–4 times that of the time-dependent viscosity slurry.
2) The mechanical properties of time-dependent slurry is great than cement-clay, and the 28 days unconfined compressive strength is 30.2–34.5 MPa and 24.6–31.3 MPa, respectively. The three# additive content of 0.5% is the optimum dosage to produce a stable grout with highest strength. A bentonite content of 3% and 0.6 w/c ratio is the optimum dosage to obtain maximum strength.
3) The permeability coefficients of the two slurry stone bodies are of the same level ($<10^{-7}$ cm/s), and the blocking rates of Hg, As, Pb and Cd heavy metal ions reach more than 99%.
4) Under the same grouting depth, the consumption of cement-clay slurry (12300 L) is 1.4 times that of time-dependent viscosity slurry (8931 L), while its grouting pressure (0.3–0.4 MPa) is 50% lower.
5) The permeability coefficient of the formation with time-dependent viscosity slurry decrease from 214.7 to 322.7 Lu to 10.3–12.3 Lu, reduced by 95.2%–96.2%. The hydromechanical behavior is changed to laminar flow, and the rock mass quality is improved from grade D to grade B-C, basically realizing the sealing of fractures.
6) The permeability of the formation with cement-clay slurry decrease from 58.1 Lu and 307.6 Lu to 28.5 Lu and 55.6 Lu, only decreased by 50.9% and 81.9%, and the mass of rock mass only increased to C-D level, with most fractures in the open state with the cement-clay slurry.

Results of the grouting test indicate that it is possible to use the method of closed local circulating grouting from top to bottom to reduce the permeability of water-bearing fault zone. In terms of grouting materials, both the grout takes and grouting quality, time-dependent viscosity slurry is better than cement-clay slurry.

## Data availability statement

The original contributions presented in the study are included in the article/supplementary material, further inquiries can be directed to the corresponding author.

## Author contributions

All authors listed have made a substantial, direct, and intellectual contribution to the work and approved it for publication.

## Funding

## Conflict of interest

The authors declare that the research was conducted in the absence of any commercial or financial relationships that could be construed as a potential conflict of interest.

## Publisher's note

All claims expressed in this article are solely those of the authors and do not necessarily represent those of their affiliated organizations, or those of the publisher, the editors and the reviewers. Any product that may be evaluated in this article, or claim that may be made by its manufacturer, is not guaranteed or endorsed by the publisher.

## References

Adamovic, D., Ishiyama, D., Kawaraya, H., Ogawa, Y., and Stevanovic, Z. (2022). Geochemical characteristics and estimation of groundwater pollution in catchment areas of Timok and Pek Rivers, Eastern Serbia: Determination of early-stage groundwater pollution in mining areas. *Groundw. Sustain. Dev.* 16, 100719. doi:10.1016/j.gsd.2021.100719

Azadi, M. R., Taghichian, A., and Taheri, A. (2017). Optimization of cement-based grouts using chemical additives. *J. Rock Mech. Geotechnical Eng.* 9, 623–637. doi:10.1016/j.jrmge.2016.11.013

Azimian, A., and Ajalloeian, R. (2015). Permeability and groutability appraisal of the Nargesi dam site in Iran based on the secondary permeability index, joint hydraulic aperture and Lugeon tests. *Bull. Eng. Geol. Environ.* 74, 845–859. doi:10.1007/s10064-014-0675-8

Benyounes, K., and Benmounah, A. (2014). Effect of bentonite on the rheological behavior of cement grout in presence of superplasticizer. *Int. J. Civ. Archit. Struct. Constr. Eng.* 8, 1095–1098.

Calvanese, G., Cioffi, R., and Santoro, L. (2002). Cement stabilization of tannery sludge using quaternary ammonium salt exchanged bentonite as pre-solidification adsorbent. *Environ. Technol.* 23, 1051–1062. doi:10.1080/09593332308618351

Carter, T. G., Dershowitz, W., Shuttle, D., and Jefferies, M. (2012). Improved methods of design for grouting fractured rock. *Grouting Deep Mix.* 228, 1472–1483 doi:10.1061/9780784412350.0123

Cioffi, R., Costanzo, S., Maffucci, L., and Santoro, L. (2001). Adsorption of the organic fraction of a tannery sludge by means of organophilic bentonite. *Environ. Technol.* 22, 83–89. doi:10.1080/09593332208618309

Eklund, D., and Stille, H. (2008). Penetrability due to filtration tendency of cement-based grouts. *Tunn. Undergr. Space Technol.* 23, 389–398. doi:10.1016/j.tust.2007.06.011

Esteller, M. V., Domínguez-Mariani, E., Garrido, S. E., and Avilés, M. (2015). Groundwater pollution by arsenic and other toxic elements in an abandoned silver mine, Mexico. *Environ. Earth Sci.* 74, 2893–2906. doi:10.1007/s12665-015-4315-9

Ewert, F.-K. (1998). Permeability, groutability and grouting of rocks related to dam sites Part 4. *Dam Eng.* 8, 271–326.

Foster, M., Fell, R., and Spannagle, M. (2000). The statistics of embankment dam failures and accidents. *Can. Geotech. J.* 37, 1000–1024. doi:10.1139/t00-030

Foyo, A., Sanchez, M. A., and Tomillo, C. (2005). A proposal for a secondary permeability index obtained from water pressure tests in dam foundations. *Eng. Geol.* 77, 69–82. doi:10.1016/j.enggeo.2004.08.007

Fransson, Å. (2001). Characterisation of a fractured rock mass for a grouting field test. *Tunn. Undergr. Space Technol.* 16, 331–339. doi:10.1016/s0886-7798(01)00060-8

Gworek, B., Dmuchowski, W., Koda, E., Marecka, M., Baczewska, A. H., Brągoszewska, P., et al. (2016). Impact of the municipal solid waste Łubna Landfill on environmental pollution by heavy metals. *Water* 8, 470. doi:10.3390/w8100470

Huang, Y., Tang, Y., Zhou, Z., and Yu, Z. (2014). Experimental investigation of contaminant migration in filled fracture. *Environ. Earth Sci.* 71, 1205–1211. doi:10.1007/s12665-013-2524-7

Hussein, M., Yoneda, K., Mohd-Zaki, Z., Amir, A., and Othman, N. (2021). Heavy metals in leachate, impacted soils and natural soils of different landfills in Malaysia: An alarming threat. *Chemosphere* 267, 128874. doi:10.1016/j.chemosphere.2020.128874

Jiang, H., and Qiu, X. (2021). Performance assessment of a newly developed and highly stable grouting material for a completely weathered granite dam foundation. *Constr. Build. Mater.* 299, 123956. doi:10.1016/j.conbuildmat.2021.123956

Khan, S. A., and Khan, M. A. (1995). Adsorption of chromium (III), chromium (VI) and silver (I) on bentonite. *Waste Manag.* 15, 271–282. doi:10.1016/0956-053x(95)00025-u

Lee, H. B., Oh, T.-M., Park, E.-S., Lee, J.-W., and Kim, H.-M. (2017). Factors affecting waterproof efficiency of grouting in single rock fracture. *Geomech. Eng.* 12, 771–783. doi:10.12989/gae.2017.12.5.771

Lisa, H., Gunnar, G., Åsa, F., and Tommy, N. (2013). A statistical grouting decision method based on water pressure tests for the tunnel construction stage–A case study. *Tunn. Undergr. Space Technol.* 33, 54–62. doi:10.1016/j.tust.2012.08.004

Liu, Y., and Chen, B. (2019). Research on the preparation and properties of a novel grouting material based on magnesium phosphate cement. *Constr. Build. Mater.* 214, 516–526. doi:10.1016/j.conbuildmat.2019.04.158

Mesboua, N., Benyounes, K., and Benmounah, A. (2018). Study of the impact of bentonite on the physico-mechanical and flow properties of cement grout. *Cogent Eng.* 5, 1446252. doi:10.1080/23311916.2018.1446252

Mortazavi, A., and Maadikhah, A. (2016). An investigation of the effects of important grouting and rock parameters on the grouting process. *Geomechanics Geoengin.* 11, 219–235. doi:10.1080/17486025.2016.1145255

Raghavendra, N. S., and Deka, P. C. (2015). Sustainable development and management of groundwater resources in mining affected areas: A review. *Procedia Earth Planet. Sci.* 11, 598–604. doi:10.1016/j.proeps.2015.06.061

Stare, D. P., Dreese, T. L., and Bruce, D. A. (2013). *Contemporary drilling and grouting methods*. Boca Raton, FL: CRC Press.

Stille, B., Stille, H., Gustafson, G., and Kobayashi, S. (2009). Experience with the real time grouting control method. *Geomech. Tunnelbau* 2, 447–459. doi:10.1002/geot.200900036

Stille, H., Gustafson, G., and Hassler, L. (2012). Application of new theories and technology for grouting of dams and foundations on rock. *Geotech. Geol. Eng. (Dordr).* 30, 603–624. doi:10.1007/s10706-012-9512-7

Tiller, K. G., Gerth, J., and Brümmer, G. (1984). The relative affinities of Cd, Ni and Zn for different soil clay fractions and goethite. *Geoderma* 34, 17–35. doi:10.1016/0016-7061(84)90003-x

Westlake, K. (2014). *Landfill waste pollution and control.* Sawston, UK: Woodhead Publishing.

Xaypanya, P., Takemura, J., Chiemchaisri, C., Seingheng, H., and Tanchuling, M. A. N. (2018). Characterization of landfill leachates and sediments in major cities of indochina peninsular countries—Heavy metal partitioning in municipal solid waste leachate. *Environments* 5, 65. doi:10.3390/environments5060065

Xu, S. F., and Yang, Y. (2006). Use of impermeable materials for refuse landfills in Japan. *Environ. Eng.* 24, 68–70.

Yao, R., Yan, Y., Wei, C., Luo, M., Xiao, Y., and Zhang, Y. (2022). Hydrochemical characteristics and groundwater quality assessment using an integrated approach of the pca, som, and fuzzy c-means clustering: A case study in the northern sichuan basin. *Front. Environ. Sci.* 648. doi:10.3389/fenvs.2022.907872

Zhang, C., Fu, J., Yang, J., Ou, X., Ye, X., and Zhang, Y. (2018). Formulation and performance of grouting materials for underwater shield tunnel construction in karst ground. *Constr. Build. Mater.* 187, 327–338. doi:10.1016/j.conbuildmat.2018.07.054

Zhang, J., Pei, X., Wang, W., and He, Z. (2017). Hydration process and rheological properties of cementitious grouting material. *Constr. Build. Mater.* 139, 221–231. doi:10.1016/j.conbuildmat.2017.01.111

Zhang, Y.-H., Yao, R.-W., Wang, Y., Duo, J., and Cao, H.-W. (2022). Zircon U–Pb and sericite Ar–Ar geochronology, geochemistry and S–Pb–Hf isotopes of the Zebuxia Pb–Zn deposit, Tibet, southwestern China. *Ore Geol. Rev.* 148, 104999. doi:10.1016/j.oregeorev.2022.104999

Zhang, Y., Dai, Y., Wang, Y., Huang, X., Xiao, Y., and Pei, Q. (2021a). Hydrochemistry, quality and potential health risk appraisal of nitrate enriched groundwater in the Nanchong area, southwestern China. *Sci. Total Environ.* 784, 147186. doi:10.1016/j.scitotenv.2021.147186

Zhang, Y., He, Z., Tian, H., Huang, X., Zhang, Z., Liu, Y., et al. (2021b). Hydrochemistry appraisal, quality assessment and health risk evaluation of shallow groundwater in the Mianyang area of Sichuan Basin, southwestern China. *Environ. Earth Sci.* 80, 1–16. doi:10.1007/s12665-021-09894-y

frontiers | Frontiers in Earth Science

# Landslide susceptibility assessment using the certainty factor and deep neural network

Wenli Ma[1,2,3], Jianhui Dong[4,5]*, Zhanxi Wei[1,2,3], Liang Peng[6], Qihong Wu[4,5], Xiao Wang[4,5], Yangdan Dong[7] and Yuanzao Wu[1,2,3]

[1]Qinghai 906 Engineering Survey and Design Institute Co Ltd, Xining, China, [2]Key Laboratory of Environmental Geology of Qinghai Province, Xining, China, [3]Qinghai Geological Environment Protection and Disaster Prevention Engineering Technology Research Center, Xining, China, [4]Sichuan Engineering Research Center for Mechanical Properties and Engineering Technology of Unsaturated Soils, Chengdu University, Chengdu, China, [5]School of Architecture and Civil Engineering, Chengdu University, Chengdu, China, [6]Qinghai Hydrogeology and Engineering Geology and Environgeology Survey Institute, Xining, China, [7]State Key Laboratory of Geohazard Prevention and Geoenvironment Protection, Chengdu University of Technology, Chengdu, China

Areas with vulnerable ecological environments often breed many geological disasters, especially landslides, which pose a severe threat to the safety of people's lives and property in these areas. To aid in landslide prevention and mitigation, an approach combining the coefficient of determination method (CF) and a deep neural network (DNN) were proposed in this study for landslide susceptibility evaluation. The deep neural network can excavate the deep features of samples and improve the accuracy of the susceptibility model. In addition, the logistic regression model (LRM) and support vector machine (SVM) were selected to create landslide susceptibility maps for comparison, which also involved the coefficient of determination method (CF). Based on landslide remote sensing interpretation and field investigations, a spatial database of mudstone landslides in the Xining area was established. Eight different conditional factors, including the elevation, slope, slope aspect, undulation, curvature, watershed, distance from a fault, and distance from a road, in the study area were selected as the evaluation factors to evaluate the susceptibility. The results revealed that four factors (i.e., the ground elevation, curvature, distance from a fault, and distance from a road) had relatively significant influences on the landslide susceptibility in the study area. Finally, the confusion matrix was used to evaluate the accuracy of the results obtained using the three methods, and the optimal result was selected to evaluate the landslide susceptibility in the study area. It was found that the combined CF-DNN method was more suitable for evaluating the landslide susceptibility in this area. Landslide susceptibility zoning was conducted to divide the study area into four sensitivity levels: low (32.65%), medium (35.12%), high (22.44%), and extremely high (9.79%) susceptibility. The high-risk areas were primarily distributed in the high-elevation areas along the eastern edge of the Huangshui Basin.

# 1 Introduction

The term "landslide" refers to the phenomenon in which the soil and rock mass constituting the slope disintegrates and slips and/or collapses under the action of gravity Landslides are regarded as one of the most common types of geological disasters in mountainous areas (Confuorto et al., 2019). They are characterized by wide distribution, high frequency of occurrence, strong concealment, and a large degree of destruction, and thus, they often have catastrophic consequences and pose a huge threat to people's lives and property, as well as social and economic development (Lin et al., 2008; Wang et al., 2018). Since the middle of the 20th century, with the increasing population and the increasing scope of human engineering activities, more and more landslides have been induced, especially in the Xining area in Qinghai Province. Xining City is one of the areas with the most vulnerable ecological environment in China, located in the transition zone between the western side of the Loess Plateau and the Qinghai-Tibet Plateau. The geological environment in this region is very complex, consisting of undulating terrain, multi-periodic tectonic movements, complex geological structures, weak formation lithology, strong river erosion, leading to a high risk of landslides. With the continuous development of economic construction in Xining, human engineering activities have intensified. Consequently, more and more geological disasters have been induced, especially landslides, seriously threatening people's lives and property in this area. For example, the Zhangjiawan Brick Factory landslide in 1960 (Bai et al., 2021; Peng et al., 2021), which had a volume of about $2.2 \times 10^7 \, \text{m}^3$, the Beishansi landslide in 2001 (Yao et al., 2014), which had a volume of about $1.38 \times 10^6 \, \text{m}^3$, and the Hanzhuang community landslide in 2011, which had a volume of about $7.326 \times 10^6 \, \text{m}^3$, were larger mudstone landslides that have occurred in this area. According to a geological survey conducted by the staff of the Qinghai Provincial Geological Environment Monitoring Station, mudstone landslides accounted for 78% of the total number of landslides investigated in the study area. The occurrence of landslides in this area is greatly related to the poor permeability of the mudstone, that is, when water collects in the slope is affected by the water resistance of the mudstone, eventually forming a soft slip zone. The deformation mechanisms and formation mechanisms of mudstone landslides in Xining have been investigated in previous studies (Xin et al., 2015). However, the distribution characteristics of mudstone landslides in Xining City have rarely been studied. Assessing the susceptibility of the study area to mudstone landslides is beneficial to providing strong support for the prediction and control of mudstone landslides.

Landslide susceptibility assessment is the basis of landslide risk assessment, which refers to the possibility of landslide occurrence caused by a combination of multiple influencing factors in a specific area (Brabb, 1984). In earlier studies, scholars mainly relied on empirical methods to qualitatively determine landslide susceptibility, such as the analytic hierarchy process (AHP), and fuzzy mathematics (Al-Harbi, 2001; Rozos et al., 2011; Giovanni et al., 2016). For small areas, the method of synthesizing the descriptions provided by experts has a certain reference value for landslide susceptibility rating; however, for large areas, such methods are subjective due to manual determination, which leads to the possibility of large errors in the results. In later studies, scholars began to use statistical methods to analyze and assess landslide susceptibility, such as the information model (IM), certainty coefficient method (CF), frequency ratio model (FR), and weight of evidence method (WEM) (Pradhan and Lee, 2010; Liu et al., 2014; Pourghasemi et al., 2014; Xu et al., 2016; Dai et al., 2017). Statistical methods have become one of several methods that are commonly used at present. Although the use of such quantitative methods avoids the disadvantages of the subjective judgment of the previous empirical experts, there are still great limitations in the prediction and evaluation of regional landslides using many evaluation indicators and the statistics of a large dataset. Therefore, with the continuous development of machine learning methods, more and more scholars have begun to use machine learning methods to assess landslide susceptibility, such as the logistic regression model (LRM), decision tree model (DTM), random forest model (RFM), support vector machine (SVM), naive bayes model (NBM), artificial neural networks (ANNs), and other methods (Bui et al., 2016; Hong et al., 2016; Wang et al., 2016; Chen et al., 2017; Le et al., 2017; Shirzadi et al., 2017; Chen et al., 2018; Sahin et al., 2018; Dou et al., 2019; Hong et al., 2019; Shariati et al., 2019; Nhu et al., 2020). However, the above models all belong to the category of shallow neural networks. When the landslide susceptibility assessment process involves diverse and interrelated evaluation factors, it is often impossible to explore the relationship between the factors to achieve more accurate results (Wang et al., 2019). Therefore, in recent years, the use of deep learning methods to extract landslide factors and characteristic information about landslides has become one of the important directions in landslide disaster research (Zheng, 2019). The structure of the deep neural network model (DNN) has more layers, leading to stronger learning ability and a stronger ability to express the characteristics of objects. When faced with a large amount of data, it has a higher recognition and evaluation accuracy. For example, training a large number of geological disaster data samples through a deep neural network model (DNN) improves the accuracy of geological disaster risk prediction and early warning (Li et al., 2018). In this study, the unified sample is compared with different models to prove that the deep neural network can still improve the accuracy in small samples.

Therefore, in this study, the DNN model was introduced into the susceptibility modeling of mudstone landslides in Xining City. In addition, based on the quantification of the sensitive factors and their correlations with the occurrence of landslides, scholars have often used two methods or even multiple methods and models coupled to reflect the characteristics of the study area. For example, Fan et al. (2017) used a combination of deterministic factors (CF) and the analytic hierarchy process (AHP) (Fan et al., 2017), Li et al. (2018) used the coefficient of determination (CF) method coupled with support vector machines (SVMs) (Luo et al., 2021), and Luo et al. (2021) coupled the CF and logistic regression model (LRM) with geographic information system (GIS) support (Akgun, 2012). All of the above studies proved that the evaluation results of coupled models are more reasonable than those of a single model. Among them, the deterministic coefficient method, as a bivariate statistical method, can be used to determine the weight of each conditional factor of the landslide to analyze the correlation between each factor and the occurrence of the landslide. Therefore, in this study, a coupled CF-DNN method was developed to analyze the mudstone landslides in Xining City. Given that the accuracy and reliability of logistic regression models and support vector machine models have been verified in previous studies (Akgun, 2012; Li et al., 2018; Luo et al., 2021), in this study, the LRM and
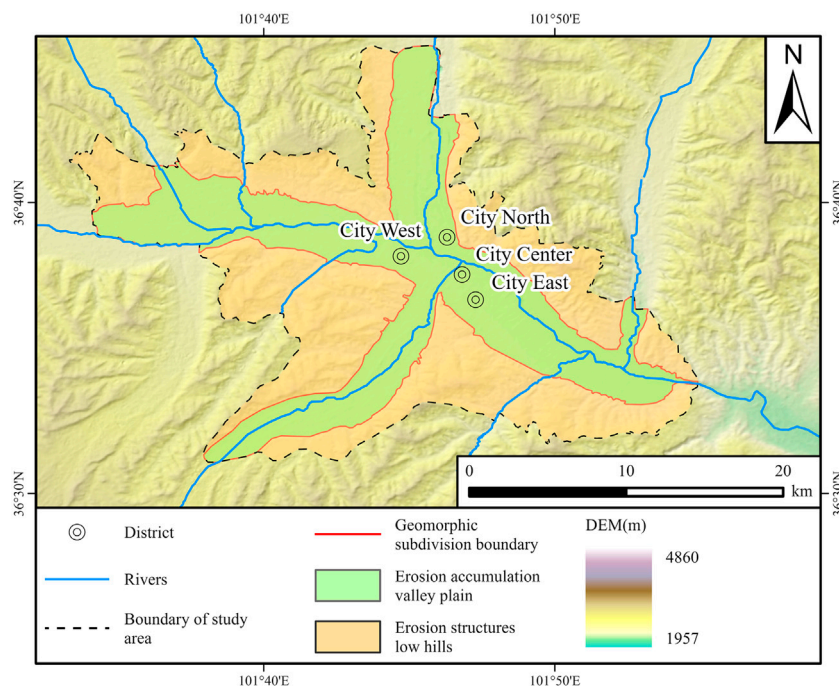
**FIGURE 1**
Outline of the geomorphic types in the study area.
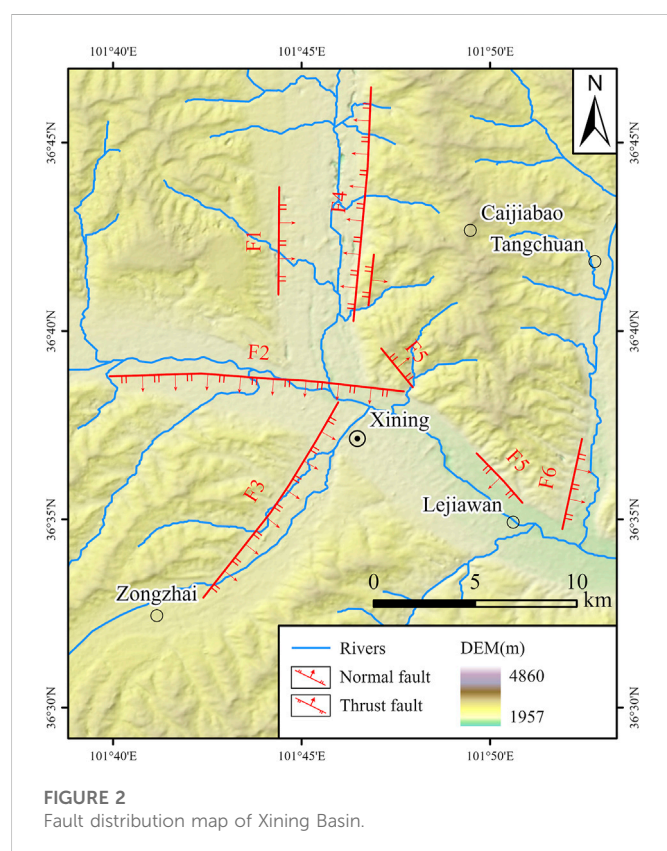


**FIGURE 2**
Fault distribution map of Xining Basin.

SVM were reasonably used as the reference models of the DNN, which was combined with the deterministic coefficient method (CF).

In this study, 1) a landslide database was constructed based on original landslide-related data obtained from landslide remote sensing interpretation and field investigations; 2) based on eight condition factors, a landslide inventory map was created and combined with the deterministic factor results to analyze the main impacts of the landslides factors; 3) a mudstone landslide susceptibility map of Xining was created using the ArcGIS software platform; and 4) the confusion matrix was used to evaluate the accuracy of the CF-DNN model.

# 2 Study area and data

In this study, Xining City, Qinghai Province, China, was taken as the study area (101°33′45″–101°56′15″E, 28°49′–29°31′N; Figure 1A). The Xining Basin is located in the northeastern part of the Qinghai-Tibet Plateau. Under the superposition of multi-stage tectonic movements, fold and fault structures have formed. The fold structure is mainly dominated by the regional Huangshui anticline (Figure 2). The fault structure is generally characterized by superficial tension. The formation and evolution of the regional landscape pattern are strictly controlled by the dominant NW-NWW trending tectonic system. Under the coupling of multi-factor mechanisms, the study area was finally shaped into the current erosion structure, with low hills and an erosion deposit valley plain (Figure 1B). The low hills of the erosion structure are distributed above the third-level terraces at the edges of the valleys of the Huangshui River and its tributaries. The hilly area covers 218.76 m², accounting for 54.63% of the total area. Due to the strong erosion of the gullies, the terrain is very fragmented. The elevation of the hilly area is 2,450–3,500 m, and the relative height difference is 100–500 m. On
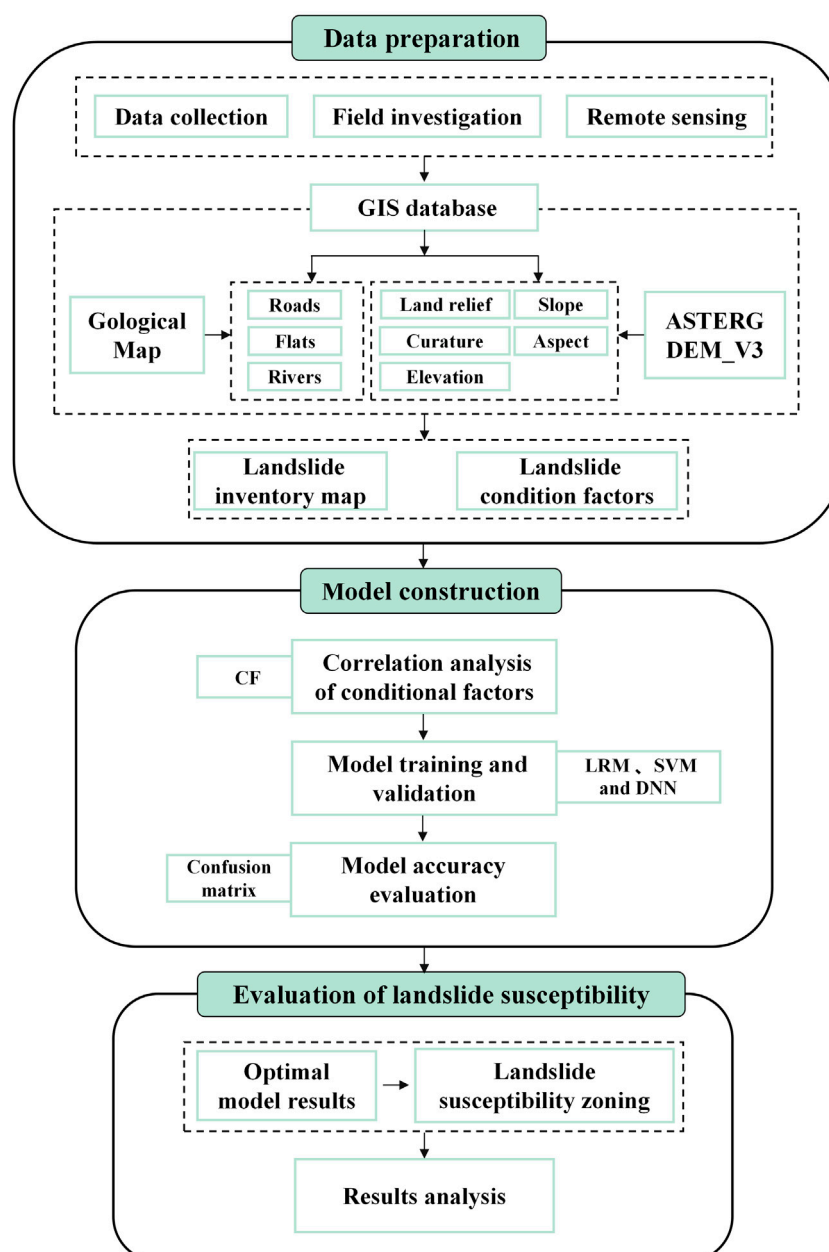
**FIGURE 3**
Workflow of the landslide susceptibility assessment conducted in this study.

the front edge of low mountains and hills, there are high and steep terrace (grades III to VII) slopes with heights of 100–300 m, and landslides are relatively more developed on these slopes. The erosion deposit valley plain is the urban area of Xining, with an area of 181.65 m², accounting for 45.37% of the study area. The terrain of the river valley area is relatively broad and is distributed in bands along the river. The terrain is high in the west and low in the east, and the terrace surface is slightly inclined toward the riverbed. The elevation is 2,200–2,450 m.

The exposed strata in the study area are relatively complex, including pre-Quaternary strata and Quaternary strata. The pre-Quaternary strata include the Changcheng system, Cretaceous

strata, and Tertiary strata, among which the Tertiary strata are the most exposed and are mainly composed of mudstone. Most of the exposed mudstone has a low strength, high degree of weathering, and poor permeability. When the water collects on the slope surface, the slope material becomes saturated due to its own water-blocking properties, making it easy for a weak sliding zone to form. A mudstone with a high degree of weathering can easily become the source of potential landslides. Thus, in this paper, the mudstone area in Xining was selected as the target research area. In terms of meteorology and hydrology, the study area has a plateau semi-arid continental climate, with a long winter and short summer, a large temperature difference, sparse but concentrated rainfall, and strong

evaporation. The Huangshui Basin is the main river basin in the study area. The Huangshui River is a first-class tributary of the Yellow River, which flows through the urban area from west to east. The river length in the study area is 35 km. The annual average flow at Xining Hydrological Station is 32.8 m³/s, the annual average minimum flow is 4.58 m³/s, and the maximum flow is 698 m³/s.

The unique tectonic, landform, lithology, meteorology, and hydrology of this area have resulted in the occurrence of a variety of disasters, and various adverse geological phenomena induced by external dynamic geological action are very prominent. Currently, according to the field investigation results reported by the staff of the Qinghai Provincial Geological Environmental Monitoring Station, a total of 294 landslide hidden danger points have been investigated, including 184 mudstone landslides, accounting for 62.58% of the total landslide hidden danger points investigated. Based on a GIS platform, five terrain factors (i.e., the elevation, slope, land relief, aspect, and curvature) and three geological factors (distance from a road, distance from a fault, and distance from a river) were selected. Topographic factors can be extracted from DEM data which is derived from the open geospatial data cloud platform. Geological factors are derived from the geological map provided by Qinghai Provincial Geological Environment Monitoring Station.

# 3 Methods

The basic workflow of the landslide susceptibility assessment conducted in this study is presented in Figure 3.

In this section, we mainly describe the methods involved in the landslide susceptibility assessment process. In this study, three different machine learning models (i.e., a logistic regression model, support vector machine, and deep neural network) were coupled with the certainty coefficient method. The data for the eight conditional factors were processed using a GIS platform. The certainty coefficient (CF) was calculated from the processed data. Then, the certainty factor was used to analyze the correlation between each condition factor and landslide. This information was then plotted on the landslide inventory map, which was convenient for the subsequent modeling of the landslide susceptibility model using *Python*.

## 3.1 Preparation of the dataset for modeling

The mudstone landslide-related data for Xining City were collected from historical data, field investigation data, and remote sensing interpretation data. A total of 184 mudstone landslides have been identified in the study area. According to the coordinates of the study area, these landslides were marked as points on the 1: 10,000terrain map of the area, and these points are considered to be the location of the geometric center of the slide. Based on the landslide data and 30 m DEM data, a preliminary landslide inventory map containing 184 landslides was generated, these landslides are all mudstone landslides. In addition, using a GIS platform, eight graded maps of the landslide condition factors were compiled in a grid format. The number of pixels of all of the factors for each classification in the reclassified grid data was counted. After conversion to vector data, each classification was connected to the space to count the number of landslides within the classification. The CF value was calculated using the number of statistical pixels and the number of landslides. The

obtained CF values were assigned in the vector layers of each factor. Before the modeling, based on the statistics of landslide scale in the study area, a circular buffer was built on the landslide point with a radius of 300 m, and non-landslide points were randomly generated outside the buffer to generate non-landslide samples equal to the number of landslide samples. The landslide and non-landslide sample points were coded as one and zero. After merging, a total of 368 samples were generated, which were randomly divided into training samples (70%) and validation samples (30%). The final dataset included a landslide inventory map, a hierarchical map of the landslide condition factors with CF values, and landslide and non-landslide samples.

## 3.2 Model

### 3.2.1 Logistic regression model

The logistic regression model (LRM) is a commonly used machine learning model for the binary classification of a dependent variable. In this paper, the relationship between the occurrence of landslides (the dependent variable) and multiple hazard factors is described (Menard, 1995; Atkinson and Massari, 1998). The independent variable in this model can be continuous or discrete, and it does not need to satisfy a normal frequency distribution (Bai et al., 2015; Wang et al., 2015). The expression of the logistic regression core function is

$$P = 1 \Big/ \Big[ 1 + e^{\left(\alpha + \beta_1 x_1 + \dots + \beta_i x_i\right)} \Big] \qquad (1)$$

where $P$ is the probability of landslide occurrence (0–1); $\alpha$ is a constant calculated *via* logistic regression; $\beta$ is the regression coefficient calculated *via* logistic regression; and i is the number of evaluation factor types. By taking the natural logarithm of both sides of Eq. 1, $In(p/(1-p))$ as the dependent variable, and the impact factor $x(i = 1, 2, \dots n)$ as the independent variable, we obtain.

$$In\left(P/\left(1-P\right)\right) = \alpha + \beta_1 x_1 + \beta_2 x_2 \dots + \beta_n x_n = \alpha + \beta x \qquad (2)$$

### 3.2.2 Support vector machine model

The support vector machine is a binary classification prediction model developed based on statistical principles (Vapnik, 1998; Abe, 2010), which is similar to a neural network but differs in that the SVM uses mathematical methods and optimization techniques. SVMs include linear support vector machines and non-linear support vector machines. In the case of linear separability, an optimal classification function is obtained by transforming a constrained extreme value problem into a dual problem. The binary classification prediction problem of landslide susceptibility zoning is often non-linear; thus, it is necessary to map the original data to a high-dimensional feature space and make it linearly separable to identify the optimal classification plane (Brenning, 2005). That is, the optimal classification plane is the plane that maximizes the separation of the data points belonging to two different classes. The core principle of identifying this plane is to introduce the corresponding kernel function after transforming it into a dual problem (Yao et al., 2008), which solves the problem of the increased complexity caused by mapping to a high-dimensional space. At present, the most commonly used kernel functions include the linear kernel function, polynomial function, radial basis function (RBF), and Sigmoid function. However, there is a certain error in the sample after the kernel function is determined. For outliers that do not meet the constraints, the slack
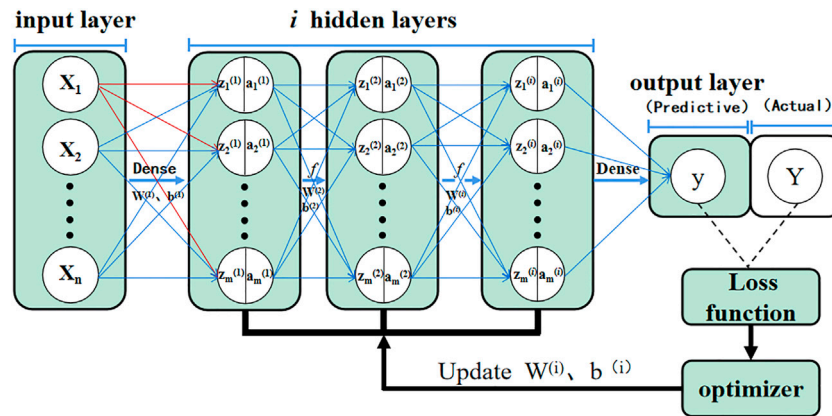
**FIGURE 4**
Schematic diagram of the DNN.

variable εi and penalty factor c are introduced for optimization. The εi value actually represents the outlier distance of the corresponding point. The larger the value is, the farther away the point is, and εi is equal to zero for non-outlier points. The penalty factor refers to the tolerance of the error, which must be determined in advance. The larger the value is, the greater the loss of the objective function, which easily leads to overfitting. Conversely, the smaller the value is, the easier it is for underfitting to occur.

The calculation process of SVM is based on a set of linearly inseparable landslide data $x_i$ ( $x_i \in R^d$ ), where i is the number of samples, $d$ is the dimension, $y_i$ is the corresponding output data, and $y_i \in \{-1, 1\}$ , which means the output results represent landslide and non-landslide points. The original data are mapped to a certain feature space through non-linear mapping $\varphi(x)$ and distinguishing landslide categories using the maximum interval $\|\omega\|^2/2$ in the hyperplane equation $\omega \cdot \varphi(x) + b = 0$ . That is, $\|\omega\|^2$ needs to be the minimum value, and the following constraints must be satisfied:

$$y_i (\boldsymbol{\omega} \cdot \boldsymbol{x}_i + \boldsymbol{b}) \geq 1 - \boldsymbol{\varepsilon}_i (\boldsymbol{\varepsilon}_i \geq 0) \tag{3}$$

While solving the hyperplane, the slack variables should be as small as possible, so the problem is transformed into a quadratic programming problem of finding the minimum value of $\|\omega\|^2/2 + c(\sum_{i=1} \varepsilon_i)$ under the constraints. The kernel function $K(x_i, y_i)$ is introduced to obtain the classification function by solving.

$$f(x) = sgn\left\{\sum_{i=1}^{n} a_i y_i \cdot K(x_i, y_i) + b\right\} \tag{4}$$

### 3.2.3 Deep neural network mode

A complete neural network consists of an input layer, a hidden layer, and an output layer. Each layer is built on multiple neurons. Each neuron can be regarded as a simple linear function, and the neurons on adjacent layers are combined in a densely connected manner. The difference is that a deep neural network has multiple hidden layers, and there is no connection within the same layer (between hidden layers). The propagation process of the DNN is divided into forward propagation composed of an input layer-hidden layer-output layer and backward propagation composed of a loss function optimizer. A schematic diagram of the DNN is shown in Figure 4.

Forward propagation refers to the calculation and recognition process of the original data starting from the input layer, through the

hidden layer calculation, finally reaching the output layer, and outputting the result from the output layer. When sample X is input, the DNN automatically assigns the initial value to the weight matrix W, and it continues the calculations in the hidden layer according to Eqs 5–7 until the result y can be output in the output layer.

$$Z^{(i)} = W^{(i)} X + b^{(i)} \tag{5}$$

$$a^{(i)} = f(Z^{(i)}) \tag{6}$$

$$y = W^{(i)} a^{(i-1)} + b^{(i)} \tag{7}$$

where $X$ is the input sample, denoted as $(x_1, x_2, ..., x_n)$ , and $n$ is characterized number. $Z$ is the output result, denoted as $(Z_1^{(i)}, Z_2^{(i)}, ..., Z_m^{(i)})$ , where $i$ is the number of hidden layers, and $m$ is the number of neurons in the next layer. $W$ is the weight matrix; $b$ is a constant term; and a is the input value of the next layer of the network, that is, substitute it into $X$ in Eq. 5 and continue to calculate forward. $f$ is the activation function, the purpose of which is to convert linear to non-linear after each layer of network calculation is completed to improve the recognition rate, and the Sigmoid function, Tanh function, and rectified linear unit (ReLu) function are commonly used.

The output result y is the predicted value, and there is a significant difference between it and the real value Y. Obtaining the correct $W$ and $b$ is the key factor affecting the output result. The essence of backpropagation is to calculate the difference between the predicted value and the true value according to the loss function to reversely adjust the parameters $W$ and $b$ and select a suitable optimizer to update the parameters. The essence of the neural network is to obtain values of the parameters $W$ and $b$ with higher accuracy through multiple forward and reverse circular training to obtain the final optimized model. For the classification problem of landslide susceptibility zoning, the loss function adopted is generally the cross entropy function, and optimizer methods such as the gradient descent and Adam method can be used.

### 3.2.4 Certainty coefficient method

The certainty coefficient method, proposed by Shortliff (1975), was used in this study to analyze the correlation between each

condition factor and the occurrence of landslides (Shortliffe and Buchanan, 1975). Although the evaluation process of the certainty coefficient model is relatively simple, the accuracy is high. The premise of the high accuracy is that the geological disasters that have occurred and the disasters that occur in the future occur under the same geological conditions. The calculation formula is as follows:

$$CF = \begin{cases} \dfrac{PP_a - PP_s}{PP_a(1 - PP_s)}, PP_a \geq PP_s \\ \dfrac{PP_a - PP_s}{PP_s(1 - PP_a)}, PP_a < PP_s \end{cases} \tag{8}$$

where $PP_a$ is the conditional probability of landslides in impact factor classification a, which is expressed as the ratio of the landslide points in classification a to the classification area; and $PP_s$ is the probability of historical landslides in the entire study area, which is expressed as the ratio of historical landslide points to the total area of the study area.

The $CF$ ranges from −1 to 1. When the $CF$ values are between zero and 1, landslides are prone to occur in this geological environment. The closer the CF value is to 1, the more sensitive the unit is to landslides. In contrast, when the $CF$ value is between −1 and zero, landslides are unlikely to occur in this geological environment.

The data mentioned in the formula are all derived from the data in the conditional factor grading diagram, including the number of landslides included in each grading, the number of landslide pixels, the total number of landslides and the total number of grids. cf values calculated according to the formula will be assigned to the attribute table of each conditional factor grading diagram.

## 3.3 Factor multicollinearity diagnostics

Multicollinearity refers to the linear correlation between independent variables. If multicollinearity exists, the matrix is irreversible when calculating the partial regression coefficient of the independent variable. The results of variance analysis of the whole model are inconsistent with the test results of regression coefficients of each independent variable. In this study, a variety of different models were used for sensitivity analysis. Here, the variance inflation factor diagnostic method and tolerance value method were combined to determine whether the selected factors could be fully incorporated into the model.

Variance inflation factor (VIF) is a measure of the severity of multicollinearity in a multiple linear regression model. It represents the ratio of the variance of the estimator of the regression coefficient to the variance when the independent variables are assumed to be not linearly correlated. When VIF is large, it indicates that there is multicollinearity between the independent variables. This diagnostic method also has the problem that the threshold value is not easy to determine, so it needs to be considered in combination with the tolerance value method. The tolerance value is actually the inverse of VIF. Its value ranges from 0 to 1. The closer Tol is to 1, the weaker the collinearity between independent variables is, indicating that the factor can be completely entered into the model through multiple collinearity diagnosis.

## 3.4 Accuracy evaluation method

There are various methods for evaluating the accuracy of landslide susceptibility results. In this study, the confusion matrix was chosen as



**FIGURE 5**
Diagram of the confusion matrix.
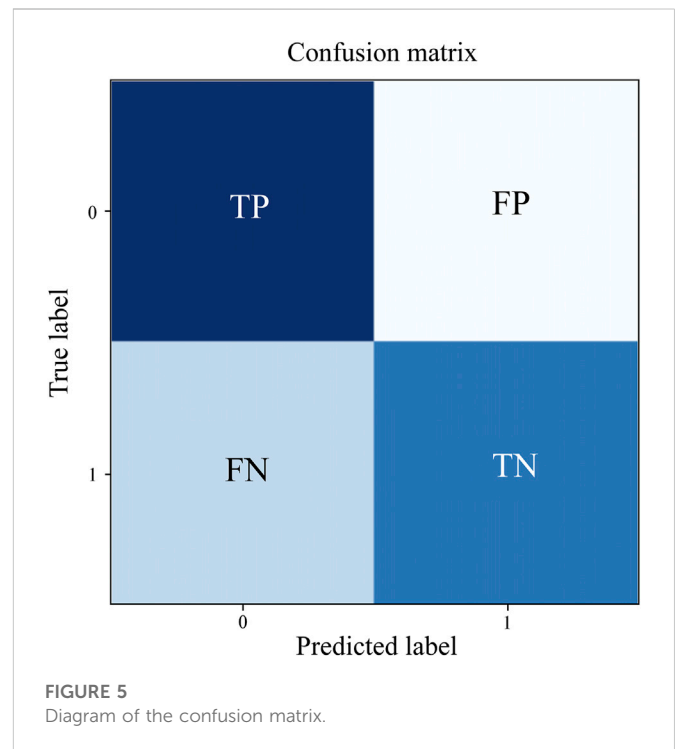
the method for evaluating the model's accuracy. The confusion matrix is an effective tool in machine learning for evaluating the accuracy of each iteration of the model, that is, it can be used to evaluate the performance of a classification model based on a set of test data with known true values. For a binary classification problem such as landslide *versus* non-landslide, when judging samples, zero is used to represent landslide, and one is used to represent non-landslide. In the early stage, we know which data are landslide and non-landslide data in the real situation through sample collection, and thus, we know the predicted value of the data through the results of the sample data output by the classification model. Therefore, four first-level indicators TP, TN, FP, and FN are formed according to the combination of the actual values of one and zero and the predicted values of one and zero (Figure 5).

For a predictive scoring model, the higher the TP and TN values are, and the lower the FP and FN values are, the higher the model accuracy is. When using a large amount of data, it is difficult to measure the reliability based only on the first-level basic indicators. Therefore, four indicators (ACC, PPV, TPR, and TNR) are added to the results of the basic statistical data of the confusion matrix. These indicators are calculated as follows:

$$ACC = \frac{TP + TN}{TP + TN + FP + FN} \tag{9}$$

$$PPV = \frac{TP}{TP + FP} \tag{10}$$

$$TPR = \frac{TP}{TP + FN} \tag{11}$$

$$TNR = \frac{TN}{TN + FP} \tag{12}$$

where ACC is the accuracy rate, which refers to the proportion of all of the results that are judged to be correct by the classification model compared to the total observations; PPV is the positive predictive
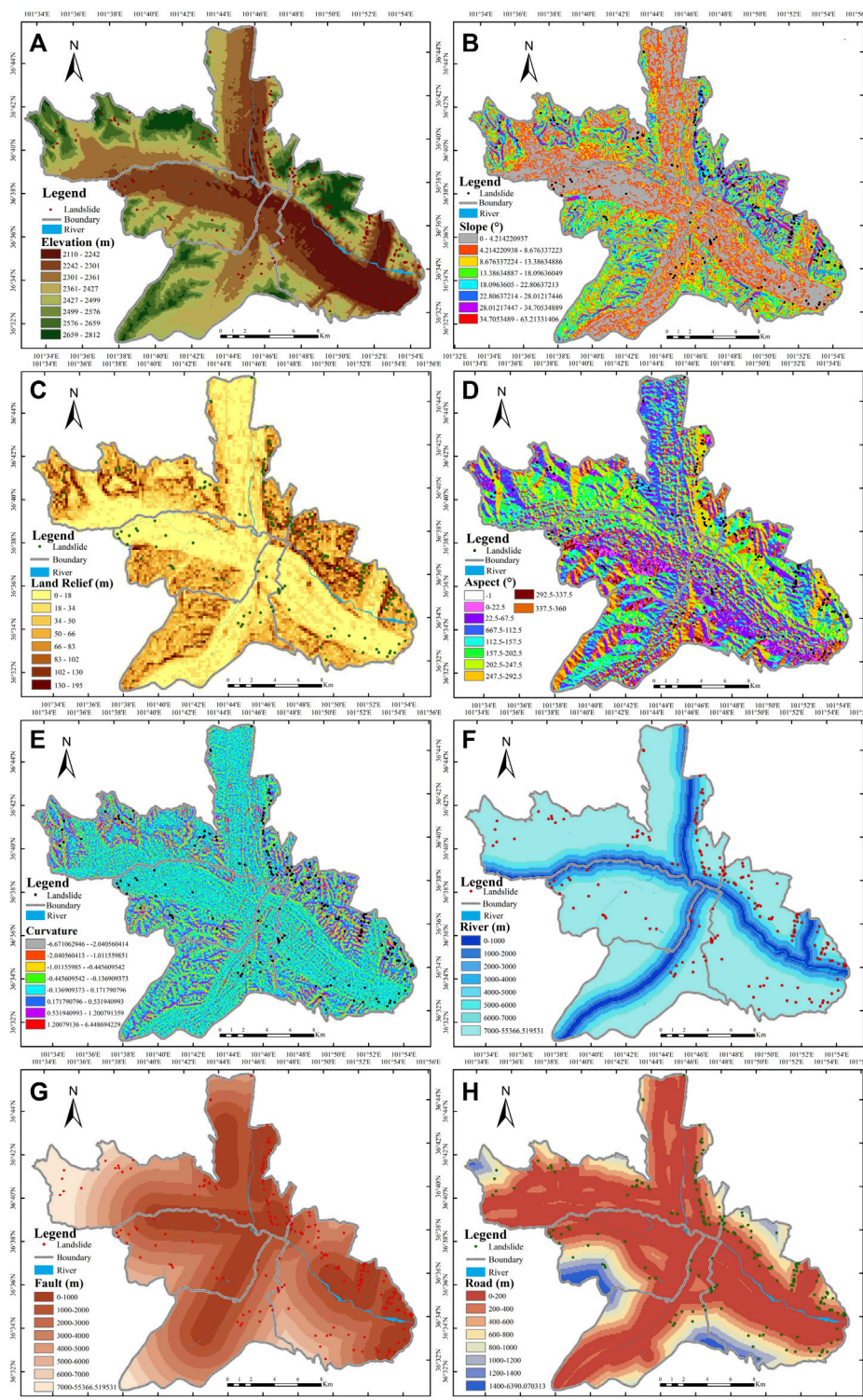
**FIGURE 6**
Grading maps of the evaluation factors for landslide susceptibility assessment in Xining City:**(A)** Elevation; **(B)** Slope; **(C)** Land relief; **(D)** Aspect; **(E)** Curvature; **(F)** Distance from a river; **(G)** Distance from a fault; and **(H)** Distance from a road.

value, which refers to the proportion of all of the results with a predicted value of landslide that the model predicts correctly; $TPR$ is the true positive rate, which refers to the proportion of all of the result with a true value of landslide that the model predicts correctly; and

$TNR$ is the true negative rate, which refers to the proportion of all of the result with a true value of non-landslide that the model predicts correctly. The larger the values of these four secondary indicators are, the better the results of the model are.

**TABLE 1 Grading of factors and CF values.**

| Evaluation factor | Elevation (m) | | | | | | | |
|---|---|---|---|---|---|---|---|---|
| Grading | 2,110–2,242 | 2,242–2,301 | 2,301–2,361 | 2,361–2,427 | 2,427–2,499 | 2,499–2,576 | 2,576–2,659 | 2,659–2,812 |
| Landslide proportion | 10.32 | 19.02 | 10.32 | 15.21 | 23.91 | 7.07 | 8.15 | 5.98 |
| Grading area ratio | 11.54 | 20.29 | 16.29 | 15.67 | 12.59 | 10.03 | 8.98 | 4.60 |
| CF | -0.1053 | -0.0627 | -0.3662 | -0.0292 | 0.4737 | -0.2955 | -0.0921 | 0.2299 |

| Evaluation factor | Slope (°) | | | | | | | | | |
|---|---|---|---|---|---|---|---|---|---|---|
| Grading | Flat | North | Northeast | East | Southeast | South | Southwest | West | Northwest | North |
| Landslide proportion | 0 | 2.17 | 14.67 | 11.96 | 8.70 | 13.59 | 12.50 | 20.65 | 8.70 | 5.98 |
| Grading area ratio | 0.17 | 6.77 | 14.80 | 15.03 | 13.00 | 12.67 | 11.73 | 11.19 | 9.77 | 4.87 |
| CF | -1 | -0.6752 | 0.0021 | -0.1959 | -0.3239 | 0.0780 | 0.0718 | 0.4641 | -0.1001 | 0.1951 |

| Evaluation factor | Land relief (m) | | | | | | | |
|---|---|---|---|---|---|---|---|---|
| Grading | 0–18 | 18–34 | 34–50 | 50–66 | 66–83 | 83–102 | 102–130 | 130–195 |
| Landslide proportion | 18.48 | 15.22 | 11.96 | 11.41 | 16.3 | 11.96 | 9.78 | 4.89 |
| Grading area ratio | 30.89 | 19.11 | 14.25 | 13.77 | 10.33 | 6.77 | 3.79 | 1.1 |
| CF | -0.675 | -0.5672 | -0.5442 | -0.5496 | -0.1657 | -0.0412 | 0.2871 | 0.5866 |

| Evaluation factor | Aspect (°) | | | | | | | |
|---|---|---|---|---|---|---|---|---|
| Grading | 0–4.21 | 4.21–8.68 | 8.68–13.39 | 13.39–18.10 | 18.10–22.81 | 22.81–28.01 | 28.01–34.71 | 34.71–63.2 |
| Landslide pproportion | 21.20 | 13.59 | 10.87 | 9.78 | 16.30 | 13.04 | 10.87 | 3.26 |
| Grading area ratio | 27.36 | 23.59 | 15.63 | 12.96 | 9.63 | 6.27 | 3.42 | 1.14 |
| CF | -0.5743 | -0.6836 | -0.618 | -0.5856 | -0.0756 | 0.1253 | 0.4283 | 0.3645 |

| Evaluation factor | Curvature | | | | | | | |
|---|---|---|---|---|---|---|---|---|
| Grading | -6.67–-2.04 | 2.04–-1.01 | -1.01–-0.45 | -0.45–-0.14 | -0.14–0.17 | 0.17–0.53 | 0.53–1.20 | 1.20–6.45 |
| Landslide proportion | 1.09 | 1.63 | 8.7 | 23.37 | 32.07 | 23.37 | 7.61 | 2.17 |
| Grading area ratio | 0.13 | 1.25 | 7.28 | 21.55 | 39.46 | 21.36 | 8.09 | 0.89 |
| CF | 0.7872 | -0.4078 | -0.5392 | -0.6972 | -0.5584 | -0.6823 | -0.4888 | 0.2477 |

| Evaluation factor | Distance from a river (m) | | | | | | | |
|---|---|---|---|---|---|---|---|---|
| Grading | 0–200 | 200–400 | 400–600 | 600–800 | 800–1,000 | 1,000–1,200 | 1,200–1,400 | 1,400–6,390 |
| Landslide proportion | 1.09 | 1.09 | 4.89 | 10.87 | 10.33 | 13.59 | 7.61 | 50.54 |
| Grading area ratio | 6.29 | 7.62 | 6.22 | 6.52 | 6.13 | 5.2 | 4.9 | 57.12 |
| CF | -0.8279 | -0.8580 | 0.2144 | 0.4022 | 0.4086 | 0.6203 | 0.3585 | -0.1157 |

| Evaluation factor | Distance from a fault (m) | | | | | | | |
|---|---|---|---|---|---|---|---|---|
| Grading | 0–1,000 | 1,000–2000 | 2000–3,000 | 3,000–4,000 | 4,000–5,000 | 5,000–6,000 | 6,000–7,000 | 7,000–1 |
| Landslide proportion | 45.65 | 17.39 | 14.13 | 9.24 | 7.07 | 3.26 | 1.09 | 2.17 |
| Grading area ratio | 25.02 | 20.9 | 17.53 | 14.62 | 8.9 | 5.33 | 3.17 | 4.54 |
| CF | 0.4544 | 0.1686 | 0.1948 | 0.3694 | 0.2067 | 0.3889 | -1.923 | 0.5227 |

| Evaluation factor | Distance from a road (m) | | | | | | | |
|---|---|---|---|---|---|---|---|---|
| Grading | 0–500 | 500–1,000 | 1,000–1,500 | 1,500–2000 | 2000–2,500 | 2,500–3,000 | 3,000–3,500 | 3,500– |
| Landslide proportion | 34.24 | 40.76 | 13.04 | 6.52 | 2.72 | 2.17 | 0.54 | 0 |
| Grading area ratio | 55.52 | 16.05 | 9.37 | 7.39 | 5.11 | 3.28 | 1.88 | 1.4 |
| CF | 0.3846 | 0.6095 | 0.2833 | -0.1178 | -0.4696 | -0.3388 | -0.7125 | -1 |

**TABLE 2 The factor multicollinearity diagnostics.**

| Variable | TOL | VIF |
|---|---|---|
| Elevation | 0.919,236 | 1.087859 |
| Slope | 0.955,998 | 1.046027 |
| Land relief | 0.482,606 | 2.072085 |
| Aspect | 0.903,503 | 1.106,803 |
| Curvature | 0.435,019 | 2.298,749 |
| Distance from a river | 0.943,796 | 1.059551 |
| Distance from a fault | 0.895,788 | 1.116,335 |
| Distance from a road | 0.952,347 | 1.050038 |

**TABLE 3 Secondary index values of each model in the confusion matrix.**

| | LRM | SVM | DNN | Best result |
|---|---|---|---|---|
| ACC | 0.7368 | 0.7456 | 0.7719 | DNN |
| PPV | 0.8245 | 0.7719 | 0.8701 | DNN |
| TPR | 0.7014 | 0.7333 | 0.7541 | DNN |
| TNR | 0.7872 | 0.7592 | 0.7924 | DNN |

# 4 Results and discussion

## 4.1 Impact factor analysis

Based on the original landslide-related data obtained from landslide remote sensing interpretation and field investigations, eight condition factors, including elevation, slope, land relief, aspect, curvature, distance from a river, distance from a fault, and distance from a road, were determined. Using a GIS platform, the data for these eight conditional factors were used to create a graded map of landslide susceptibility evaluation factors (Figure 6), which was combined with the deterministic factor results (Table 1) to analyze the influence of each factor on the occurrence of landslides. All of these eight factors have passed the multicollinearity diagnosis and can be completely entered into different models. See Table 2 for details.

### 4.1.1 Elevation

The elevation reflects the land changes to a certain extent and is an important factor affecting the stress value of the slope. Based on the DEM data, in this study, the natural discontinuity method was used to divide the elevation. The natural break method considers variation in groups of LSI values by calculating the minimum sum of variance of different groups for the optimal classification of LSI values and can be conveniently applied in ArcGIS software. In this method, statistical principle is considered to avoid subjectivity in obtaining susceptibility zonation. Combined with the chart, we can see that the terrain of the Xining urban area is relatively flat and broad and distributed in a band along the valley. The terrain is high in the west and low in the east. The terrace surface slopes slightly towards the riverbed. The altitude is higher farther away from the urban area, and this is also the main distribution area of landslides.

### 4.1.2 Slope

The slope represents the steepness of the surface. The size of the slope not only affects the stress distribution inside the slope but also controls the surface runoff, groundwater recharge, and rainfall infiltration. In this study, based on the DEM data, the slope analysis function in ArcGIS based on the gridded surface was used to analyze the slope in the study area. Combined with the chart, we can see that the landslides are mainly distributed in the slope range of 28.01°–63.2°. The greater the slope is, the greater the probability of landslide occurrence when the slope is affected by adverse external environmental factors.

### 4.1.3 Land relief

The land relief factor represents the difference between the highest point and the lowest point in a certain area. The greater the land relief is, the greater the possibility of landslide occurrence. Based on the DEM data, in this study, the block statistics and raster calculator functions in ArcGIS were used to analyze the land relief in the study area Combined with the chart, we can see that the area most prone to landslides is mainly distributed in the land relief range of 102–195 m, and the area with this land relief range accounts for 4.89% of the total area of the study area, including 14.67% of the landslide area. The CF value becomes closer to one as the land relief increases, which is consistent with the principle that landslides are prone to occur in areas with a large land relief.

### 4.1.4 Aspect

Different slopes receive different sunshine hours and solar radiation intensity. This leads to differences in the soil moisture content and weathering degree on the slope, which ultimately affects the stability of the slope. Based on the DEM data, in this study, the aspect analysis function of the grid surface in ArcGIS was used to analyze the slope aspect in the area. Combined with the chart, we can see that the slopes most prone to landslides mainly had due west aspects (247.5°–292.5°), accounting for 11.19% of the study area, including 20.65% of the landslide area. As can be seen from the CF values, in the study area, the slopes with aspects ranging from the south to west (sunny slope) were more susceptible to landslides. This is related to the higher degree of weathering of the rock and soil mass due to prolonged exposure to sunlight.

### 4.1.5 Curvature

The curvature represents the degree of deformation of a point on the surface of the slope. A positive value indicates a convex slope, a negative value indicates a concave slope, and a value of zero or close to zero indicates a relatively flat slope. Based on the DEM data, in this study, the curvature analysis function of the ArcGIS grid surface was used to analyze the curvature of the area. Combined with the chart, we can see that the areas most prone to landslides mainly have curvatures of −6.67 to −2.04 and 1.2–6.45 m$^{-1}$, and the area with this curvature accounts for 1.02% of the study area, including 3.26% of the landslide area. The closer the curvature is to zero, the closer the CF value is to −1, indicating that the greater the curvature of the slope is, the greater the probability of landslide occurrence.

### 4.1.6 Distance from a river

Different degrees of scouring and erosion on both sides of the river lead to instability of the slope foot, which eventually induces landslides. Based on the geological map data, in this study, the Euclidean distance function in ArcGIS was used to analyze the
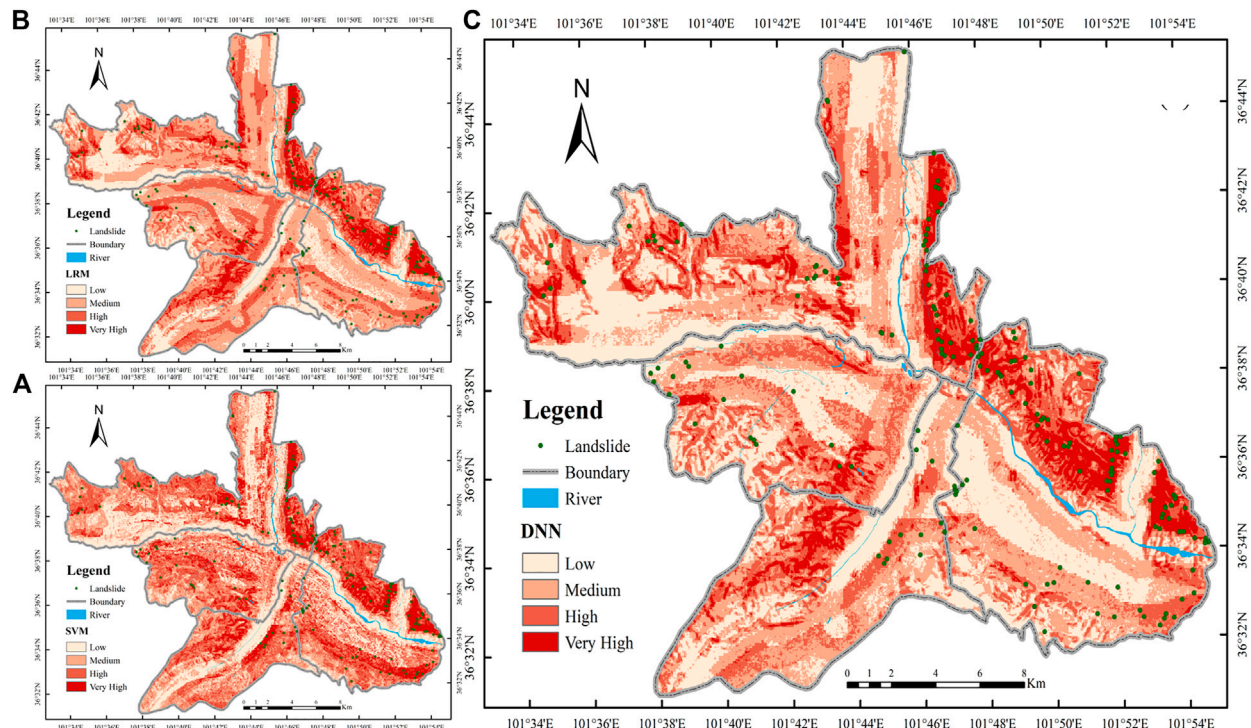
**FIGURE 7**
The results of the susceptibility evaluation of the coupled model: **(A)** Support vector machine model susceptibility zoning; **(B)** the logistic regression model susceptibility zoning; **(C)** Deep learning susceptibility zoning.

water system in the study area, and the distance from a river was divided into eight grades with 200 m intervals (Table 3). Combined with the chart, we can see that the areas most prone to landslides are mainly distributed in the range of 1,000–1,200 m. The area within this range accounts for 5.2% of the total area of the study area, including 13.59% of the landslide area. Based on the CF values, the 400–1,400 m area is prone to the occurrence of landslides.

### 4.1.7 Distance from a fault

The regional fault structure plays a controlling role in the development of joints and fissures in the geological bodies. Based on the geological map data, in this study, the Euclidean distance function in ArcGIS was used to perform fault analysis in the study area, and the distance from a fault was divided into eight grades with 1,000 m intervals (Table 1). Combined with the chart, we can see that the areas most prone to landslides are mainly distributed in the range of up to 1,000 m. The area within this range accounts for 25.02% of the total area of the study area, including 45.65% of the landslides. It can be seen that the fault factor has a great influence on landslide susceptibility. As the distance from a fault increased, the proportion of landslides and the CF value gradually decrease, indicating that the more fragmented the rock mass is, the more prone to landslides it is.

### 4.1.8 Distance from a road

The large-scale cutting and excavation of roads in urban areas has changed the stress state of the cut slopes and aggravated the occurrence of landslides. Based on the geological map data, in this

study, the Euclidean distance function in ArcGIS was used to analyze the roads in the study area, and the distance from a road was divided into eight grades with 500 m intervals (Table 1). Combined with the chart, we can see that the areas most prone to landslides are mainly distributed in the range of 500–1,000 m. The area within this range accounts for 16.05% of the total area of the study area, including 40.76% of the landslide area. As the distance from a road increases, the landslide proportion and CF value gradually decrease, indicating that human activities such as road construction have a certain impact on the development of landslides.

## 4.2 Model accuracy evaluation and verification

After grading and quantifying each evaluation factor and using the certainty coefficient model to calculate the CF value of each grading index, the logistic regression model (LR), the support vector machine model (SVM), and the deep neural network model (DNN) were used for the coupled calculations. The evaluation results are presented in Figure 7. In the verification, 70% of the 368 landslide and non-landslide samples were used as training samples for the model calculation, and 30% were used as test samples. The confusion matrix was used to compare the results of the above three models, and the reliability was verified. The results are presented in Table 2.

It can be seen from the comprehensive results presented in Table 2 that the ACC, PPV, TPR, and TNR of the deep neural network are

**FIGURE 8**
Comparison of the number of landslides in each sensitivity area generated using the three models.
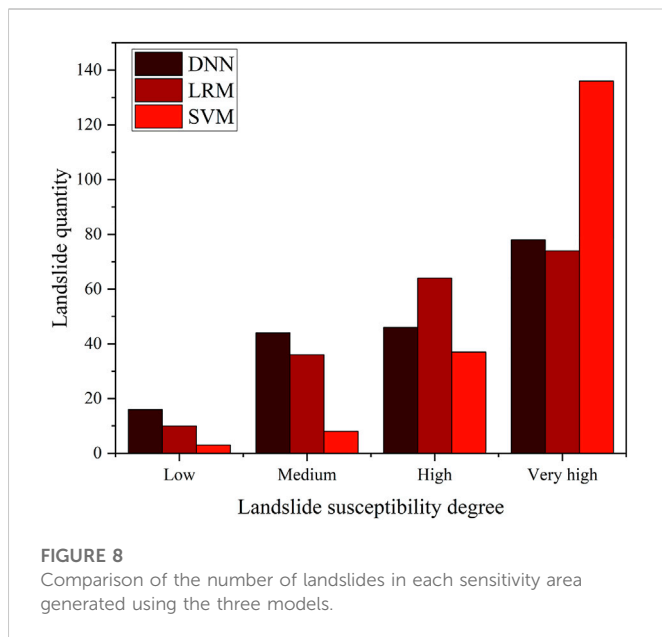
greater than those of the other two models, so it is the optimal model among the three models. This study proves that the model accuracy of deep neural network in small samples is still improved. Of course, for small samples, the improved accuracy is smaller than that of large samples.

## 4.3 Sensitivity analysis

The principles of the three models were outlined in Section 3, and their algorithms can all be implemented using *Python*. First, the model was constructed using the training dataset, and then, the prediction ability of the trained model was tested using the validation dataset. In addition, the trained model was applied to calculate the landslide sensitivity index (LMI) for each raster layer in the study area. Theoretically, the LSI ranges from zero to 1, reflecting the probability of landslide occurrence. In this case, the LSI values calculated using the three models did not reach the breakpoint value. The LSI values calculated using the SVM model ranged from zero to 0.993, the LSI values calculated using the LR model ranged from zero to 0.595, and the LSI values calculated using the DNN model ranged from 0.146 to 0.853. To avoid subjectivity in obtaining the sensitivity partitions, the most widely used Jenks natural discontinuity method was used in this study to classify the landslide sensitivity categories as extremely high, high, medium, and low (Figure 7).

The results presented in Section 4.2 show that the DNN produced the optimal results for this study area, so the sensitivity analysis was carried out based on the evaluation results of this model. According to the landslide sensitivity zoning map obtained using the CF-DNN (Figure 7C), 32.1% of the study area had an extremely high and high landslide susceptibility, with 124 landslides in these areas. The extremely high and high susceptibility areas were mainly distributed in the higher elevation areas along the eastern edge of the Huangshui watershed, which is in good agreement with the landslide

distribution observed in the field. In addition, the areas with moderate susceptibility accounted for about 35.1% of the study area and included 25% of the landslide area. The low susceptibility area accounted for 32.6% of the study area and 8.7% of the landslide area. The low and medium sensitivity zones accounted for a large proportion of the area and were mainly distributed within the urban area of Xining City. Figure 8 presents a comparison of the model results.

## 5 Conclusion

In this study, based on remote sensing interpretation and field investigations, eight evaluation factors were selected: elevation, slope, land relief, aspect, curvature, distance from a river, distance from a fault, and distance from a road. According to the landslide susceptibility assessment factor classification map of these eight condition factors and the certainty factor results, the influence of each factor on the occurrence of landslides in the study area was analyzed. The results showed that four factors—elevation, curvature, distance from a fault, and distance from a road—had relatively significant influences on the landslide susceptibility in the study area.

The certainty coefficient method was used to couple the logistic regression, support vector machine, and deep neural network models, and the confusion matrix was used to evaluate the accuracy of these three models. The results indicated that the combined CF-DNN method was the most suitable for evaluating the landslide susceptibility in the study area.

According to the evaluation results obtained using the coupled CF and deep neural network model, the study area was divided into four landslide susceptibility zones: low (32.65%), medium (35.12%), high (22.44%), and extremely high (9.79%). The low and medium susceptibility areas accounted for the largest proportions and were distributed in the urban area of Xining; while the extremely high susceptibility areas were distributed in the high-elevation areas along the eastern edge of the Huangshui Basin.

## Data availability statement

The raw data supporting the conclusion of this article will be made available by the authors, without undue reservation.

## Author contributions

Writing—original draft preparation, WM; writing—review and editing, ZW; writing—review and editing, JD; resources, LP; supervision, QW; methodology, XW; visualization, YD; investigation, YW; All authors have read and agreed to the published version of the manuscript.

## Funding

Conversion and Utilization Technology (GF2022YB005). Study on deformation evolution and stability criterion of Mining slope with Gentle stratified structure under complex conditions (41877273); Study on Unloading Law of Overlying Sandstone in Steeply inclined Coal Goaf under High and Steep Slope (2021YJ0053).

## Conflict of interest

WM, ZW, and YW were employed by Qinghai 906 Engineering Survey and Design Institute Co Ltd.

The remaining authors declare that the research was conducted in the absence of any commercial or financial relationships that could be construed as a potential conflict of interest.

## Publisher's note

All claims expressed in this article are solely those of the authors and do not necessarily represent those of their affiliated organizations, or those of the publisher, the editors and the reviewers. Any product that may be evaluated in this article, or claim that may be made by its manufacturer, is not guaranteed or endorsed by the publisher.

## References

Abe, S. (2010). *Support vector machines for pattern classification*. London: Springer.

Akgun, A. (2012). A comparison of landslide susceptibility maps produced by logistic regression, multi-criteria decision, and likelihood ratio methods: A case study at izmir, Turkey. *Landslides* 9 (1), 93–106. doi:10.1007/s10346-011-0283-7

Al-Harbi, K. M. A. S. (2001). Application of the AHP in project management. *Int. Proj. Manage* 19, 19–27. doi:10.1016/S0263-7863(99)00038-1

Atkinson, P. M., and Massari, R. (1998). Generalized linear modeling of susceptibility to landsliding in the central Apennines, Italy. *Comput. Geosciences* 24 (4), 373–385. doi:10.1016/s0098-3004(97)00117-9

Bai, C. N., Peng, L., and Shen, Y. (2021). Characteristics and mechanism of large landslide in Zhangjiawan. *Xining. Sci. Technol. Eng.* 21 (03), 927–934.

Bai, S. B., Lu, P., and Wang, J. (2015). Landslide susceptibility assessment of the Youfang catchment using logistic regression. *J. Mt. Sci-engl* 12 (4), 816–827. doi:10.1007/s11629-014-3171-5

Brabb, E. E. (1984). "Innovative approaches to landslide hazard and risk mapping," in Proc Fourth International Symposium on landslide, Toronto, Canada, 23-31 August 1985 (Toronto: Canadian Geotechnical Society), 307–324.

Brenning, A. (2005). Spatial prediction models for landslide hazards: Review, comparison and evaluation. *Nat. Hazards. E. Sys.Sci* 5, 853–862. doi:10.5194/nhess-5-853-2005

Bui, D. T., Tuan, T. A., Klempe, H., Pradhan, B., and Revhaug, I. (2016). Spatial prediction models for shallow landslide hazards: A comparative assessment of the efficacy of support vector machines, artificial neural networks, kernel logistic regression, and logistic model tree. *Landslides* 13 (2), 361–378. doi:10.1007/s10346-015-0557-6

Chen, W., Xie, X., Peng, J., Shahabi, H., Hong, H., Bui, D. T., et al. (2018). GIS-based landslide susceptibility evaluation using a novel HybridIntegration approach of bivariate statistical based random forest method. *Catena* 164, 135–149. doi:10.1016/j.catena.2018.01.012

Chen, W., Xie, X., Peng, J., Wang, J., Duan, Z., and Hong, H. (2017). GIS-Based landslide susceptibility modelling: A comparative assessment of kernel logistic regression, naïve-bayes tree, and alternating decision tree models. *Nat. Hazrisk* 8 (2), 950–973. doi:10.1080/19475705.2017.1289250

Confuorto, P., Di Martire, D., Infante, D., Novellino, A., Papa, R., Calcaterra, D., et al. (2019). Monitoring of remedial works performance on landslideaffected areas through ground- and satellite-based techniques. *Catena* 178, 77–89. doi:10.1016/j.catena.2019.03.005

Dai, L. X., Qiang, X., Xuanmei, F., Ming, C., Qin, Y., Fan, Y., et al. (2017). Preliminary study on spatial distribution and susceptibility evaluation of earthquake-induced geological disasters in Jiuzhaigou, Sichuan province on August 8, 2017. *Chin.J. Eng. Geol.* 25 (4), 1151–1164. doi:10.13544/j.cnki.jeg.2017.04.030

Dou, J., Yunus, A. P., Tien Bui, D., Sahana, M., Chen, C. W., Zhu, Z., et al. (2019). Evaluating GIS-based multiple statistical models and data mining for earthquake and rainfall-induced landslide susceptibility using the LiDAR DEM. *Remote Sens.* 11 (6), 638. doi:10.3390/rs11060638

Fan, W., Wei, X., Cao, Y., and Zheng, B. (2017). Landslide susceptibility assessment using the certainty factor and analytic hierarchy process. *J. Mt. Sci-engl* 14 (5), 906–925. doi:10.1007/s11629-016-4068-2

Giovanni, L., Rocco, P., and Francis, C. (2016). Landslide susceptibilitym apping using a fuzzy approach. *Procedia Eng.* 161, 380–387. doi:10.1016/j.proeng.2016.08.578

Hong, H., Pradhan, B., Jebur, M. N., Bui, D. T., Xu, C., and Akgun, A. (2016). Spatial prediction of landslide hazard at the luxi area (China) using support vector machines. *Environ. Earth. Sci.* 75, 40. doi:10.1007/s12665-015-4866-9

Hong, H., Shahabi, H., Shirzadi, A., Chen, W., Chapi, K., Ahmad, B. B., et al. (2019). Landslide susceptibility assessment at the wuning area, China: A comparison between multi-criteria decision making, bivariate statistical and machine learning methods. *Nat. Hazards.* 96 (1), 173–212. doi:10.1007/s11069-018-3536-0

Le, L., Lin, Q., and Wang, Y. (2017). Landslide susceptibility mapping on a global scale using the method of logistic regression. *Nat. Hazards Earth Syst. Sci.* 17 (8), 1411–1424. doi:10.5194/nhess-17-1411-2017

Li, Y. Y., Mei, H. B., and Ren, X. J. (2018). Geological disaster susceptibility evaluation based on certainty factor and support vector machine. *J. Geo. Hnformation. Sci.* 20 (12), 1699–1709.

Lin, W. T., Chou, W. C., and Lin, C. Y. (2008). Earthquake-induced landslide hazard and vegetation recovery assessment using remotely sensed data and a neural network based classifier: A case study in central taiwan. *Nat. Hazards.* 47 (3), 331–347. doi:10.1007/s11069-008-9222-x

Liu, L. N., Xu, C., and Chen, J. (2014). Sensitivity analysis of landslide factors in 2013 Lushan earthquake based on CF method supported by GIS. *Chin.J. Eng. Geol.* 22 (6), 1176–1186.

Luo, L. G., Pei, X. J., and Huang, R. Q. (2021). Evaluation of landslide susceptibility in Jiuzhaigou Scenic Area based on CF and Logistic regression model with GIS support. *J. Eng. Geol.* 29 (02), 526–535. doi:10.13544/j.cnki.jeg.2019-202

Menard, S. (1995). *Applied logistic regression analysis*. Berlin: Sage University Paper Series on Quantitative.

Nhu, V. H., Shirzadi, A., Shahabi, H., Singh, S. K., Al Ansari, N., Clague, J. J., et al. (2020). Shallow landslide susceptibility mapping: A comparison between logistic model tree, logistic regression, naïve bayes tree, artificial neural network, and support vector machine algorithms. *Int. J. Environ. Res. Public Health.* 17 (8), 2749. doi:10.3390/ijerph17082749

Peng, L., Du, W. X., and Tian, H. (2021). *Sci. Technol. Eng.* 21 (18), 7806–7813.

Pourghasemi, H. R., Moradi, H. R., Fatemi Aghda, S. M., Gokceoglu, C., and Pradhan, B. (2014). GIS-based landslide susceptibility mapping with probabilistic likelihood ratio and spatial multi-criteria evaluation models (North of Tehran, Iran). *Arab. J. Geosci.* 7 (5), 1857–1878. doi:10.1007/s12517-012-0825-x

Pradhan, B., and Lee, S. (2010). Landslide susceptibility assessment and factor effect analysis: Backpropagation artificial neural networks and their comparison with frequency ratio and bivariate logistic regression modelling. *Envir. Model. Softw.* 25 (6), 747–759. doi:10.1016/j.envsoft.2009.10.016

Rozos, D., Bathrellos, G. D., and Skilodimou, H. D. (2011). Comparison of the implementation of rock engineering system and analytic hierarchy process methods, upon landslide susceptibility mapping, using GIS: A case study from the eastern achaia county of peloponnesus, Greece. *Environ. Earth. Sci.* 63 (1), 49–63. doi:10.1007/s12665-010-0687-z

Sahin, E. K., Colkesen, I., and Kavzoglu, T. (2018). A comparative assessment of canonical correlation forest, random forest, rotation forest and logistic regression methods for landslide susceptibility mapping. *Geocarto Int.* 1–23, 341–363. doi:10.1080/10106049.2018.1516248

Shariati, M., Mafipour, M. S., Mehrabi, P., Bahadori, A., Zandi, Y., Salih, M. N. A., et al. (2019). Application of a hybrid artificial neural network-particle swarm optimization (ANN-PSO) model in behavior prediction of channel shear connectors embedded in normal and high-strength concrete. *Appl. Sci.* 9 (24), 5534. doi:10.3390/app9245534

Shirzadi, A., Bui, D. T., Pham, B. T., Solaimani, K., Chapi, K., Kavian, A., et al. (2017). ShallowLandslide susceptibility assessment using a NovelHybrid intelligence approach. *Environ.E. Sci.* 76, 60. doi:10.1007/s12665-016-6374-y

Shortliffe, E. H., and Buchanan, G. G. (1975). A model of inexact reasoning in medicine. *Math. Biosci.* 23 (3-4), 351–379. doi:10.1016/0025-5564(75)90047-4

Vapnik, V. N. (1998). *Statistical learning theory*. Hoboken, New Jersey, United States: Wiley-Interscience.

Wang, L. J., Guo, M., Sawada, K., Lin, J., and Zhang, J. (2016). A comparative study of landslide susceptibility maps using logistic regression, frequency ratio, decision tree, weights of evidence and artificial neural network. *Geosci. J.* 20 (1), 117–136. doi:10.1007/s12303-015-0026-1

Wang, T., Wu, S., Shi, J., Xin, P., and Wu, L. (2018). Assessment of the effects of historical strong earthquakes on large-scale landslide groupings in the Wei river midstream. *Eng. Geol.* 235, 11–19. doi:10.1016/j.enggeo.2018.01.020

Wang, Y., Fang, Z. C., and Hong, H. Y. (2019). Comparison of convolutional neural networks for landslide sus-ceptibility mapping in yanshan county, China. *Sci. Total. Environ.* 666, 975–993. doi:10.1016/j.scitotenv.2019.02.263

Wang, Y. T., Seijmonsbergen, A. C., Bouten, W., and Chen, Q. (2015). Using statistical learning algorithms in regional landslide susceptibility zonation with limited landslide field data. *J. Mt. Sci-engl* 12 (2), 268–288. doi:10.1007/s11629-014-3134-x

Xin, P., Wang, T., and Wu, S. R. (2015). Study on the formation mechanism of mudstone multistage rotaryLandslide in hanjiashan, datong county, xining, Qinghai province. *J. E. Sci.* 36 (06), 771–780.

Xu, Y. Z., Lu, Y. N., and Li, D. Y. (2016). Evaluation of landslide susceptibility of granite distribution area in guangxi based on GIS and information quantity model. *Chin.J. Eng. Geol.* 24 (4), 693–703.

Yao, S. H., Li, Z. M., and Zhang, J. Q. (2014). Study on the relationship between the beishan landslide in xining and the fault on the north bank of huangshui river. *Sci. Technol. Eng.* 14 (04), 161–163+169.

Yao, X., Tham, L. G., and Dai, F. C. (2008). Landslide susceptibility mapping based on support vector machine: A case study on natural slopes of Hong Kong, China. *Geomorphology* 101, 572–582. doi:10.1016/j.geomorph.2008.02.011

Zheng, Y. (2019). *Geological hazard prediction and evaluation based on multi-source data and deep learning*. China: Hefei University of Technology.

Check for updates

# *In situ* stress distribution law of fault zone in tunnel site area based on the inversion method with optimized fitting conditions

Tiansheng Li[1,2], Ziquan Chen[1], Zihan Zhou[1]* and Yeming Bao[2]

[1]Key Laboratory of Transportation Tunnel Engineering, Ministry of Education, Southwest Jiaotong University, Chengdu, Sichuan, China, [2]China Railway 12th Bureau Group Co., Ltd., Taiyuan, Shanxi, China

Tunnel construction in high geo-stress strata faces the risk of extreme natural disasters such as large squeezing deformation and rockburst. Therefore, it is of great significance to adopt a high-precision inversion method to investigate the distribution law of *in situ* stress in the tunnel site area. In this paper, the *in situ* stress inversion research was carried out based on a plateau tunnel with a buried depth of more than 1000 m. The idea of improving the inversion accuracy by unifying displacement constraints was proposed by aiming at the defects of the traditional method on the boundary conditions. Furthermore, the impact of the constant term in the regression model on the fitting accuracy was discussed. According to the inversion method with optimized fitting conditions, the *in situ* stress distribution characteristics in the tunnel site area were obtained, and the variation law of the *in situ* stress near the fault zone was discussed. The results showed that after unifying displacement constraints, the comprehensive inversion accuracy comprehensive indicator reflecting the inversion accuracy decreased from 15.291 to 12.895, indicating that the inversion error was effectively controlled. Whether the constant term should be retained had a random effect on the inversion accuracy, so it was recommended that this issue be independently verified when fitting the data. When approaching the inner side of the fault from the outer side, the *in situ* stress first increased slightly and then decreased significantly. Moreover, the wider the fault impact zone and the farther the fault distribution distance, the more significant the amplitude of stress change, e.g., the maximum amplitude of stress change reached 9.0 MPa. In addition, the *in situ* stress orientation near the fault can be significantly deflected. And the wider the fault impact zone, the more pronounced the deflection.

KEYWORDS

tunnel engineering, deep-buried tunnel, *in situ* stress, fault zone, inversion method

# 1 Introduction

Affected by the intense tectonic movements of the Indian Ocean and the Eurasian plates, the Qinghai-Tibet Plateau has natured many faults and high tectonic *in situ* stress (Zhang D. L. et al., 2022; Wang et al., 2022). Tunnel project constructed in this stratum faces the significant risk of geological disasters, such as squeezing large deformation disasters in soft rock (Hu et al., 2022; Liu et al., 2022) and rockburst disasters in hard rock (Fan et al., 2021; Zhang H. et al., 2022). Therefore, it is significant to investigate the *in situ* stress distribution law in deep-buried tunnels crossing fault zone strata to guide the structural design and prevent and control geological disasters.

Since there are no conditions for measuring inside the tunnel in the geological exploration stage, the hydraulic fracturing method is the only means to measure the *in situ* stress in this stage (Zhang et al., 2014). The multiple linear regression method developed based on the elastic stress assumption of the hydraulic fracturing method is one of the commonly used methods for *in situ* stress inversion (Zhang et al., 2012). Figueiredo et al. (2014) used the multiple linear regression method to reveal that the *in situ* stress of the granite formation of a hydropower station in northern Portugal was controlled by self-weight stress and shear stress. Li et al. (2015) proposed the local least squares regression measure to improve the inversion accuracy based on the multiple linear regression method and applied it to a dam project. Meng et al. (2020) adopted the multiple linear regression method to put forward the idea of *in situ* stress inversion for high geo-temperature tunnels considering the temperature stress component. Based on the multiple linear regression method, Xu et al. (2021) proposed an *in situ* stress inversion system that comprehensively considered information such as geological tectonic background and topography. Meng et al. (2021) discussed the effect of using ridge regression to improve the inversion accuracy of the multiple linear regression method. However, the displacement constraints of each calculation condition in these applications are not strictly consistent, likely leading to significant inversion errors.

Some scholars have revealed the *in situ* stress distribution law in tectonic strata based on the inversion results. Han et al. (2016) found no direct linear relationship between the horizontal tectonic stress and the burial depth in the syncline, and the stress orientation was deflected inside and outside the syncline. Li G. et al. (2020) studied the distribution law of *in situ* stress in gully strata relying on a hydropower station in the mountainous area of southwest China, and the conclusion showed that buried depth had a positive effect on the *in situ* stress level. Based on the *in situ* stress inversion results of tunnel engineering of the Sichuan-Tibet Railway, Li X. P. et al. (2020) concluded that the *in situ* stress dropped suddenly inside the fault. Ning et al. (2021) studied the *in situ* stress distribution characteristics in the valley area considering geological tectonic movement and river erosion and believed that the stress relaxation effect occurred in the unloading and rebound area of the slope. Zhou et al. (2022) studied the *in situ* stress distribution law of the intrusive rock strata through the segmented inversion method and believed that there was a sudden stress change phenomenon at the intrusive rock interface. However, although these studies have investigated the *in situ* stress distribution of some structural strata, few studies have systematically analyzed the *in situ* stress distribution characteristics of dense fault zones.

Relying on a deep-buried Plateau tunnel in Southwest China, this paper first analyzed the optimization effect of unified displacement constraints on inversion accuracy. Then, the random effect of the constant term in the regression model on the inversion error was discussed. The *in situ* stress distribution law when the tunnel crosses the fault zone was revealed based on the multiple linear regression method with optimized fitting conditions. Furthermore, the change law of the value and orientation of the *in situ* stress near the fault was emphatically discussed.

# 2 Engineering background and measured *in situ* stress

## 2.1 Engineering background

The plateau tunnel is located on the eastern edge of the Qinghai-Tibet Plateau, passing through Zheduo Mountain, the first high mountain in Sichuan Province to enter Tibet. Its south is the Indian Ocean plate, and its north is the Eurasian plate. The plate compression has created an active neotectonic movement in this area (Figure 1). Affected by the intense geological tectonic action, the tunnel site area is densely covered with mountains and ravines. Figure 1B shows the typical plateau landform characteristics of the tunnel site area, and its surface elevation is about 3460–4730 m. In addition, the strong stratigraphic cutting action formed the famous Y-shaped active fault zone in southwest China near the tunnel site. The tunnel is located on the Xianshuihe active fault zone on the northwest side of this area (Figure 1D).

The tunnel entrance is in Zheduotang Village, and its exit is in Shuiqiao Village. Its total length and maximum buried depth are about 20.8 km and 1215 m, respectively (Figure 2). The strata traversed by the tunnel include quartz sandstone, biotite adamellite, and slate. Affected by the Xianshuihe active fault zone, 12 faults are distributed in the tunnel site area. Among them, the Zheduotang fault covers the range of 3–4 km in the entrance, which is only represented by the actual strata. Among them, the faults with a wider impact range include the Zheduotang branch fault with a width of 302 m, the Jinlongsi-mozigou fault with a width of 198 m, the F15 fault with a width of 296 m, and the Yulongxi fault with a width of 614 m. Besides, the rest of the faults are roughly 100 m wide.
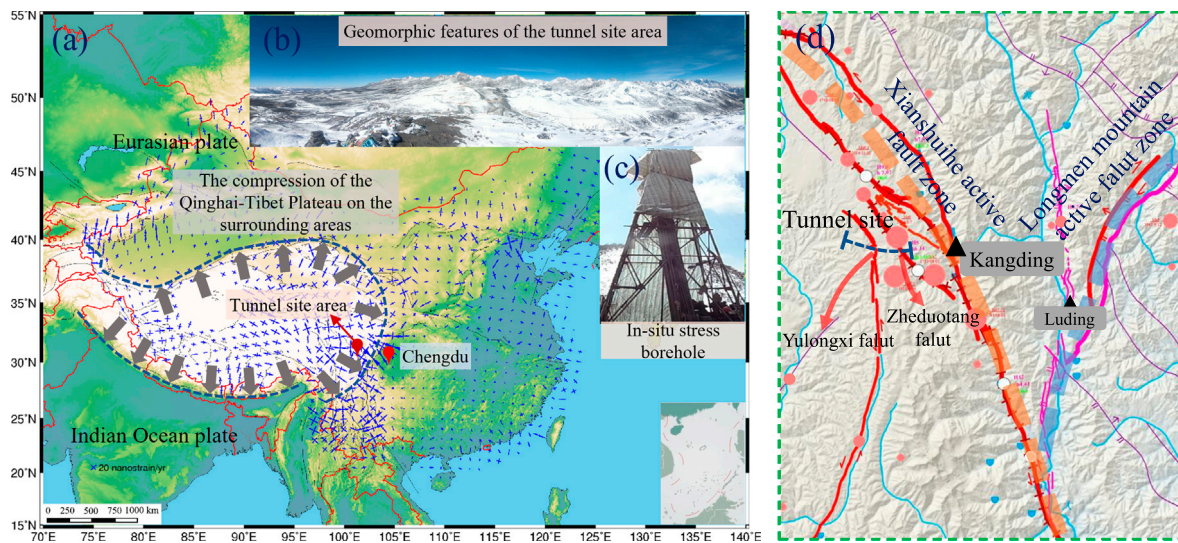
**FIGURE 1**
Geological background of the tunnel: **(A)** stress field of China; **(B)** plateau landform characteristics; **(C)** *in situ* stress measurement; **(D)** main fault zone around tunnel site.
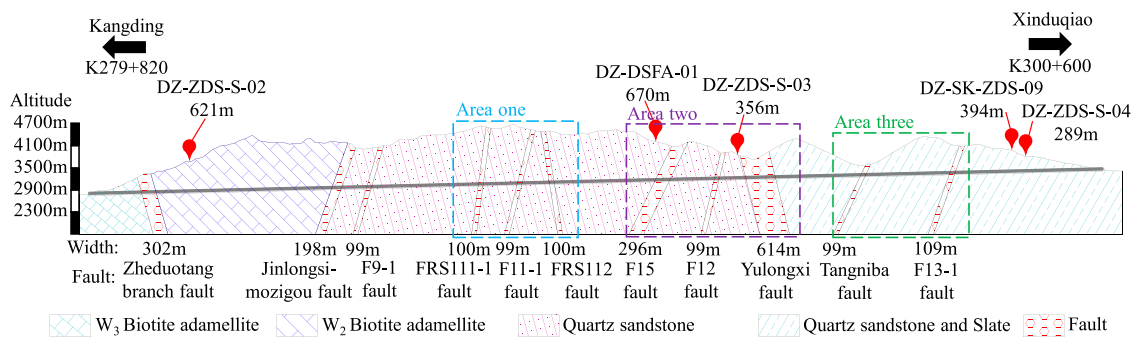


**FIGURE 2**
Longitudinal profile of the tunnel.

## 2.2 Measured *in situ* stress

The large buried depth and complex tectonic geological environment are typic features of the tunnel. Generally, in addition to the self-weight stress, there is a nonnegligible horizontal tectonic stress in the strata with active geological movement (Yuan et al., 2022). Furthermore, in this geological environment, the horizontal tectonic stress is even greater than the vertical self-weight stress (Zhao et al., 2021). In order to investigate the *in situ* stress distribution characteristics in the tunnel site area, field measurement was carried out by the hydraulic fracturing method during the geological exploration stage. There are five *in situ* stress boreholes in total. Among them, the maximum depth of DZ-ZDS-S-02, DZ-DSFA-01, DZ-ZDS-

S-03, DZ-SK-ZDS-09, and DZ-ZDS-S-04 boreholes is 621 m, 670 m, 356 m, 394 m, and 289 m, respectively (Figure 2). Except for the DZ-DSFA-01 borehole, which has five measuring points, the other boreholes have four.

Figure 3 shows the measured *in situ* stress at different measuring points of each borehole. It can be seen that for a single borehole, the *in situ* stress of each measuring point increases almost linearly with the increase of the buried depth. Especially the vertical stress ($\sigma_V$), the measured *in situ* stress of all boreholes maintains the same linear growth relationship. On the other hand, the maximum horizontal principal stress ($\sigma_H$) and the minimum horizontal principal stress ($\sigma_h$) between different boreholes show an apparent nonlinear relationship. Among them, the DZ-ZDS-S-02, DZ-SK-ZDS-09, and DZ-ZDS-S-
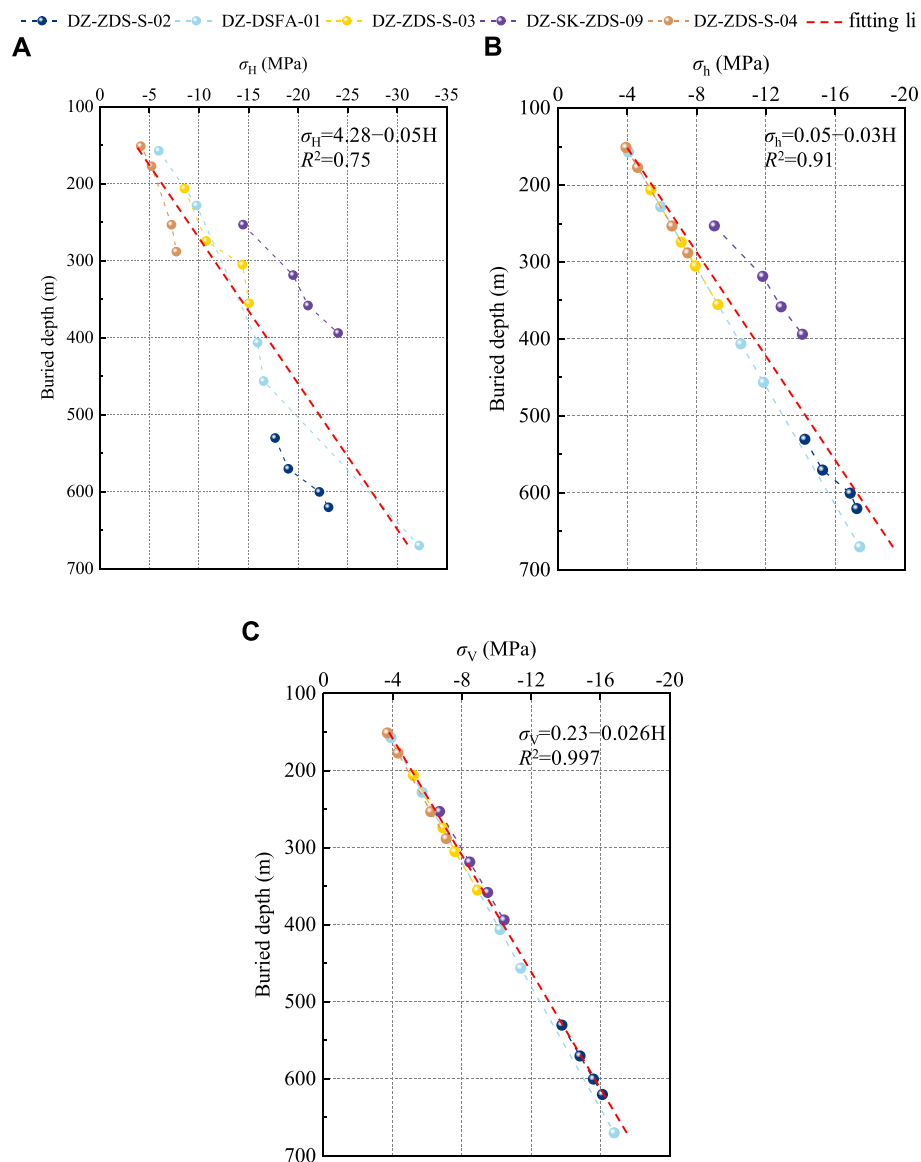
**FIGURE 3**
Measured *in situ* stress: **(A)** maximum horizontal principal stress; **(B)** minimum horizontal principal stress; **(C)** vertical stress.

04 boreholes are particularly significant. Comparing Figure 2, it can be seen that these three boreholes are located on both sides of the tunnel site area and are far away from the two middle boreholes. Therefore, there are certain differences in the distribution characteristics of *in situ* stress in different local areas.

To further demonstrate the linear relationship between each stress component and the buried depth, Figure 3 also shows the linear fitting results of the measured data. Among them, the linear relationship between $\sigma_V$ and burial depth (H) is the most significant, and its goodness of fit $R^2$ reaches 0.997. Secondly, $\sigma_h$ also has a good linear correlation with buried depth, and the corresponding goodness of fit $R^2$ is 0.91. In addition, the linear

correlation between $\sigma_H$ and burial depth is the weakest, and the corresponding goodness of fit $R^2$ is only 0.75.

The buried depth range of the DZ-ZDS-S-02, DZ-DSFA-01, DZ-ZDS-S-03, DZ-SK-ZDS-09, and DZ-ZDS-S-04 boreholes is 530–620 m, 157–670 m, 206–355 m, 253–394 m, and 151–288 m, respectively. The corresponding $\sigma_H$ range of each borehole is $-17.73 \sim -23.08$ MPa, $-6.02 \sim -32.20$ MPa, $-8.47 \sim -15.11$ MPa, $-14.53 \sim -24.06$ MPa, and $-4.09 \sim -7.72$ MPa, respectively, the $\sigma_h$ range of each borehole is $-14.30 \sim -17.32$ MPa, $-4.11 \sim -17.43$ MPa, $-5.38 \sim -9.17$ MPa, $-9.01 \sim -14.06$ MPa, and $-3.92 \sim -7.46$ MPa, respectively, and the $\sigma_V$ range of each borehole is $-13.83 \sim -16.12$ MPa, $-3.90$

**FIGURE 4**
Three-dimensional numerical model of the tunnel site area.
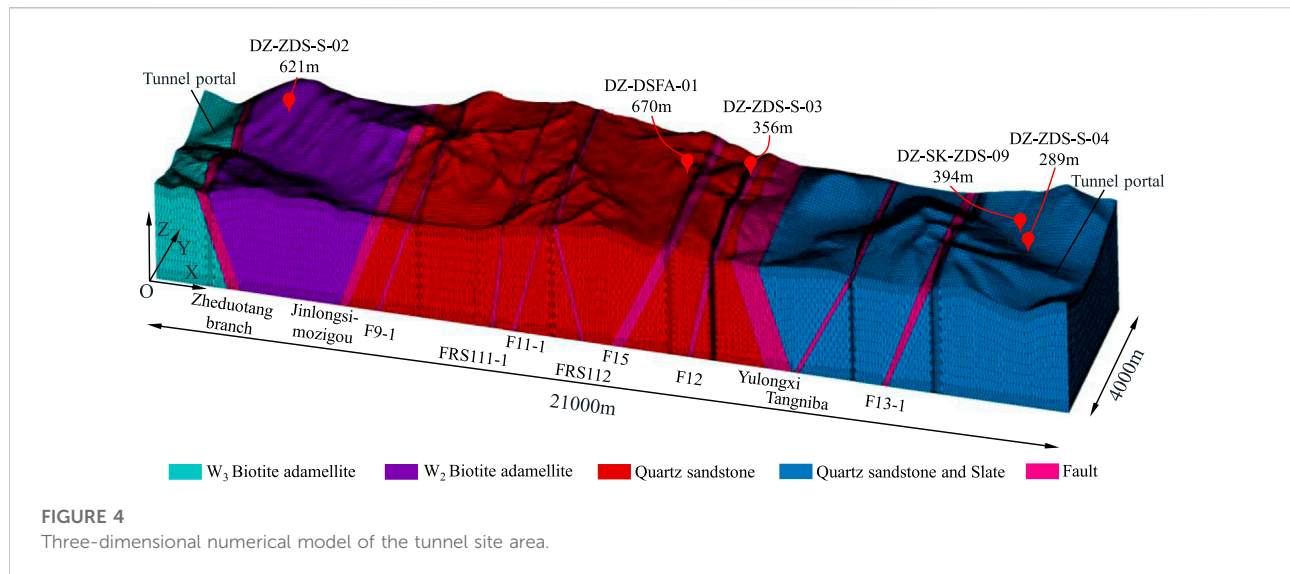
TABLE 1 Physical and mechanical parameters of the rock masses.

| Rock | Elastic modulus (GPa) | Poisson's ratio | Density (kg/m³) | Cohesion strength (MPa) | Internal friction angle (°) |
|---|---|---|---|---|---|
| W₃ Biotite adamellite | 13.00 | 0.27 | 2300.00 | 1.10 | 45.00 |
| W₂ Biotite adamellite | 33.00 | 0.20 | 2500.00 | 2.00 | 60.00 |
| Quartz sandstone | 26.00 | 0.23 | 2500.00 | 1.80 | 55.00 |
| Quartz sandstone and Slate | 22.00 | 0.24 | 2450.00 | 1.60 | 53.00 |
| Fault | 1.50 | 0.43 | 2100.00 | 0.30 | 35.00 |

$\sim -16.84$ MPa, $-5.18 \sim -8.91$ MPa, $-6.74 \sim -10.37$ MPa, and $-3.66 \sim -7.08$ MPa, respectively.

The *in situ* stress gradient in the tunnel site can be obtained by dividing the stress increment by the buried depth increment. The calculation indicates that the average increment gradients per 100 m buried depth of $\sigma_H$, $\sigma_h$, and $\sigma_V$ are 4.32 MPa, 2.81 MPa, and 2.53 MPa, respectively. In other words, $\sigma_H$ is 1.54 times $\sigma_h$ and 1.71 times $\sigma_V$. Hence, the *in situ* stress field of the tunnel presents $\sigma_H > \sigma_h > \sigma_V$. This indicates that the horizontal tectonic movement of the strata in this area is strong, and the *in situ* stress is dominated by the horizontal principal stress.

# 3 Inversion method with optimized fitting conditions

## 3.1 Inversion principle

Since there is no field condition for measuring *in situ* stress inside the tunnel, the measurement by the hydraulic fracturing method is the only means in the geological exploration stage (Zhang et al., 2014). The principle of the hydraulic fracturing method indicates that its stress components are derived based on elastic assumptions (Pei et al., 2016). That is to say, the measured *in situ* stresses obtained by the hydraulic fracturing method are all elastic stresses. Based on this, the multiple linear regression method using the least squares optimization criterion according to the principle of linear superposition is widely used in the field of *in situ* stress inversion. In short, the inversion principle of the multiple linear regression method is to approximate the observed value through the regression value to solve the regression coefficient. In other words, the residual sum of squares between the regression value and the observed value is minimized based on the least squares method. The regression model of the multiple linear regression method is as follows:

$$\hat{\sigma}_{jk} = a_0 + \sum_{i=1}^{n} a_i \sigma_{jk}^i \tag{1}$$

where $\hat{\sigma}_{jk}$ is the $j$-th regression stress component of the $k$-th observed point, $a_0$ is the constant term, $n$ is the total number of

**FIGURE 5**
Genetic mechanism of the fault: **(A)** original rock mass; **(B)** fault.
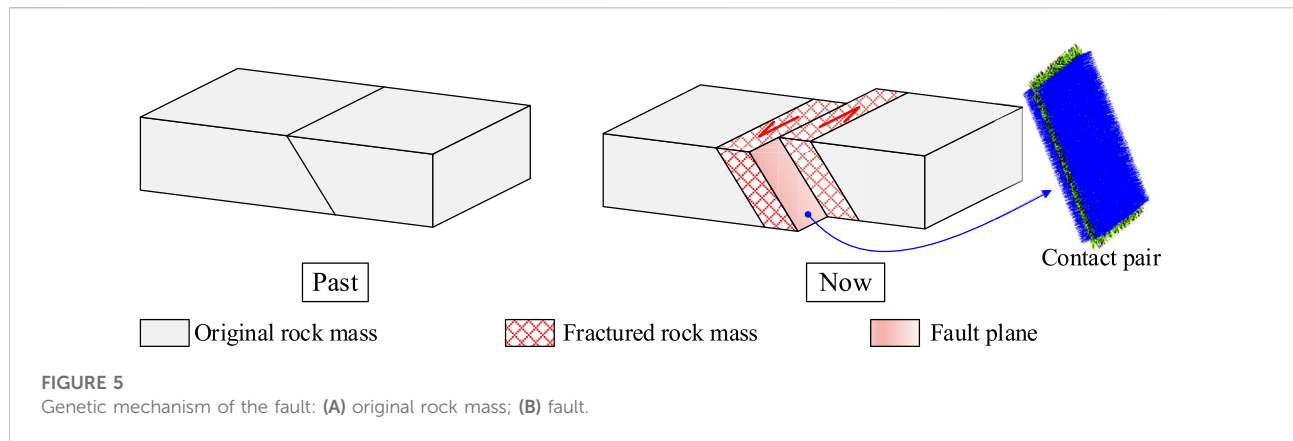
TABLE 2 Measured *in situ* stresses after coordinate transformation.

| Borehole | $\sigma_x$ (MPa) | $\sigma_y$ (MPa) | $\sigma_z$ (MPa) | $\tau_{xy}$ (MPa) | Orientation |
|---|---|---|---|---|---|
| DZ-ZDS-S-02 | −17.72 | −14.28 | −13.83 | −0.38 | N67°W |
| | −18.96 | −15.32 | −14.76 | −0.42 | |
| | −22.11 | −16.91 | −15.59 | −0.43 | |
| | −23.02 | −17.34 | −16.12 | −0.67 | |
| DZ-DSFA-01 | −5.87 | −4.06 | −3.87 | 0.28 | N51°W |
| | −9.74 | −5.96 | −5.73 | 0.39 | |
| | −15.88 | −10.59 | −10.16 | 0.33 | |
| | −−16.26 | −12.11 | −11.39 | 1.12 | |
| | −30.83 | −18.83 | −16.84 | 4.41 | |
| DZ-ZDS-S-03 | −8.41 | −5.50 | −5.22 | 0.58 | N50°W |
| | −10.62 | −7.23 | −6.93 | 0.63 | |
| | −14.14 | −8.26 | −7.61 | 1.38 | |
| | −14.85 | −9.39 | −8.90 | 0.92 | |
| DZ-SK-ZDS-09 | −12.79 | −10.65 | −6.67 | 2.53 | N28°W |
| | −17.50 | −13.81 | −8.48 | 3.38 | |
| | −20.13 | −13.83 | −9.52 | 2.59 | |
| | −18.31 | −19.88 | −10.39 | 4.91 | |
| DZ-ZDS-S-04 | −4.14 | −3.87 | −3.72 | 0.03 | N52°W |
| | −5.18 | −4.62 | −4.28 | 0.12 | |
| | −7.22 | −6.63 | −6.16 | 0.14 | |
| | −7.67 | −7.51 | −7.13 | 0.05 | |

boundary conditions, $a_i$ is the regression coefficient of the $i$-th boundary condition, and $\sigma_{jk}^i$ is the calculated stress.

The residual sum of squares, i.e., $Q = (e_{jk})^2$, between the regression and observed values is as follows:

$$Q = \left(e_{jk}\right)^2 = \sum_{k=1}^{m}\sum_{j=1}^{s}\left(\sigma_{jk}^m - a_0 - \sum_{i=1}^{n} a_i \sigma_{jk}^i\right)^2, \qquad (2)$$

where $m$ is the total number of observed points, $s$ is the total number of stress components, $\sigma_{jk}^m$ is the measured stress, which is also called observed stress.

Furthermore, the regression coefficient can be obtained by taking the minimum value of the residual sum of squares based on the least squares method. The solution equation is as follows:
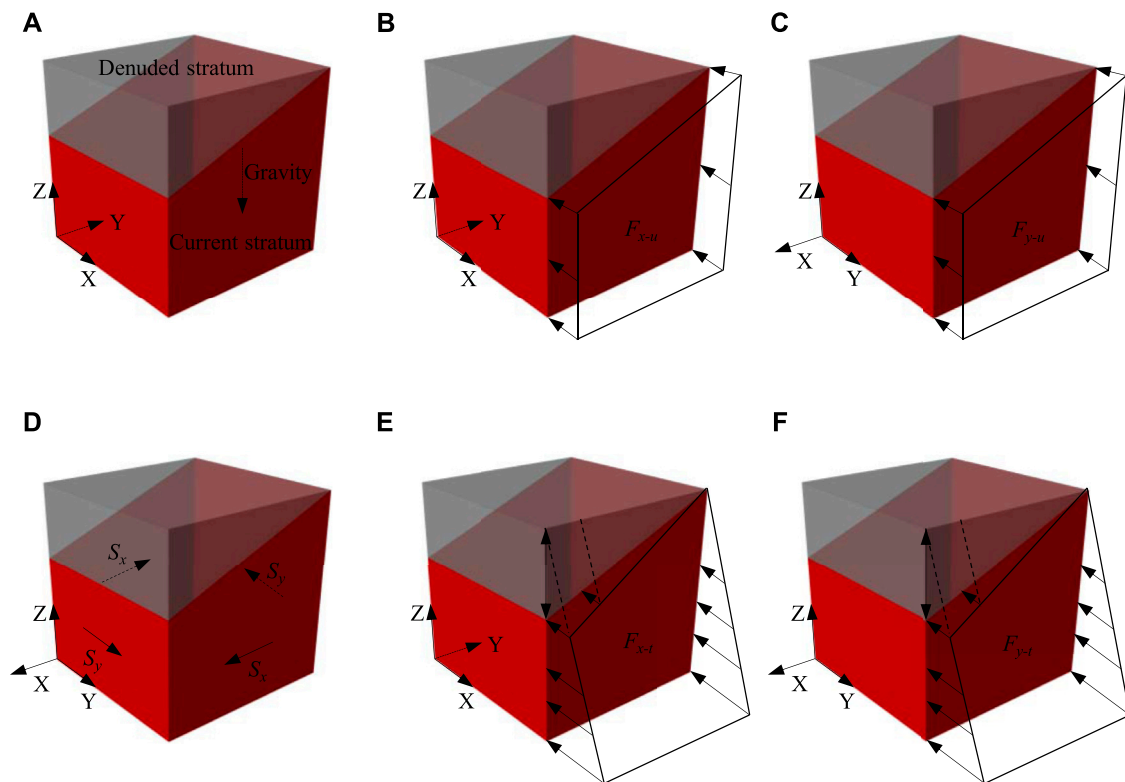
**FIGURE 6**
Boundary conditions of multiple linear regression method: **(A)** self-weight stress; **(B)** uniform load in X direction; **(C)** uniform load in Y direction; **(D)** shear load in XOY plane; **(E)** triangular gradient load in X direction; **(F)** triangular gradient load in Y direction.

$$
\begin{bmatrix}
ms & \sum_{k=1}^{m}\sum_{j=1}^{s}\sigma_{jk}^{1} & \sum_{k=1}^{m}\sum_{j=1}^{s}\sigma_{jk}^{2} & \cdots & \sum_{k=1}^{m}\sum_{j=1}^{s}\sigma_{jk}^{n} \\
\cdot & \sum_{k=1}^{m}\sum_{j=1}^{s}\left(\sigma_{jk}^{1}\right)^{2} & \sum_{k=1}^{m}\sum_{j=1}^{s}\sigma_{jk}^{1}\sigma_{jk}^{2} & \cdots & \sum_{k=1}^{m}\sum_{j=1}^{s}\sigma_{jk}^{1}\sigma_{jk}^{n} \\
\cdot & \cdot & \sum_{k=1}^{m}\sum_{j=1}^{s}\left(\sigma_{jk}^{2}\right)^{2} & \cdots & \sum_{k=1}^{m}\sum_{j=1}^{s}\sigma_{jk}^{2}\sigma_{jk}^{n} \\
\cdot & \cdot & \cdot & \cdot & \vdots \\
\cdot & \cdot & \cdot & \cdot & \sum_{k=1}^{m}\sum_{j=1}^{s}\left(\sigma_{jk}^{n}\right)^{2}
\end{bmatrix}
\times
\begin{bmatrix}
a_0 \\ a_1 \\ a_2 \\ \vdots \\ a_n
\end{bmatrix}
$$

$$
=
\begin{bmatrix}
\sum_{k=1}^{m}\sum_{j=1}^{s}\sigma_{jk} \\
\sum_{k=1}^{m}\sum_{j=1}^{s}\sigma_{jk}^{1}\sigma_{jk} \\
\sum_{k=1}^{m}\sum_{j=1}^{s}\sigma_{jk}^{2}\sigma_{jk} \\
\vdots \\
\sum_{k=1}^{m}\sum_{j=1}^{s}\sigma_{jk}^{n}\sigma_{jk}
\end{bmatrix}, \tag{3}
$$

where the left matrix is a symmetric matrix.

The regression model representing the *in situ* stress field in the tunnel site area can be obtained by putting $(a_0, a_i)$ solved in Eqn. 3 into Eqn. 1.

The multiple linear regression method has the characteristics of high computational efficiency and unique output solution, so it is widely used in engineering. However, two issues are not clearly agreed upon in the practical application of this method. One is that the boundary conditions of the calculation conditions have not been unified, and the other is that multiple linear regression can be performed even if the constant term $a_0$ is deleted. Engineering practices show that these two issues are very likely to impact the inversion accuracy. Therefore, the multiple linear regression method urgently needs to be improved in these two aspects.

## 3.2 Three-dimensional numerical model

Import the geological plan of the tunnel site area into Surfer software to obtain the three-dimensional coordinate information of the surface. Input this information into ANSYS finite element
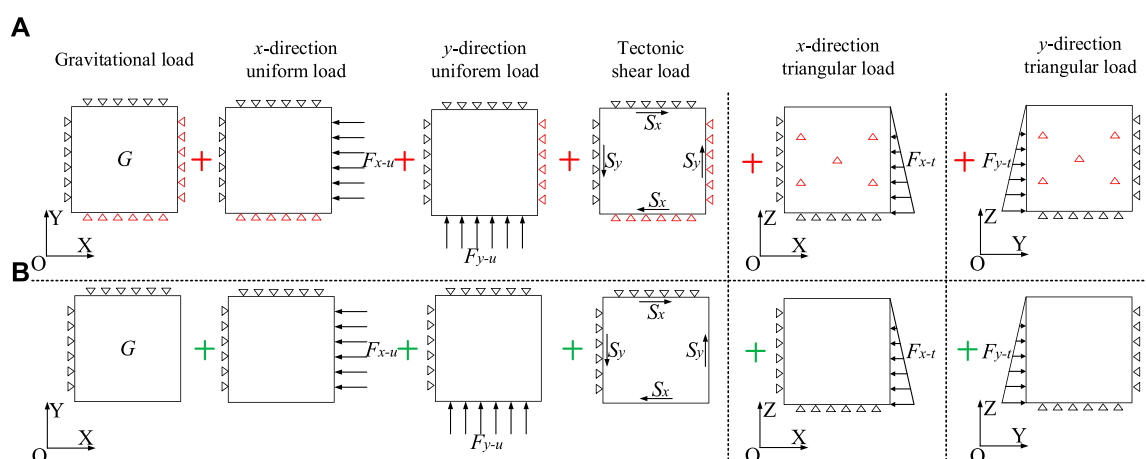
**FIGURE 7**
Linear superposition principle in multiple linear regression method: **(A)** not unified displacement constraints; **(B)** unified displacement constraints.

software to establish the top surface of the model. The $Z$ direction of the model includes the range of 3000 m below the tunnel portal, the Y direction is 4000 m, and the X direction is 21,000 m. As shown in Figure 4, the tunnel axis is basically located in the central area of the three-dimensional numerical model. In order to avoid the deformed grid caused by the irregular surface, the grid refinement process is carried out in some local areas. In the end, the total number of meshes exceeds six million. The physical and mechanical parameters of rock mass were derived from geological exploration data, as shown in Table 1. Literature researches shows that the value range of rock mass parameters around tunnel areas in previous studies is basically consistent with that in Table 1 (Meng et al., 2021; Zhou et al., 2022). In addition, these rock mass parameters are generally consistent with the recommended values in the Code for Design of Railway Tunnel (National Railway Administration of PRC 2017).

For the fault simulation method in the numerical model, the Boolean operation was firstly used to cut the model to form the impact area of the fault fracture zone. Then, the following assumptions were made on the mechanical parameters and contact relationship of the fault based on its genesis. Taking strike-slip faults as an example, Figure 5 shows the genetic mechanism of the fault. When the stress difference exceeds the strength level, the original rock mass begins to fracture. A fault plane, i.e., the fault plane where the two fault walls slide relative to each other, is gradually formed with the development of micro-fractures. Once the fault plane is formed and the stress difference exceeds the frictional resistance, the two fault walls begin to slide relative to each other, forming a fault. With the sliding of the fault, the surrounding rock mass is fractured under the action of friction and shear (Li, 2022). Based on the above

mechanism, it was first assumed that the closer to the fault plane, the more fragmented the rock mass. Then the physical and mechanical parameters of the rock mass inside the fault satisfy Eqn. 4.

$$p_L = p_{fp} + \alpha L, \tag{4}$$

where $p_L$ is the physical and mechanical parameter of the rock mass $L$ m away from the fault plane, $p_{fp}$ is the physical and mechanical parameter at the fault plane, $\alpha = p_o - p_{fp}/W$ is the gradient of the physical and mechanical parameters, $p_o$ is the physical and mechanical parameter of the original rock mass, and $W$ is the impact range of the fault.

Secondly, it was assumed that the fault plane was located in the middle of the fractured rock mass (Li et al., 2017), and its frictional constitutive relation adopted the Coulomb friction-slip criterion.

$$\frac{\sigma_1 - P_0}{\sigma_3 - P_0} = \left( \sqrt{1 + \mu^2} + \mu \right)^2, \tag{5}$$

where $\sigma_1$ and $\sigma_3$ are the first principal stress and the third principal stress, respectively, $\mu$ is the friction coefficient of the fault plane, $P_0$ is the pore pressure.

The contact pair in ANSYS software was used to simulate the above fault frictional relationship, shown in Figure 5B.

## 3.3 Accuracy improvement effect for unifying boundary condition

Due to the coordinate system of the measured stress being different from that of the three-dimensional numerical model, the coordinate system of the measured stress needs to be
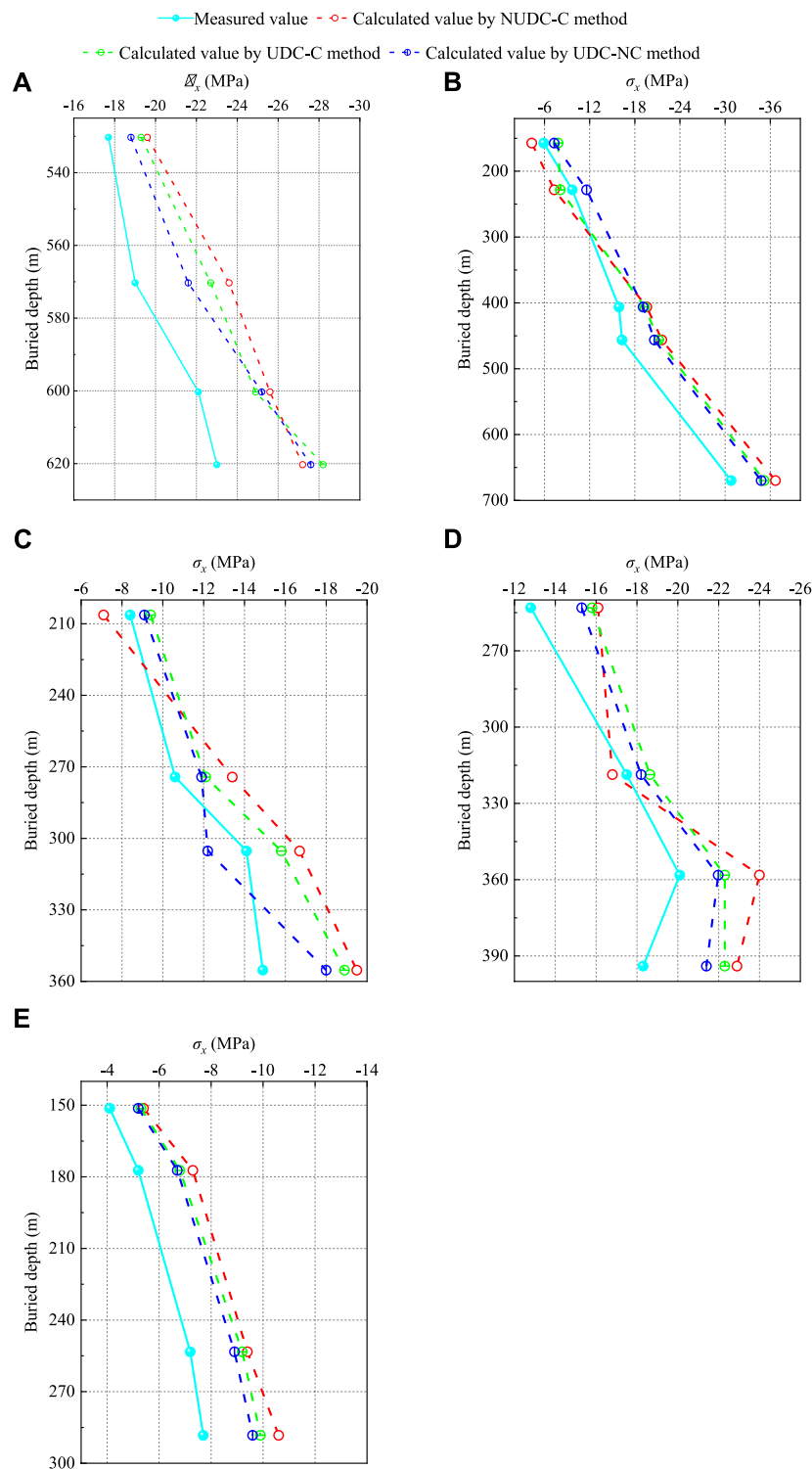
**FIGURE 8**
Comparison of the measured values and the inversion values: **(A)** DZ-ZDS-S-02 borehole; **(B)** DZ-DSFA-01 borehole; **(C)** DZ-ZDS-S-03 borehole; **(D)** DZ-SK-ZDS-09 borehole; **(E)** DZ-ZDS-S-04 borehole.

TABLE 3 Statistical indicators of $\sigma_x$ for different inversion methods.

| Indicator | NUDC-C method | UDC-C method | UDC-NC method |
|---|---|---|---|
| $\delta_r$ | 23.9% | 20.1% | 17.4% |
| VAF | 95.6% | 96.3% | 97.2% |
| RMSE | 3.4 | 2.9 | 2.5 |
| CIA | 3.683 | 3.138 | 2.702 |

TABLE 4 Overall statistical indicators of the stress value for different inversion methods.

| Indicator | NUDC-C method | UDC-C method | UDC-NC method |
|---|---|---|---|
| $\delta_r$ | 21.3% | 18.0% | 16.4% |
| VAF | 94.5% | 95.5% | 96.3% |
| RMSE | 2.6 | 2.3 | 2.1 |
| CIA | 2.868 | 2.525 | 2.301 |

TABLE 5 Overall statistical indicators of the stress orientation for different inversion methods.

| Indicator | NUDC-C method | UDC-C method | UDC-NC method |
|---|---|---|---|
| $\delta_r$ | 25.2% | 18.1% | 15.9% |
| VAF | 92.9% | 91.1% | 99.1% |
| RMSE | 12.1 | 10.1 | 7.3 |
| CIA | 12.423 | 10.370 | 7.468 |

transformed before inversion. The coordinate transformation formula in elastic mechanics is as follows:

$$\sigma_{1'q'} = \alpha_{1'p}\alpha_{q'q}\sigma_{pq} \tag{6}$$

$$\sigma_{2'q'} = \alpha_{2'p}\alpha_{q'q}\sigma_{pq} \tag{7}$$

$$\sigma_{3'q'} = \alpha_{3'p}\alpha_{q'q}\sigma_{pq} \tag{8}$$

where $1'$, $2'$, and $3'$ are, $x'$, $y'$, and $z'$, respectively, and $p, q = x, y, z$.

The measured stress after coordinate transformation is shown in Table 2.

Apply boundary conditions simulating self-weight and different tectonic actions to the numerical model to obtain the calculated stress, and then use the inversion principle to obtain the regression model of the *in situ* stress field in the tunnel site area. Common boundary conditions include self-weight stress (Figure 6A), 1 MPa uniform load in the X direction (Figure 6B), 1 MPa uniform load in the Y direction (Figure 6C), unit shear load in the XOY plane (Figure 6D), triangular gradient load in the X direction (Figure 6E), and triangular gradient load in the Y direction (Figure 6F). Among them, the XOY plane adopts the method of forced displacement to simulate the shear effect of

plane structure (Meng et al., 2021), and the triangular load is applied with a gradient of 1 kPa/m.

The principle of linear superposition has strict preconditions, one of which is that the material must satisfy Hooke's law, i.e., the mechanical constitutive model of the material is linear elastic. The second is that the boundary conditions of each load condition need to be consistent. In this way, the stress superposition value of each load condition can be equal to the stress value after all loads are applied simultaneously. However, due to the failure to strictly adhere to the boundary requirements of the linear superposition principle, the error of the multiple linear regression method will increase in practical applications. Specifically, the boundary conditions in Figure 6 were transformed into those in Figure 7A (Li et al., 2015). It can be seen from Figure 7A that the displacement constraints under each calculation condition are different. Nevertheless, the essential requirement of the linear superposition principle is that the displacement constraints of each calculation condition need to be consistent. The main reason for this phenomenon is that some scholars assume that the opposite boundary is fixedly
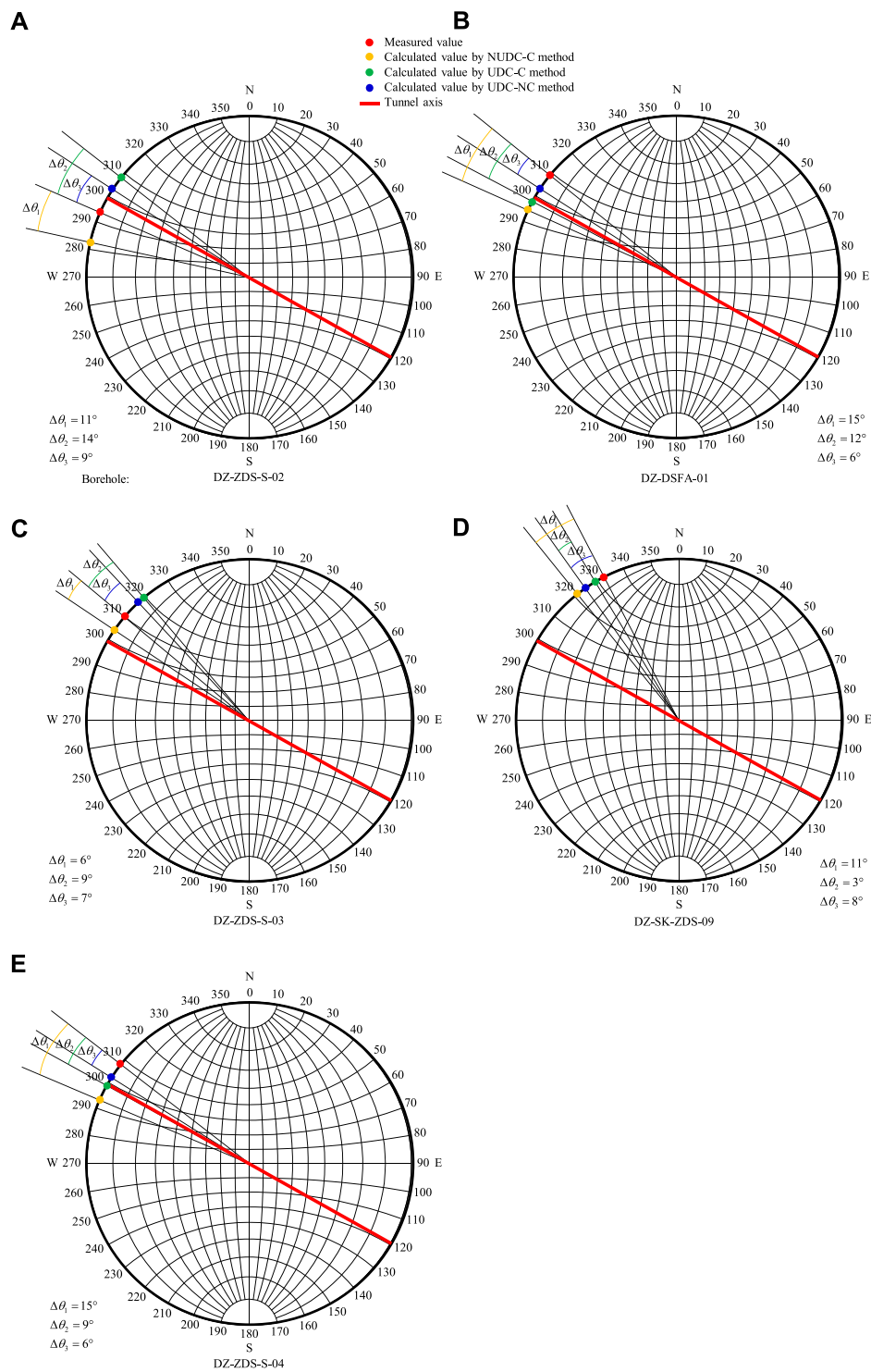
**FIGURE 9**
Comparison of the measured orientations and the inversion orientations: **(A)** DZ-ZDS-S-02 borehole; **(B)** DZ-DSFA-01 borehole; **(C)** DZ-ZDS-S-03 borehole; **(D)** DZ-SK-ZDS-09 borehole; **(E)** DZ-ZDS-S-04 borehole.

| Indicator | NUDC-C method | UDC-C method | UDC-NC method |
|-----------|---------------|--------------|---------------|
| CIA       | 15.291        | 12.895       | 9.769         |



FIGURE 10
Influence of the constant term on data fit: **(A)** not contain a constant term; **(B)** contain a constant term.
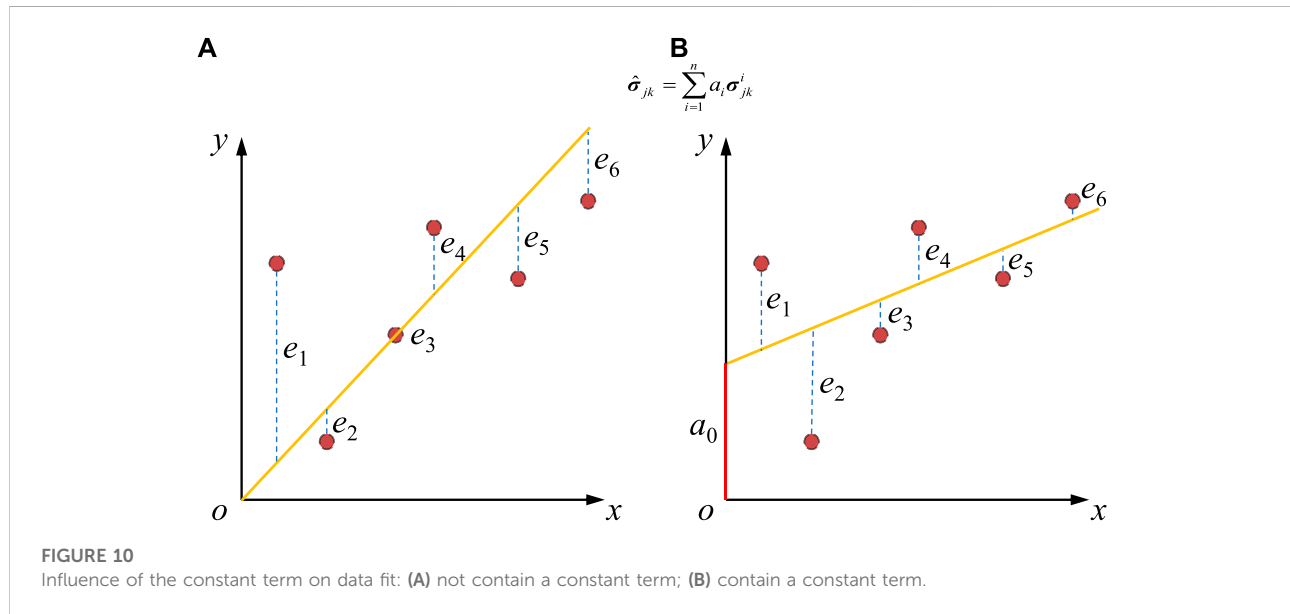
constrained when applying tectonic loads (Meng et al., 2020; Zhou et al., 2022). Then, the boundary conditions strictly following the linear superposition principle are shown in Figure 7B. It can be seen from Figure 7B that the displacement constraint conditions of all calculation conditions are consistent. The displacement constraint range of each working condition includes a boundary surface parallel to the X direction, a boundary surface parallel to the Y direction, and the bottom surface.

In order to verify the optimization effect of unified displacement constraints condition on the inversion accuracy, the regression models of two boundary types were solved according to the principle of multiple linear regression. Eqn .9 corresponds to the boundary condition in Figure 7A, i.e., not unified displacement constraints (NUDC-C method), and Eqn. 10 corresponds to the boundary condition in Figure 7B, i.e., unified displacement constraints (UDC-C method). Among them, the last C at the abbreviation represents whether the regression model has a constant term, which will be discussed in the next section.

$$\sigma_{jk}^{\mathrm{NUDC-C}} = 1.40 + 0.92\sigma_{jk}^{g} - 5.36\sigma_{jk}^{x-u} + 10.78\sigma_{jk}^{y-u} + 5.99\sigma_{jk}^{xoy}$$
$$+ 3.31\sigma_{jk}^{x-t} + 2.67\sigma_{jk}^{y-t}, \tag{9}$$

$$\sigma_{jk}^{\mathrm{UDC-C}} = 1.17 + 0.89\sigma_{jk}^{g} - 3.87\sigma_{jk}^{x-u} + 13.26\sigma_{jk}^{y-u} + 10.03\sigma_{jk}^{xoy}$$
$$+ 1.96\sigma_{jk}^{x-t} + 2.01\sigma_{jk}^{y-t}, \tag{10}$$

where $\sigma_{jk}^{\mathrm{NUDC-C}}$ and $\sigma_{jk}^{\mathrm{UDC-C}}$ are the regression stresses solved by the NUDC-C and UDC-C methods, respectively, $\sigma_{jk}^{g}$ is the calculated stress under self-weight, $\sigma_{jk}^{x-u}$ and $\sigma_{jk}^{y-u}$ are the calculated stresses under the uniform load in the $X$ and $Y$ directions, respectively, $\sigma_{jk}^{xoy}$ is the calculated stress under the shear load in the XOY plane, and $\sigma_{jk}^{x-t}$ and $\sigma_{jk}^{y-t}$ are the calculated stresses under the triangular load in the $X$ and $Y$ directions, respectively.

Due to space limitations, only $\sigma_x$ is selected to show the inversion effects of the two methods, as shown in Figure 8. In addition, their inversion accuracies of all stress components at all measuring points are listed in Table 4 and Table 5. On this basis, the regression orientation of $\sigma_{\mathrm{H}}$ at the observed point can be solved by Eqs. 11, 12; Figure 9 shows the inversion effects of the two methods on orientation.

$$\begin{cases} \sigma_{\mathrm{H}} \\ \sigma_{\mathrm{h}} \end{cases} = \frac{\sigma_x + \sigma_y}{2} \pm \sqrt{\left(\frac{\sigma_x + \sigma_y}{2}\right)^2 + \left(\tau_{xy}\right)^2}, \tag{11}$$

$$tan\,\theta = \frac{(\sigma_{\mathrm{H}} - \sigma_x)}{\tau_{xy}}, \tag{12}$$
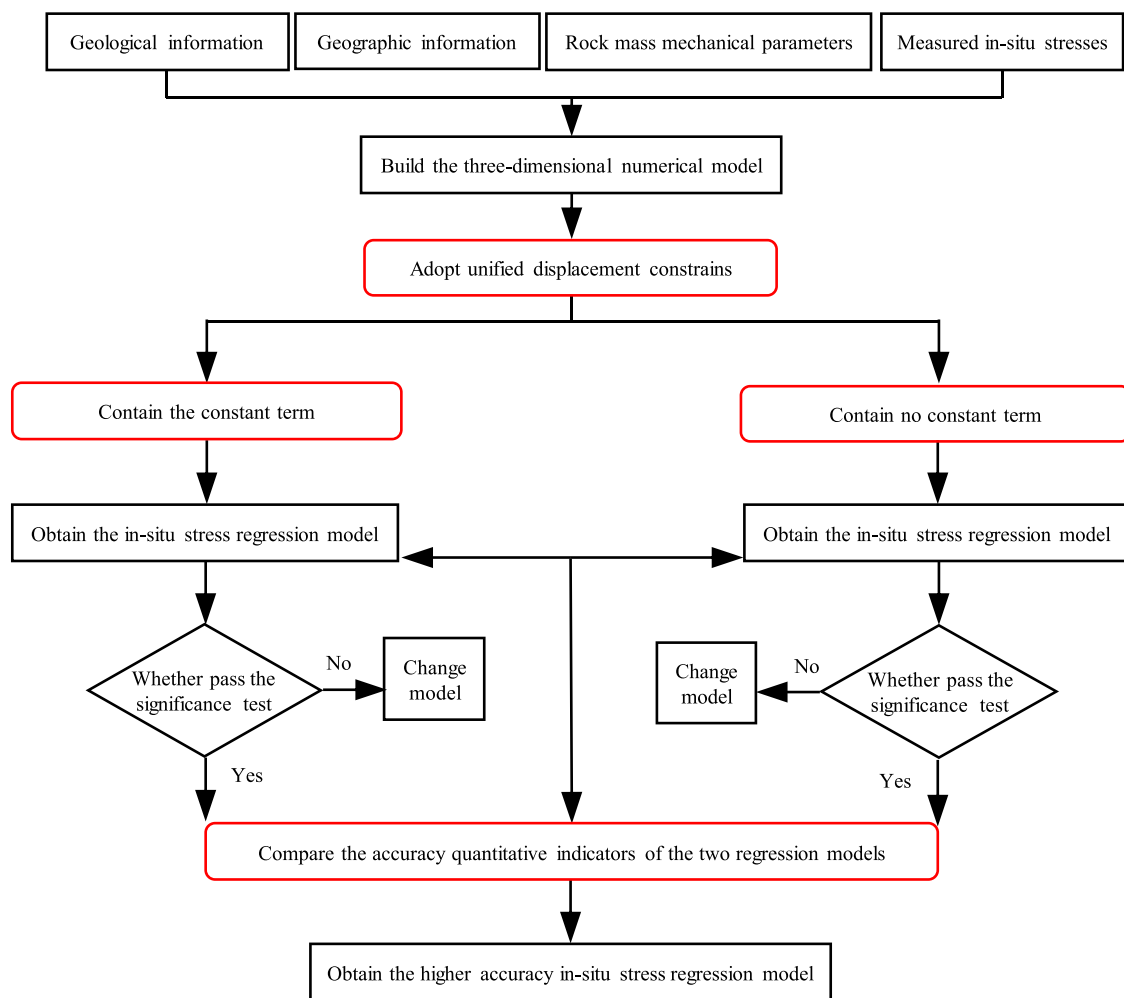
**FIGURE 11**
Optimized process of the *in situ* stress inversion.

where $\theta$ is the angle between $\sigma_H$ and X-axis.

It can be seen from Figure 8 that the inversion results of the NUDC-C method and the UDC-C method generally maintain a consistent distribution law with the measured values. However, especially at DZ-ZDS-S-03, DZ-SK-ZDS-09, and DZ-ZDS-S-04 boreholes, the distribution law of the inversion results of the UDC-C method is more similar to the measured values. At the same time, the absolute error of the UDC-C method is smaller than that of the NUDC-C method for all other measuring points except for the measuring points with 620 m buried depth in the DZ-ZDS-S-02 borehole, and 319 m buried depth in the DZ-SK-ZDS-09 borehole. Figure 9 also shows that the inversion effect of the UDC-C method is better than that of the NUDC-C method. Except for the DZ-ZDS-S-02 and DZ-ZDS-S-03 boreholes, where the absolute error of the UDC-C method increases by 3°, the absolute errors of the other boreholes decrease significantly. For example,

from the NUDC-C method changed to the NDC-C method, the absolute error of the DZ-DSFA-01 borehole is reduced from 15° to 12°, and that of the DZ-SK-ZDS-09 borehole is reduced from 11° to 3°, and that of the DZ-ZDS-S-04 borehole is reduced from 15° to 9°.

Furthermore, the statistical indicators, including the relative error ($\delta_r$), the statistical analysis performance indicators of ANOVA (VAF), and the root mean square (RMSE), are used to comprehensively evaluate the accuracy level of each inversion method (She et al., 2022). Their calculation formulas are shown in Eqs. 13–15, respectively. Among them, the smaller the relative error, the larger the VAF, and the smaller the RMSE, indicating the higher the inversion accuracy. According to this principle, the comprehensive evaluation indicator, i.e., comprehensive inversion accuracy (CIA), can be obtained by normalizing the three statistical indicators and superimposing them. The CIA indicator can be calculated by Eqn. 16.
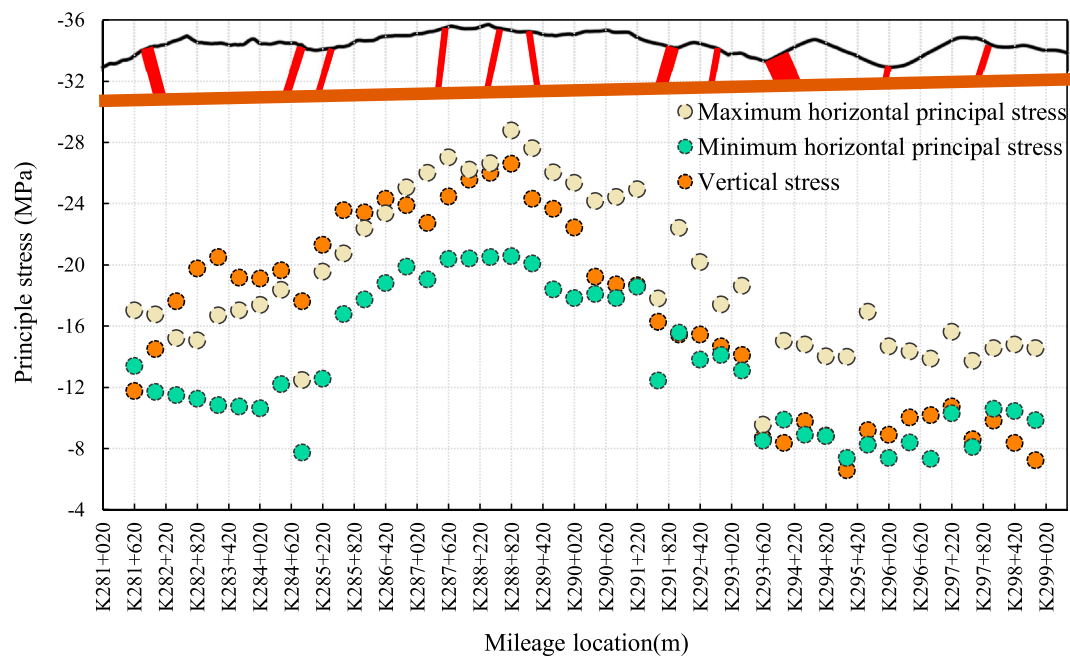
**FIGURE 12**
Distribution of the *in situ* stress along tunnel axis.

$$\delta_r = \frac{\left|\sigma_{jk}^m - \hat{\sigma}_{jk}\right|}{\left|\sigma_{jk}^m\right|} \times 100\% \quad (13)$$

$$VAF = \left(1 - \frac{Variance\left(\sigma_{jk}^m - \hat{\sigma}_{jk}\right)}{Variance\left(\sigma_{jk}^m\right)}\right) \times 100\% \quad (14)$$

$$RMSE = \sqrt{\frac{1}{N}\sum_{i=1}^{N}\left(\sigma_{jk}^m - \hat{\sigma}_{jk}\right)^2}, \quad (15)$$

where $N$ is the total number of samples.

$$CIA = CIA_{value} + CIA_{orientation}$$
$$= [\delta_r + (1 - VAF) + RMSE]_{value} + [\delta_r + (1 - VAF) + RMSE]_{orientation}, \quad (16)$$

where $CIA_{value}$ refers to the comprehensive inversion accuracy of the stress value, and $CIA_{orientation}$ refers to the comprehensive inversion accuracy of the stress orientation.

Table 3 lists the statistical indicators of $\sigma_x$ for different inversion methods. It can be seen that all indicators of the UDC-C method are superior to the NUDC-C method. For example, $\delta_r$ decreases from 23.9% to 20.1%, VAF increases from 95.6% to 96.3%, and RMSE decreases from 3.4 to 2.9. Finally, the CIA indicator decreases from 3.683 to 3.138. In addition, Table 4 and Table 5 list the statistical indicators of all inversion results of the stress value and orientation, respectively. The UDC-C method outperforms the NUDC-C method in all statistical indicators except the VAF indicator of stress orientation. Based on this, calculate the total CIA indicator of

stress value and orientation using Eqn. 16. The comprehensive CIA indicators of the UDC-C method and NUDC-C method are 12.895 and 15.291, respectively (Table 6). To sum up, these data all show that the inversion accuracy is improved after unifying the displacement constraints.

## 3.4 Effect of constant term on accuracy

The multiple linear regression method also has an uncertain factor in the data fitting: whether the regression model should contain the constant term $a_0$. Traditional practice generally includes the constant term $a_0$ (Li et al., 2015; Meng et al., 2021; Zhou et al., 2022), in which case the regression model is Eqn. 1. However, some regression models do not contain the constant term (Figueiredo et al., 2014; Meng et al., 2020; Xu et al., 2021), in which case the regression model is Eqn. 17. In fact, whether to include a constant term is just a matter of choice between the two fitting methods. However, this choice will likely affect the accuracy level of the inversion results. Figure 10 shows the effect of the constant term on the data fit. Obviously, the sum of the errors in Figure 10A, i.e., does not contain a constant term, and that in Figure 10B, i.e., contains a constant term, are probably not equal. Moreover, it is impossible to know in advance which method is more accurate. Therefore, it is necessary to judge whether the constant term should be included before determining the final regression model. Based on this, taking

**FIGURE 13**
Distribution characteristics of *in situ* stress value inside and outside the fault: **(A)** F11-1 fault; **(B)** Yulongxi fault; **(C)** F13-1 fault.
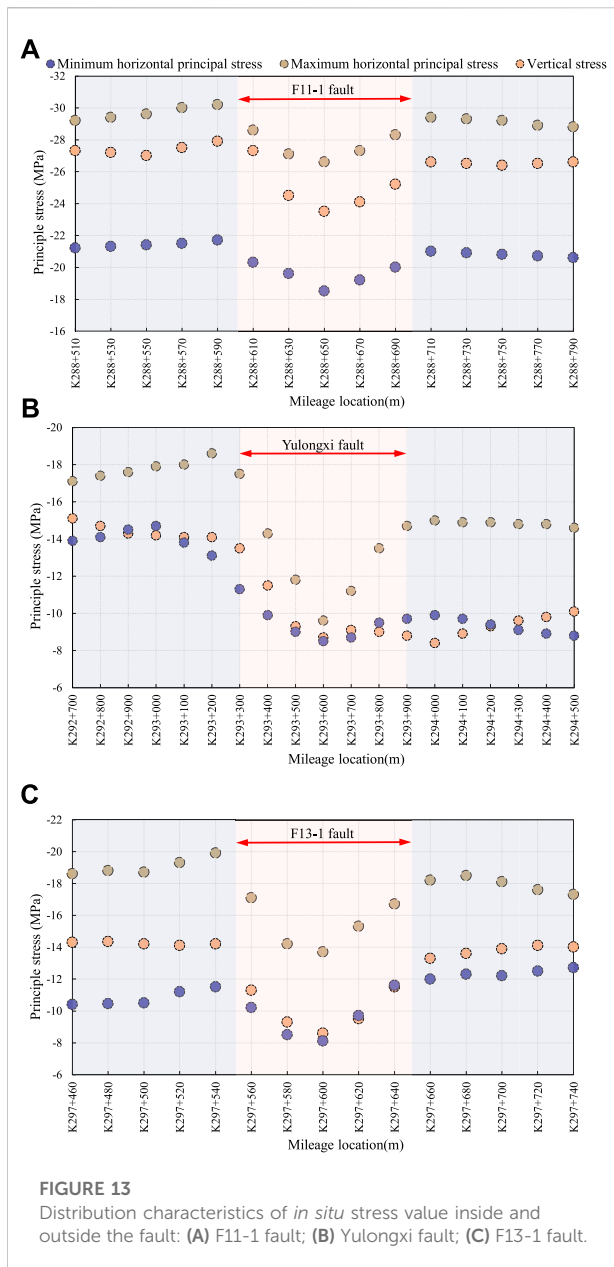
the model with the unified displacement constraints as the standard, the accuracy difference between the inversion methods with a constant term (UDC-C method) and with no constant term (UDC-NC method) is further discussed.

$$\hat{\sigma}_{jk} = \sum_{i=1}^{n} a_i \sigma_{jk}^i \qquad (17)$$

According to the same inversion principle, the data fitting is performed after removing the constant term, and the obtained regression model is as follows:

$$\sigma_{jk}^{\text{UDC-NC}} = 1.06\sigma_{jk}^{g} - 1.73\sigma_{jk}^{x-u} + 16.11\sigma_{jk}^{y-u} + 9.72\sigma_{jk}^{xoy} + 3.50\sigma_{jk}^{x-t} + 4.06\sigma_{jk}^{y-t} \qquad (18)$$

The inversion results of $\sigma_x$ by the UDC-NC method are shown in Figure 8. The absolute errors of all other measuring points reach the smallest, except for the measuring points with 600 m and 620 m buried depths in the DZ-ZDS-S-02 borehole and 228 m buried depth in the DZ-DSFA-01 borehole. In addition, the statistical indicators of $\sigma_x$ in Table 3 also show that the UDC-NC method has the highest inversion accuracy, and its CIA indicator is 2.702. At the same time, Figure 9 shows that the inversion method with no constant term gives the highest inversion accuracy for the orientation of $\sigma_H$. For example, the absolute errors of DZ-ZDS-S-02, DZ-DSFA-01, DZ-ZDS-S-03, and DZ-ZDS-S-04 are 9°, 6°, 7°, and 6°, respectively, all reaching the minimum value. Table 4, Table 5, and Table 6 list the statistical indicators of all inversion results of the UDC-NC method. Regardless of stress value or orientation, the $\delta_r$, VAF, and RMSE all reach the minimum value. Among them, the overall CIA indicator of the stress value, stress orientation, and comprehensive index of the UDC-NC method are 2.301, 7.468, and 9.769, respectively, which are the minimum values among the three methods. This shows that the *in situ* stress inversion accuracy using the regression model with no constant term is much higher.

It should be emphasized that although the inversion accuracy of the UDC-NC method in this tunnel engineering is higher than that of the UDC-C method, it does not prove that the fitting method with no constant term will obtain more accurate inversion results. In fact, according to the fitting principle in Figure 10, the influence of the constant term on the inversion accuracy is random. In other words, higher inversion accuracy may appear in regression models with no constant terms or regression models with a constant term. Therefore, it is recommended that the effect of the constant term on the inversion error must be discussed before determining the regression model.

Based on the above improvement measures for the multiple linear regression method in terms of fitting conditions, the optimized process of *in situ* stress inversion is summarized as follows (Figure 11). The first step is to collect the geological information, geographic information, rock mass mechanical parameters, and measured *in situ* stresses. The second step is to build a three-dimensional numerical model based on the information. The third step is to keep the displacement constraints of the model consistent under each working condition. The fourth step is to discuss the effect of the constant term on accuracy. The fifth step is to select the regression model with higher inversion accuracy to obtain the *in situ* stress field in the tunnel site area.
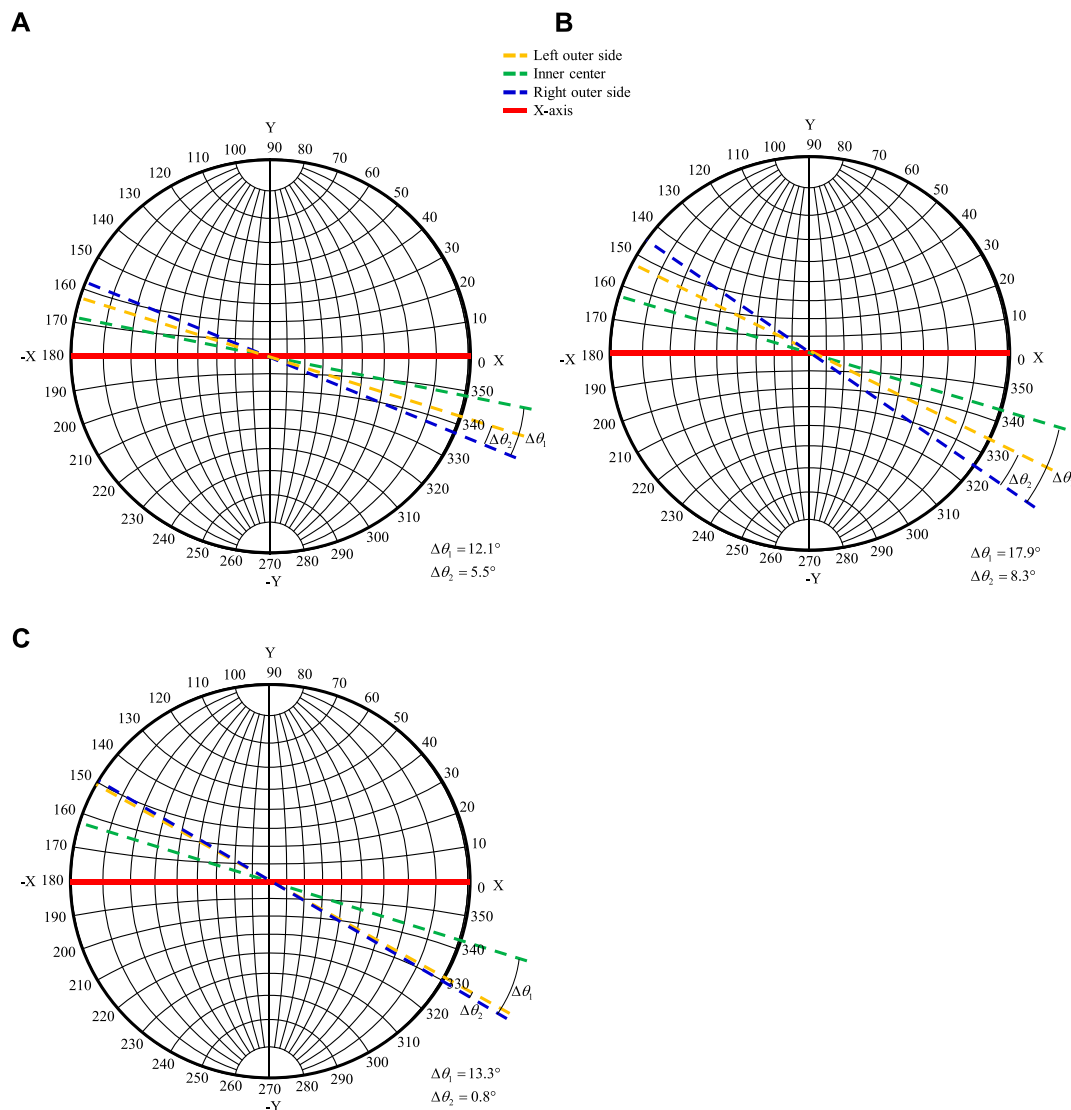
**FIGURE 14**
Distribution characteristics of *in situ* stress orientation inside and outside the fault: **(A)** F11-1 fault; **(B)** Yulongxi fault; **(C)** F13-1 fault.

# 4 Distribution characteristics of the *in situ* stress field in fault zone

Affected by the stress concentration effect at the model boundary, the data about 2000 m on both sides of the tunnel axis should be excluded. Figure 12 shows the *in situ* stress distribution in the range of the tunnel axis K281+620 ~ K298+820. From a macro perspective, the $\sigma_H$, $\sigma_h$, and $\sigma_V$ are positively correlated with the buried depth of the tunnel. Among them, the vertical stress is the most representative, and its change is basically consistent with the fluctuation of the ground surface and the variation of the buried depth. Specifically, in the range of K285+820 ~ K291+220, the tunnel passes through the maximum

buried depth area, and these three stresses all reach the peak range. For example, the range of $\sigma_H$ is -22.4 MPa ~ -28.8 MPa, the range of $\sigma_h$ is -17.7 MPa ~ -20.6 MPa, and the range of $\sigma_V$ is -23.4 MPa ~ -26.6 MPa. At mileage K288+820, the tunnel burial depth reaches the maximum value of about 1215 m, and the corresponding three stresses are -28.8 MPa, -20.6 MPa, and -26.6 MPa, respectively.

On the other hand, their distribution laws are different from the perspective of local areas. Taking the mileage K286+420 as the boundary, the stress distribution law on the left side shows that $\sigma_V$ is greater than $\sigma_H$ greater than $\sigma_h$, and the stress distribution law on the right shows that $\sigma_H$ is greater than $\sigma_V$ greater than $\sigma_h$. In the range of K281+620 ~ K286+420, the range

of $\sigma_H$, $\sigma_h$, and $\sigma_V$ is -12.5 MPa ~ -23.4 MPa, -7.7 MPa ~ -18.8 MPa, and -17.6 MPa ~ -24.3 MPa, respectively, and in the range of K286+420 ~ K298+820, the range of $\sigma_H$, $\sigma_h$, and $\sigma_V$ is -13.9 MPa ~ -28.8 MPa, -7.3 MPa ~ -20.6 MPa, and -10.2 MPa ~ -26.6 MPa, respectively. This shows that the stress distribution characteristics of ultra-long tunnels are not invariant, and there are significant differences between their local areas.

In addition, Figure 12 also shows that there are large fluctuations in stress near the fault. This phenomenon is particularly significant in mileage K284+820 and mileage K291+620. For example, at mileage K284+820, the $\sigma_H$, $\sigma_h$, and $\sigma_V$ are reduced from -19.6 MPa, -12.5 MPa, and -21.3 MPa to -12.5 MPa, -7.7 MPa, and -17.6 MPa, respectively. At mileage K291+620, the $\sigma_H$, $\sigma_h$, and $\sigma_V$ are reduced from -24.9 MPa, -18.5 MPa, and -18.6 MPa to -17.8 MPa, -12.4 MPa, and -16.3 MPa, respectively. This shows that the distribution of faults has a significant disturbance to the *in situ* stress field. On this basis, the three areas in Figure 2 are selected to investigate the disturbance law of the fault distribution to the *in situ* stress field. Among them, compare Area one and Area two to analyze the influence of fault width and compare Area one and Area three to analyze the influence of fault distribution distance.

Select the F11-1 fault in Area one, the Yulongxi fault in Area two, and the F13-1 fault in Area three to analyze the *in situ* stress distribution law in the fault zone (Figure 13). In general, on the outside of the fault, the *in situ* stress slightly increases as it approaches the fault, and inside the fault, the *in situ* stress decreases as it approaches the fault plane. For example, while approaching the fault from outside, $\sigma_H$ of the F11-1 fault, Yulongxi fault, and F13-1 fault increase by a maximum of 1.1 MPa, 1.5 MPa, and 1.3 MPa, respectively. On the other hand, what is remarkable is that the *in situ* stress inside the fault manifests as a sudden stress drop. Comparing Figures 13A,B, it can be seen that the amplitudes of stress change inside the Yulongxi fault are more evident than that of the F11-1 fault. The maximum amplitude of stress change of the $\sigma_H$, $\sigma_h$, and $\sigma_V$ in the F11-1 fault are 3.6 MPa, 3.2 MPa, and 4.4 MPa, respectively. The maximum amplitudes of stress change of the $\sigma_H$, $\sigma_h$, and $\sigma_V$ in the Yulongxi fault are 9.0 MPa, 5.6 MPa, and 6.4 MPa, respectively. It can be seen that under the same fault distribution distance, the amplitude of stress change increases by an average of 1.9 times when the width of the fault impact zone increases from 99 m to 614 m. Therefore, the wider the fault, the more significant its disturbance to the *in situ* stress. Comparing Figures 13A,C, it can be seen that the amplitude of stress change inside the F13-1 fault is more evident than that of the F11-1 fault. The maximum amplitudes of stress change of the $\sigma_H$, $\sigma_h$, and $\sigma_V$ in the F13-1 fault are 6.2 MPa, 4.6 MPa, and 5.8 MPa, respectively. It can be seen that under the same fault width, the amplitude of stress change increases by an average of 1.5 times when the fault distribution distance increases by

about 2.0 times. This shows that the denser the fault distribution, the more minor its disturbance to the *in situ* stress.

Figure 14 shows the variation of $\sigma_H$ inside and outside the three faults. In Figure 14, the inner center represents the position of the fault plane, and the left and right outer sides are both located at the center of the outer sides of two adjacent faults. It can be seen that the *in situ* stress orientation is deflected between both the outer sides of the fault and between the inside and outside sides. In general, the disturbance of the fault impact zone width and the fault distribution distance on the stress orientation is similar to the disturbance on the stress value. For example, comparing Figures 14A,B, it can be found that the wider the fault impact zone is, the more significant the *in situ* stress orientation changes. $\Delta\theta_1$ and $\Delta\theta_2$ of the F11-1 fault are 12.1° and 5.5°, respectively, while those of the Yulongxi fault are 17.9° and 8.3°, respectively. Comparing Figures 14A,C, it can be found that after the distribution distance between the faults increases, the variation between the inner and outer orientations increases slightly. The $\Delta\theta_1$ of the F13-1 fault increases to 13.3°. Nevertheless, on the other hand, as the distribution distance between faults increases, the orientations of the two outer sides of the fault remain almost unchanged, e.g., $\Delta\theta_2$ is only 0.8°.

# 5 Conclusion

In this paper, an inversion method with unified displacement constraints was proposed to improve the inversion accuracy. On this basis, the influence of the constant term in the regression model on the inversion accuracy was discussed, and the specific process of the inversion method with optimized fitting conditions was proposed. By using this optimized method, the *in situ* stress field distribution law between the densely distributed faults in the tunnel site area was revealed. The main conclusions are summarized as follows:

1) Combining the statistical indicators with $\delta_r$, VAF, and RMSE, a CIA indicator that can comprehensively evaluate the *in situ* stress inversion accuracy is proposed. The smaller the CIA indicator, the higher the inversion accuracy.
2) The inversion method with unified displacement constraints has been verified can improve the inversion accuracy. Before and after the unification of displacement constraints, the CIA indicators between the measured and inversion values at all measuring points are 15.291 and 12.895, respectively.
3) Whether keep the constant term in the regression model has an impact on the inversion error. Therefore, it is recommended to investigate the effect of the constant term before determining the regression model.
4) From the outer side of the fault to the inner side, the *in situ* stress increases slightly and then decreases significantly. A significant stress drop develops inside the fault. On the other hand, the wider the fault impact zone, the larger the fault

distribution distance, and the more significant the amplitude of stress change. When the width of the fault impact zone increases from 99 m to 614 m, the maximum amplitude of stress change increases from 4.4 MPa to 9.0 MPa. When the fault distribution distance increases by 2.0 times, the maximum amplitude of stress change increases from 4.4 MPa to 6.2 MPa.

5) Furthermore, the wider the fault impact zone, the greater the deflection of the *in situ* stress orientation between inside and outside the fault. When the width of the fault impact zone becomes wider, the variation between the inner and outer sides increases from 12.1° to 17.9°. In addition, the fault distribution distance has no significant effect on the variation between the inner and outer *in situ* stress orientation. However, after the fault distribution distance increases, the *in situ* stress orientations on the two outer sides of the fault are basically consistent.

## Data availability statement

The original contributions presented in the study are included in the article/supplementary material, further inquiries can be directed to the corresponding author.

## Author contributions

TL has performed the numerical analysis, data analysis, and draft manuscript. ZC supervised the whole research, performed the data analysis and discussion. ZZ designed the overall structure and innovation and reviewed and did the final editing. YB performed the data processing of some figures and tables.

## Funding

## Conflict of interest

TL and YB were employed by the company China Railway 12th Bureau Group Co., Ltd.

The remaining authors declare that the research was conducted in the absence of any commercial or financial relationships that could be construed as a potential conflict of interest.

## Publisher's note

All claims expressed in this article are solely those of the authors and do not necessarily represent those of their affiliated organizations, or those of the publisher, the editors and the reviewers. Any product that may be evaluated in this article, or claim that may be made by its manufacturer, is not guaranteed or endorsed by the publisher.

## References

Fan, Y., Cui, X. Z., Leng, Z. D., Zheng, J. W., Wang, F., and Xu, X. L. (2021). Rockburst prediction from the perspective of energy release: A case study of a diversion tunnel at jinping II hydropower station. *Front. Earth Sci. (Lausanne).* 9, 711706. doi:10.3389/feart.2021.711706

Figueiredo, B., Cornet, F. H., Lamas, L., and Muralha, J. (2014). Determination of the stress field in a mountainous granite rock mass. *Int. J. Rock Mech. Min. Sci. (1997).* 72, 37–48. doi:10.1016/j.ijrmms.2014.07.017

Han, J., Zhang, H. W., Liang, B., Rong, H., Lan, T. W., Liu, Y. Z., and Ren, T. (2016). Influence of large syncline on *in situ* stress field: A case study of the kaiping coalfield, China. *Rock Mech. Rock Eng.* 49 (11), 4423–4440. doi:10.1007/s00603-016-1039-4

Hu, D., Liang, X. Q., Li, Y. S., Wu, Y. P., and Jiang, L. (2022). Deformation prediction of tunnel-surrounding rock considering the time effect of the viscosity coefficient: A case of an NATM-excavated tunnel. *Front. Earth Sci. (Lausanne).* 10, 843545. doi:10.3389/feart.2022.843545

Li, G., Hu, Y., Li, Q. B., Yin, T., Miao, J. X., and Yao, M. D. (2020a). Inversion method of *in-situ* stress and rock damage characteristics in dam site using neural network and numerical simulation—A case study. *IEEE Access* 8, 46701–46712. doi:10.1109/access.2020.2979024

Li, P., Guo, Q. F., Miao, S. J., and Cai, M. F. (2017). Comparisons of *in-situ* stress fields and stability of faults in shallow and deep engineering areas. *J. Harbin Inst. Technol.* 49 (9), 10–16. doi:10.11918/j.issn.0367-6234.201608057

Li, X. P., Zhou, X. J., Xu, Z. X., Feng, T., Wang, D., Deng, J. H., Zhang, G. Z., Li, C. B., Feng, G., Zhang, R., Zhang, Z. L., and Zhang, Z. T. (2020b). Inversion method of initial *in situ* stress field based on BP neural network and applying loads to unit body. *Adv. Civ. Eng.* 2020, 1–15. doi:10.1155/2020/8840940

Li, X. Y. (2022). Investigation of genetic mechanism of the Shigang fault zone in the Northern Jiangsu basin using physical analog sand-box modeling. *Energy Rep.* 8, 9379–9391. doi:10.1016/j.egyr.2022.07.034

Li, Y., Guo, Y. H., Zhu, W. S., Li, S. C., and Zhou, H. (2015). A modified initial *in-situ* stress inversion method based on FLAC3D with an engineering application. *Open Geosci.* 7 (1), 824–835. doi:10.1515/geo-2015-0065

Liu, Y. X., Zhang, Y. Q., Su, P. D., Zhang, G. Z., Qiu, P., and Tang, L. (2022). Risk prediction of rock bursts and large deformations in YL tunnel of the chongqing–kunming high-speed railway. *Front. Earth Sci. (Lausanne).* 10, 892606. doi:10.3389/feart.2022.892606

Meng, W., and He, C. (2020). Back analysis of the initial geo-stress field of rock masses in high geo-temperature and high geo-stress. *Energies* 13 (2), 363. doi:10.3390/en13020363

Meng, W., He, C., Zhou, Z. H., Li, Y. Q., Chen, Z. Q., Wu, F. Y., et al. (2021). Application of the ridge regression in the back analysis of a virgin stress field. *Bull. Eng. Geol. Environ.* 80 (3), 2215–2235. doi:10.1007/s10064-020-02043-y

National Railway Administration of Prc (2017). *Code for design of Railway tunnel.* Beijing China: China Railway Press.

Ning, Y., Tang, H., Smith, J. V., Zhang, B., Shen, P., and Zhang, G. (2021). Study of the *in situ* stress field in a deep valley and its influence on rock slope stability in Southwest China. *Bull. Eng. Geol. Environ.* 80 (4), 3331–3350. doi:10.1007/s10064-020-02094-1

Pei, Q. T., Ding, X. L., Lu, B., Zhang, Y. T., Huang, S. L., and Dong, Z. H. (2016). An improved method for estimating *in situ* stress in an elastic rock mass and its engineering application. *Open Geosci.* 8 (1), 523–537. doi:10.1515/geo-2016-0047

She, L., Zhang, S. R., Wang, C., Du, M., and Yang, P. (2022). A cutting mechanics model of constant cross-section type disc cutter and its application based on dense core theory. *Int. J. Rock Mech. Min. Sci. (1997).* 150, 105025. doi:10.1016/j.ijrmms.2021.105025

Wang, Z. S., Xiang, H., Wang, L. B., Xie, L., Zhang, Z. G., Gao, L. F., Yan, Z. F., and Li, F. L. (2022). Fracture characteristics and its role in bedrock reservoirs in the Kunbei fault terrace belt of Qaidam basin, China. *Front. Earth Sci. (Lausanne).* 10, 865534. doi:10.3389/feart.2022.865534

Xu, D. P., Huang, X., Jiang, Q., Li, S. J., Zheng, H., Qiu, S. L., Xu, H. S., Li, Y. H., Li, Z. G., and Ma, X. D. (2021). Estimation of the three-dimensional *in situ* stress field around a large deep underground cavern group near a valley. *J. Rock Mech. Geotechnical Eng.* 13 (3), 529–544. doi:10.1016/j.jrmge.2020.11.007

Yuan, D., Zhang, L. B., Liu, X. L., Feng, T., Zhang, G. Z., Xu, Z. X., Wang, Z. W., Yi, X. J., Lin, Z. H., Ren, Y., Zhang, R., and Ren, L. (2022). Influence of the Xianshuihe fault zone on *in situ* stress field of a deep tunnel and its engineering effect. *Front. Earth Sci. (Lausanne).* 10, 886876. doi:10.3389/feart.2022.886876

Zhang, C. Q., Feng, X. T., and Zhou, H. (2012). Estimation of *in situ* stress along deep tunnels buried in complex geological conditions. *Int. J. Rock Mech. Min. Sci. (1997).* 52, 139–162. doi:10.1016/j.ijrmms.2012.03.016

Zhang, D. L., Sun, Z. Y., and Fang, Q. (2022a). Scientific problems and research proposals for Sichuan-Tibet railway tunnel construction. *Undergr. Space* 7, 419–439. doi:10.1016/j.undsp.2021.10.002

Zhang, H., Ouyang, Z. H., Li, T., Liu, S., Yi, H. Y., Wang, H. L., Chen, J. Q., and Li, K. (2022b). An investigation into the mechanism of rock bursts in mines for tunnel-cut isolated areas with multiple stress fields. *Front. Earth Sci. (Lausanne).* 9, 809839. doi:10.3389/feart.2021.809839

Zhang, S. K., and Yin, S. D. (2014). Determination of *in situ* stresses and elastic parameters from hydraulic fracturing tests by geomechanics modeling and soft computing. *J. Pet. Sci. Eng.* 124, 484–492. doi:10.1016/j.petrol.2014.09.002

Zhao, T., Hu, W. G., Zhao, R., Yang, M., Wang, Q., Lin, H. X., Ru, Z. X., Bao, D., and Cao, F. (2021). Present *in-situ* stress distribution characteristics of strike-slip in SH oilfield, Tarim basin. *Arab. J. Geosci.* 14, 1223. doi:10.1007/s12517-021-07552-y

Zhou, Z. H., Chen, Z. Q., He, C., Meng, W., Wu, F. Y., Kou, H., and Yan, J. (2022). *in situ* stress field along the axis of deeply buried tunnel in Southwest China employing the segmented single-borehole inversion method. *Int. J. Geomech.* 22 (6), 04022064. doi:10.1061/(ASCE)GM.1943-5622.0002377

Frontiers | Frontiers in Earth Science

# Offshore subsurface characterization enabled by fiber-optic distributed acoustic sensing (DAS): An East China Sea 3D VSP survey example

Yuanzhong Chen[1,2], Jingjing Zong[1]*, Chengxin Liu[3], Zhonglin Cao[2], Pengfei Duan[2], Jianguo Li[2] and Guangmin Hu[1]

[1]University of Electronic Science and Technology of China, Chengdu, China, [2]BGP Inc. China National Petroleum Co., Zhuozhou, China, [3]Shanghai Petroleum Corporation Ltd., Shanghai, China

Recent advances in distributed acoustic sensing (DAS) technology have allowed more intense measurements of subsurface and environment events, providing improved geohazard monitoring and subsurface characterization. This study discussed the subsurface evaluation enabled by the DAS-vertical seismic profiling (DAS-VSP) system in the East China Sea, China. Taking advantage of a continuous recording of the vibrational wavefields through the strain deformation of the fiber deployed along the borehole, DAS-VSP is considered an emerging and promising alternative borehole acquisition method. It provides a wider-spectrum range of recordings in a cheaper, denser, and more continuous tense compared to conventional geophones. We explored the 3D DAS-VSP signal processing and imaging strategy. Based on a set of 3D DAS-VSP data of exceptional quality, this study reviewed the common processing challenges and practical solutions for de-noise, de-ghosting, de-multiple, and wavefield separation arising from the DAS acquisition mechanism in the offshore VSP scenario. High-quality down-going multiples were separated and imaged using the pre-stack Gaussian beam depth migration in addition to the primary reflection wavefield, providing significant additional illumination to support the subsurface evaluation. The current results validated the efficiency of the DAS-VSP survey and encouraged better geological interpretation.

## 1 Introduction

Uncertainties in subsurface/geohazard evaluation are among the main concerns for safe offshore drilling (Hadley et al., 2008; Acocella, 2015). Better subsurface characterization using geophysical methods can reduce these uncertainties. The emerging fiber-optic distributed acoustic sensing (DAS) technology has demonstrated strengths in monitoring environmental changes (Zhu et al., 2021), near-surface hazards (Fang et el., 2020), and deep subsurface events (Daley et al., 2013). The DAS system uses a fiber optic cable to provide distributed strain sensing based on the internal natural flaws of the thin glass fibers (Krohn et al., 2014). Compared to conventional geophysical sensors (e.g., seismic geophones), the stable performance of the optic fiber under high-temperature, high-hydrogen, and corrosive environments makes it well adapted for ultra-deep wellbore and deep water settings (Zhan, 2020; Li et al., 2021). The past decade has witnessed the rapid development of
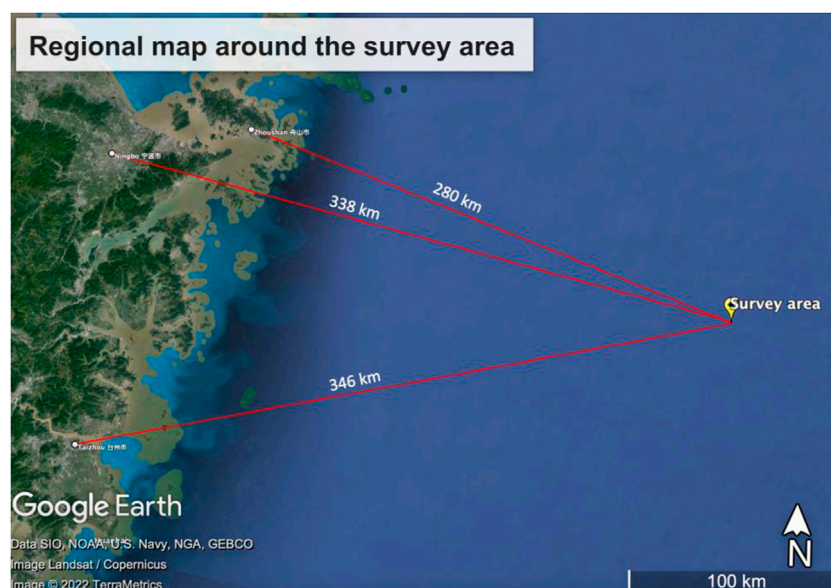
**FIGURE 1**
Survey area (marked in yellow) is located on the Pinghu slope to the west of the Xihu Sag, East China Sea, China. The distances between the survey area and three adjacent cities, namely, Zhoushan, Ningbo, and Taizhou are 280 km, 338 km, and 346 km, respectively. The map was created using Google Earth.

DAS surveys in many geophysical surveys, including ocean bottom acquisition, vertical seismic profiling (VSP), integrated borehole and surface seismic surveys, 4D reservoir monitoring, and micro-seismic monitoring (Mateeva et al., 2012, 2017, Yu et al., 2016; Zhan et al., 2019).

Unlike surface seismic surveys, whose source and receiver arrays are deployed on the surface, VSP surveys equip three-component (3-C) geophones along the wellbore. Therefore, VSP is advantageous in providing reliable time-depth registration of wave propagation and higher-quality subsurface reflectivity measurements around the wellbore (Stewart et al., 1984; Oristaglio, 1985). Owing to the shortened travel path, the subsurface receivers record higher-resolution and higher signal-to-noise ratio (SNR) wavefields. As the receivers are deployed closer to the subsurface targets, more reliable kinematic and dynamic seismic wave information on the formations (e.g., seismic velocity, quality factor, seismic wavelets, and anisotropy) can be obtained (Gaiser 2016; Wo et al., 2021; Huang et al., 2022).

DAS-VSP, in particular, has gained increased attention as the DAS recording system facilitates cheaper, repeatable, and denser spatial sampling, as well as time-lapse monitoring of subsurface formations and reservoirs (Li et al., 2015; Willis et al., 2021). Several studies have reported on subsurface formation parameters and images from DAS-VSP. Zhang et al. (2020) reported quality factor (Q) estimation for the DAS-VSP data. Horne et al. (2020) analyzed the anisotropy parameters from a walkaway DAS-VSP case. Mizuno and Ali (2021) reported satisfactory results of the application of generalized radon transform migration to DAS-VSP data. Wilson et al. (2021) evaluated carbonate sequestration using a time-lapse 3D DAS-VSP survey.

The present work reviewed a 3D offshore DAS-VSP case in the Pinghu oilfield, East China Sea, China. We explored a list of typical signal processing challenges related to the DAS acquisition system as well as promising solutions.
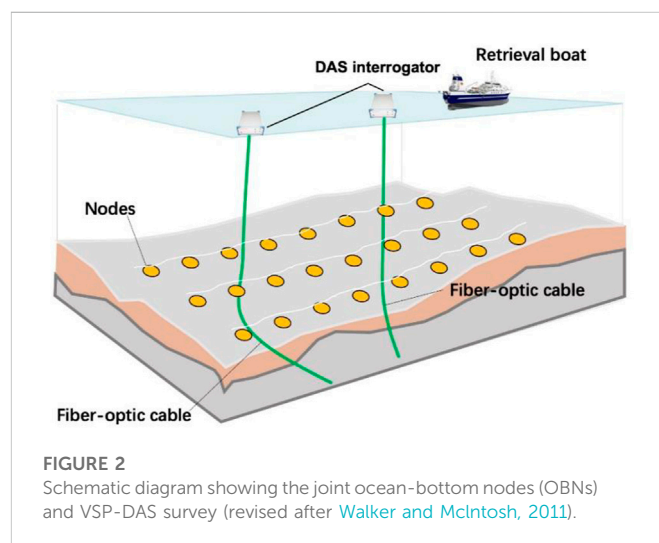


**FIGURE 2**
Schematic diagram showing the joint ocean-bottom nodes (OBNs) and VSP-DAS survey (revised after Walker and McIntosh, 2011).

## 2 Geologic background

The study area was located on the Pinghu slope to the west of the Xihu Sag, East China Sea (Figure 1). The Pinghu oilfield comprises eight geologic structures, including the Fangheting, Bajiaoting, Wanghuting, and Shuangzhaoting. All of them have provided commercial oil and gas flow from drilled wells. The reservoirs are reported primarily controlled by fractured anticlines (Su et al., 2018). Therefore, the delineation of the fault and fracture networks may provide key clues to understanding the reservoir distribution.

The dominant fault system extends over 100 km along the north-northeast (NNE) direction and plays a key role in retaining the gas accumulation. Early surface seismic surveys with steamer met great challenges in supplying quality data for deep targets. Moreover, lateral

**TABLE 1 3D DAS-VSP acquisition parameters.**

| Well name | Depth range (m) | Sampling interval (m) | Source azimuth (°) | Source offset (m) | Source interval (m) | Source array interval (m) | Total shot number |
|-----------|-----------------|------------------------|---------------------|--------------------|----------------------|----------------------------|--------------------|
| B1 | 1-3580 | 1 | 120 | -4000–4000 | 37.5 | 50 | 48411 |
| B2 | 1-3170 | 1 | 120 | -4000–4000 | 37.5 | 50 | 62473 |



**FIGURE 3**
Fold coverage map calculated under the designed acquisition configuration for wells **(A)** B1 and **(B)** B2. The outermost coral areas mark the coverage of shots while the green lines denote the receiver array.
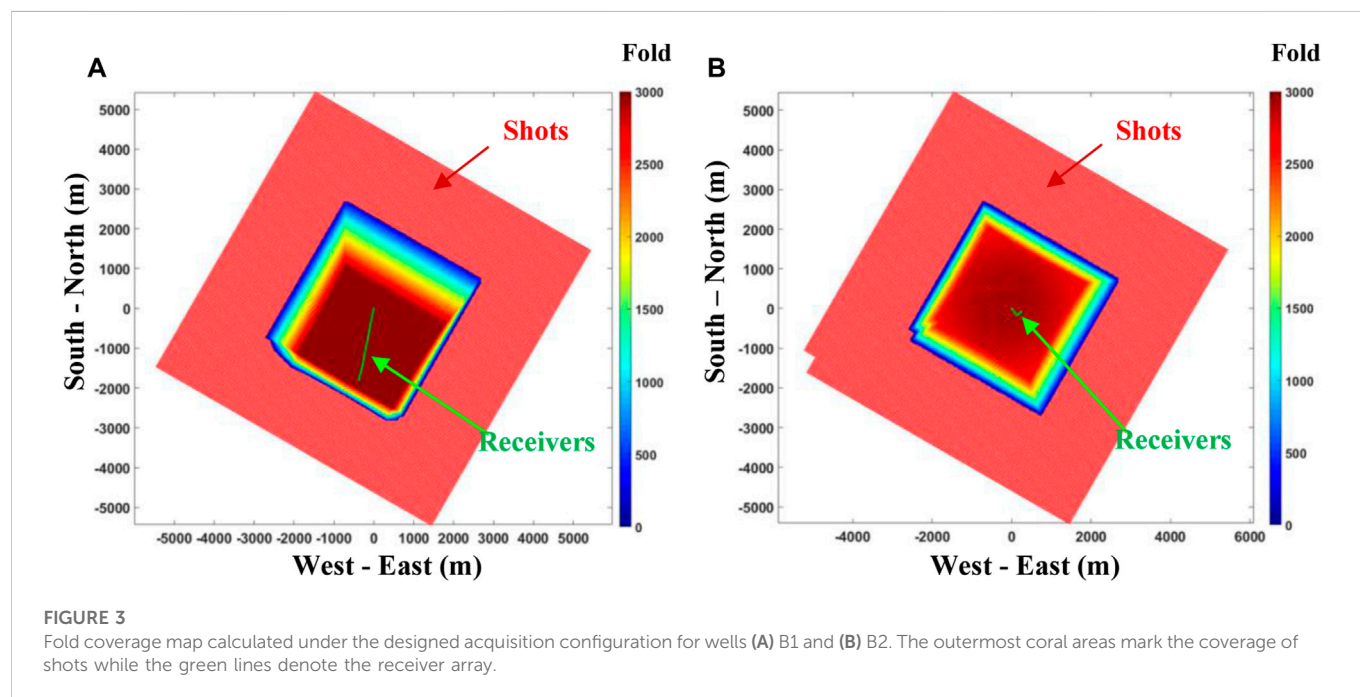
variation around the reservoir in the survey area complicates reservoir characterization given the less-satisfactory image quality of the streamer data. Therefore, in 2021, a new 3D survey with joint ocean-bottom nodes (OBN) and DAS-VSP was carried out to provide an integrated surface and borehole seismic image. Figure 2 shows a schematic configuration of the 3D joint OBN and DAS-VSP survey revised after Walker and McIntosh (2011). The present paper focused on the 3D DAS-VSP survey with the fiber-optical cables deployed in two wells (B1 and B2). The primary objective of this survey was to provide better illumination and finer characterization of the reservoir around the wellbore. This study examined the common challenges in processing the 3D DAS-VSP data and focused on providing an optimized solution and imaging strategy to supply an enhanced final image.

## 3 3D VSP survey acquisition

To improve the seismic illumination around the target area, the 3D-VSP survey was designed based on the following considerations: 1. to extend the borehole receiver range closely to, if not to penetrate, the target formation at a depth of around 3500 m below the mudline; and 2. to increase the lateral illumination within the maximum capacity of the length of the source array. Therefore, we designed a DAS fiber covering measured depths of 3580 m and 3170 m for wells B1 and B2,

respectively. In addition, both wells were planned to deviate to allow wider lateral illumination. The bottoms of the well offsets were 1530 m and 350 m for wells B1 and B2, respectively. Table 1 lists the detailed acquisition parameters.

We calculated the theoretical fold coverage at wells B1 and B2 around the target formation as shown in Figure 3 based on the designed acquisition parameters. For both wells, the fold counts were >3000 around the wellbore, with a bin size of 20 m. The premium imaging areas were > 8 $km^2$. This survey configuration was believed to be adequate for the 3D-VSP imaging around the target area.

Figure 4 shows examples of the raw shot gathers at different offsets from near to far (500 m, 1000 m, 2000 m, 3000 m, and 4000 m, respectively). The raw data were generally of good quality, with high signal-to-noise ratio (SNR) events observed throughout the entire depth range in both the down-going and up-going wavefields. In the up-going wavefield, we noticed strong converted-wave events below a depth of 2000 m, which required designated wavefield separation efforts given the acoustic imaging strategy. Both surface and interval multiples appeared to be fairly strong, especially at the near and middle offset ranges. Reverberating noises were observed at several shallow depths, showing zigzag patterns due to the poor cable coupling effect. To ensure a satisfactory image, the signal processing focused on these issues and ensured that the processed wavefield mainly contained the P-wave primary reflections.
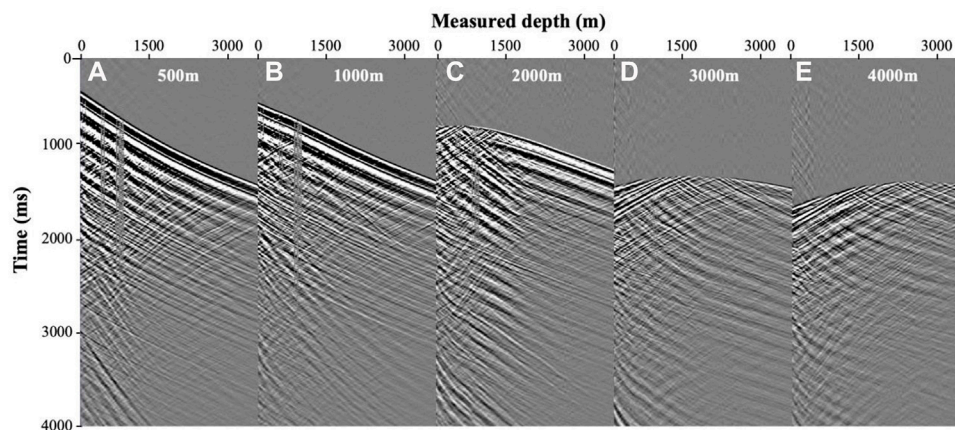
**FIGURE 4**
DAS-VSP raw shot gathers at different offset ranges from near to far (500 m, 1000 m, 2000 m, 3000 m, and 4000 m, respectively).
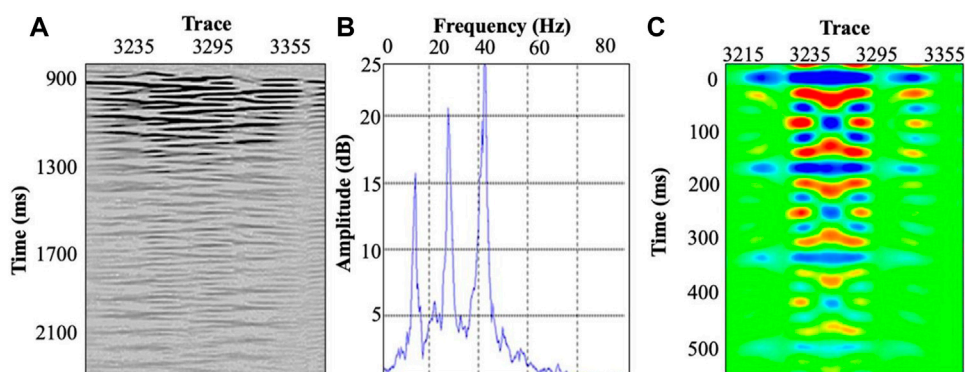


**FIGURE 5**
Characteristics of the DAS-VSP zigzag reverberation noise. **(A)** Raw record. **(B)** Frequency spectrum. **(C)** Autocorrelation of the reverberation noise.
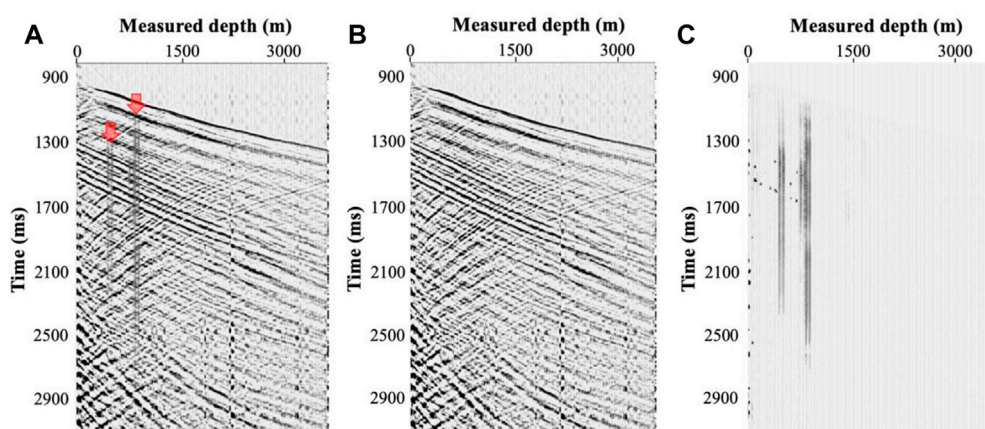


**FIGURE 6**
Example shot gathers **(A)** before and **(B)** after the zigzag cable-reverberation noise is removed, as shown in **(C)**. Red arrows: appearance of cable-reverberation noises.
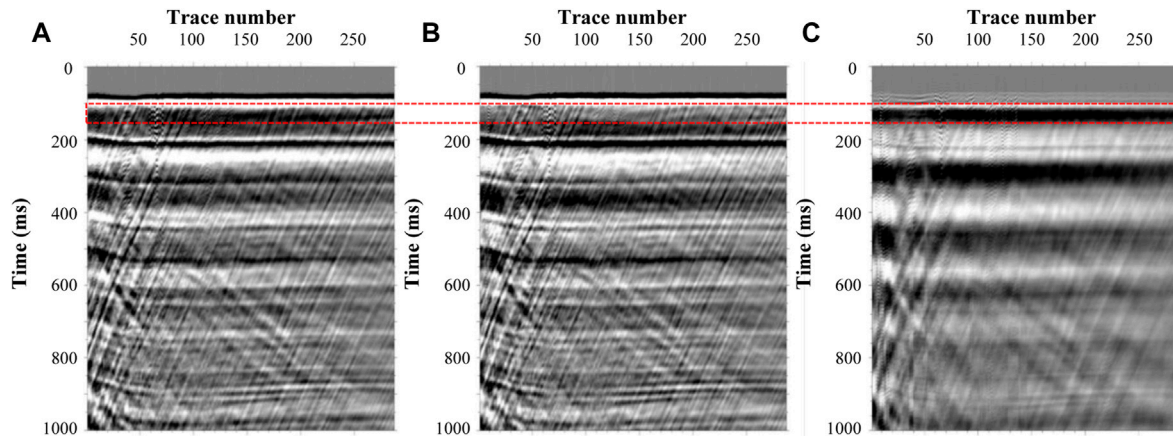
FIGURE 7
Example shot gather showing the **(A)** raw record flattened by the first arrivals, **(B)** de-ghosting record, and **(C)** removed ghost wave. Red dashed box: ghost wave following the first arrival with the identical move-out but reversed polarity.
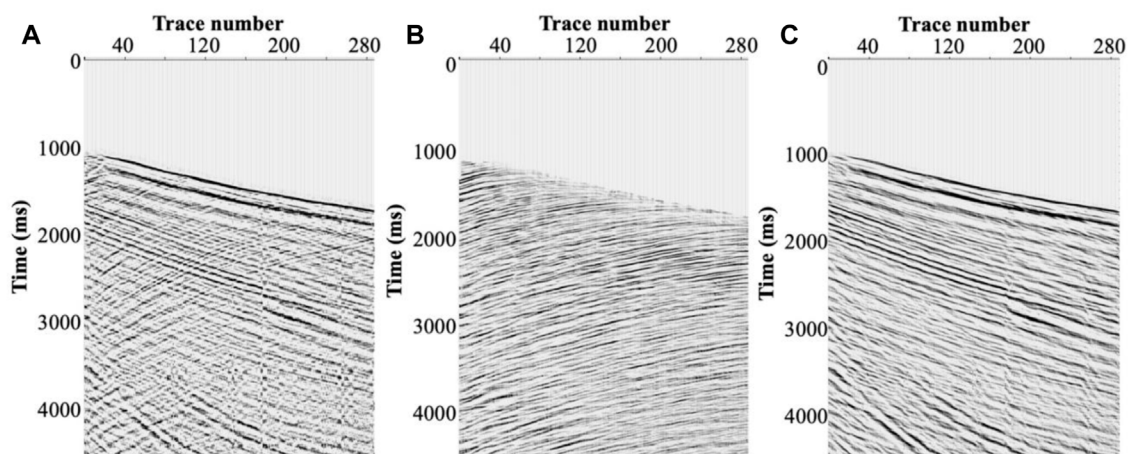


FIGURE 8
Example shot gather showing the wavefield separation processing. **(A)** Raw shot gather. **(B)** Separated P-wave primary reflection. **(C)** Removed down-going field.

# 4 3D DAS-VSP data preparation

The general process of offshore 3D VSP imaging processing includes data loading, geometry setup, trace editing, first break picking, static correction, de-noising, amplitude compensation, deconvolution, wavefield separation, velocity analysis, and migration imaging. Several new challenges in processing offshore DAS-VSP data are reviewed in the following sections.

## 4.1 Cable-reverberation suppression

Although fiber-optical cables can easily cover the entire borehole with densely distributed sensors, one common issue with fiber cable recording is that proper cable coupling or wellbore cementation cannot always be guaranteed. Poorly coupled sections result in coherent reverberation noise, often referred to as "ringing" or "zigzag" noises (Martuganova et al., 2021). Figure 5A shows a raw section with cable-reverberation noise in the time domain. The signal behaves periodically in both the frequency spectrum and its auto-correlation spectrum, as shown in Figures 5B, C, respectively. The cable reverberations share a frequency range with the primary P-wavefield. Thus, eliminating the cable-reverberation noise at a specific depth range without affecting the reflections can be complicated (Willis et al., 2019).

The present study applied a cable-reverberation suppression method based on a $\tau - p$ transform, where $\tau$ refers to the two-way intercept time at the slowness $p = 0$, given the periodic feature in the cable-reverberation's auto-correlation spectrum domain. This transforms the offset-time (x-t) domain seismic records to the
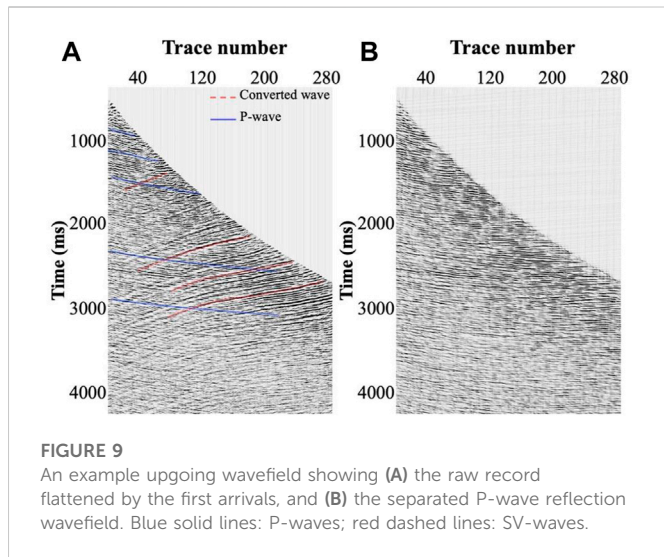
**FIGURE 9**
An example upgoing wavefield showing **(A)** the raw record flattened by the first arrivals, and **(B)** the separated P-wave reflection wavefield. Blue solid lines: P-waves; red dashed lines: SV-waves.



**FIGURE 10**
Cross-section of the smoothed 3D P-wave velocity model used for VSP imaging plotted on top of the surface seismic image. Red solid line: projected trajectory of Well B1.

which shows strong impedance contrast at nearly a reflectivity coefficient around -1, a strong reflection (often referred to as a "ghost wave") with a reversed polarity occurs and propagates downwards. Hence, the ghost wave appears to be similar to the primary wave with a reversed polarity and a delay time window in the shot record. Attenuating ghost waves is critical to ensure the quality of the final image of the primary reflection wavefield. The present study adopted a de-ghost method based on the frequency–wavenumber domain filtering, which is briefly described as follows (Bernth and Sonneland, 1983; Weglein and Dragoset, 2005; Yilmaz and Baysal, 2015; Wang et al., 2016).

We first simplified our problem by assuming that the seismic records contained only the primary and the ghost wavefields. We assumed that other types of noises of interferences were already separated.

Thus, the seismic record ( 'S') can be expressed as follows:

$$S = P + G, \qquad (1)$$

where P and G represent the primary reflections and ghost waves, respectively.

With the time delay between the ghost wave and the first arrival of the primary wave, denoted by $\Delta\tau$, we can represent the ghost wavefield as

$$G = Re^{-i\omega\triangle\tau}P, \qquad (2)$$

where R is the reflectivity coefficient at the boundary of the sea surface to air, which is close to -1. Hence, the polarity of the ghost wave is reversed compared to the primary wave. We further introduce Eq. 2 to equation (1) and rewrite the total wavefields in the frequency-slowness (f-p) domain (or, equivalently, frequency–wavenumber domain) as

$$Re^{-i\omega\triangle\tau}P + Re^{-i\omega\triangle\tau}e^{-i\omega\triangle\tau}P = e_{pr}^{-i\omega\triangle\tau}S. \qquad (3)$$

Thus, $D_\mu = e^{-i\omega\triangle\tau}$, which is the linear f-p transform operator. Therefore, Eq. 1 can be represented as

$$D_M + RD_M E^{-I\Omega\triangle T}P = D_M S. \qquad (4)$$

The resulting Eq. 4 corresponds to a linear decomposition of the ghost and the primary wavefields that can be solved using the conjugate gradient method by approximating the least-squares solution.

Figure 7 shows the applied de-ghosting result in an example flattened shot gather. Figure 7A shows the raw record with its first arrival event aligned at 100 ms. The dashed red box indicates the strong ghost wave following the first arrival event with identical move-out but reversed polarity, as opposed to the first arrivals. After applying the f-p domain de-ghosting filter, the ghost waves (Figure 7C) were efficiently attenuated, resulting in a more focused primary wavefield (Figure 7B).

## 4.3 Wavefield separation

After noise suppression, we next separated the P-wave reflection field for imaging. The wavefield separation plays a critical role in VSP data preparation and greatly affects the final image. One of the most common and effective references to differentiate different wave modes is through their varying apparent velocities. A variety of velocity-based filters have been designed for desired wave modes, including the median filter, F-K filter, and $\tau - p$ filter (Blias, 2007).

time-slowness ($\tau - p$) domain, allowing the periodically appearing ringing noises to be predicated using a least-squares linear fit (Turner, 1990).

Figure 6A shows an example of the raw shot gather with the cable-reverberation noises appearing at the shallow depths (indicated by red arrows). Figures 6B, C show the processed shot gather using a $\tau - p$ domain filter and the removed cable-reverberation noises, respectively. The $\tau - p$ domain allows better separation of the primary reflection from the cable-reverberation noise. By subtracting the predicted noise from the full record and applying the inverse $\tau - p$ transform, we obtain the primary wavefields without sacrificing many of the useful signals. The current application proves that the $\tau - p$ filter can efficiently eliminate DAS-VSP cable-reverberation ringing noise.

## 4.2 De-ghosting in the frequency-slowness domain

Another source of noise is the offshore acquisition environment. Offshore acquisition often utilizes an airgun source that fires below the sea surface. When the up-going wave travels across the sea surface,

**FIGURE 11**
Final images of the 3D DAS-VSP primary reflection wavefields from wells **(A)** B1 and **(B)** B2. The original depth migration profiles are converted to the time domain for display.



**FIGURE 12**
Schematic diagram showing the first-order multiple imaging principle.

The current study primarily utilized P-wave and compared it to the surface seismic image. However, the S-wave field showed a fairly strong recording even at the near-offset range, given the well deviation. Figure 9 shows an example up-going wavefield of a near-offset shot gather in two-way-time (TWT). The P- and converted S-wave reflections are marked by blue solid and red dashed lines, respectively. Both wavefields are of sufficient quality for utilization. In this example, we further separated the P- and S-mode using an F-K filter in TWT. The separated P-wavefield for acoustic imaging is shown in Figure 9B. A shear-wave image can be achieved when a reasonable S-wave velocity model is available, which is not covered in the present study.

## 4.4 3D DAS-VSP imaging

Among a variety of well-developed depth migration algorithms, the pre-stack Gaussian beam migration (GBM) has proven advantages in efficiency compared to wave-equation-based methods (e.g., reverse-time-migration) as well as high imaging accuracy compared to the standard Kirchhoff migration (Hill, 1990 and 2001; Etgen et al., 2009). Therefore, we applied this method to migrate the 3D VSP datasets of considerable volume. By constructing the Green's function with the Gaussian beams, the GBM method allows a weighted summation of the effective rays around the imaging point, which can be expressed as

$$G\left(x, x', \omega\right) = \frac{i}{4\pi} \int \frac{dP_x}{P_z} u_{GB}\left(x, x', \omega\right) = \frac{i}{4\pi} \int \frac{dP_x}{P_z} A_{GB} \exp\left\{i\omega t_{GB}\right\},$$

(5)

where the positions of the source and the calculation point are represented by x and $x'$, respectively. The horizontal and vertical components of the initial slowness of the central ray are denoted by $P_x$ and $P_z$, respectively. $t_{GB}$ and $A_{GB}$ are the complex travel time and amplitude, respectively. Finally, $u_{GB}$ represents the energy of the Gaussian beam.

Figure 8A shows an example raw shot gather. As the raw record includes complex wavefields whose behaviors can be differentiated in various domains, we utilized a combination of filters to separate the P-wave primary reflections: we first applied the median and $\tau - p$ filters to isolate the down-going and up-going fields. As the reflections in this area are distributed mostly in the up-going wavefield, we further separated the P-wave reflections using the F-K and the median filters, as shown in Figure 8B. Figure 8C shows the removed down-going field, which contained the transmitted P- and S-waves.

**FIGURE 13**
Separation of upgoing wavefield and down-going multiples in the $\tau - p$ domain for wells **(A)** B1 and **(B)** B2.
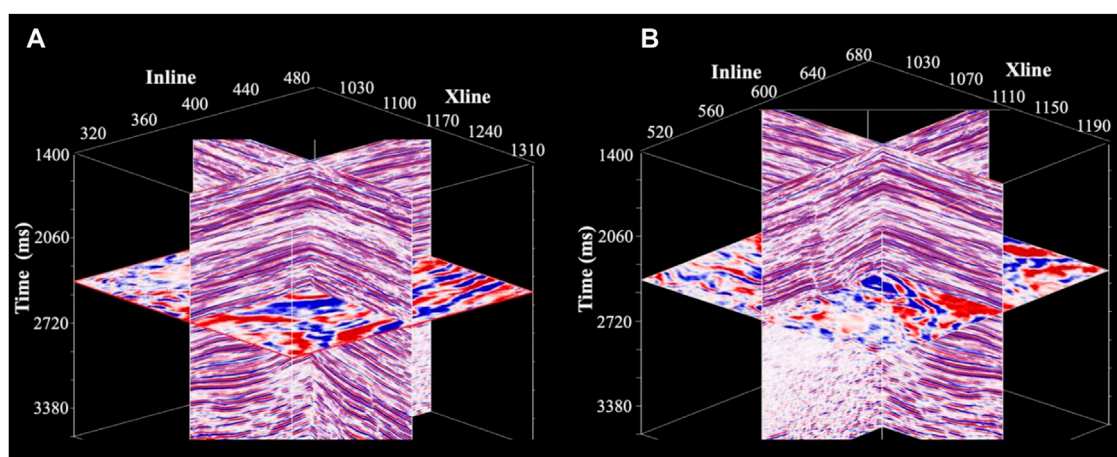


**FIGURE 14**
Final images of the 3D DAS-VSP down-going multiples from wells **(A)** B1 and **(B)** B2. The original depth migration profiles are converted to the time domain for display.
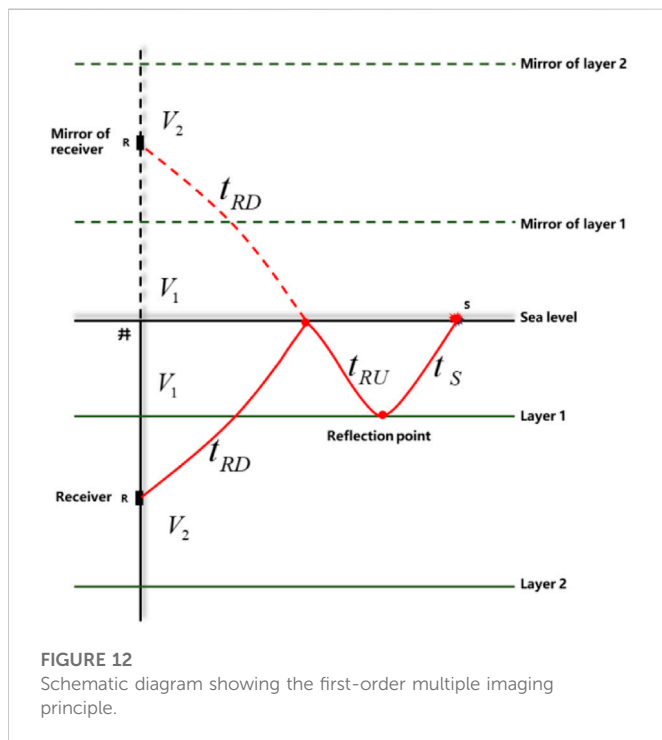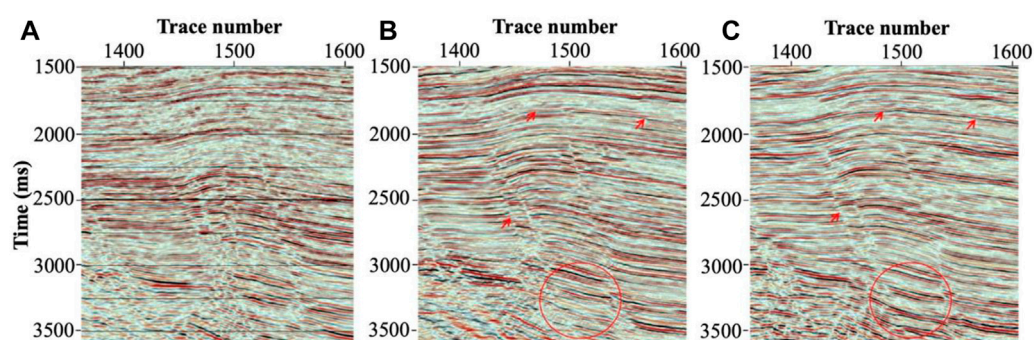


**FIGURE 15**
Comparisons of images from the **(A)** streamer, **(B)** OBN, and **(C)** DAS-VSP data.
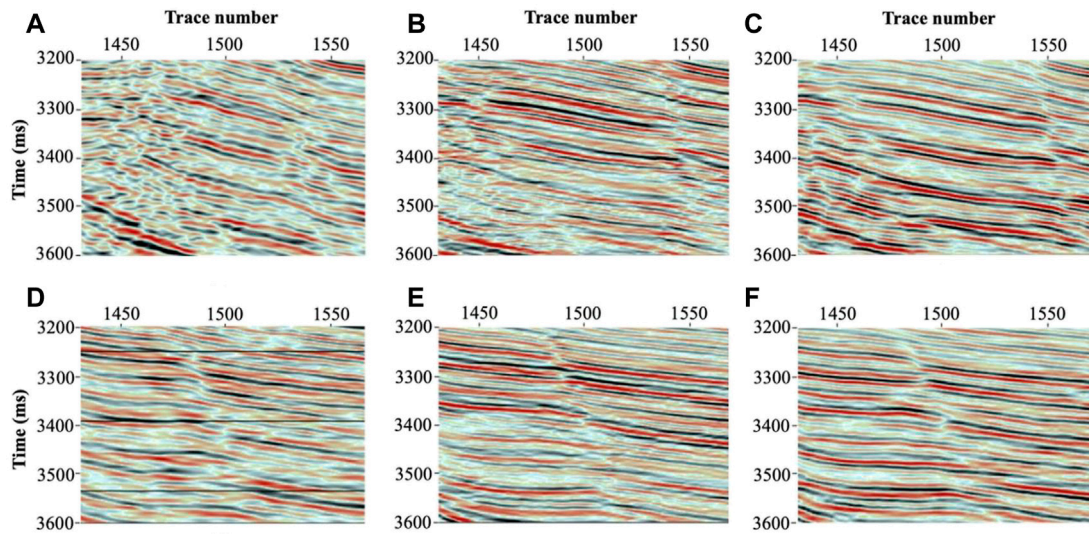
**FIGURE 16**
Enlarged images around the target areas of the **(A)** streamer data, **(B)** OBN data and **(C)** DAS-VSP data from Well B1; as well as the **(D)** streamer data **(E)** OBN data and **(F)** DAS-VSP data from Well B2.

Based on the characteristics of the VSP acquisition configuration, the down-going wavefield from the source to the reflector is considered a forward wavefield, while the up-going wavefield from the reflection point to the receiver is taken as a reverse wavefield. The VSP common-shot-gather pre-stack Gaussian beam depth migration is implemented by first tracing the ray between the source and the receiver. Then, the forward wavefield on the source side and the reverse wavefield on the receiver side are calculated. Finally, we obtain the VSP image by cross-correlating the forward and reverse wavefields. Eq. 6 gives the image condition of the offset VSP common-shot-gather pre-stack Gaussian beam depth migration:

$$I(X) = \frac{-1}{2\pi} \int d\omega \int dX_S \int dX_S \frac{\partial G^*(X, X_R, \omega)}{\partial z_R}$$
$$\times G^*(X, X_S, \omega) D_S(X_S, X_R, \omega), \quad (6)$$

where $G^*(X, X_S, \omega)$ and $G^*(X, X_R, \omega)$ denote the Green's function from the source to the image point and from the image point to the receiver, respectively.

### 4.4.1 Migration of the primary P-wave reflection wavefield

We first image the primary P-wavefield using a 3D velocity profile built from the surface seismic survey. Figure 10 displays an example cross-section of the velocity model projecting the trajectory of Well B1. The final 3D DAS-VSP imaging profiles for both wells are shown in Figure 11. Some fine and enriched details of the layer boundaries, as well as the fault planes around the borehole region, can be revealed on the VSP images to support a better interpretation of the fault/fracture networks and the subsurface evaluation.

### 4.4.2 Migration of down-going multiples

The offshore DAS-VSP data recorded high-quality down-going wavefields, as shown in Figure 8C, which includes not only the primary transmissions but also rich multiples following the first arrivals, which can potentially be utilized for imaging. As the corresponding reflectors of the multiples showed a much wider distribution than the primary reflectors, they can effectively broaden the VSP image range given the proper imaging condition. Although many studies have discussed the mirror migration of down-going multiples in VSP, including interferometric migration by He et al. (2007), generalized Radon transform (GRT) migration by Li et al. (2019), and reverse time migration (RTM) by Jiang et al. (2016); Cheng et al. (2022), no or very few publications have yet proposed migrating the multiples in a DAS-VSP survey using GBM. Inspired by the idea of mirror migration of the down-going wave of the OBN data (as illustrated in Figure 12), we performed mirror migration in the VSP common-receiver gather to migrate the down-going multiples using the GBM method (Jiang et al., 2022; O'Brien et al., 2013). In addition, the down-going multiples show attenuation and dispersion due to the increased travel distances compared to the primaries. Thus, the Q-compensated GBM (Gray and Bleistein, 2009) was reinforced to achieve higher-resolution images.

A separated down-going multiple wavefield is a prerequisite before imaging. As shown in Figure 13, the primary reflection in the P-wave upgoing domain and the down-going multiples (after the first arrivals were rejected) were mostly separated in the $\tau - p$ domain. The primary upgoing reflections appeared to be more focused in the negative wavenumber domain, while the down-going multiples were likely to be more extensively distributed in the positive wavenumber domain. However, it remains challenging to distinguish the first- and higher-order multiples for the massive volume of 3D field data when the velocity model is highly uncertain. Future studies are needed to further improve the first- and higher-order multiple wavefields separation for more enhanced images.

The 3D DAS-VSP down-going wavefields for wells B1 and B2 are migrated and displayed in Figures 14A, B. Both images were converted

to the time domain to compare time domain surface seismic sections. Figures 15A–C show a comparison of the 2D projected images of the streamer data, OBN data, and the DAS-VSP, respectively. Among the three images, that of the streamer data was more contaminated by noises, especially deeper in the section. The OBN image showed better SNR compared to the streamer image. However, the image quality degraded in the deeper section. The DAS-VSP image was superior, with (1) greatly improved SNR even for deep targets, as indicated by the red circle; and (2) more continuous and smoother events compared to the other two images. Moreover, some details (indicated by the red arrows) were enhanced in the DAS-VSP image, which might support better formation and fault network interpretation. Enlargement of the portion around the target area (marked by the red circles in Figure 15) for the streamer, OBN, and DAS-VSP data, respectively, as shown in Figures 16A–C, showed that the deep target was clearly improved in the 3D DAS-VSP survey, with higher SNR and better amplitude recovery. Similarly, we observed enhancements in the 3D DAS-VSP image (Figure 16F) obtained from Well B2 compared to those from the streamer (Figure 16D) and OBN (Figure 16E) surveys.

## 5 Conclusion

The results of this study demonstrated the capability of the evolving DAS technology to characterize the subsurface complexity using an offshore 3D VSP survey acquired in the East China Sea. We explore practical solutions to several characteristic challenges related to this emerging fiber-optic sensing technology applied in a marine VSP acquisition case. We analyzed the cable-reverberation ringing noise in the DAS acquisition system and effectively eliminate it using the $\tau - p$ domain filter. The strong ghost waves/surface multiples often observed in offshore seismic surveys were separated and suppressed in the $f - k/f - p$ domain. We migrated both the primary reflection wavefield and the down-going multiples using the pre-stack Gaussian beam depth migration. Taking advantage of the high-quality down-going multiples, we provided illumination coverage in addition to the primary reflection field. The Q-compensated migration can be helpful to improve the resolution of the images of multiples. Given that the incident angle of the multiples is often smaller than the primary waves to the same source–receiver pair for the flat layers investigated by a VSP configuration, utilizing the multiple wavefields might benefit the DAS sensing system, as the fiber cable loses its sensitivity large-angle incident P-wavefields. The final image of the down-going multiple supplements the primary reflection image with significantly improved lateral illumination of shallower depth ranges. The current 3D DAS-VSP image showed improvement compared to both streamer and OBN surveys, allowing better subsurface interpretation and formation evaluation.

## Data availability statement

The raw data supporting the conclusion of this article will be made available by the authors, without undue reservation.

## Author contributions

YC, JZ, CL, ZC, and PD contributed to the study conception and design. GH and JL supervised and outlined the manuscript, respectively. YC and PD processed the data and prepared the plots. JZ and YC wrote the manuscript. All authors contributed to the manuscript revision and approved the submitted version.

## Conflict of interest

YC, ZC, PD, and JL were employed by BGP Inc. China National Petroleum Co., and CL was employed by Shanghai Petroleum Corporation, Ltd.

The remaining authors declare that the research was conducted in the absence of any commercial or financial relationships that could be construed as a potential conflict of interest.

## Publisher's note

All claims expressed in this article are solely those of the authors and do not necessarily represent those of their affiliated organizations, or those of the publisher, the editors, and the reviewers. Any product that may be evaluated in this article, or claim that may be made by its manufacturer, is not guaranteed or endorsed by the publisher.

## References

Acocella, V. (2015). Grand challenges in Earth science: Research toward a sustainable environment. *Front. Earth Sci.* 3, 68. doi:10.3389/feart.2015.00068

Bernth, H., and Sonneland, L. (1983). Society of Exploration Geophysicists, 264–265.Wave field extrapolation techniques for prestack attenuation of water reverberations, *SEG Int. Expo. Annu. Meet*,

Blias, E. (2007). VSP wavefield separation: Wave-by-wave optimization approach. *Geophysics* 72 (4), T47–T55. doi:10.1190/1.2744124

Cheng, L., Simmons, J., and Tura, A. (2022). Society of Exploration Geophysicists, 3594–3598.Imaging and fold comparison of mirror reverse time

migration vs. interferometric imaging for VSP data, *SEG Tech. Program Expand. Abstr*,

Daley, T. M., Freifeld, B. M., Ajo-Franklin, J., Dou, S., Pevzner, R., Shulakova, V., et al. (2013). Field testing of fiber-optic distributed acoustic sensing (DAS) for subsurface seismic monitoring. *Lead. Edge* 32 (6), 699–706. doi:10.1190/tle32060699.1

Etgen, J., Gray, S. H., and Zhang, Y. (2009). An overview of depth imaging in exploration geophysics. *Geophysics* 74 (6), WCA517–WCA17. doi:10.1190/1.3223188

Fang, G., Li, Y. E., Zhao, Y., and Martin, E. R. (2020). Urban near surface seismic monitoring using distributed acoustic sensing. *Geophys. Res. Lett.* 47 (6), e2019GL086115. doi:10.1029/2019gl086115

Gaiser, J. (2016). 3C seismic and VSP: Converted waves and vector wavefield applications. *Soc. Explor. Geophys.* 36.

Gray, S. H., and Bleistein, N. (2009). True-amplitude Gaussian-beam migration. *Geophysics* 74 (2), S11–S23. doi:10.1190/1.3052116

Hadley, C., Peters, D., Vaughan, A., and Bean, D. "Gumusut-Kakap project: Geohazard characterization and impact on field development plans," in Proceedings of the International Petroleum Technology Conference, Bangkok, Thailand, March 2008 (European Association of Geoscientists & Engineers). cp-148.

He, R., Hornby, B., and Schuster, G. (2007). 3D wave-equation interferometric migration of VSP free-surface multiples. *Geophysics* 72 (5), S195–S203. doi:10.1190/1.2743375

Hill, N. R. (1990). Gaussian beam migration. *Geophysics* 55 (11), 1416–1428. doi:10.1190/1.1442788

Hill, N. R. (2001). Prestack Gaussian-beam depth migration. *Geophysics* 66 (4), 1240–1250. doi:10.1190/1.1487071

Horne, S., Armstrong, P., and Soulas, S. (2020). Society of Exploration Geophysicists, 495–499.Deepwater DAS walkaway VSP analysis, *SEG Tech. Program Expand. Abstr,*

Huang, X., Greenhalgh, S., Han, L., and Liu, X. (2022). Generalized effective biot theory and seismic wave propagation in anisotropic, poroviscoelastic media. *J. Geophys. Res. Solid Earth* 127 (3), e2021JB023590. doi:10.1029/2021jb023590

Jiang, T., Zhan, G., HanceSugianto, T. S., Soulas, S., and Kjos, E. (2016). Society of Exploration Geophysicists, 5582–5586.Valhall dual-well 3D DAS VSP field trial and imaging for active wells, *SEG Tech. Program Expand. Abstr,*

Jiang, Z., Sheng, J., Yu, J., Schuster, G. T., and Hornby, B. E. (2007). Migration methods for imaging different order multiples. *Geophys. Prospect.* 55 (1), 1–19. doi:10.1111/j.1365-2478.2006.00598.x

Krohn, D. A., MacDougall, T., and Mendez, A. (2014). *Fiber optic sensors: Fundamentals and applications*. Bellingham, WA, USA: Spie Press, 233–310.

Li, W., Mao, W., and Liang, Q. (2019). Society of Exploration Geophysicists, 5325–5329.Joint imaging with primaries and multiples of VSP data by GRT migration, *SEG Tech. Program Expand. Abstr,*

Li, Y., Karrenbach, M., and Ajo Franklin, J. B. (2021). A literature review: Distributed acoustic sensing (DAS) geophysical applications over the past 20 years. *Distributed Acoust. Sens. Geophys. Methods Appl.*, 229–291.

Li, Y., Wu, H., Wong, W., Hewett, B., Liu, Z., and Mateeva, A. (2015). Society of Exploration Geophysicists, 5285–5289.Velocity analysis and update with 3D DAS-VSP to improve borehole/surface seismic images, *SEG Tech. Program Expand. Abstr,*

Martuganova, E., Stiller, M., Bauer, K., Henninges, J., and Krawczyk, C. M. (2021). Cable reverberations during wireline distributed acoustic sensing measurements: Their nature and methods for elimination. *Geophys. Prospect.* 69 (5), 1034–1054. doi:10.1111/1365-2478.13090

Mateeva, A., Lopez, J., Chalenski, D., Tatanova, M., Zwartjes, P., Yang, Z., et al. (2017). 4D DAS VSP as a tool for frequent seismic monitoring in deep water. *Lead. Edge* 36 (12), 995–1000. doi:10.1190/tle36120995.1

Mateeva, A., Mestayer, J., Cox, B., Kiyashchenko, D., Wills, P., Lopez, J., et al. (2012). Advances in distributed acoustic sensing (DAS) for VSP. SEG technical program expanded abstracts. *Soc. Explor. Geophys.* 5.

Mizuno, T., and Ali, S. (2021). Society of Exploration Geophysicists, 422–426.Benchmarking DAS VSP migration methods with geophone VSP migration: Case study for the generalized Radon transform migration, *First Int. Meet. Appl. Geoscience Energy,*

O'Brien, J., Farmani, B., and Atkinson, B. (2013). VSP imaging using free-surface multiples: A case study from the gulf of Mexico. *Lead. Edge* 32 (10), 1258–1266. doi:10.1190/tle32101258.1

Oristaglio, M. L. (1985). A guide to current uses of vertical seismic profiles. *Geophysics* 50 (12), 2473–2479. doi:10.1190/1.1441878

Stewart, R. R., Huddleston, P. D., and Kan, T. K. (1984). Seismic versus sonic velocities: A vertical seismic profiling study. *Geophysics* 49 (8), 1153–1168. doi:10.1190/1.1441745

Su, A., Chen, H., Chen, X., He, C., Liu, H., Li, Q., et al. (2018). The characteristics of low permeability reservoirs, gas origin, generation and charge in the central and Western Xihu depression, East China Sea Basin. *J. Nat. Gas Sci. Eng.* 53, 94–109. doi:10.1016/j.jngse.2018.01.034

Turner, G. (1990). Aliasing in the tau-p transform and the removal of spatially aliased coherent noise. *Geophysics* 55 (11), 1496–1503. doi:10.1190/1.1442797

Walker, C., and McIntosh, S. "Autonomous nodes–the future of marine seismic data acquisition?," in Proceedings of the 12th International Congress of the Brazilian Geophysical Society & EXPOGEF, Rio de Janeiro, Brazil, August 2011 (Society of Exploration Geophysicists and Brazilian Geophysical Society), 1–6.

Wang, C., Gu, H. M., Xu, Z. Q., Fang, Z. Y., Tang, Y. J., Zhang, J. N., et al. (2016). The application of adaptive iteration inversion algorithm to deghost for marine variable-depth streamer data in frequency-slowness domain. *Chin. J. Geophys.* 59 (12), 4677–4689.

Weglein, A. B., and Dragoset, W. H. (2005). *Multiple attenuation*. Tulsa, Oklahoma: Society of Exploration Geophysicists.

Willis, M. E., Ellmauthaler, A., Wu, X., and LeBlanc, M. J. (2021). Important aspects of acquiring distributed acoustic sensing (DAS) data for geoscientists. *Distributed Acoust. Sens. Geophys. Methods Appl.*, 33–44.

Willis, M. E., Wu, X., Palacios, W., and Ellmauthaler, A. (2019). Society of Exploration Geophysicists, 5310–5314.Understanding cable coupling artifacts in wireline-deployed DAS VSP data, *SEG Int. Expo. Annu. Meet.*

Wilson, G. A., Willis, M. E., and Ellmauthaler, A. (2021). Evaluating 3D and 4D DAS VSP image quality of subsea carbon storage. *Lead. Edge* 40 (4), 261–266. doi:10.1190/tle40040261.1

Wo, Y., Zong, J., Hu, H., Zhou, H. W., and Stewart, R. R. (2021). Velocity model building for single-offset VSP data via deformable-layer tomography: A Texas salt dome example. *Geophysics* 86 (4), U63–U73. doi:10.1190/geo2020-0394.1

Yilmaz, O., and Baysal, E. European Association of Geoscientists & Engineers, June 2015, An effective ghost removal method for marine broadband seismic data processing, Proceedings of the 77th EAGE Conference and Exhibition, Madrid, Spain,

Yu, G., Cai, Z., Chen, Y., Wang, X., Zhang, Q., Li, Y., et al. (2016). Walkaway VSP using multimode optical fibers in a hybrid wireline. *Lead. Edge* 35 (7), 615–619. doi:10.1190/tle35070615.1

Zhan, G., Li, Y., Tura, A., Willis, M., and Martin, E. (2019). Introduction to special section: Distributed acoustic sensing and its oilfield potential. *Interpretation* 7 (1). doi:10.1190/int-2019-0116-spseintro.1

Zhan, Z. (2020). Distributed acoustic sensing turns fiber optic cables into sensitive seismic antennas. *Seismol. Res. Lett.* 91 (1), 1–15. doi:10.1785/0220190112

Zhang, M., Zhao, X., Wilson, G. A., Willis, M. E., and Barrios, O. (2020). Q estimation from geophone and DAS VSPs. SEG technical program expanded abstracts. *Soc. Explor. Geophys.*, 475–479.

Zhu, T., Shen, J., and Martin, E. R. (2021). Sensing Earth and environment dynamics by telecommunication fiber-optic sensors: An urban experiment in Pennsylvania, USA. *Solid earth.* 12 (1), 219–235. doi:10.5194/se-12-219-2021

# Mechanical mechanism of rock mass slabbing aggravating toppling failure

Junchao Cai[1,2,3,4], Shuqiang Lu[4]*, Kan Li[5], Zhongteng Wu[2,3], Rui Zhao[6] and Junping Wang[1]

[1]School of Civil Engineering, Henan University of Science and Technology, Luoyang, China, [2]State Key Laboratory of Geohazard Prevention and Geoenvironment Protection, Chengdu University of Technology, Chengdu, China, [3]Fujian Key Laboratory of Geohazard Prevention, Fuzhou, China, [4]Key Laboratory of Geological Hazards on Three Gorges Reservoir Area (China Three Gorges University), Ministry of Education, Yichang, China, [5]Chengdu East Group Co., Ltd, Chengdu, China, [6]Shuifa Planning and Design Limited Company, Jinan, China

Many slabbing rock masses have emerged in hydropower slopes and underground engineering, with the construction of basic engineering and resource development projects along the zone of the Belt and Road. The anti-dip slabbing rock mass is prone to toppling and the degree of slabbing controls the development of toppling deformation. There are a few reports on the mechanical mechanism of rock mass toppling deformation after slabbing. Based on the analysis of the genetic conditions of rock mass slabbing, the influence of rock mass after slabbing on toppling deformation was explored by means of the mechanics method. The toppling bending deflection (TBD) and the toppling fracture depth (TFD) were selected as the analysis indexes, and the response regularity of slabbing on toppling rock mass was analyzed with examples. The results show that the width and thickness of the slabbing rock mass become narrower and thinner, the toppling bending deflection (TBD) increases, the toppling fracture depth (TFD) decreases, and the toppling deformation and failure intensify. The TBD is independent of the width of rock mass slabbing under self-weight, and the change of TBD is slow when the slab beam slabbing number ($n$) of thickness is <4 and fast when the slabbing number is above 4. The first TFD decreases fast when $w$ is <2.0m and it tends to be stable when $w$ is above 2.0m. The first TFD reduces relatively fast with the decrease in the thickness ($t$) of the slab beam. The result of this study can provide a reference for the treatment and evaluation of slabbing rock mass toppling deformation.

KEYWORDS

rock mass slabbing, toppling failure, mechanical model, mechanism of slabbing, TFD

## 1. Introduction

   With the implementation of the Belt and Road strategy, many infrastructure projects and resource development projects along the zone have been put into construction. The excavation of hydropower slopes, hydropower underground chambers, and deep tunnels exposes a large number of rock mass slabbing failures (Wu et al., 2010; Sun et al., 2012; Qiu et al., 2014; Zhou et al., 2015; Liu et al., 2017; Zhou et al., 2018; Qin et al., 2020; Xu et al., 2021; Fujii et al., 2022).

The rock mass with slab fracture structure is divided by fracture surfaces (slab fracture surfaces) that are nearly parallel to a certain extent. The rock mass among the slab fracture surfaces presents a slab-like feature. The slabbing rock mass structure is called the slab fracture structure. The slabbing failure rock mass consists of a slab fracture structure formed by excavation unloading of intact rock mass, relatively intact rock mass, and massive rock mass, and a natural slab fracture structure formed by long-term geological processes. Due to the difference in output characteristics of the slab fracture rock mass, the rock slab with anti-dip characteristics is prone to toppling deformation and failure, which are common in hydropower, traffic engineering slopes, hydropower buildings, and tunnels (Goodman, 2013). Toppling failure has been reported in more and more situations with the construction of mines, highways, hydropower stations, and so on. Many scholars have carried out research on the evolution mechanism of toppling failure and identification of instability failure (Huang, 2008; Huang et al., 2017; Tao et al., 2019; Bao et al., 2022; Nie et al., 2022; Zhu et al., 2022; Li et al., 2022a). The cantilever beam theory was introduced to study the rock mass with slab fracture structure (Goodman and Bray, 1976; Sun and Zhang, 1985; Aydan and Kawamoto, 1992; Amini et al., 2009, 2012; Liu H. J. et al., 2016; Alejano et al., 2018; Zheng et al., 2018; Cai et al., 2022a). Ni and Ye (1987) compared and analyzed the similarities and differences between the slab fracture structure rock mass and the layered rock mass, and concluded that the failure forms of the slab fracture structure are flexural toppling failure and buckling instability. Many scholars have carried out research on the slabbing rock mass and its genetic mechanism and achieved fruitful results. Some scholars analyzed the characteristics of slope rock mass slabbing under different stress modes caused by valley undercutting, excavation, and long-term geological processes from the perspective of supergene transformation and aging deformation (Huang et al., 1994; Tao et al., 2000; Huang, 2008; Huang et al., 2017; Cai et al., 2019; Liang et al., 2022; Li et al., 2022b). The latest research show that a large number of slabbing failures have also emerged in the excavation of underground chambers and tunnels (Du et al., 2016; Gong et al., 2018, 2020; Pan et al., 2020; Jiang et al., 2021; He et al., 2022; Tang et al., 2022; Wang et al., 2022). Huang (2008) and Huang et al. (2017) proposed the three stages of the development process of high slope and the characteristics of slope stress field with undercutting or excavation unloading, which is of great significance to reveal the causes of rock mass slabbing under stress conditions at different development stages of the slope and also deepen the understanding of rock mass slabbing phenomena exposed by the excavation of deep tunnels and hydropower underground chambers.

Slabbing transformed the toppled rock mass, making the original rock slab and rock block thinner and narrower. The mechanical strength parameters (rock block and structural plane) are reduced due to long-term geological action, which further aggravates the degree of rock mass toppling deformation, indicating that the occurrence of toppling deformation is closely related to the mechanical and geometric characteristics of the rock slab. There are few reports on the regularity and mechanical mechanism of rock mass toppling deformation after slabbing. This study mainly analyzes

the geometric size of the rock slab of the toppled rock mass after slabbing, which is mainly reflected in the influence of the width and thickness of the rock slab. Based on the causes analysis of rock mass slabbing, this study uses mechanical methods to analyze the mechanical mechanism by which rock mass slabbing aggravates toppling deformation and explains its influence degree from two aspects: the toppling bending deflection (TBD) and the toppling fracture depth (TFD), and analyzes the influence law of rock mass slabbing on toppling deformation with examples.

# 2. Genetic condition of rock mass slabbing

The rock mass slabbing process of slope can be described as follows: the stress redistribution of slope caused by valley undercutting or engineering excavation, and the difference of unloading rebound value caused by the difference of rock mass structure, lithological composition, and mechanical properties produces tensile stress and shear stress concentrations within the unloading influence depth range. The stress differentiation makes the tensile stress concentration zone produce a tension fracture surface, and the compressive stress concentration area forms shear- and compression-induced tension fracture surfaces, which are nearly parallel to the unloading surface (Figures 1, 2). With the late transformation, the rock mass with the slab fracture structure has further deteriorated. The different cutting combination relationship between the slab fracture structure rock mass and the slope surface or free face where it is located forms the types of slope such as anti-dip slope, dip slope, and oblique slope, and the toppling bending deformation occurs on the anti-dip slope under the influence of external factors and self-weight (Huang et al., 1994; Huang, 2008; Huang et al., 2017). Meanwhile, considering the rheological properties of rock mass, the deterioration of rock mass properties caused by water and weathering and the toppling deformation of the anti-dip rock slope intensified.

The rock mass slabbing is the result of the combined action of internal and external factors. The internal factors are the decisive condition, and the external factors play the role of triggering and inducing. The internal factors include the mineral composition characteristics and internal structure of rocks. The external factors include stress state, excavation, earthquake, weathering, and other deterioration factors.

## 2.1. Internal defect of rock mass

Mineral particles constitute the rock, and the boundary between mineral particles and the trace cutting through mineral particles are the places where subtle cracks (such as cracks, small weak surfaces, and other defects) are generated. The size, arrangement, and combination of mineral particles in the rock and the connection between particles are the internal factors of rock mass slabbing. The anisotropy of rock caused by the directional arrangement of mineral particles determines the dominant orientation of the slab fracture

**FIGURE 1**
Rock mass slabbing of slope under different stress states.



**FIGURE 2**
Differential resilience of rock strength differences. **(A)** loading and **(B)** unloading.
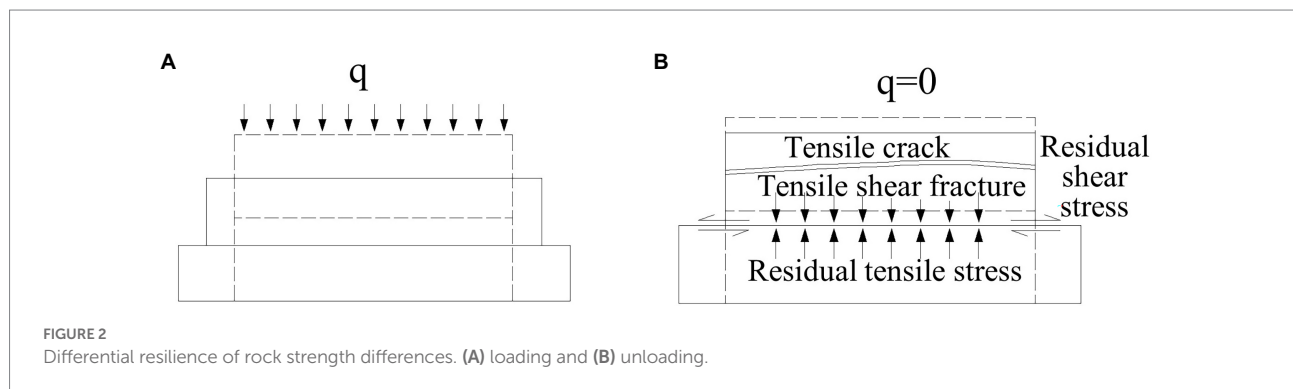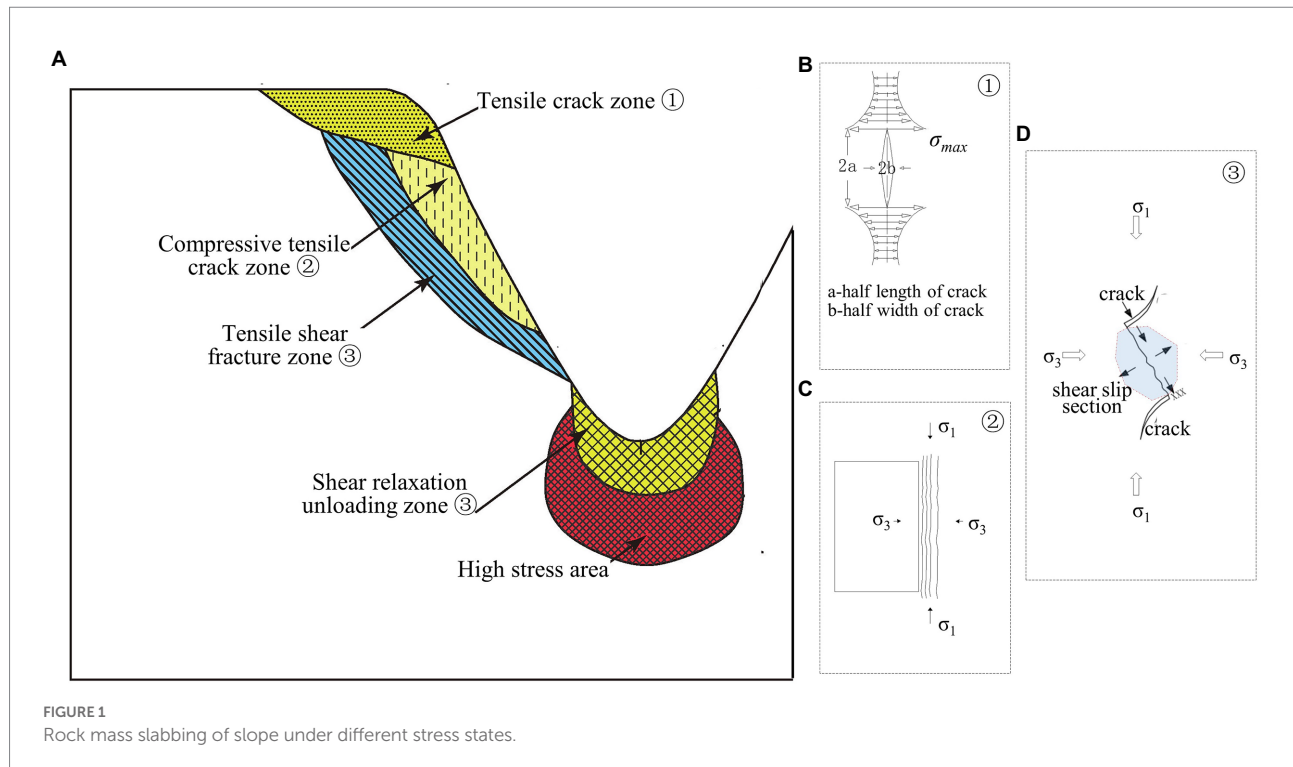
surface. When the condition of stress concentration is sufficient, the rock will undergo intergranular fracture, Peristaline fracture, and cleavage transgranular fracture. With the increase of deformation, the rock will undergo microcracks to slab fracture. Therefore, the grain arrangement and internal defects lay the material structure foundation for the rock mass slabbing and affect the development direction and degree of rock mass slabbing.

## 2.2. External environmental factors

The external factors that affect the rock mass slabbing mainly include stress state (stress differentiation and differential unloading), weathering, water action, earthquake (dynamic load), and human activities.

Slabbing of rock mass may be caused by valley undercutting and excavation of slope, chamber, etc. The stress state of rock mass transits from the initial compression state to the tensile

state. The stress state goes through compression, shear, and tension (Figure 1). Under various mechanical behaviors, the rock mass deteriorates into a slab-like rock mass. The tension, shear, and compression generated in the stress differentiation and the difference in rock mass material properties lead to the differential unloading rebound, and the stress concentration and residual stress occur in the rock mass within a certain range of the unloading surface, intensifying the slabbing failure (Figure 2).

In addition to the influence of the change of stress state on rock mass slabbing, weathering, earthquake, water, and human activities, all promote the occurrence of slabbing and further fragmentation and deterioration of slabbing rock mass.

1. Under the weathering of minerals and rocks, the connection degree of particles in the rock mass, the undulation and roughness of slab fracture surface weaken,

the overall strength decreases, and the porosity increases, further providing a channel for the action of water.

2. In the process of stress wave propagation under dynamic load, the reflection will occur at the relatively free interface with different medium characteristics. At the interface, the incident wave will generate a tensile wave (tensile stress), and the greater the difference in elastic modulus between the two mediums, the greater the tensile stress. The cumulative effect of repeated dynamic loads aggravates the development of rock mass slabbing.

3. The water combines with the hydrophilic substances on the slab fracture surface for lubrication, or some minerals on the slab fracture surface will be hydrolyzed and dissolved. The expansion of frozen volume, hydrostatic pressure, and hydrodynamic pressure of water in the slab fracture surface will further aggravate the expansion of fractures.

4. The excavation and reconstruction of human activities provide free space for unloading and forming slabbing. The blasting, vibration, and other artificial dynamic loads will further trigger and intensify the rock mass slabbing.

# 3. Slabbing effect of toppling deformation based on bending deflection

## 3.1. Mechanical model analysis

The influence of rock mass slabbing under self-gravity on toppling bending deflection (TBD) is considered. The thickness and width of the rock slab are reduced due to slabbing, and the adhesion between the slab fracture surfaces is lost or decreased due to various factors, which makes it easier to produce interlaminar dislocation in the process of toppling and bending.

Before rock mass slabbing, the toppling bending deflection (TBD) caused by the self-weight is estimated by Equation 1. After rock mass slabbing, the flexural stiffness of the rock slab decreases greatly and the toppling bending deflection (TBD) increases significantly. It is assumed that the slabbing of the isothick slab in rock formation forms $n$ layer m segment (Figure 3), and then the toppling bending deflection (TBD) caused by the bending moment provided by the self-weight is estimated by Equation 2 as follows:

$$\omega_1 = \frac{3 \cdot \gamma \cdot l^4 \cdot \sin\alpha}{2 \cdot E \cdot t^2} \qquad (1)$$

$$\omega_2 = \frac{3 \cdot n^2 \cdot \gamma \cdot l^4 \cdot \sin\alpha}{2 \cdot E \cdot t^2} \qquad (2)$$

where $\alpha$ is the dip angle of the rock beam, $l$ is the length of the cantilever beam segment, $t$ is the thickness of the beam, $r$ is the beam weight, and $E$ is the deformation modulus of the slabbing rock mass. It can be seen from Equation 2 that the toppling bending deflection (TBD) of the rock slab increases after the rock mass slabbing.

Moreover, the more serious the rock mass slabbing is, the more severe the toppling flexural stiffness of the rock slab is reduced, and the more easily the rock slab is inclined to topple and bend. Then, the toppling deformation will develop gradually and enter the creeping stage considering the time effect (Cai et al., 2022b).

Considering the particularity of rock lithology, there will be a tension-neutral layer not located on the geometric central axis of its section. There is a difference between the deformation and the assumption (Figures 4, 5).

According to Figures 4, 5, $w$ is beam width, $t$ is beam thickness, $A$ is the area of beam section, $t_t$ is tension zone height, and $t_c$ is compression zone height. $E_c$ and $E_t$ are compression deformation modulus and tensile deformation modulus, respectively. If $E_c = E_t$, the neutral axis position coincides with the symmetry axis of the section, that is, $t_t = t_c$. But the tensile modulus and compressive modulus of rock mass are obviously different, that is, $E_c \neq E_t$, and even if the section has a symmetry axis position, the neutral axis position is inconsistent with the symmetry axis position of the section, that is, $t_t \neq t_c$.

$$N = \int_0^A \sigma(y)\,dA = E_t \cdot \frac{1}{\rho} \cdot w \cdot \frac{t_t^2}{2} - E_c \cdot \frac{1}{\rho} \cdot w \cdot \frac{t_c^2}{2} = 0 \qquad (3)$$

$$t_t = t_c\sqrt{\frac{E_c}{E_t}} = t \left/ \left(1 + \sqrt{\frac{E_c}{E_t}}\right)\right. \qquad (4)$$

The moment of inertia of the rock slab section can be processed by the equal-generation method, and $E_t$ is used instead of $E_c$, then the width above the neutral axis increases to $w'$, which is introduced and called the equivalent width of the section, and $\frac{w'}{w} = \frac{E_c}{E_t}$, the moment of inertia of the entire section can be expressed as Equation 5, then simplified to Equation 6.

$$I = \int_0^{t_c} w' \cdot y^2 \cdot dy + \int_0^{t_t} w \cdot y^2 \cdot dy = \frac{1}{3} \cdot w' \cdot t_c^3 + \frac{1}{3} \cdot w \cdot t_t^3 \qquad (5)$$
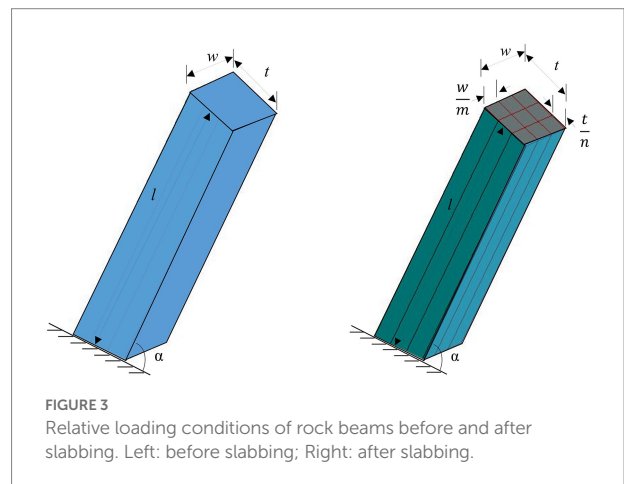


**FIGURE 3**
Relative loading conditions of rock beams before and after slabbing. Left: before slabbing; Right: after slabbing.
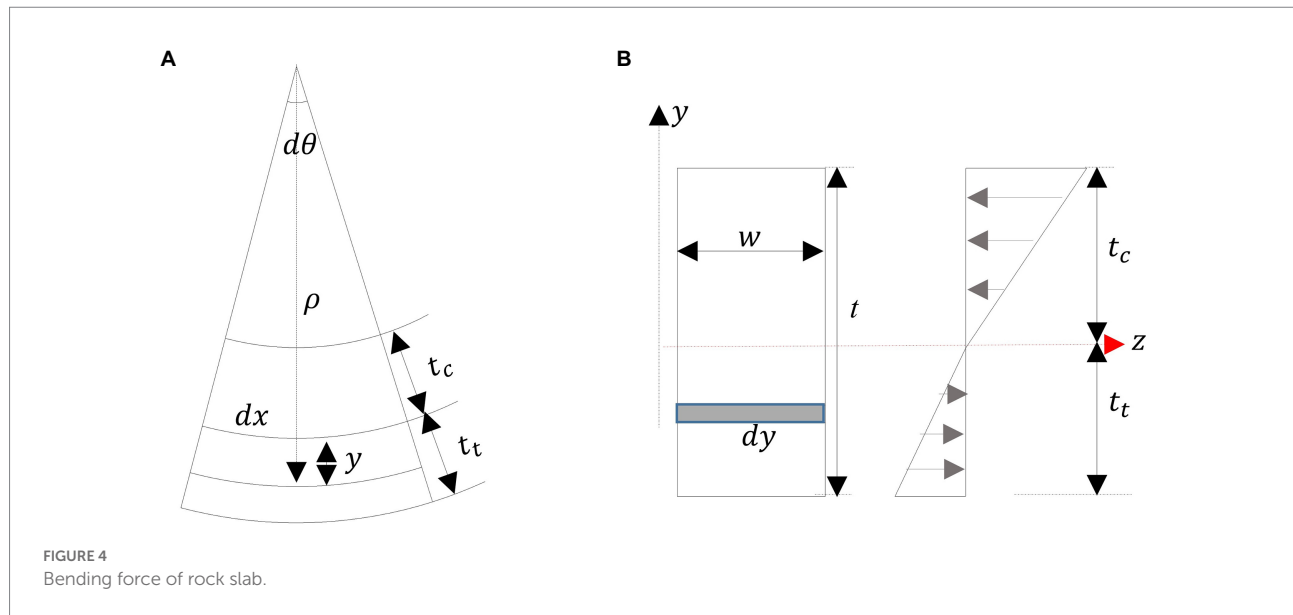
**FIGURE 4**
Bending force of rock slab.
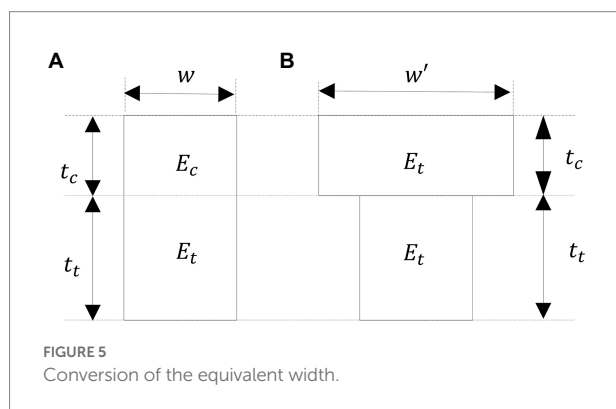


**FIGURE 5**
Conversion of the equivalent width.

$$I = w \cdot t^3 \cdot \frac{1 + \left(\frac{E_t}{E_c}\right)^{0.5}}{3 \cdot \left[1 + \left(\frac{E_c}{E_t}\right)^{0.5}\right]^3} \qquad (6)$$

Then, the difference in tensile and compressive characteristics of rock mass is considered, and the toppling bending deflection (TBD) caused by self-weight is estimated by Equation 7. The toppling bending deflection (TBD) caused by the bending moment provided by the self-weight of each rock slab after isopach slabbing is estimated by Equation 8.

$$\omega_1 = \frac{3 \cdot \gamma \cdot l^4 \cdot \sin\alpha}{8 \cdot E \cdot t^2} \cdot \frac{\left[1 + \left(\frac{E_c}{E_t}\right)^{0.5}\right]^3}{1 + \left(\frac{E_t}{E_c}\right)^{0.5}} \qquad (7)$$

$$\omega_2 = \frac{3 \cdot n^2 \cdot \gamma \cdot l^4 \cdot \sin\alpha}{8 \cdot E \cdot t^2} \cdot \frac{\left[1 + \left(\frac{E_c}{E_t}\right)^{0.5}\right]^3}{1 + \left(\frac{E_t}{E_c}\right)^{0.5}} \qquad (8)$$

## 3.2. Example analysis

An example was selected to analyze the slabbing effect of toppling deformation based on toppling bending deflection (TBD). The inclination angle of the rock slab $\alpha = 60°$, $\gamma = 26.0\,\text{kN/m}^3$, and $t = 5\,\text{m}$, the length of cantilever beam segment $l$ is $10\,\text{m}$, and the compression deformation modulus $E_c$ and the tensile deformation modulus $E_t$ are $5 \times 10^3\,\text{MPa}$ and $1 \times 10^4\,\text{MPa}$, respectively. The deformation modulus of slabbing rock mass $E$ is similar to the $E_c$.

According to Equation 8, the slabbing segment of width m is eliminated, which reflects that the toppling bending deflection (TBD) is independent of the width of rock mass slabbing under self-weight of slabbing rock mass, as the thickness of the slab beam becomes thinner. The TBD is closely related to the thickness of the slab beam.

The slabbing numbers of slab beam thickness were selected as an example (Table 1). The control variable method is supposed to study further the toppling bending deflection (TBD) and the slabbing numbers of slab beam thickness, and the curves of the relationship between the slabbing numbers and the toppling bending deflection (TBD) presented in Figure 6 are concluded. It can be seen from Figure 6 that the toppling bending deflection (TBD) increases remarkably with the number of rock mass slabbing. The change of toppling bending deflection (TBD) is slow when the slabbing number ($n$) of thickness is <4 and fast when the slabbing number is above 4. The existing research

reflects that the toppling bending deflection of thin phyllite is stronger than that of thick massive sand slate (Liu M. et al., 2016; Cai et al., 2019; Zhao et al., 2021).

# 4. Slabbing effect of toppling failure based on toppling fracture depth

## 4.1. Three-dimensional mechanical model analysis

A three-dimensional mechanical model was established for a single slab beam, $H$ is the height of the slope, $\alpha$ is the dip angle of the strata ($0 < \alpha < 90°$), $\beta$ is the angle of the slope ($0 < \beta < 90°$), $t$ is the thickness of the single-layer slab beam, and $w$ is the width of the slab beam. The slab beam is simplified always in a quasi-equilibrium state during the process of bending and toppling and is subjected to self-weight, the friction resistance of the upper and lower adjacent layers, and the lateral constraining force of the left and right sides (Figure 7). The rock layer is homogeneous and uniform in thickness, and the distribution of normal stress and shear stress between layers and lateral joints is linear and only related to the buried depth. In addition, the cohesion and internal frictional angle of the strata are the same, and the lateral joints are also uniform. It is assumed that the parameters of the joint surface are equal to those of the stratum plane. Meanwhile, considering that the joint surface is almost open after unloading, and the cohesion of the joint surface is limited, the influence of the cohesion of the lateral joint surface is not considered in this study. According to the geometric relationship of the model, $\sigma_i$ and $\sigma_{i+1}$ are the normal stresses of the slab beam, respectively. $\tau_i$ and $\tau_{i+1}$, respectively, are the shear stresses of the slab beam surface, and $\tau k_i$ is the lateral constraint force. $W$ is the self-weight of the slab beam. Therefore, $W = \gamma t x w$. $M$ is the difference between the bending moment $M_T$ and the resisting moment $M_R$, is the total bending moment of the slab beam. $M$ can be abbreviated as Equation 9. The deduction process details of Equation 9 are shown in Equations A.1–A.4 in Appendix A.

$$
\begin{aligned}
M = &\ w \int_0^{x_i} \left( \int_0^{x_i} \sigma_i dx \right) \frac{dx}{2} - w \int_0^{x_{i+1}} \left( \int_0^{x_{i+1}} \sigma_{i+1} dx \right) \frac{dx}{2} - \\
&\ \frac{t}{2} w \int_0^{x_i} \tau_i dx - w \frac{t}{2} \int_0^{x_{i+1}} \tau_{i+1} dx + \frac{x}{2} W \cos\alpha - \\
&\ t \int_0^x \left( \int_0^x Kn \tan\varphi \, \sigma_v dx \right) \frac{dx}{2} \\
= &\ -\frac{1}{4} \gamma x^2 t w \lambda \frac{\cos(\alpha + \beta)}{\cos\beta} - \\
&\ \frac{1}{2} \gamma x^2 t w \tan\varphi \lambda \frac{\sin(\alpha + \beta)}{\cos\beta} + \frac{1}{2} \gamma x^2 t w \cos\alpha - \\
&\ cx t w + \frac{1}{12} t x^3 \frac{\sin(\alpha + \beta)}{\cos\beta} Kn\gamma\tan\varphi
\end{aligned}
\tag{9}
$$

where $\propto$ is Poisson's ratio, $n$ is the lateral stress coefficient, and its calculation formula is $n = \mu / (1 - \mu)$. The introduced lateral constraint coefficient $K$ presented lateral constraint conditions, which reflected the boundary condition of the slab beam. Supposing $K \in [0, 2]$, 0 means no constraint, which reflects the three-way conditions of the free face; 1 shows a unilateral constraint that reflects the condition on either side of the free face; and 2 signifies three constraints and only one side opening condition. The values of (0, 1) or (1, 2) correspond to different combinations of opening conditions, considering unloading crack conditions (including two free faces, unloading conditions, and one free face). Those values are determined according to the opening and filling degree of unloading cracks. Due to the limited contribution of cohesion after opening, only the friction angle effect is taken into consideration.

Since the compressive strength of the rock mass is much higher than its tensile strength, tensile failure is likely to occur. In other words, the condition of toppling failure of the slab beam is $M > 0$, and $\sigma_t > [\sigma_T]$. $\sigma_t$ and $[\sigma_T]$ are the tensile stress of the slab beam and the tensile strength of the rock mass, respectively. The tensile stress on the normal section of the beam can be expressed as Equation 10.

$$
\begin{aligned}
\sigma_t = &\ \frac{My}{I} - \frac{N}{A} + w \int_0^x \frac{\tau_{i+1} - \tau_i}{tw} dx = \\
&\ -\frac{1}{4} \gamma x^2 t w \lambda \frac{\cos(\alpha + \beta)}{2\cos\beta} - \\
&\ \frac{\frac{1}{2} \gamma x^2 t w \tan\varphi \lambda \frac{\sin(\alpha + \beta)}{\cos\beta} + \frac{1}{2} \gamma x^2 t w \cos\alpha - cxtw}{\frac{t^2 w}{6}} + \\
&\ \frac{\frac{1}{12} t x^3 \frac{\sin(\alpha + \beta)}{\cos\beta} Kn\gamma\tan\varphi}{\frac{t^2 w}{6}} + \\
&\ \gamma x \tan\varphi \lambda \frac{\cos(\alpha + \beta)}{\cos\beta} - \gamma x \sin\alpha = \\
&\ -\frac{3}{2} \gamma x^2 \lambda \frac{\cos(\alpha + \beta)}{2\cos\beta} - \\
&\ \frac{3\gamma x^2 \tan\varphi \lambda \frac{\sin(\alpha + \beta)}{\cos\beta} + 3\gamma x^2 \cos\alpha - 6cx}{t} + \\
&\ \frac{\frac{1}{2} x^3 \frac{\sin(\alpha + \beta)}{\cos\beta} Kn\gamma\tan\varphi}{tw} + \\
&\ \gamma x \tan\varphi \lambda \frac{\cos(\alpha + \beta)}{\cos\beta} - \\
&\ \gamma x \sin\alpha > [\sigma_T]
\end{aligned}
\tag{10}
$$

where $N$ is the axial force exerted on the slab beam, which is the component force of the self-weight of the slab beam in the $x$-direction, $N = W \sin\alpha$. $A$ is the normal cross-sectional area of the slab beam, $A = tw$. $y$ is the distance in the $y$-direction from the fracture point on the normal section to the centroid of the section,

**TABLE 1** The relationship between the slabbing number and rock slab thickness.

| Thickness ($t$)/m | 5 | 2.5 | 1.67 | 1.25 | 1 | 0.83 | 0.71 | 0.63 | 0.56 | 0.5 |
|---|---|---|---|---|---|---|---|---|---|---|
| Slabbing number ($n$) | 1 | 2 | 3 | 4 | 5 | 6 | 7 | 8 | 9 | 10 |



**FIGURE 6**
Relationship between the slabbing number and toppling bending deflection.
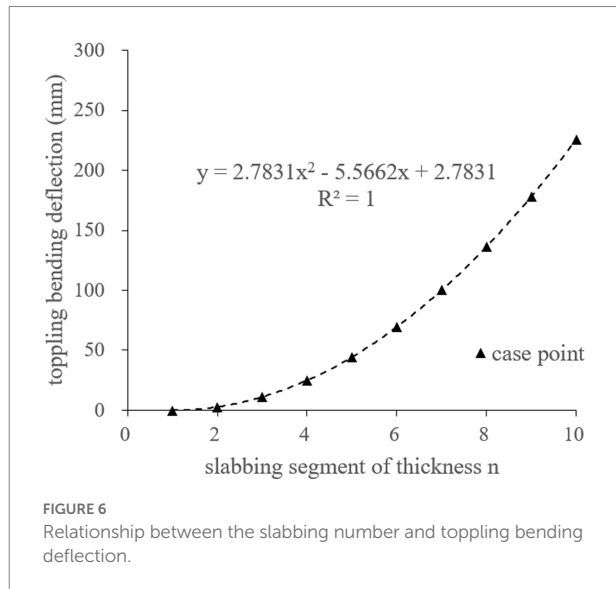
$y = t/2$. $I$ is the section moment of inertia, $I = t^3 w/12$. Equation 10 can be rewritten as Equation 11. $A_1$, $B_1$, $C_1$, $D_1$ are shown in Equation A.5 in Appendix A.

$$A_1 x^3 + B_1 x^2 + C_1 x + D_1 = 0 \qquad (11)$$

According to Cardin's formula, if $A_1 \uparrow 0$, there must be a real solution of the unary cubic equation, $A_1$, $B_1$, $C_1, D_1 \in R$. Moreover, the solution is the first toppling fracture depth (TFD) of the slab beam. $A_0$, $B_0$, $C_0$, $D_0$ are shown in Equation A.6 in Appendix A.

According to Cardin's formula, the first toppling fracture depth $x$ of the slab beam is as follows:

$$x = A_0 + \sqrt[3]{B_0 + C_0} + \sqrt[3]{B_0 - C_0} \qquad (12)$$

If $A_1 = 0$, Equation 12 is simplified to a unary quadratic equation, namely, $B_1 x^2 + C_1 x + D_1 = 0$, the first toppling fracture depth $x$ of the slab beam is as follows:

$$x = \frac{-C_1 + \sqrt{C_1^2 - 4B_1 D_1}}{2B_1} \qquad (13)$$

It is consistent with the format of the previous two-dimensional mechanical model of the slab beam and will not be described in detail. From equation 12, it can be inferred that the first toppling fracture

depth (TFD) of the slab beam is closely related to the slope angle $\beta$, rock inclination angle $\alpha$, the weight of the slab beam $\gamma$, thickness $t$, width $w$, lateral constraint coefficient $n$, internal friction angle of the rock layer $\varphi$, cohesion of the rock layer $c$, and lateral constraint factor $K$. The following example analysis further analyzed the slabbing effect of toppling failure based on toppling fracture depth (TFD).

## 4.2. Example analysis

The toppling slope of the highway, proposed by Liu H. J. et al. (2016), in the southern mountainous area of Anhui was taken as an example. The slope lithology is composed of metamorphic sand slate, and the inclination angle of the rock layer $\alpha = 56°$, the slope angle $\beta = 50°$, $\gamma = 26.0 \, \text{kN/m}^3$, Poisson's ratio $\propto = 0.2$, $t = 0.25 \, \text{m}$, the tensile strength $[\sigma_T] = 9,000 \, \text{kPa}$, $\varphi = 20°$, and $c = 50 \, \text{kPa}$. The $K$ values of (0, 1) or (1, 2) correspond to different combinations of opening conditions, considering including two free faces or unloading conditions and one free face. This site point is located on the mountain ridge, and there is a gully on one side and an excavation surface of the highway on the other side of the slope. This site point approximately presented two free faces, then $w = 2.0 \, \text{m}$, and the coefficient of lateral constraint $K = 0.01$ can be determined according to the geological conditions in the field. According to Equation 12, the TFD of the three-dimensional mechanical model is 14.7 m. The TFD calculated by the two-dimensional mechanical model is 14.0 m, and the toppling development depth measured in the field is ~15.5 m.

The two-dimensional mechanical model with a width of 1.0 m indicates that the lateral joint spacing is the unit width. In most cases, lateral spacing is generally $w \neq 1.0 \, \text{m}$, and there is no lateral constraint force caused by the principal stress. Obviously, Equation 12 derived from the three-dimensional mechanical model can be used to accurately calculate the toppling fracture depth (TFD) of the slab beam, and the results are consistent with the depth of the statistical field.

The control variable method is supposed to study further the first toppling fracture depth (TFD) of the slab beam and the related variables. The variables including the thickness $t$ and the width $w$ of the slab beam were mainly selected, and the curves of the relationship between the variables and the first toppling fracture depth (TFD) presented in Figure 8 are concluded.

According to the parameter analysis (Figure 8), the toppling fracture depth decreases with the decrease in the width and thickness of the rock slab, and the first toppling fracture depth (TFD) increases inversely with the increase in the width of the slab beam. The first toppling fracture depth (TFD) decreases fast when $w < 2.0 \, \text{m}$, and it tends to be stable when w is above 2.0 m. The first fracture depth grows relatively fast with the thickness of the
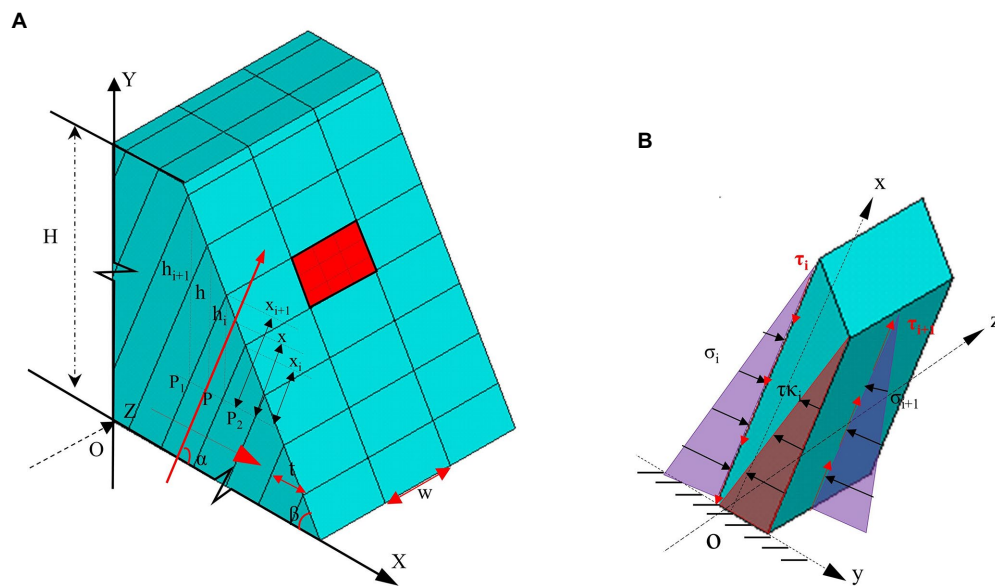
FIGURE 7
Geometry of the mechanical model. **(A)** Three-dimensional mechanical model; and **(B)** a single slab beam.
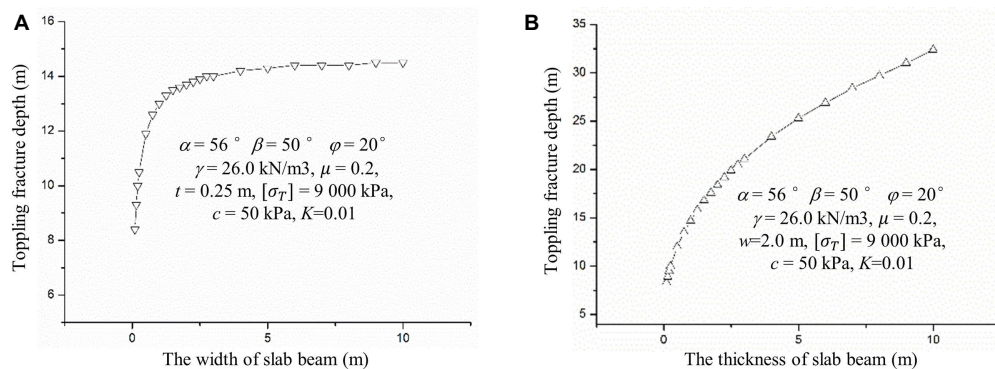


FIGURE 8
Relationship between toppling fracture depth and width and thickness of the slab beam.

decreased slab beam. The smaller the toppling fracture depth (TFD), the more likely the toppling failure will occur.

# 5. Conclusion

1. There are many factors inducing the rock mass slabbing, which are mainly divided into internal and external factors. The internal factors are the decisive condition, and the external factors play the role of triggering and inducing. The internal factors are mainly the internal texture and structural factors of rock mass, while the external factors are mainly stress differentiation, differential unloading, dynamic load, weathering, artificial activities, etc.

2. Slabbing makes the section size of the rock slab beam narrower and thinner, thus increasing the bending deflection of the toppling failure, indicating that the slabbing of the rock slab aggravates the development of toppling deformation. The toppling bending deflection (TBD) is independent of the width of rock mass slabbing under self-weight, and the toppling bending deflection (TBD) is closely related to the thickness of the slab beam. The change of toppling bending deflection (TBD) is slow when the slab beam slabbing number ($n$) of thickness is <4 and fast when the slabbing number is above 4.

3. According to the analysis of the three-dimensional mechanical model, the toppling fracture depth (TFD) decreases with the decrease in the width and thickness of the section size of the rock slab. The first toppling fracture

depth (TFD) decreases fast when $w$ is <2.0 m, and it tends to be stable when $w$ is above 2.0 m. The first toppling fracture depth (TFD) reduces relatively fast with the thickness $t$ of the decreased slab beam. The smaller the toppling fracture depth (TFD) is, the more likely the toppling failure will occur.

4. The section size of slabbing rock mass is mainly concerned, and the influence of rock mass slabbing on mechanics parameters of rock mass is not considered, especially the amplification effect of the crack tip and the time-varying effect of slabbing rock mass mechanics parameters caused by weathering, which can be regarded as the focus of future research.

## Data availability statement

The original contributions presented in the study are included in the article/supplementary material, further inquiries can be directed to the corresponding author.

## Author contributions

JC and SL conceived and designed the paper and analyzed the mechanical model. KL and ZW analyzed and interpreted the data. JC wrote the paper. JW, RZ, and ZW revised the paper. All authors contributed to the article and approved the submitted version.

## Funding

## Acknowledgments

## Conflict of interest

KL is employed by Chengdu East Group Co., Ltd. RZ is employed by Shuifa Planning and Design Limited Company.

The remaining authors declare that the research was conducted in the absence of any commercial or financial relationships that could be construed as a potential conflict of interest.

## Publisher's note

All claims expressed in this article are solely those of the authors and do not necessarily represent those of their affiliated organizations, or those of the publisher, the editors and the reviewers. Any product that may be evaluated in this article, or claim that may be made by its manufacturer, is not guaranteed or endorsed by the publisher.

## References

Alejano, L. R., Alonso, C. S., Rey, I. P., Arzua, J. R., Alonso, E. S., Gonzalez, J., et al. (2018). Block toppling stability in the case of rock blocks with rounded edges. *Eng. Geol.* 234, 192–203. doi: 10.1016/j.enggeo.2018.01.010

Amini, M., Majdi, A., and Aydan, Ö. (2009). Stability analysis and the stabilisation of flexural toppling failure. *Rock Mech. Rock. Eng.* 42, 751–782. doi: 10.1007/s00603-008-0020-2

Amini, M., Majdi, A., and Veshadi, M. A. (2012). Stability analysis of rock slopes against block flexure toppling failure. *Rock Mech. Rock. Eng.* 45, 519–532. doi: 10.1007/s00603-012-0220-7

Aydan, O., and Kawamoto, T. (1992). The stability of slopes and underground openings against flexural toppling and their stabilization. *Rock Mech. Rock. Eng.* 25, 143–165. doi: 10.1007/BF01019709

Bao, Y. D., Chen, J. P., Su, L. J., Zhang, W., and Zhan, J. (2022). A novel numerical approach for rock slide blocking river based on the CEFDEM model: a case study from the Samaoding paleolandslide blocking river event. *Eng. Geol.* 312:106949. doi: 10.1016/j.enggeo.2022.106949

Cai, J. C., Ju, N. P., Huang, R. Q., Zheng, D., Zhao, W. H., Li, L. Q., et al. (2019). Mechanism of toppling and deformation in hard rock slope: a case of bank slope of Hydropower Station, Qinghai Province, China. *J. Mt. Sci.* 16, 924–934. doi: 10.1007/s11629-018-5096-x

Cai, J. C., Zheng, D., Ju, N. P., Huang, R. Q., and Zhao, W. H. (2022a). Boundary effect of toppling failure based on three-dimensional mechanical model. *J. Mt. Sci.* 19, 3314–3322. doi: 10.1007/s11629-022-7337-2

Cai, J. C., Zheng, D., Ju, N. P., Wang, J., Zhou, X., and Li, D. (2022b). Time-varying effect of ductile flexural toppling failure on antidip layered rock slope. *Front. Earth Sci.* 10:943700. doi: 10.3389/feart.2022.943700

Du, K., Tao, M., and Li, X. B. (2016). Experimental study of Slabbing and Rockburst induced by true-Triaxial unloading and local dynamic disturbance. *Rock Mech. Rock. Eng.* 9, 3437–3453. doi: 10.1007/s00603-016-0990-4

Fujii, Y., Ikeda, N., Onoe, Y., Kanai, Y., Hayakawa, T., Awaji, D., et al. (2022). A case study on severe damage at a tunnel in serpentinite rock mass. *SN Appl Sci.* 4:34. doi: 10.1007/s42452-021-04924-7

Gong, F. Q., Luo, Y., Li, X. B., Si, X. F., and Tao, M. (2018). Experimental simulation investigation on rockburst induced by spalling failure in deep circular tunnels. *Tunn Undergr Sp Tech.* 81, 413–427. doi: 10.1016/j.tust.2018.07.035

Gong, F. Q., Wu, W. X., and Li, T. B. (2020). Simulation test of spalling failure of surrounding rock in rectangular tunnels with different height-to-width ratios. *Bull. Eng. Geol. Environ.* 79, 3207–3219. doi: 10.1007/s10064-020-01734-w

Goodman, R. E. (2013). "Toppling-A fundamental failure mode in discontinuous materials description and analysis," in *2013 Congress on Stability and Performance of Slopes and Embankments III, Geo-Congress 2013, San Diego, United States.* Geotechnical Special Publication, ASCE, 2348–2378.

Goodman, R. E., and Bray, J. W. (1976). "Toppling of rock slopes," in *Rock Engineering for Foundations & Slopes.* Boulder, Colorado: ASCE, 201–234.

He, M. C., Sui, Q. R., Li, M. N., Wang, Z., and Tao, Z. (2022). Compensation excavation method control for large deformation disaster of mountain soft rock tunnel. *Int. J. Min. Sci. Techno.* 32, 951–963. doi: 10.1016/j.ijmst.2022.08.004

Huang, R. Q. (2008). Geodynamic process and stability control of high rock slope development. *Chin. J. Rock Mech. Eng.* 8, 1525–1544. doi: 10.3321/j.issn:1000-6915.2008.08.002

Huang, R. Q., Li, Y. S., and Yan, M. (2017). The implication and evaluation of toppling failure in engineering geology practice. *Chin. J. Eng. Geol.* 25, 1165–1181. doi: 10.13544/j.cnki.jeg.2017.05.001

Huang, R. Q., Zhang, Z. Y., and Wang, S. T. (1994). Epigenetic reformation of Rockmass structure. *Hydroge. Eng. Geol.* 4, 1–6.

Jiang, Q., Zhang, M., Yan, F., Su, G., Feng, X., Xu, D., et al. (2021). Effect of initial minimum principal stress and unloading rate on the spalling and rockburst of marble: a true triaxial experiment investigation. *Bull. Eng. Geol. Environ.* 80, 1617–1634. doi: 10.1007/s10064-020-01995-5

Li, H. J., He, Y. S., Xu, Q., Deng, J., Li, W., and Wei, Y. (2022b). Detection and segmentation of loess landslides via satellite images: a two-phase framework. *Landslides* 19, 673–686. doi: 10.1007/s10346-021-01789-0

Li, H. J., He, Y. S., Xu, Q., Deng, J., Li, W., Wei, Y., et al. (2022a). Sematic segmentation of loess landslides with STAPLE mask and fully connected conditional random field. *Landslides.* doi: 10.1007/s10346-022-01983-8

Liang, X., Tang, S. B., Tang, C. A., Hu, L. H., and Chen, F. (2022). Influence of water on the mechanical properties and failure behaviors of sandstone under Triaxial compression. *Rock Mech. Rock. Eng.* doi: 10.1007/s00603-022-03121-1

Liu, G. F., Feng, X. T., Jiang, Q., Yao, Z., and Li, S. (2017). In situ observation of spalling process of intact rock mass at large cavern excavation. *Eng. Geol.* 226, 52–69. doi: 10.1016/j.enggeo.2017.05.012

Liu, M., Liu, F. Z., Huang, R. Q., and Pei, X. J. (2016). Deep-seated large-scale toppling failure in metamorphic rocks: a case study of the Erguxi slope in Southwest China. *J. Mt. Sci.* 13, 2094–2110. doi: 10.1007/s11629-015-3803-4

Liu, H. J., Zhao, J. J., and Ju, N. P. (2016). Mechanical analysis of toppling failure of rock slope. *Rock Soil Mech.* 37, 289–294. doi: 10.16285/j.rsm.2016.S1.038

Ni, G. R., and Ye, M. X. (1987). Mechanical analysis of rock mass with the "plate fracture" structure. *Yantu Gongcheng Xuebao* 9, 99–108.

Nie, W., Wang, W. Q., Tao, Z. G., Zhu, C., and Chen, Y. (2022). Numerical modeling of the NPR-cable and its applications for analysis of a slide-toe-toppling failure. *Comput. Geotech.* 149:104852. doi: 10.1016/j.compgeo.2022.104852

Pan, P. Z., Miao, S. T., Wu, Z. H., Feng, X. T., and Shao, C. (2020). Laboratory observation of Spalling process induced by tangential stress concentration in hard rock tunnel. *Int. J. Geomech.* 20:4020011. doi: 10.1061/(ASCE)GM.1943-5622.0001620

Qin, C. A., Chen, G. Q., Zhu, J., and Tang, P. (2020). A precursor of bedding rockslide: rock spalling in the key block triggered by tensile cracks. *Bull. Eng. Geol. Environ.* 79, 2513–2528. doi: 10.1007/s10064-019-01703-y

Qiu, S. L., Feng, X. T., Zhang, C. Q., and Xiang, T. (2014). Estimation of rockburst wall-rock velocity invoked by slab flexure sources in deep tunnels. *Can. Geotech. J.* 51, 520–539. doi: 10.1139/cgj-2013-0337

Sun, Z. H., Hou, Z. S., and Zhang, A. P. (2012). Research on tensile Slabbing failure of marble at Jinping II Hydropower Station. *J. Water Resour. Archit. Eng.* 10, 24–27. doi: 10.3969/j.issn.1672-1144.2012.01.008

Sun, G. Z., and Zhang, W. B. (1985). A common rock structure-board crack structure and its mechanical model. *J. Eng. Geol.* 28, 275–282.

Tang, S. B., Li, J. M., Ding, S., and Zhang, L. (2022). The influence of water-stress loading sequences on the creep behaviour of granite. *B Eng. Geol. Environ.* 81:482. doi: 10.1007/s10064-022-02987-3

Tao, L. J., Chang, C., Huang, R. Q., Chai, H. J., and Li, P. F. (2000). Epigenetic reformation of the Rockmass structure in a deep downcutting gorge. *J. Chengdu Univ. Technol.* 27, 383–387. doi: 10.3969/j.issn.1671-9727.2000.04.010

Tao, Z. G., Geng, Q., Zhu, C., He, M., Cai, H., Pang, S., et al. (2019). The mechanical mechanism of large-scale toppling failure for counter-inclined rock slopes. *J. Geophys. Eng.* 16, 541–558. doi: 10.1093/jge/gxz020

Wang, Y., Zhu, C., He, M. C., Wang, X., and le, H. (2022). Macro-meso dynamic fracture behaviors of Xinjiang marble exposed to freeze thaw and frequent impact disturbance loads: a lab-scale testing. *Geomech. Geophys. Geo.* 8:154. doi: 10.1007/s40948-022-00472-5

Wu, S. Y., Gong, Q. M., Wang, G., Hou, Z. S., and She, Q. R. (2010). Experimental study slabbing failure for deep-buried marble at Jinping II Hydropower Station and its influences on TBM excavation. *Chin. J. Rock Mech. Eng.* 29, 1089–1095.

Xu, Y. X., Wang, G. F., Li, M. Z., Xu, Y. J., Zhou, C. T., and Zhang, J. H. (2021). Mechanism of slabbed spalling failure of the coal face in fully mechanized caving face with super large cutting height. *J. Min. Saf. Eng.* 38, 19–30. doi: 10.13545/j.cnki.jmse.2019.0416

Zhao, W. H., Zhang, C. Q., and Ju, N. P. (2021). Identification and zonation of deep-seated toppling deformation in a metamorphic rock slope. *Bull. Eng. Geol. Environ.* 80, 1981–1997. doi: 10.1007/s10064-020-02027-y

Zheng, Y., Chen, C. X., Liu, T. T., Zhang, H., Xia, K., and Liu, F. (2018). Study on the mechanisms of flexural toppling failure in anti-inclined rock slopes using numerical and limit equilibrium models. *Eng. Geol.* 237, 116–128. doi: 10.1016/j.enggeo.2018.02.006

Zhou, H., Lu, J. J., Xu, R. C., Zhang, C. Q., and Meng, F. Z. (2015). Critical problems of study of slabbing failure of surrounding rock in deep hard rock tunnel and research progress. *Rock Soil Mech.* 36, 2737–2749. doi: 10.16285/j.rsm.2015.10.001

Zhou, Y., Sun, Z., Wang, L., Wang, Y., and Ding, Y. P. (2018). Meso research on mechanical properties and slab failure mechanism of pre-fractured rock mass under the condition of one side restriction loading. *Rock Soil Mech.* 39, 4385–4394. doi: 10.16285/j.rsm.2017.2597

Zhu, C., Xu, Y. Z., Wu, Y. X., He, M., Zhu, C., Meng, Q., et al. (2022). A hybrid artificial bee colony algorithm and support vector machine for predicting blast-induced ground vibration. *Earthq. Eng. Eng. Vib.* 21, 861–876. doi: 10.1007/s11803-022-2125-0

# Appendix A

Figure 7 presents the mechanical model under the global coordinate system.

$$h = x \sin(\alpha + \beta) / \cos\beta$$

$$h_i^{i+1} = \frac{\dfrac{x \, \sin(\alpha + \beta)}{\cos\beta \pm t \, \cos(\alpha + \beta)}}{2\cos\beta} \tag{A1}$$

Because $n\sigma_v = \sigma_h$, the stress state at a point in the slab beam is as follows:

$$\sigma_\alpha = \gamma h \left[ \frac{1+n}{2} + \frac{1-n}{2} \cos 2\alpha \right] \tag{A2}$$

where $n$ is the lateral stress coefficient and its calculation formula is as follows:

$$n = \mu / (1 - \mu) \tag{A3}$$

where $\mu$ is Poisson's ratio.

Because the toppling is still in the quasi-static equilibrium of dislocation each other and meets $\tau_i > [\tau] = \sigma \tan\varphi + c$, the rock slab can slide along with the plane of the rock layer. Thus, $\lambda = \frac{1+n}{2} + \frac{1-n}{2} \cos 2\alpha$, the stress state at $P_1$ and $P_2$ can be rewritten as follows:

$$\begin{aligned}
\sigma_i &= \gamma h_i \lambda \\
\sigma_{i+1} &= \gamma h_{i+1} \lambda \\
\tau_i &= \tan\varphi \gamma h_i \lambda + c \\
\tau_{i+1} &= \tan\varphi \gamma h_{i+1} \lambda + c
\end{aligned} \tag{A4}$$

Similarly, the lateral constraint force of the lateral section can be expressed as $\tau k_i = K \tan\varphi n \gamma h_i + c$.

$$\begin{aligned}
A_1 &= \frac{\dfrac{\sin(\alpha+\beta)}{\cos\beta} K n \gamma \tan\varphi}{2tw} \\[2mm]
B_1 &= \frac{-\dfrac{3}{2}\gamma\lambda \dfrac{\cos(\alpha+\beta)}{2\cos\beta} - 3\gamma \tan\varphi\lambda \dfrac{\sin(\alpha+\beta)}{\cos\beta} + 3\gamma\cos\alpha}{t} \\[2mm]
C_1 &= \frac{-6c}{t} + \gamma\tan\varphi\lambda \dfrac{\cos(\alpha+\beta)}{\cos\beta} - \gamma\sin\alpha \\[2mm]
D_1 &= -[\sigma_T]
\end{aligned} \tag{A5}$$

$$\begin{aligned}
A_0 &= -\frac{B_1}{3A_1} \\[2mm]
B_0 &= -\frac{27A_1 2D_1 - 9A_1B_1C_1 + 2B_1 3}{54A_1 3} \\[2mm]
C_0 &= \sqrt{\left(\frac{27A_1^2 D_1 - 9A_1 B_1 C_1 + 2B_1^3}{54A_1^3}\right)^2 + \left(\frac{3A_1 C_1 - B_1^2}{9A_1^2}\right)^3}
\end{aligned} \tag{A6}$$

frontiers | Frontiers in Earth Science

Check for updates

# Calculation method for reinforcement spacing of bilaterally wrapped reinforced embankments under seismic force

Qingwei Yan[1] and Shiguo Xiao[2]*

[1]Faculty of Geosciences and Environmental Engineering, Southwest Jiaotong University, Chengdu, China, [2]Key Laboratory of High-Speed Railway Engineering of Ministry of Education, Southwest Jiaotong University, Chengdu, China

The vertical spacing among reinforcements in geosynthetic-reinforced earth embankment is crucial to its overall stability. Based on the upper bound theorem of plastic limit analysis and pseudo-static approach, an overall stability analysis method for bilaterally wrapped reinforced embankments under strip surcharge and seismic action is put forward in view of the planar and log-spiral failure mechanism of the reinforced embankments, which quantitatively expresses the relationship between the reinforcement spacing and the factor of safety of the embankments. Some examples show that the maximum relative error of the factor of safety between the proposed method and some existing methods is around 10% under a specified reinforcement spacing. The factor of safety is nonlinearly decreasing as the reinforcement spacing increases, and the results by the log-spiral mode are slightly more conservative than those by the planar mode. The proposed method can quantitatively reflect the influence of the filling properties, reinforcement strength, seismic forces, strip surcharge, and embankment geometry on the reinforcement spacing. The nonlinear negative relationship between the factor of safety and the reinforcement spacing is noticeable under different reinforcement strengths. The reinforcement spacing is almost linearly reducing with the increase of the vertical seismic coefficient increases, while it decreases clearly nonlinearly as the horizontal seismic coefficient increases.

KEYWORDS

geosynthetic-reinforced embankment, reinforcement spacing, upper bound limit analysis method, factor of safety, seismic forces

## 1 Introduction

Geosynthetic reinforcement technology has been widely used in embankment reinforcement, soft ground improvement, as well as slope engineering, and has achieved good practical results and economic benefits (Romstad et al., 1976; Zou et al., 2016; Holtz, 2017; Tatsuoka, 2019; Venkateswarlu and Hegde, 2020). The

stability of the geosynthetic-reinforced soil structures is influenced by some factors such as soil parameters, reinforcement strength, reinforcement spacing, seismic conditions and seepage effect (Li et al., 2021). Many scholars have carried out some laboratory model tests (Zhussupbekov et al., 2015; Hajiazizi et al., 2018; Ma et al., 2022a) and numerical simulations on the issue (Basha and Babu, 2011; Ruan and Sun, 2013; Pain et al., 2017; Ma et al., 2022b). Based on the horizontal slice method, Choudhury et al. (2006) analyzed the tensile force and length of reinforcements required to maintain the stability of a geosynthetic-reinforced soil retaining wall (GRSW) under seismic action. They investigated the influence of soil friction angle, horizontal and vertical seismic accelerations on the stability of the GRSW. Sitar and Nova-Roessig (1999) used a numerical method to study the influence of dynamic load on GRSW. The results show that vertical spacing of reinforcement, stiffness of reinforcement, backfill and panel type have important effects on the stability of the walls. Weerasekara et al. (2017) established an interface friction model, combined it with the reinforcement stiffness to form an analytical model, and fully considered the displacement, strain, force, and friction length of reinforcements to evaluate the stability of the GRSW.

Among the factors influencing the stability of GRSW, the vertical spacing among reinforcements is an essential parameter in design. Leschinsky (2007) discussed the influence of reinforcement spacing on the failure mechanism of the walls by the finite element method. Chen et al. (2015) conducted centrifugal model tests on the GRSW. A low-strength clay was used as the backfill to investigate the effect of reducing the reinforcement spacing on the wall stability. It was found that the deformation mode of the wall panel depended greatly on the vertical spacing. Xie and Leshchinsky (2015) studied the stability of GRSW under surcharge by changing reinforcement spacing, strength, and position. The results indicate that placing dense reinforcements near the wall top under the surcharge significantly improves the wall stability. Also, Leschinsky and Vulova, 2001 analyzed the influence of reinforcement spacing, filling strength, foundation strength, reinforcement stiffness, and interface strength on the failure mechanism of the wall. Ren et al. (2016) applied the dynamic finite element method to systematically simulate the shaking table test of a segmented retaining wall (SRW). It is found that increasing the reinforcement length can improve the stability of SRW more effectively than reducing the vertical spacing among reinforcements. Lee et al. (2010) introduced the numerical simulation results of three full-scale GRSW models under seismic load. The computation results show that the wall displacement is positively related to the reinforcement spacing. In some of the past investigations on reinforced Earth retaining walls, it seems to imply that reinforcement strength and spacing play the same role in the structural stability. However, Wu and Pham, 2013 recent studies have clearly shown that the effect of reinforcement spacing is much more significant than that of reinforcement strength. The beneficial effect of geosynthetics on the GRSW stability is obviously enhanced

under relatively small reinforcement spacing (≤0.3 m). Also, the finite element program Plaxis 2D is used to simulate the reinforced soil structure under the condition of plane strain (Gebremariam et al., 2021), and the numerical results show that the vertical reinforcement spacing has more influences on the design members than the reinforcement stiffness.

Apart from the GRSW, some researchers investigated the performance of reinforced Earth structures. Li et al. (2019) conducted some experiments on the geogrid reinforced embankment and monitored pressure and displacement distribution inside the embankment. The results show that the optimal embedded depth and spacing between geogrid reinforcement layers can improve slope stability effectively. Zheng and Fox (2016) introduced a numerical simulation of the performance of a geosynthetic reinforced soil abutment under static load. The results show that the relative compaction of backfill, reinforcement spacing, and bridge load significantly influence the lateral displacement of the abutment and the settlement of the foundation. Abu-Farsakh et al. (2007) conducted a finite element analysis to evaluate the effect of reinforcing medium and low plastic embankment soils with geogrids under strip foundations regarding ultimate bearing capacity and foundation settlement. The research results show that the optimal depth of the first reinforcement layer exists in the position where the highest bearing capacity can be achieved. Xu et al. (2019) used a centrifuge model to evaluate the deformation behaviors, vertical stress, strain, and failure mode of a 14 m high geogrid-reinforced subgrade supporting an 8 m high embankment. As the layer spacing increases, the potential sliding surface moves away from the slope surface, and the overall stability of the reinforced slope decreases.

These existing investigations have indicated that with the increase of the reinforcement spacing, the overall stability of the GRSW gradually decreases obviously and the corresponding slip surface tends to develop towards the embankment interior. Moreover, the deformation of the reinforced soil structure increases with the reinforcement spacing, and the wall displacement is positively correlated with it. In fact, previous studies mainly focus on the influence of reinforcement spacing on the overall stability of reinforced Earth structures. However, the theoretical calculation of the vertical spacing among reinforcement layers in the geosynthetic reinforced soil structures is absent. In particular, the bilaterally wrapped reinforced Earth embankment is less involved in existing reports. In this regard, we propose a calculation method for vertical spacing among reinforcements in the bilaterally wrapped embankment based on the upper bound limit analysis method (Chen, 1975; Yang, 2007; Khoshzaban et al., 2021). The formula of external force power and internal energy consumption rate of the reinforced embankment under strip surcharge is derived, and the relationship between the overall stability of the embankment and the vertical spacing is determined further *via* the shear strength reduction method (Chen et al., 2014). Matlab programming can efficiently perform
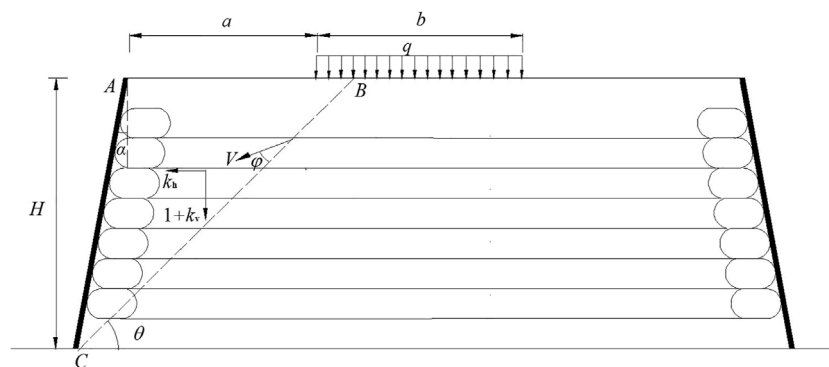
**FIGURE 1**
Analysis model of planar failure mode.

the calculation procedure (Farshidfar et al., 2020). Based on the proposed method, the minimum reinforcement spacing meeting the design requirement for the overall stability of the bilaterally wrapped reinforced embankment can be reasonably obtained in the practical design.

# 2 Analysis model and formula derivation

The results of a large number of shaking table and centrifugal tests on the geosynthetics-reinforced soil slopes show that the most common slip surfaces of the slopes under seismic action are of log-spiral shape (Zornberg et al., 1998) or planar pattern (Nouri et al., 2008). So, the planar failure mode (Narasimha Reddy et al., 2008; Ahmadabadi and Ghanbari, 2009) and log-spiral failure mode (Segrestin, 1992; Michalowski, 1998) are assumed in the present investigation to analyze the vertical spacing among the reinforcement layers in the bilaterally wrapped reinforced embankment.

## 2.1 Planar failure mode

### 2.1.1 Analysis model

A bilaterally wrapped reinforced embankment is shown in Figure 1. The sliding wedge ABC sliding surface BC with sliding velocity $V$ is a velocity discontinuity surface, which can be assumed to be a plane with dip angle $\theta$, particularly under high internal friction angle $\varphi$ of the filling. According to the associated flow rule, the angle between the sliding surface BC and velocity $V$ equals $\varphi$. A series of horizontally-arranged geogrids with layer spacing $h$ are rewound to wrap local filling at lateral two ends of the embankment. In addition, $H$ is the vertical height of the embankment; $\alpha$ is the inclination angle of the panel to the vertical direction; $k_h$ and $kv$ are horizontal and vertical seismic

coefficients, respectively; and $q$ is strip surcharge with distribution width $b$ and horizontal offset to the embankment crest $a$.

### 2.1.2 Derivation of work rates
#### 2.1.2.1 Gravity work rate

The soil in zone ABC is regarded as a rigid-plastic body, and the area of the sliding wedge is

$$S_{ABC} = \frac{1}{2}H^2\frac{\cos(\alpha + \theta)}{\sin\theta \cdot \cos\alpha} \tag{1}$$

Because the admissible velocity field is translational, the velocity component along the gravity direction in the mechanism is equal to $V\sin(\theta-\varphi)$, then the work rate of the sliding wedge gravity is

$$W_G = \frac{\gamma H^2 V}{2}\frac{\cos(\alpha + \theta) \cdot \sin(\theta - \varphi)}{\sin\theta \cdot \cos\alpha} \tag{2}$$

where $\gamma$ is the unit weight of the soil.

#### 2.1.2.2 Work rate of seismic force

Considering the effect of horizontal and vertical seismic forces on the wedge, the corresponding work rates are, respectively

$$W_h = k_h G \cdot V \cos(\theta - \varphi) \tag{3}$$

$$W_v = k_v G \cdot V \sin(\theta - \varphi) \tag{4}$$

where $G$ is the sliding wedge weight.

#### 2.1.2.3 Surcharge work rate

The work rate of the surcharge on the embankment top surface can be expressed as

$$W_q = q l_q V \sin(\theta - \varphi) \tag{5}$$

where $l_q$ is the distribution width of the strip surcharge on the sliding wedge.

### 2.1.2.4 Work rate related to lateral Earth pressure on the wrapped constraint ends

Since the surcharge distributes on a certain width, it only influences the lateral Earth pressure on the wrapped constraint ends at a limited height of the embankment. So, the expression of the Earth pressure in the $i$th layer can be divided into two cases.

$$E_i = \begin{cases} \dfrac{\gamma(2i-1)h^2K}{2} & 0 < H_i < a\tan\left(45° + \dfrac{\varphi}{2}\right) \text{or}\, (a+b)\tan\left(45° + \dfrac{\varphi}{2}\right) < H_i < H \\ \dfrac{1}{2}\gamma(2i-1)h^2K + qKh & a\tan\left(45° + \dfrac{\varphi}{2}\right) < H_i < (a+b)\tan\left(45° + \dfrac{\varphi}{2}\right) \end{cases}$$

$$(6)$$

Thus, the work rate corresponding to the lateral Earth pressure of the $i$th slice is

$$W_{iE} = -E_i \cdot V\cos(\theta - \varphi) \tag{7}$$

where $K$ is the Earth pressure coefficient, and $H_i$ is the vertical distance from the reinforcements' layer to the embankment's top surface.

Assuming that there are $n$ layers of the reinforcements, then the total work rate related to the Earth pressure is

$$W_E = \sum_{i=1}^{n} W_{iE} \tag{8}$$

### 2.1.2.5 Dissipation power on the slip surface

According to the Mohr-Coulomb yield criterion and associated flow rule, the energy dissipation power on slip surface due to the friction is

$$W_{BC} = \frac{cVH\cos\varphi}{\sin\theta} \tag{9}$$

where $c$ is the cohesion of the filling soil.

### 2.1.2.6 Dissipation power of reinforcement failure

There are two possible failures for the reinforcements, including tensile cut-off and pull-out failure. For the former, Leschinsky and Reinschmidt (1985) believed that because the reinforcements are flexible materials and can only bear the tensile force, the reinforcement at the sliding surface can gradually adjust its position with the soil movement until it is in the same direction as the velocity $V$ of the soil.

The energy dissipation power of the reinforcements in the sliding layer owing to tensile cut-off failure depends on generally two aspects. One is the power of reinforcement tensile force. The other is the power of friction between the reinforcement and soil. The frictional force can be regarded as a positive correlation with the small thickness of the sliding layer. It is assumed that the power of the friction is an ignored high-order small quantity compared with the power of the tensile force.

In the sliding layer, the tensile strain rate of the reinforcement $\dot{\varepsilon}$ can be written as

$$\dot{\varepsilon} = \frac{\varepsilon}{\Delta T} = \frac{\Delta l/\Delta T}{l} = \frac{V\sin\theta}{t} \tag{10}$$

where $\varepsilon$ is the axial strain of the reinforcement; $\Delta l$ is the axial elongation of the reinforcement segment; $t$ is the thickness of the sliding layer; $l$ is the original length of the reinforcement in the sliding layer, and $\Delta T$ is a minimal time increment.

Thus, the energy dissipation power of the $i$th reinforcement can be expressed as

$$W_{i\_off} = \int_0^{t/\sin\theta} T\dot{\varepsilon}dx = TV \tag{11}$$

where $T$ is the ultimate tensile strength per meter of the reinforcement.

For the pull-out failure of the $i$th layer reinforcement, it is necessary to overcome the sum of the reinforcement-soil friction in the sliding soil and the corresponding lateral Earth pressure on the wrapped constraint ends or that in the stable soil. Namely, the pulling force of the reinforcement for this failure mode should be adopted as

$$F_{i\_out} = \min\left[(F_{iL} + E_i), (F_{iR} + E_i)\right] \tag{12}$$

where $F_{iL}$ and $F_{iR}$ are the reinforcement-soil frictional resistance in the sliding soil and stable soil, respectively; and they can be expressed as

$$F_{iL} = 2c_0 L_{iL} + 2N_{iL}\tan\phi_0 \tag{12a}$$
$$F_{iR} = 2c_0 L_{iR} + 2N_{iR}\tan\phi_0 \tag{12b}$$

where $c_0$ and $\varphi_0$ are the cohesion and frictional angle of the reinforcement-soil interface, respectively; $N_{iL}$ and $N_{iR}$ are the normal force on the $i$th layer reinforcement in the slide and stable soil, respectively; $L_{iL}$ and $L_{iR}$ are the lengths of the $i$th layer reinforcement in the slide and stable soil, respectively, and there are

$$L_{iL} = (H - i \cdot h)(\cot\theta - \tan\alpha) \tag{12c}$$
$$L_{iR} = L_i - (H - i \cdot h)(\cot\theta - \tan\alpha) \tag{12d}$$

The upper and lower reinforcement-soil interfaces are velocity discontinuities for the $i$th layer reinforcement, and the corresponding velocity is $V\cos(\theta-\varphi)$. So, the pullout dissipation power of the reinforcement can be derived as

$$W_{i\_out} = \min\left[(F_{iL} + E_i), (F_{iR} + E_i)\right] \cdot V\cos(\theta - \phi) \tag{13}$$

In the tensile failure state of the reinforcement, there is the minimum energy dissipation power between the tensile cut-off and pullout mode. Thus, the dissipation power of the $i$th reinforcement failure can be expressed as:

$$W_{iT} = \min(W_{i\_off}, W_{i\_out}) \tag{14}$$
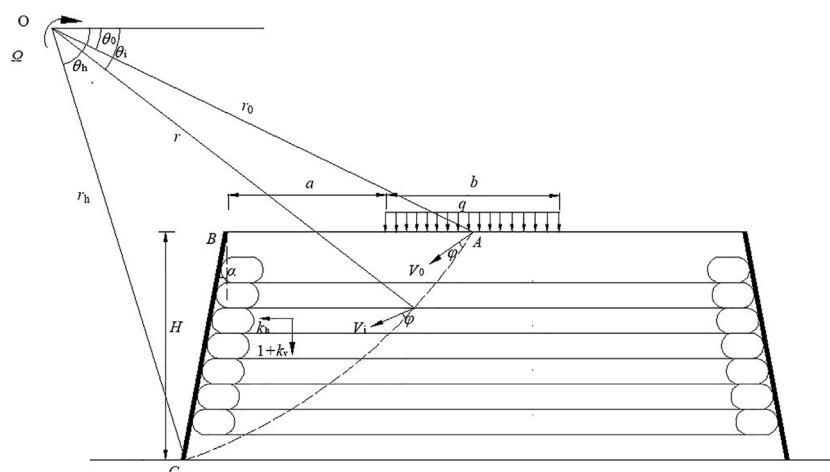
**FIGURE 2**
Analysis model of log-spiral failure mode.

Naturally, the total energy dissipation power of $n$ layers of reinforcement is

$$W_T = \sum_{i=1}^{n} W_{iT} \qquad (15)$$

According to the upper-bound theory of plastic limit analysis (Chen, 1975), the total work rate of external forces is equal to the total dissipation power of internal energy. Namely, there is

$$W_G + W_q + W_h + W_v + W_E = W_{BC} + W_T \qquad (16)$$

Besides, it should be noted that the shear strength reduction approach can be introduced in the above analysis with the factor of safety $F_s$ of the soil slope stability (Zienkiewicz et al., 1975). Namely, there is

$$\begin{cases} c' = \dfrac{c}{F_s}, \\[2mm] \varphi' = \arctan \dfrac{\tan \varphi}{F_s} \end{cases} \qquad (17)$$

where $\varphi'$ and $c'$ are the soil's internal friction angle and cohesion after strength reduction, respectively.

Thus, by replacing $\varphi$ and $c$ with $\varphi'$ and $c'$ respectively in the previously related formulas and then substituting Eqs 2–5, 8, 9, 15 into Eq. 16, the relationship between the safety factor $F_s$ and dip angle of the potential slip surface $\theta$ can be obtained. Therefore, the minimum $F_s$ and the corresponding slip surface can be determined by

$$\frac{\partial F_s}{\partial \theta} = 0 \qquad (18)$$

The computational procedure can be easily carried out *via* computer programs such as Microsoft Excel or Matlab.

## 2.2 Log-spiral failure mode

### 2.2.1 Analysis model

As shown in Figure 2, the potential sliding surface can be generally assumed as a curved plane. For simplification, a log-spiral slip surface is adopted herein, and its equation can be written as (Chen and Snitbhan, 1975)

$$r = r_0 \exp\left[ (\theta - \theta_0) \tan \varphi \right] \qquad (19)$$

where $r$ is the distance from any point on the slip surface AC to its rotation center O, $r_0$ and $r_h$ are the length of lines OA and OC, respectively; $\theta$ is the inclination angle between the radius of the slip surface AC and the horizontal direction, where subscripts 0, i, h stands for starting radius OA, the $i$th layer of reinforcements, and ending radius OC, respectively; $\Omega$ is the angular velocity of the sliding wedge rotating around point O; $L_{AB}$ is the distance between points A and B on the top of the reinforced embankment.

The following geometric relationships can be obtained from Figure 2 as

$$\frac{H}{r_0} = \sin \theta_h \cdot \exp\left[ (\theta_h - \theta_0) \tan \varphi \right] - \sin \theta_0 \qquad (20)$$

$$\frac{L_{AB}}{r_0} = \cos \theta_0 - \exp\left[ (\theta_h - \theta_0) \tan \varphi \right] \cos \theta_h - \frac{H}{r_0} \tan \alpha \qquad (21)$$

### 2.2.2 Derivation of work rates

#### 2.2.2.1 Gravity work rate

The sliding body ABC is equal to the area OAC minus areas OAB and OBC (see Figure 2). So, the gravity work rate of mass ABC can be obtained by superpositioning the corresponding work rates of the three areas.

The gravity work rate of zone OAC can be calculated by the integral method to be derived as

$$W_{OAC} = \frac{1}{3}\gamma\Omega \int_{\theta_0}^{\theta_h} r^3 \cos\theta d\theta = \gamma\Omega r_0^3 f_1 \tag{22}$$

The gravity work rate of zones OAB and OBC can also be derived respectively as

$$W_{OAB} = \gamma S_{OAB} V_{OAB} = \gamma r_0^3 \Omega f_2 \tag{23}$$

$$W_{OBC} = \gamma r_0^3 \Omega f_3 \tag{24}$$

Thus, the gravity work rate of slide mass ABC can be expressed as

$$W_G = \gamma r_0^3 \Omega (f_1 - f_2 - f_3) \tag{25}$$

where the calculation coefficients $f_i$ ($i = 1, 2, 3$) are

$$f_1 = \frac{\{(3\tan\varphi\cos\theta_h + \sin\theta_h)\cdot\exp[3(\theta_h - \theta_0)\tan\varphi] - 3\tan\varphi\cos\theta_0 - \sin\theta_0\}}{3(1 + 9\tan^2\varphi)} \tag{25a}$$

$$f_2 = \frac{1}{6}\frac{L_{AB}}{r_0}\left[2\cos\theta_0 - \frac{L_{AB}}{r_0}\right]\sin\theta_0 \tag{25b}$$

$$f_3 = \frac{1}{6}\exp[(\theta_h - \theta_0)\tan\varphi]\left[\sin(\theta_h - \theta_0) - \frac{L_{AB}}{r_0}\sin\theta_h\right]$$
$$\left[\cos\theta_0 - \frac{L_{AB}}{r_0} + \cos\theta_h\exp[(\theta_h - \theta_0)\tan\varphi]\right] \tag{25c}$$

#### 2.2.2.2 Work rate of seismic force

Similar to the determination approach of the gravity work rate of mass ABC, the work rate of the corresponding vertical and horizontal seismic force can be derived, respectively as

$$W_v = k_v \gamma r_0^3 \Omega (f_1 - f_2 - f_3) \tag{26}$$

$$W_h = k_h \gamma r_0^3 \Omega (f_4 - f_5 - f_6) \tag{27}$$

where the calculation coefficients $f_i$ ($i = 4, 5, 6$) are

$$f_4 = \frac{\{(3\tan\varphi\sin\theta_h - \cos\theta_h)\cdot\exp[3(\theta_h - \theta_0)\tan\varphi] - 3\tan\varphi\sin\theta_0 + \cos\theta_0\}}{3(1 + 9\tan^2\varphi)} \tag{27a}$$

$$f_5 = \frac{1}{3}\frac{L_{AB}}{r_0}\cdot\sin^2\theta_0 \tag{27b}$$

$$f_6 = \frac{1}{3}\left(\exp[(\theta_h - \theta_0)\tan\varphi]\cdot\sin\theta_h - \frac{H}{2r_0}\right)$$
$$\cdot\left(\frac{H}{r_0}\cdot\exp[(\theta_h - \theta_0)\tan\varphi]\cdot\frac{\cos(\alpha - \theta_h)}{\cos\alpha}\right) \tag{27c}$$

#### 2.2.2.3 Surcharge work rate

Considering three possible location relationships between the surcharge and slide mass ABC, the surcharge work rate $W_q$ can be expressed as three cases as

$$W_q = \begin{cases} 0 & (l_{AB} < a) \\ \Omega q l_q r_0 f_7 & (a < l_{AB} < a + b) \\ \Omega q l_q r_0 f_8 & (l_{AB} > a + b) \end{cases} \tag{28}$$

where the calculation coefficients $f_i$ ($i = 7$ and $8$) are

$$f_7 = \frac{1}{2}\left\{\cos\theta_h\exp[(\theta_h - \theta_0)\tan\varphi] + \cos\theta_0 + \frac{H}{r_0}\tan\alpha + \frac{a}{r_0}\right\} \tag{28a}$$

$$f_8 = \cos\theta_h\exp[(\theta_h - \theta_0)\tan\varphi] + \frac{H}{r_0}\tan\alpha + \frac{b + 2a}{2r_0} \tag{28b}$$

#### 2.2.2.4 Work rate related to lateral Earth pressure on the wrapped constraint ends

According to the direction of the velocity at the intersection between the slip surface and each reinforcement layer, the work rate related to the lateral Earth pressure on the wrapped constraint end of the $i$th reinforcements can be derived as

$$W_{iE} = -E_i r_0 \exp[(\theta_i - \theta_0)\tan\varphi]\Omega\sin\theta_i \tag{29}$$

Similarly, the total work rate related to the lateral Earth pressure can be written in the same format as Eq. 8.

#### 2.2.2.5 Dissipation power on the slip surface

The energy dissipation power on the slip surface AC can be obtained by integral calculus as

$$W_{AC} = \int_{\theta_0}^{\theta_h} c \left( V \cos \varphi \right) \frac{r d\theta}{\cos \varphi} = r_0{}^2 c \Omega f_9 \qquad (30)$$

where the calculation coefficient $f_9$ is

$$f_9 = \frac{\{\exp[2(\theta_h - \theta_0)\tan\varphi] - 1\}}{2\tan\varphi} \qquad (30a)$$

### 2.2.2.6 Dissipation power of reinforcement failure

As shown in Figure 3, the axial strain rate of the linear segment of the $i$th reinforcement in the sliding layer can be expressed as

$$\dot{\varepsilon} = \frac{\varepsilon}{\Delta T} = \frac{r_i \Omega}{r_i \Delta \theta} = \frac{\Omega}{\Delta \theta} \qquad (31)$$

where $\Delta\theta$ is the increment of the inclination angle between the starting and ending radius corresponding to the linear segment of the $i$th reinforcement in the sliding layer.

If the reinforcement is in the tensile cut-off state, the energy dissipation power of the $i$th layer can be expressed as

$$W_{i\_off} = \int_0^{r_i \Delta\theta} T\dot{\varepsilon} dx = Tr_i\Omega = Tr_0 \exp\left[(\theta_i - \theta_0)\tan\phi\right]\Omega \quad (32)$$

Based on the direction of the velocity at the intersection between the slip surface and the $i$th reinforcement, if the $i$th reinforcement is in the pulling-out state, the corresponding energy dissipation power can be derived as

$$W_{i\_out} = \min\left[(F_{iL} + E_i),(F_{iR} + E_i)\right]r_0 \exp\left[(\theta_i - \theta_0)\tan\phi\right]\sin\theta_i\Omega \qquad (33)$$

where the two lengths $L_{iL}$ and $L_{iR}$ are respectively expressed as

$$L_{iL} = \cos\theta_i r_0 \exp\left[(\theta_i - \theta_0)\tan\varphi\right] - \cos\theta_h r_0 \exp\left[(\theta_h - \theta_0)\tan\varphi\right] \\ - (H - i \cdot D)\tan\alpha \qquad (33a)$$

$$L_{iR} = L_i - r_0 \exp\left[(\theta_i - \theta_0)\tan\varphi\right]\cos\theta_i \\ + r_0 \exp\left[(\theta_h - \theta_0)\tan\varphi\right]\cos\theta_h + (H - i \cdot h)\tan\alpha \qquad (33b)$$

Further, the expression of the pulling-out energy dissipation power of the $i$th reinforcement and the total dissipation power of all reinforcements are the same as Eqs 14, 15, respectively.

Similarly, the factor of safety of the soil slope stability can be introduced *via* Eq. 17, and the relationship between $F_s$ and variables $\theta_0$ and $\theta_h$ can be determined *via* Eq. 16. Then the minimum safety factor and the corresponding slip surface can be obtained by

$$\begin{cases} \dfrac{\partial F_s}{\partial \theta_0} = 0 \\[2mm] \dfrac{\partial F_s}{\partial \theta_h} = 0 \end{cases} \qquad (34)$$

## 3 Practical example and verification

A geogrid-reinforced embankment on a stable foundation in a single-track railway in Bangladesh is shown in Figure 4. The width of the top surface of the embankment is 10.6 m, and there is an equivalent strip surcharge of 70 kPa with a 3.7 m distribution width in the middle of the top of the embankment with a 6 m height. The horizontal net distance between the surcharge and the slope crest is 3.45 m. The angle between the wall panel and the vertical direction is 3°, and the unit weight and internal friction angle of the sandy filling are 20 kN/m³ and 30°, respectively. The designed ultimate tensile force of the geogrids is 24 kN/m after the requirement of safety margin. According to the field seismic conditions, the horizontal and vertical seismic coefficients are specified as $k_h = 0.2$ and $k_v = 0.1$, respectively.

The factors of safety of the reinforced embankment obtained using the proposed method are shown in Figure 5. As can be seen, the safety factor is nonlinearly decreasing with the increase of the reinforcement spacing. There are similar results between the planar mode and log-spiral failure mode. To verify the proposed method, numerical modeling *via* FLAC³ᴰ (Rai et al., 2012; Mabrouk et al., 2018) is established (see Figure 6) for the reinforced embankment. The elastic-perfectly plastic constitutive model, the Mohr-Coulomb yield criterion, and the associative flow rule are assumed to simulate the soils. The panels are simulated with the linear elastic model. The geogrids are modeled with the Geogrid Element inserted in FLAC³ᴰ, and the shear characteristics of the geogrid-soil interface obey the elastic-perfectly plastic mode. The left and right boundaries of the numerical model are fixed in the horizontal direction, while the bottom is fixed in both the horizontal and vertical directions. The hexahedral mesh is used to divide the entity model to form a total of 239,520 elements and 254,851 nodes. Equivalent seismic forces are exerted on each element based on the pseudo-static approach. The main physical and mechanical parameters involved in the numerical model are shown in Tables 1, 2, which is determined mainly according to the related laboratory material tests with enough number to eliminate possible accidental error, as well as the empirical references in FLAC³ᴰ.

It can also be seen from Figure 5 that the factors of safety by FLAC³ᴰ are slightly larger than the proposed results under different reinforcement spacing, and the relationships between $F_s$ and $h$ using the analytical and numerical methods are similar. If the geogrid spacing is 0.3 m, the factors of safety of using FLAC³ᴰ and the proposed method with planar mode and log-spiral mode are 1.66, 1.52, and 1.49, respectively, and the maximum relative error is 10.2%. So, the proposed results are in good agreement with the numerical value. According to Li et al. (2006), the safety factor of embankment stability should not be less than 1.3 in some cases. The maximum vertical spacing of the geogrids is accordingly figured out to be 0.46 m by the planner mode and 0.43 m by the log-spiral mode. So the latter can be conservatively adopted as
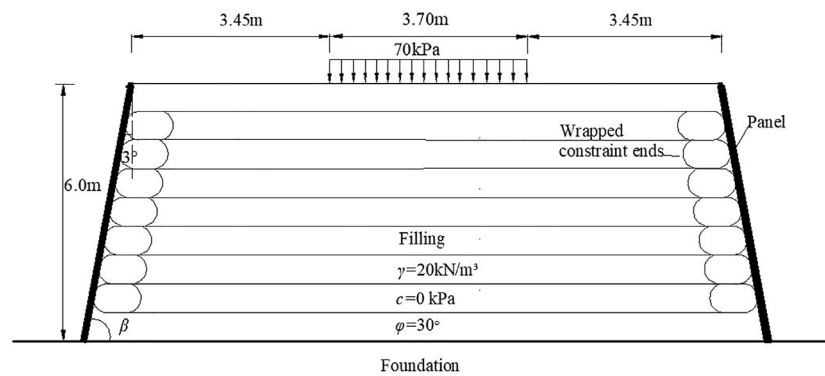
FIGURE 4
Cross-sectional diagram of a bilaterally wrapped geogrid-reinforced embankment.
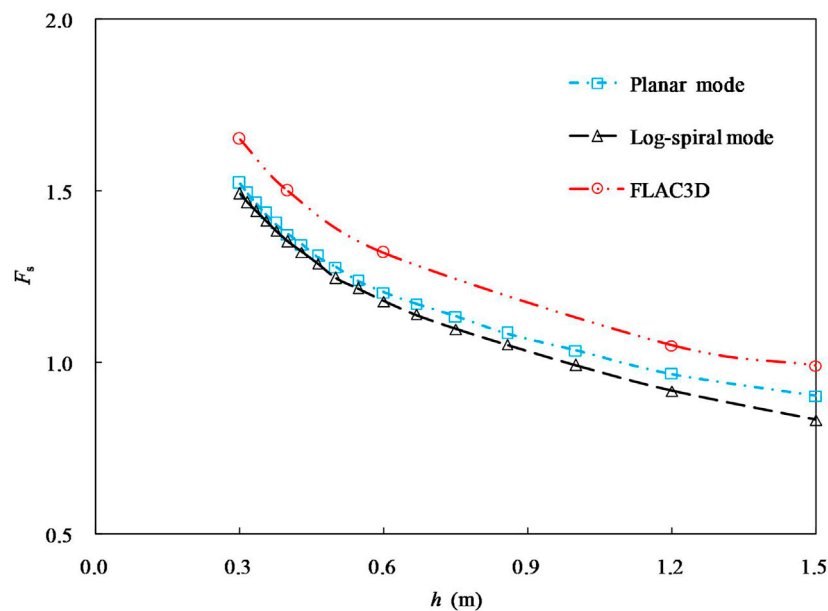


FIGURE 5
Calculation results of factor of safety using different methods.

the design control value. There are some differences of the calculation results between the two failure surface modes. The reason lies mainly that the shape of the slip surface has close influence on the internal and external power of the failure mechanism. In particular, the dissipation power of the log-spiral slip surface is more significant than that of the planar slip surface, which means the required reinforcement spacing under the former is possibly smaller than that under the latter. In addition, from the perspective of deformation mechanism of the reinforced embankment, the reinforcement tension in the planar mode is much more developed than that in the log-spiral mode,

which naturally allows a higher reinforcement spacing to maintain the specified stability of the embankment.

The other geosynthetics-reinforced embankment with vertical slope face under different seismic actions is adopted herein to further verify the proposed method. The embankment height is 6 m and the reinforcement spacing is 0.6 m. The unit weight and internal friction angle of the sandy filling are 16 kN/m³ and 32°, respectively. The horizontal seismic coefficient is 0.25, and the reinforcement strength is 90 kN/m. The proposed results are shown in Figure 7, where they are compared with the results by FHWA (2009) and Xu and Hatami (2019). As can be

**FIGURE 6**
Numerical model *via* FLAC3D for the example.
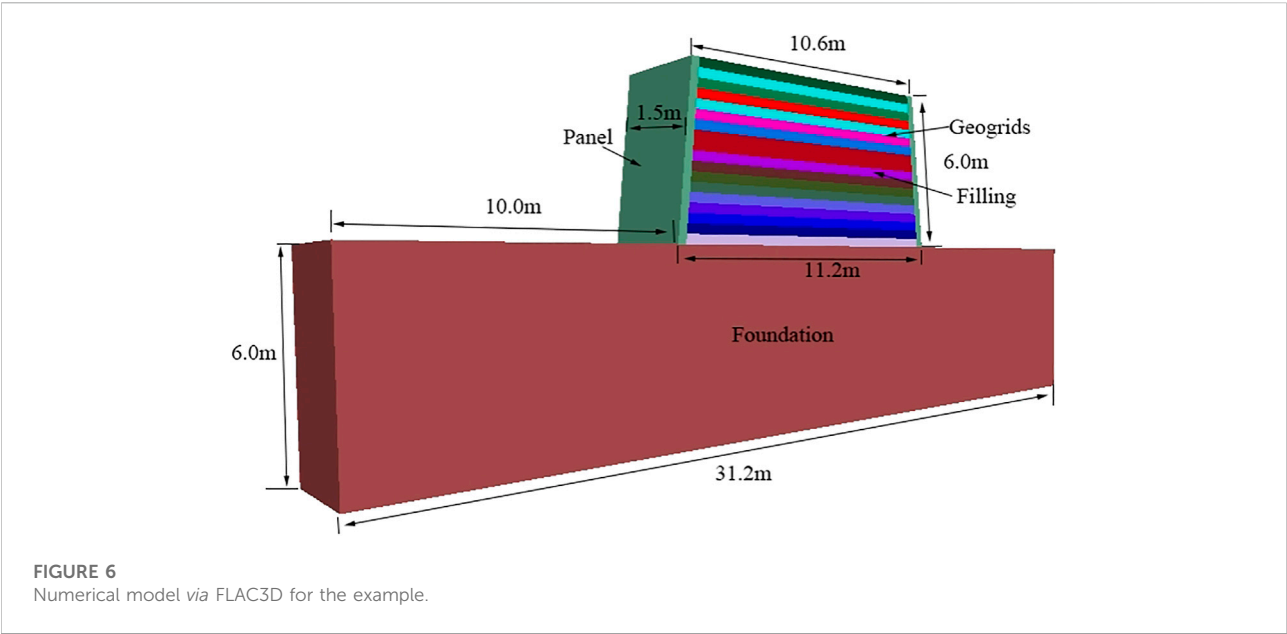
TABLE 1 Material properties of the numerical model.

| Material | Bulk modulus (MPa) | Shear modulus (MPa) | Cohesion (kPa) | Internal friction angle (°) | Unit weight (kN/m3) |
|---|---|---|---|---|---|
| Filling | 9.5 | 8.7 | 0 | 30 | 20 |
| Foundation | 80 | 32 | 10 | 45 | 25 |
| Panel | 16.6 | 7.7 | — | — | 22 |

TABLE 2 Geogrid and geogrid-soil interface parameters.

| Elastic modulus (MPa) | Poisson's ratio | Coupling stiffness (MPa) | Coupling cohesion (kPa) | Coupling internal friction angle (°) | Thickness(mm) |
|---|---|---|---|---|---|
| 50 | 0.33 | 23 | 2 | 30 | 2 |

seen, the proposed results are fairly close to those using the existing methods, particularly in most cases of $-1 \leq k_v/k_h \leq 1$. If $k_v/k_h = 0.5$, the proposed safety factors under the planer and log-spiral modes are individually 1.303 and 1.290, whose relative errors with those by FHWA (2009) and Xu and Hatami (2019) are 0.5% and 1.3%, 1.5% and 0.3%, respectively.

# 4 Parameter study and discussion

According to the proposed analysis model and derived formulas, many factors have influences on the reinforcement spacing. The reinforced embankment shown in Figure 4 is taken herein as an example to discuss the influences by the essential

parameters, including $T$, $\gamma$, $c$, $\varphi$, $q$, $k_h$ and $k_v$. The parameter study is conducted using the controlling variable tactic with specified basic values $c = 0$ kPa, $\varphi = 30°$, $\gamma = 18$ kN/m$^3$ $\alpha = 3°$, $a = 3.45$ m, $b = 3.7$ m, $H = 6$ m, $T = 24$ kN/m, $q = 70$ kPa, $k_h = 0.2$ and $k_v = 0.1$. The values of each parameter are assumed mainly according to the common range in practical engineering as well as the related empirical data. Besides, vertical seismic coefficient is usually half of the horizontal seismic coefficient (Kavazanjian, 1995).

## 4.1 Reinforcement strength

The variation of the safety factor with the reinforcement spacing under different reinforcement strengths is shown in
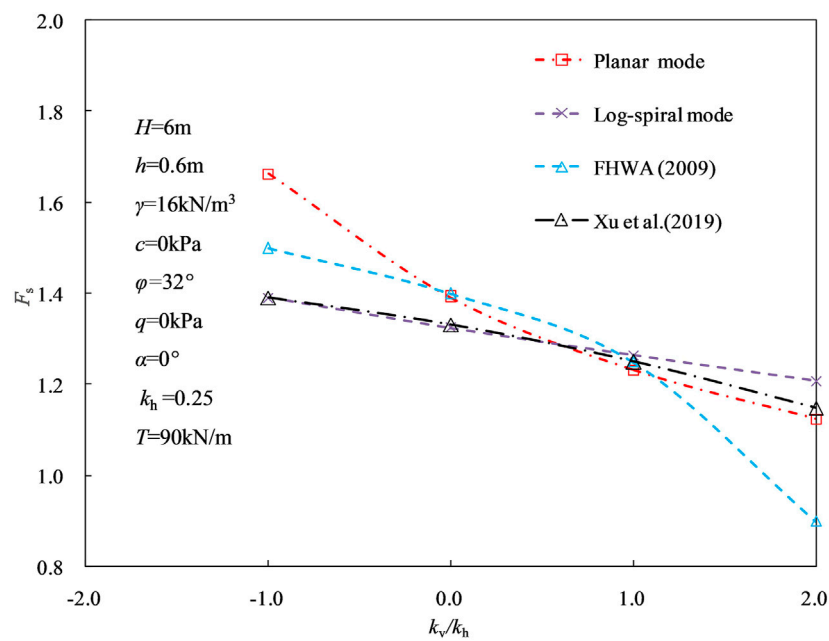
**FIGURE 7**
Comparison of factor of safety of another example using different methods.
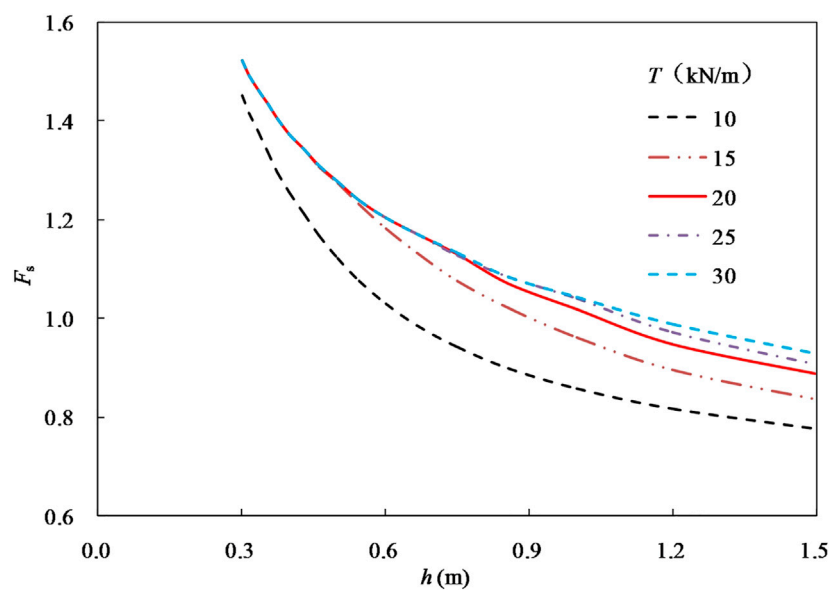


**FIGURE 8**
Relationship between $F_s$ and $h$ under different $T$.

Figure 8. It can be seen that the nonlinear negative relationship between the factor of safety and the reinforcement spacing is noticeable under different $T$. Figure 9 shows that the spacing is

nonlinearly increasing with the reinforcement strength under $F_s = 1.0$. However, the nonlinear characteristics are not obvious with the increase of $F_s$. Additionally, the spacing is almost not
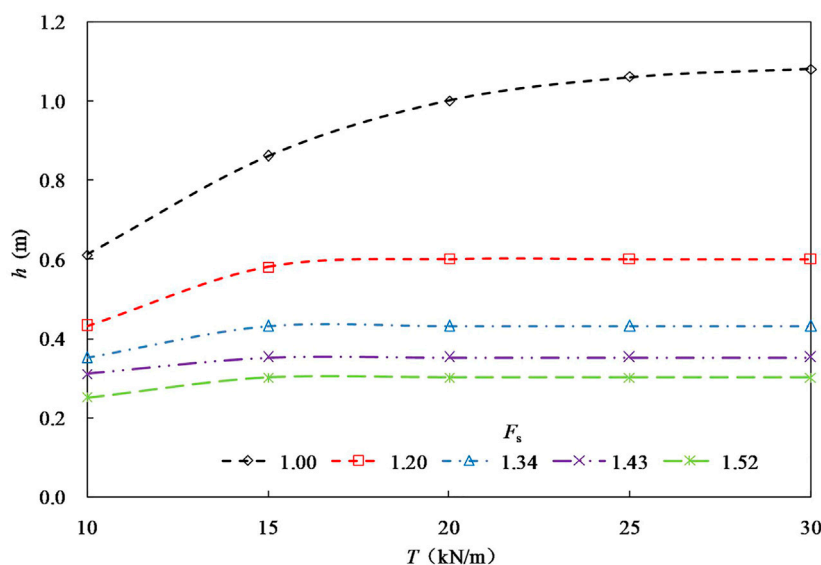
**FIGURE 9**
Relationship between $h$ and $T$ under different $F_s$.

influenced as expected under a designed safety factor if the reinforcement strength reaches a relatively high value.

## 4.2 Unit weight of filling

Figure 10 shows the relationship between the reinforcement spacing and the unit weight of the filling under different factors of safety. As can be seen, the unit weight has almost no effect on the reinforcement spacing. Under the same unit weight, the required spacing is nonlinearly decreasing with the safety factor increase. Taking the unit weight of 18 kN/m³ as an example, the reinforcement spacing required to meet the overall stability with designed safety factors of 1.20, 1.34, and 1.43 is 0.6, 0.43, and 0.38 m, respectively.

## 4.3 Cohesion of filling

The influence of the filling cohesion on the reinforcement spacing is shown in Figure 11. It can be seen that the spacing is generally nonlinearly increasing with cohesion. However, if the designed safety factor is small, there is an approximately linear relationship between the spacing and the cohesion, and the spacing necessary is considerably increasing with the cohesion. The filling shear strength is liable to meet the requirement of the overall stability of the reinforced embankment under lower factors of safety. In these cases, the effect of the reinforcements on the embankment stability is not significant to naturally allow fairly high reinforcement spacing.

## 4.4 Internal friction angle of filling

Figure 12 shows the relationship between the reinforcement spacing and the internal friction angle of the filling. As can be seen, with the increase of the internal friction angle, the reinforcement spacing required to meet the overall stability almost increases linearly. However, the increased gradient is closely related to the factor of safety. If the factor of safety is small and close to 1.0, the increasing gradient is relatively obvious; but if the factor of safety is high enough, the required spacing is almost not varied with the internal friction angle.

## 4.5 Strip surcharge

Figure 13 reveals the variation of the reinforcement spacing with the strip surcharge under different safety factors. As the strip surcharge increases, the reinforcement spacing is approximately linear decreasing. The decrease gradient depends to some extent on the specified factor of safety. With the increase of safety factor, the decrease gradient is reduced.

## 4.6 Seismic coefficients

The relationships between the reinforcement spacing and the horizontal and vertical seismic coefficient under different safety factors are shown in Figure 14 and Figure 15, respectively. It can be seen from Figure 14 that the reinforcement spacing decreases
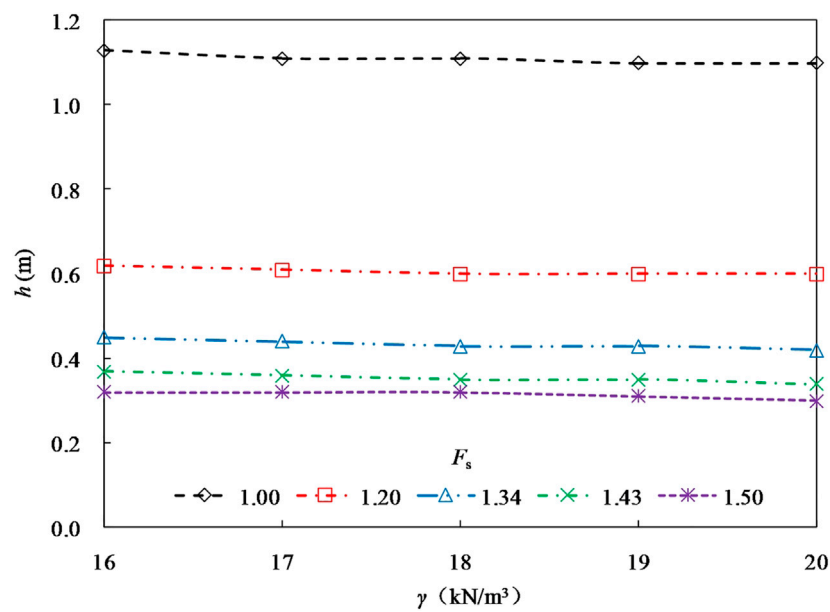
**FIGURE 10**
Relationship between $h$ and $\gamma$ under different $F_s$.
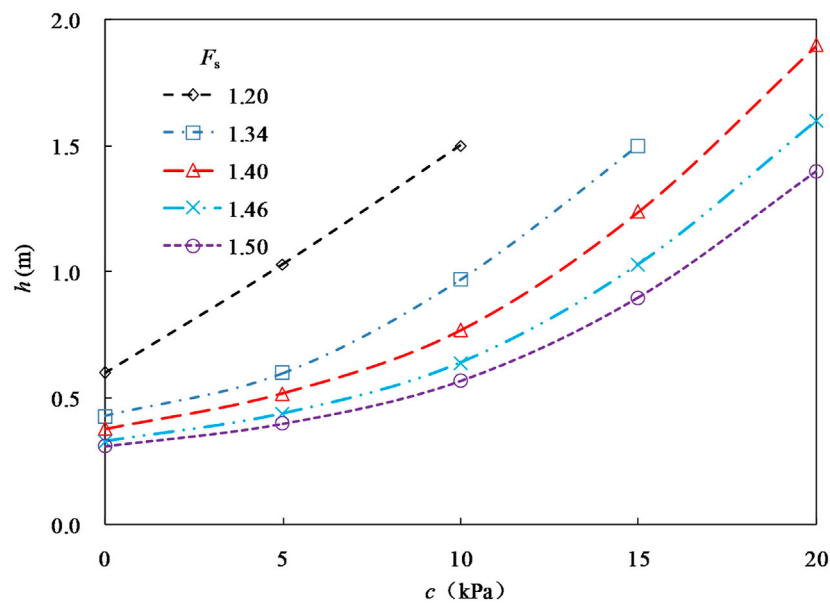


**FIGURE 11**
Relationship between $h$ and $c$ under different $F_s$.

nonlinearly with the increase of the horizontal seismic coefficient. As the specified factor of safety increases, the nonlinear characteristics lessen to some extent. Figure 15 reveals the spacing is almost linearly reducing as the vertical seismic coefficient increases. With the rise of the designed safety factor, the decrease gradient reduces gradually. Under high safety factors, the vertical seismic coefficient has a minor effect on the reinforcement spacing.
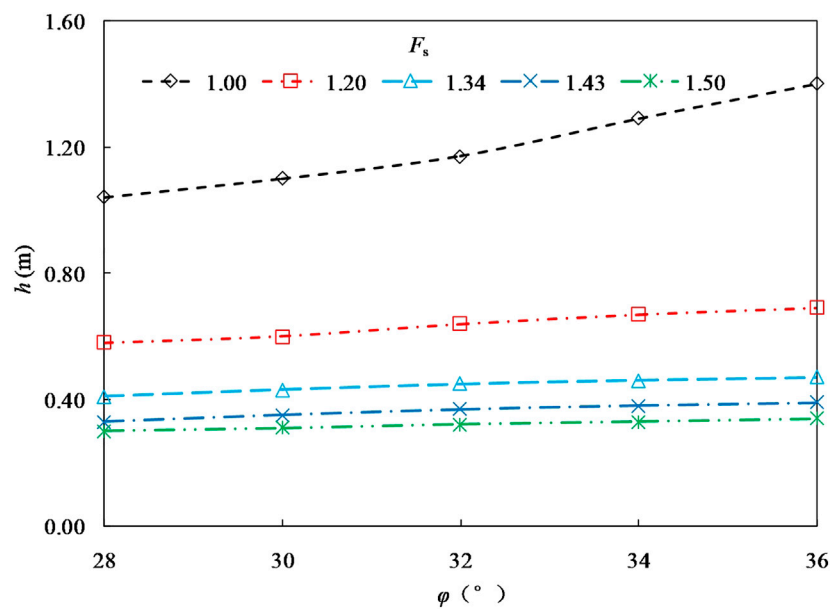
**FIGURE 12**
Relationship between $h$ and $\varphi$ under different $F_s$.
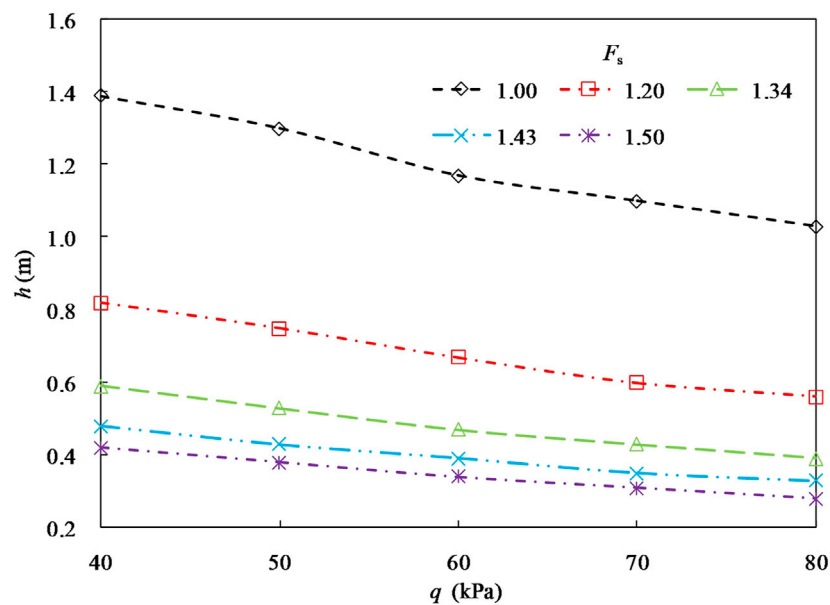


**FIGURE 13**
Relationship between $h$ and $q$ under different $F_s$.

## 4.7 Sensitivity analysis

The sensitivity of the vertical spacing to the seven independent parameters mentioned-above can be further analyzed by an orthogonal test design. According to the empirical range of physical and mechanical indexes of embankment filling, four levels are assumed for this test, and the specific values are shown in Table 3. So, the total number of
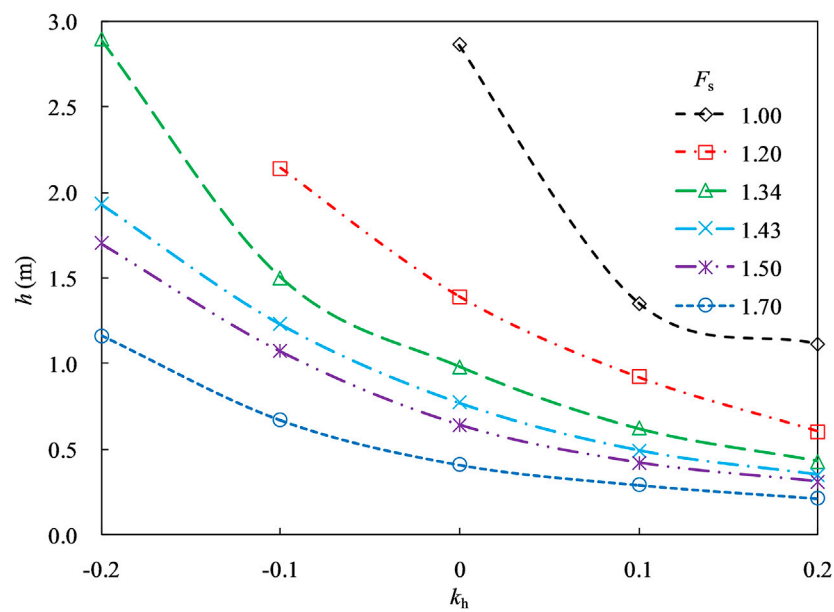
**FIGURE 14**
Relationship between $h$ and $k_h$ under different $F_s$.
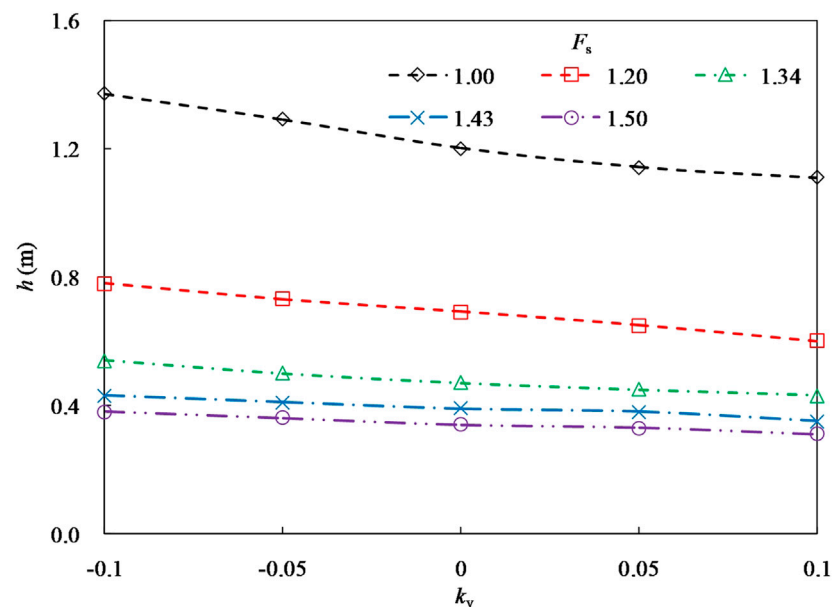


**FIGURE 15**
Relationship between $h$ and $k_v$ under different $F_s$.

the orthogonal test can be assumed as 32 to effectively reflect the combination of different factors. The range analysis results of the orthogonal test are listed in Table 4, where $K_1$, $K_2$, $K_3$ and $K_4$ as well as $m_1$, $m_2$, $m_3$ and $m_4$ are the sum and arithmetic mean values of the corresponding test results if the level is 1, 2, 3 and 4, respectively; and $R$ is the range of $m$. As can be seen that the range value of the seven factors $T$, $\gamma$, $c$, $\varphi$, $q$, $k_h$ and $k_v$ are 0.048, 0.056, 0.388, 0.086, 0.212, 0.653 and 0.126, respectively. Therefore, the

TABLE 3 Factors and levels of the orthogonal test.

| Levels | Influence factors | | | | | | |
|---|---|---|---|---|---|---|---|
| | $T$ (kN/m) | $\varphi$ (°) | $c$ (kPa) | $\gamma$ (kN/m3) | $q$ (kPa) | $k_h$ | $k_v$ |
| 1 | 10 | 28 | 0 | 17 | 50 | 0 | 0 |
| 2 | 15 | 30 | 5 | 18 | 60 | 0.1 | 0.05 |
| 3 | 20 | 32 | 10 | 19 | 70 | 0.2 | 0.1 |
| 4 | 25 | 34 | 15 | 20 | 80 | 0.3 | 0.15 |

TABLE 4 Range analysis results of the orthogonal test.

| | Influence factors | | | | | | |
|---|---|---|---|---|---|---|---|
| | $T$ (kN/m) | $\varphi$ (°) | $c$ (kPa) | $\gamma$ (kN/m³) | $q$ (kPa) | $k_h$ | $k_v$ |
| $K_1$ | 14.969 | 14.962 | 13.710 | 15.275 | 16.080 | 17.799 | 15.589 |
| $K_2$ | 15.352 | 14.968 | 14.401 | 15.097 | 15.302 | 16.032 | 15.245 |
| $K_3$ | 15.085 | 14.980 | 15.631 | 15.316 | 14.788 | 14.147 | 15.140 |
| $K_4$ | 15.150 | 15.646 | 16.814 | 14.868 | 14.386 | 12.578 | 14.582 |
| $m_1$ | 1.871 | 1.870 | 1.714 | 1.909 | 2.010 | 2.225 | 1.949 |
| $m_2$ | 1.919 | 1.871 | 1.800 | 1.887 | 1.913 | 2.004 | 1.906 |
| $m_3$ | 1.886 | 1.873 | 1.954 | 1.915 | 1.849 | 1.768 | 1.893 |
| $m_4$ | 1.894 | 1.956 | 2.102 | 1.859 | 1.798 | 1.572 | 1.823 |
| $R$ | 0.048 | 0.086 | 0.388 | 0.056 | 0.212 | 0.653 | 0.126 |

sensitivity order of these factors from large to small is subsequentially horizontal seismic coefficient, filling cohesion, strip surcharge, vertical seismic coefficient, filling internal friction angle, filling unit weight, and reinforcement strength.

# 5 Conclusion

Based on the upper-bound limit analysis method and pseudo-static approach, a stability analysis method of the bilaterally wrapped reinforced embankment under strip surcharge and seismic action is provided considering the planar and log-spiral failure mechanism of the reinforced embankment, which can substantially reflect the relationship between the reinforcement spacing and the overall stability of the reinforced embankment. Under a specified factor of safety of the overall stability, the required spacing can be consequently figured out. The main conclusions are drawn as follows:

- The safety factor of the reinforced embankment decreases nonlinearly with the increase of reinforcement spacing, and similar results are obtained in the planar and log-spiral failure mechanisms. Under the same safety factor for the stability

requirement, the allowable reinforcement spacing calculated using the log-spiral mode is smaller and more conservative than that using the planar mode. Under a specified reinforcement spacing in some examples, the maximum relative error of the safety factor between the proposed method and some existing methods, including FLAC3D, is around 10%.

- The proposed method can quantitatively reflect the influence of properties of the filling, reinforcement strength, seismic forces, strip surcharge, and geometry of the embankment on the reinforcement spacing under a specified safety factor. The reinforcement spacing is nonlinearly positively related to the filling cohesion and approximately linearly positively related to the internal friction angle of the filling, while the unit weight of the filling does not almost influence it.

- The nonlinear negative relationship between the factor of safety and the reinforcement spacing is noticeable under different reinforcement strengths, but the nonlinear characteristics are not obvious with the increase of the design factor of safety. The spacing is scarcely influenced under a design factor of safety if the reinforcement strength reaches a relatively high value. The spacing is almost linearly reduced as the strip surcharge or vertical seismic coefficient

increases, whereas it decreases nonlinearly with the rise of the horizontal seismic coefficient.

## Data availability statement

The original contributions presented in the study are included in the article/Supplementary Material, further inquiries can be directed to the corresponding author.

## Author contributions

QY: conceptualization, methodology, software analysis, data curation, writing- original draft preparation. SX: supervision, reviewing and editing.

## Conflict of interest

The authors declare that the research was conducted in the absence of any commercial or financial relationships that could be construed as a potential conflict of interest.

## Publisher's note

All claims expressed in this article are solely those of the authors and do not necessarily represent those of their affiliated organizations, or those of the publisher, the editors and the reviewers. Any product that may be evaluated in this article, or claim that may be made by its manufacturer, is not guaranteed or endorsed by the publisher.

## References

Abu-Farsakh, M. Y., Gu, J., Voyiadjis, G., and Tao, M. J. (2007). Numerical parametric study of strip footing on reinforced embankment soils. *Transp. Res. Rec.* 2004, 132–140. doi:10.3141/2004-14

Ahmadabadi, M., and Ghanbari, A. (2009). New procedure for active Earth pressure calculation in retaining walls with reinforced cohesive-frictional backfill. *Geotext. Geomembranes* 27, 456–463. doi:10.1016/j.geotexmem.2009.06.004

Basha, B. M., and Babu, G. L. S. (2011). Seismic reliability assessment of internal stability of reinforced soil walls using the pseudo-dynamic method. *Geosynth. Int.* 18, 221–241. doi:10.1680/gein.2011.18.5.221

Chen, H. T., Hung, W. Y., Chen, P. W., and Lee, C. J. (2015). Improvement of the stability of a vertical geotextile reinforced Earth wall backfilled with low strength clayey soil. *Int. J. Phys. Model. Geotechnics* 7, 35–45. doi:10.1680/ijpmg.2007.070203

Chen, J. F., Liu, J. X., Xue, J. F., and Shi, Z. M. (2014). Stability analyses of a reinforced soil wall on soft soils using strength reduction method. *Eng. Geol.* 177, 83–92. doi:10.1016/j.enggeo.2014.05.018

Chen, W. F. (1975). *Limit analysis and soil plasticity*. Amsterdam, Netherlands: Elsevier Scientific Publishing Company. doi:10.1016/b978-0-444-41249-2.x5001-x

Chen, W. F., and Snitbhan, N. (1975). On slip surface and slope stability analysis. *Soils Found.* 15, 41–49. doi:10.3208/sandf1972.15.3_41

Choudhury, D., Mandal, J. N., and Nimbalkar, S. S. (2006). Seismic stability of reinforced-soil wall by pseudo-dynamic method. *Geosynth. Int.* 13, 111–119. doi:10.1680/gein.2006.13.3.111

Farshidfar, N., Keshavarz, A., and Mirhosseini, S. M. (2020). Pseudo-static seismic analysis of reinforced soil slopes using the horizontal slice method. *Arab. J. Geosci.* 13, 1–14. doi:10.1007/s12517-020-5269-0

Fhwa (2009). *Mechanically stabilized earth walls and reinforced soil slopes design and construction guidelines*. Washington, D C, USA: Federal Highway Administration.

Gebremariam, F., Tanyu, B. F., Guler, E., Urgessa, G. S., and Shen, P. (2021). Numerical investigation of reinforced soil structures with GRS-IBS design features. *Geosynth. Int.* 28, 1–50. doi:10.1680/jgein.20.00031

Hajiazizi, M., Bavali, M., and Fakhimi, A. (2018). Numerical and experimental study of the optimal location of concrete piles in a saturated sandy slope. *Int. J. Civ. Eng.* 16, 1293–1301. doi:10.1007/s40999-017-0155-1

Holtz, R. D. (2017). 46th terzaghi lecture: Geosynthetic reinforced soil: From the experimental to the familiar. *J. Geotech. Geoenviron. Eng.* 143, 03117001. doi:10.1061/(asce)gt.1943-5606.0001674

Kavazanjian, E. (1995). "Hanshin earthquake-replyCalifornia, CA, USA," in *NSF earthquake hazard mitigation program* (Los Angeles: Geotechnical Bulletin Board).

Khoshzaban, A., Askari, F., and Farzaneh, O. (2021). Introduction of plastic block method in the upper bound limit analysis of soil stability problems. *Int. J. Civ. Eng.* 19, 897–910. doi:10.1007/s40999-020-00596-3

Lee, K. Z. Z., Chang, N. Y., and Ko, H. Y. (2010). Numerical simulation of geosynthetic-reinforced soil walls under seismic shaking. *Geotext. Geomembranes* 28, 317–334. doi:10.1016/j.geotexmem.2009.09.008

Leschinsky, D. (2007). Discussion of the influence of facing stiffness on the performance of two geosynthetic reinforced soil retaining walls. *Can. Geotech. J.* 44, 1479–1482. doi:10.1139/t07-100

Leschinsky, D., and Reinschmidt, A. J. (1985). Stability of membrane reinforced slopes. *J. Geotech. Eng.* 111, 1285–1300. doi:10.1061/(asce)0733-9410

Leschinsky, D., and Vulova, C. (2001). Numerical investigation of the effects of geosynthetic spacing on failure mechanisms in MSE block walls. *Geosynth. Int.* 8, 343–365. doi:10.1680/gein.8.0199

Li, X. H., Qin, L. X., Bao, L. M., Feng, J. D., and Wu, L. H. (2006). *Code for design for applications of geosynthetics on subgrade of railway*. Beijing, China: China Railway Publishing House.

Li, L. H., Cui, F. L., Ferreira, P., Xiao, H. L., and Jie, H. (2019). Experimental study of embankments with different reinforcement materials and spacing between layers. *Geotext. Geomembranes* 47, 477–482. doi:10.1016/j.geotexmem.2019.03.003

Li, Q., Ma, D., Zhang, Y. D., Liu, Y., and Ma, Y. J. (2021). Insights into controlling factors of pore structure and hydraulic properties of broken rock mass in a geothermal reservoir. *Lithosphere-Us* 5. doi:10.2113/2022/3887832

Ma, D., Duan, H. Y., Zhang, J. X., Liu, X. W., and Li, Z. H. (2022b). Numerical simulation of water–silt inrush hazard of fault rock: A three-phase flow model. *Rock Mech. Rock Eng.* 55, 5163–5182. doi:10.1007/s00603-022-02878-9

Ma, D., Duan, H. Y., and Zhang, J. X. (2022a). Solid grain migration on hydraulic properties of fault rocks in underground mining tunnel: Radial seepage experiments and verification of permeability prediction. *Tunn. Undergr. Space Technol.* 126, 104525. doi:10.1016/j.tust.2022.104525

Mabrouk, T., Ahmed, R., Mustapha, B., and Belkacem, A. (2018). Experimental and numerical analysis of geogrid-reinforced soil systems. *Arab. J. Sci. Eng.* 43, 5295–5303. doi:10.1007/s13369-018-3158-6

Michalowski, R. L. (1998). Limit analysis in stability calculations of reinforced soil structures. *Geotext. Geomembranes* 16, 311–331. doi:10.1016/s0266-1144(98)00015-6

Narasimha Reddy, G. V., Madhav, M. R., and Saibaba Reddy, E. (2008). Pseudo-static seismic analysis of reinforced soil wall-Effect of oblique displacement. *Geotext. Geomembranes* 26, 393–403. doi:10.1016/j.geotexmem.2008.02.002

Nouri, H., Fakher, A., and Jones, C. J. F. P. (2008). Evaluating the effects of the magnitude and amplification of pseudo-static acceleration on reinforced soil slopes and walls using the limit equilibrium horizontal slices method. *Geotext. Geomembranes* 26, 263–278. doi:10.1016/j.geotexmem.2007.09.002

Pain, A., Choudhury, D., and Bhattacharyya, S. K. (2017). Effect of dynamic soil properties and frequency content of harmonic excitation on the internal stability of reinforced soil retaining structure. *Geotext. Geomembranes* 45, 471–486. doi:10.1016/j.geotexmem.2017.07.003

Rai, R., Khandelwal, M., and Jaiswal, A. (2012). Application of geogrids in waste dump stability: A numerical modeling approach. *Environ. Earth Sci.* 65, 1459–1465. doi:10.1007/s12665-011-1385-1

Ren, F. F., Zhang, F., Xu, C., and Wang, G. (2016). Seismic evaluation of reinforced-soil segmental retaining walls. *Geotext. Geomembranes* 44, 604–614. doi:10.1016/j.geotexmem.2016.04.002

Romstad, K. M., Herrmann, L. R., and Shen, C. K. (1976). Integrated study of reinforced Earth–I: Theoretical formulation. *J. Geotech. Engrg. Div.* 102, 457–471. doi:10.1061/ajgeb6.0000269

Ruan, X. B., and Sun, S. L. (2013). Seismic stability of reinforced soil walls under bearing capacity failure by pseudo-dynamic method. *J. Cent. South Univ.* 20, 2593–2598. doi:10.1007/s11771-013-1773-7

Segrestin, P. "Design of sloped reinforced fill structure," in Proceedings of the conference organized by the institution of civil engineers and robinson college, Cambridge, MA, USA, July 1992, 574–584.

Sitar, N., and Nova-Roessig, L. A. "Review of experimental studies of seismic behavior of reinforced soil structures," in Proceedings of the Second International Conference On Earthquake Geotechnical Engineering, Rotterdam, Netherlands, June 1999, 1083–1088.

Tatsuoka, F. (2019). Geosynthetic-reinforced soil structures for railways and roads: Development from walls to bridges. *Innov. Infrastruct. Solut.* 4, 49. doi:10.1007/s41062-019-0236-x

Venkateswarlu, H., and Hegde, A. (2020). Isolation prospects of geosynthetics reinforced soil beds subjected to vibration loading: Experimental and analytical studies. *Geotech. Geol. Eng.* 38, 6447–6465. doi:10.1007/s10706-020-01447-7

Weerasekara, L., Hall, B., and Wijewickreme, D. (2017). A new approach for estimating internal stability of reinforced soil structures. *Geosynth. Int.* 24, 419–434. doi:10.1680/jgein.17.00012

Wu, J. T. H., and Pham, T. Q. (2013). Load-carrying capacity and required reinforcement strength of closely spaced soil-geosynthetic composites. *J. Geotech. Geoenviron. Eng.* 139, 1468–1476. doi:10.1061/(asce)gt.1943-5606.0000885

Xie, Y. G., and Leshchinsky, B. (2015). MSE walls as bridge abutments: Optimal reinforcement density. *Geotext. Geomembranes* 43, 128–138. doi:10.1016/j.geotexmem.2015.01.002

Xu, H., Ren, X., Chen, J. N., Liu, C. N., Xia, L., and Liu, Y. W. (2019). Centrifuge model tests of geogrid-reinforced slope supporting a high embankment. *Geosynth. Int.* 26, 629–640. doi:10.1680/jgein.19.00027

Xu, P., and Hatami, K. (2019). Sliding stability and lateral displacement analysis of reinforced soil retaining walls. *Geotext. Geomembranes* 47, 483–492. doi:10.1016/j.geotexmem.2019.03.004

Yang, X. L. (2007). Upper bound limit analysis of active earth pressure with different fracture surface and nonlinear yield criterion. *Theor. Appl. Fract. Mech.* 47, 46–56. doi:10.1016/j.tafmec.2006.10.003

Zheng, Y. W., and Fox, P. J. (2016). Numerical investigation of geosynthetic-reinforced soil bridge abutments under static loading. *J. Geotech. Geoenviron. Eng.* 142, 04016004. doi:10.1061/(asce)gt.1943-5606.0001452

Zhussupbekov, A. Z., Tanaka, T., and Aldungarova, A. K. (2015). Model tests of the influence of reinforcement on levee stability. *Soil Mech. Found. Eng.* 52, 131–134. doi:10.1007/s11204-015-9318-8

Zienkiewicz, O. C., Humpheson, C., and Lewis, R. W. (1975). Associated and non-associated visco-plasticity and plasticity in soil mechanics. *Geotechnique* 25, 671–689. doi:10.1680/geot.1975.25.4.671

Zornberg, J. G., Sitar, N., and Mitchel, J. K. (1998). Performance of geosyn-thetic reinforced slopes at failure. *J. Geotech. Geoenviron. Eng.* 124, 670–683. doi:10.1061/(asce)1090-0241(1998)124:8(670)

Zou, C., Wang, Y. M., Lin, J. Y., and Chen, Y. K. (2016). Creep behaviors and constitutive model for high density polyethylene geogrid and its application to reinforced soil retaining wall on soft soil foundation. *Constr. Build. Mat.* 114, 763–771. doi:10.1016/j.conbuildmat.2016.03.194

Frontiers | Frontiers in Earth Science

Check for updates

# Risk analysis and countermeasures of TBM tunnelling over the operational tunnel

Feng Lu[1,2,3], Linlong Li[1], Zhenyu Chen[1], Maoyi Liu[4], Pinpin Li[3], Xinqiang Gao[2]*, Changjun Ji[5]* and Lun Gong[3]

[1]School of Emergency Management, Xihua University, Chengdu, Sichuan, China, [2]State Key Laboratory of Mechanical Behavior and System Safety of Traffic Engineering Structures, Shijiazhuang Tiedao University, Shijiazhuang, China, [3]Key Laboratory of Transportation Tunnel Engineering, Ministry of Education, School of Civil Engineering, Southwest Jiaotong University, Chengdu, Sichuan, China, [4]Chongqing Urban Construction Investment (Group) Co., Ltd., Chongqing, China, [5]Institute of Geomechanics, Chinese Academy of Geological Sciences, Beijing, China

To study the risk and control countermeasures of the TBM tunnel construction adjacent to the operational railway tunnel, based on the TBM tunnel project of Chongqing Rail Transit Line 5, this paper first evaluates the quality health degree of the operational tunnel lining (OTL) structure according to the on-site structural inspection. Then, the displacement, internal force, and proximity influence scope influenced by the metro TBM tunnel construction are studied using numerical simulation. Finally, the corresponding control countermeasures are proposed. The results show that: (1) The adjacent construction of the upper TBM tunnel will lead to the uplift deformation trend of the lower operational tunnel, and the uplift deformation of the vault is greater than that of the ballast bed. The influence scope is roughly a parallelogram, with the long axis parallel to the operational tunnel and the short axis parallel to the new TBM subway tunnel. (2) TBM tunnelling over the operational tunnel will cause the transformation of the mechanical mode of the OTL structure from the small eccentric compression mode to the large eccentric compression mode. The OTL structure between the left and right lines of TBM is unfavorable. (3) The longitudinal curve of the bending moment and axial force of the OTL fluctuates greatly within the influence range. The bending moment and axial force are reduced in operational tunnel construction joints. Based on field evaluation and numerical analysis, this paper puts forward some risk control countermeasures, such as TBM tunnelling parameters control, pea-gravel backfilling, backfill grouting, and bottom grouting, which can effectively solve the risk of the operational tunnel structure in the adjacent construction. This study has important reference value for risk control and safety assessment of tunnel in complex adjacent tunnel construction.

KEYWORDS

TBM tunnel, adjacent construction, risk analysis, structural safety, control countermeasures

## 1 Introduction

With the rapid development of subway construction in China, more and more subways are constructed adjacent to existing tunnels. Moreover, the construction risk will be further increased when multiple tunnels are constructed close to each other. Being one of the riskiest engineering projects, the adjacent-tunnel construction will lead to adverse effects on the adjacent structures, such as causing cracks in adjacent

buildings and threatening the operational safety of existing tunnels (Zhang and Huang, 2014).

Some countries in the world started earlier in adjacent tunnel research, for example, Japan has formed a technical construction guide based on its comprehensive study and summary of various problems on construction adjacent to existing tunnels. In China, Qiu (2003) put forward the definition and classification of the adjacent construction, the theory of adjacent impact zoning, the concept of adjacent, and the corresponding countermeasures; Zheng (2007), Gong (2008), and Kong (2016) continually to conduct in-depth research on the impact degree and impact zoning of different types of adjacent projects. The impact analysis of the construction adjacent to the existing tunnels mainly falls into two groups: the analytical method and numerical simulation. Because of the advantages of low cost, short cycle, repeatability, and suitability for parametric analysis, numerical simulation has been widely used in the research of tunnel adjacent. Li et al. (2016) adopted numerical simulation to analyze the response of deformation, stress, and plastic zone of tunnel intersection. Moreover, the influence scope of the tunnel lining was analyzed, and thus proposed control countermeasures of the locally thickened support structure to improve tunnel stability. Fang et al. (2015) analyzed the settlement of the existing tunnel caused by the new two newly-built shield tunnels by numerical simulation, and used superposition technology to fit the settlement profile of the existing tunnel affected by the new tunnels. Choi and Lee (2010) used numerical simulation method, found that the size of newly-built tunnel, centre spacing of tunnels, and earth pressure coefficient have an influence on the mechanical behaviours of both the existing and new tunnels during construction. Akbari et al. (2020) used numerical method to study the influence of the horizontal distance between the double-line tunnel and the single-line tunnel on the lining deformation, the lining stress, the ground settlement, and the structure stability. It was found that the influence can be ignored when the distance is more than three times the diameter of the single-line tunnel. Jiang et al. (2017) based on the actual project of double tunnels passing through the existing tunnel and found that the adverse effect of the later excavation on the existing tunnel is less than that of the earlier excavation of the tunnel by numerical analysis. It can be seen that, the numerical simulation has become an important research method to analysis the risk of complex tunnel proximity construction, which can provide a basis for risk evaluation and risk control measures.

The risk control measures for proximity construction often adopt the risk control methods such as reinforcing the existing tunnel structure, optimizing the adjacent construction measures, and improving the surrounding rock parameters within the influence area. The safety of the existing tunnel structure can be improved by compensating grouting behind the lining (Zhang et al., 2018). Gauge tie rods, guard rails, and rail fastening beams are usually added to the existing tunnel structure. At the same time, lifting grouting and filling grouting are used to deal with the settlement and the separation between the ballast bed and the tunnel invert (Zhang et al., 2009), to improve the operational safety of the existing tunnel during construction. In addition, measures such as advanced small conduits and surrounding rock grouting reinforcement are taken to improve the strength of surrounding rock between tunnels, which can reduce the tunnel stratum disturbance during the close construction and the impact of new tunnel construction on existing tunnels. Pre-reinforcement measures of pipe shed and pipe curtain (Cui et al., 2022) and temporary invert (Zheng et al., 2009) are adopted to reduce the

settlement of existing and new tunnels during the excavation of adjacent tunnels. However, the research on tunnel proximity risk control mainly focuses on construction control measures and structural safety analysis. The research cases of risk analysis and corresponding control measures for TBM tunnelling over the existing tunnels are rarely involved and need to be further studied. Therefore, based on the Chongqing Rail Transit Line 5 tunnel adjacent to the operational railway tunnel project, this paper systematically studies the risk problems and control methods of complex adjacent tunnels through field investigation and numerical simulation.

Based on the project of the Chongqing Rail Transit Line 5 tunnel adjacent to the operational railway tunnel, this paper systematically studies the risk problems and control methods of complex adjacent tunnels through field investigation and numerical analysis. Firstly, the structural safety of the operational tunnel is comprehensively evaluated using on-site inspection. Secondly, the structural displacement, lining internal force, and overall safety of the tunnel complex adjacent-tunnel project are analyzed using numerical analysis. Finally, the influence scope of the TBM tunnelling over the operational railway tunnel is determined, and the corresponding risk control countermeasures are proposed. The research results are of reference value to the risk control and construction safety of complex adjacent projects.
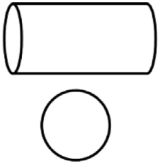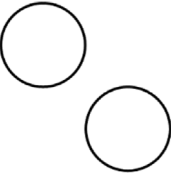
# 2 Risk control methods of complex adjacent tunnels

## 2.1 Construction risk

The redistribution of the stress field caused by the construction of a new tunnel will lead to the release of stratum stress in the surrounding area of the tunnel, and the stratum will move toward the new tunnel, which adversely affected the adjacent tunnel structure. The smaller the center distance between adjacent tunnels, the higher the adjacent impact. The elastic-plastic deformation caused by the stress release of the surrounding rock, the compaction deformation caused by the increase of effective earth pressure, and the elastic-plastic and creep deformation caused by the change of soil physical properties (Zheng, 2007) will lead to adverse phenomena of the existing tunnel, such as subsidence, inclination, torsion, structural deformation, etc. The deformation impact of the new tunnel on the existing tunnel is mainly divided into longitudinal deformation and transverse deformation. Transverse deformation shall be detected by bending moment and axial force of lining cross section (Gong, 2008), to prevent torsional deformation during construction. Longitudinal deformation is mainly the lining deformation caused by tunnel settlement or uplift. The longitudinal bending moment plays a decisive role in tunnel cracking, water leakage, and other structural damages (Min et al., 2020).

At the same time, when the existing tunnel has been in service for many years, the state of the tunnel has changed. The construction of the new tunnel may further lead to the change of the structural internal force and the increase of the structural deformation of the existing tunnel. It is difficult to ensure the structural safety of the existing tunnel during construction. According to the classification of the adjacent underground engineering (Qiu, 2003; Guan, 2011), combined with the analysis of burial depth and construction sequence (Boonyarak and Ng, 2014; Islam and Iskander, 2021), the construction risk types of adjacent tunnels are summarized, as shown in Table 1. It can be seen from

TABLE 1 Types and influence factors of adjacent tunnels.

| Type | Mechanical model | Influence factor | | Mechanical characteristic |
|---|---|---|---|---|
| | | Burial depth | Construction sequence | |
|  | Plane model of lateral effect | With the increase in burial depth, the ground settlement will be smaller and the settlement trough will be wider | When the tunnel is excavated at the same time, the surface settlement has the greatest impact | The surrounding rock around the existing tunnel is relaxed, and the lining load increases, causing tensile deformation to the new tunnel |
|  | Plane model of longitudinal effect | As the buried depth of existing tunnels and new tunnels increases, the settlement of existing tunnels due to the new tunnels excavated below decreases. When the new tunnel is above, the uplift of the existing tunnel increases with the increase of C/D* | The vertical displacement of the existing tunnel caused by the excavation of the new tunnel below is far greater than that of the new tunnel above | When the new tunnel is above, the existing tunnel will deform upward due to unloading. When the new tunnel is under, the existing tunnel will continue to sink with the excavation |
|  | Plane model of lateral effect | The greater the burial depth, the smaller the surface settlement | The new tunnel above will usually cause the uplift of the lower tunnel. When the new tunnel is below, the existing tunnel will settle due to interaction | When the new tunnel is above, the existing tunnel will deform upward, the arching effect of surrounding rock will be damaged. When the new tunnel is below, the existing tunnel will continue to sink with the excavation |
|  | Plane model of lateral effect | | The first construction of the upper tunnel will lead to higher ground settlement than the first construction of the lower tunnel | The surrounding rock around the existing tunnel is relaxed, and the lining load increases, causing tensile deformation to the new tunnel |

*C is the coverage depth of the new tunnel from the ground, D is the diameter of tunnel.

Table 1 that the construction types of adjacent tunnels can be divided into four categories: parallel, intersection, overlapping, and interlacing. The mechanical model of the intersection type is the longitudinal effect, and the others are the plane models of the lateral effect. Different types of adjacent tunnels face different risks. Parallel tunnels, overlapping tunnels, and interlacing tunnels mainly control the stress redistribution and displacement of surrounding rock caused by excavation, while tunnel crossing is to control the displacement of surrounding rock and existing structural deformation caused by excavation. The uplift deformation of the existing tunnel caused by the parallel tunnel and interlacing tunnel is usually greater than that of the overlapping tunnel. If the distance between the new tunnel and the existing tunnel is fixed, the influence of large-diameter tunnel excavation on the existing tunnel is greater than that of small-diameter excavation (Liang et al., 2021).

This paper relied on the adjacent project of Chongqing Rail Transit Line 5 which belongs to the construction of new subway tunnels close to the operational railway tunnels. Two parallel TBM tunnels are passing through the two operational tunnels, which belong to the adjacent problem of multiple tunnels. The minimum vertical net distance between the new TBM tunnels and the operational Chongqing-Huaihua Railway tunnels is 8.946 m. The small tunnel spacing can cause a great impact on the operational tunnel, and the construction difficulty is high (Zhen et al., 2019). The distance between the edges of the left and right lines of the subway section is 14 m, and the construction load superimposed on the left and right lines will cause structural damage to the operational railway tunnel. In addition,

the stress reorganization caused by the simultaneous excavation of double tunnels may lead to an increase in the settlement of the tunnel (Do et al., 2014). At the same time, the Chongqing-Huaihua Railway Tunnel has been in service for many years, and the safety state of the structure has changed. The construction of the subway TBM tunnels will cause further changes in structural internal force and structural deformation of the existing tunnel. It is difficult to ensure the structural safety and operational safety of existing tunnels during the construction period.

## 2.2 Risk control methods

At present, the risk assessment method for proximity tunnel construction is not particularly perfect, especially in the field of the complex adjacent tunnel (N.H. Krishnan, 2000). With the wide application of computers, digital technology has been gradually applied to the field of tunnel evaluation, and intelligent tunnel construction has been started for underground projects. I. Yamaguchi and Kiritani. (1998) proposed a safety assessment system and the analytical expression of the ground performance during the adjacent construction. Li and Yuan (2012) used an automatic measurement system to monitor the displacement changes of existing tunnels caused by new tunnels at different crossing stages in real time and provided some ideas for evaluating the influence of shield tunneling on existing tunnels. The subway

intelligent deformation prediction model proposed by Qiu et al. (2012) can realize intelligent, automatic deformation measurement, and early warning during the construction process, which can ensure the operational and structural safety of existing tunnels during construction. Clarke and Laefer (2014) proposed a comprehensive risk assessment method and a pre-construction risk assessment procedure for underground projects. Azadi et al. (2013) combined the finite element method and neural network method to assess the risk of the proximity tunnel construction but did not make more detailed planning for the proximity construction. Zheng et al. (2018) evaluated the influence of the new tunnel excavation on the deformation of the adjacent lateral tunnels from the aspects of the excavation depth, the horizontal displacement of the support structure, and the relative tunnel position. Luo et al. (2019) comprehensively analyzed the risk factors that have a greater impact on the construction of the new tunnel under crossing the existing tunnel and established the safety risk evaluation index system and safety risk evaluation model. The risk treatment idea proposed by Lei et al. (2018) is to first find out the key control indicators of the project for an evaluation, then propose the risk control measures and analyze the feasibility by numerical simulation, and finally obtain a complete risk control scheme. Mou et al. (2020) gave the influence area of overlapping tunnels based on surrounding rock parameters, and the transverse and longitudinal effects of orthogonal excavation tunnels, which provides a basis for subsequent construction risk control measures. The analysis method proposed by Zhang et al. (2019) and Liu et al. (2021) can predict the potential risk of new tunnel excavation on existing tunnel, and study the impact of the new tunnel construction on existing tunnel, including longitudinal shear stiffness, volume loss, gap between two tunnels, and the relative stiffness coefficient of surrounding rock.

The main purpose of risk control in the construction of adjacent tunnels is to build new tunnels without affecting the structural stability and operational safety of existing tunnels. The measures to control the influence of TBM tunnel adjacent construction can be divided into active control measures and passive control measures (Hua, 2008). Passive control countermeasures are taken from the perspective of protecting existing tunnels, including changing construction parameters such as tunnelling speed, jack thrust, grouting time, and shield posture (Zhang, 2018), as well as multiple construction parts, short footage, and precision blasting (Zhou et al., 2017), isolation of impacts and other measures. Active control measures are taken to reduce the disturbance of surrounding rock caused by tunnelling, including surrounding rock grouting (Liu et al., 2022), compensation grouting (Gan et al., 2022), and stratum reinforcement. It is a common method to take preventive measures for existing tunnels, which can be divided into basic measures, maintenance measures, and strengthening measures. Among them, strengthening existing tunnels to improve the bearing capacity of the structure has a significant effect, which is one of the common methods to control adjacent construction risks. The risk control of complex adjacent tunnels is a systematic project. It is necessary to take targeted control countermeasures for the protection of existing tunnel structures and reduction of the impact of adjacent construction according to the adjacent tunnel types and risks of the actual engineering project.

Based on the structural inspection and assessment of existing tunnel structures, this paper proposes the risk control method for complex adjacent tunnels. The analysis method mainly includes the

structural inspection, assessment of existing tunnels, the optimization design of the tunnel construction, the analysis of the interaction forces under adjacent construction, and the safety impact zoning. The risk control process of TBM tunnel construction is shown in Figure 1. First of all, conduct a structural inspection on the lining thickness, concrete strength, defects behind the lining, lining cracks, and surrounding rock state of the existing tunnel, to obtain the health status of the existing tunnel. Then, conduct the safety and risk analysis on the complex adjacent tunnels, mainly including the influence of tunnel face spacing, the displacement and internal force of the existing tunnel structure, and the longitudinal internal force of the existing tunnel lining after the adjacent construction. According to the analysis results, specific measures of risk control are proposed, such as tunnelling parameters, pea-gravel backfilling, backfill grouting, consolidation grouting at the bottom of segments, and other measures.

# 3 Engineering background

## 3.1 Project overview

The section tunnel between Renhechang Station and Xingfu Square Station of Chongqing Rail Transit Line 5 starts from Renhechang Station and goes westward along Jinkai Avenue, and then crosses successively above 2# construction inclined shaft of Shanghai-Chengdu Railway, Renhechang Tunnel of Shanghai-Chengdu Railway, Xinrenhechang Tunnel of Chongqing-Huaihua downward line and Renhechang Tunnel of Chongqing-Huaihua upward line. The geographical location and tunnel layout of this line is shown in Figure 2.

The mileage range of the section where the section tunnel of Chongqing Rail Transit Line 5 crosses above the Chongqing-Huaihua Railway tunnel is YDK16+911.681 ~ YDK17+194.572, in a total length of the section is 282.9 m. The tunnel is constructed with a single shield TBM. The lining is Type II (ordinary type), the waterproof concrete is C50, and the impermeability grade is P12. The lining section of the new TBM tunnel is shown in Figure 3A. The designed running speed of the Xinrenhechang tunnel of the Chongqing-Huaihua downward line is 120 km/h. The starting and ending mileage is K12+796 ~ DK17+567. The surrounding rock of the adjacent area is Grade IV, and the concrete strength grade is C25 corrosion-resistant concrete. The starting and ending operational mileage of the Renhechang tunnel of the Chongqing-Huaihua upward line is K12+765 ~ DK17+499. The surrounding rock of the adjacent tunnel is Grade IV, and the concrete strength grade is C20 corrosion-resistant concrete. The lining section of the operational tunnel is shown in Figure 3B.

The original landform of the complex adjacent tunnel section of Chongqing Metro belongs to the tectonic denudation hilly area, with gentle terrain and small undulation, and the gradient is generally less than 5°. The ground elevation along the line is 290~375, and the relative elevation difference is about 85 m. The exposed strata along the whole line are relatively simple, basically in the Quaternary Holocene loose soil layer and the Jurassic Middle Shaximiao Formation bedrock of continental river lake clastic deposits, mainly composed of sandy mudstone and sandstone. The stratum where the tunnel is located is mainly artificial fill and silty clay. The thickness of the soil layer varies greatly. The bedrock is continental clastic rock with sandstone and mudstone interbedding. The hydrogeological conditions are simple. The groundwater in the site is mainly
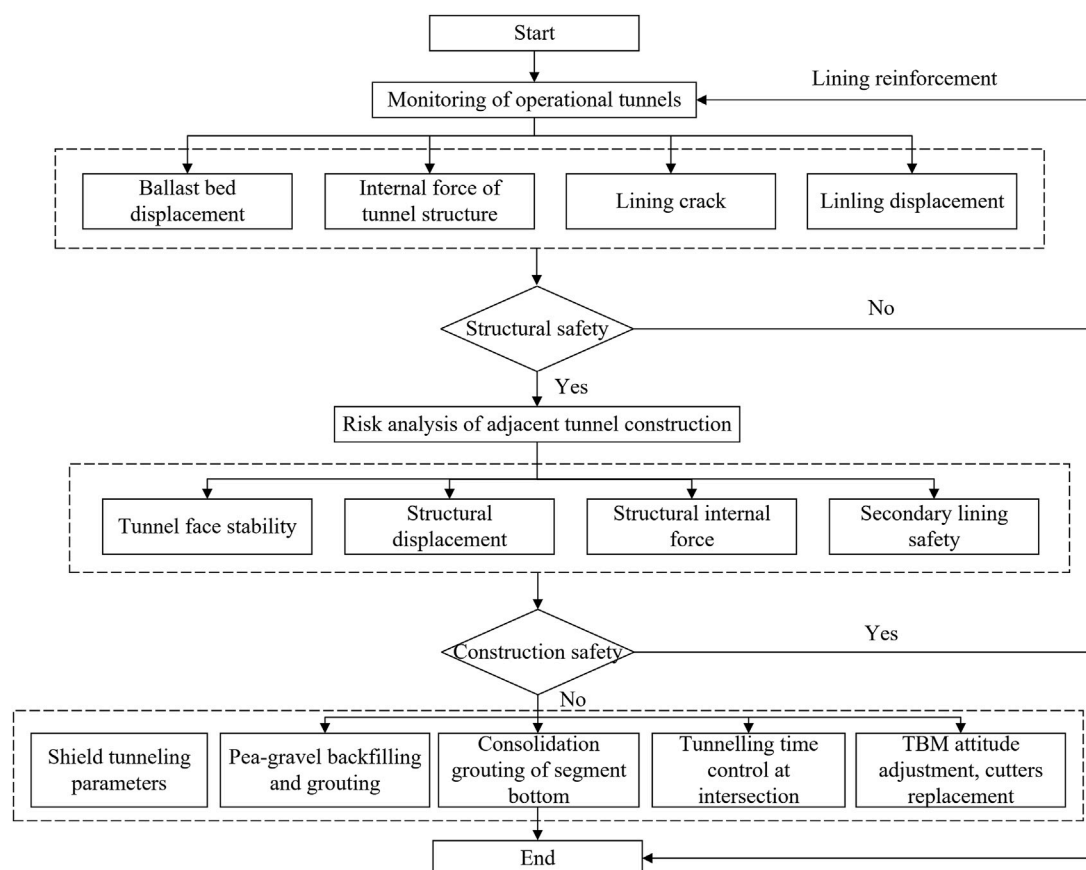
FIGURE 1
Risk control process of adjacent tunnel construction.



FIGURE 2
Location plan of the adjacent tunnel.

perched water and bedrock weathering fissure water. The water content in rock and soil layers is generally weak. The profile of the complex adjacent section of Chongqing Rail Transit Line 5 is shown in Figure 4.

## 3.2 Complex adjacent situations

The newly-built Chongqing Rail Transit Line 5 crosses above the Renhechang tunnels of the Chongqing-Huaihua Railway upward line
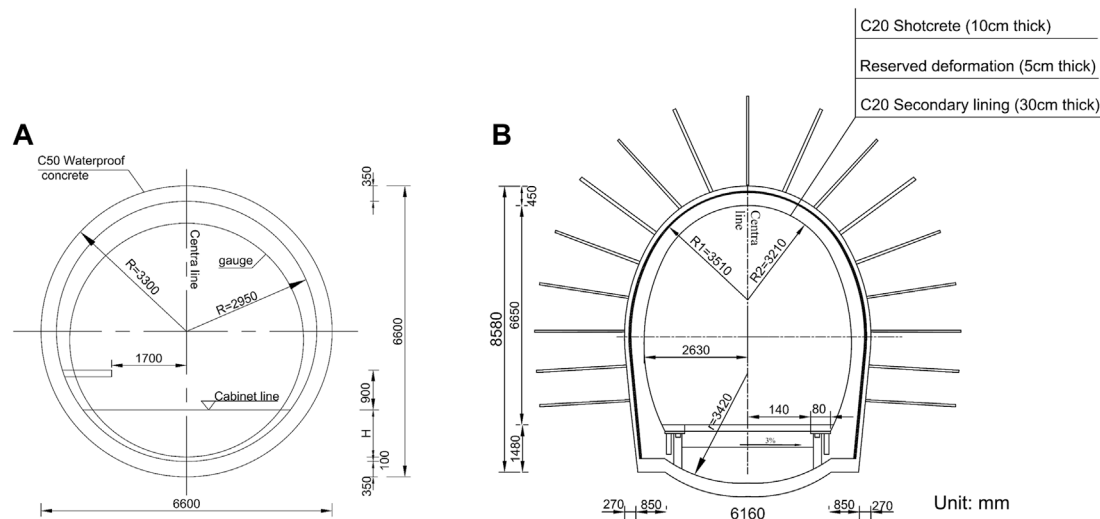
**FIGURE 3**
Schematic diagram of adjacent tunnel lining section. **(A)** TBM subway tunnel. **(B)** Upward operational tunnel.
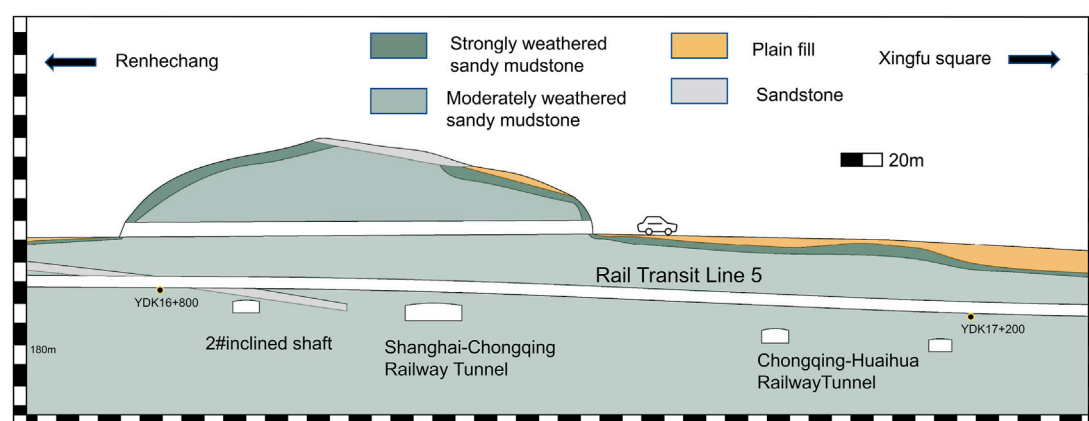


**FIGURE 4**
Profile and stratum distribution of adjacent tunnel.

and downward line. The right-line tunnel of the subway intersects with the Chongqing-Huaihua Railway downward tunnel at DK14+803, at a clear distance of 10.743 m, and intersects with the Chongqing-Huaihua Railway upward tunnel at DK14+786, in a clear distance of 10.69 m; the left line tunnel of the subway intersects DK14+831 of Chongqing-Huaihua Railway downward tunnel in a clear distance of 8.946 m, and DK14+758 of Chongqing-Huaihua Railway upward tunnel in a clear distance of 11.944 m. The specific adjacent spatial relationship is shown in Figure 5. The corresponding mileage range of complex adjacent tunnels of Chongqing Metro is shown in Table 2.

## 3.3 Inspection of the operational tunnels

The TBM tunnel construction of Chongqing Rail Transit Line 5 will cause the stress redistribution of the surrounding rock, which

will change the longitudinal and transverse internal forces of the operational tunnels, thus affecting the safety of the tunnel structure. In this paper, the health monitoring of the operational Renhechang railway tunnel structures is conducted to understand the structural performance of the operational tunnel structures. To further ensure the structural integrity and operational safety of the existing tunnels. The monitoring instruments include ground penetrating radar (SIR-3000), concrete rebound instrument (ZC3-A), laser profiler (BJSD-2E), core drilling machine (DZ47-63), and ultrasonic detector (NM-4A). The monitoring technology adopted in this paper is based on TB10417-2003, 2003, TB10223-2004, 2004, TB/T 2820.1-1997, 1997 and Railway transport letter, 2004.

The soundness rating table of the Renhechang tunnels of the Chongqing-Huaihua railway is shown in Table 3. There are fourteen voids behind the lining of the operational upward tunnel inspection section. The voids with a cumulative length of 30 m account for 5.5%
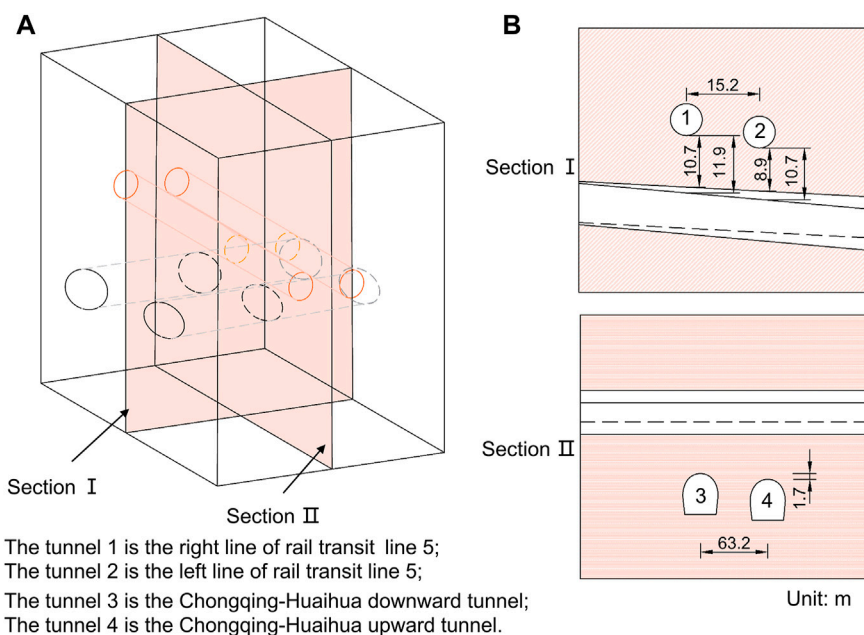
**FIGURE 5**
Spatial position relationship of the complex adjacent tunnel. **(A)** Overall schematic diagram. **(B)** Section diagram.

**TABLE 2** Data sheet of adjacent tunnel.

| | Clear distance (m) | | Intersection mileage | | included angle (°) | |
|---|---|---|---|---|---|---|
| | Right line | Left line | Right line | Left line | Right line | Left line |
| Chongqing-Huaihua Downward | 10.743 | 8.946 | Mileage: DK14+803 Tunnel signpost: 2+008 | Mileage: DK14+831 Tunnel signpost: 2+036 | 35.4 | 35.4 |
| Chongqing-Huaihua Upward | 11.944 | 10.69 | Mileage: DK14+758 Tunnel signpost: 1+908 | Mileage: DK14+786 Tunnel signpost: 1+936 | 35.4 | 35.4 |

**TABLE 3** Soundness rating form of operational tunnels of Chongqing-Huaihua railway.

| Lining | Detection results | | Rating | | Comprehensive assessment | | Remarks | |
|---|---|---|---|---|---|---|---|---|
| | Upline | Downline | Upline | Downline | Upline | Downline | Upline | Downline |
| Thickness | > δ | > δ | 0 | 0 | 1 | 1 | | |
| Concrete strength | $f_{cu}^t$:40.8 MPa > $f_{cu,k}(c25)$ | $f_{cu}^t$:21.5 MPa < $f_{cu,k}(c25)$ | 0 | 1 | | | | 1 |
| Defects behind lining | Length:1~3 m | Length < 3 m width>1.5 mm | 1 | 1 | | | 1 | 1 |
| Cracking | Length < 7 m width < 2 mm | Length < 3 m width < 1.5 mm | 1 | 1 | | | 1 | 1 |
| Surrouding rock | Joint fissures (small range) | Joint fissures (small range) | 0 | 0 | | | | |

Note: 1) δ indicates design thickness of lining; 2) $f_{cu}^t$ indicates detection value of concrete strength; $f_{cu,k}$ indicates the design strength; 3) 0 indicates minor impact, 1 indicates slight impact.

of the total length of the upward line inspection section. The spacing of the steel bars in the secondary lining is 21~25 cm, and the spacing of the steel frames in the primary support is 1.2 m. Among the twelve tested sections, intrusion in the design clearance is found in eleven sections, accounting for 91.7%, and the maximum intrusion clearance is 5.95 cm. Only one section is found with intrusion into the tunnel construction clearance, accounting for 8.3%, and the intrusion value is 0.51 cm. In all sections, no intrusion is found within the basic construction clearance. The monitoring shows that the tunnel lining has the following diseases: six cracks (two at the arch waist

**FIGURE 6**
Numerical model. **(A)** Overall model. **(B)** Adjacent tunnel. **(C)** Lining construction joint. **(D)** TBM tunneling construction.

and four at the arch foot, including four oblique cracks), one longitudinal construction gap joint with water leakage, and one circumferential crack. The surrounding rock within 29~45 cm behind the support is relatively broken, and the wave velocity of rock mass is 2.82~3.55 km/s.

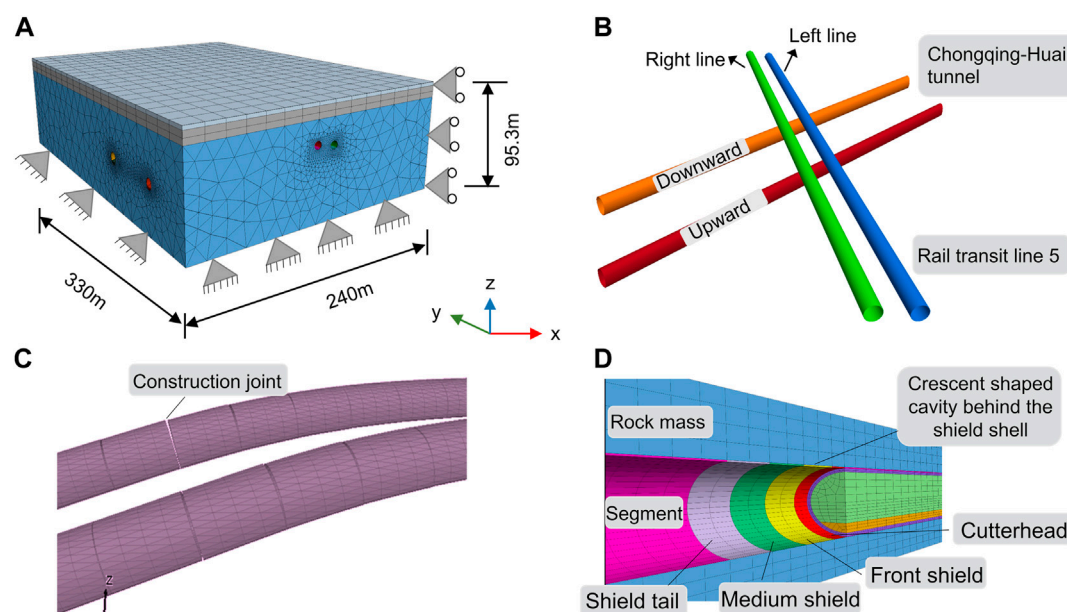There are twenty-three voids behind the lining of the operational downward tunnel inspection section. The voids with a cumulative length of 48 m account for 7.3% of the total length of the downward line inspection section. There are steel bars in the secondary lining, with a spacing of 20~24 cm. There are steel frames in the primary support, and the spacing of some steel frames is 1.0 m. Among the twelve tested sections, eleven sections (91.7%) are found with intrusion in the design clearance. The maximum intrusion clearance is 3.7 cm. No intrusion is found within the tunnel construction clearance or the basic construction clearance. The monitoring shows that the tunnel lining has the following diseases: four cracks (three at the vault and one at the arch foot, including one diagonal crack), one longitudinal crack, and two circumferential cracks, and all cracks have no water leakage. The surrounding rock behind the left wall is complete, and the surrounding rock within 77~114 cm behind the right wall is relatively broken, with a rock wave velocity of 3.06~3.11 km/s.

# 4 Numerical simulation

## 4.1 Numerical model

This paper uses the FLAC 3D finite-difference program for numerical simulation. The three-dimensional spatial relationship of adjacent tunnel groups is simulated through fine modeling, and the stress response and lining deformation are calculated to analyze the safety risks. According to the actual project situation, the longitudinal length of the model is 330m, the transverse length is 240m, and the

**TABLE 4 Mechanical parameters of geotechnical materials.**

| Category | $\gamma$ (kN/m³) | $E$ (MPa) | $\mu$ | $c$ (KPa) | $\varphi$ (°) |
|---|---|---|---|---|---|
| Plain fill | 21.0 | 500 | 0.3 | 40 | 28.0 |
| Sandy mudstone 1# | 25.6 | 1660 | 0.36 | 750 | 33.3 |
| Sandy mudstone 2# | 25.6 | 1738 | 0.36 | 900 | 33.9 |

depth under the invert of the tunnel is 60 m. The tunnel construction process is simulated according to the actual project. The front, back, left and right edges of the model are subject to horizontal constraints, the bottom boundary is subject to vertical constraints, and the top boundary is a free plane. The stratum and initial support are simulated by the elastic-plastic element, and the secondary lining is simulated by Liner structural element. The numerical calculation model is shown in Figure 6A. The adjacent tunnel model is shown in Figure 6B.

Geological parameters in the numerical simulation are determined according to the *Geotechnical Investigation Report of Chongqing Rail Transit Line 5*. The mechanical parameters of each stratum are shown in Table 4. Physical parameters of the lining are according to TB 10003-2005, 2005. The detailed mechanical parameters are shown in Table 5. Considering that the waterproof board is laid between the initial support and the secondary lining, the model achieves the effect of sliding by setting the contact surface parameters. Considering the construction joint setting of the secondary lining during the calculation, the secondary lining of the operational railway tunnel is set with a ring of construction joints every 9 m along the longitudinal direction. The construction joint is realized by changing the link between the liner. The parameters of the contact element are shown in Table 6. The simulation of the construction joint is shown in Figure 6C. The construction steps of the TBM tunnel are determined by reference to the construction design data. Figure 6D

**TABLE 5 Mechanical parameters of support materials.**

| Concrete | $\gamma$ (KN/m³) | $E$ (GPa) | $\mu$ |
|---|---|---|---|
| Primary lining | 22 | 20.0 | 0.2 |
| Secondary Lining of Chongqing-Huaihua Upward | 25 | 28.0 | 0.2 |
| Segment | 25 | 25.0* | 0.2 |
| Shield shell of the shield machine | — | 210.0 | 0.2 |

*Consider stiffness reduction.

**TABLE 6 Calculation parameters of the contact surface.**

| Name | $c$ (MPa) | $\varphi$ (°) | $t$ (MPa) | kN (N/m³) | $k_s$ (N/m³) |
|---|---|---|---|---|---|
| Contact face | 0.001 | 1.0 | 0.001 | 15e10 | 15e10 |

shows the TBM tunnel excavation and segment construction. To simulate the TBM tunnel construction, the first step is TBM tunnelling, then activating the shell element of the shield shell, releasing 70% of the load on the tunnel face and 30% of the load on the radial direction of the tunnel, and the simulation calculation is carried out until the balance is achieved. Then, the segments shall be constructed at the tail of the shield, and the crescent-shaped cavities behind the segments shall be backfilled. After that, the calculation is conducted until the balance is achieved, and the next construction cycle is carried out.

## 4.2 Weight distribution parameters of TBM

TBM is a large mechanical equipment, and the influence of TBM's heavy weight on the tunnel structure shall be considered. TBM weight distribution shall be determined according to the construction design data as shown in Table 7, and TBM weight distribution in the numerical calculation is shown in Figure 7.

## 4.3 Measurement schemes

To analyze the influence of adjacent tunnel construction on lining internal force and structural deformation of the operational tunnel, this paper analyzes the influence of TBM tunnel cutterhead position on lining internal force and structural deformation of different sections of an operational railway tunnel in the construction process. Figure 8 shows the layout of measuring points for structural impact analysis of the operational tunnel. The intersection point between the right line of the new tunnel and the central axis of the operational upward tunnel is 0. Figure 8A shows the layout of monitoring points for the longitudinal displacement of the operational upward tunnel structure during TBM tunnelling, that is, when

the TBM working face reaches the set point, the longitudinal displacement of the operational tunnel is extracted once. The numbers in the figure represent the distance from the TBM face position to point 0. A negative value indicates that it has not yet passed through the centerline intersection, while a positive value indicates that it has passed through the centerline intersection. Figure 8B shows the structural monitoring section layout of the operational tunnel at different positions of the TBM cutterhead. Wherein, points a, b, and c represent the position of the TBM tunnel cutterhead and points a and c are −6.87 m and 7.6 m away from point b, respectively. Points 1, 2, and 3 represent different sections of the operational tunnel. Points 1 and 3 are −9.02 m and 9.02 m away from the section of point 0, respectively.

## 4.4 Longitudinal spacing of TBM tunnel face

To analyze the influence of TBM tunnel face spacing of the TBM tunnel on the deformation of the operational tunnel structure during tunnel adjacent construction, the right line of the TBM tunnel is excavated above the centre line of the operational railway tunnel, and then the left line tunnel is excavated, with footage of 1.5 m. The distance between the centerline of the double tracks of the TBM tunnel is 15.2 m. During the construction, the vertical displacement of the ballast bed at the intersection of the operational railway tunnel was monitored. By analyzing the influence of the tunnel face distance on the deformation of the operational tunnel structure, the minimum distance between the new TBM tunnel faces during the excavation is determined.

Figure 9 shows the influence curve of different distances of tunnel face on the displacement of the operational tunnel ballast bed during the TBM tunnelling. It can be seen that when the tunnel face spacing of the TBM tunnel decreases from 16 m to 4m, the displacement of the operational tunnel ballast bed increases from 0.116mm to 2.78 mm. Based on the previous geological data, operational tunnel structural detection, and the experience of the railway administration, the deformation of the operational railway tunnel ballast bed caused by subway tunnel excavation shall not exceed 0.5 mm. According to the numerical simulation results, when the TBM tunnel face spacing of Rail Transit Line 5 is 10 m, the vertical displacement of the ballast bed near the tunnel

**TABLE 7 TBM weight distribution (kg).**

| Type | Cutterhead | Front shield | Medium shield | Shield tail |
|---|---|---|---|---|
| TBM337(Single shield) | 12712 | 8297 | 6356 | 1989 |
| TBM338(Single shield) | 12809 | 4517 | 5356 | 1741 |
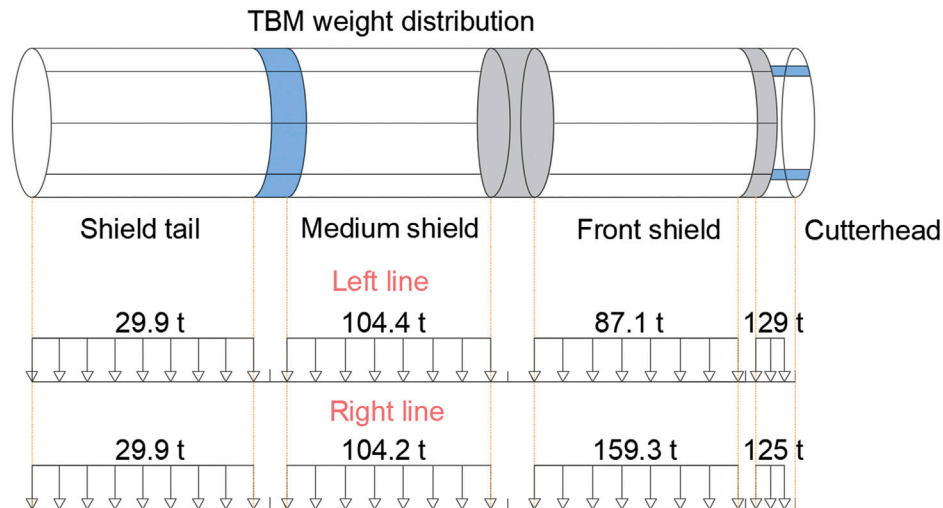
**FIGURE 7**
TBM tunnel weight distribution.
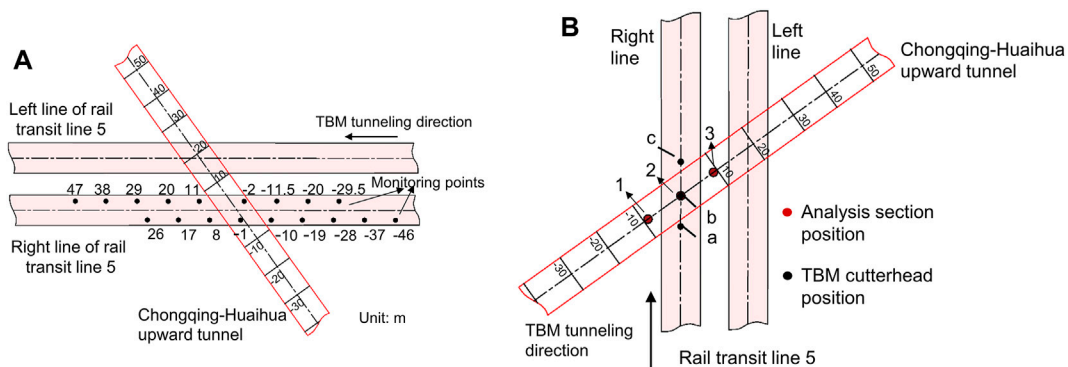


**FIGURE 8**
Layout of monitoring points of the operational tunnel. **(A)** Displacement monitoring. **(B)** Internal force monitoring.

intersection reaches 0.5 mm. The double-line subway construction will have a superposition effect on the deformation of the operational railway structure. Therefore, the minimum longitudinal spacing (safety spacing) of the TBM tunnel face during the tunnelling of the new subway tunnel is determined as 15.0 m.

# 5 Results and discussion

## 5.1 Effect of longitudinal displacement of the operational tunnel

By simulating the actual construction process of the TBM subway tunnels, an analysis is done here on the displacement changes in the vault and ballast bed structure of the operational railway tunnel at different TBM tunnel face positions. The evaluation of the displacement impact of the operational tunnel lining and its influence scope was also analyzed. Considering that the two operational tunnels affected by the TBM tunnel have similar adjacent influence rules, only the up-line operational tunnel is selected for analysis in this paper. The analysis scope covers the right line of the new tunnel from 46 m outside the intersection to 26 m across the intersection. The displacement of the operational tunnel is recorded every 9 m of tunnelling.

The vault displacement curve of the operational tunnel changes in the process of TBM tunnel excavation is shown in Figure 10A. The analysis scope is from - 46m to 26 m from the intersection of the right line of the new TBM tunnel, and the longitudinal displacement of the operational tunnel is recorded every 9 m of TBM tunnelling. The longitudinal displacement analysis length of the operational tunnel is 100 m. The vault displacement of the operational tunnel at the monitoring point shows an overall upward trend. At first, when the TBM tunnel face was −46 m from the intersection, the influence scope of displacement of the operational tunnel was only between −30 m and −9 m, with an affected length of about 22 m long. When the excavation is near the intersection, the operational tunnel will heave longitudinally from −38 m to 26 m, with an affected length

**FIGURE 9**
Curve of influence of different distances of tunnel face on the displacement of tunnel ballast bed of operational tunnel during TBM tunneling.

intersection, more parts of the operational tunnel are affected by proximity, and the uplift displacement increases accordingly. When the tunnel face of the right TBM tunnel crosses the intersection by 17m, the left TBM tunnel is just above the center line of the operational tunnel, and the displacement change of the operational tunnel reaches the peak value. In addition, with the TBM tunnelling, the peak displacement points of the vault have a trend of changing from left to right. The vault displacement of the operational tunnel is respectively −16 m, −14 m, −9 m, −8 m, −5 m, −0.8 m, 5 m, 5.3 m, and 5.3 m.

The ballast bed displacement curve of the operational tunnel changing with the TBM tunnel excavation is shown in Figure 10B. The analysis scope is from −29.5 m to 47 m from the intersection of the right line of the new TBM tunnel, and the longitudinal displacement of the operational tunnel is recorded every 9 m of TBM tunnelling. The longitudinal displacement analysis length of the operational tunnel is 100 m. The maximum displacement of the ballast bed of the operational tunnel is 0.56mm, which is 0.472 mm smaller than the maximum displacement of the vault. As a whole, the displacement change of the ballast bed is smaller than that of the vault.

The displacement change curve of the vault and ballast bed at the intersection of the operational tunnel and the new tunnel is shown in Figure 10C. Points A and B are the displacement monitoring points of the vault and the ballast bed, respectively, at the intersection of the operational tunnel and the new right-line tunnel. Points C and D are the displacement monitoring points of the vault and ballast bed, respectively, at the intersection of the new left-line tunnel and the operational tunnel. The maximum uplift of two points A and B of the new right line tunnel are 0.76 mm and 0.47 mm respectively, and the

of 64 m. The maximum vault displacement of the operational tunnel is 1.032 mm. In the process of TBM tunnelling from far to near toward the intersection, the affected area of the operational tunnel shows a multiple growth trend. The tunnel uplift displacement increases significantly, and the displacement change curve gradually changes from gentle to steep. Because of the certain included angle between the TBM tunnel and the operational tunnel, with the tunnelling of the TBM tunnel, the displacement of the tunnel vault on the left side of the intersection (along the tunnelling direction) first appears to uplift. As the TBM face approaches the tunnel



**FIGURE 10**
Displacement curve and influence scope of the operational tunnel. **(A)** Vault. **(B)** Ballast bed. **(C)** Cross section. **(D)** Influence area.

**FIGURE 11**
Bending moment, axial force, and safety factor of sections 1, 2, and 3. **(A)** The cutterhead is at point a. **(B)** The cutterhead is at point b. **(C)** The cutterhead is at point c.
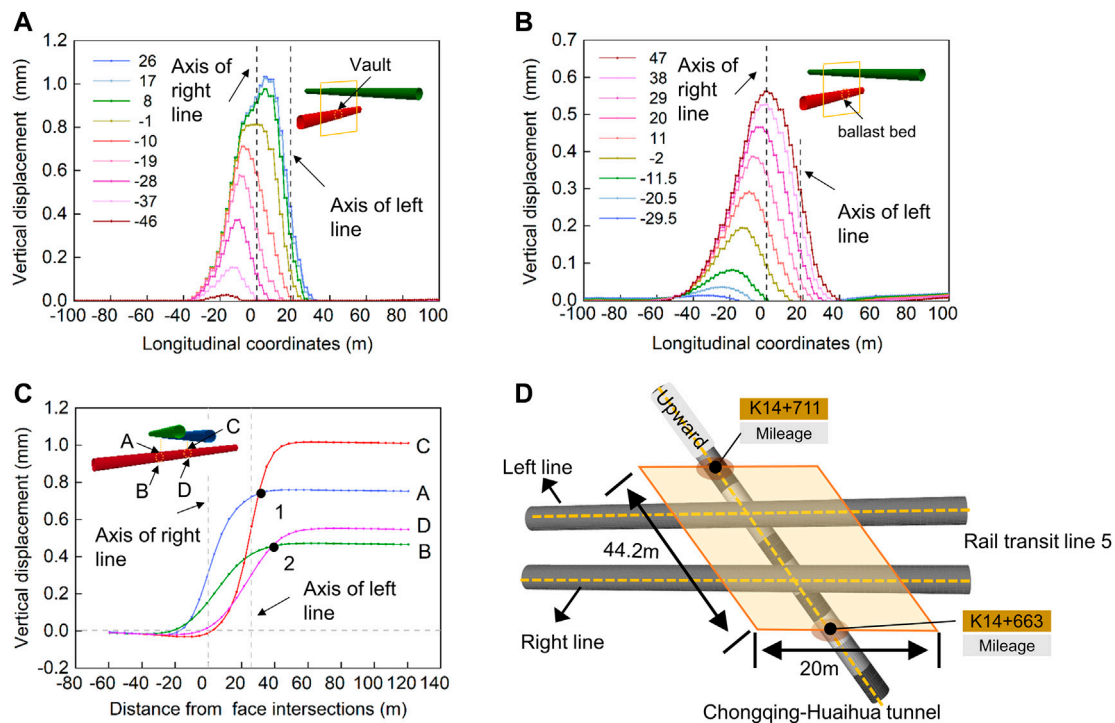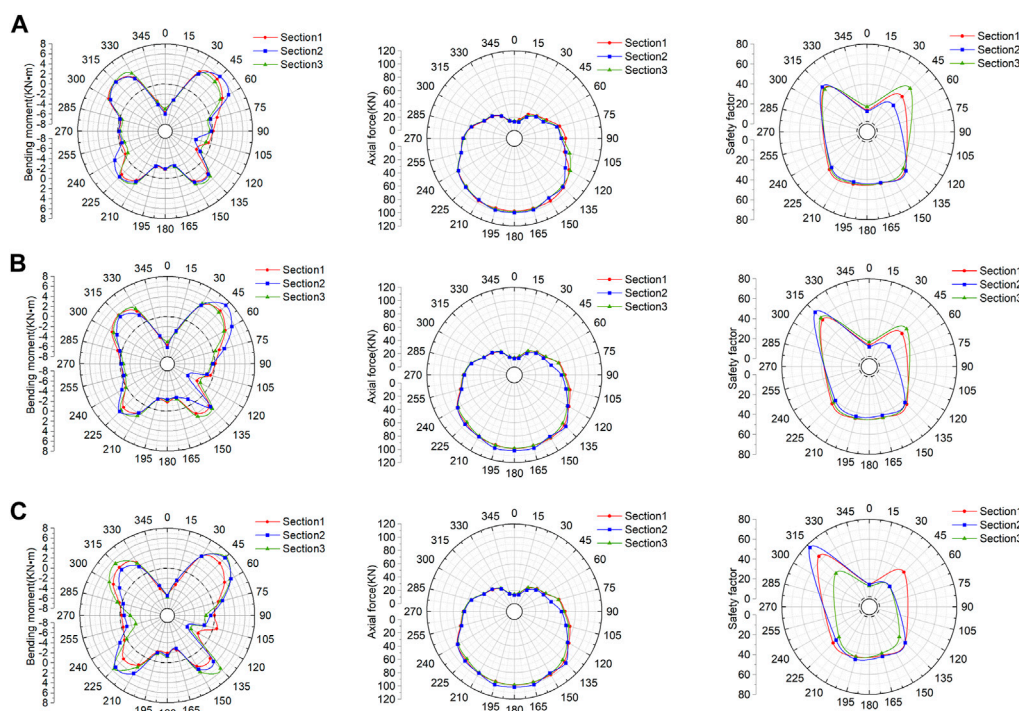
displacement tends to be stable 40 m after the TBM tunnel face crosses the intersection. The maximum uplift of C and D points of the new left line tunnel is 1.02 and 0.55 mm respectively, and the displacement tends to be stable at 57.5 m after the TBM face crosses the intersection. The displacement of point D lags behind that of points A and B, mainly because the TBM tunnel face of the right line is 15 m ahead of the left line.

As shown in Figure 10C, when the TBM face of the right line tunnel reaches the intersection (0 m), the displacement of points A and B are 0.29 mm and 0.15 mm, respectively, and the value is greater than that of points C and D. When the new left line is driven to the intersection of the left line and the operational tunnel (29.2 m), the displacement curves of points A and C intersect at point 1 at this time, and then the displacement curves of points B and D also intersect at point 2. Take intersection point 1 as an example, the displacement at the intersection of A and C at point 1 is 0.75 mm, and the displacement at point A reaches the peak value and keeps stable. However, the displacement change of the left line intersection is continuing until the TBM left line tunnel crosses the left line intersection by 31.7 m and then tends to be stable.

As mentioned in the previous section 4.4, the displacement of the operational tunnel ballast bed caused by subway tunnel excavation shall not exceed 0.5 mm. Combined with the displacement data and the actual field data, the influence scope of the tunnel is obtained, as shown in Figure 10D. The mileage of the influence area of the operational tunnel is between K14+663 and K14+711, and the whole influence area is roughly a parallelogram. The long axis is 44.2 m parallel to the operational tunnel, and the short axis is 20 m parallel to the new subway tunnel.

## 5.2 Effect of internal force of operational tunnel lining cross-section

The disturbance caused by the TBM tunnelling will have a certain impact on the stress of the operational tunnel structure. This section analyzes the internal force changes of the operational tunnel lining when TBM is excavated near the intersection and the TBM cutterhead is far away from the intersection. The variation law of the internal force of the operational tunnel lining is analyzed, and the safety factor of the lining structure is calculated.

Figure 11 A, B, and C show the distribution of the bending moment and axial force of the lining in Section 1, Section 2, and Section 3 in the operational tunnel when the TBM cutterhead excavates in positions a, b, and c of the right line, respectively. On the whole, when the TBM cutterhead is at points a, b, and c, the distribution laws of bending moment, axial force, and safety factor of the operational tunnel are similar, and the changes of bending moment and axial force of Section 1, Section 2, and Section 3 are not significant. Among them, the bending moment is relatively small at the vault, left and right side walls, and invert arch; contrarily, the bending moment is relatively large at the left and right arch waists and the left and right wall feet, showing a 'butterfly-like' distribution characteristics. For the axial force, the minimum axial force is at the vault and the maximum is at the invert. From the vault to the inverted arch, the axial force increases gradually, and the axial force presents the 'apple-like' distribution characteristics. For the safety factor, the safety factor of the left arch waist is the largest, the vault is the smallest. For the right arch waist, when the TBM cutterhead is located at points a and b, the safety factor is sorted from large to small as Section 3 > Section 2 > Section 1; when the TBM cutterhead is at point c, the safety factor of the

**TABLE 8 Summary of structural stress of Section 2**

| Location | Part | M (kN·m) | N (kN) | $e_0/h$* | Eccentric compression mode | Safety factor |
|----------|------|----------|--------|----------|---------------------------|---------------|
| a | Vault | 5.99 | −13.07 | 1.528 | Large | 12.530 |
| | Left arch waist | 4.43 | −35.26 | 0.419 | Large | 55.549 |
| | Right arch waist | 5.96 | −34.00 | 0.584 | Large | 29.451 |
| | Left wall foot | 3.45 | −91.86 | 0.125 | Small | 42.399 |
| | Right wall foot | 2.24 | −91.46 | 0.082 | Small | 47.244 |
| | Left inverted arch | 2.32 | −99.73 | 0.078 | Small | 43.776 |
| | Right inverted arch | 2.13 | −99.33 | 0.071 | Small | 44.639 |
| b | Vault | 6.22 | −12.73 | 1.629 | Large | 11.740 |
| | Left arch waist | 3.83 | −35.39 | 0.361 | Large | 68.826 |
| | Right arch waist | 7.04 | −34.11 | 0.688 | Large | 20.226 |
| | Left wall foot | 4.00 | −93.21 | 0.143 | Small | 40.160 |
| | Right wall foot | 2.73 | −97.88 | 0.093 | Small | 42.922 |
| | Left inverted arch | 2.12 | −102.06 | 0.069 | Small | 43.697 |
| | Right inverted arch | 2.47 | −102.05 | 0.081 | Small | 42.443 |
| c | Vault | 5.47 | 13.31 | 1.370 | Large | 14.460 |
| | Left arch waist | 3.43 | 35.17 | 0.325 | Small | 76.249 |
| | Right arch waist | 6.81 | 33.06 | 0.687 | Large | 20.960 |
| | Left wall foot | 5.13 | 85.18 | 0.201 | Small | 39.043 |
| | Right wall foot | 3.54 | 88.70 | 0.133 | Small | 43.143 |
| | Left inverted arch | 1.74 | 98.47 | 0.059 | Small | 46.538 |
| | Right inverted arch | 2.60 | 97.31 | 0.089 | Small | 43.590 |
| d** | Vault | 5.63 | 13.33 | 1.408 | Large | 13.856 |
| | Left arch waist | 3.29 | 35.27 | 0.311 | Small | 77.747 |
| | Right arch waist | 6.94 | 33.53 | 0.690 | Large | 20.445 |
| | Left wall foot | 5.08 | 85.38 | 0.198 | Small | 39.135 |
| | Right wall foot | 3.46 | 89.35 | 0.129 | Small | 43.209 |
| | Left inverted arch | 1.72 | 98.16 | 0.058 | Small | 46.747 |
| | Right inverted arch | 2.63 | 96.91 | 0.090 | Small | 43.619 |

*$e_0$ represents the eccentricity; h represents the thickness of lining cross-section.
**Position d refers to location of the TBM, tunnel face crosses the intersection for a long distance.

left arch waist of Section 1 is the largest, followed by Section 2, and finally Section 3. In the process of TBM tunnelling from point a to point c, the safety factors of all parts of Section 3 gradually decrease, especially the left and right arch waists, where the safety factors of the left arch waists decrease by about 20% and the right arch waists decrease by about 60%. The main reason is that Section 3 locates between the left and right TBM tunnels, within the cross-influence range, and is greatly affected by the adjacent construction.

The summary of the structural stress in Section 2 when the TBM tunnel face is located at a, b, c, and after the TBM tunnel face crosses the intersection for a long distance is shown in Table 8. The maximum positive bending moment of tunnel lining is inside the vault, the maximum negative bending moment is outside the arch foot, and the

maximum axial force is at the invert. When the TBM cutterhead is close to the intersection, the bending moment increases. When it crosses the intersection and starts to move away, the bending moment decreases. Similar change laws can also be found in axial force. After the TBM tunnel face is far away from the intersection, the bending moment and axial force of the existing lining are finally stable (See data at position d in Table 8), and their values are the same as those of the cutterhead at position c.

It can also be seen from the internal force in Table 8 that the left arch waist of Section 2 is in the large eccentric compression mode when the TBM cutterhead is at a and b positions. When the TBM tunnel crosses the intersection point, it changes to the small eccentric compression mode again and then keeps the small eccentric
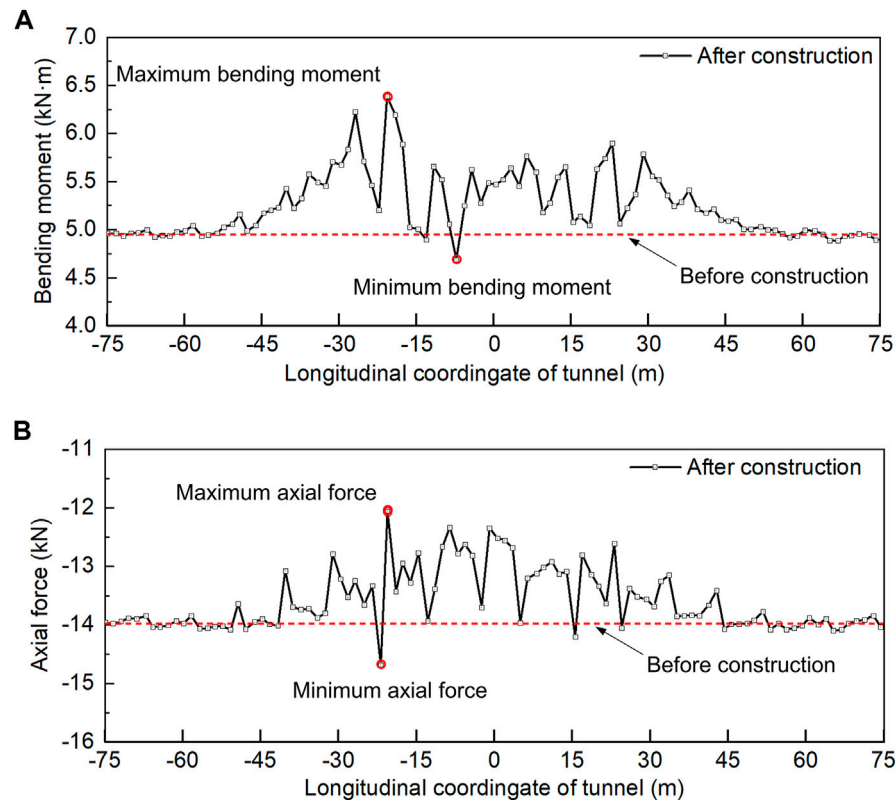
**FIGURE 12**
Variation curves of longitudinal internal force. **(A)** Bending moment. **(B)** Axial force.

compression mode unchanged. It shows that the TBM tunnel construction above the operational tunnel will change the local stress mode of the lining structure, and the lining structure will have a local tension trend. Moreover, the displacement change results of the vault and ballast bed of the operational tunnel in Section 5.1 also show that the uplift displacement of the vault is greater than that of the ballast bed. The lining structure shows a tensile trend in the vertical direction. Therefore, corresponding risk control measures should be taken to ensure the safety of the operational tunnel structure during the construction of the TBM tunnel up-crossing the operational tunnel.

## 5.3 Longitudinal influence of the internal force of operational tunnel lining

To study the internal force changes of the operational tunnel lining after the adjacent construction, this paper analyzes the longitudinal bending moment and axial force changes of the tunnel lining when the tunnel face of the TBM tunnel is located directly above the tunnel crossing point. Figure 12 shows the longitudinal curves of the bending moment and axial force at the vault of the operational tunnel. The dotted line in Figure 12A represents the longitudinal bending moment value of the operational tunnel before the construction of the TBM tunnel, which is 4.9 kN·m. The dotted line in Figure 12B represents the longitudinal axial force of the operational tunnel before the construction of the TBM tunnel. Its value is 14 kN, where positive values represent tension and negative values represent compression. The bending moment and axial force

change curves show an increasing tendency and regular fluctuation within a certain range (−30~30 m). The maximum bending moment after construction is 6.4 kN·m, which increases by 1.5 kN·m and 30.6% compared with that before construction. The minimum bending moment after construction is 4.7 kN·m, which is 0.2 kN·m and 4.1% less than that before construction. The maximum value of axial force after construction is −12.6 kN, which increases by 1.4 kN and 10% compared with that before construction. The minimum axial force after construction is −14.6 kN·m, which is 0.6 kN·m and 4.3% less than that before construction. The maximum value of bending moment and axial force both appeared at −16.8m, mainly because there was a certain intersection angle between the TBM tunnel and the operational tunnel. It can also be seen that the bending moment and axial force of the operational tunnel fluctuate more violently in the area of - 30~0 m. This is mainly because the left area of the intersection (point b in Figure 8 (b)) enters the influence area of the excavation in advance. It can be found from the bending moment change curve that there are two obvious peaks within the influence range, but the axial force variation curve has no obvious peak. Moreover, because a construction joint is installed every 9 m along the longitudinal lining, the construction joint of the lining weakens the longitudinal transmission of the bending moment and axial force, and the bending moment and axial force at the construction joint along the tunnel both show a decreasing trend. In general, the TBM tunnel has a great influence on the internal forces of the operational tunnel lining within the influence scope. However, the variation of bending moment and internal force is within the controllable range, and the overall influence is within the acceptable range. The risk is controllable for the complex adjacent tunnel.

# 6 Risk control countermeasures

Based on the above analysis results, this paper mainly proposes four risk control countermeasures. The details are as follows.

## 6.1 Tunnelling parameters

To effectively reduce the influence of the TBM tunnel on stratum disturbance and operational railway tunnels, TBM tunnel construction parameters need to achieve low thrust, low penetration, low speed, low torque, and continuous working. The rated driving thrust is 3900 t, 900~1700 t for the normal section, 780~1200 the for upper span section, and the average thrust is 20~30% of the rated value. The normal driving speed is 40~60 mm/min, and the upper span is 20~30 mm/min. The rated speed of the cutterhead is 5~6 rad/min, the normal section is 4.0~4.5 rad/min, and the upper span section is 3.0~3.5 rad/min. The rated torque of the cutterhead is 4000 kN·m, 900~1300 kN·m for the normal section, and 700~1100 kN·m for the upper span section.

## 6.2 Pea-gravel backfilling and grouting

In the TBM tunnel construction, the method of synchronous pea-gravel backfilling and grouting can be used to improve the contact state between segments and rock mass, which can effectively reduce the stratum settlement. To ensure full backfill of pea-gravel and prevent lateral displacement caused by uneven stress on segments, pea-gravel shall be filled from bottom to top and both sides shall be symmetrically filled. After ensuring the pea-gravel is filled, the first grouting shall be carried out in time, and then the second supplementary grouting shall be conducted at the rear of the trailer to improve the waterproofness of the grouting layer, make the grouting body fill evenly, and effectively reduce the formation loss.

## 6.3 Consolidation grouting of segment bottom

Considering the existence of joints and fissures in the surrounding rock and it will be softening after encountering water. Therefore, the surrounding rock near the bottom of the affected area of the new tunnel is reinforced by grouting during the TBM tunnelling. The grouting range is 90° of the inverted arch, the depth is 3 m, and the grouting pressure shall not exceed 2 MPa.

## 6.4 Other countermeasures

Conduct attitude adjustment and cutters replacement for TBM in advance. Adjust the host machine attitude and key parameters to ensure good attitude and control of TBM. Check and replace the cutters to avoid a midway pause. The single shield TBM always keeps rising during the tunnelling. The stability of the segment guide system and the segment assembly quality shall be ensured through regular retesting. TBM tunnelling time control at the intersection: when the

construction is carried out within one time of the tunnel diameter (1D) before and after the intersection of the operational tunnel, the excavation must be conducted within the skylight time of the railway. The deformation and stress of the operational tunnel shall be inspected and monitored in real-time to ensure the controllability of construction safety.

# 7 Conclusion

Based on the complex adjacent project of the TBM tunnelling of Chongqing Rail Transit Line 5, through on-site inspection and numerical simulation, this paper studies the impact of new TBM tunnel construction on the structural stability of operational tunnel, and proposes the impact zoning of proximity construction and corresponding risk control measures. The main conclusions are as follows.

1) When TBM tunnelling over the operational tunnel, it will result in uplift deformation of the operational tunnel below. The maximum uplift deformation of the ballast bed is less than that of the vault, and the lining structure shows a tensile trend in the vertical direction.
2) The influence of the tunnelling construction of the new TBM tunnels on the operational tunnel below is roughly a parallelogram. The long axis of the parallelogram is parallel to the operational tunnel, with a length of about 44.2m; the short axis is parallel to the new TBM tunnel, with a length of about 20 m.
3) The new TBM tunnels have little influence on the internal force of the operational tunnel structure, and the safety factors of the key monitoring sections meet the requirements of the bearing capacity.
4) Under the influence of the construction of the above TBM tunnel, the longitudinal bending moment and axial force change curve of the operational tunnel fluctuate greatly within the close influence scope (within 30 m around the intersection of the new tunnel and the operational tunnel). At the construction joint, the bending moment and axial force are reduced.
5) Risk control measures such as TBM tunnelling parameter optimization, pea-gravel backfilling and grouting, grouting reinforcement at the bottom of new tunnels, TBM attitude adjustment, TBM cutters replacement, and tunnelling time control are proposed.

# Data availability statement

The original contributions presented in the study are included in the article/supplementary material, further inquiries can be directed to the corresponding authors.

# Author contributions

FL: contributed to Conceptualization, Resources, Funding acquisition, Analysis, and Writing; LL and ZC: contributed to Validation, Analysis, and Writing; PL and ML: contributed to Field test, Analysis, Review editing, and Data collection; LG, XG, and CJ: contributed to Investigation, Supervision, Methodology, and Review editing. All authors have read and agreed to the published version of the manuscript.

## Funding

## Conflict of interest

## Publisher's note

## References

Akbari, S., Zare, S., Chakeri, H., and Mirzaei, H. (2020). A 3D finite-difference analysis of Interaction between a newly-driven Large tunnel with twin tunnels in urban areas. *J. Min. Environ.* 11 (03), 809–823. doi:10.22044/jme.2020.9444.1851

Azadi, M., Pourakbar, S., and Kashfi, A. (2013). Assessment of optimum settlement of structure adjacent urban tunnel by using neural network methods. *Tunn. Undergr. Space Technol.* 37, 1–9. doi:10.1016/j.tust.2013.03.002

Boonyarak, T., and Ng, C. (2014). Effects of construction sequence and cover depth on crossing-tunnel interaction. *Can. Geotechnical J.* 52 (07), 851–867. doi:10.1139/cgj-2014-0235

Choi, J., and Lee, S. (2010). Influence of existing tunnel on mechanical behavior of new tunnel. *KSCE J. Civ. Eng.* 14 (05), 773–783. doi:10.1007/s12205-010-1013-8

Clarke, J., and Laefer, D. (2014). Evaluation of risk assessment procedures for buildings adjacent to tunnelling works. *Tunn. Undergr. Space Technol.* 40, 333–342. doi:10.1016/j.tust.2013.10.014

Cui, G., Tian, Y., Xiao, Y., He, J., and Meng, L. (2022). Optimization of construction scheme for metro small clear distance tunnel close to tunnel group in high-risk urban environment. *J. Saf. Sci. Technol.* 18 (03), 156–161. In Chinese. doi:10.1016/j.csite.2021.101130

Do, N., Dias, D., Oreste, P., and Djeran-Maigre, I. (2014). Three-dimensional numerical simulation of a mechanized twin tunnels in soft ground. *Tunn. Undergr. Space Technol.* 42, 40–51. doi:10.1016/j.tust.2014.02.001

Fang, Q., Zhang, D., Li, Q., and Wong, L. (2015). Effects of twin tunnels construction beneath existing shield-driven twin tunnels. *Tunn. Undergr. Space Technol.* 45, 128–137. doi:10.1016/j.tust.2014.10.001

Gan, X., Yu, J., Gong, X., Hou, Y., Liu, N., and Zhu, M. (2022). Response of operating metro tunnels to compensation grouting of an underlying large-diameter shield tunnel: A case study in hangzhou. *Undergr. Space* 7 (02), 219–232. doi:10.1016/j.undsp.2021.07.006

Gong, L. (2008). *Mechanics of vertical construction of vertical cross sectioned tunnel.* Chengdu: Southwest Jiaotong University. Doctor's thesis. In Chinese.

Guan, B. (2011). *Key points of tunnel construction.* Beijing: China Communications Press.

Hua, K. (2008). *Prediction and control method for subway shield tunnel approaching cross adjacent structure.* Master's thesis. In Chinese: Chengdu: Southwest Jiaotong University.

Islam, M., and Iskander, M. (2021). Twin tunnelling induced ground settlements: A review. *Tunn. Undergr. Space Technol.* 110, 103614. doi:10.1016/j.tust.2020.103614

Jiang, B., Chen, L., Yang, J., Wang, S., and Ng, C. (2017). Effects of twin-tunnel excavation on an existing horseshoe-shaped tunnel considering the influence of a settlement joint. *Can. Geotechnical J.* 54 (09), 1346–1355. doi:10.1139/cgj-2015-0389

Kong, C. (2016). *Study on the construction mechanics behavior of large and adjacent urban tunnel groups.* Chengdu: Southwest Jiaotong University. Doctor's thesis. In Chinese.

Krishnan, R. (2000). *Tunnels and Underground Structures: Proceedings Tunnels & Underground Structures, Singapore 2000.* 1st Edn. London: Routledge. doi:10.1201/9780203734926

Lei, M., Lin, D., Huang, Q., Shi, C., and Huang, L. (2018). Research on the construction risk control technology of shield tunnel underneath an operational railway in sand pebble formation: A case study. *Eur. J. Environ. Civ. Eng.* 24, 1558–1572. doi:10.1080/19648189.2018.1475305

Li, X., and Yuan, D. (2012). Response of a double-decked metro tunnel to shield driving of twin closely under-crossing tunnels. *Tunn. Undergr. Space Technol.* 28, 18–30. doi:10.1016/j.tust.2011.08.005

Li, Y., Jin, X., Lv, Z., Dong, J., and Guo, J. (2016). Deformation and mechanical characteristics of tunnel lining in tunnel intersection between subway station tunnel and construction tunnel. *Tunn. Undergr. Space Technol.* 56, 22–33. doi:10.1016/j.tust.2016.02.016

Liang, R., Kang, C., Xiang, L., Li, Z., Lin, C., Gao, K., et al. (2021). Responses of in-service shield tunnel to overcrossing tunnelling in soft ground. *Environ. Earth Sci.* 80, 183. doi:10.1007/s12665-021-09374-3

Liu, B., Yu, Z., Zhang, R., Han, Y., Wang, Z., and Wang, S. (2021). Effects of undercrossing tunneling on existing shield tunnels. *Int. J. Geomechanics* 21 (08), 04021131. doi:10.1061/(asce)gm.1943-5622.0002102

Liu, X., Jiang, A., Fang, Q., Wan, Y., Li, J., and Guo, X. (2022). Spatiotemporal deformation of existing pipeline due to new shield tunnelling parallel beneath considering construction process. *Appl. Sci.* 12, 500. doi:10.3390/app12010500

Luo, Z., Zeng, L., Pan, H., Hu, Q., Liang, B., and Han, J. (2019). Research on construction safety risk assessment of new subway station close-attached undercrossing the existing operating station. *Math. Problems Eng.* 2019, 1–20. doi:10.1155/2019/3215219

Min, B., Zhang, C., Zhang, X., Wang, H., Li, P., and Zhang, D. (2020). Cracking performance of asymmetric double-arch tunnels due to the voids behind linings. *Thin-Walled Struct.* 154, 106856. doi:10.1016/j.tws.2020.106856

Mou, Z., Zhang, H., Tian, M., and Qiu, W. (2020). Research on the influence zone dividing of tunneling adjacent to existing tunnel based on ultimate strain criterion. *IOP Conf. Ser.: Mater. Sci. Eng.* 741, 012102. doi:10.1088/1757-899X/741/1/012102

Qiu, D., Huang, H., and Song, D. (2012). Deformation monitoring and prediction technique of existing subway tunnel: A case study of guangzhou subway in China. *Geodesy, Photogrammetry Cartogr.* 30 (6-2), 623–629. doi:10.7848/ksgpc.2012.30.6-2.623

Qiu, W. (2003). *The study on mechanics principle and countermeasure of approaching excavation in underground works.* Chengdu: Southwest Jiaotong University. Doctor's thesis. In Chinese.

TB 10003-2005 (2005). *Code for design on tunnel of railway.* Beijing: China Railway Publishing House.

TB 10417-2003 (2003). *Standard for constructional quality acceptance of railway tunnel engineering.* Beijing: China Railway Publishing House.

TB/T 2820.1-1997 (1997). *Standard for deterioration assessment of railway bridge and tunnel buildings Tunnel.* Beijing: Standards Press of China.

TB10223-2004 (2004). *Code for undestructive detecting of railway tunnel lining.* Beijing: China Railway Publishing House.

Railway transport letter (2004). *Interim provisions on assessment of lining safety grade of railway operation tunnels.* Beijing: Ministry of railways of the People's Republic of China.

Yamaguchi, I., and Kiritani, Y. (1998). Study of ground-tunnel interactions of four shield tunnels driven in close proximity, in relation to design and construction of parallel shield tunnels. *Tunn. Undergr. Space Technol.* 13 (03), 289–304. doi:10.1016/S0886-7798(98)00063-7

Zhang, C., Zhang, D., Wu, J., and Luo, J. (2009). Construction control of a newly-built subway station undercrossing the existing subway tunnel. *China Railw. Sci.* 30 (01), 69–73. In Chinese. doi:10.3969/j.issn.1006-2106.2009.01.016

Zhang, C., Zhang, X., and Fang, Q. (2018). Behaviors of existing twin subway tunnels due to new subway station excavation below in close vicinity. *Tunn. Undergr. Space Technol.* 81, 121–128. doi:10.1016/j.tust.2018.07.020

Zhang, D., Huang, Z., Li, Z., Zong, X., and Zhang, D. (2019). Analytical solution for the response of an existing tunnel to a new tunnel excavation underneath. *Comput. Geotechnics* 108, 197–211. doi:10.1016/j.compgeo.2018.12.026

Zhang, Q. (2018). Field observation and theoretical study on an existing tunnel underpassed by new twin tunnels. *Adv. Civ. Eng.* 2018, 1–16. doi:10.1155/2018/1598672

Zhang, Z., and Huang, M. (2014). Geotechnical influence on existing subway tunnels induced by multiline tunneling in Shanghai soft soil. *Comput. Geotechnics* 56, 121–132. doi:10.1016/j.compgeo.2013.11.008

Zhen, Q., Li, S., Zheng, G., Feng, X., and Chi, Z. (2019). Influence of excavation of loess tunnel on stability of adjacent existing tunnels. *IOP Conf. Ser. Earth Environ. Sci.* 371, 022053. doi:10.1088/1755-1315/371/2/022053

Zheng, B., Chen, W., and Hu, G. (2009). Analysis and monitoring of ground subsidence caused by excavation of adjacent and crossing metro tunnel with shallow-depth and subsurface excavation method. *J. Railw. Eng. Soc.* (01), 72–76. In Chinese. doi:10.3969/j.issn.1006-2106.2009.01.016

Zheng, G., Yang, X., Zhou, H., Du, Y., Sun, J., and Yu, X. (2018). A simplified prediction method for evaluating tunnel displacement induced by laterally adjacent excavations. *Comput. Geotechnics* 95, 119–128. doi:10.1016/j.compgeo.2017.10.006

Zheng, Y. (2007). *Study on the influence degree of adjacent construction of three parralell shield tunnels*. Chengdu: Southwest Jiaotong University. Doctor's thesis. In Chinese.

Zhou, J., Luo, Y., Li, X., Guo, Y., and Liu, T. (2017). Numerical evaluation on dynamic response of existing underlying tunnel induced by blasting excavation of a subway tunnel. *Shock Vib.* 2017, 1–10. doi:10.1155/2017/8628671

# Experimental investigation on the reinforcement of a high-pressure jet grouting pile for an ultra-shallow tunnel in a strongly weathered stratum

Pinpin Li[1], Xun Huang[2], Feng Lu[1,3]*, Wenge Qiu[1], Huan Liu[4], Linlong Li[3], Yi Wang[3], Zhenyu Chen[3] and Zhihao He[3]*

[1]Key Laboratory of Transportation Tunnel Engineering, Ministry of Education, School of Civil Engineering, Southwest Jiaotong University, Chengdu, Sichuan, China, [2]Faculty of Geosciences and Environmental Engineering, Southwest Jiaotong University, Chengdu, Sichuan, China, [3]School of Emergency Management, Xihua University, Chengdu, Sichuan, China, [4]Anhui Transport Consulting and Design Institute Co., Ltd., Hefei, Anhui, China

In this paper, the performance of a high-pressure grouting material and consolidation body, the key parameters of tunnel surrounding rock reinforcement, and the field reinforcement effect are compared and studied. The results show that 1) the compressive strength, elastic modulus, and seepage resistance of the consolidation body are related to the water−cement ratio. The permeability of the consolidation body increases with increasing water−cement ratio under the constant head; under the condition of a certain water−cement ratio, the strength increases with an increase in cement content. To meet the construction requirements and the slurry stability, a small water−cement ratio is appropriate. 2) Slurry pressure, rotary spray speed, and lifting speed on the single pile static load bearing capacity have a significant impact. Under the same static load conditions, the greater the slurry pressure, the lower the cumulative settlement value of the single pile, the cumulative settlement value increases less, and the amount of change in rebound is the same; with the increase in the rotational speed of the rotary spray, the lower the cumulative settlement value of the single pile, and the rate of change of the cumulative settlement value of the single pile decreases; and with the increase in the lifting speed, the cumulative settlement value of the single pile increases and the rate of change of the cumulative settlement value decreases. 3) The pile body cement soil is more uniform, has high strength, and is brittle, and the stratum where the slurry part is located is a loose powder clay layer and sandy layer. 4) After high-pressure jet grouting pile reinforcement, the top surrounding rock is more stable after the excavation of an ultra-shallow buried tunnel, the fissures between the surrounding rocks are filled with cement soil consolidation, and the integrity is improved. Certain piles also play a certain role in stopping water; high-pressure jet grouting pile reinforcement to improve the integrity of the surrounding rock played a role in consolidating the weak soil layer above the tunnel vault, creating conditions for the safe excavation of the shallow buried section of the tunnel.

# 1 Introduction

With the rapid development of high-speed railroad network construction, highway tunnels often encounter the problem of excavating ultra-shallow buried tunnels in strongly weathered strata. Due to the very shallow burial depth, the stratum in which the tunnel is located is severely weathered, rock fissures are developed, and the surrounding rock is poorly self-stabilized and prone to surface cracking and collapse after tunnel excavation (Davis et al., 1981; Zhou et al., 2013; Cui et al., 2022), which poses a great threat to the service life and operation safety of the tunnel (Li et al., 2022; Lu et al., 2022). The common accident types and frequency statistics of tunnels are shown in Figure 1. Due to the high frequency of collapse accidents in tunnel construction and the highest number of single fatalities among all accident types (Wang et al., 2009; Zhang et al., 2014; Li et al., 2022), often accompanied by damage to the structure, engineering delays, and serious environmental impacts in the surrounding area, collapse accident prevention is at the top of disaster prevention and control. Many factors cause collapse, including geological factors, survey factors, design factors, and construction factors, and the latter three are controlled by geological factors, so dealing with geological factors is the focus of collapse prevention and control (Hu and Qin, 2013). Due to the complex geological conditions and the lack of mature experience and corresponding standard specifications, effective reinforcement of the stratum, prevention of collapse of the surrounding rock, and ensuring construction safety are the key factors for ultra-shallow buried tunnel construction in strongly weathered strata (Chen et al., 2013).

To improve the surrounding rock in strongly weathered strata and reduce the risk of a tunnel collapse, it is often necessary to pre-reinforce the tunnel-surrounding rock before the excavation of ultra-shallow buried tunnels. High-pressure jet grouting piles are created by using high-pressure cement mortar after drilling holes in the ground and using high-pressure slurry to quickly cut and mix the soil to create the cement and soil mix. High-pressure jet grouting piles have become a reinforcement technique used to improve the ground and solve most of the weak ground problems (Brandsttter et al., 2001). Jet grouting systems are divided into three types according to the delivery mechanism (see Figure 2): single-fluid, two-fluid, and three-fluid (Nikbakhtan and Osanloo, 2009). In a single-fluid system, the injected fluid is cement soil; in a two-fluid system, cement soil and compressed air are injected. The combined action of high-pressure grout and air results in a greater percentage of soil being removed and replaced by the grout; in the three-fluid system, slurry, air, and water are injected. This triple combination removes a much higher percentage of soil and the system can be used to replace soil almost completely with cement soil. In general, the most important parameters affecting the design of jet grouting are the soil type, the inflow of the slurry mixture, the injection energy, the slurry flow rate, the rotational speed, and the lifting speed (Nikbakhtan and Rahmani, 2010). The rotary jet pile system can be applied to different application scenarios with different types of soils by adjusting the technical parameters, such as increasing the bearing capacity, increasing the permeability of gravelly soils, reducing the settlement of soft
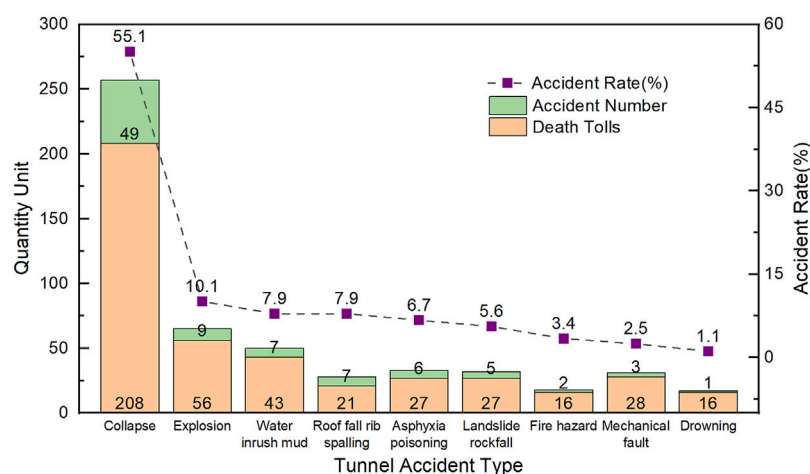


**FIGURE 1**
Statistics of tunnel accident type and occurrence frequency.
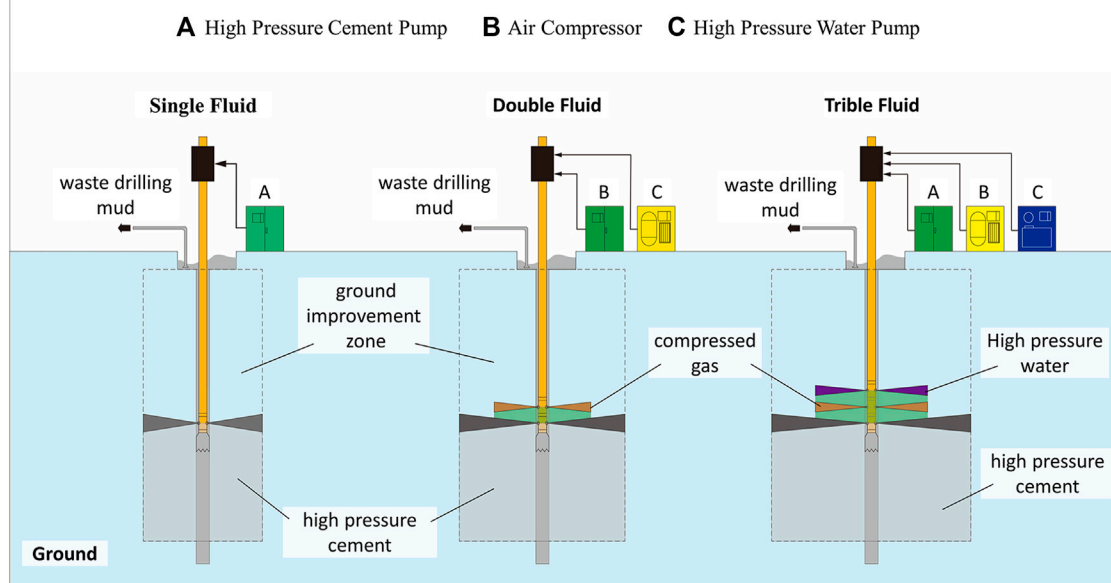
**FIGURE 2**
Classification of high-pressure jet grouting piles.

clay soils, and resisting the liquefaction of sandy soils (Hasan and Canakci, 2022).

Nowadays, shallow buried tunnels of highways gradually adopt high-pressure jet grouting pile construction technology for surface soft surrounding rock reinforcement and achieve good results. Wang et al. (2017) used high-pressure jet grouting piles for soft foundation reinforcement in the combined bridge-tunnel section of the Hong Kong–Zhuhai–Macao Bridge, with a replacement rate of 31.4%–40.3% in the reinforced area and a water–cement ratio of 0.8. The *in situ* field test proved that the high-pressure jet grouting pile composite foundation can effectively improve the stratum elastic mode and reduce the permeability of the stratum. Ren (2009) applied high-pressure jet grouting piles to the construction of shallow buried tunnels in saturated water-bearing layers, using a slurry pressure of 20–23 MPa, a rotation speed of 10–15 r/min, and a lifting speed of 10–15 cm/min. It was found that the quality of high-pressure jet grouting piles is greatly affected by adverse geology, and on-site rotary tests should be conducted before large-scale rotary spraying to achieve a better reinforcement effect. Que (2009) studied high-pressure jet grouting piles for ground reinforcement in shallow buried tunnels with sandy soil, using a cement dosage of 400 kg/m, a water–cement ratio of 0.8, and an unconfined compressive strength of 1.5 MPa, which shows that the piles have the effect of improving the force form, improving the effect of water stopping in the ground, and speeding up the construction of the tunnel. Ou et al. (2016) compared four shield tunnel ground reinforcement schemes by numerical analysis, and

the study showed that high-pressure jet grouting piles can effectively play the role of water isolation, reduce ground loss, and reduce surface settlement.

Previous studies on the field tests and applications of high-pressure jet grouting pile reinforcement in ultra-shallow buried tunnels with strong weathering strata are rare. In this paper, based on the ultra-shallow buried tunnel construction of the new Wu Tunnel as the engineering background, the innovation of the application and evaluation of the reinforcement effect of high-pressure jet grouting pile ground reinforcement technology in the ultra-shallow buried tunnel excavation in the strongly weathered stratum is studied through field tests and theoretical analyses, to provide some reference significant for the high-pressure jet grouting pile in the ultra-shallow buried tunnel ground reinforcement in the strongly weathered stratum.

# 2 Project overview

## 2.1 Project background

The new Wu tunnel is a separate tunnel; the total length of the tunnel is 2,500 m, the slope of the whole tunnel is −2.3%, and the maximum depth of the tunnel is about 218.4 m. The tunnel body crosses two ultra-shallow buried sections; the ultra-shallow buried tunnel left line longitudinal section is shown in Figure 3. The main influence range of the first section is ZK84 + 450–ZK84 + 476 (the left line tunnel), and K84 + 453–K84 + 475 (the right
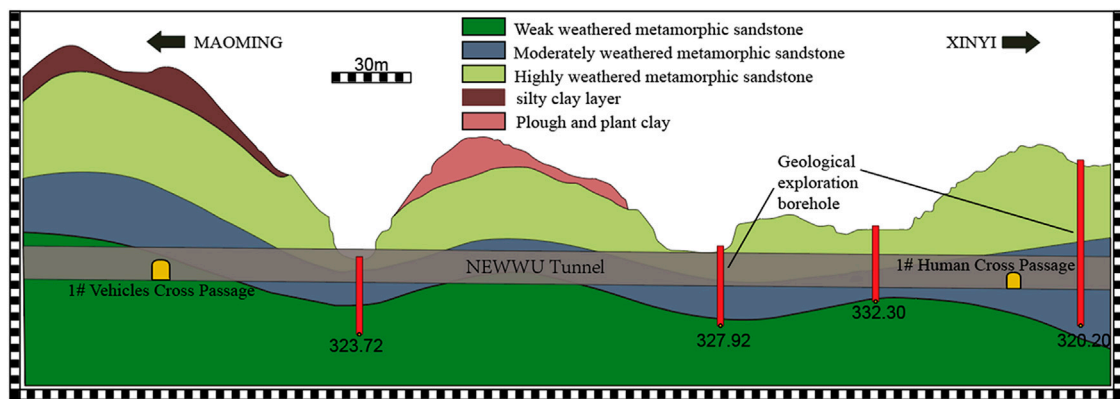
**FIGURE 3**
Longitudinal section of the left line.

**TABLE 1 Geological distribution of tunnel stratigraphy.**

| Stratigraphic number | Layer thickness (m) | Floor elevation (m) | Stratigraphic description |
|---|---|---|---|
| 1 | 1.1 | 342.92 | Powdery clay: brownish yellow, moist, good plasticity, average cohesiveness |
| 2 | 3.1 | 339.82 | Silty powdery clay: gray–brown, saturated, soft plastic, with a fishy odor |
| 3 | 3.2 | 336.62 | Powdery clay: brownish yellow, moist, soft plastic, containing more powder particles |
| 4 | 2.4 | 334.22 | Fine sand: brownish yellow, saturated state, slightly dense particles |
| 5 | 2.7 | 331.52 | Strongly weathered metamorphic sandstone: yellowish brown, grayish brown, weathering fissures developed, cores are fragmented and blocky, the rock quality is soft |
| 6 | 3.7 | 327.82 | Medium-weathering metamorphic sandstone: yellowish brown, greenish gray, fine-grained metamorphic structure, blocky structure, fissure development, cores are mostly fragmented and blocky, a few short columns, fissure surface is mostly discolored, the rock quality is hard |
| 7 | 4.1 | 323.72 | Weakly weathered metamorphic sandstone: grayish-blue, fine-grained metamorphic structure, massive structure, fissures are more developed, cores are mostly columnar, locally massive, nodes are 10–33 cm long, cores account for about 60%, rock is fresh and hard |

line tunnel). The left line exposed top is about 1 m, and the minimum cover layer of the right line is about 2 m thick, with surface water development and ditch development; the main impact area of the second section is ZK84 + 628 to ZK84 + 829 (the left line tunnel) and K84 + 644 to K84 + 795 (the right line tunnel). The surface above the tunnel is undulating, mostly paddy fields, large basin area, and some sections are ditches; multiple reservoirs, wells and houses are distributed in the upstream shallow buried section of the tunnel.

Dynasty Yunkai Rock Group, Garidonian granite, and its weathering layer. From the surface to the bottom of the tunnel, the rocks are, from top to bottom, cultivated soil, chalky clay, silty chalky clay, fine sand, chalky clay, and strongly weathered metamorphic sandstone, and below is medium-weathered metamorphic sandstone (below the bottom of the tunnel). The groundwater level in the section is located at the original ground level, with surface water flowing all year round. The geological longitudinal distribution of the layers is shown in Table 1.

## 2.2 Engineering geology

The stratigraphic lithology of the tunnel site area is Quaternary slope residual powder clay, metamorphic sandstone of the Yuan

## 2.3 Construction design

The tunnel (ZK84 + 450–ZK84 + 476 and K84 + 453–K84 + 475) construction method adopts the single sidewall excavation
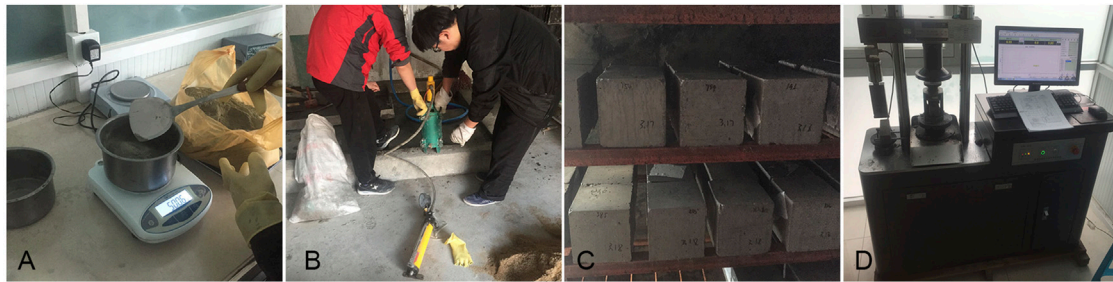
**FIGURE 4**
Test of the consolidation body properties. **(A)** Mix ratio test, **(B)** Water separation test rate, **(C)** Sample maintenance, **(D)** Compressive strength test.

method, the composite lining of XS-Va type, the double-layer small conduit for overrun support, small conduit spacing of 0.4 m, single length 4 m, 37 per ring, longitudinal 2.4 m/ring, a φ25 hollow grouting anchor rod for initial support, single length 3.5 m, spacing 100*60 (circumferential*longitudinal) cm, I20a I-beam spacing 0.6 m, locking foot anchors φ22 pill roll anchors, single length 3 m, and 8 per ring. The second lining adopts C30-reinforced waterproof concrete, with a thickness of 50 cm.

# 3 High-pressure grouting material test

This experimental study conforms to the Highway Engineering Cement Test Code (JTG3420-2020) (Transport, 2005) to investigate the characteristics of the consolidation formed by using a high-pressure jet grouting pile. The cement soil slurry consists of four parts: water, cement, admixture, and soil body. The main factors affecting the consolidation performance of cement soil are cement strength grade, curing agent mixing ratio, maintenance age, soil parameters, and admixtures. In the test, the soil samples were used in a certain range of powder clay above the tunnel at the construction site, and the cement used to prepare the slurry was 42.5# normal silica cement with a compressive strength of 45.0 MPa at 28 d. The replacement rate of the high-pressure jet grouting pile used in the test was 0.34. The performance test of cement soil and the compressive strength test of specimens are shown in Figure 4.

## 3.1 Performance of cement soil

According to the requirements of the high-pressure jet grouting pile, four cement soil types with water–cement ratios of 0.8, 1.0, 1.2, and 1.5 were modulated and mixed with the clay soil samples according to the replacement ratio of 0.34 test requirements (as shown in Figure 4A). The cement soil density, funnel viscosity, and water separation rate (as shown in Figure 4B) measured in this study

are shown in Table 2. It can be seen that the slurry density decreases, the water separation rate increases, and the viscosity decreases as the water–cement ratio increases. Therefore, under the premise of satisfying the construction requirements and considering the stability of the slurry, the water–cement ratio should be small.

## 3.2 Compressive strength of specimens

The soil samples at the site of the compressive strength test were mixed with cement paste materials of different proportions, and the test blocks were molded with a cube with a side length of 7.00 cm. After the molds were removed, the compressive strength test was carried out after curing for 28 days at standard conditions (20°C ± 1°C and RH ≥ 95%) according to GB/T 50082-2009 (Lu et al., 2022) (as shown in Figures 4C, D). From the compressive strength test results shown in Table 3, it can be seen that under the conditions of a certain water–cement ratio, the consolidation strength increases when the cement increases; under a certain cement content, the consolidation strength decreases when the water–cement ratio increases. The sudden change in the strain–stiffness curve of the load-displacement curve of the axial compression test marks the development of cracks in the consolidated sample (Gao et al., 2018). The on-site high-pressure consolidation strength can be analyzed by the inlet weight, return weight, and sand content of the return slurry. The high-pressure consolidation strength can be determined by the inlet weight, return weight, and sand content of the slurry, and consolidation strength of the return slurry. Concerning the indoor test results for preliminary estimation, the parameters can be adjusted during the construction test.

## 3.3 Modulus of elasticity of specimens

The cement soil with different water–cement ratios was mixed with the base material and then molded with a 15 cm × 30 cm test mold. The mold was removed after 48 h of wet maintenance on the

**TABLE 2 Cement soil property test results.**

| Work condition number | Water-to-ash ratio | Density (g*cm⁻³) | Funnel viscosity | Water separation rate | Test temperature (°C) |
|---|---|---|---|---|---|
| S-M1 | 0.75 | 1.61 | 20.5 | 17.3 | 23.5 |
| S-M2 | 1.00 | 1.49 | 19.8 | 28.6 | 23.3 |
| S-M3 | 1.25 | 1.39 | 19.0 | 37.7 | 24.2 |
| S-M4 | 1.50 | 1.31 | 18.2 | 41.6 | 24.5 |

The absolute value error of test measurement is 2%.

**TABLE 3 Mechanical properties of solid test results.**

| Work condition number | Water-to-ash ratio | Compressive strength (MPa) | | | | | 28-d modulus of elasticity (Mpa) |
|---|---|---|---|---|---|---|---|
| | | 150 | 200 | 250 | 300 | 350 | |
| S-P1 | 0.75 | 2.41 | 3.44 | 5.74 | 7.55 | 11.19 | 3,755 |
| S-P2 | 1.00 | 1.41 | 2.17 | 3.02 | 4.92 | 7.06 | 3,214 |
| S-P3 | 1.25 | 1.12 | 1.60 | 2.57 | 4.14 | 5.81 | 3,165 |

1) The cement content of the modulus of elasticity specimen is 300 kg*m⁻³.

2) The absolute value error of test measurement is 2%–3%.



**FIGURE 5**
Stress−strain curve of the solid body.
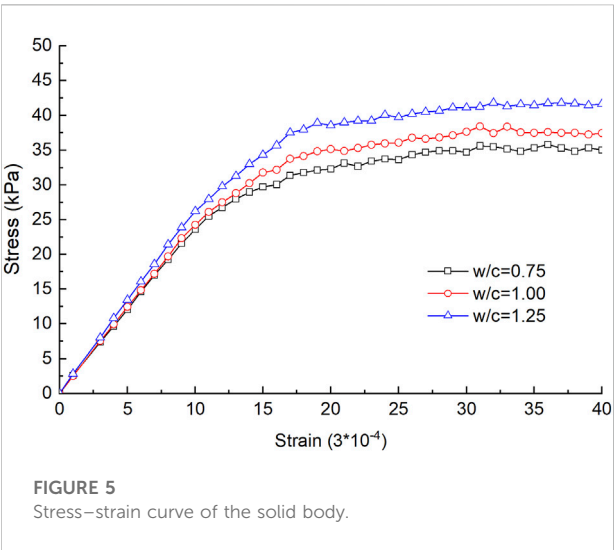
surface. Test specimens were moved to the maintenance room and taken out until 28 d and loaded on the testing machine until destruction while measuring the deformation relative to both sides. This test provides a set of useful test data for evaluating the effect of stratum reinforcement, the static load-bearing capacity of the foundation, and the stability analysis of tunnel excavation (Gao et al., 2022). The results of the spring mold test are shown in Table 3, and the stress–strain curve is shown in Figure 5.

## 3.4 Seepage resistance of specimens

The soil samples collected in the field were mixed with cement soil and molded with a 7.5 cm upper, 8.5 cm lower, and 3 cm high test mold, and after demolding, they were maintained in the maintenance room until 28 d of age and tested on the mortar impermeability meter to determine the permeability coefficient at the constant head, and the results are shown in Table 4. The test results show that the permeability of the consolidation body increased with increasing water–cement ratio at the same room temperature.

## 4 High-pressure jet grouting pile piling test

The construction process of high-pressure jet grouting piles is complex, and the geological conditions and hydrology of the shallow buried section of the reinforced tunnel are complicated, so field trial piling tests must be carried out to determine the key technical indicators to ensure the reinforcement and impermeability effects and to guarantee the safety and speed of the tunnel construction. To test the piling effect of high-pressure jet grouting piles, and the ground reinforcement, piling load tests, and pile core drilling tests were carried out.

**TABLE 4 Specimen seepage resistance test results.**

| Work condition number | Water-to-ash ratio | Permeability coefficient (cm*s$^{-1}$) | Test temperature (°C) |
|---|---|---|---|
| S-W1 | 0.75 | 6.6*10$^{-8}$ | 23.4 |
| S-W2 | 1.00 | 2.3*10$^{-7}$ | 23.3 |
| S-W3 | 1.25 | 5.1*10$^{-7}$ | 24.5 |
| S-W4 | 1.50 | 6.4*10$^{-7}$ | 24.3 |

1) The cement content of the specimen is 300 kg*m$^{-3}$.
2) The absolute value error of the test result is 2%–3%.

**TABLE 5 Rotary pile surface test condition design table.**

| Condition number | Slurry pressure (Mpa) | Spin spray speed (r*min$^{-1}$) | Lifting speed (cm*min$^{-1}$) | Hole diameter (cm) | Jet diameter (cm) | Length of pile (m) |
|---|---|---|---|---|---|---|
| S-D1 | 20 | 20 | 25 | 50 | 3 | 10 |
| S-D2 | 22 | 20 | 25 | 50 | 3 | 10 |
| S-D3 | 25 | 20 | 25 | 50 | 3 | 10 |
| S-R1 | 20 | 18 | 25 | 50 | 3 | 10 |
| S-R2 | 20 | 20 | 25 | 50 | 3 | 10 |
| S-R3 | 20 | 22 | 25 | 50 | 3 | 10 |
| S-T1 | 20 | 20 | 20 | 50 | 3 | 10 |
| S-T2 | 20 | 20 | 25 | 50 | 3 | 10 |
| S-T3 | 20 | 20 | 25 | 50 | 3 | 10 |

S-D stands for slurry pressure condition, S-R stands for spin spray speed condition, and S-T stands for lifting speed condition. Each group of conditions has three test groups: single-pile static load test, composite foundation static load test, and borehole coring test.

## 4.1 Program design

The spray pressure needs to be considered in terms of the compactness, compressive strength, and scour resistance of the soil. The lifting speed has a great influence on the quality and diameter of the pile consolidation body. The spray speed and the lift speed are two correlated parameters. According to the construction experience, single-tube spin spray pile lifting heights per revolution ranges from 0.5–1.25 mm. To satisfy the construction parameters that the soil within 0.25 m can be subjected to five jet impacts, we selected 20, 22, and 25 r/min as test parameters. The test is arranged with 18 high-pressure jet grouting pile test piles, consisting of nine groups of test piles (three piles in each group). The single-pile static load test and drill core sampling test were conducted, and the specific design of the working conditions is shown in Table 5. The test piles follow the positive triangular arrangement, the standard working conditions of the pile diameter of 0.5 m, and spacing of 1.5 m. The standard test pile has a rotating speed of 20 r/min, an injection pressure of 25 Mpa, and a mechanical lifting speed of 25 cm/min. The total length of the pile is about 10 m.

## 4.2 Test equipment

The static load test equipment includes one set of RSM-JCIII static load test system, one set of 300T jack, one set of pressure transducers, and four sets of displacement transducers. The load value is measured using the pressure transducer and the pile settlement value is recorded using displacement meters symmetrically distributed on the load plate. The displacement meter is fixed by a magnetic base to the reference beam, and the distance between the reference amount and the center point of the load plate is 2.5 m. The schematic diagram of pile static loading is shown in Figure 6.

## 4.3 Test loading

The static load test adopts the graded load settlement relative stability method. The maximum design test load is 300 kN divided into 10 grades, and each grade loading value (taking 1/10 of the design limit load) is 30 kN. After the test loads to the expected maximum load, the loading is terminated. The single-pile load test uses a round bearing plate with a diameter of 0.5 m.
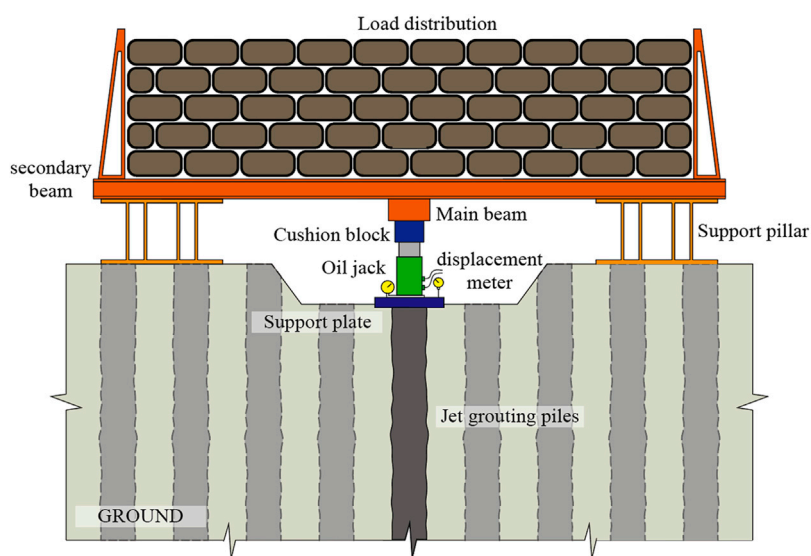
**FIGURE 6**
Pile static load schematic diagram.

After the test, the test pile body is excavated to check the integrity of the pile and the slurry situation, as well as the bearing capacity. The core test is conducted by the conventional coring method according to the construction specification.

# 5 Analysis results of the piling test

The parameters of the high-pressure jet grouting pile need to be combined with the project geological conditions and the empirical data of similar projects should be referred to for verification, combined with the field piling test (Pan et al., 2021). Ultra-shallow buried tunnel ground reinforcement should also consider tunnel design requirements, minimum depth of burial, and construction safety (Li, 2004). The pile load settlement curves under different test conditions are shown in Figure 7. The statistics of the single-pile bearing capacity test results are shown in Table 6.

## 5.1 Single-pile static load test

### 5.1.1 The effect of injection pressure

The three groups of working conditions, S-D1, S-D2, and S-D3, are the test piles of high-pressure jet grouting piles under different slurry pressure conditions. Under the requirements of the monopile static load test, incremental loading is carried out until the design load of 300 kPa is reached. From Figure 7A, it can be seen that under the first loading condition of a static load of

30 kPa, the cumulative settlement value of the pile top is 2.85 mm; when the static load is loaded to the 5th load level of 180 kPa, the cumulative settlement value of the pile top is 5.38 mm; the maximum cumulative settlement value of the pile top is 34.97. After reaching the maximum design load value and unloading, the residual settlement value of the pile top is 26.9 and the rebound amount is 8.07 mm s-D2. The cumulative settlement at the top of the pile is 2.80 mm at the first load, 4.91 mm at the fifth load, and 29.6 at the maximum load. After unloading, the residual settlement of the pile top was 22.25 and the rebound was 5.93 mm.

From the test results, it can be found that the slurry pressure has a significant effect on the static load-bearing capacity of the monopile; the higher the slurry pressure, the lower will be the cumulative settlement value of the monopile under the same static load condition. When the slurry pressure was increased from 20 Mpa to 22 Mpa, the cumulative settlement value of the single pile under the maximum design load condition was reduced by 5.37 mm and the rebound was reduced by 1.12 mm. When the slurry pressure was increased from 22 Mpa to 25 Mpa, the cumulative settlement value of the single pile under the maximum design load condition was reduced by 1.42 mm and the rebound was reduced by 1.02 mm, and the cumulative settlement value increased by a smaller amount. The amount of change in rebound is the same.

### 5.1.2 The effect of jet rotation speed

The three groups of working conditions, S-R1, S-R2, and S-R3, are test piles of high-pressure jet grouting piles under
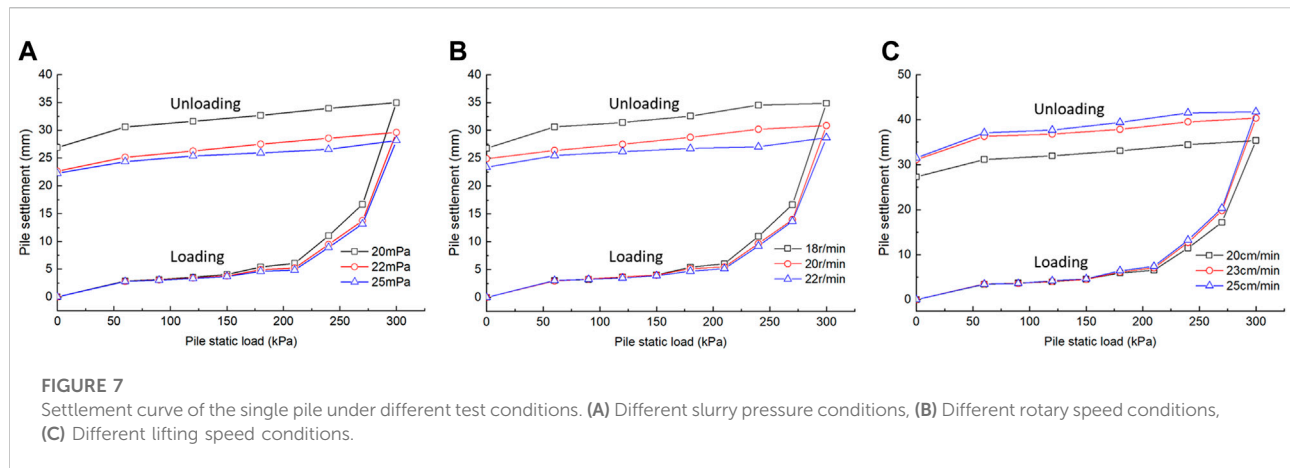
**FIGURE 7**
Settlement curve of the single pile under different test conditions. **(A)** Different slurry pressure conditions, **(B)** Different rotary speed conditions, **(C)** Different lifting speed conditions.

TABLE 6 Statistics of static load test data of the single pile.

| Work conditions | Load value (kN) | | | | Rebound amount/mm | Rebound ratio (%) |
|---|---|---|---|---|---|---|
| Type | 60 | 180 | 300 | Uninstallation | | |
| S-D1 | 2.85 | 5.38 | 34.97 | 26.9 | 8.07 | 23.1 |
| S-D2 | 2.8 | 4.91 | 29.6 | 22.65 | 6.95 | 23.5 |
| S-D3 | 2.78 | 4.61 | 28.18 | 22.25 | 5.93 | 21.0 |
| S-R1 | 3.02 | 5.42 | 34.87 | 26.79 | 8.08 | 23.2 |
| S-R2 | 2.95 | 5.16 | 30.85 | 24.9 | 5.95 | 19.3 |
| S-R3 | 3.01 | 4.69 | 28.69 | 23.38 | 5.31 | 18.5 |
| S-T1 | 3.43 | 5.95 | 35.4 | 27.32 | 8.08 | 22.8 |
| S-T2 | 3.49 | 6.13 | 40.34 | 31.13 | 9.21 | 22.8 |
| S-T3 | 3.47 | 6.43 | 41.76 | 31.53 | 10.23 | 24.5 |

1) The unit of settlement is mm.
2) The absolute value error of the test result is 2%–3%.

different rotary speed conditions. The test results are shown in Figure 7B. The cumulative settlement at the top of the pile for S-R1 was 3.02 mm at the first load; the maximum cumulative settlement at the top of the pile was 34.87 at the fifth load stage; after reaching the maximum design load, the pile was unloaded to 0 at 60 kPa step-by-step; after completion of unloading, the residual settlement at the top of the pile was 26.79 and the rebound was 8.08 mm. After unloading, the residual settlement at the top of the pile was 24.9, with a rebound of 5.95 mm. The residual settlement value of the pile top after unloading is 23.39 and the rebound is 5.31 mm.

From the test results, it can be found that when the spin spray speed increased from 18 to 20 r/min, the cumulative settlement value of the single pile under the maximum design load condition was reduced by 4.02 mm, and the amount of rebound was reduced by 2.13 mm. When the spin-spray speed increased

from 20 to 22 r/min, the cumulative settlement value of the single pile under the maximum design load condition was reduced by 2.16 mm, and the amount of rebound was reduced by 0.64 mm. The rotational speed of rotary spraying has a significant effect on the static load-bearing capacity of the single pile; the larger the rotational speed of rotary spraying, the lower will be the cumulative settlement value of the single pile under the same static load conditions. With the increase in the rotational speed of rotary spraying, the rate of change of the cumulative settlement value of the single pile decreases, and the rate of change of the rebound volume also decreases.

### 5.1.3 Effect of lifting speed
The three groups of working conditions, S-T1, S-T2, and S-T3, are the test piles of High-pressure jet grouting piles under different lifting speed conditions. The test results are shown in
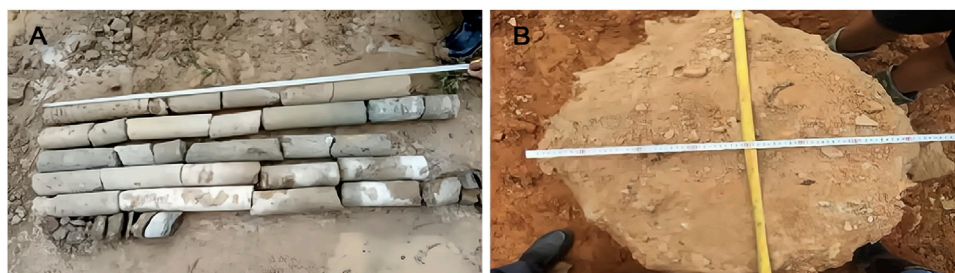
**FIGURE 8**
Drill core sampling of the high-pressure jet grouting pile. **(A)** Drill core sampling, **(B)** The pile diameter.

Figure 7C, from which it can be seen that the cumulative settlement at the top of the pile at the first load was 3.43 mm for S-T1, 5.95 mm at the fifth load level, and 35.40 for the maximum cumulative settlement at the top of the pile. After unloading, the residual settlement at the top of the pile is 31.13, with a rebound of 9.21 mm. The residual settlement value after unloading is 31.53, and the rebound is 10.23 mm.

From the test results, it can be found that when the lifting speed increased from 20 cm/min to 25 cm/min, the cumulative settlement value of the monopile under the maximum design load increased by 4.94 mm, and the rebound increased by 1.13 mm. When the lifting speed increased from 25 cm/min to 30 cm/min, the cumulative settlement value of the monopile under the maximum design load increased by 1.42 mm and the rebound increased by 1.02 mm. The rotational speed of the rotary spray has a significant effect on the static load-bearing capacity of the single pile; the higher the slurry pressure, the higher will be the cumulative settlement value of the single pile under the same static load condition. With the increase of the lifting speed, the increase of the cumulative settlement value decreases, and the rate of the change of rebound remains the same.

## 5.2 Drilling core test

After the test pile, the high-pressure jet grouting pile was completed in 14 days and the test pile was drilled core. The high-pressure jet grouting pile coring condition is shown in Figure 8A. A borehole depth of 1.5 m–7.5 m is a mixed layer of water and soil, grayish white, more uniform in color, with bubbles. Through the analysis of high-pressure jet grouting pile coring, it is found that the height of the mud spillover is basically above the strongly weathered metamorphic sandstone layer, and the stratum where the mud spillover is located is mainly a loose powdered clay layer and sandy layer. After the pile excavation, it was found that the maximum mud spillover height at the top of the rotary pile was 0.8 m, and the cement soil strength was not high. The hydro clay of the pile was more uniform, and the strength was high and

brittle. After the test pile construction is completed, the pile body is sampled using the drilling core. It is found that the quality of the pile is good through drilling, and the pile diameter is up to 60–75 cm (see Figure 8B), to meet the design requirements. The piles played a role in consolidating the weak soil layer above the tunnel vault, to create conditions for the safe excavation of the shallow buried section of the tunnel.

## 6 Surrounding rock reinforcement field applications

### 6.1 Tunnel reinforcement

The sections ZK84 + 645 to ZK84 + 820 (the left line) and K84 + 650 to K84 + 705 (the right line) are the test sections of the tunnel stratum reinforcement. The reinforcement test of a high-pressure rotary jet grouting pile is carried out on an ultra-shallow tunnel, and the surrounding rock integrity, deformation around the tunnel, the support structure stress, and permeability are monitored to evaluate the reinforcement effect of the tunnel.

Before the test, the surface vegetation, rooted soil, and flow-plastic silt were cleaned up, and the silt was excavated and refilled. In the test, the grouting pressure of the high-pressure rotary jet grouting pile is 22–24 mpa, the lifting speed is 18–22 cm/min, the rotation speed is 20 r/min, the pile spacing is 1.5 m, and the water–cement ratio of the grouting pile is 1:1. After the reinforcement of the piles, the shallow buried section is constructed in the construction sequence. The process of tunnel high-pressure jet grouting pile reinforcement is shown in Figure 9.

The reinforcement range of the high-pressure rotary jet grouting pile is 6 m on both sides of the tunnel, and the pile spacing is 1 m. The piles are reinforced to the depth of the tunnel invert, and the length of the pile is 10–13 m, depending on the length of the pile passing through the fully weathered soft layer. The high-pressure jet grouting pile site plan layout is shown in Figure 10. The cross-section of the pile reinforcement range is shown in Figure 11.
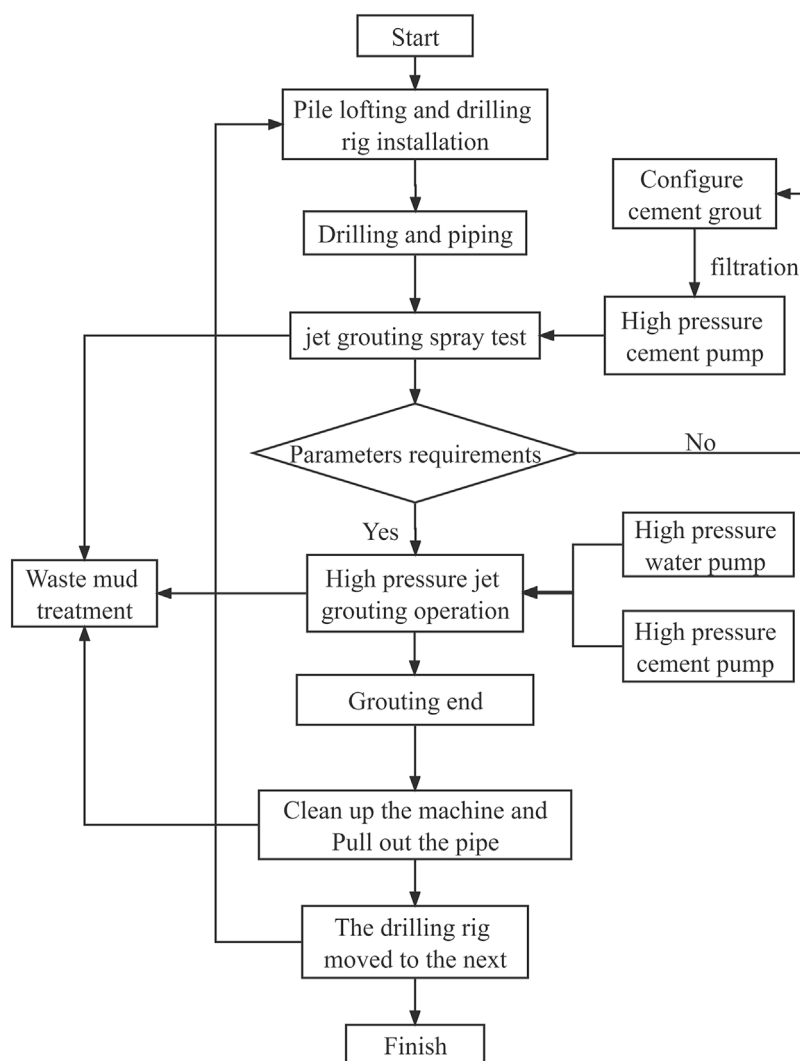
**FIGURE 9**
Flow chart of tunnel reinforcement.

## 6.2 Reinforcement effect

### 6.2.1 Integrity and deformation of the surrounding rock

The tunnel structure of the shallow buried section is a composite lining structure, including two parts: primary lining and secondary lining (Lu et al., 2022a). In the early stage of construction, the primary lining subjected to a large formation slack load is usually implemented to stabilize the ground (Qiu et al., 2019). In order to ensure construction safety, the tunnel excavation construction is carried out by strengthening the tunnel surrounding rock with the high-pressure rotary jet grouting pile. Tunnel excavation of the test section after reinforcement of the high-pressure jet grouting pile is shown

in Figure 12. The surrounding rock between the piles has a high cement content and well integrity with a compaction effect between the piles. Compared with the soil outside the depth range of the high-pressure jet grouting pile, the strength of the piles is greatly improved. As a result of high-pressure jet grouting pile ground reinforcement, the pile body plays a supporting role for the soil layer, limiting the lateral displacement of the soil layer, and the tunnel lateral convergence is small, indicating that the high-pressure jet grouting pile anti-extrusion effect is obvious. The high-pressure rotary jet grouting pile can improve the integrity of the surrounding rock, and the self-stability ability to surround rock can be effectively played during tunnel excavation, indicating that the high-pressure rotary jet grouting pile has played a good reinforcement role.
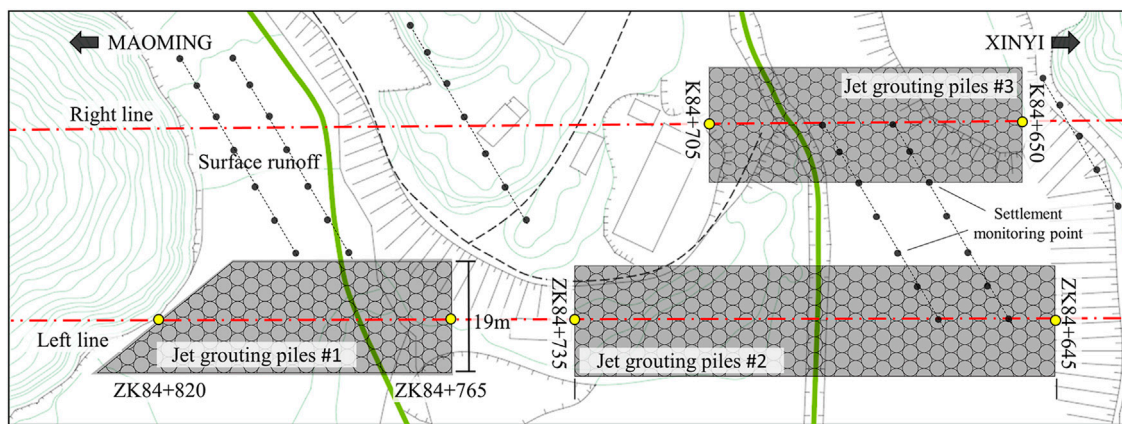
**FIGURE 10**
Layout plan of the high-pressure jet grouting pile.
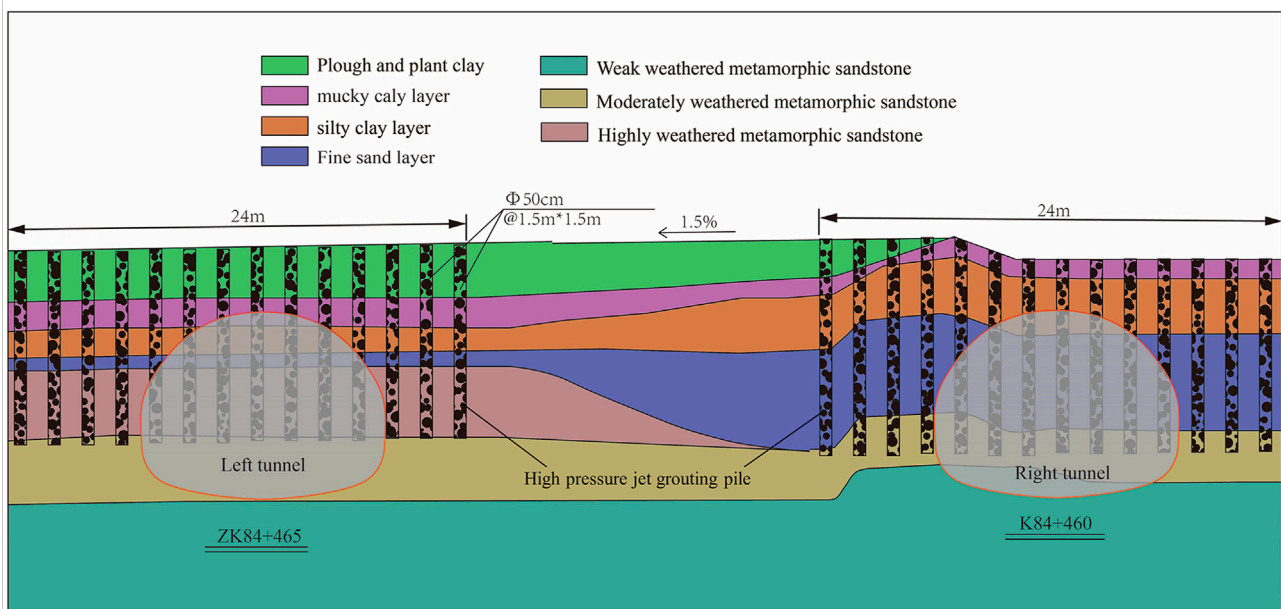


**FIGURE 11**
Cross section of the pile reinforcement range.

## 6.2.2 Support structure force and pore water pressure

According to the on-site monitoring results, in the early stage of tunnel support, the surrounding rock pressure is released quickly and finally stabilizes at about 6 KPa, within the reasonable range of treatment. The stress of the steel arch developed rapidly in the early stage and gradually balanced in the later stage. The maximum internal force of the arch was stable at 0.3 Mpa, which was within the allowable design range. The surface settlement is stable and the settlement value is within the allowable range of the design; the pore pressure is stable at 5 KPa. Comprehensive analysis shows that the stress and deformation of the support structure in the shallow buried section are allowable after reinforcement of a high-pressure jet grouting pile, and the pore water pressure of formation is greatly reduced. The high-pressure jet grouting pile can effectively reduce the stress and deformation of the support structure in shallow buried sections and reduce the
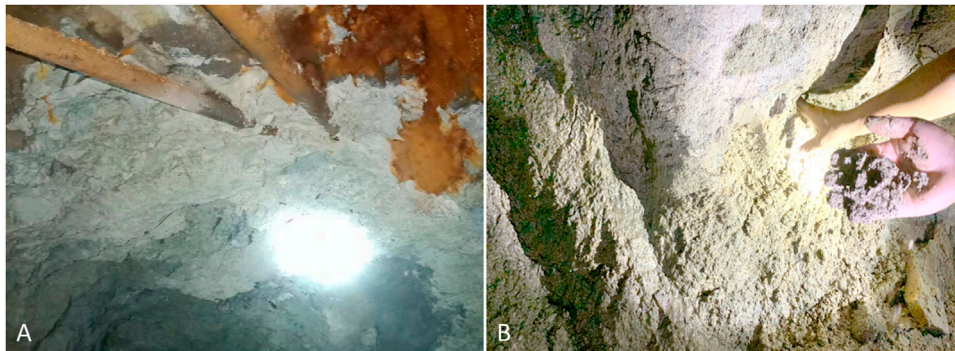
**FIGURE 12**
Tunnel arch after excavation. **(A)** Tunnel vault, **(B)** Tunnel arch foot.
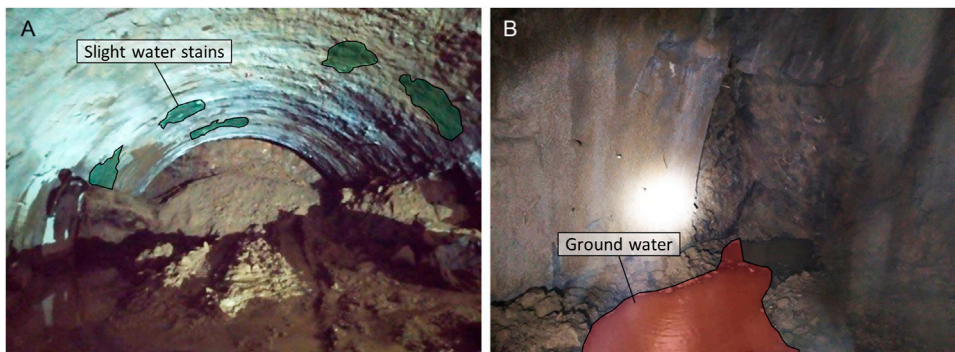


**FIGURE 13**
Water seepage in tunnel lining. **(A)** Tunnel arch, **(B)** tunnel side wall.

pore water pressure of the surrounding rock. According to the excavation condition, there were slight water stains on the initial supporting local surface of the upper bench and the whole surface was relatively dry (see Figure 13A). The groundwater mainly flows into the tunnel on both sides of the middle step and is discharged from the drainage ditch (see Figure 13B). To better show the lining water leakage water distribution, the lining surface scanning can be carried out using a 3D laser (Li et al., 2021). After the reinforcement of the high-pressure rotary jet grouting pile, the top of the ultra-shallow tunnel is stable after excavation, and the cracks between surrounding rocks are filled and consolidated by cement slurry. The strength and integrity of the surrounding rock are improved. The water seepage on the surface of the upper step is small, and the groundwater flows out along the arch feet on both sides, and the pile body plays a certain role in the water stop.

# 7 Conclusion

Based on the mechanical property test of the grouting material, the static load-bearing capacity of the test pile, and field application, this paper studies the application effect of a high-pressure rotary jet grouting pile in the reinforcement of an ultra-shallow tunnel in a strongly weathered stratum. The conclusions are as follows:

1) The compressive strength, elastic modulus, and seepage resistance of the cement soil are related to the water–cement ratio. The permeability of the consolidation body increases with increasing water–cement ratio under the constant head; under a certain water–cement ratio, the strength increases with increasing cement content.
2) Field piling tests were carried out to determine the key technical indicators to ensure the reinforcement and

impermeability effects. The static load test results of a single pile show that the greater the slurry pressure, the lower the cumulative settlement value, the greater the rotational speed, the lower the cumulative settlement value of the single pile, the greater the slurry pressure, and the lower the cumulative settlement value.

3) The height of mud spillover is basically above the strongly weathered metamorphic sandstone layer. The maximum mud spillover height at the top of the rotary pile is 0.8 m. The pile body is uniform with high strength and is brittle. The pile diameter reaches 60–75 cm, which meets the design requirements.

4) After the reinforcement of the high-pressure jet grouting pile, the cracks in the surrounding rock are filled and consolidated by cement slurry. The strength and integrity of the surrounding rock are improved. The water seepage on the surface of the upper step is small, and the groundwater flows out along the arch feet which means that the pile body plays a certain role in the water stop. The high-pressure rotary jet grouting pile has played a good reinforcement role.

## Data availability statement

The original contributions presented in the study are included in the article/Supplementary Material; further inquiries can be directed to the corresponding authors.

## Author contributions

PL: conceptualization, methodology, analysis, and writing; WQ and FL: validation, resources, and funding acquisition; XH, HL, and ZH: experiment design and data collection; and ZC, LL, and YW: investigation, supervision, and review editing. All authors read and agreed to the published version of the manuscript.

## Funding

## Conflict of interest

Author HL was employed by the company Anhui Transport Consulting & Design Institute Co., Ltd.

The remaining authors declare that the research was conducted in the absence of any commercial or financial relationships that could be construed as a potential conflict of interest.

## Publisher's note

All claims expressed in this article are solely those of the authors and do not necessarily represent those of their affiliated organizations, or those of the publisher, the editors, and the reviewers. Any product that may be evaluated in this article, or claim that may be made by its manufacturer, is not guaranteed or endorsed by the publisher.

## References

Brandsttter, C., Lackner, R., Pichler, C., and Mang, H. A. (2001). *Computational mechanics–new Frontiers for the new millennium*, 3–15. doi:10.1016/B978-0-08-043981-5.50007-9 Application of jet grouting in NATM tunneling - ScienceDirect.

Chen, L. J., Liang, B., and Wang, G. (2013). Study of excavation method for shallow-buried subway station tunnels with super-large section. *Chin. J. Undergr. Space Eng.* 9 (4), 6.

Cui, S. H., Wu, H., Pei, X., Yang, Q. W., Huang, R. Q., and Guo, B. (2022). Characterizing the spatial distribution, frequency, geomorphological and geological controls on landslides triggered by the 1933 Mw 7.3 Diexi Earthquake, Sichuan, China. *Geomorphology* 403, 108177. doi:10.1016/j.geomorph.2022.108177

Davis, E. H., Gunn, M. J., and Mair, R. J. (1981). Stability of shallow tunnels and underground openings in cohesive material. *Int. J. Rock Mech. Min. ences Geomechanics Abstr.* 18 (3), 51. doi:10.1016/0148-9062(81)91080-9

Gao, M. B., Cui, S. H., Li, T. B., Ma, C., Wu, Z., Zhang, Y., et al. (2022). Investigation on the expression ability of a developed constitutive model for rocks based on statistical damage theory. *Lithosphere* 2021 (7), 9874408. doi:10.2113/2022/9874408

Gao, M. B., Li, T. B., Meng, L. B., Ma, C., and Xing, H. (2018). Identifying crack initiation stress threshold in brittle rocks using axial strain stiffness characteristics. *J. Mt. Sci.* 15 (6), 1371–1382. doi:10.1007/s11629-018-4847-z

Hasan, M. F., and Canakci, H. (2022). An investigation of geomechanical and microstructural properties of full-scale jet grout column constructed in organic soil. *Arab. J. Sci. Eng.* 47 (4), 4605–4621. doi:10.1007/s13369-021-06189-z

Hu, Q. F., and Qin, J. B. (2013). Statistical analysis on accidents of subway tunnel construction from 2003 to 2011 in China. *Chin. J. Undergr. Space Eng.* 9 (3), 6.

Li, H. J., He, Y. S., Xu, Q., Deng, J. H., Li, W., and Wei, Y. (2022). Detection and segmentation of loess landslides via satellite images: A two-phase framework. *Landslides* 19 (3), 673–686. doi:10.1007/s10346-021-01789-0

Li, P. P., Qiu, W. G., Cheng, Y. J., and Lu, F. (2021). Application of 3D laser scanning in underground station cavity clusters. *Adv. Civ. Eng.* 2021, 1–12. doi:10.1155/2021/8896363

Li, P., Qiu, W., Lu, F., Yang, Q., Chen, Z., Li, L., and Deng, Z. (2021). Quasi-static test study of tunnel with resistance-limiting shock absorption layer in high-intensity seismic. *Front. Earth Sci.* doi:10.3389/feart.2022.1029929

Li, X. J. (2004). Analysis of calculation methods for bearing capacity and settlement of high-pressure chemical churning pile composite foundation. *Rock Soil Mech.* 25 (9), 4. doi:10.3969/j.issn.1000-7598.2004.09.004

Lu, F., Li, P. P., Zheng, Y. C., and Qiu, W. G. (2022). Experimental investigation on the mechanical performance of retrofitted cracked linings with mesh-bolts and plate-bolts. *China J. Highw. Transp.* 35 (5), 128. doi:10.19721/j.cnki.1001-7372.2022.05.012

Lu, F., Wang, H. Y., Wang, L. C., Zhao, K., and Zhang, J. R. (2022a). Degradation law and service life prediction model of tunnel lining concrete suffered combined effects of sulfate attack and drying–wetting cycles. *Materials* 15 (13), 4435. doi:10.3390/ma15134435

Nikbakhtan, A. H. A. N. G. A. R. I., Rahmaniand Rahmani, N. (2010). Estimation of jet grouting parameters in Shahriar dam, Iran. *Min. Sci. Technol.* 20 (3), 472–477. (English Edition. doi:10.1016/S1674-5264(09)60228-3

Nikbakhtan, B., and Osanloo, M. (2009). Effect of grout pressure and grout flow on soil physical and mechanical properties in jet grouting operations. *Int. J. Rock Mech. Min. Sci. (1997).* 46 (3), 498–505. doi:10.1016/j.ijrmms.2008.10.005

Ou, Y. l., Yang, S. f., and Zhang, D. M. (2016). Subgrade settlement analysis in shield tunnel construction process using high-pressure rotary jet grouting pile joint with sleeve valve barrel grouting reinforcement method. *Railw. Surv.*, 64–67. doi:10.19630/j.cnki.tdkc.2016.04.021

Pan, H. L., Qian, H. P., Cai, Z., Lan, Y., Guo, X., and Hong, Y. (2021). Field test of high pressure jet grouting pile for strengthening highly sensitive soft soil foundation. *J. Ground Improv.* 3 (1), 5.

Qiu, W., Lu, F., Wang, G., Huang, G., Zhang, H., Zhang, Z., et al. (2019). Evaluation of mechanical performance and optimization design for lattice girders. *Tunn. Undergr. Space Technol.* 87, 100–111. doi:10.1016/j.tust.2019.02.008

Que, S. H. (2009). Application of high pressure spinning jetting pile in consolidating surrounding rock in tunnel. *Technol. Highw. Transp.* (2), 4. doi:10.3969/j.issn.1009-6477.2009.02.035

Ren, X. W. (2009). Tests on high-pressure whirly-sprayed piles in construction of shallow tunneh with mining method at dynamic watery saturated gravel layer and

diseussion on its application. *Railw. Stand. Des.* (7), 5. doi:10.3969/j.issn.1004-2954.2009.07.028

Transport (2005). *Highway engineering cement and cement concrete test code (JTG3420-2020.*

Wang, S., Zhao, M., and Lin, Z. (2009). Summary of common geologic hazards during highway tunnel construction. *Highw. traffic Technol.* (1), 102–106. doi:10.3969/j.issn.1009-6477.2009.01.029

Wang, Y. N., Jiang, B. S., Yu, J., Gao, C., and Fang, D. Y. (2017). *In-situ* experiment on composite foundation of high pressure jet grouting piles of Hong Kong-Zhuhai-Macau Bridge. *Chin. J. Rock Mech. Eng.* 36 (6), 8. doi:10.13722/j.cnki.jrme.2016.1005

Zhang, C. P., Han, K. H., Zhang, D. L., Li, H., and Cai, Y. (2014). Test study of collapse characteristics of tunnels in soft ground in urban areas. *Chin. J. Rock Mech. Eng.* 33 (12), 10. doi:10.13722/j.cnki.jrme.2014.12.008

Zhang, J., Chen, Y., Chen, T., Mei, Z., Liu, Z., Wang, F., et al. (2018). Law and Characteristics Analysis of Domestic Tunnel Construction Accidents from 2006 to 2016[J]. *Mod. Tunn. Technol.* 55 (3), 10–17. doi:10.13807/j.cnki.mtt.2018.03.003

Zhou, Z. Q., Li, S. C., Li, L. P., Sui, B., Shi, S., and Zhang, Q. (2013). Causes of geological hazards and risk control of collapse in shallow tunnels. *Rock Soil Mech.* 34 (5), 8. doi:10.16285/j.rsm.2013.05.028

Check for updates

# Revealing karst water circulation based on the GIS and environmental isotopes methods—A case study in eastern Sichuan, southwestern China

Zixuan Qin[1], Qiang Zhang[1]*, Siyao Yu[1], Yanna Yang[1], Jiasen Zhang[1], Mo Xu[1], Yang Liu[2], Maoyi Liu[3] and Mi Nie[3]

[1]State Key Laboratory of Geohazard Prevention and Geoenvironment Protection, College of Environment and Civil Engineering, Chengdu University of Technology, Chengdu, China, [2]Chongqing Survey Institute, Chongqing, China, [3]Chongqing Urban Infrastructure Construction Co., Ltd., Chongqing, China

Jura-type folds in eastern Sichuan Basin have created unique multi-type karst water circulation patterns. Understanding the karst water circulation features is helpful to the protection and management of water resources in this area. In this study, a typical Jura-type fold Mingyueshan in eastern Sichuan, Southwestern China is taken as an example. The geological conditions, natural geographical factors, and environmental isotopes data ($\delta^2$H, $\delta^{18}$O, $\delta^3$H) are analyzed, the GIS method was used to construct the groundwater flow system. The results reveal the karst water circulation patterns under the control of multiple drainage base levels. Finally, it comes to the conclusion that the north, middle and south sections of Mingyueshan present three water circulation patterns: unidirectional shallow circulation system, bidirectional shallow circulation system and unidirectional shallow-deep nested circulation system, respectively. These results are essentially qualitative, some numerical simulations of groundwater flow can be considered in future work, which will help to determine the groundwater flow system quantitatively. The research results can provide reference for the studies of karst aquifers in eastern Sichuan Jura-type folds area and other areas with similar characteristics.

## 1 Introduction

Karst is widely distributed all over the world, which cover 7%–12% of the Earth's land surface, meanwhile, karst aquifers contain rich fresh water resources (Ford and Williams, 2007; Lorette et al., 2018; Liu et al., 2021). Therefore, it is essential to accurately grasp the groundwater circulation characteristics in karst area. The groundwater flow theory creatively proposed by Tóth (1962) and Tóth (1963) gives better description of the law of regional groundwater circulation, which does not completely depend on the geological factors, and it is also controlled by the natural geographical factors (Tóth, 2009; Liang et al., 2012; Liang et al., 2022). Different groundwater flow systems have different flow mechanics characteristics, there are great differences in water chemistry and isotopes. Although the strong spatial heterogeneity of karst aquifers causes challenges for research, existing studies have shown that hydrogen and oxygen isotopes can perform well in complex karst water systems (Kattan, 1997; Vasic et al., 2019; Gil-Marquez et al., 2019; Torresan et al., 2020; Deng et al., 2022; Ma et al., 2022), which

**FIGURE 1**
**(A)** Map of study area. **(B)** Altitude DEM rendering map of study area. **(C)** Overview map of the study area indicating water samples.
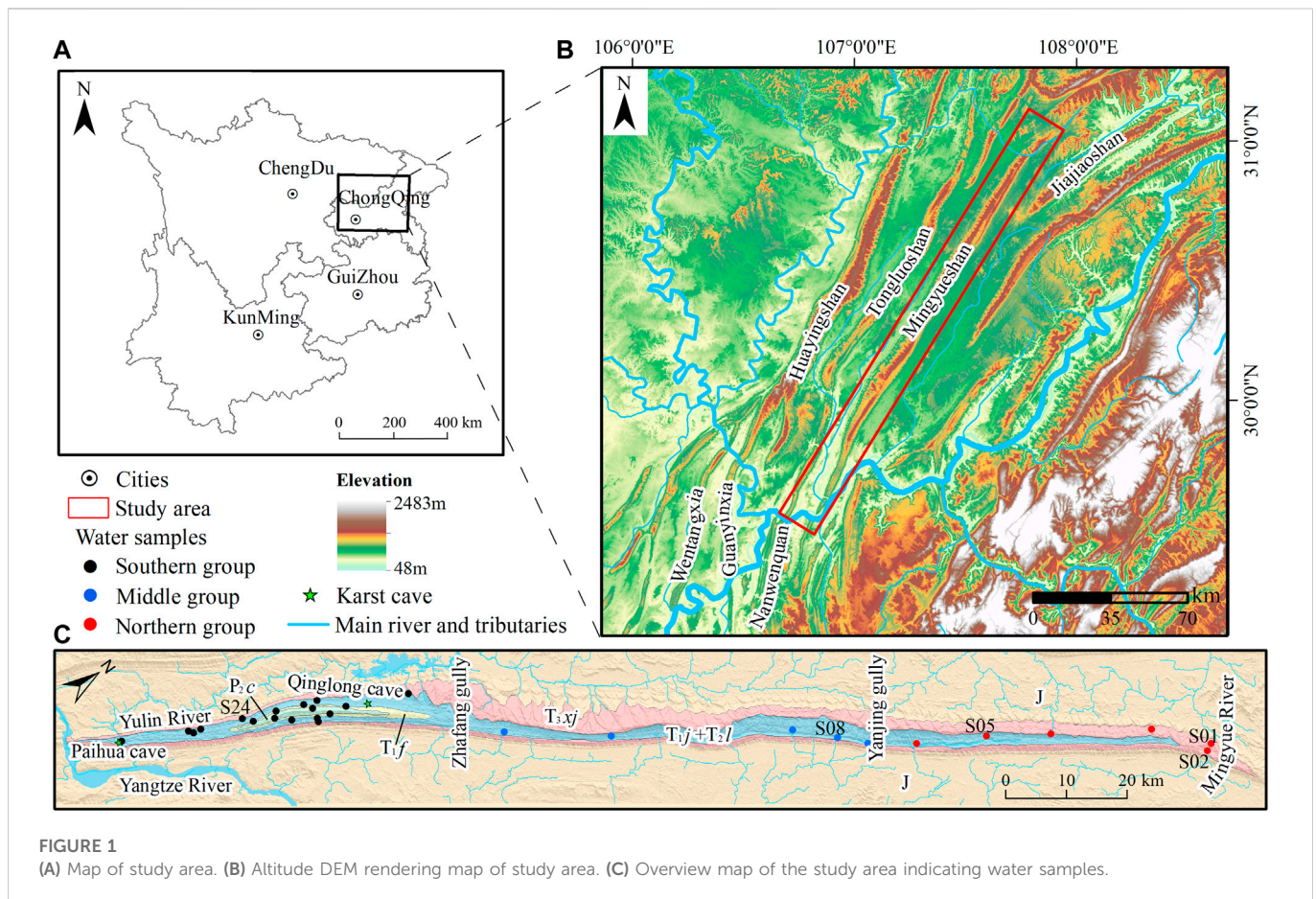
provides a theoretical basis for application of hydrogen and oxygen environmental isotopes to reveal karst water flow systems.

The Jura-type folds, also known as the detachment folds, which evaporates incompetent Triassic and develops a serial of parallel "comb-like and trough-like" folds (Laubscher, 1977; Wang et al., 2012). Typical examples are the Jura Mountains of the Swiss, the foreland region of the Appalachian Orogenic Belt, the foreland region of the Cordillera Orogenic Belt (Rich, 1934; Davis, 1980; Suppe, 1983). A serial of NNE–SSW trending "comb-like and trough-like" fold belts in eastern Sichuan Basin are caused by multi-layer detachment, belonging to typical Jura-type folds (Wang et al., 2010; Wang et al., 2022). The concrete manifestation is that the soluble rock is exposed in the core of the high-steep anticline and the east and west limbs are clamped by the relative water-isolated sandstone and mudstone. Under this special tectonic condition, the near east-west (EW) direction gullies, or transverse gullies briefly, largely control the groundwater discharge and circulation in karst mountainous areas. Neotectonic movement caused regional crustal uplift, resulting in continuous downward cutting of the hydrological network and the development of transverse rivers with different cutting depths and lengths. According to the degree of transverse gullies cutting through the soluble rock strata, they can be divided into three types: fully-cut, partly-cut, and uncut gully. Typical Jura-type folds in eastern Sichuan Basin such as Wentangxia, Huayinshan, Tongluoshan, Mingyueshan, and Jiajiaoshan show a variety of gully cutting and groundwater drainage types. Up till to now, there are many studies on karst

aquifers in the Jura-type folds area of the eastern Sichuan Basin. However, existing studies mainly focus on the physicochemical properties, occurrence condition or quality evaluation of karst water (Pu et al., 2014; Xiao et al., 2018; Chen et al., 2020; Zhang et al., 2022), few researches pay attention to karst water cycle pattern in this area. To be more specific, how multiple drainage base levels and their combinations affect and control the karst water circulation in this area remains a question worth exploring.

In this study, theoretical controlling factors of karst water flow, the GIS method and environmental isotopes data were analyzed to reveal the karst water circulation patterns under the control of different drainage base levels in Mingyueshan. Finally, the different karst water circulation patterns in the north, middle and south sections of the Mingyueshan was summarized. This work is beneficial to the management of water resources and the safety of underground engineering in the study area, provides reference for the study of karst aquifers with similar characteristics in eastern Sichuan Jura-type folds area and other area.

# 2 Study area

## 2.1 Physical geography conditions

The Mingyueshan, located on the Chongqing Municipality, lies between latitudes 29°28′–31°01′ N and longitudes 106°45′–107°56′ E.
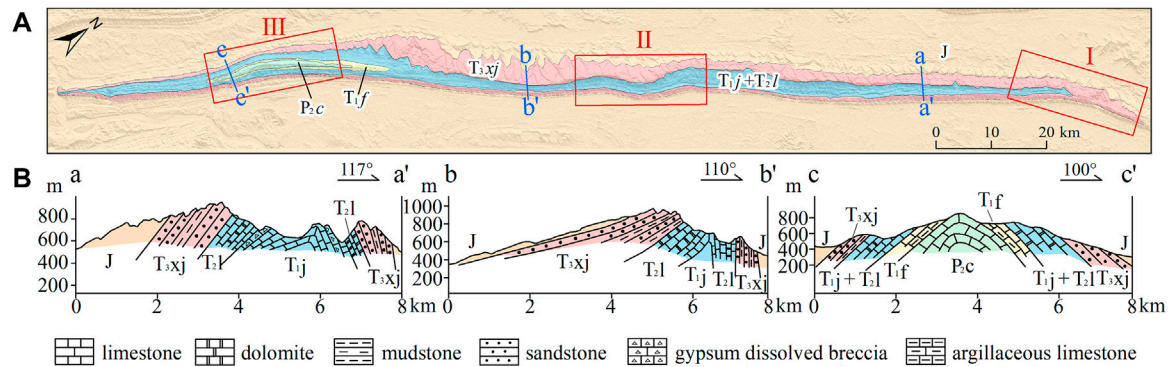
FIGURE 2
(A) Structural trace of Mingyueshan anticline. (B) Two limbs morphology shown in sections a−a′, b−b′, and c−c′.

It is a 210-km typical eastern Sichuan Jura-type fold with narrow axis and asymmetrical limbs. The Yulin river and the Mingyue river pass through the south and north of the long anticline, respectively (Figure 1).

The study area is controlled by the semitropical climate, with distinct seasons. The average temperature is 16°C–18°C throughout the year. The rainfall is abundant and there is an obvious vertical zonation of rainfall, in which the average annual rainfall in the basin and river valley is about 998 mm, while the rainfall in the mountain area exceeds 1,100 mm (Yang et al., 2019). The river systems in the study area are well developed with a dendritic distribution.

## 2.2 Geological conditions

The Eastern Sichuan fold-thrust belt (ESFTB) is situated in the eastern margin of the middle and upper Yangtze blocks in the South China Craton (Charvet, 2013; Lu et al., 2014). It had experienced Yanshan and Himalayas movement, then developed a serial of NNE–SSW trending asymmetric high-steep folds, one of which is Mingyueshan anticline. The Mingyueshan anticline is located in the southwest area of ESFTB, which is a narrow and long structural belt and subjected to the combined action of west-east compression and bottom-up uplift during the tectonic deformation. Therefore, the structural features and two limbs of the north, middle and south parts are presented differently (Figure 2).

The northern part of Mingyueshan was affected by the southward thrust and nappe of the South Dabashan mountains tectonic belt in the north of Mingyueshan, leading to the south-east bending of Mingyueshan fold belt and its continued northward expansion. The influence of the southward thrust and nappe of the South Dabashan mountains was getting more intense (Wen and Li, 2020). As a result, the limbs of the northern anticline are roughly symmetrical (Figure 2A and section a–a′). In the middle part, the lithology phase transition occurred in part of the area, the difference of lithology led to the concentration of stress and displacement, appearance of multiple rotation axis segments. The rock strata in the west limb of the middle part were inclined gently, while the rock strata in the east limb were steep (Figure 2B and section b–b′). In the southern part, affected by the thickness of the weak layer (detachment layer), the tectonic stress and displacement were more likely to transfer to the west along the detachment layer, resulting in the uplift of the anticlinal
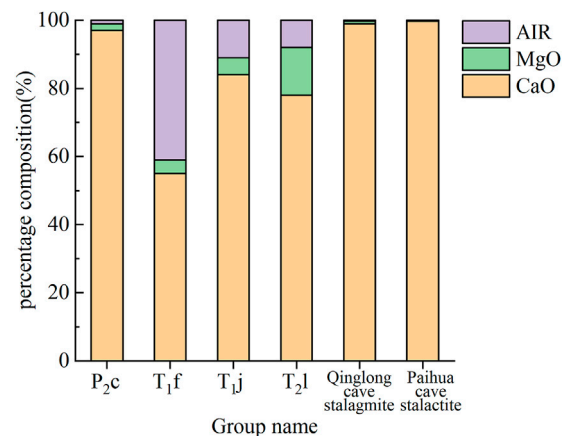


FIGURE 3
Carbonated rocks composition of water-bearing formation and two karst caves.

core. The difference in detachment layer thickness led to a significant difference in the transfer of tectonic deformation from east to west in the study area. The two limbs of the south part were roughly symmetrical (Figure 2C and section c–c′).

The soluble rocks in the anticline are only exposed in the core area, while the east and west limbs are clamped by the water-isolated sandstone and mudstone of the Upper Triassic Xujiahe Formation ($T_3xj$) (Chen et al., 2016; Szczygieł et al., 2018). The soluble rocks in the northern part are mainly limestone and dolomite in the Middle Triassic Leikoupo ($T_2l$) and the Lower Triassic Jialingjiang Formations ($T_1j$), with a small amount of gypsum dissolved breccia. The middle part has the same soluble rock lithology as the north part, which consists of limestone and dolomite. In addition to Leikoupo and Jialingjiang Formation, there are argillaceous limestone of the Upper Permian Changxing Formation ($P_2c$) and the Lower Triassic Feixianguan Formation ($T_1f$) in the anticline core of the southern soluble rocks (Figure 2). The carbonated rocks composition such as CaO, MgO and AIR (acid-insoluble residue) of water-bearing formation and two caves in the Mingyueshan area is shown in Figure 3.

# 3 Methods

## 3.1 Tóth's groundwater flow system built by the GIS

Tóth (1962) and Tóth (1963) obtained the groundwater flow system in a basin of undulating topographic surface by analytical solution. Tóth's study showed the nested groundwater systems of local, intermediate, and regional flow systems, discussed the geological force of groundwater flow (Tóth, 1999). In general, groundwater circulation is not entirely dependent on geological factors, but also controlled by natural geographical factors such as topographic potential energy and drainage system (Tóth, 2009; Liang et al., 2012; Liang et al., 2022). The difference of topographic potential energy is the main driving force of groundwater movement. Recharge areas with high terrain accumulate potential energy with recharge, while discharge area with low-lying terrain is difficult to accumulate potential energy. Therefore, topography usually controls the spatial distribution of topographic potential energy.

During the intermittent uplift of crust, the karst water circulation is closely related to the evolution of karst topography (Hill and Polyak, 2010). On the one hand, the evolution of karst topography is a process that changes with time, the alternate water cycle conditions control the evolution of karst topography. On the other hand, topographical control over hydrology can be manifested in a short period of time. The diversity and difference of karst landforms lead to different hydrological functions of karst systems, groundwater shows regional and local drainage characteristics. In order to obtain the relationship between karst topography and hydrological system clearly in the study area, transverse gully cut points and karst depressions were extracted automatically using digital elevation model (DEM) and geographic information system (GIS) data (Pavel et al., 2016; Wu et al., 2016; Meng et al., 2018).

## 3.2 Environmental isotopes

### 3.2.1 Water sampling

Water sampling campaigns were conducted in the study area during the period of 27th August to 2nd September 2018 (sampling sites are shown in Figure 1). A total of 33 groups of samples were collected from the north, middle and south parts of Mingyueshan for environmental isotope testing, among which 28 groups from all sampling sites were tested for $\delta^2H$ and $\delta^{18}O$ isotope, and the rest, five groups were tested for $\delta^3H$ isotope, marked as from S01, S02, S05, S08 and S24 sites. Sampling bottles were rinsed with sample water at least five times before collection. The water samples collected in the field being sealed in 500 mL polyethylene bottles and stored in a low-temperature environment above zero. The samples were sent to the Institute of Karst Geology, Chinese Academy of Geological Sciences for isotope testing within 7 days after collection. $\delta^2H$ and $\delta^{18}O$ were tested by MAT253 stable isotope mass spectrometer, tritium was tested by Qnantulus1220 ultra-low local liquid scintillation spectrometer.

### 3.2.2 $\delta^3H$ dating

Environmental isotope tritium is a radioactive isotope of hydrogen with a half-life of 12.43a (Lucas and Unterweger 2000). Generally, the tritium content in groundwater is only affected by the decay rule, does not exchange with rock medium. Therefore, it is often used as the tracer signal of precipitation input to study the dating of groundwater (Solomon and Sudicky 1991; Kaufman et al., 2003; Gleeson et al., 2016; Cauquoin et al., 2017). Relevant studies show that the annual variation curve of tritium concentration in global atmospheric precipitation has similar morphological characteristics, there is correlation between the data (Taylor 1966; Koster et al., 1989; Michel 1989). Therefore, the application of factor analysis method to the analysis of the average annual tritium concentration in atmospheric precipitation has a longer time and larger space applicability (Doney et al., 1992; Zhang et al., 2011). The MGMTP (Yang and Ye 2018) model of factor analysis was used to recover the annual average tritium concentration of atmospheric precipitation in the study area from 1953 to 2018.

Groundwater in Chongqing area is mainly replenished by atmospheric rainfall. The tritium values of atmospheric precipitation in the study area from 1953 to 2017 are taken as the input function, the piston flow model (PFM) of a single input-output system is calculated and selected to establish the relationship between the groundwater output age and the tritium output concentration. The PFM assumes that groundwater flow in an ideal aquifer is similar to piston motion, i.e. equal-scale mixing model, which means that the recharge is punctual and all tracer concentrations arrive as a unique peak without mixing between flow lines (Nir, 1964; Silva and Cota, 2021). Therefore, the retention age of groundwater can be deduced by measuring the tritium value of the samples.

$$C_{out}(t) = C_{in}(t - \tau)e^{-\lambda\tau}$$

where, $t$ is the time series of isotope output; $\tau$ is the transmission time of isotope, i.e., the age. $t - \tau$ is isotope input time series. $C_{out}(t)$ is the tritium output function of groundwater system. $C_{in}(t - \tau)$ is the tritium input function of groundwater system. $\lambda$ is the tritium decay constant, equals to 0.055764.

# 4 Results and discussions

## 4.1 Karst hydro-geomorphology

Transverse gully cut points and karst depressions were extracted (Figure 4) and the elevation and development density of transverse gullies were calculated (Table 1) in each part of Mingyueshan. From north to south, the number of transverse gullies cut points increase, the depth of karst depression changes from shallow to deep, the development density and range of karst depressions also increase. In the area close to the fully-cut gully, groundwater circulation gradually adapts to the downward cutting of the fully-cut gully, the surface basically has no gully development, then the partly-cut gully loses the drainage ability. The terrain landform of the study area is obviously controlled by the geological structure and lithologic characteristic, the groundwater migrates mainly along the tectonic line from north to south to the Yulin river (the primary tributary of the Yangtze river), the lowest drainage base level. The dynamic conditions of groundwater are mainly controlled by the Yulin river which fully cuts through the anticline karst formation, the gullies, which partly cut into the anticline karst rock.

The depth of groundwater circulation is largely determined by the relative height of recharge and discharge zones (Stringfield et al., 1979). Under the unique background of the Jura-type folds in eastern
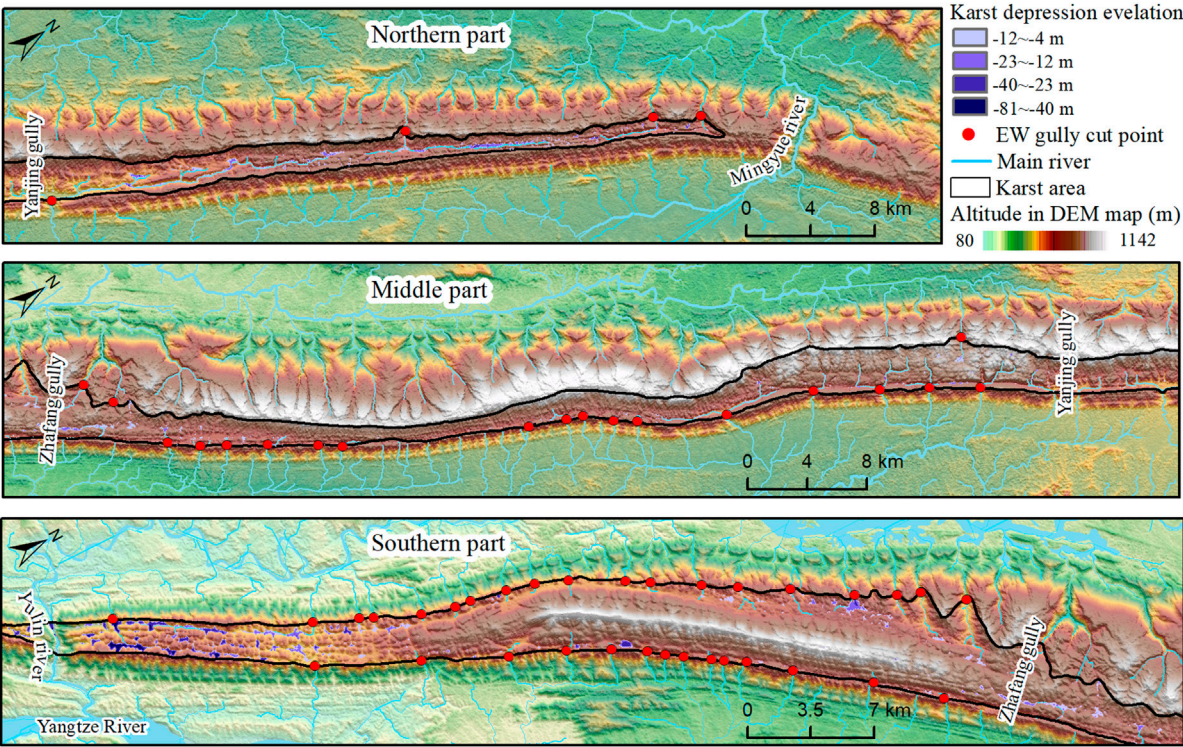
**FIGURE 4**
Distribution of surface gullies development and karst depressions in Mingyueshan.

**TABLE 1 Statistics of EW gullies elevation and density in Mingyueshan.**

| Area | Lowest elevation (m) | | Number of EW gully | | Density (number of EW gully/km) | |
|---|---|---|---|---|---|---|
| | East limb | West limb | East limb | West limb | East limb | West limb |
| Mingyue river to Yanjing gully | 488 | 662.6 | 1 | 3 | 0.021 | 0.063 |
| Yanjing gully to Zhafang gully | 517.9 | 472 | 16 | 3 | 0.230 | 0.041 |
| Zhafang gully to Yulin river | 185 | 185 | 14 | 20 | 0.263 | 0.376 |

Sichuan, the east-west direction transverse gullies that cut into anticline soluble rock play an essential role in discharging nearby karst water, the cutting length and depth determine the ability and control range of discharging groundwater. According to the degree to which the transverse river cuts through the soluble rock strata, it is divided into three types: fully-cut, partly-cut, and uncut gully. Their ability of discharging groundwater also ranks from strong to weak. The fully-cut and partly-cut gullies correspond to the deep and shallow circulation of groundwater respectively. A multilevel groundwater circulation system is formed under the control of combination of drainage base level with different cutting forms. At the dip end of the northern anticline, the Mingyue river valley, with an elevation of 420 m, was developed in the non-solvable rocks of the Xujiahe Formation and did not cut into the karst rocks of the anticline, therefore the Mingyue river valley should not be considered as an effective drainage area for karst water. Yanjing gully and Zhafang gully are the gullies that partly cut into the soluble rock, with the elevations of 488 m and 472 m respectively. Yulin river fully cut into the soluble rock with 185 m elevation and it is the regional drainage base level in the study area. Yanjin gully, Zhafang gully and Yulin river formed the local drainage base level of the water in the Mingyueshan and controlled the local karst landform features and groundwater circulation conditions. According to the spatial location of these drainage base levels, the anticline was divided into north, middle and south sections. The groundwater circulation characteristics of each section will be analyzed later.

## 4.2 $\delta^2$H and $\delta^{18}$O isotope analysis

The stable isotope values of the southern group samples are −46.40‰ to −40.70‰ for $\delta^2$H, and −7.59‰ to −6.48‰ for $\delta^{18}$O. The isotope values

**TABLE 2** $\delta^2$H and $\delta^{18}$O isotope information of water samples.

| Group | Sample ID | Elevation (m) | $\delta^2$H (‰) | $\delta^{18}$O (‰) | *d*-excess |
|---|---|---|---|---|---|
| Northern | S01 (hot water hole) | 523 | −58.1 | −8.91 | 13.18 |
| | S02 | 668 | −56.3 | −8.46 | 11.38 |
| | S03 | 779 | −52.5 | −8.13 | 12.54 |
| | S04 | 743 | −49.9 | −7.94 | 13.62 |
| | S05 | 682 | −49.7 | −7.81 | 12.78 |
| | S06 | 650 | −49.2 | −7.73 | 12.64 |
| Middle | S07 | 615 | −49.7 | −7.81 | 12.78 |
| | S08 | 614 | −50.4 | −7.92 | 12.96 |
| | S09 | 701 | −50.2 | −7.78 | 12.04 |
| | S10 | 656 | −47.7 | −7.69 | 13.82 |
| | S11 | 597 | −49.8 | −7.85 | 13.00 |
| Southern | S12 | 779 | −46.4 | −7.59 | 14.32 |
| | S13 | 743 | −43.8 | −7.39 | 15.32 |
| | S14 | 672 | −45 | −7.36 | 13.88 |
| | S15 | 647 | −46.2 | −7.52 | 13.96 |
| | S16 | 507 | −41.5 | −6.69 | 12.02 |
| | S17 | 530 | −42.2 | −6.58 | 10.44 |
| | S18 | 638 | −46.2 | −7.44 | 13.32 |
| | S19 | 513 | −44.2 | −7.08 | 12.44 |
| | S20 | 658 | −45.2 | −7.51 | 14.88 |
| | S21 | 647 | −44.6 | −7.43 | 14.84 |
| | S22 | 600 | −43.8 | −7.19 | 13.72 |
| | S23 | 626 | −42.6 | −6.93 | 12.84 |
| | S24 | 542 | −40.7 | −6.48 | 11.14 |
| | S25 | 507 | −41.7 | −6.69 | 11.82 |
| | S26 | 507 | −41.4 | −6.53 | 10.84 |
| | S27 | 507 | −41.6 | −6.52 | 10.56 |
| | S28 | 218 | −40.9 | −6.59 | 11.82 |

of the middle group varied between −50.40‰ and −47.70‰-for $\delta^2$H, from −7.92‰ to −7.69‰ for $\delta^{18}$O. The $\delta^2$H values of the northern group ranges from −58.10‰ to −49.20‰, $\delta^{18}$O ranges from −8.910‰ to −7.730‰ (Table 2). A binary scatter plots of $\delta^2$H and $\delta^{18}$O were drawn from 28 sets of isotopic data of water samples in the north, middle and south parts of the Mingyueshan (Figure 5). The samples are between the global meteoric water line (GMWL: $\delta^2$H = 8.14 × $\delta^{18}$O + 10.9; Craig 1961) and the local meteoric water line (LMWL: $\delta^2$H =7.85 × $\delta^{18}$O + 14.12; Wen 2017), indicating that there is a close relationship between the recharge source of the samples and atmospheric precipitation. It also reflects that the region is inland far from the steam source and at a high altitude, which is consistent with the actual situation in the study area.

In general, the terrain of Mingyue Mountain decreases from north to south, the average elevation of water samples in the northern and middle sections is generally higher than the southern section. The

stable isotope is affected by the altitude, the southern section of Mingyueshan shows obvious subdivision compared with the northern and middle sections: the water samples in the south section are concentrated in the upper right of the scatter diagram, are distributed obviously denser in heavy isotopes $\delta^{18}$O and $\delta^2$H than those in the middle and north sections. The slope of stable isotope linear curves of the middle and northern group is parallel to that of LMWL and GMWL, which reflects wet climate and weak evaporation in the study area. However, the slope of isotope linear curve of the southern group is significantly less than that of LMWL and GMWL, showing positive $\delta^{18}$O deviation, which results from the water-rock interaction. The content of $\delta^2$H in rocks is very low, which is not enough to significantly affect the $\delta^2$H value in water, while the rocks are more enriched in $\delta^{18}$O than water (Pu, 2013). The long-term retention of karst water in the aquifer leads to the enhancement of
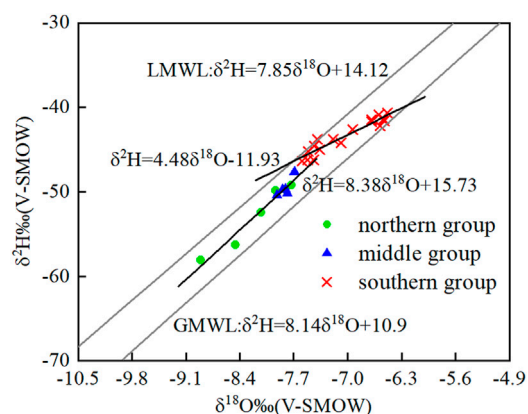
**FIGURE 5**
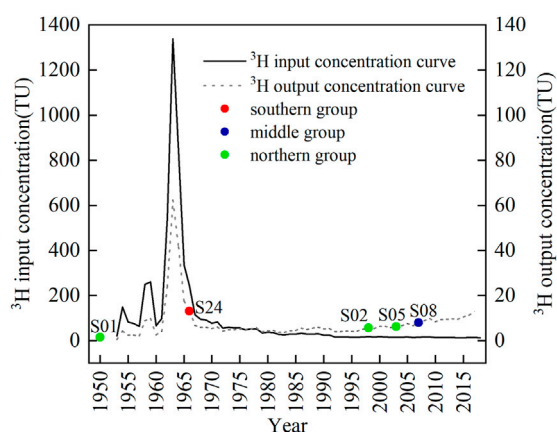Isotopes $\delta^2H$ and $\delta^{18}O$ binary graph.



**FIGURE 6**
$^3H$ input concentration in precipitation and $^3H$ output concentration curves.

water-rock interaction in the system, $\delta^{18}O$ in the rock will transfer to the water, resulting in $\delta^{18}O$ enrichment in the southern group. It is inferred that the south section groundwater has larger exchange capacity of material components than middle and north sections, and the groundwater circulation in the southern section is deeper than middle and north sections.

## 4.3 Groundwater residence time

$^3H$ input concentration in precipitation curved graph and $^3H$ output concentration curved graph from the PEM in study area were established (Figure 6). S01, S02 and S05 are all in the north section of the anticline. The tritium values of S02 and S05 springs are ranging from 5.58 to 6.1Tu. It is estimated that the groundwater runoff time is roughly 15–20 years and the formation time lies from year 1998 to 2003. S01 is a hot water hole involved in deep circulation and has a low $^3H$ abundance less than 2. It should have been formed before the nuclear explosion in 1953 and has a

long groundwater detention time. S08 is an ascending spring in the middle section of the anticline, the measured tritium value is 7.97Tu, which is presumed to have been formed around year 2007 and the groundwater circulation path is short and shallow. S24 is an outcropping spring in the south section of the anticline with 13.01TU tritium value, the groundwater retention age is relatively long, about 50 years. It is speculated that the groundwater of S24 migrates through the deep circulation system and is discharged to the inner spring mouth in the negative terrain. The estimation of the age of tritium retention in groundwater can provide a reliable basis for the classification of groundwater circulation patterns in Mingyueshan.

## 4.4 Karst water circulation patterns

The north section is from Mingyue river to Yanjin gully, about 46 km long, with few transverse gullies, undeveloped surface water systems and shallow karst depressions. The main karst landforms on the surface are ridge-shallow troughs. The scale of karst development is weak, in which karst troughs of west limb are not obvious, while karst troughs of the east limb are more apparent. In the north section, due to the large area of non-soluble rock strata exposed by the overturning of the anticline, the penetrating valley of Mingyue river does not cut into the soluble rocks, as a result it does not act as an effective drainage area for the inland water of the anticline. Retention time of S02 and S05 spring are short, accompanied with weak water-rock reaction, corresponding to shallow circulation. While the sampling depth of S01 hot water borehole is deep, the groundwater $^3H$ dating is old and the retention time is long. It is speculated that the overall flow of groundwater in this section is from north to south, the shallow groundwater is discharged through the deep transverse gullies of Yanjing gully, the deep groundwater migrates to the Yulin river. Under the control of the depth and drainage capacity of the deep transverse gullies, there are almost no other transverse gullies development in a certain range near this area. The groundwater in this section is mainly controlled by a single deep transverse gully, which is a unidirectional shallow circulation pattern (Figure 7).

The middle section is from Yanjin gully to Zhafang gully, about 70 km long. The karst landforms developed in this section are ridge-single troughs. The soluble rock strata of Leikoupo and Jialingjiang Formation formed valleys after dissolution, while the non-carbonate rocks on both limbs formed monocline ridge. The structural stress in the middle section is not distributed evenly, resulting in asymmetry between the two limbs of the anticline. To be more concrete, the Xujiahe Formation in the west limb stands up and goes inverted, with steepness occurring in parts of the area. The dip angle of east limb formation is gentle, forming a single plane structure. In this area, the outcrop of Xujiahe Formation is thin, which is vulnerable to the trace-back erosion of cross-cut gullies and cut into the core of the anticline. Rainfall is mainly discharged by lateral runoff from the west limb to the east limb gullies through slope flows, forming deep circulating karst water within a certain depth range below the drainage base level, and leading to longitudinal runoff to the Yulin river. Far away from the control area of fully cut valley, the non-soluble rock strata formation holding karst layer groups are cut open by transverse gullies, as the main drainage channel of groundwater in karst trough valleys. With the continuous tractive erosion of groundwater, the groundwater between adjacent gullies and valleys continuously attacks and
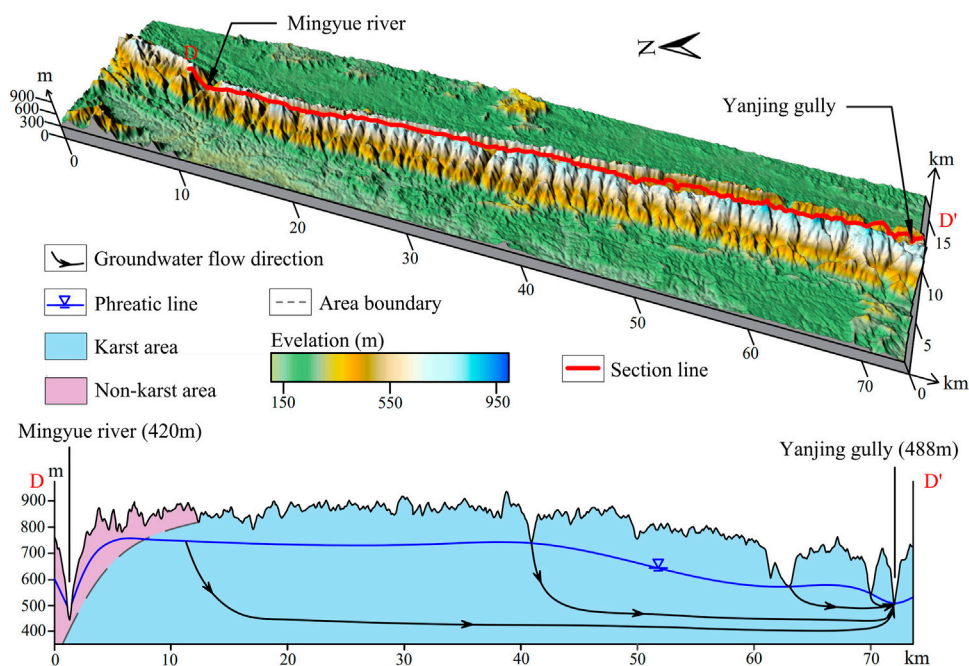
**FIGURE 7**
Karst water circulation pattern in north section of Mingyueshan.
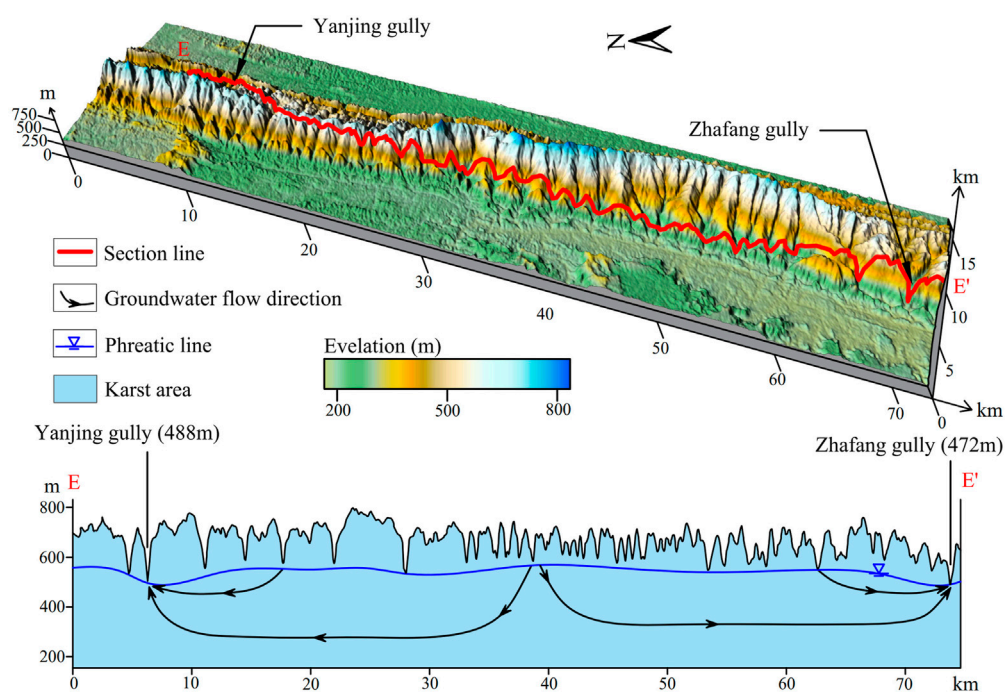


**FIGURE 8**
Karst water circulation pattern in middle section of Mingyueshan.

merges with each other, leading to the increasing difference in the depth and shallow degree of the transverse gully development. In the development of a series of shallow transverse gullies, a deep cutting gully with a large control range appeared, which controls the discharge of groundwater in the trough valley together with the shallow transverse gullies. Isotope sampling data from the middle section

**FIGURE 9**
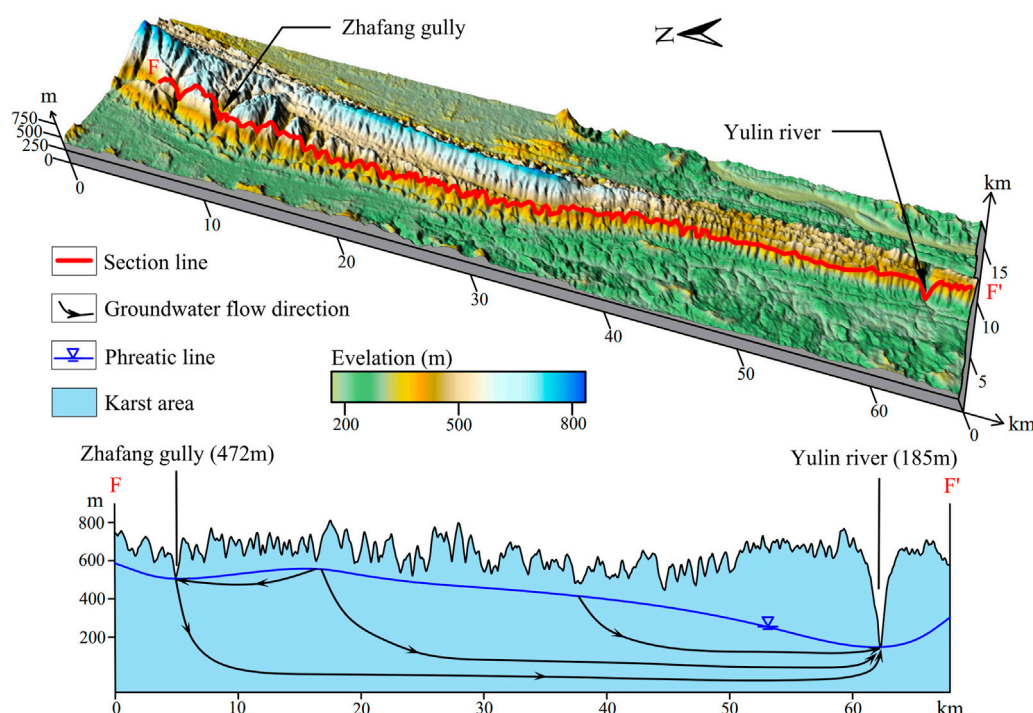Karst water circulation pattern in south section of Mingyueshan.

indicate weak water-rock interaction and a short groundwater retention age. The groundwater in the middle section is jointly controlled by the two partly cut transverse gullies Yanjing gully and Zhafang gully, forming a bidirectional shallow circulation pattern (Figure 8).

The south section is from Zhafang gully to Yulin river, with a length about 54 km. The karst landforms, mainly ridge-double troughs and transverse gullies and valleys, are developed along both limbs of the anticline. The karst depressions are distributed roughly in a beaded shape, the bottom elevation of the depressions decreases from north to south. In this section, the rainfall in the trough valleys is discharged to the syncline area through the cross-cutting gullies on both sides. Meanwhile, due to the development of the surface karst negative terrain in this section, the atmospheric rainfall is rapidly introduced into the underground through the negative terrain, and is discharged along the east-west trough valleys of the anticline to the southern side of the Yulin river. Impacted by the tectonic stress extrusion in the south section, the Feixianguan Formation and Changxing Formation exposed in the core, controlled by the non-soluble rocks of the Feixianguan Formation, the hydraulic connection between the east and west limbs of the anticline is hindered, with a manifestation that the shallow groundwater is mainly discharged through partly cut transverse gullies. In a certain range away from the fully cut valley, where groundwater circulation has not adapted to the valley down-cutting, the valley has a weak influence on the transverse valleys, resulting in the strong development of transverse gullies and valleys and forming shallow depth of groundwater level. Groundwater, is discharged through the shallow transverse gullies, with a small amount of groundwater

circulating deeply through the deep dissolution gap. For areas close to the Yulin river, under the control of crustal uplift, fully cut river valley continues to cut down, which controls the groundwater circulation to the deep, leading to a deep depth of groundwater level. When groundwater circulation is adapted to the down-cutting of fully cut valleys, there is basically no gully development on the surface, transverse gullies and valleys will lose the discharge ability. The stable isotopes of the water samples data in the southern section far away from the Yulin River basically fall on the LMWL, indicating that the groundwater is excreted by temporary runoff and belongs to shallow circulation. The stable isotopes of the water samples to the south showed a trend of $\delta^{18}O$ enrichment, the $^{3}H$ dating also showed that the groundwater retention time was long, which was a deep circulation area. It's inferred that the fully-cut Yulin river valley and partly-cut Zhangfang gully together constitute a multilevel discharge base level of karst water, thus forming a unidirectional shallow-deep nested circulation system jointly controlled by fully cut river valley and partly cut gully (Figure 9).

Under the special conditions of the east Sichuan Basin, where a series of NNE–SSW trending Jura-type folds developed, we considered that the near east-west (EW) direction gullies determine the drainage of karst water largely. In this study, according to the degree of transverse gullies cutting through the soluble rock strata, it can be divided into three types: fully-cut, partly-cut, and uncut gully. Based on geomorphic and environmental isotopes analysis, the karst water circulation under the control of multiple drainage base levels and their combinations is discussed in typical Jura-type fold Mingyueshan. However, these discussions are essentially qualitative, some numerical simulations of groundwater flow can be considered in

future work. The combination of numerical simulation and field data helps to determine the groundwater flow system quantitatively.

# 5 Conclusion

Under the special tectonic conditions of the Jura-type folds in eastern Sichuan, the down-cutting degree and depth of the near EW gully cutting into soluble rocks determine the drainage capacity of groundwater in the anticline area. According to the morphology of transverse gullies which cut into the soluble rocks in anticline area, transverse gullies can be divided into three types: fully-cut, partly-cut, and uncut. The transverse gullies with different combinations control the shallow circulation and deep circulation of karst water. In this study, the geological and natural geographical factors that control the karst water circulation in the Mingyueshan area were analyzed from the geographical three-dimensional perspective. The groundwater flow system was built by GIS, the direct evidence of the karst water circulation was obtained by the environmental isotopes ($\delta^2$H, $\delta^{18}$O, $\delta^3$H) methods. Based on the above, the karst water circulation patterns under the control of different drainage base levels were explored. It is concluded that the north section of Mingyueshan is a unidirectional shallow circulation pattern controlled by a partly-cut gully. The middle section is a bidirectional shallow circulation pattern controlled by two partly-cut gullies. The karst water circulation in the south section is controlled by a fully-cut gully and a partly-cut gully and forms a unidirectional shallow-deep nested circulation system pattern.

# Data availability statement

The original contributions presented in the study are included in the article/supplementary material, further inquiries can be directed to the corresponding author.

# Author contributions

ZQ: Conceptualization, writing-original draft, methodology, investigation, formal analysis, and visualization; QZ: Conceptualization, resources, supervision, validation, writing-review and editing; SY: Writing-original draft, methodology, and visualization; YY: writing-review and editing; JZ: Validation and data curation; MX: Resources and supervision; YL: Data curation; ML: Investigation; MN: Investigation. All authors contributed to the article and approved the submitted version.

# Funding

This study was supported by the National Natural Science Foundation of China's project under No. 42272318.

# Conflict of interest

Authors ML and MN are employed by Chongqing Urban Construction Investment (Group) Co., Ltd.

The remaining authors declare that the research was conducted in the absence of any commercial or financial relationships that could be construed as a potential conflict of interest.

# Publisher's note

All claims expressed in this article are solely those of the authors and do not necessarily represent those of their affiliated organizations, or those of the publisher, the editors and the reviewers. Any product that may be evaluated in this article, or claim that may be made by its manufacturer, is not guaranteed or endorsed by the publisher.

# References

Cauquoin, A., Jean, B. P., Risi, C., Fourre, E., and Landais, A. (2017). Modeling the global bomb tritium transient signal with the AGCM LMDZ-iso: A method to evaluate aspects of the hydrological cycle. *J. Geophys. Res.* 121 (21), 12612–12629. doi:10.1002/2016JD025484

Charvet, J. (2013). The neoproterozoic-early paleozoic tectonic evolution of the South China block: An overview. *J. Asian Earth Sci.* 74, 198–209. doi:10.1016/j.jseaes.2013.02.015

Chen, K. L., Wu, H. N., Cheng, W. C., Zhang, Z., and Chen, J. (2016). Geological characteristics of strata in Chongqing, China, and mitigation of the environmental impacts of tunneling-induced geo-hazards. *Environ. Earth Sci.* 76 (1), 10–16. doi:10.1007/s12665-016-6325-7

Chen, S., Tang, Z. H., Wang, J., Wu, J. L., Yang, C., Kang, W. L., et al. (2020). Multivariate analysis and geochemical signatures of shallow groundwater in the main urban area of chongqing, southwestern China. *Water* 12 (2833), 2833. doi:10.3390/w12102833

Craig, H. (1961). Isotopic variations in meteoric waters. *Science* 133, 1702–1703. doi:10.1126/science.133.3465.1702

Davis, G. H. (1980). Structural characteristics of metamorphic core complexes. *South. Ariz. Geol. Soc. Am. Memoirs,Cordilleran Metamorph. Core Complexes* 153, 35–77. doi:10.1130/MEM153-p35

Deng, X., Xing, M., Yu, M., Zhao, Z. H., Li, C. S., and Su, Q. W. (2022). Characteristics of the water cycle of Jinan karst spring in northern China. *Water Pract. Technol.* 17 (7), 1470–1489. doi:10.2166/wpt.2022.075

Doney, S. C., Glover, D. M., and Jenkins, W. J. (1992). A model function of the global bomb tritium distribution in precipitation, 1960-1986. *J. Geophys. Res.* 97 (C4), 5481–5492. doi:10.1029/92JC00015

Ford, D., and Williams, P. D. (2007). *Karst hydrogeology and geomorphology*. Hoboken, NJ: John Wiely & Sons.

Gil-Marquez, J. M., Andreo, B., and Mudarra, M. (2019). Combining hydrodynamics, hydrochemistry, and environmental isotopes to understand the hydrogeological

functioning of evaporite-karst springs. An example from southern Spain. *J. Hydrology* 576, 299–314. doi:10.1016/j.jhydrol.2019.06.055

Gleeson, T., Befus, K. M., Jasechko, S., Luijendijk, E., and Cardenas, B. M. (2016). The global volume and distribution of modern groundwater. *Nat. Geosci.* 9 (2), 161–167. doi:10.1038/ngeo2590

Hill, C. A., and Polyak, V. J. (2010). Karst hydrology of grand canyon, Arizona, USA. *J. Hydrology* 390 (3-4), 169–181. doi:10.1016/j.jhydrol.2010.06.040

Kattan, Z. (1997). Environmental isotope study of the major karst springs in damascus limestone aquifer systems: Case of the figeh and barada springs. *J. Hydrology* 193, 161–182. doi:10.1016/S0022-1694(96)03137-X

Kaufman, A., Bar-Matthews, M., Ayalon, A., and Carmi, I. (2003). The vadose flow above soreq cave, Israel: A tritium study of the cave waters. *J. Hydrology* 273, 155–163. doi:10.1016/S0022-1694(02)00394-3

Koster, R. D., Broecker, W. S., Jouzel, J., Suozzo, R. J., Russell, G. L., Rind, D., et al. (1989). The global geochemistry of bomb-produced tritium: General circulation model compared to available observations and traditional interpretations. *J. Geophys. Res. Atmos.* 94 (D15), 18305–18326. doi:10.1029/JD094iD15p18305

Laubscher, H. P. (1977). Fold development in the Jura. *Tectonophysics* 37 (4), 337–362. doi:10.1016/0040-1951(77)90056-7

Liang, X., Zhang, R. Q., Luo, M. M., Sun, R. Q., Jin, M. G., Zhou, H., et al. (2022). Discussion on methodology in research of groundwater flow system: A review of research on groundwater flow systems at CUG-wuhan. *Bull. Geol. Sci. Technol.* 41 (01), 30–42. (In Chinese and English Abstract). doi:10.19509/j.cnki.dzkq.2022.0005

Liang, X., Zhang, R. Q., Niu, H., Jin, M. G., and Sun, R. L. (2012). Development of the theory and research method of groundwater flow system. *Bull. Geol. Sci. Technol.* 31 (05), 143–151. (In Chinese and English Abstract).

Liu, R. T., Wang, J. G., Zhan, H. B., Chen, Z., Li, W. J., Yang, D., et al. (2021). Influence of thick karst vadose zone on aquifer recharge in karst formations. *J. Hydrol.* 592, 125791. doi:10.1016/j.jhydrol.2020.125791

Lorette, G., Lastennet, R., Nicolas, P., and Denis, A. (2018). Groundwater-flow characterization in a multilayered karst aquifer on the edge of a sedimentary basin in Western France. *J. Hydrology* 566, 137–149. doi:10.1016/j.jhydrol.2018.09.017

Lu, G., Zhao, L., Zheng, T., and Kaus, P. (2014). Strong intracontinental lithospheric deformation in south China: Implications from seismic observations and geodynamic modeling. *J. Asian Earth Sci.* 86, 106–116. doi:10.1016/j.jseaes.2013.08.020

Lucas, L., and Unterweger, M. P. (2000). Comprehensive review and critical evaluation of the half-life of tritium. *J. Res. Natl. Inst. Stand. Technol.* 105, 541–549. doi:10.6028/jres.105.043

Ma, J. F., Li, X. L., Liu, F., Fu, C. C., Zhang, C. C., Bai, Z. X., et al. (2022). Application of hydrochemical and isotopic data to determine the origin and circulation conditions of karst groundwater in an alpine and gorge region in the qinghai–xizang plateau: A case study of genie mountain. *Environ. Earth Sci.* 81 (10), 291–309. doi:10.1007/s12665-022-10414-9

Meng, X., Xiong, L. Y., Yang, X. W., Yang, B. S., and Tang, G. A. (2018). A terrain openness index for the extraction of karst Fenglin and Fengcong landform units from DEMs. *J. Mt. Sci.* 15 (4), 752–764. doi:10.1007/s11629-017-4742-z

Michel, R. L. (1989). Tritium deposition in the continental United States, 1953-1983. *J. Fujian Agric. For. Univ.* 179, 107–115. doi:10.1002/pola.27791

Nir, A. (1964). On the interpretation of tritium 'age' measurements of groundwater. *J. Geophys. Res.* 69 (12), 2589–2595. doi:10.1029/JZ069i012p02589

Pavel, B., Michal, V., Ludovit, G., and Jozef, M. (2016). Josvafo paleo-polje: Morphology and relation to the landform evolution of aggtelek karst and josva river valley, Hungary. *Z. Fur Geomorphol.* 60 (3), 219–235. doi:10.1127/zfg/2016/0212

Pu, J. B., Cao, M., Zhang, Y. Z., Yuan, D. X., and Zhao, H. P. (2014). Hydrochemical indications of human impact on karst groundwater in a subtropical karst area, Chongqing, China. *Environ. Earth Sci.* 72 (5), 1683–1695. doi:10.1007/s12665-014-3073-4

Pu, J. B. (2013). Hydrogen and oxygen isotope geochemistry of karst groundwater in chongqing. *Acta Geosci. Sin.* 34 (6), 713–722. (In Chinese and English Abstract). doi:10.3975/cagsb.2013.06.08

Rich, J. L. (1934). Mechanics of low-angle overthrust faulting as illustrated by Cumberland thrust block, Virginia, Kentucky, and Tennessee. *AAPG Bull.* 18, 1584–1596. doi:10.1306/3D932C94-16B1-11D7-8645000102C1865D

Silva, A., and Cota, S. (2021). Groundwater age dating using single and time-series data of environmental tritium in the Moeda Synclyne, Quadrilátero Ferrífero, Minas Gerais, Brazil. *J. S. Am. Earth Sci.* 107, 103009. doi:10.1016/j.jsames.2020.103009

Solomon, D. K., and Sudicky, E. A. (1991). Tritium and helium 3 isotope ratios for direct estimation of spatial variations in groundwater recharge. *Water Resour. Res.* 27 (9), 2309–2319. doi:10.1029/91WR01446

Stringfield, V. T., Rapp, J. R., and Anders, R. B. (1979). Effects of karst and geologic structure on the circulation of water and permeability in carbonate aquifers. *J. Hydrology* 12, 313–332. doi:10.1016/0022-1694(79)90178-1

Suppe, J. (1983). Geometry and kinematics of fault-bend folding. *Am. J. Sci.* 283, 684–721. doi:10.2475/ajs.283.7.684

Szczygieł, J., Golicz, M., Hercman, H., and Lynch, E. (2018). Geological constraints on cave development in the plateau-gorge karst of South China (Wulong, Chongqing). *Geomorphology* 304, 50–63. doi:10.1016/j.geomorph.2017.12.033

Taylor, C. B. (1966). Tritium in southern hemisphere precipitation 1953-1964. *Tellus* 18, 105–131. doi:10.1111/j.2153-3490.1966.tb01449.x

Torresan, F., Fabbri, P., Piccinini, L., Dalla, L. N., Pola, M., and Zampieri, D. (2020). Defining the hydrogeological behavior of karst springs through an integrated analysis: A case study in the berici mountains area (vicenza, NE Italy). *J. Hydrology* 28, 1229–1247. doi:10.1007/s10040-020-02122-0

Tóth, J. (1963). A theoretical analysis of groundwater flow in small drainage basins. *J. Geophys. Res.* 68 (16), 4795–4812. doi:10.1029/JZ068i016p04795

Tóth, J. (1962). A theory of groundwater motion in small drainage basins in central Alberta, Canada. *J. Geophys. Res.* 67 (11), 4375–4388. doi:10.1029/JZ067i011p04375

Tóth, J. (2009). *Gravitational system of groundwater: Theory evaluation, utilization.* New York: Cambridge University Press.

Tóth, J. (1999). Groundwater as a geologic agent: An overview of the causes, processes, and manifestations. *Hydrogeology J.* 7 (1), 1–14. doi:10.1007/s100400050176

Vasic, L., Palcsu, L., and Fen, H. (2019). Groundwater gravitational circulation of karst veliko vrelo and malo vrelo springs by isotope and the noble gas method: Case study of the beljanica massif. *Environ. Earth Sci.* 78 (10), 307–314. doi:10.1007/s12665-019-8294-0

Wang, Y. S., Xu, M., Yang, Y. N., Xia, Q., Jiang, B., Yang, C., et al. (2022). Structural characteristics and deformation evolution of an intra-continental fold-thrust belt in eastern sichuan: Insights into analogue sandbox models. *Front. Earth Sci.* 10, 1–23. doi:10.3389/feart.2022.897882

Wang, Z. X., Zhang, J., Tao, L., Xie, G., and Ma, Z. J. (2010). Structural analysis of the multi-layer detachment folding in eastern sichuan province. *Atca Geol. Sin. Engl. Ed.* 84 (003), 497–514. doi:10.1111/j.1755-6724.2010.00269.x

Wang, Z. X., Zhang, J., Tao, L., Zhou, X. G., Ma, Z. J., Tang, L. G., et al. (2012). Structural traps in detachment folds: A case study from the comb- and troughtrough-like' deformation zone/s, east Sichuan, China. *Atca Geol. Sin. Engl. Ed.* 86 (4), 828–841. doi:10.1111/j.1755-6724.2012.00709.x

Wen, K., and Li, C. X. (2020). The geometry and kinematics of the intersection area of eastern Sichuan and the Dabashan fold-thrust belt. *Atca Geol. Sin. Engl. Ed.* 94, 426–438. doi:10.19762/j.cnki.dizhixuebao.2020005

Wen, Y. R. (2017). *Variations of stable isotope in daily precipitation and the response to the ENSO phases in Chongqing, Southwest, China.* Chongqing: Southwest University. (In Chinese and English Abstract).

Wu, Q. S., Deng, C. B., and Chen, Z. Q. (2016). Automated delineation of karst sinkholes from LiDAR-derived digital elevation models. *Geomorphology* 266, 1–10. doi:10.1016/j.geomorph.2016.05.006

Xiao, Q., Jiang, Y. J., Shen, L. C., and Yuan, D. X. (2018). Origin of calcium sulfate-type water in the triassic carbonate thermal water system in chongqing, China: A chemical and isotopic reconnaissance. *Appl. Geochem.* 89, 49–58. doi:10.1016/j.apgeochem.2017.11.011

Yang, P. H., Luo, D., Groves, C., and Xie, S. Y. (2019). Geochemistry and Genesis of geothermal well water from a carbonate–evaporite aquifer in Chongqing, SW China. *Environ. Earth Sci.* 78, 33. doi:10.1007/s12665-018-8004-3

Yang, P., and Ye, S. J. (2018). Global model of the annual mean concentration of Tritium in precipitation, 1960-2014. *Acta Sci. Circumstantiae* 38 (5), 1759–1767. (In Chinese and English Abstract). doi:10.13671/j.hjkxxb.2017.0475

Zhang, J. R., Yang, P. H., Groves, C., Luo, X. H., and Wang, Y. Y. (2022). Influence of geological structure on the physicochemical properties and occurrence of middle-deep groundwater in Chongqing, Southwest China. *J. Hydrology* 610, 127782. doi:10.1016/j.jhydrol.2022.127782

Zhang, Y. H., Ye, S. J., and Wu, J. C. (2011). A modified global model for predicting the tritium distribution in precipitation, 1960-2005. *Hydrol. Process.* 25 (15), 2379–2392. doi:10.1002/hyp.8001

Check for updates

# Characterization of true triaxial rock bursts in sandstones with different water contents

Kezhu Chen[1], Weijin Zhou[1]*, Yuangui Pan[2]*, Ying Zhuo[3] and Guoqiang Zheng[1]

[1]Sichuan Communication Surveying and Design Institute Co., Ltd., Chengdu, Sichuan, China, [2]Sichuan Huadi Construction Engineering Co., Ltd., Chengdu, Sichuan, China, [3]School of Emergency Management, Xihua University, Chengdu, Sichuan, China

The rockburst phenomenon occurs in dry red sandstone under high *in situ* stress, and the rockburst effect is weaker for a water-bearing rock. The rockburst effect on red sandstone with different water contents is analyzed in this paper. A true triaxial testing machine is used to conduct the loading, and acoustic emission recording equipment and a high-speed camera are used to monitor the acoustic signal inside the rock and the rock-caving situation throughout the entire process in order to analyze the characteristics of the acoustic emissions and the ejection form of the rockburst. The results show that rockburst occurs in dry red sandstone and 50% saturated red sandstone but not in saturated red sandstone. The phrase characteristics of the stress−strain curve of the dry rock vary more significantly than those of the water-bearing rock, and the elastic strain energy inside the rock decreases gradually as the water content increases. The double peak of the acoustic emissions curve occurs during the failure process of the dry rock and gradually transitions to a stepped pattern as the water content increases. The ejected fragments of dry red sandstone during the rockburst are abundant and large. The true triaxial test results illustrate the characteristic effect of the rockburst on red sandstone with different water contents, reveal the failure mode and ejection characteristics of red sandstone with different water contents, and demonstrate the influence of the water content on the rockburst characteristics of red sandstone. The results of this study provide a theoretical reference for the study of the rockburst mechanisms of similar hard rocks.

KEYWORDS

water content, rockburst, true triaxial, energy, acoustic emission

## Introduction

Rockburst, a common geological disaster in the process of deep engineering construction, often occurs suddenly and destructively, threatening the safe construction and production in the engineering industry (Mazaira and Konicek, 2015). With the increase in construction depth, rockburst disasters are becoming more serious. Suorineni et al. (2014) even described rockburst as a cancer, indicating

the danger of rockbursts in engineering projects. A railway tunnel (Liu et al., 2013) with a length of 16,449 m contained a rockburst section of up to 9,500 m (58% of the total) according to statistics. The Mount Longmen highway tunnel (design stage) in western China is approximately 25,000 m long, and more than 19,000 m of the tunnel located at depths of greater than 500 m, so the rockburst section of this tunnel is expected to be 15,000 m. Rockburst disasters have been reported worldwide and have caused significant losses of life and property. Rockburst is an inevitable problem in deep engineering construction. Mechanical mechanisms, monitoring and early warning, excavation optimization, and dynamic control have been the key research topics in the last decade (Feng et al., 2019). Among them, rockburst mechanics is the foundation of other research fields, and thus, this topic has notable theoretical significance and engineering value.

Even though there is currently no consensus on the formation of the rockburst mechanism, academics have explored and explained the mechanism of rockburst through methods such as field research, theoretical analysis, mechanical tests, numerical simulations, and similarity tests, yielding fruitful results (Afraei et al., 2018; Zhou et al., 2018). In the early days of this research, rockburst studies mainly focused on rockburst damage modes. Li et al. (2017) summarized six types of geomechanical models of rockburst based on geological analysis. Early uniaxial rock mechanics test (Zhao and Jiang, 2010) have evolved into a true triaxial excavation simulation, including the installation of various monitoring instruments to observe the rockburst process (He et al., 2012), analyze the shape and kinetic energy of rockburst blocks (Su et al., 2017a; Su et al., 2017b), and study the acoustic emission spectrum characteristics, energy release (Zhao and Cai, 2014; Zhao et al., 2014), and rockburst tendency (Gong et al., 2020). (Zhang et al., 2019a; 2019b; 2019c; Zhang et al., 2021) proposed a strain energy determination method for rocks under true triaxial compression (TTC), and investigated the energy evolution process and mechanism of different hard rocks under true triaxial compression (TTC) using strain energy analysis (Qu et al., 2022). In order to accurately and effectively predict the occurrence of rock bursts, a multi-indicator evaluation method for the occurrence of rock bursts at deep subsurface rock openings was established (Xu et al., 2022). explored the effects of temperature on energy storage and dissipation properties and rockburst susceptibility, revealing that high temperatures can damage the ESC of rocks, which is essential for reducing rockburst susceptibility. To accurately predict rockburst hazards among complex influencing factors, a rockburst hazard prediction model based on binary classification of Gaussian processes (GPC) was proposed after determining the intrinsic relationship between multiple factors and rockbursts in coal mines (Lan et al., 2022). (Du et al., 2022) established an analytical model to quantitatively describe the physical process of rockburst in mine tunnels, and investigated the calculation

method of dynamic release of elastic properties during the physical process of rockburst (Chen et al., 2022). proposed a bagged ensemble of Gaussian process classifiers (GPCs) to evaluate the rockburst damage potential of unbalanced data sets. The macroscopic block characteristics of rockburst fragments reflect the degree of rock fragmentation, which increases with the loading rate (Sun et al., 2022). (Yan et al., 2022) found that the prediction results of the rockburst intensity classification prediction model and SVM discriminant method based on the analysis of a large number of sample data processing were in good agreement with the actual rockburst intensity (Xia et al., 2022). proposed a data-driven approach based on spectral clustering to predict rockburst intensity (Yang et al., 2020). investigated the degree of influence of red sandstone specimen shape and rock material on rockburst sensitivity, and it was found that cubic specimens exhibited stronger rockburst sensitivity than cylindrical specimens. The rockburst characteristics of red sandstone with different arrangements of prefabricated holes were investigated by uniaxial compression tests, and it was found that the rockburst effect of red sandstone containing prefabricated holes was weaker than that of intact specimens (He et al., 2021). It was found that water gushing is highly likely to occur within the broken enclosure section, and the permeability and porosity of the enclosure increases with time due to the granular structure of the broken enclosure that easily forms water-conducting channels (Ma et al., 2022a). Li investigated the pore structure and hydraulic properties of fractured rock masses and found that at lower compressive stress levels, fractured rock masses showed greater compressibility, while fractured gangue with more small particles showed greater stress sensitivity (Li et al., 2022). Studying the hydraulic characteristics of fault rocks during water-silt scouring, the higher the silt concentration, the higher the erosion effect is inhibited by silt flow (Ma et al., 2022b). Liu conducted rockburst tests on horizontally laminated surface sandstones under double-sided unloading and found that rockbursts occur asynchronously on two free surfaces (Liu et al., 2021). Rockbursts are very likely to occur after excavation and unloading of deep rock masses, and it was found that water injection into the rock mass before excavation can effectively reduce the rockburst effect (Cai et al., 2021). It can be seen that the water content of the rock and the rock burst effect, the study of rock burst effect of different water content of the rock, rock burst prevention and control has important significance.

Because the different mechanical properties of red sandstone with different water contents are different, we believe that the rockburst tendency of the rock is related not only to the stress state but also to the water content. According to the published literature, few studies have been carried out on the rockburst characteristics of rocks with different water contents under true triaxial conditions. Thus, based on laboratory true triaxial compression tests, in this study, the energy characteristics of red sandstone with different water contents were systematically
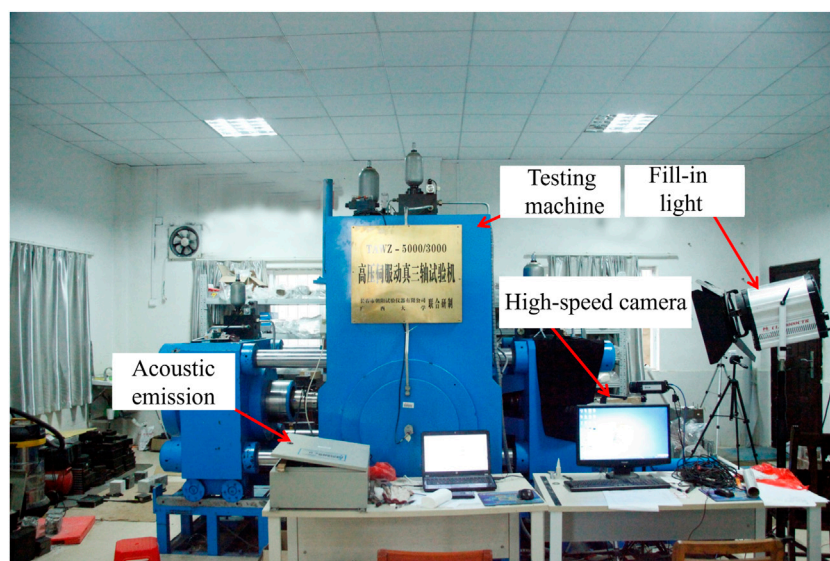
**FIGURE 1**
Test loading system.

investigated. In addition, a high-speed camera and Micro-II acoustic emission control acquisition system were used to reveal the failure modes and ejection characteristics of the specimens under true triaxial conditions and to determine the rockburst characteristics of red sandstone, providing a reference for similar rockburst mechanism research.

# Laboratory experiments

## Experimental equipment

The test system is mainly composed of test loading system, measurement and control system, and monitoring system. The loading system is a high-pressure servo dynamic true triaxial tester, which can perform uniaxial tensile, compression, shear test and conventional triaxial test as well as true triaxial test and other comprehensive rigidity testing machine, as shown in Figure 1. The maximum vertical loading pressure of the test host is 5,000 kN, and the maximum loading pressure in the horizontal direction is 3,000 kN. The tester can realize the special function of unloading the excavation under high ground stress conditions by quickly unloading the single-sided pressurizing device under the simultaneous loading of three directions and six sides. The measurement and control system is mainly composed of servo controller, computer and sensing elements, which can monitor the whole process of the test and has powerful data and graphic processing capability. The monitoring system is divided into an acoustic emission monitoring system and a high-speed camera to monitor the damage process of the specimen from the inside out in a comprehensive manner. The load compression rate of the true triaxial loading system is 10 N/s-10 kN/s, the displacement measurement range is 0–10 mm, and the deformation measurement range is 0–10 mm.

Acoustic emission monitoring instrument is the Micro-II Digital AE System acoustic emission acquisition system developed by the U.S. PAC, the main core component of the system is an eight-channel acquisition analysis and waveform processing acoustic emission function card PCI-8 board, the acoustic emission system can simultaneously use four sensors for array data acquisition. The high-speed digital camera is developed by SVSI, the maximum resolution of the camera is 1,280×1,024 pixels, and the maximum frame rate is 532 fps.

## Test program

In the tests, three-direction and five-side loading were adopted, that is, one horizontal direction remained free, and the other five sides were loaded to the set stress. The loading method of the test was as follows: 1) At a rate of 0.5 MPa/s, the stress was simultaneously loaded to the minimum principal stress in the three-directions. $\sigma_3$ remained unchanged, and the sample was loaded to the intermediate principal stress at a rate of 0.5 MPa/s $\sigma_2$ and $\sigma_3$ remained unchanged, and the sample was loaded to the maximum principal stress at a rate of 1 MPa/s, until failure of the specimen occurred. The minimum principal stress $\sigma_3$ was 5 MPa, and the intermediate principal stress $\sigma_2$ was 10 MPa. 2) After installing the fixture for the specimen, the specimen was placed in the holder, carefully leveled, and fixed in
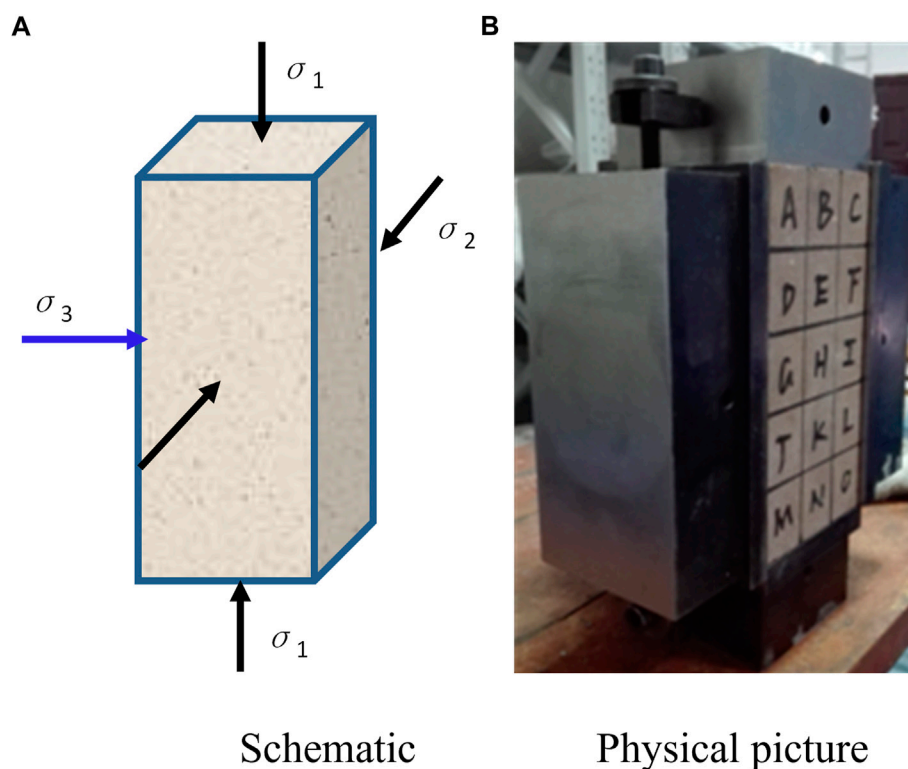
**FIGURE 2**
Schematatic diagram of the true triaxial loading test with a single face in the air. Panel **(A)** is the schematic picture of the rock sample, Panel **(B)** is the physical picture of the rock sample.

place. The displacement sensors and acoustic emission probes were installed, the monitoring and observation equipment was debugged and prepared for the tests. 3) The load and strain data were recorded in real-time during the tests. An acoustic emission instrument was used to record the acoustic emission data throughout the entire process of the true triaxial sandstone rockburst tests. The high-speed camera recorded continuously to capture the failure process of the specimen. 4) After the test, the rockburst fragments that peeled off and were ejected from the free face were collected in order to analyze the scale and mass distribution characteristics of the rockburst fragments. After the fragments were collected, the specimen was removed from the testing machine, and the fixture was disassembled to preliminarily protect the parent rock and collect a morphological map of the parent rock at various angles after failure occurred. A schematic diagram of the loading and a physical diagram of the specimens are presented in Figure 2.

The specimens were standard 100 mm × 100 mm × 200 mm blocks. The specimens were divided into three different water contents: dry, 0.5 K (i.e., 50% saturated), and saturated ($K_s$ is the saturation coefficient). The maximum water content was 2.2% after the rock water absorption test. The dry rock samples were numbered GZ-1–GZ-5. The 0.5-Ks rock samples were numbered HS-1–HS-5, and the saturated rock samples were numbered BH-1–BH-5, resulting in a total of 15 samples with five samples for each working condition.

## Analysis of test results

### Analysis of ejection process and fracture characteristics

Five rock samples were tested under each set of working conditions, and those with relatively good test phenomena were selected for analysis, namely, GZ-3 was selected for the dry rock samples, HS-2 was selected for the 0.5-$K_s$ rock samples, and BH-4 was selected for the saturated rock samples. The ejection process during the failure of the red sandstone with different water contents is shown in Figure 3.

For GZ-3 sample, first, a small number of particles were ejected in the lower M region. As the axial pressure increased, particles were ejected in the AB area on the upper-end surface of the sample. At the same time, plate-like debris was ejected in the MNO area on the lower part of the rock sample, with a fast ejection speed, long distance, and severe destruction.

**FIGURE 3**
Ejection process of red sandstone destruction under different water content.
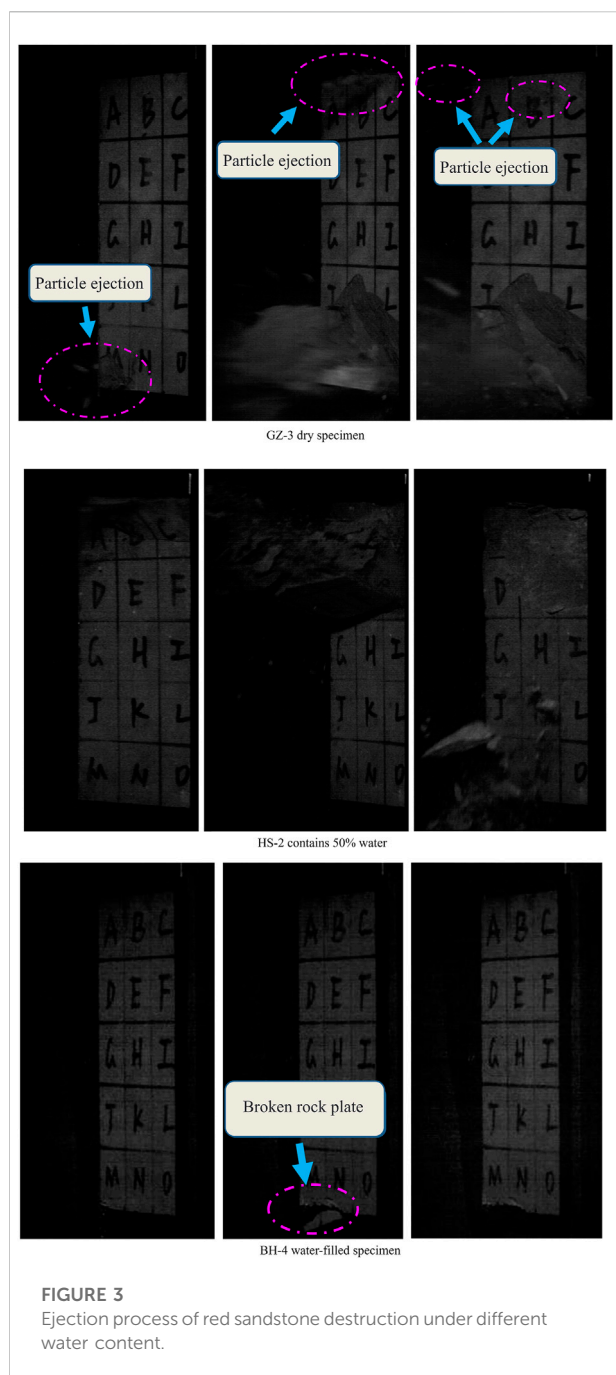
First, the upper end of HS-2 split into plates and collapsed. Then, the middle and upper part of the sample collapsed, with many fragments but no ejection, and sliding only occurred along the free face. During the entire failure process, there was no ejection of rock debris, but severe damage occurred.

Sample BH-4 did not undergo rockburst, and only a local rock plate fracture formed in the lower surface, with a small number of fragments slipping and mild damage.

According to the failure process of the red sandstone with three different water contents, the dry rock was damaged very violently, accompanied by a large number of ejection fragments. When the damage to the rock block involved a fast ejection speed and long ejection distance, the rockburst phenomenon was very violent. For the red sandstone with a water content of 50%, no debris ejection occurred, but the rock block collapsed and a small number of fragments formed in the upper part during the failure process, so the rockburst effect was significantly reduced. The saturated red sandstone did not undergo rockburst, and the failure mode was dominated by the formation of a fracture and sliding of the rock blocks.

Figure 4 shows the failure modes of the red sandstone with different water contents. As can be seen from Figure 4A, the failure modes of the dry red sandstone involved the cracking of small thin sections in area B at the free face, but no fragments were ejected. The deep ejection area was located in the lower part. The cracks were mainly concentrated in the rear of the specimen (opposite to the free surface). There were a vertical crack and shear crack in the upper part, and two shear cracks in the lower part, which extended through the middle of the specimen, forming an X shape. Finally, the specimen was damaged by splitting, shearing, and rockburst. Figure 4B shows the sample with 50% saturation. Plate-like fragments were ejected from the shallow surface of the free face, and multiple small vertical splitting cracks formed in the upper-end surface of the rock sample without obvious crack expansion. A shear oblique crack extended from the lower left corner of the specimen to the middle of the upper-end surface, leading to the final failure of the rock sample. Figure 4C shows the sample in the saturated state. As can be seen from Figure 4C, no rockburst or rock block ejection from the free face occurred, and the free face remained intact without pits. Two obvious shear cracks penetrated from the tips on both sides of the lower-end face and converged in the middle of the upper-end face, forming a staggered shear zone. There was no splitting crack, no plate crack bulging, and no rockburst during the failure of this specimen.

## Analysis of stress–strain characteristics

Figure 5 shows the stress–strain curves of the red sandstone with different water contents. The changes in the characteristics were analyzed and compared. In terms of the peak stress, the peak stress of the dry red sandstone was the highest, reaching 155.8 MPa; the peak stress of the 50% saturated specimen was 148.5 MPa, and the peak stress of the saturated specimen was 117.2 MPa. It can be seen that as the water content increased, the stress required to cause failure of the red sandstone gradually decreased. The most obvious decrease occurred under the saturated condition.
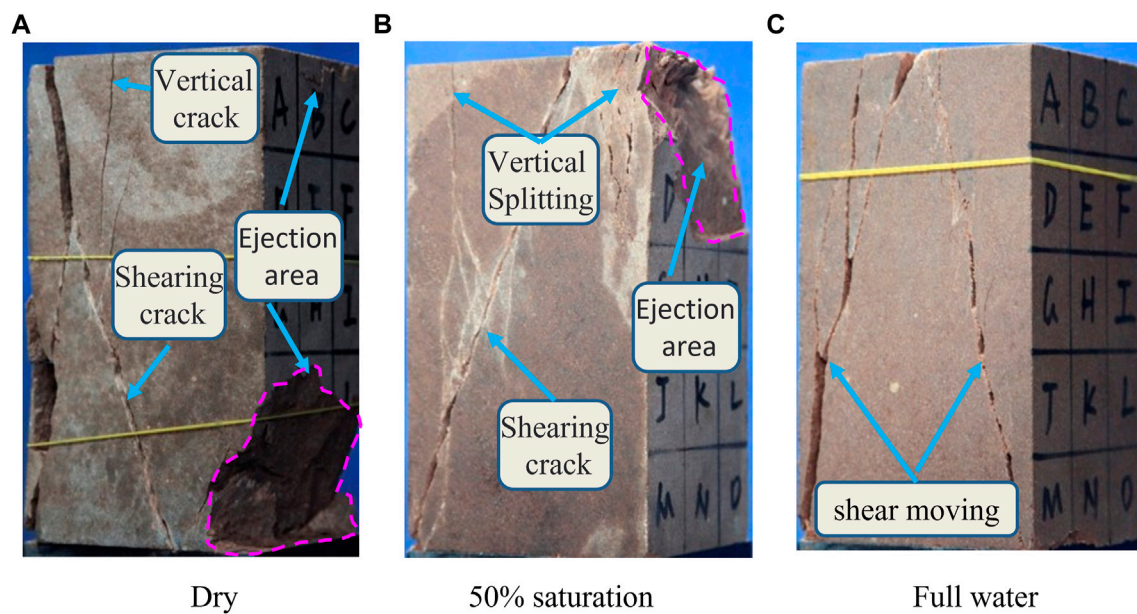
**FIGURE 4**
Destruction patterns of red sandstone at different water contents. Panel **(A)** shows the dry rock samples, Panel **(B)** shows the 50% saturation rock samples, Panel **(C)** shows the full water rock samples.



**FIGURE 5**
Stress-strain curves of red sandstone at different water contents.

According to the slope of the stress–strain curve, the overall change in the stress–strain curve in the dry state can be divided into three stages. The first stage is the gently increasing stage, in which the stress–strain curve gradually rises gently with a small overall slope. The second stage is the sharp increase stage, in which the stress–strain curve is steeper and has a large slope. The

**FIGURE 6**
Stress-strain curve of the whole process of deformation and damage of red sandstone. Panel **(A)** shows the dry rock samples, Panel **(B)** shows the 50% saturation rock samples, Panel **(C)** shows the full water rock samples.
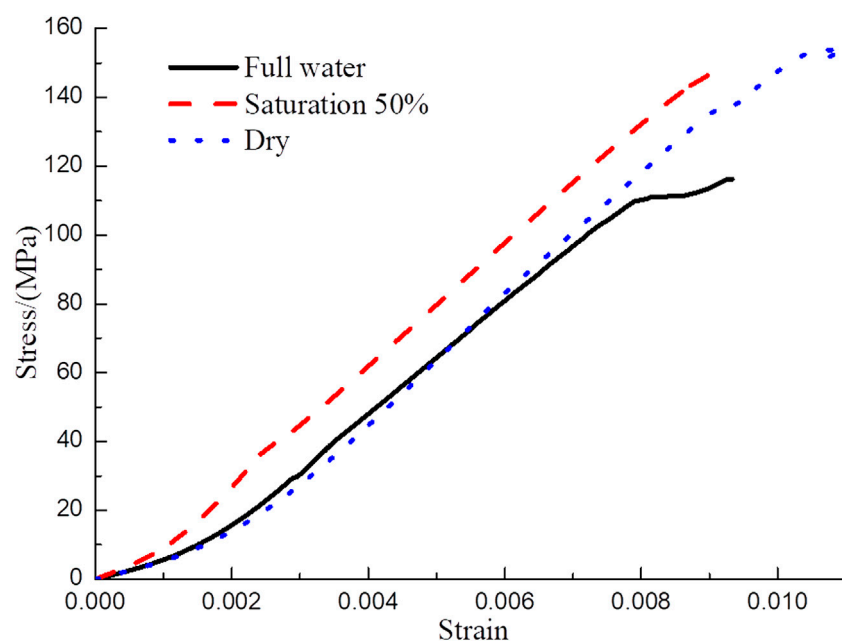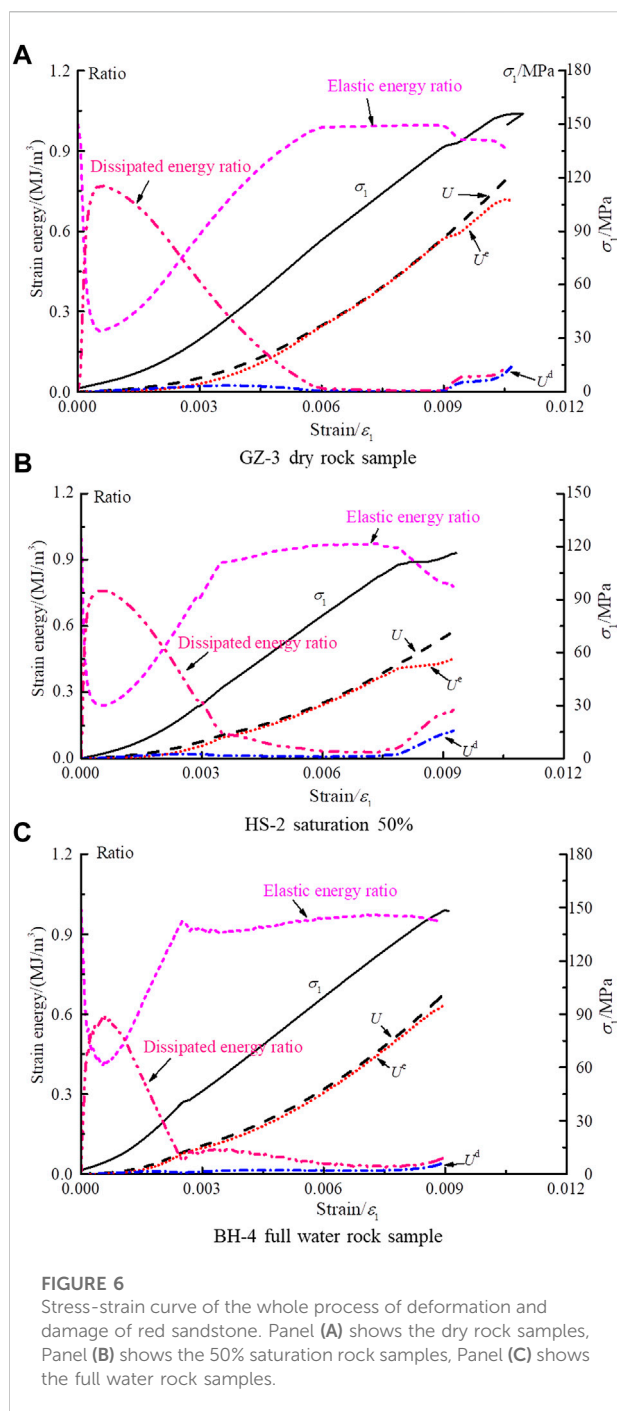
third stage is the gentle stage, in which the slope of the stress–strain curve changes from steep to slow. For 50% saturation, the stress–strain curve is generally an inclined straight line without any phrase change characteristics. For the saturated state, the stress–strain curve exhibits a gentle shape in the early stage, increases linearly in the middle stage, and becomes gentle before failure occurs. By analyzing the

stress–strain curves of the red sandstone with three different water contents through comparison, it was found that the stress–strain curve of the dry red sandstone has a strong phrase characteristic and a large slope. As the water content increases, the phase characteristic of the stress–strain curve weakens and the slope decreases. Therefore, it can be concluded that if the dry rock is more brittle, the rockburst is more serious, and increasing the water content will reduce the brittleness of the rock and weaken the rockburst phenomenon.

## Analysis of energy evolution characteristics

According to the first law of thermodynamics, if a volume unit of a rock mass is considered to deform under the action of external forces, it can be assumed that there is no heat exchange between the physical process and the outside world, that is, all of the work done by the external forces can be absorbed by the rock. According to the principle of the conservation of energy,

$$U = U^e + U^d \tag{1}$$

where U is the energy produced by the work done by the external force, $U^e$ is the releasable elastic strain energy, and $U^d$ is the dissipative energy.

Figure 6 shows the stress–stress–strain curve of the entire process of rock deformation and failure. The damage to the internal units of the rock and the resulting plastic deformation consume part of the energy absorbed by the rock, which is irreversible, i.e., the dissipative energy $U^d$ in Figure 6. The elastic deformation generated by the rock is recoverable after the external force is unloaded. Another part of the energy absorbed by the rock is converted into elastic strain energy to form elastic deformation, which is the releasable elastic strain energy $U^e$ in Figure 6 and is reversible under certain conditions. In Figure 6, $E$ is the elastic modulus.

The total strain energy and elastic strain energy in the principal stress space are expressed as follows:

$$U = \int_0^{\varepsilon_1} \sigma_1 d\varepsilon_1 + \int_0^{\varepsilon_2} \sigma_2 d\varepsilon_2 + \int_0^{\varepsilon_3} \sigma_3 d\varepsilon_3 \tag{2}$$

$$U^e = \frac{1}{2}\sigma_1\varepsilon_1^e + \frac{1}{2}\sigma_2\varepsilon_2^e + \frac{1}{2}\sigma_3\varepsilon_3^e \tag{3}$$

where $\sigma_1$, $\sigma_2$, and $\sigma_3$ are the maximum principal stress, intermediate principal stress, and minimum principal stress in three directions, respectively; $\varepsilon_1$, $\varepsilon_2$, and $\varepsilon_3$ are the principal strains in the three principal stress directions; and $\varepsilon_1^e$, $\varepsilon_2^e$, and $\varepsilon_3^e$ are elastic strains in the three principal stress directions.

According to the generalized form of Hooke's law, the elastic strain can be expressed as follows:

$$\varepsilon_i^e = \frac{1}{E}\left[\sigma_i - \mu_i\left(\sigma_j + \sigma_k\right)\right] \tag{4}$$

where $\sigma_i, \sigma_j$, and $\sigma_k$ $(i, j, k = 1, 2, 3)$ are the principal stresses, and $E$ and $\mu_i$ are the unloaded elastic modulus and Poisson's ratio, respectively. In order to facilitate calculation, the elastic modulus and Poisson's ratio in the late elastic stage are uniformly adopted in this paper.

In the late elastic stage, two points a and b are taken, and $\varepsilon_{ia}$ and $\varepsilon_{ib}$ $(i=1, 2, 3)$ are the principal strains at these two points in the three principal stress directions, respectively. In the true triaxial state, the Poisson's ratio can be expressed as follows:

$$\mu_{1-2} = \frac{\varepsilon_{2b} - \varepsilon_{2a}}{\varepsilon_{1b} - \varepsilon_{1a}} \tag{5}$$

$$\mu_{1-3} = \frac{\varepsilon_{3b} - \varepsilon_{3a}}{\varepsilon_{1b} - \varepsilon_{1a}} \tag{6}$$

$$\mu_{2-3} = \frac{\varepsilon_{3b} - \varepsilon_{3a}}{\varepsilon_{2b} - \varepsilon_{2a}} \tag{7}$$

where $\mu_{1-2}$ is the Poisson's ratio in the direction of the maximum principal stress and intermediate principal stress, $\mu_{1-3}$ is the Poisson's ratio in the direction of the maximum principal stress and minimum principal stress, and $\mu_{2-3}$ is the Poisson's ratio in the direction of the intermediate principal stress and minimum principal stress.

According to Eqs. 2–7, the equation for calculating the elastic strain energy in the true triaxial stress state is

$$U^e = \frac{1}{2E} \left[ \sigma_1^2 + \sigma_2^2 + \sigma_3^2 - 2 \left( \mu_{1-2}\sigma_1\sigma_2 + \mu_{1-3}\sigma_1\sigma_3 + \mu_{2-3}\sigma_2\sigma_3 \right) \right] \tag{8}$$

Therefore, the total energy absorbed, the elastic strain energy, the dissipative energy, and their respective proportions in the process of the deformation and damage of the rock can be calculated using the above principles and equations to analyze the change.

It can be seen from Figure 6 that the elastic strain energy $U^e$ of the rock in the dry state is consistent with the total energy $U$ absorbed during the failure process, and the dissipative energy $U^d$ approximates the horizontal change, with the peak value of the elastic strain energy reaching 0.71 MJ/m³ and the peak value of total energy absorbed reaching 0.73 MJ/m³. In the rock with 50% saturation, the peak value of the elastic strain energy is 0.68 MJ/m³, the peak value of the total absorbed energy is 0.70 MJ/m³, and the dissipated energy approximates the horizontal change where $U^e$ is in good agreement with $U$. In the saturated state, the elastic strain energy and total absorbed energy of the rock decrease more significantly, with a peak elastic strain energy of 0.45 MJ/m³, a peak total absorbed energy of 0.57 MJ/m³, and an approximate horizontal change in the dissipative energy.

Based on the analysis of the total stress–strain curves for the three different water contents through comparison, it can be concluded that the elastic strain energy of the rock in the dry state is the highest, the total energy absorbed in the failure process is greater, the energy released during the failure is greater, and the rockburst phenomenon is more prominent. As the water content increases, the elastic strain
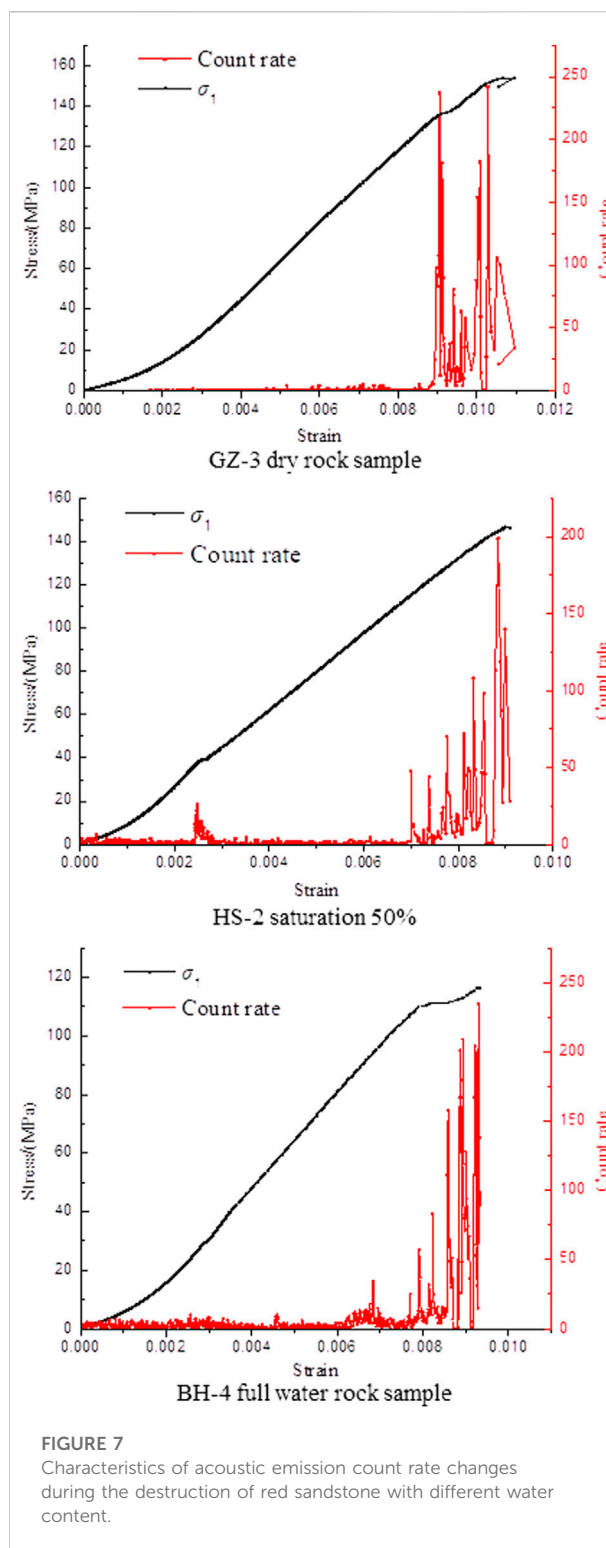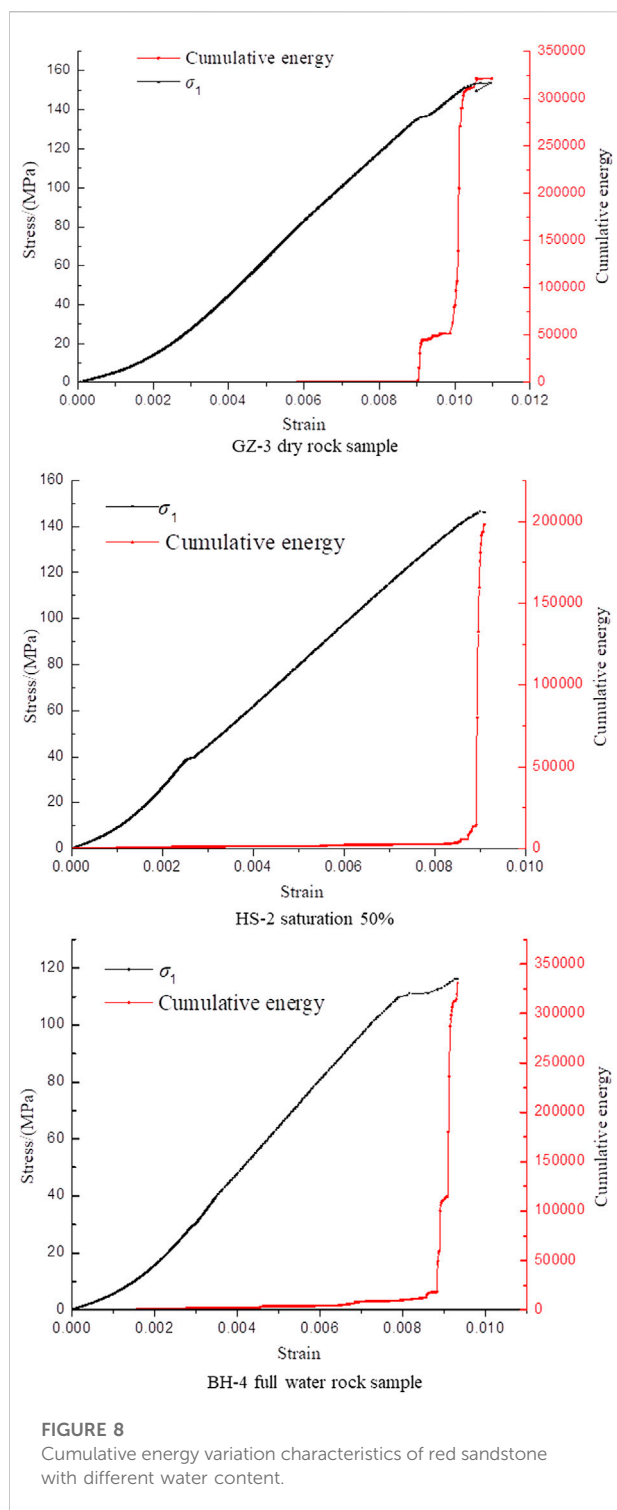


FIGURE 7
Characteristics of acoustic emission count rate changes during the destruction of red sandstone with different water content.

energy of the rock decreases. The total energy absorbed during the failure decreases, and the energy released during the failure decreases, gradually weakening the rockburst phenomenon.

**FIGURE 8**
Cumulative energy variation characteristics of red sandstone with different water content.

## Analysis of acoustic emission characteristics

Figure 7 shows that the acoustic emission activity of the dry sample is quiet in the compaction stage and the elastic deformation

stage, with almost no formation of cracks. However, due to the instantaneous release of a large amount of elastic energy before the failure of the specimen, the acoustic emission count rate increases suddenly and double peaks of the count rate appear. Between the two peaks, there is a very short quiet period with obvious brittle failure. The acoustic emission record of the sample with 50% saturation is more active than that of the dry sample in the compaction-density stage, and the count rate increases in a stepwise manner near the failure time. This indicates that when the rock is weakened by the presence of water, the microcrack expansion is more stable, and the brittle damage occurs with a sudden increase of about twice the count rate at the time the final damage occurs. The acoustic emission record of the saturated sample is also more pronounced than that of the dry sample in the compaction stage. The acoustic emission signal continues to be active and has a higher count rate value in the yielding stage, and the microcracks continue to accelerate, expand, and penetrate, resulting in shear failure.

As can be seen from Figure 8, the cumulative energy of the dry sample in the compaction-density and elastic deformation stages does not fluctuate, and the curve rises in a stepwise manner before the damage occurs. According to the acoustic emission count rate, the rock sample is damaged once before the final failure occurs; however, at this time, the failure strength does not reach the point where the overall sample becomes unstable. Subsequently, the cumulative energy increases sharply and the acoustic emission activity increases substantially in an instant. The cumulative energy of the sample with 50% water saturation increases slightly in the elastic stage, then the curve rises steeply during the failure stage, suddenly releasing a large quantity of energy. Unlike the sample count rate, the damage count rate increases with the activity signal, indicating that after immersion, the microcracks continue to form before failure occurs due to the softening effect of the water on the sample. In addition, the final energy released is about 33% lower than that released in the dry state. In the saturated state, due to the continuous development of microcracks, the cumulative energy continues to increase after the compaction stage. The final cumulative energy of the failure is greater than those of the dry and 50% water-saturated samples because the static brittle failure is an overall failure mode. In addition, violent ejection only occurs on the surface of the free face during the failure of the sample through rockburst. It can be seen from Figure 4 that two shear cracks penetrate the water-saturated sample from top to bottom, while only one crack forms under the other two working conditions, indicating that the penetrating shear cracks need to release more and more energy.

## Analysis of characteristics of rockburst fragments

The rockburst fragments can be used to visually analyze the amount of energy released during the damage. According to the results of the true triaxial rockburst tests on samples with different water contents, statistical analysis of the scale characteristics of the

**TABLE 1 Rockburst debris scale statistics results.**

| Specimen number | Number of statistics | Length/Thickness | | | Length/Width | | | Width/Thickness | | |
|---|---|---|---|---|---|---|---|---|---|---|
| | | max | min | ave | max | min | ave | max | min | ave |
| GZ-3 | 167 | 14.56 | 2.29 | 6.57 | 3.28 | 1.02 | 1.53 | 9.80 | 1.40 | 4.41 |
| HS-2 | 122 | 13.51 | 2.31 | 5.79 | 3.07 | 1.06 | 1.55 | 8.25 | 1.37 | 3.73 |
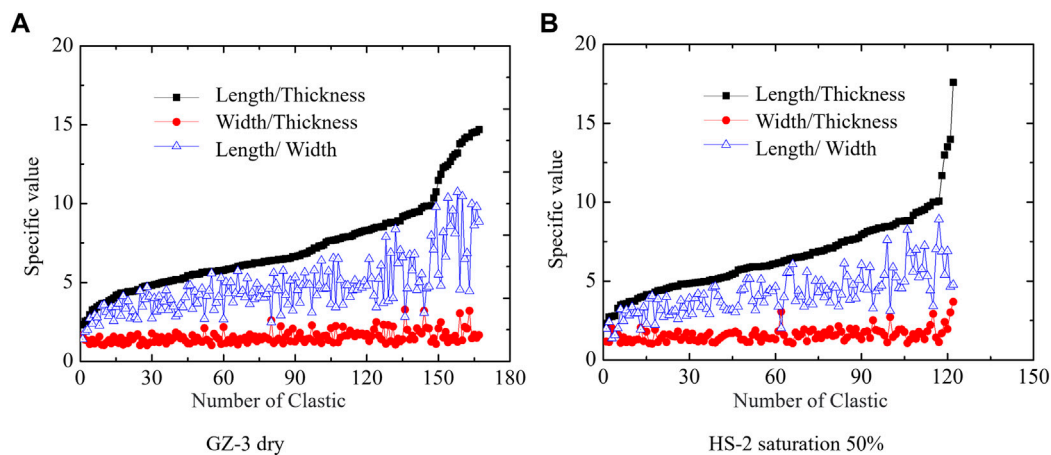


**FIGURE 9**
Rock explosion debris scale ratios of red sandstone with different water content. Panel **(A)** shows the dry rock samples, Panel **(B)** shows the 50% saturation rock samples.

rockburst fragments and the mass distribution characteristics of the different particle groups of samples GZ-3 and HS-2 with rockburst characteristics was conducted and the fractal dimension of the rockburst fragments was calculated based on the statistical results of the mass distribution characteristics.

## Scale and weight characteristics of rockburst fragments

Table 1 shows the statistical results of the scale of the rockburst fragments. The main statistical object used to obtain the scale distribution characteristics of the rockburst fragments of the samples with different water contents was the rockburst fragments with a maximum length of greater than 5 mm. The same standard was adopted to measure the maximum values of the three directions (i.e., the length, width, and thickness). A total of 167 rockburst fragments from the dry sample and 122 rockburst fragments from sample HS-2 (soaked in water for 8 h, water content of 1.18, 50% saturation) were analyzed. The longest rockburst fragments from samples GZ-3 and HS-2 were 63.88 mm and 75.16 mm, respectively; the widest rockburst fragments from samples GZ-3 and HS-2 were 58.74 mm and 66.46 mm,

respectively; and the thickest rockburst fragments from samples GZ-3 and HS-2 were 11.10 mm and 8 mm, respectively.

It can be seen from Figure 9 that as the length to thickness ratio increased, the oscillations of the width to thickness ratios of both specimens were small and the increasing trend was not obvious; while the oscillations of the length to width ratios were larger and both samples exhibited an increasing trend. The distributions of the three ratios were obvious, and each ratio exhibited significant variability, illustrating the characteristics of the two rock samples in the form of clastic plates.

Figure 10 shows the results after sieving and measuring the rockburst ejection fragments from the two samples according to four particle size ranges: particles (<0.075), fine (0.075–5), medium (5–30), and coarse (>30).

Figure 10A shows the rockburst ejection fragments from the dry sample, and it can be seen that most of the coarse fragments are flaky and irregular in shape, but there are a few blocky fragments, which are rectangular and small in scale. Most of the medium fragments are flakes, followed by blocks with irregular shapes. The rockburst ejection fragments from the 50% saturation sample are shown in Figure 10B. Most of the coarse and medium fragments are flakes, and there are fewer blocky fragments with irregular shapes. Based on the
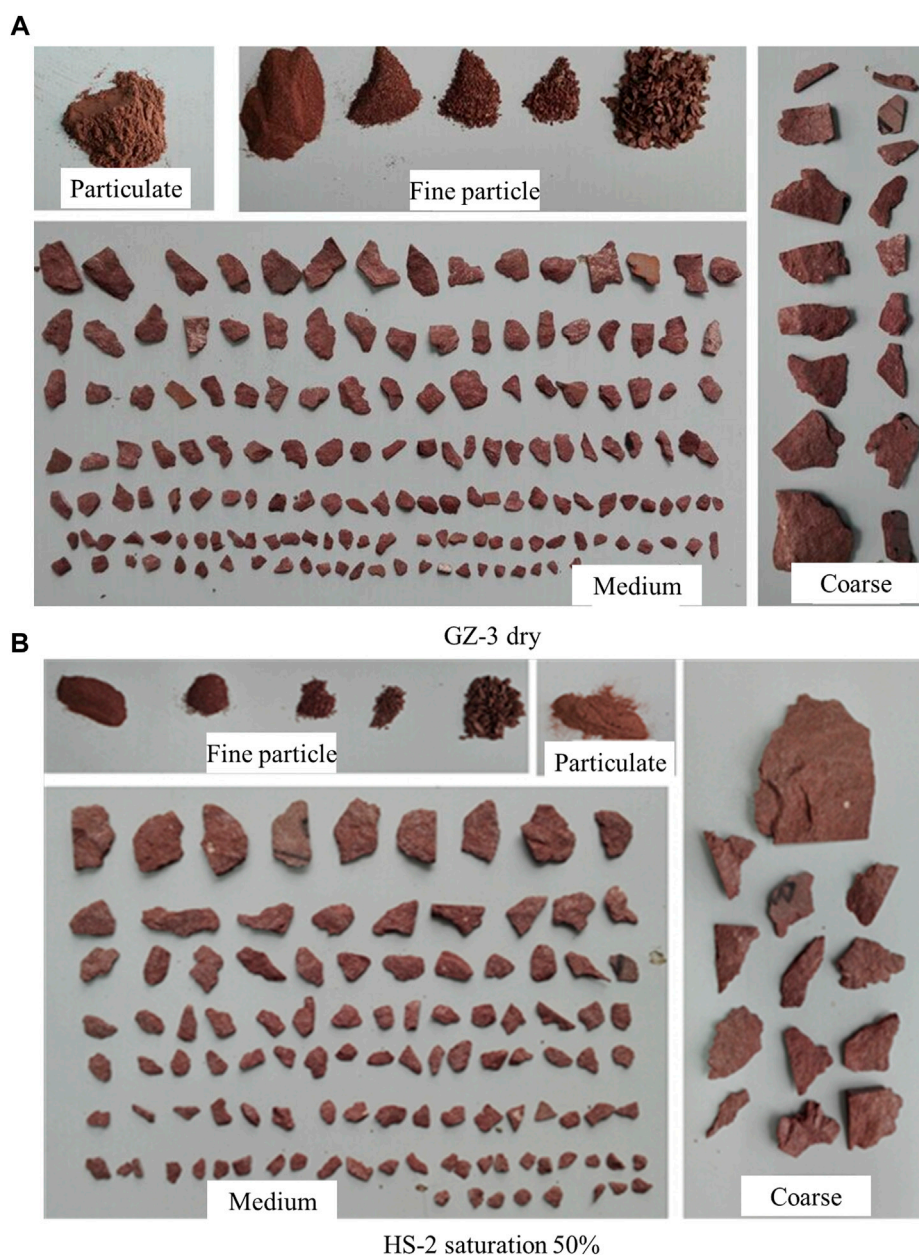
**FIGURE 10**
Sieving results of rock-burst ejected debris from red sandstone with different water content.

symmetrical weight, the total mass of the rockburst fragments from sample GZ-3 is significantly higher (nearly 40%) than that of the fragments from sample HS-2. The masses of the particles and fine particle fragments from sample GZ-3 account for 2.19% and 14.3% of the total mass of the fragments; while those from sample HS-2 account for 1.48% and 9.62%, respectively. Compared with sample HS-2, the particles and fine particles from sample GZ-3 not only have significantly higher masses, but they also account for significantly higher proportions.

Table 2 shows the masses of the rockburst ejection fragments with different particle sizes. As can be seen from Table 2, the mass of each fragment size category for the dry sample is higher than for the 50% saturation sample. In particular, the mass of the coarse particles is 37% higher. The rockburst effect on the dry rock is intense, and many fragments are ejected. Figure 11 shows the percentages of the rock fragments with different particle sizes. The coarse particles account for the largest percentage of the total mass (61.19–63.92%), while the particles account for the smallest percentage (1.48–2.19%).

TABLE 2 Different particle size debris mass.

| Classification | Particle diameter/mm | Weight/g | |
|---|---|---|---|
| | | GZ-3 | HS-2 |
| Micro- grained | <0.075 | 5.31 | 2.13 |
| Fine-grained | 0.075–5 | 35.03 | 13.89 |
| Medium-grained | 5–30 | 53.85 | 36.07 |
| Coarse-grained | >30 | 148.54 | 92.31 |
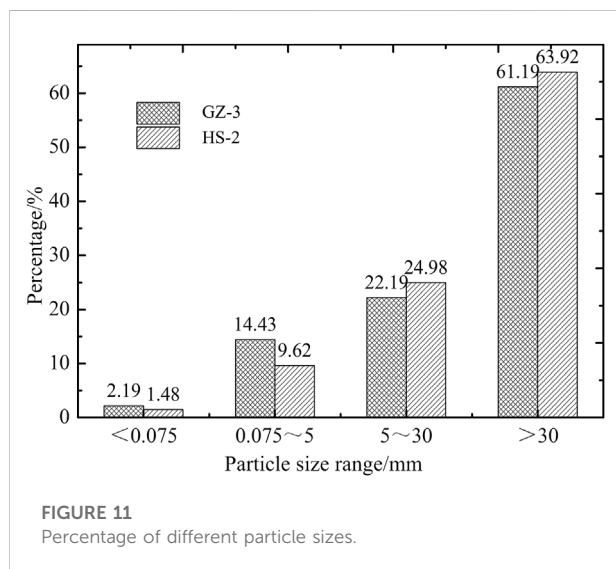


FIGURE 11
Percentage of different particle sizes.

It can be seen that the proportion of the coarse particles formed by the rockburst process is the highest.

The mass distribution characteristics of the rockburst fragments from the two samples with different water contents show that the formation of the rockburst fragments from the dry red sandstone sample consumed more energy than the formation of the fragments from the water-bearing sample, which indirectly demonstrates that as the soaking time and the water content increase, the energy provided by the sample during the rockburst decreases. This also reflects the degree by which the strength of the rockburst decreases.

## Energy consumption characteristics of rockburst fragments

Rockburst, which is a non-linear dynamic phenomenon, consumes a large amount of energy in the production of the fragments formed by fracturing and fragmentation under compression. The larger the area of the fragment is, the greater the energy consumed is. The fractal dimension can be used to relate the fracture fragmentation to the energy dissipation.

The basic definition of the fractal dimension is as follows:

$$N = CR^{-D} \qquad (9)$$

$R$ is the feature scale, N is the number of objects with a feature scale of greater than or equal to $R$, $C$ is the scale coefficient, and $D$ is the fractal dimension.

According to the above definition, the most basic expression of the fractal dimension and the mass-frequency relationship are as follows:

$$N = N_0 \left( R/R_{\max} \right)^{-D} \qquad (10)$$

$$N = N_0 \left( M/M_{\max} \right)^{-b} \qquad (11)$$

where $R$ is the characteristic size of the fragments, $R_{\max}$ is the maximum characteristic size of the fragments, $N$ is the number of fragments with a scale that is greater than or equal to the characteristic scale, $N_0$ is the number of fragments with a scale that is greater than or equal to the characteristic scale, $M$ is the mass of the debris, $M_{\max}$ is the maximum mass of the debris, $b$ is the mass-frequency distribution index, and $D$ is the fractal dimension.

By comparing the equations, it can be concluded that the fractal dimension $D$ and the mass-frequency distribution index b have the following relationship:

$$D = 3b \qquad (12)$$

The $b$ value can be obtained through fitting, and then, the fractal dimension $D$ can be calculated. The calculation results are presented in Table 3.

It can be seen from Table 3 that the fractal dimension values of the rockburst of the red sandstone with two different water contents are both greater than 2, which are similar to the fractal dimension values of rockburst debris of different lithologies obtained by Miao, (2008) and Miao, (2009). The rockburst debris formed during the rockburst consumes a large amount of energy, and the fractal dimension decreases as the water immersion time and water content increase. From the perspective of the fractal results, the energy consumed by the formation of the rockburst debris from the water-bearing red sandstone specimen soaked for a long time is smaller than that of the dry rock sample. This is conducive to the accumulation and instantaneous release of energy, leading to the formation of a large amount of rockburst debris and thus consuming a large amount of energy.

## Failure mechanism of red sandstone with different water contents and engineering construction understanding

The red sandstone used in this study was characterized by a high porosity, and its main components were clastic minerals, as well as clay minerals such as montmorillonite and kaolin.

**TABLE 3 *b*-value and *D*-value of different particle size debris.**

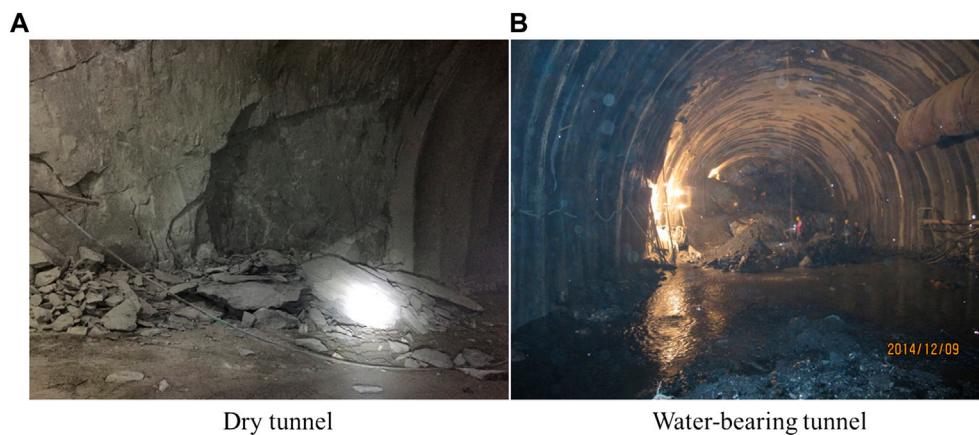| Number | Saturation (%) | *b* | *D* | Number of debris | $\sigma_1$/MPa |
|--------|---------------|-----|-----|------------------|-------|
| GZ-3 | 0 | 0.72 | 2.16 | 167 | 155.8 |
| HS-2 | 50% | 0.69 | 2.07 | 122 | 148.5 |



**FIGURE 12**
Rockburst characteristic effects in dry and water-bearing tunnel. Panel **(A)** is the dry tunnel, Panel **(B)** is the water-bearing tunnel.

Montmorillonite disintegrates and softens when exposed to water, which compresses the internal voids. In addition, kaolin particles flow under the action of pore water pressure, resulting in the redistribution of the particles and filling of the pores and cracks. Therefore, the porosity of the saturated sample was lower than that of the dry sample. In fracture mechanics and damage mechanics, the rockburst mechanism not only refers to the energy release speed but also to the stress concentration caused by the uneven stress on the microcracks, voids, and defect areas in the rock mass on the molecular scale in the area where the energy is concentrated and released. For the saturated sample with a low porosity, the impact of the stress concentration inside the specimen was greatly reduced, which was not conducive to the occurrence of rockburst. The compressive capacity of montmorillonite decreased after expansion, increasing the deformation during compression. The water content also reduced the friction coefficient between the clastic minerals, leading to increased deformation. The plastic deformation ratio of the specimens increased substantially, while the elastic energy decreased, so the failure phenomenon of the samples changed from plate crack failure during rockburst to static brittle failure as the water content increased.

According to the conclusions drawn from the contents of this paper, the water content has a large influence on the rockburst incubation process of red sandstone. Project construction process, the choice of appropriate rockburst prevention measures can effectively reduce the risk and intensity level of rockburst. In the construction of projects with similar surrounding rock conditions, rock bursts are reduced by increasing the water content of the surrounding rock mass. In the excavation, immediately after the palm face and excavation hole wall spray high-pressure water, and at the same time can use the gunhole and anchor borehole to inject water into the deep part of the rock body, through this way to improve the physical and mechanical properties of the surrounding rock body, change the damage form of the surrounding rock, reduce the elastic strain energy reserve capacity, so as to effectively reduce the risk of rockburst.

Figure 12 reflects the rockburst effect in a dry tunnel and a water-bearing tunnel with similar burial depths in both tunnels. After the excavation of dry tunnels, the rock explosion effect is significant, mostly manifested as stone projectile avalanche, avalanche distance and stone volume is inversely proportional relationship. There is almost no rock explosion in water-bearing tunnels, and the fractured surrounding rocks are collapsing under hydraulic conditions in a falling block. There is a large area of water in the tunnel for a long time, the water content of the rock in the tunnel is high, it is difficult to occur rock explosion phenomenon. According to these two

engineering examples can be seen, the actual project, the rock explosion phenomenon mainly exists in the burial depth and dry hard rock tunnel, high water content of the tunnel rock explosion effect is weak, rock explosion phenomenon is relatively small. According to the engineering examples, it can be seen that the relationship between the realistic tunnel rock burst effect and the water content coincides with the results of this experimental study.

## Conclusion

(1) Rockbursts are evident in the destruction of dry red sandstone. When the water content as increased, rock fragments were not ejected when the rock was damaged, indicating that the rockburst phenomenon was weakened. The failure modes of the dry red sandstone were mainly splitting, shearing, and rockburst. As the water content increased, the failure mode tended toward shear failure.

(2) The stress–strain curve of the dry rock exhibited obvious phase characteristics and had a relatively large slope. As the moisture content increases, the phase characteristics of the overall stress-strain curve diminish and the overall slope becomes smaller. In addition, the peak stress decreased as the water content increased.

(3) The acoustic emission activity of the dry sample was quiet in the compaction stage and the elastic deformation stage. The acoustic emission count rate suddenly increased, accompanied by a double peak value of the count rate, when the rock sample was damaged. The acoustic emission record of the 50% saturation sample was more active in the compaction stage than that of the dry sample, and the count rate increased in a stepwise manner near the time of the failure.

(4) The dry rock produced abundant rockburst debris with larger particle sizes, while the 50% saturation sample produced less debris with smaller particle sizes. The fractal dimension values for the rockburst of the red sandstone with different water contents were all greater

than 2, and the fractal dimensions of the rockburst of the samples with different water contents were similar.

## Data availability statement

The original contributions presented in the study are included in the article/Supplementary Material, further inquiries can be directed to the corresponding authors.

## Author contributions

KC, WZ, and YP were responsible for writing. YP and GZ were responsible for analysis of characteristics of rockburst fragments. YZ was responsible for analysis of test results. KC and YP were responsible for analyzing the destruction mechanism of red sandstone. WZ and GZ were responsible for review and proofreading.

## Conflict of interest

The authors of KC, WZ, and GZ are employed by Sichuan Communication Surveying and Design Institute Co., Ltd. The authors of YP is employed by Sichuan Huadi Construction Engineering Co., Ltd.

The remaining author declares that the research was conducted in the absence of any commercial or financial relationships that could be construed as a potential conflict of interest.

## Publisher's note

All claims expressed in this article are solely those of the authors and do not necessarily represent those of their affiliated organizations, or those of the publisher, the editors and the reviewers. Any product that may be evaluated in this article, or claim that may be made by its manufacturer, is not guaranteed or endorsed by the publisher.

## References

Afraei, S., Shahriar, K., and Madani, S. H. (2018). Statistical assessment of rockburst potential and contributions of considered predictor variables in the task. *Tunn. Undergr. Space Technol.* 72, 250–271. doi:10.1016/j.tust.2017.10.009

Cai, X., Cheng, C. Q., Zhou, Z. L., Konietzky, H., Song, Z. Y., and Wang, S. F. (2021). Rock mass watering for rock-burst prevention: Some thoughts on the mechanisms deduced from laboratory results. *Bull. Eng. Geol.* 80 (11), 8725–8743. doi:10.1007/S10064-021-02467-0

Chen, Y., Da, Q., Liang, W. Z., Xiao, P., Dai, B., and Zhao, G. (2022). Bagged ensemble of Gaussian process classifiers for assessing rockburst damage potential with an imbalanced dataset. *Math. (Basel).* 10 (18), 3382. doi:10.3390/MATH10183382

Du, F., Ma, J., Guo, X. F., Wang, T., Dong, X., Li, J., et al. (2022). Rockburst mechanism and the law of energy accumulation and release in mining

roadway: A case study. *Int. J. Coal Sci. Technol.* 9 (1), 67. doi:10.1007/S40789-022-00521-0

Feng, X. T., Xiao, Y. X., Feng, G. L., Yao, Z. B., Chen, B. R., Yang, C. X., et al. (2019). Study on the development process of rockbursts. *J. Chin. J. Rock Mech. Eng.* 38 (04), 649–673. doi:10.13722/j.cnki.jrme.2019.0103

Gong, F. Q., Wang, Y. L., and Luo, S. (2020). Rockburst proneness criteria for rock materials: Review and new insights. *J. Cent. South Univ.* 27 (10), 2793–2821. doi:10.1007/s11771-020-4511-y

He, M. C., Jia, X. N., Coli, M., Livi, E., and Sousa, L. (2012). Experimental study of rockbursts in underground quarrying of Carrara marble. *Int. J. Rock Mech. Min. Sci. (1997).* 52, 1–8. doi:10.1016/j.ijrmms.2012.02.006

He, Z. C., Gong, F. Q., and Luo, S. (2021). Evaluation of the rockburst proneness of red sandstone with prefabricated boreholes: An experimental study from the

energy storage perspective. *Geomat. Nat. Hazards Risk* 12 (1), 2117–2154. doi:10.1080/19475705.2021.1955754

Lan, T. W., Zhang, Z. J., Sun, J. W., Zhao, W., Zhang, M., Jia, W., et al. (2022). Regional prediction and prevention analysis of rockburst hazard based on the Gaussian process for binary classification. *Front. Earth Sci. (Lausanne).* 10. doi:10.3389/FEART.2022.959232

Li, Q., Ma, D., Zhang, Y. D., Liu, Y., and Ma, Y. (2022). Insights into controlling factors of pore structure and hydraulic properties of broken rock mass in a geothermal reservoir. *J. Lithosphere.* 5. doi:10.2113/2022/3887832

Li, T. B., Ma, C. C., Zhu, M. L., Meng, L., and Chen, G. (2017). Geomechanical types and mechanical analyses of rockbursts. *Eng. Geol.* 222, 72–83. doi:10.1016/j.enggeo.2017.03.011

Liu, D. Q., Ling, K., Li, D., He, M. C., Li, J. Y., Han, Z. J., et al. (2021). Evolution of anisotropy during sandstone rockburst process under double-faces unloading. *J. Cent. South Univ.* 28 (8), 2472–2484. doi:10.1007/S11771-021-4780-0

Liu, J. P., Feng, X. T., Yuan, H. L., Xu, S. d., and Sheng, Y. (2013). Studies on temporal and spatial variation of microseismic activities in a deep metal mine. *Int. J. Rock Mech. Min. Sci. (1997).* 60, 171–179. doi:10.1016/j.ijrmms.2012.12.022

Ma, Dan., Duan, H. Y., Zhang, J. X., Liu, X. W., and Li, Z. (2022b). Numerical simulation of water-silt inrush hazard of fault rock: A three-phase flow model. *Rock Mech. Rock Eng.* 55 (8), 5163–5182. doi:10.1007/s00603-022-02878-9

Ma, Dan., Duan, H. Y., and Zhang, J. X. (2022a). Solid grain migration on hydraulic properties of fault rocks in underground mining tunnel: Radial seepage experiments and verification of permeability prediction. *Tunn. Undergr. Space Technol.* 126, 104525. doi:10.1016/J.TUST.2022.104525

Mazaira, A., and Konicek, P. (2015). Intense rockburst impacts in deep underground construction and their prevention. *Can. Geotech. J.* 52 (10), 1426–1439. doi:10.1139/cgj-2014-0359

Miao, J. L. (2008). Compound energy dynamic mechanism of rockburst. *J. Metal. Mine.* 11, 16–24.

Miao, J. L. (2009). *Experimental analysis of energy characteristics of rock burst*. Beijing: D. China University of Mining and Technology.

Qu, H. L., Yang, L. H., Zhu, J. B., Chen, S., Li, B., and Li, B. (2022). A multi-index evaluation method for rockburst proneness of deep underground rock openings with attribute recognition model and its application. *Int. J. Rock Mech. Min. Sci. (1997).* 159, 105225. doi:10.1016/J.IJRMMS.2022.105225

Su, G. S., Feng, X. T., Wang, J. H., Jiang, J., and Hu, L. (2017a). Experimental study of remotely triggered rockburst induced by a tunnel axial dynamic disturbance under true-triaxial conditions. *Rock Mech. Rock Eng.* 50 (8), 2207–2226. doi:10.1007/s00603-017-1218-y

Su, G. S., Zhai, S. B., Jiang, J. Q., Zhang, G., and Yan, L. (2017b). Influence of radial stress gradient on strainbursts: An experimental study. *Rock Mech. Rock Eng.* 50 (10), 2659–2676. doi:10.1007/s00603-017-1266-3

Sun, F. Y., Guo, J. Q., Fan, J. Q., and Liu, X. (2022). Experimental study on rockburst fragment characteristic of granite under different loading rates in true triaxial condition. *Front. Earth Sci. (Lausanne).* 10. doi:10.3389/FEART.2022.995143

Suorineni, F. T., Hebblewhite, B., and Saydam, S. (2014). Geomechanics challenges of contemporary deep mining: A suggested model for increasing future mining safety and productivity. *J. JS Afr. Inst. Min. Metall.* 114 (12), 1023–1032.

Xia, Z. Z., Mao, J. Y., and He, Y. (2022). Rockburst intensity prediction in underground buildings based on improved spectral clustering algorithm. *Front. Earth Sci. (Lausanne).* 10. doi:10.3389/FEART.2022.948626

Xu, L., Gong, F. Q., and Liu, Z. X. (2022). Experiments on rockburst proneness of pre-heated granite at different temperatures: Insights from energy storage, dissipation and surplus. *J. Rock Mech. Geotechnical Eng.* 14 (5), 1343–1355. doi:10.1016/J.JRMGE.2021.08.004

Yan, S. H., Zhang, Y. B., Liu, X. X., and Liu, R. (2022). Rock burst intensity classification prediction model based on a bayesian hyperparameter optimization support vector machine. *Math. (Basel).* 10 (18), 3276. doi:10.3390/MATH10183276

Yang, J. J., Gong, F. Q., Liu, D. Q., and Liu, Z. X. (2020). Experimental study on the influence of specimen shape on rockburst proneness of red sandstone. *Shock Vib.* 2020 (9), 1–17. doi:10.1155/2020/4182861

Zhang, Y., Feng, X. T., Yang, C. X., Han, Q., Wang, Z., and Kong, R. (2021). Evaluation method of rock brittleness under true triaxial stress states based on pre-peak deformation characteristic and post-peak energy evolution. *Rock Mech. Rock Eng.* 54, 1277–1291. doi:10.1007/S00603-020-02330-W

Zhang, Y., Feng, X. T., Yang, C. X., Zhang, X., Sharifzadeh, M., and Wang, Z. (2019c). Fracturing evolution analysis of Beishan granite under true triaxial compression based on acoustic emission and strain energy. *Int. J. Rock Mech. Min. Sci. (1997).* 117, 150–161. doi:10.1016/j.ijrmms.2019.03.029

Zhang, Y., Feng, X. T., Zhang, X. W., Wang, Z., Sharifzadeh, M., and Yang, C. (2019a). A novel application of strain energy for fracturing process analysis of hard rock under true triaxial compression. *Rock Mech. Rock Eng.* 52, 4257–4272. doi:10.1007/s00603-019-01868-8

Zhang, Y., Feng, X. T., Zhang, X. W., Wang, Z., Sharifzadeh, M., Yang, C., et al. (2019b). Strain energy evolution characteristics and mechanisms of hard rocks under true triaxial compression. *Eng. Geol.* 228, 105222–105281. doi:10.1016/j.enggeo.2019.105222

Zhao, X. G., and Cai, M. (2014). Influence of specimen height-to-width ratio on the strainburst characteristics of Tianhu granite under true-triaxial unloading conditions. *Can. Geotech. J.* 52 (7), 890–902. doi:10.1139/cgj-2014-0355

Zhao, X. G., Wang, J., Cai, M., Cheng, C., Ma, L. K., Su, R., et al. (2014). Influence of unloading rate on the strainburst character-istics of Beishan granite under true-triaxial unloading conditions. *Rock Mech. Rock Eng.* 47 (2), 467–483. doi:10.1007/s00603-013-0443-2

Zhao, Y. X., and Jiang, Y. D. (2010). Acoustic emission and thermal infrared precursors associated with bump-prone coal failure. *Int. J. Coal Geol.* 83 (1), 11–20. doi:10.1016/j.coal.2010.04.001

Zhou, J., Li, X., and Mitri, H. S. (2018). Evaluation method of rockburst: State-of-the-art literature review. *Tunn. Undergr. Space Technol.* 81, 632–659. doi:10.1016/j.tust.2018.08.029

# Stability analysis of rock slopes using the interface contact model and strength reduction method

Rui Yang[1], JiaCheng Li[1], Xue Bai[1] and Cheng Zeng[2]*

[1]Key Laboratory of Urban Underground Engineering of Ministry of Education, Beijing Jiaotong University, Beijing, China, [2]Discipline of Civil, Surveying and Environmental Engineering, Priority Research Centre for Geotechnical Science and Engineering, The University of Newcastle, Callaghan, NSW, Australia

The assessment of rock slope stability is usually controlled by the presence of discontinuities. The block theory is an established method in practical engineering to predict the stability of rock slopes. A maximum of two discontinuity planes are considered in the application of the block theory. It would lead to inaccurate prediction of slopes with multiple discontinuity planes. A novel method for estimating the safety margin of rock slopes is proposed, which is capable of considering the contribution of all discontinuities to the stability problem. The discontinuity planes are simulated by an interface contact model within the theoretical framework of the finite difference method. The factor of safety is obtained by the strength reduction method. The failure criteria of rock slopes are also discussed. The proposed model can simulate discontinuous planes in a more realistic manner and thus is more effective in engineering practice. To demonstrate the effectiveness of the proposed model, several numerical examples are presented, which showcase its superiority for predicting the stability of blocks composed of multiple discontinuities. Several numerical examples are analyzed to confirm the effectiveness of the proposed model and its superiority in stability prediction of blocks formed by multiple discontinuities.

## 1 Introduction

Rock slope stability is generally governed by the presence of discontinuities which developed in rocks. The combination of these discontinuities may result in a set of removable key blocks that significantly decrease the overall stability of slopes. It is vital to develop an effective method for evaluating the stability of key blocks for safe rock slope excavation and construction.

Extensive research studies have been conducted to investigate the stability of rock slopes. Goodman and Shi (1985) proposed the block theory to analyze the stability of the rock wedge, and it has been widely adopted in engineering because of its simplicity of concept. Chen (2004) developed a theoretical method for assessing the stability of the rock wedge based on limit equilibrium analysis. Ma et al. (2019) explored the applicability of the block theory to the wedge probability analysis by considering the variabilities of the geometric and rock properties of blocks. Deng (2021) established a spatial model of rock slopes based on the characteristics of discontinuities and slope surfaces. However, these block theory-based methods have some limitations for a general rock block formed by multiple discontinuities. The factor of safety and failure modes can be inaccurately estimated when these methods are adopted for the stability of rock blocks formed by multiple structural planes. Jiang and Zhou

FIGURE 1
Components of the bonded interface constitutive model.
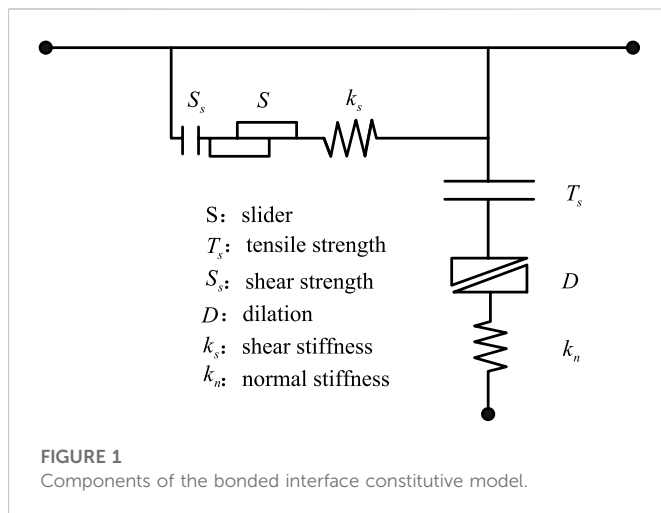
(2017) proposed a rigorous solution based on the limit equilibrium method (LEM) and kinematic analysis for the stability of polyhedral rock blocks formed by multiple discontinuities. Nevertheless, when analyzing the stability of a rock block, LEM does not completely take into account the shear forces acting on the sliding surfaces of either side of the rock block.

Zienkiewicz et al. (1975) first applied the strength reduction method (SRM) to evaluate the slope stability. Since then, some researchers have employed the SRM with finite element methods (FEMs) and finite difference methods (FDMs) to analyze the stability of slopes. The factor of safety (FS) is comparable with the result from LEM as found by Ugai and Leshchinsky (1995), Griffiths and Lane (1999), Zheng et al. (2007), and Griffiths and Marquez (2007). In comparison to the LEM, the SRM has a number of advantages including the abilities to model complex geometric and boundary conditions, the nonlinear behavior of rocks and soils, and the progressive collapse of slopes (Wei et al., 2009; Xi et al., 2014; Zhao et al., 2019). It is noted, however, most of the applications are for soil slopes. The applications of SRM to rock slopes are rare with a few exceptions including Jiang et al. (2015) and Lu et al. (2020). The existing rock slope applications of SRM involve modeling the discontinuities based on solid elements neglecting the significant disparity in the physical and mechanical characteristics of intact rocks and discontinuities. In addition, the failure criterion of the soil slope is directly applied to the rock slope despite the distinction failure mode of soil slopes and rock slopes.

In this paper, an FDM interface contact model developed for rock slopes is first introduced. The proposed model is capable of modelling discontinuities by interface contact elements, and it is reasonable considering the contribution of multiple discontinuities. The shear reduction approach is adopted to assess the stability of rock slopes. Then, the failure criterion of rock slopes is discussed. To validate the reliability of the proposed method, four typical examples are analyzed by FlAC³D. The effects of the stiffness of interfaces, mesh size, and failure criteria on the FS and computation time are also investigated. Moreover, the proposed method is applied in the stability analysis of the right dam abutment of the Yinpan Hydropower Station in Wulong County, Chongqing Province, China. The results show that the proposed method is effective in assessing multiple structural planes.



FIGURE 2
Three-dimensional mesh discretization for rock slopes with a symmetrical wedge. **(A)** Symmetrical wedge **(B)** Rock slope.
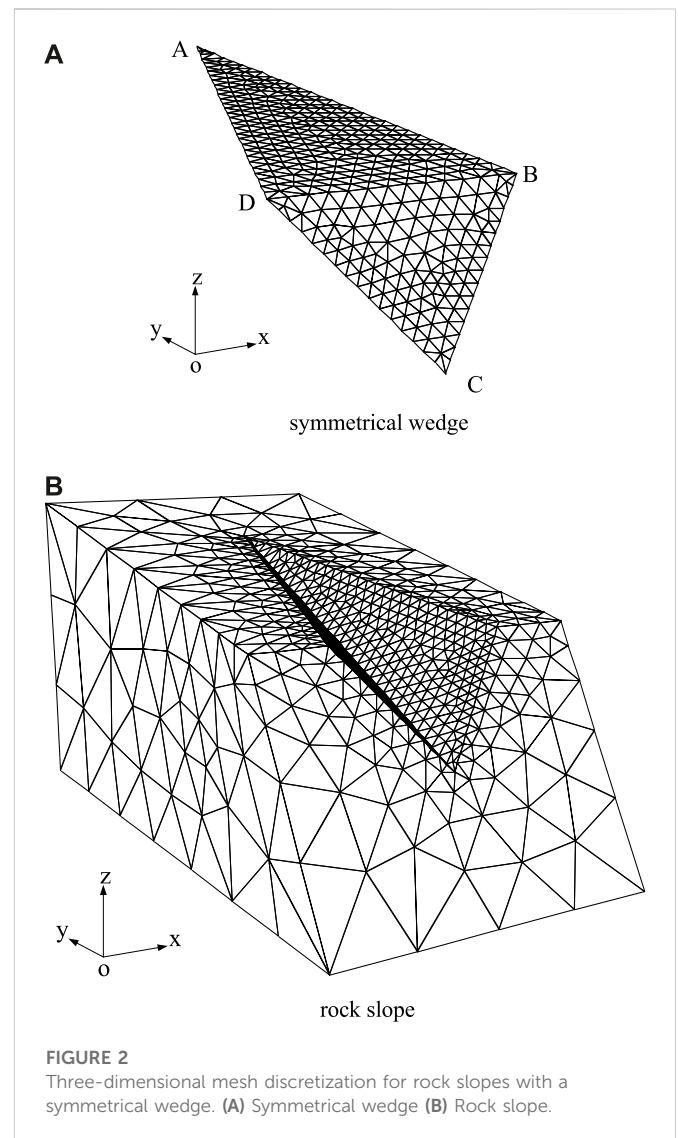
## 2 Methodology

### 2.1 Constitutive relation of the interface contact model

Advanced numerical models provide two approaches for modelling rock discontinuities: zero-thickness interface contact elements to facilitate the transmission of both shear and normal stress from the rock to the discontinuity structure planes and solid elements with finite depth. The interface contact elements in FlAC³D with zero thickness are used to model the discontinuities in rock slopes.

Figure 1 illustrates the constitutive model of the interface elements. The Coulomb sliding law (Itasca 2000) is used to characterize the shear strength of the interface, which is represented by a linear Coulomb shear-strength criterion, normal and shear stiffnesses, tensile and shear bond strengths, and a dilation angle. The dilation angle is assumed to be zero in this paper, and a non-associate flow rule is used, which limits the shear force acting at an interface node and causes an increase in effective normal force on the target face after the shear-strength limit is reached.

**TABLE 1 Geometrical and material parameters of example 1.**

| Surface | Dip direction/(°) | Dip angle/(°) | Shear strength | |
|---|---|---|---|---|
| | | | $c$ (kPa) | $\phi$ (°) |
| Discontinuity ADC | 115 | 45 | 20 | 20 |
| Discontinuity ABC | 245 | 45 | 20 | 20 |
| Slope top surface | 180 | 10 | — | — |
| Slope surface | 180 | 45 | — | — |

**TABLE 2 Geometrical and material parameters of example 2.**

| Surface | Dip direction/(°) | Dip angle/(°) | Shear strength | |
|---|---|---|---|---|
| | | | $c$ (kPa) | $\phi$ (°) |
| Discontinuity ADC | 120 | 40 | 50 | 30 |
| Discontinuity ABC | 240 | 60 | 50 | 30 |
| Slope upper surface | 180 | 0 | — | — |
| Slope surface | 180 | 60 | — | — |



**FIGURE 3**
Three-dimensional mesh discretization for the asymmetrical wedge. 3) Example 3
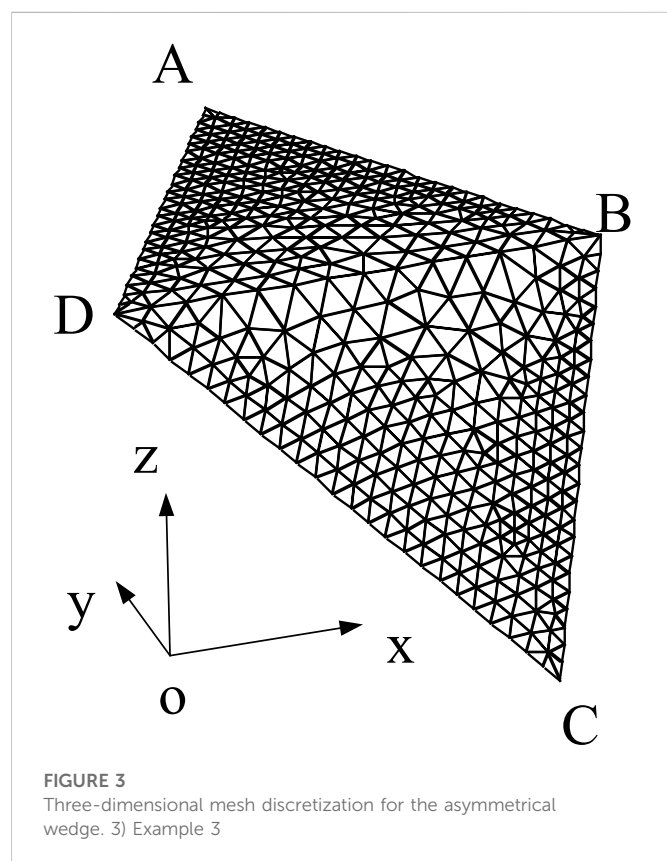
The absolute normal penetration and the relative shear velocity of every interface node and its corresponding target face are determined at every time step. The interface constitutive model utilizes these values to generate a normal force and a shear-force vector. They are calculated at time $t + \Delta t$ as follows:

$$\begin{cases} F_n^{(t+\Delta t)} = k_n u_n A + \sigma_n A, \\ F_{si}^{(t+\Delta t)} = F_{si}^t + k_n \Delta u_{si}^{(t+\Delta t/2)} A + \sigma_{si} A, \end{cases} \quad (1)$$

where $F_n^{(t+\Delta t)}$ and $F_{si}^{(t+\Delta t)}$ are the normal force and shear force at time $t + \Delta t$, respectively; $k_n$ and $k_s$ denote the normal and shear stiffnesses, respectively; $u_n$ is the absolute normal penetration of the interface node into the target face; $\Delta u_{si}$ is the incremental relative shear displacement; $\sigma_n$ is the additional normal stress that is generated as a result of interface stress initialization; $\sigma_{si}$ is the extra shear stress that results from the interface stress initialization; and A is an area that is associated with the node in the contact model.

The Coulomb shear-strength criterion restricts the magnitude of the shear force according to a specific equation.

$$F_{s\,\max} = cA + \tan\varphi\left(F_n - pA\right), \quad (2)$$

where $F_{s\,\max}$ is the maximum shear force, $c$ is the cohesion along the interface, $\varphi$ is the friction angle of the interface surface, and $p$ is the pore pressure (interpolated from the target face). The sliding along the interface shall occur when the criterion $|F_s| \geq F_{s\,\max}$ is fulfilled. The shear force should be adjusted to the maximum shear stress ($|F_s| = F_{s\,\max}$), and the direction remains unchanged.

If either the shear stress is greater than the shear strength or the tensile effective normal stress is more than the normal strength, the bond will be broken. Then the normal force and shear force turn to be zero. The interface elements can well simulate the deformation and stress characteristics of the discontinuous plane.

The intercalation capacity of two contact surfaces is determined by normal stiffness $k_n$ and shear stiffness $k_s$. The analysis is significantly influenced by the interface shear and normal stiffnesses. The bigger the stiffness, the more difficult it is to penetrate between two contact surfaces. Utilizing stiffnesses of a high magnitude will result in a slow convergence rate of the solution (Rosso, 1976; Bandis et al., 1983). The equivalent stiffness proposed by Fossum (1985) for a zone in the normal direction can be determined as follows:

**TABLE 3** Geometrical and material parameters of example 3.

| Surface | Dip direction/(°) | Dip angle/(°) | Shear strength | |
|---|---|---|---|---|
| | | | $c$ (kPa) | $\phi$ (°) |
| Discontinuity ABED | 225 | 50 | 150 | 30 |
| Discontinuity ACFD | 150 | 45 | 150 | 30 |
| Discontinuity ABC | 180 | 30 | 20 | 30 |
| Slope upper surface | 180 | 0 | — | — |
| Slope surface | 180 | 60 | — | — |



**A**

upper slope surface 3

discontinuity plane 1

discontinuity plane 2

discontinuty plane 5

slope face 4

**B**

Geometry of a typical movable block forming by three discontinuities

vertical view of the movable block

**FIGURE 4**
Three-dimensional model for example 3 **(A)** Geometry of a typical moveable block forming by three discontinuities. **(B)** Vertical view of the movable block.

$$k_e = \frac{K + 4G/3}{\Delta z_{\min}}, \tag{3}$$



**FIGURE 5**
Effect of the cohesion of discontinuities ABED and ACFD on slope stability analysis. 4) Example 4

where $k_e$ is the equivalent stiffness; $K$ and $G$ are the bulk and shear moduli, respectively; and $\Delta z_{\min}$ is the smallest width in the normal direction of an adjoining zone. To join two sub-grids, the interface must be utilized with the higher shear and normal stiffnesses than the equivalent stiffness ($k_s$ and $k_n$ higher than $k_e$) to prevent any movement.

## 2.2 Strength reduction method

The strength reduction finite difference method is proposed to predict the stability of a rock slope. The SRM is intended to reduce the cohesion $c_j$ and internal friction angle $\tan \phi_j$ of rock discontinuities progressively until the critical failure state, as described in the next section, is reached. The shear strength parameters $c_j'$ and $\phi_j'$, which have been factored, are represented by

$$c_j' = \frac{c_j}{SRF}, \tag{4}$$

$$\phi_j' = \arctan\left(\frac{\tan \phi_j}{SRF}\right), \tag{5}$$

where $SRF$ is the strength reduction factor. When the critical state is determined, the factor of the safety of the rock slope is the same as $SRF$

**A** Geometry of a typical movable block forming by three discontinuities

**B** vertical view of the movable block

**FIGURE 6**
Three-dimensional model for example 4. **(A)** Geometry of a typical movable block forming by three discontinuities. **(B)** Vertical view of the movable block.

2) The non-convergence of a numeral model computation.
3) Plastic shear strain runs through the slope.

Using the displacement mutation of specific points as failure criteria is not objective enough due to specific points' selection and the determination of whether the displacement mutation of these points depends on subjective judgment. The convergence speed of a numeral model is influenced by grid partitioning. The occurrence of a plastic zone stretching from the bottom to the top of a slope does not necessarily signify slope failure.

Research studies on the failure criteria of rock slopes are rare. Most of the researchers adopted failure criteria for soil slopes to obtain the *FS* of rock slopes. The assessment of *FS* based on soil slope failure criteria could give a misleading conclusion regarding the rock slope stability. It is assumed that the critical state is reached when all the nodes of interface contact elements are either sliding or opening, as the rock slope stability is generally governed by multiple structural planes. The new failure criteria are more effective in depicting the failure behavior of a rock mass.

## 3 Examples

The stability assessment of a rock slope that includes either a wedge formed by two discontinuities or a pentahedron formed by three discontinuities is of great interest in rock slope engineering. To verify the effectiveness of the proposed method, four rock slope examples are analyzed by the traditional method and proposed method. The analysis is carried out using the high-performance laptop with Intel(R) Core(TM) i7-10875H CPU @ 2.30 GHz. The movable block in examples 1 and 2 is formed by two discontinuities, while that in examples 3 and 4 is formed by three discontinuities.

1) Example 1: Symmetrical wedge

The first problem deals with a symmetrical wedge with two discontinuities, as illustrated in Figure 2. The rock slope surface of this wedge has an inclination of 45° with a dip direction of 185°, while the upper surface of slope dips has an inclination of 10° with a dip direction of 180°. The wedge has a height of 64.89 m and is intersected by two discontinuities (i.e., ADC and ABC). Details of discontinuities for geometry and geotechnical properties are given in Table 1. The unit weight is $\gamma = 26kN/m^3$, the bulk modulus is $K = 10$ GPa, and the elastic modulus is $G = 3$ GPa. The discontinuities are modelled by interface contact elements comprising 456 nodes and 818 elements.

and *FS* = *SRF*. Therefore, the failure criteria directly influence the value of *FS*.

## 2.3 Failure criteria in strength reduction for rock slopes

The failure criteria for evaluating if a soil slope has reached its critical state have been widely discussed. The most widely used failure criteria for soil slopes are presented as follows.

1) Strain and displacement mutation of specific points.

**TABLE 4 Geometrical and material parameters of example 4.**

| Surface | Dip direction/(°) | Dip angle/(°) | Shear strength | |
|---|---|---|---|---|
| | | | $c$ (kPa) | $\phi$ (°) |
| Discontinuity ABED | 235 | 45 | 20 | 30 |
| Discontinuity ACFD | 105 | 45 | 20 | 30 |
| Discontinuity ABC | 180 | 45 | 20 | 30 |
| Slope upper surface | 180 | 0 | — | — |
| Slope surface | 180 | 60 | — | — |

**FIGURE 7**
Effect of the dip angle of discontinuity ABC on slope stability analysis.
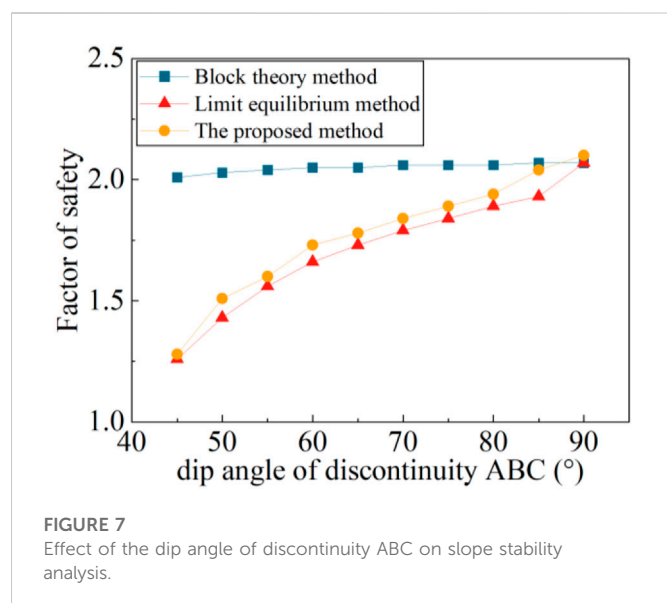
**TABLE 5 Effects of** $k_s, k_n$ **on the** *FS* **and computation time for wedges.**

| Symmetrical wedge | | | Asymmetrical wedge | | |
|---|---|---|---|---|---|
| $k_s, k_n$ | FS | Time step | $k_s, k_n$ | FS | Time step |
| $k_e$ | 1.310 | 4921 | $k_e$ | 1.643 | 9065 |
| 10 $k_e$ | 1.316 | 8595 | 10 $k_e$ | 1.644 | 30,856 |
| 50 $k_e$ | 1.315 | 16,090 | 50 $k_e$ | 1.642 | 46,141 |
| 80 $k_e$ | 1.314 | 19,219 | 80 $k_e$ | 1.642 | 69,341 |
| 100 $k_e$ | 1.314 | 20,587 | 100 $k_e$ | 1.642 | 79,765 |

The obtained rock mass consisted of 1161 nodes and 4508 elements. The tetrahedron mesh of the symmetrical wedge is shown in Figure 2.

Through the procedure of shear strength reduction on the discontinuities ADC and ABC, the *FS* can be determined. When *SRF* attains 1.316, all the nodes of interface contact elements are either sliding or opening and the limit failure state is reached. For this example, the *FS* is 1.316. For comparison, the block theory is also undertaken to evaluate the stability of this example. According to the principles of the block theory, the movable block is determined to be sliding along the juncture where two sliding surfaces intersect. The

block theory derived closed-form equations for this failure mode to calculate the *FS*. The *FS* has an exact value of 1.293. It was found that *FS* estimated by the proposed method is consistent with the block theory, which is proved to be an accurate method for evaluating stability of symmetrical wedges. Thus, the rationality and effectiveness of the proposed method have been demonstrated.

2) Example 2: Asymmetrical wedge

Example 2 consists of an asymmetrical wedge with two discontinuities ADC and ABC. The shear strength and geometric features of the example are provided in Table 2. In this case, the rock unit weight is $\gamma = 26kN/m^3$, the bulk modulus is $K = 10$ GPa, and the elastic modulus is $G = 3$ GPa. FLAC$^{3D}$ is employed to develop a numerical model of the rock slope. Figure 3 shows the tetrahedron mesh of the asymmetrical wedge with 256 nodes and 451 interface contact elements The obtained rock mass consisted of 632 nodes and 2350 elements. Both the proposed method and block theory-based method are employed to evaluate the stability of this example. The *FS* obtained by the proposed method is 1.644, which is very close to the result (*FS*=1.640) estimated by the block theory. The effectiveness of the proposed method is further confirmed.

Example 3 is a rock slope with a movable block formed by three discontinuity surfaces (ABED, ACFD, and ABC) as shown in Figure 3A. In this case, the volume of the block is 6076 m$^3$. The area of structural surfaces ABED, ACFD, and ABC is 573 m$^2$, 878 m$^2$, and 81 m$^2$, respectively. The strengths and orientations of the three discontinuities are given in Table 3. The rock unit weight is $\gamma = 26kN/m^3$, the bulk modulus is $K = 10$ GPa, and the elastic modulus is $G = 3$ GPa. Discontinuities are simulated using interface contact elements within the theoretical framework of the finite difference method. The tetrahedron mesh of the rock block is shown in Figure 3B. The mesh of the interface comprised 69 nodes and 106 elements.

The *FS* for this example is obtained by the proposed method and block theory. When *SRM* is equal to 2.875, as shown in Figure 4, all the nodes of interface contact elements are either sliding or opening and the limit failure state is reached. For this problem, the *FS* is 2.875. The sliding mode of this example determined by the block theory is the single plane sliding (along ABC). In the estimation, the block theory only considers the normal and shear stresses of the sliding surface, ignoring the influence of other discontinuities. The *FS* estimated by the block theory is 1.156. It is shown that the block theory method seriously underestimates the rock slope's stability.

**TABLE 6 Effects of element size of interface contact elements on the** *FS***.**

| Symmetrical wedge | | | | Asymmetrical wedge | | | |
|---|---|---|---|---|---|---|---|
| Element size | Number of elements | FS | Computational cost (s) | Element size | Number of elements | FS | Computational cost (s) |
| $l_1/50$ | 1562 | 1.320 | 170 | $l_2/50$ | 2321 | 1.642 | 240 |
| $l_1/40$ | 1098 | 1.315 | 106 | $l_2/40$ | 1754 | 1.640 | 210 |
| $l_1/30$ | 818 | 1.316 | 48 | $l_2/30$ | 912 | 1.640 | 60 |
| $l_1/20$ | 308 | 1.317 | 15 | $l_2/20$ | 451 | 1.644 | 25 |

Notes: $l_1$ and $l_2$ are the lengths of intersection for symmetrical and asymmetrical wedges, respectively.
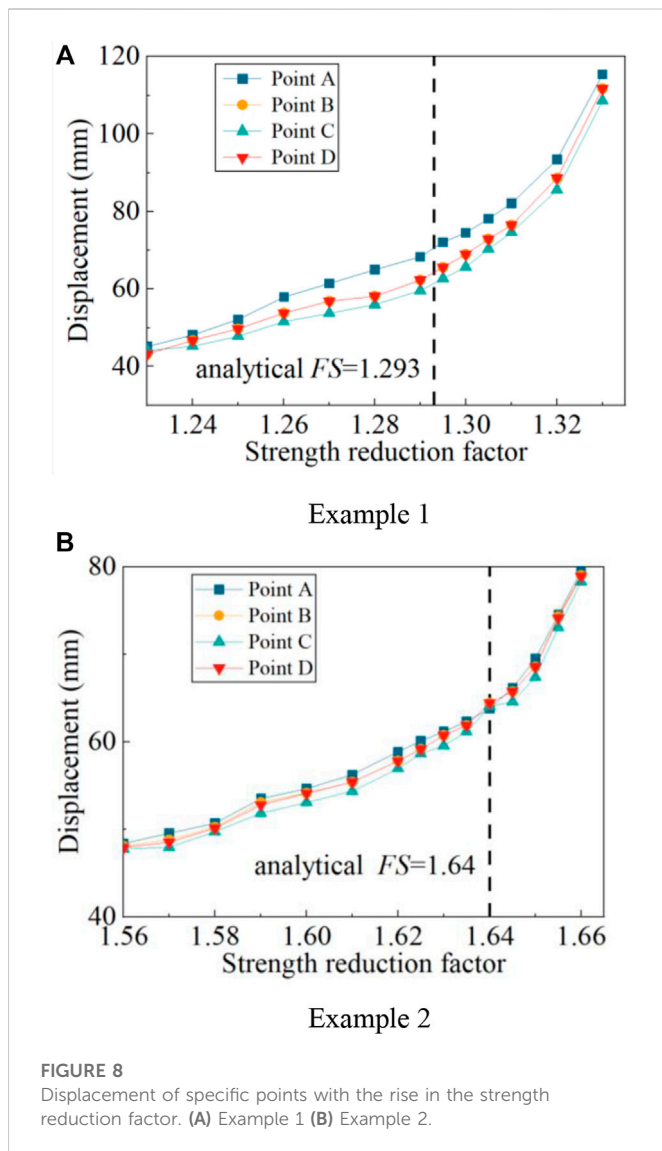
FIGURE 8
Displacement of specific points with the rise in the strength reduction factor. **(A)** Example 1 **(B)** Example 2.



FIGURE 9
Percentage of failure nodes with the increase in the strength reduction factor. **(A)** Example 1 **(B)** Example 2.

To investigate the influence of discontinuities ABED and ACFD on the slope stability assessment, the $c$ of these two planes is varied in the range of 0–150 kPa, while all other parameters remain unchanged as described in this section. For comparison, the proposed method and block theory method are carried out to estimate $FS$. The obtained results from both methods pertaining to $c$ of discontinuities ABED and ACFD are demonstrated in Figure 5. It is evident that discontinuities ABED and ACFD have significant impact on the slope stability. The contribution of these structural planes is omitted by the block theory which will result in the underestimation of $FS$. The proposed method which considers the shear strength on all discontinuities would yield accurate results for rock slopes controlled by three discontinuities.

Figure 6 shows an example of a rock slope with three discontinuities developed in the rock mass. Figure 6A exhibits a tetrahedron mesh of the pentahedron. The mesh of the interface comprised 116 nodes and 172 elements. The shear strength characteristics and geometry of discontinuities are listed in Table 4. In this case, the potentially unstable block formed by the spatial intersection of discontinuities ABED, ACFD, and ABC has a volume
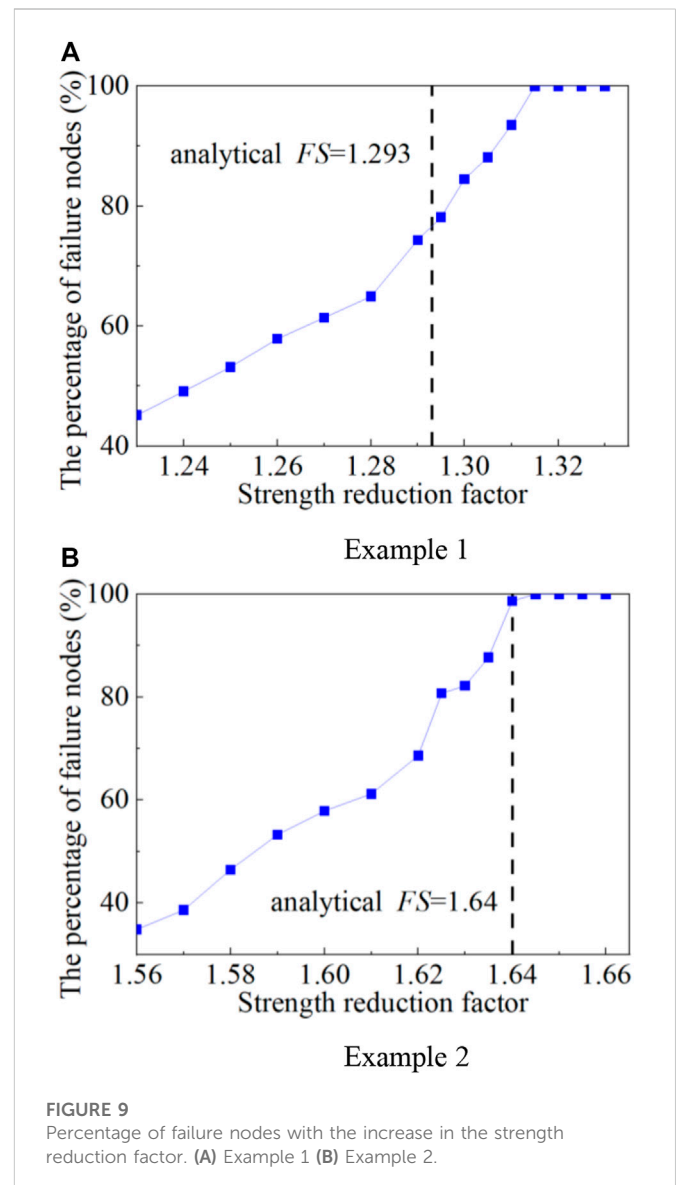
of 10,870 m³. The area of structural surfaces ABED, ACFD, and ABC is 683 m², 580 m², and 764 m², respectively.

For comparison and validation, the block theory, the three-dimensional LEM implemented using 3D slope software, and the proposed method are adopted to analyze the stability of the example rock slope. The $FS$ of 1.28 obtained by the proposed method shows good agreement with that predicted by LEM ($FS=1.26$). Within the framework of the block theory, it is essential to first evaluate the failure mode. The example slope sliding direction is congruent with the junction of the two failure planes (ABED and ACFD) on the horizontal projection. The $FS$ obtained from the block theory only considers normal and shear stresses of the two sliding surfaces, ignoring the influence of the tension crack. The $FS$ is found to be 2.01, which overestimated the stability of the slope.

The effect of the tension crack (i.e., discontinuity ABC) on the stability of the example slope has been discussed by varying the dip angle. As depicted in Figure 7, when the tension crack dip angle is 90°, the difference in the $FS$ obtained by the proposed method, block theory, and LEM is negligible. This indicates that the tension crack
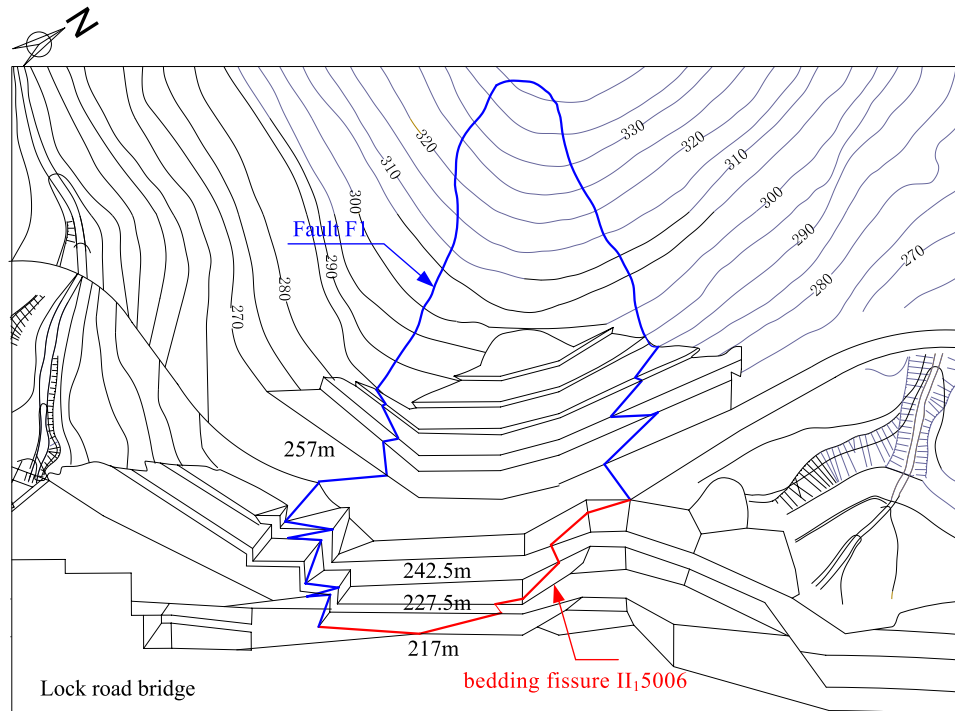
**FIGURE 10**
Plan layout of excavation on the right dam slope.

barely influences the analysis of slope when the dip angle is equal to 90°. It can also be found from Figure 7 that the *FS* calculated by the block theory increases slightly with the increasing tension crack dip angle. The varied volume of movable blocks and areas of sliding surfaces leads to minor difference in *FS* for different dip angles. The difference between the proposed method and block theory is increased with the decreasing tension crack dip angle. When the dip angle is equal to 45°, the relative difference in *FS* between the proposed method and block theory is 36.5%. The block theory can lead to inaccurate outcomes due to ignoring the tension crack of unstable slopes, thus overestimating the stability of slopes. The proposed method and LEM can consider the roles of all the structural planes in the stability problem, which provides a new and effective way of solving the stability problem of movable blocks. The *FS* calculated by these two methods is very close. To accurately assess the stability of rock slopes, the shear strength of all discontinuities should be considered, and their unfavorable effects on the rock stability assessment should also be reflected for calculating the *FS*.

# 4 Discussion

## 4.1 Effects of shear and normal stiffnesses on slope stability analysis

The discontinuities developed in rocks are simulated by interface contact elements. To analyze the impact of normal and shear stiffnesses on the stability of a slope, the symmetrical wedge and asymmetrical wedge are adopted and analyzed. The bulk and shear moduli of the rock

mass were set at $K = 10$ GPa and $G = 3$ GPa, respectively, while $k_s$ and $k_n$ varied in the range of $k_e \sim 100k_e$. The effects of stiffness on the *FS* and time steps for estimating the stability of the wedges are shown in Table 5.
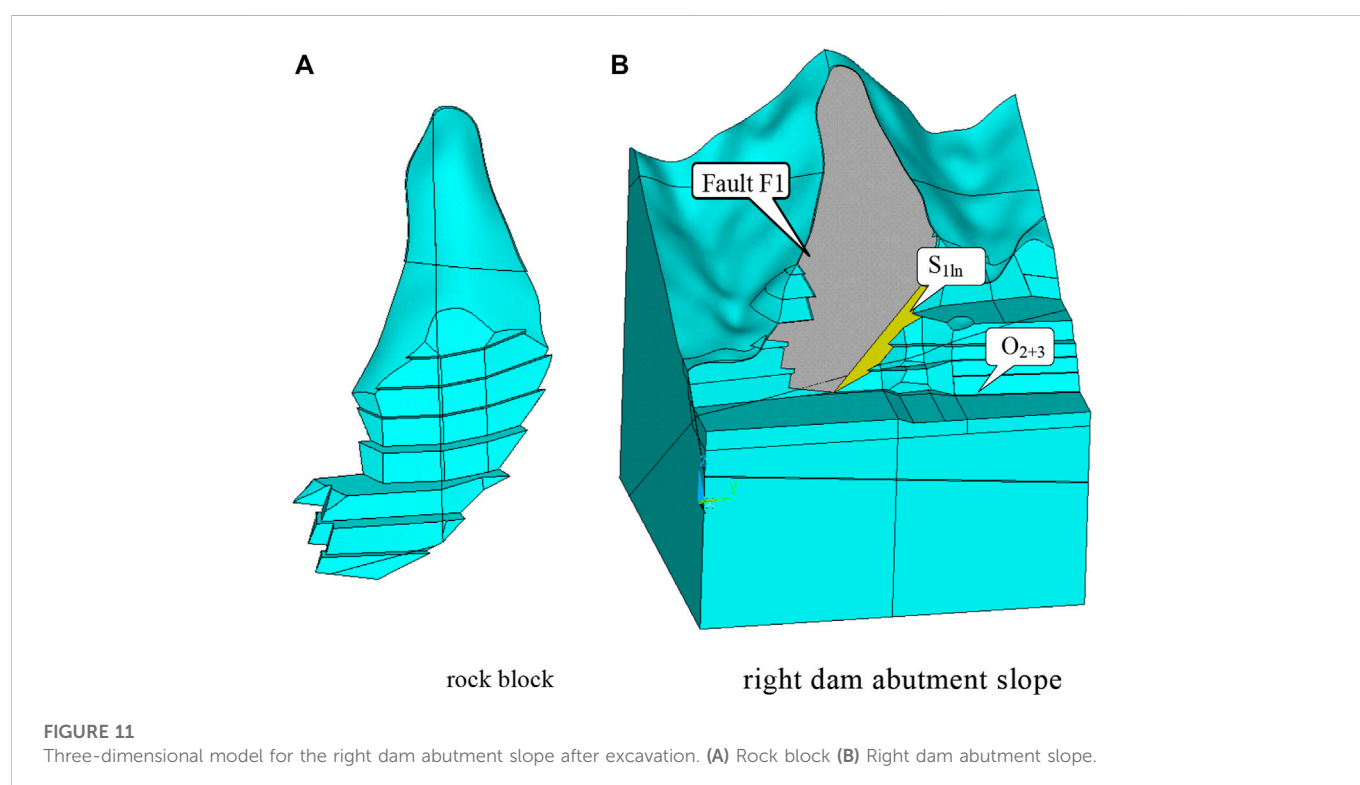
For the illustrative examples, although the values of stiffnesses are different, the values of *FS* are very similar. If normal stiffness $k_s$ and shear stiffness $k_n$ of interface contact elements are less than ten times that of $k_e$ of adjacent zones, these stiffnesses have no influence on the estimation of *FS* and computational efficiency. If the ratio between $k_s$ and $k_e$ is much more than ten, the computational cost will be significantly increased. Careful consideration should be given to improve computational efficiency. It is recommended that the stiffness of a zone ($k_s$; $k_n$) should be set to ten times the stiffness of the stiffest adjacent zone.

## 4.2 Effects of element size on slope stability analysis

To discuss the effects of size of the interface contact element on the estimation of rock slope stability, various element sizes are utilized in the analysis. To discretize symmetrical and asymmetrical wedges, four different element sizes are employed. $k_s$ and $k_n$ of these two examples are set to ten times that of $k_e$. The results of *FS* corresponding to different element sizes are presented in Table 6. The estimation of *FS* appears to remain unchanged regardless of the size of the element. The proposed method can reach the high level of precision even when the large element size is adopted. As the number of elements increases, the computational cost also increases. To maximize efficiency, it is advisable to use a small number of elements for the proposed method.

TABLE 7 Physical and mechanical parameters of the rock mass for the right dam abutment slope.

| Material | Unit weight/kN/m³ | Deformation modulus/GPa | Poisson's ratio | Shear strength | |
|---|---|---|---|---|---|
| | | | | $\tan\phi$ | $c$/MPa |
| $S_{1ln}$ | 25.1 | 6.0 | .28 | 1.01 | .81 |
| $O_{2+3}$ | 26.5 | 12.5 | .23 | 1.10 | 1.00 |
| $O_{1d}$ | 27.0 | 11.0 | .20 | 1.11 | 1.13 |
| $II_1$-5006 | — | — | — | .75 | .50 |
| $F_1$ | — | — | — | .35 | .05 |



FIGURE 11
Three-dimensional model for the right dam abutment slope after excavation. **(A)** Rock block **(B)** Right dam abutment slope.

## 4.3 Effects of failure criteria on slope stability analysis

To investigate the effects of different criteria on the rock slope stability, both displacement mutation criterion and the proposed failure criterion (all the nodes of interface contact elements are either sliding or opening) are used to obtain the *FS* of the rock slope for examples 1 and 2. The displacements of four points (A, B, C, and D) are recorded with the rise in *SRF* as illustrated in Figure 8. The displacements of all selected points increased with the rise in *SRF*. The analytical *FS* (estimated by the block theory) of example 1 is 1.293. The displacement mutation phenomenon has not been easily observed with the increasing strength reduction. When the shear strength reduction method is applied with the displacement mutation as the slope failure criteria, the estimation of *FS* involved subjectivity. As shown in Figure 9, the number of failed nodes is increased with the increasing *SRF*. The turning points are found when *SRF*=1.316 of

example 1. All the nodes of interface contact elements are either sliding or opening when *SRF*=1.316. Thus, *FS* is 1.316 according to the failure criteria. The turning points of example 2 can also be obtained when *SRF*=1.644. The results show that the *FS* estimated in the strength reduction method by the new failure criteria has good agreement with the block theory. The interface element node failure criteria are recommended for examining the stability of rock slopes because of its objectivity and clear concept.
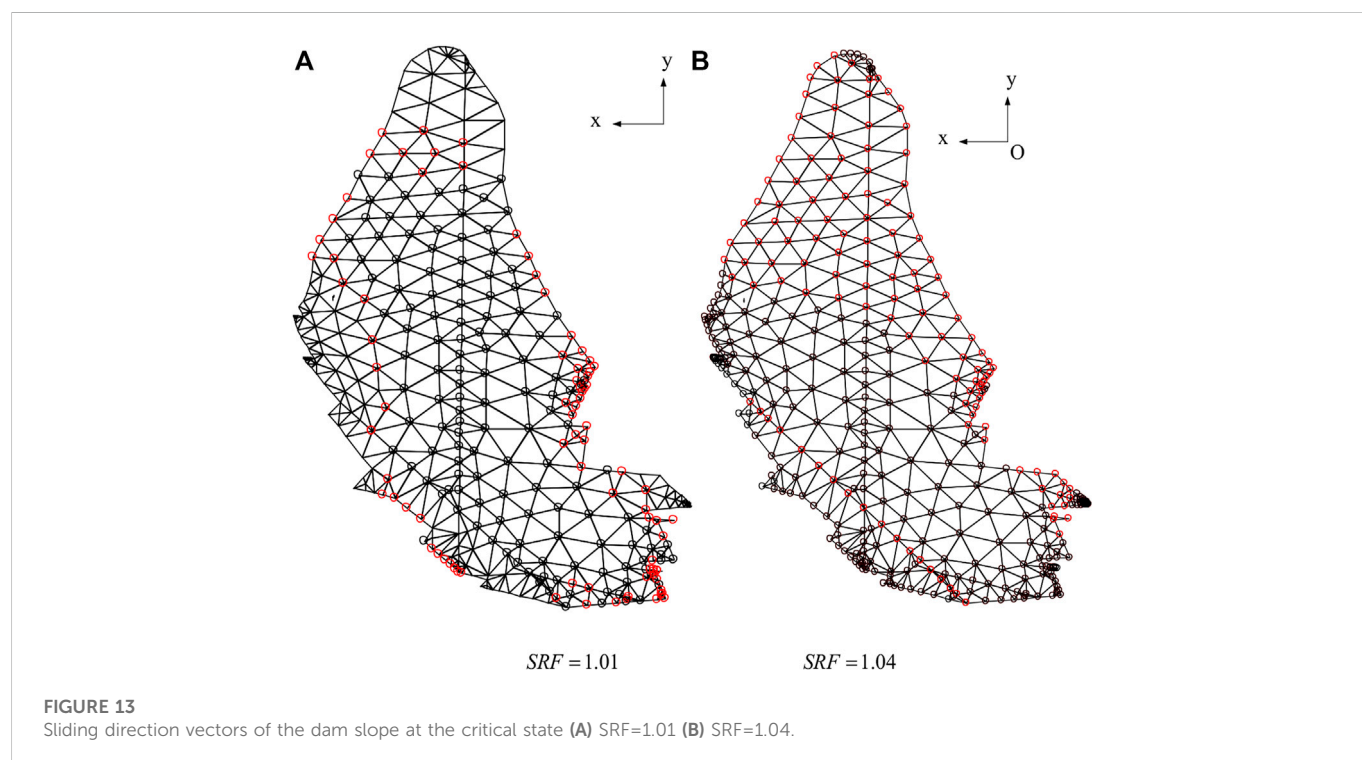
## 5 Engineering application

The Yinpan Hydropower Station is situated in Wulong County, Chongqing Province, China, which is 4 km downstream from Jiangkou Town. The Yinpan Hydropower Station, as the 11th cascade development on the main stream of the Wujiang River, is a comprehensive hydro-project designed for electric power

**FIGURE 12**
States of interface nodes for the rock block of the right dam slope.
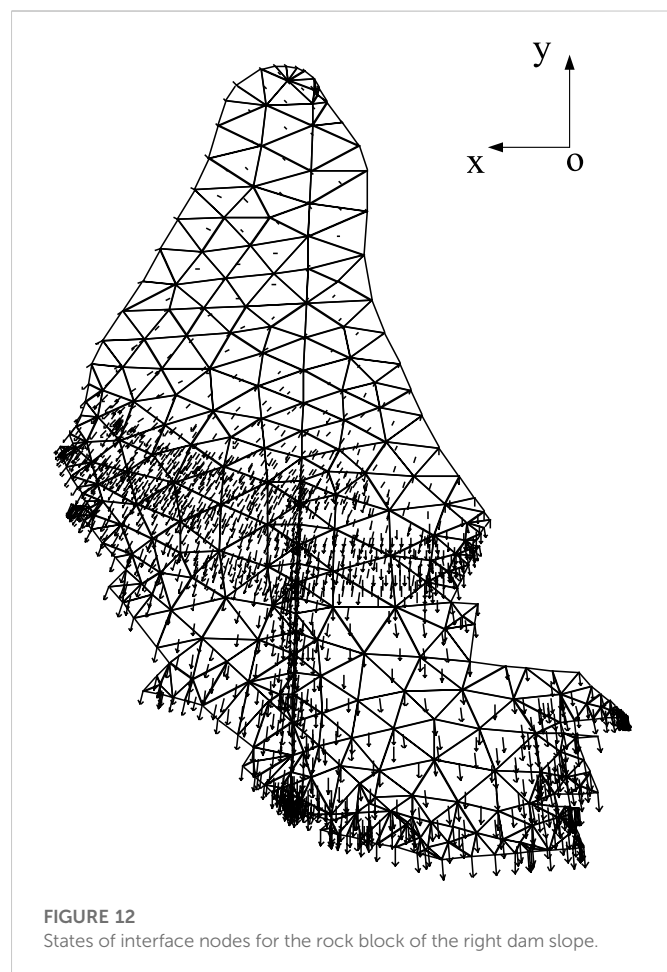
generation in combination with navigation. The hydropower station includes the construction of a 653.8-m-long and 80-m-high concrete gravity dam.

The gradient of natural rock slopes on the right bank is about 35°. The rock of the slope is composed of $S_{ln}^1$ shale, $O_{3w}$ shale, $O_{2+3}$ limestone, $O_{1d}$ sandstone, and shale from the top to bottom. Figure 10 depicts the geological plan layer of excavation on the right abutment slope. As indicated in the field geological investigation and geological survey of the right bank, there is a latent large block generated by fault $F_1$ and bedding fissure $II_15006$ that developed in $S_{ln}^1$ shale, as shown in Figure 10. The intersection angle between $F_1$ and slope strike is about 12°. The altitude of fault $F_1$ is 110°∠38°. The composition of fault $F_1$ is muddy intercalation within broken shale. The broken rock has a diameter of 5–15 cm and a general width of .5–3 cm. After excavation, the lower part of fault $F_1$ exposure led to right abutment slope failure. The altitude of bedding fissure $II_15006$ is 272°∠41° whose joint connectivity is 20% consisting of the calcite membrane. According to the engineering geological investigation, the physical and mechanical properties of the dam abutment slope and the shear strength parameters of the slip surfaces are listed in Table 7.

A model is built to analyze the *FS* after excavation based on the geological reveals in the right slope. The numerical model for the right dam abutment slope is presented in Figure 11. The numerical model is composed of 1161 nodes and 4508 elements. The volume of the potential failure block is 21,445 m3. Fault F1 and bedding fissure $II_15006$ are simulated by interface contact elements within the theoretical framework of the finite difference method. The mesh of the interface comprised 402 nodes. For the right dam abutment slope, the *SRF* is 1.04 when all the nodes of interface contact elements are either sliding or opening. Therefore, the *FS* is 1.04. Figure 12 shows the states of interface nodes with different reduction factors of shear



**FIGURE 13**
Sliding direction vectors of the dam slope at the critical state **(A)** SRF=1.01 **(B)** SRF=1.04.

strength. Circles at nodes represent that the interface has slipped in the shear or normal direction. Red circles represent opening contact nodes, and black circles represent sliding contact nodes. Figure 13 represents the plane sliding direction vectors of the right dam abutment slope at a critical state.

The failure mode of right slopes obtained by the block theory is single plane sliding with fault $F_1$. When considering a potential sliding of the right dam slope along fault $F_1$, a unique decomposition of forces on the sliding body is induced into a component along the sliding direction and a component perpendicular to the sliding direction. Thus, the *FS* obtained from the block theory is .72. However, when the block fails, $II_15006$ would resist sliding of the movable block and change the sliding direction. Since the block theory method ignores the role of bedding fissure $II_15006$, the block theory underestimated the stability of the right dam abutment slope. The proposal method can consider roles of all the structural planes in the stability problem and obtain credible results Figure 13.

# 6 Conclusion

In order to analyze rock slopes with multiple discontinuities, which can induce ill-advised results by the conventional block theory, this paper proposes a method for estimating the *FS* of complex blocks, in which the discontinuities are simulated by interface contact elements within the theoretical framework of the finite difference method based on the strength reduction method. The effects of shear and normal stiffnesses, element size of wedges, and failure criteria on the stability analysis were further investigated by the proposal method. The following conclusions can be drawn from the results and discussion of this paper:

1) The validity of the proposed model is demonstrated by some typical examples of wedges. For wedge examples, the *FS* values calculated by the proposed method are consistent with the traditional method. For the stability analysis of blocks formed by multiple structural planes, the proposed method can consider roles of all the structural planes in the stability problem. Thus, the proposed method provides engineers with a practical method for 3D jointed rock slope stability analysis.

2) The stiffnesses of the interface contact element and element size have no influence on the estimation of *FS*. However, large values of stiffnesses and small element size will result in low computational efficiency. Therefore, it is of great importance for adopting the suitable stiffnesses of the interface element and element size to improve solution efficiency. The failure criteria of the interface contact node provide a more accurate way to indicate the failure behavior of a rock slope.

3) The proposed method is utilized to assess the stability of the Yinpan Hydropower Station right abutment slope. The traditional block theory method fails to accurately assess the stability of the slope due to its inability to consider the contributions of all the structural planes. However, the proposed method takes into account all the structural planes and produces more reliable results.

# Data availability statement

The original contributions presented in the study are included in the article/Supplementary Material; further inquiries can be directed to the corresponding author.

# Author contributions

RY: methodology, software, validation, investigation, formal analysis, data curation, writing—original draft, writing—review and editing, and visualization. CZ: conceptualization, methodology, software, validation, formal analysis, writing—original draft, writing—review and editing, visualization, supervision, and project administration. JL: software, validation, and writing—review and editing. XB: software, validation, and writing—review and editing.

# Funding

# Conflict of interest

The authors declare that the research was conducted in the absence of any commercial or financial relationships that could be construed as a potential conflict of interest.

# Publisher's note

All claims expressed in this article are solely those of the authors and do not necessarily represent those of their affiliated organizations, or those of the publisher, the editors, and the reviewers. Any product that may be evaluated in this article, or claim that may be made by its manufacturer, is not guaranteed or endorsed by the publisher.

# References

Bandis, S. C., Lumsden, A. C., and Barton, N. R. (1983). Fundamentals of rock joint deformation. *Int. J. Rock Mech. Min.* 20 (6), 249–268. doi:10.1016/0148-9062(83)90595-8

Chen, Z. (2004). A generalized solution for tetrahedral rock wedge stability analysis. *Int. J. Rock Mech. Min. Sci.* 41 (4), 613–628. doi:10.1016/j.ijrmms.2003.12.150

Deng, D. (2021). Limit equilibrium analysis on the stability of rock wedges with linear and nonlinear strength criteria. *Int. J. Rock Mech. Min. Sci.* 148, 104967. doi:10.1016/j.ijrmms.2021.104967

Fossum, A. F. (1985). Effective elastic properties for a randomly jointed rock mass. *Int. J. Rock Mech. Min. Sci. Geomechanics Abstr.* 22 (6), 467–470. doi:10.1016/0148-9062(85)90011-7

Goodman, R. E., and Shi, G. H. (1985). *Block theory and its application to rock engineering*. USA: Prentice-Hall.

Griffiths, D. V., and Lane, P. A. (1999). Slope stability analysis by finite elements. *Geotechnique* 49, 387–403. doi:10.1680/geot.1999.49.3.387

Griffiths, D. V., and Marquez, R. M. (2007). Three-dimensional slope stability analysis by elasto-plastic finite elements. *Geotechnique* 57 (6), 537–546. doi:10.1680/geot.2007.57.6.537

Itasca, F. (2000). *Fast Lagrangian analysis of continua*. Minneapolis, Minn: Itasca Consulting Group Inc.

Jiang, Q., Qi, Z., Wei, W., and Zhou, C. (2015). Stability assessment of a high rock slope by strength reduction finite element method. *Bull. Eng. Geol. Environ.* 74 (4), 1153–1162. doi:10.1007/s10064-014-0698-1

Jiang, Q., and Zhou, C. (2017). A rigorous solution for the stability of polyhedral rock blocks. *Comput. Geotechnics* 90, 190–201. doi:10.1016/j.compgeo.2017.06.012

Lu, R., Wei, W., Shang, K., and Jing, X. (2020). Stability analysis of jointed rock slope by strength reduction technique considering ubiquitous joint model. *Adv. Civil Eng.*, 1–13. doi:10.1155/2020/8862243

Ma, Z., Qin, S., Chen, J., Lv, J., Chen, J., and Zhao, X. (2019). A probabilistic method for evaluating wedge stability based on blind data theory. *Bull. Eng. Geol. Environ.* 78 (3), 1927–1936. doi:10.1007/s10064-017-1204-3

Rosso, R. S. (1976). A comparison of joint stiffness measurements in direct shear, triaxial compression, and *in Situ*. *Int. J. Rock Mech. Min. Sci. Geomechanics Abstr.* 13 (6), 167–172. doi:10.1016/0148-9062(76)91282-1

Ugai, K., and Leshchinsky, D. (1995). Three-dimensional limit equilibrium and finite element analyses: A comparison of results. *Soils Found.* 35 (4), 1–7. doi:10.3208/sandf.35.4_1

Wei, W. B., Cheng, Y. M., and Li, L. (2009). Three-dimensional slope failure analysis by the strength reduction and limit equilibrium methods. *Comput. Geotechnics* 36 (1–2), 70–80. doi:10.1016/j.compgeo.2008.03.003

Xi, C., Wu, Y., Yu, Y., Liu, J., Xi, F. X., and Ren, J. (2014). A two-grid search scheme for large-scale 3-D finite element analyses of slope stability. *Comput. Geotechnics* 62, 203–215. doi:10.1016/j.compgeo.2014.07.010

Zhao, M., Guo, W., Chen, L. Y., and Wang, S. Y. (2019). Experiment on the frost resistance of modified phospho gypsum: A case used to improve baozhong railway subgrade loess. *J. Mt. Sci.* 16 (12), 2920–2930. doi:10.1007/s11629-018-5014-2

Zheng, Y., Deng, C., Zhao, S., and Tang, X. (2007). Development of finite element limiting analysis method and its applications in geotechnical engineering. *Sciences* 2007 (3), 10–36.

Zienkiewicz, O. C., Humpheson, C., and Lewis, R. (1975). Associated and non-associated visco-plasticity and plasticity in soil mechanics. *Geotechnique* 25 (4), 671–689. doi:10.1680/geot.1975.25.4.671

# Detection of former goaf and analysis of deformation characteristics of overburden in Dameidong coal mine

Zhan-Xi Wei[1,2,3†], Meng Zhao[4*†], Fei-Hong Xie[4],
Sheng-Hong Cao[1,2,3], Jian-Hui Dong[4] and Yang-Dan Dong[5]

[1]Qinghai Bureau of Environmental Geological Exploration, Xining, China, [2]Qinghai 906 Project Survey and Design Institute, Xining, China, [3]Qinghai Geological Environmental Protection and Disaster Prevention Engineering Technology Research Center, Xining, China, [4]Sichuan Engineering Research Center for Mechanical Properties and Engineering Technology of Unsaturated Soils, Chengdu University, Chengdu, China, [5]State Key Laboratory of Geological Disaster Prevention and Geological Environment Protection, Chengdu University of Technology, Chengdu, China

In order to analyze the deformation of the old goaf in Dameidong Coal Mine and its influence on the surrounding rock and soil layer, it provides guidance for the prevention and control of geological disasters in the region. In this paper, the transient electromagnetic method and numerical simulation method were used to study the deformation law of the overlying strata in the mining area. The results of transient electromagnetic detection showed that the subsidence area of the goaf in Dameidong Coal Mine was within the range of the elliptical water-rich area, and the average buried depth of the goaf was expected to be 90 m. The model was established by discrete element numerical simulation to study the variation law of mining overburden rock. The results showed that the stress change in coal mining was mainly reflected at both ends of the goaf, which was a stress concentration phenomenon. Overburden rock deformation changed with the mining process. The stress concentration area and the displacement change area were highly coincident, consisted with the displacement monitoring map, showing a "U"-type distribution. The results proved that the numerical simulation results do have theoretical guidance for mining subsidence control.

KEYWORDS

geological disaster prevention, coal seam mining, former goaf detection, discrete element numerical simulation, strata deformation

## 1 Introduction

Since the 21st century, ecological construction had been an indispensable part of the global sustainable development strategy (Liu et al., 2010; Xia et al., 2006). However, with the gradual increase of the depth of coal mine development, the deformation and destruction of the overlying strata would lead to surface subsidence and trigger a series of mine geological disasters. Therefore, the detection of the range of coal mine goaf and the exploration of the deformation law of rock strata had become the research focus of many scholars.

First of all, in the field of geological disaster prevention and control, many scholars have done a lot of research. Zhang et al. (2022) proposed a prediction method of creep landslide by using mathematical model, which has important guiding significance for the prevention and control of landslide disaster. Through triaxial compression (RTC ) test, Zhang et al. (2020) analyzed the deformation characteristics and mechanical response of unloading soil, and

revealed the instability mechanism and response mechanism of loess slope under unloading. Zhang et al. (2019a), Zhang et al. (2019b) proposed an early warning threshold model for rainfall-induced slope instability by studying the characteristics of slope deformation and failure caused by the continuous rise of groundwater level, which provided a new framework for early warning. Pei et al. (2016) revealed the importance of geological disaster prevention by studying the complete failure process of high fill slope. In the field of mining area exploration, Yin (2022) combined with audio magnetotelluric sounding (AMT) to detect the apparent resistivity of the karst development area in the mining area found out the distribution of the goaf in mining area and explained the feasibility of audio magnetotelluric sounding (AMT) and high density resistivity tomography to detect fault location. Qiang et al. (2021) applied the transient electromagnetic method to detect the apparent resistivity anomaly area of coal seam roof and floor and divided the relative water-rich anomaly area in the stratum. The importance of the transient electromagnetic method in the field of goaf detection is proved. In addition, Yang and Guo (2020), Wang and Liu (2013), Sun et al. (2021), and Wang (2009) used the high-density electrical method to detect the range of coal mine goaf and achieved effective results.

With the in-depth study of the stress distribution of overlying rock mass caused by underground mining by many scholars, physical models and numerical simulation experiments are more and more widely used. Yu and Gui (2014) used numerical simulation software to simulate the gently inclined coal seam with two-dimensional discrete element numerical simulation. The results show that compared with the horizontal coal seam in the plain area, the cracks caused by the shallow buried inclined coal seam in the mountainous area are more developed, the stability is poor, and it is easy to lose stability and cause landslides. Guan et al. (2012) used discrete element UDEC software to study the working face of the shallow coal seam subsidence area and concluded that the shallow coal seam rock layer and the main key layer have coupling effect on surface subsidence. Liang (2020) used two-dimensional discrete element UDEC numerical simulation software to study the dynamic development of cracks and the movement process of overlying strata in the shallow coal seam working face and obtained the caving step of immediate roof and the dynamic change law of overlying strata after mining in the shallow coal seam working face. Chen et al. (2016), through the physical similarity simulation experiment, proved that the use of the local filling coordination mining method can effectively control the fracture development height and for green mining energy and ecological environment protection to find a more effective and more efficient method. Liiu (2017) used two-dimensional discrete element UDEC software to study the feasibility and necessity of mining close-distance protective layers and concluded that the expansion rate of the protected layer reached 3‰. In addition, the stress changes and collapse caused by close-distance protected layers are in line with relevant regulations. Li (2016) used UDEC numerical simulation software to simulate the excavation direction of the shallow coal seam working face and monitored the dynamic change process of subsidence displacement and stress of different strata in the model during the gradual excavation process, so as to obtain the movement and deformation law of overlying strata after the gradual excavation of different coal seams, which provided relevant basis for the control of rock and soil layers in coal mines.

Through UDEC numerical simulation software, Gao et al. (2013) simulated the overlying coal and rock strata of the coal mine working
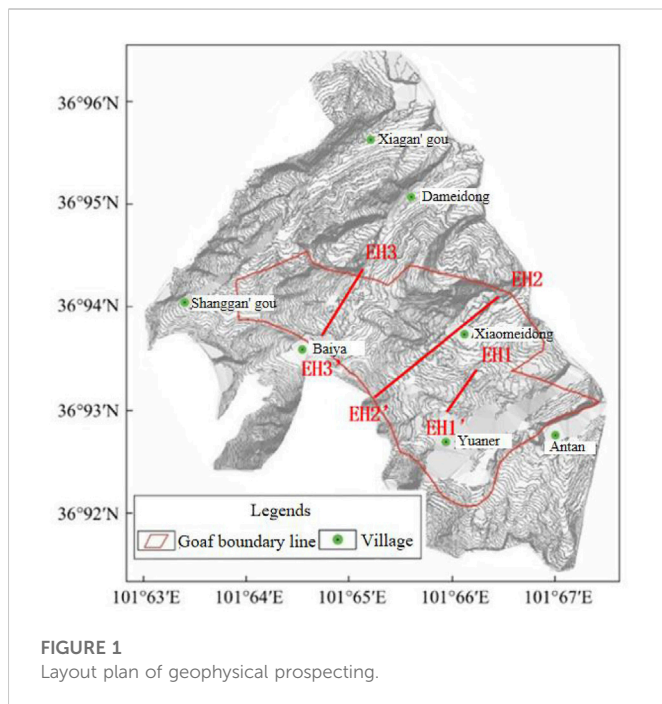
face. The calculation results show that there are obvious vertical fracture cracks in the 20–30 m range of the two sides of the goaf in the coal mine. The results of the two-dimensional discrete element numerical simulation software are in good agreement with the field investigation results. This research results also provide a certain basis for other similar mine stope conditions and gas control in the goaf. It is demonstrated that the dynamic movement process of the overburden caused by coal seam mining simulated by the software can predict the dynamic distribution of gas migration channels during mining in the actual process. This also has important guiding significance for preventing gas overflow. Guo et al. (2010) used two-dimensional discrete element simulation software to demonstrate the relationship between force and force between rock mass blocks, which directly reflects that two-dimensional discrete element has been widely used in coal mine rock mechanics and mine pressure research. The aforementioned research shows that in the detection field of coal seam goaf, magnetotelluric method and transient electromagnetic method can accurately detect the approximate range and location of goaf and have the characteristics of easy construction, high detection accuracy, and strong directivity. It has become a mainstream detection method. The aforementioned research showed that in the field of coal seam goaf detection, the magnetotelluric method and transient electromagnetic method could indeed detect the approximate range and location of goaf, and numerical simulation could also study the deformation of overburden strata in the process of mining. However, there was no complete and specific research on the detection of mined-out area and the law of stress–strain settlement in the alpine region where the mining situation was more complex.

In this paper, the large coal tunnel of Datong Coal Mine in Datong County, Xining City, Qinghai Province, was taken as the research object. Combined with the geological and hydrological data of the study area, the transient electromagnetic method was used to detect the goaf and draw the goaf profile. Combined with two-dimensional discrete element numerical simulation software, the model was established with the old goaf of Datong Coal Mine in Datong County, Xining City, Qinghai Province, as the research background. The variation law of stress–strain of rock and soil layers was obtained by calculation. On the basis of this numerical simulation, combined with the actual monitoring of the coal mine goaf displacement variation, the deformation of the old goaf in Datong Coal Mine and the influence of the evaluation on the surrounding rock and soil layers were analyzed.

# 2 Engineering geology background

## 2.1 Meteorological and hydrological conditions

The key coal mining subsidence area of Datong County was located in the southeastern part of Datong Hui and Tu Autonomous County, Xining City, Qinghai Province, involving seven villages in Qiaotou Town and Liangjiao Township. The study area had village roads and mining area roads. The north national road G227 ran through Qiaotou Town, the county seat where the key coal mining subsidence area was located. The Dameidong Coal Mine was located in the southeast of Datong Hui and Tu Autonomous County, Xining City, Qinghai Province, China. The key research area belonged

**FIGURE 1**
Layout plan of geophysical prospecting.



**FIGURE 2**
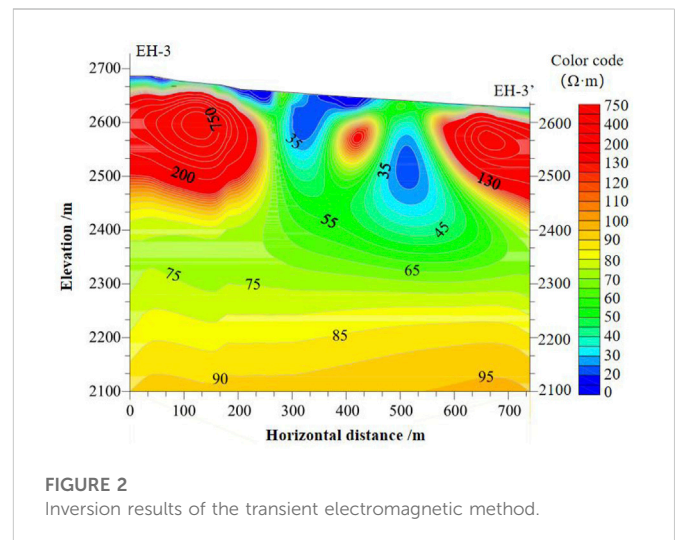Inversion results of the transient electromagnetic method.

to plateau continental climate. The mean annual temperature ranged 2.8°C–3.9°C. Temperature difference 25.3°C, average daily temperature difference 13.2°C ~ 13.8°C, average annual precipitation; between 508.7 and 532.6 mm. Summer and autumn witnessed more southeast wind, and the wind speed was small. Winter and spring witnessed more northwest wind, and the average wind speed was 2 m/s, the maximum wind speed was 17 m/s, and the average frost-free period was of 96.3 days.

## 2.2 Geological condition

The study area was located in the southern margin of the Xining–Datong Basin, which was composed of eroded and eroded low hills and eroded valley plains. The erosion and denudation hills in the area are mainly composed of Cretaceous, Paleogene mud, sandstone, and Quaternary loess. The altitude was 2,450–2,750 m, the relative height difference was 300 m, the mountain was high and the slope was steep, the ravines were cross, the terrain was undulating, the topography was complex, the vegetation was scarce, and the soil erosion was serious.

In view of the characteristics of underground mined-out area, such as strong concealment, poor regularity of spatial distribution characteristics, and difficult prediction of roof caving and collapse in mined-out area, how to quantitatively evaluate the distribution range, spatial morphological characteristics, and caving condition of the underground mined-out area had always been a key technical problem for engineers to evaluate the potential hazard of the mined-out area and reasonably determine the treatment measures of the mined-out area. At the same time, due to the underground mining of Datong Coal Mine, there were many private small coal mines in the past, which made the underground mining roadways densely distributed. The "cavity" produced by coal mining under the surface of the coal mine formed a large area of goaf, and the coal mining activities continued, causing various geological disasters.

The distribution range of goaf in Dameidong Coal Mine was obtained by a comprehensive analysis of field investigation, survey data provided by different coal mining enterprises, and transient electromagnetic exploration results. The distribution characteristics of the mined-out area were consistent with the distribution characteristics of the ore body. The task of transient electromagnetic exploration was to explore the distribution range and depth of the mined-out area in Dameidong Coal Mine. The obtained geophysical prospecting results showed that the collapse area of the mined-out area in Dameidong Coal Mine was elliptical, with a length of 770 m, a width of 400 m, and an area of 200,036 m². The length of the roadway in Dameidong Coal Mine was 6,891 m, of which the underground chamber volume of the roadway in Dameidong Coal Mine was about $940.04 \times 104$ m³. The distribution of the mined-out area in Dameidong Mine was shown in detail in the present situation diagram and prediction diagram.

## 3 Analysis of geophysical results

The transient electromagnetic method was a method used to detect the resistivity of a medium by using an ungrounded loop or ground line source to emit a primary pulse magnetic field to the ground, and using coil or ground electrode to observe the secondary induced eddy current field caused by an underground medium during the intermittent period of primary pulse magnetic field. It had the advantages of automatically eliminating the main noise source, no terrain influence, combined observation at the same point, best coupling with the detection target, strong abnormal response, simple shape, and strong resolution. Based on the actual situation of the study area, in order to efficiently monitor the *status quo* of the goaf, this paper intended to use the transient electromagnetic method to arrange geophysical survey lines in the three main coal mine areas. The geophysical survey line set by the large coal mine was E3-E3′. The detailed geophysical layout plan is shown in Figure 1.

Combined with the original data of resistivity obtained by line detection, the terrain data were added to invert the apparent resistivity model, and the error value was obtained by comparing the forward calculation of the model data with the original data. The data error did not exceed 15%, which was the qualified inversion model. The inversion result is shown in Figure 2. The horizontal axis of the
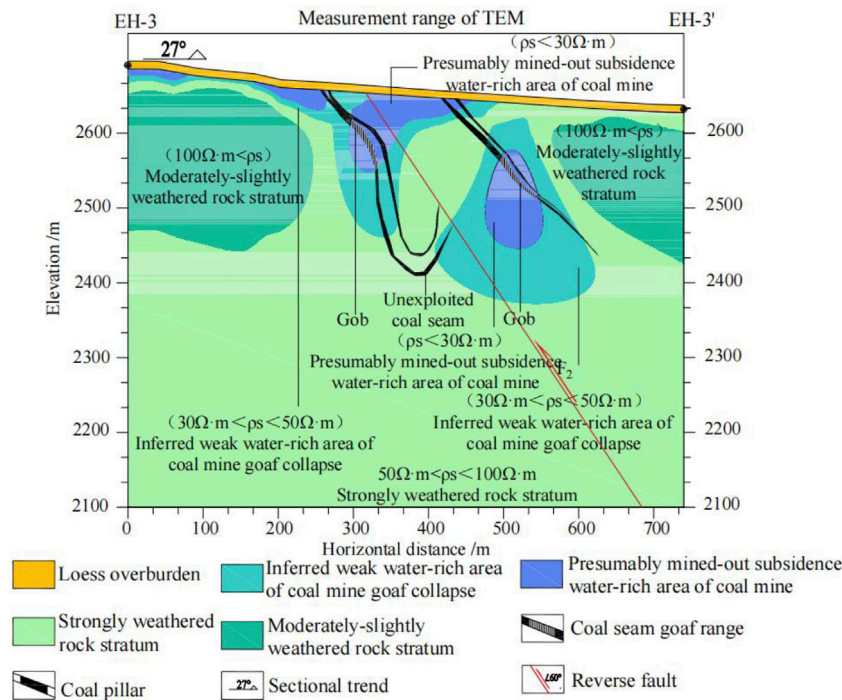
**FIGURE 3**
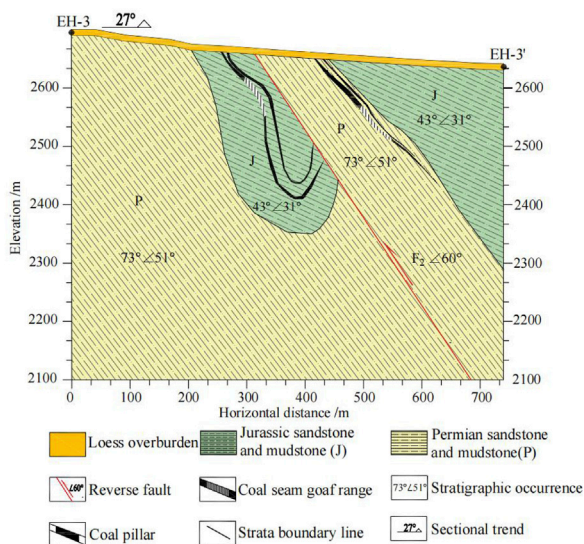Interpretation of the inversion results of the transient electromagnetic method.



**FIGURE 4**
Geological profile of the eh3-3 'survey line.

profile was horizontal distance (unit m), and the vertical axis was elevation (unit m). This interpretation work was based on the inversion profile, combined with the geological data and the actual situation to interpret each section.

Figure 3 shows the predicted goaf map obtained by using the transient electromagnetic method to survey the large coal mine. The terrain range measured between EH-3 and EH-3′ was relatively flat,

and the surface layer was mainly loess cover. It could be seen from the aforementioned figure that when the apparent resistance was less than 30 Ωm, it was speculated that it was a water-rich area of coal mine goaf collapse. When the apparent resistance was greater than 30 Ωm and less than 50 Ωm, it was presumed to be a weak water-rich area of coal mine goaf collapse. When the apparent resistance was greater than 50 Ωm, less than 100 Ωm was strongly weathered rock; when the apparent resistance was greater than 100 Ωm, it was a medium-lightly weathered rock layer. The profile of the study area was 27°, and there was a reverse fault between the two excavated coal seams with a dip angle of 60°.

Figure 4 shows a cross-sectional view of the mining coal seams M1 and M3 in the Dameidong Coal Mine. The profile of the study area was 27°, where the thickness of the coal seams mined at both locations was 2.4 m. The thinner coal seams next to the two indicate that the coal seam had not been mined. There were two stratigraphic occurrences in the study area. The stratigraphic strike of Permian sandstone and mudstone was 73°, and the dip angle was 51°. The strike of Zhuluo sandstone and mudstone was 43°, and the dip angle was 31°. There was also a reverse fault between the two excavated coal seams with a dip angle of 60°.

The mechanical properties of each coal seam are detailed in Tables 1, 2.

# 4 Discrete element numerical simulation of goaf overlying strata deformation analysis

With the gradual improvement of computer technology, numerical simulation calculation gradually played an important

**TABLE 1 Coal seam M1 mining parameters.**

| M1 coal seam mining area | Mining thickness/m | Tilt angle/° | Mining length/m | Mining upper roof elevation/m | Mining upper floor elevation/m |
|---|---|---|---|---|---|
| M1 | 2.4 | 51 | 103 | +2660 | +2648 |

**TABLE 2 Coal seam M3 mining parameters.**

| M3 coal seam mining area | Mining thickness/m | Tilt angle/° | Mining length/m | Mining upper roof elevation/m | Mining upper floor elevation/m |
|---|---|---|---|---|---|
| M3 | 2.4 | 31 | 82 | +2626 | +2614 |

**TABLE 3 Physical and mechanical parameters of rock strata.**

| Lithological characters | Density/ kN·m$^{-3}$ | Bulk modulus/GPa | Shear modulus/GPa | Cohesion/ MPa | Internal friction angle/° | Tensile strength/MPa |
|---|---|---|---|---|---|---|
| Sandstone | 2400 | 6 | 2.3 | 0.7 | 30 | 0.6 |
| Coal seam | 1400 | 3.9 | 1.1 | 0.5 | 30 | 1.04 |

**TABLE 4 Rock joint parameters.**

| Tangential stiffness/Gpa | Normal stiffness/Gpa | Internal friction angle/° | Cohesion/Mpa | Tensile strength/Kpa |
|---|---|---|---|---|
| 5 | 2.5 | 15 | 0.2 | 10 |

role in scientific research projects. Numerical simulation calculation and analysis of rock and soil movement in coal seam mining was one of the important means of scientific research. It could reflect the deformation of coal mine excavation strata and showed the dynamic process of damage, which provided a quantitative analysis basis for the subsequent formulation of control schemes and support technology (Hao, et al., 2007; Zhang and Huang, 2010; Che et al., 2022). Discrete element software was widely used in underground engineering research such as coal mining and played an important role in the research of coal mining support and surrounding rock stability control theory. This numerical simulation method regarded the rock mass as a collection of two basic elements of rock and structural planes and continuously judged and updated the contact state of the block during the calculation process. According to these contact states, the load transfer mode between the blocks was judged, and the corresponding mechanical laws were selected for contact. The stress and deformation behavior of these basic elements were defined. By establishing a two-dimensional numerical model, the variation displacement, stress variation law, and surface subsidence of overlying strata after coal seam excavation were calculated and analyzed, which provided a quantitative analysis basis for safe mining on site.

## 4.1 Model establishment and survey line setting

Due to the complex stratum structure in the study area, in the process of establishing the numerical model, the rock and soil bodied with similar physical and mechanical properties were appropriately simplified, and the coal seams were divided into upper and lower sections, and the upper and lower sections are mined simultaneously.

The model was assumed to be an isotropic continuous homogeneous medium, and the mechanical model was the Mohr–Coulomb elastic-plastic model. The top surface of the model was free surface, the bottom was fixed constraint, and the surrounding was horizontal displacement constraint. The initial stress of the mining area was mainly self-weight stress. The gravity acceleration was set to 9.81 m/s², and the direction was vertical downward. The physical and mechanical parameters of the rock strata are shown in Table 3.

According to the M-C criterion and Bandis empirical formula method, the theoretical joint shear stiffness and normal stiffness could be calculated. Combined with the field measured data and the joint contact embedding degree in the two-dimensional discrete element numerical simulation software, the joint normal stiffness of this model was set to 2.5 Gpa, and the joint shear stiffness was set to 5 Gpa. Detailed joint material parameters are shown in Table 4.

For the constitutive model, the elastoplastic model was used in the modeling, and the block obeyed cons = 2 in the discrete element software; the joint constitutive model obeyed jcons = 3.

When establishing the model, we first used the round command to set the block fillet d = 0.1. We needed to set a reasonable calculation area according to the Saint–Venant principle. The size of the established geometric model should be based on the regional length of the excavated coal seam. On this basis, the side length was extended by 30%–50%. Therefore, a numerical simulation model was established according to the geological survey data of Datong Coal Mine in Xining City, Qinghai Province. After properly simplifying its area, the left excavation boundary was 50 m away from the established
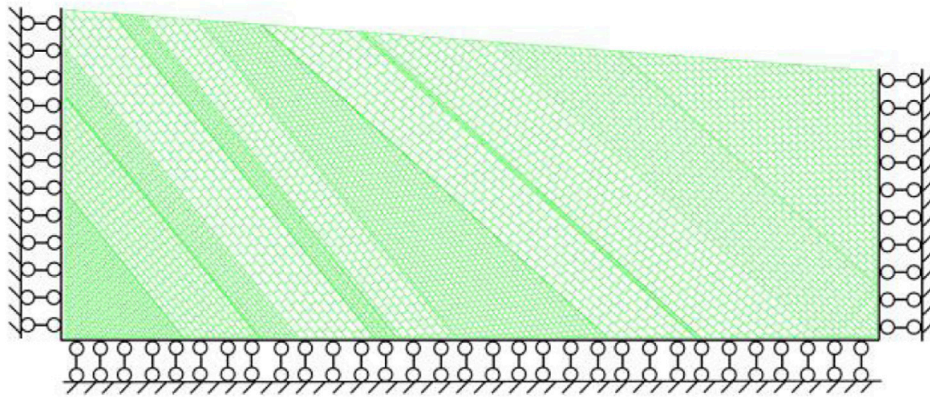
**FIGURE 5**
Schematic diagram of thee numerical model.

geometric model boundary, and the right excavation coal seam area was 200 m away from the established geometric model boundary. In this design, Block command was used to establish a 670 m long, 270 m high on one side, and 220 m high trapezoidal block on the other side as the research and calculation area. Arc command was used to divide each joint layer in the coal seam of Dameidong Coal Mine, so as to facilitate the dynamic simulation of excavation in this area. The loading method in UDEC software was used to simulate the actual stress of the overlying strata in the excavation process of the numerical model. A total of 15 layers of coal mine rock strata were simulated and divided by the excavation model. The rock mass in this area was divided into two large blocks, one part of the rock mass joint inclination angle was 51°, and the other part of the rock mass joint inclination angle was 31°.

When the geometric model of the computational domain was established, the block boundary conditions must be defined and consistent with the boundary conditions of the actual engineering situation, otherwise the calculated data would be inaccurate. Here, the vertical stress was the self-weight stress of the rock mass. According to the density of the rock mass and the excavation depth of the coal seam, the vertical stress of the numerical model was calculated. The calculated vertical stress was −9.09201 Mpa. In the two-dimensional discrete software, the compressive stress was negative, the tensile stress was positive, and the lateral stress was calculated according to the Poisson effect. The lateral stress was −4.5886 Mpa. Numerical simulation of unexcavated coal seam is shown in Figure 5.

## 4.2 Analysis of numerical calculation results

Based on the Dameidong mining area of Datong Coal Mine in Xining City, Qinghai Province, as the main research area, combined with the field research survey data and the measured data, the geometric calculation model was constructed. The excavation area was divided into single excavation of inclined coal seam M1 and simultaneous excavation of inclined coal seam M1 and gently inclined coal seam M3. In this section, the displacement variation law and stress variation law of rock and soil layers after coal seam excavation were analyzed by the results obtained by simulation calculation.

First, the numerical calculation of single-layer excavation of coal seam M1 was carried out. When the geometric numerical model under the action of the original rock stress in this working condition was iteratively calculated to achieve balance, we used the delete range reg command to delete the rock and soil blocks that need to be excavated in the model. First, find out the four node coordinates of the excavation area, enter them clockwise, and then delete the blocks in the area to simulate the dynamic excavation work. After excavation, the number of iteration steps was superimposed by 10,000 steps to reach the balance. Different commands were input to output the corresponding graphics, and the coal seam M1 after excavation was explained and analyzed according to the obtained graphics.

Second, the numerical calculation of simultaneous excavation of coal seams M1 and M3 was carried out. When the geometric numerical model under the action of *in situ* rock stress was iteratively calculated to achieve balance, the goafs in coal seams M1 and M3 were deleted clockwise to simulate the dynamic excavation work. After the iteration steps were superimposed for 10,000 steps, the balance was achieved. Different commands were input to output the corresponding graphics, and the coal seams M1 and M3 after excavation were explained and analyzed according to the obtained graphics.

### 4.2.1 Coal seam M1 excavation stress field analysis

The stress cloud diagram was mainly used to observe the stress distribution of the rock mass in the working condition, which had more intuitive advantages than the contour map.

Figure 6 shows the distribution of stress after coal seam M1 mining. Among them, Figure 6A illustrates the distribution of horizontal stress after M1 coal seam mining reaches equilibrium under the initial state condition. The horizontal stress cloud map after excavation took 1 Mpa as the equivalent interval of stress size, with a minimum of 0Mpa and a maximum of −6 Mpa. The negative value was expressed as compressive stress, and the stress range of most areas in the horizontal stress cloud map was 1–2 Mpa. The stress state gradually decreases with the increase of elevation, and the bottom stress was larger. As shown in the figure, there were stress concentration areas at the front and back ends of the coal mine goaf, and the horizontal stress was distributed in the range of 2–4 Mpa. The goaf area of the coal mine rock and soil layers was also due to coal
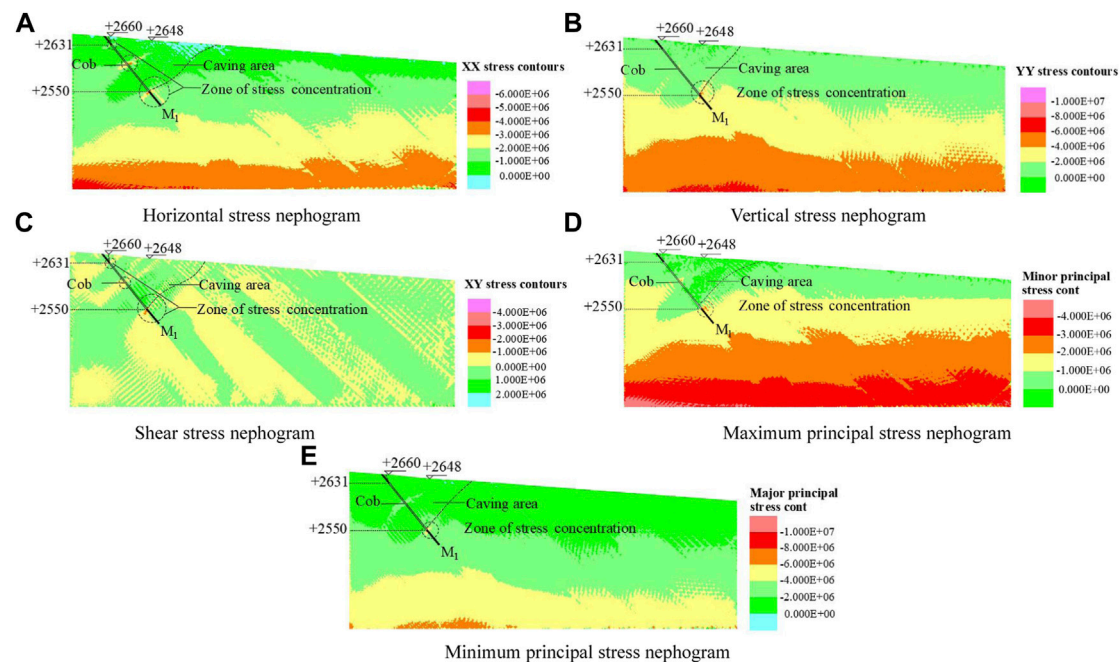
**FIGURE 6**
Stress distribution of coal seam M1 after mining. **(A)** Horizontal stress nephogram, **(B)** vertical stress nephogram, **(C)** shear stress nephogram, **(D)** maximum principal stress nephogram, and **(E)** minimum principal stress nephogram.

seam excavation. The stress release of the goaf area was reduced from the original equilibrium stress of 1–2 Mpa–0–1 Mpa. It could be seen in the horizontal stress cloud map after this excavation that when the excavated coal seam was again calculated to reach the stress balance, a caving zone would be formed above the goaf, and the stress range of the caving zone was distributed in 0–2 Mpa.

Figure 6B illustrates the distribution of vertical stress of coal seam M1 rock mass under the initial excavation condition. Under the action of self-weight stress, the vertical stress layers were evenly distributed. The vertical stress state decreased gradually with the increase of coal seam elevation, and the bottom stress was larger. After the excavation of the coal seam, the balance of the original rock stress was destroyed, and the stress field was redistributed. As shown in the diagram, the vertical stress cloud map took 2 Mpa as the equivalent interval, the minimum was 0 Mpa, the maximum was −8 Mpa (expressed as compressive stress), and the large area was 0–2 Mpa. The vertical stress at the bottom of the coal seam mining area was larger, and the stress at the upper roof of the coal seam goaf was smaller. The stress in the mined-out area of coal seam M1 was also released due to the excavation of coal seam, and the vertical stress in the mined-out area was reduced from the original equilibrium stress 2–4 Mpa to 0–2 Mpa. There were stress concentration areas at the front and back ends of the coal mine goaf, and the stress concentration areas were distributed in the range of 4–8 Mpa.

Figure 6C shows the distribution of shear stress after the mining of coal seam M1 reached equilibrium under the initial excavation condition. It could be seen from the figure that the shear stress of the rock strata near the mining area of coal mine rock and soil layers had positive and negative values. The positive value of shear stress indicated that it was consistent with the direction of movement along the inclined layer. When the excavated coal seam was recalculated to

reach the stress balance, a caving area would be formed above the goaf, and the shear stress of the subsidence area reached 0–2 Mpa. As shown in the figure, in the front and back ends of the coal mine goaf were stress concentration areas, and the shear stress was negative, distributed in 1–3 Mpa.

Figures 6D, E show the distribution of the maximum principal stress and the minimum principal stress after the balanced mining of inclined coal seam M1. From the diagram, it could be seen that the distribution of the maximum principal stress and the minimum principal stress appears stress stratification. The stress size gradually decreased with the increase of the elevation of the coal mine area, and the bottom layer stress was larger, which was consistent with the abovementioned stress cloud diagram in all directions. The maximum principal stress cloud diagram took 1 Mpa as the equivalent interval, the minimum was 0 Mpa, the maximum was −4 Mpa, and the large area of the caving zone was 0–1 Mpa; the minimum principal stress cloud map took 2 Mpa as the equivalent interval, the minimum was 0 Mpa, the maximum was −10 Mpa, and the large area of the collapse area was within the area of 0–4 Mpa. From the diagram, it could be seen that there was a more obvious stress concentration area at the lower end of the excavation area in the maximum principal stress cloud diagram and the minimum principal stress cloud diagram, and the stress concentration area at the upper end of the goaf was not obvious.

### 4.2.2 Coal seam M1 excavation displacement field analysis

After the coal seam was mined out, the original stress balance state around the goaf was destroyed, causing the redistribution of stress, which caused the deformation, damage, and movement of the rock layer and develops from the bottom up to the surface causing the
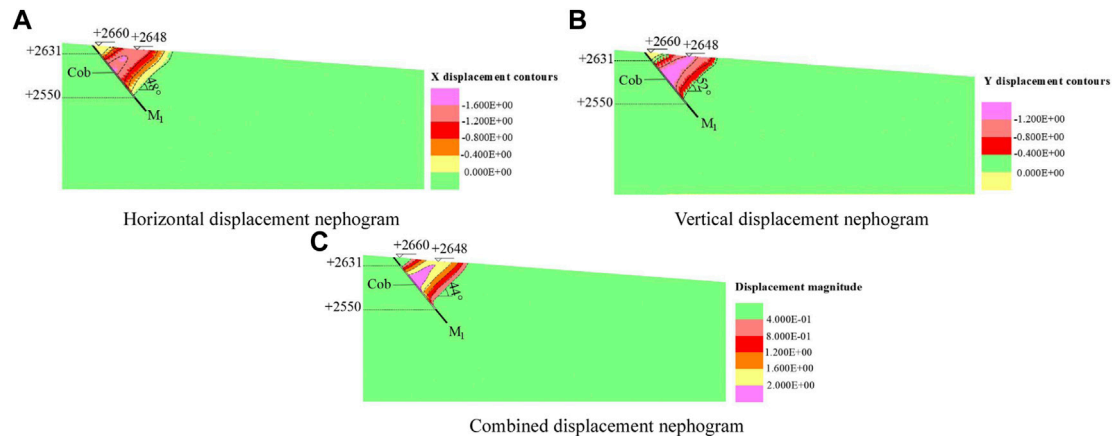
**FIGURE 7**
Coal seam M1 displacement cloud after mining. **(A)** Horizontal displacement nephogram, **(B)** vertical displacement nephogram, and **(C)** combined displacement nephogram.
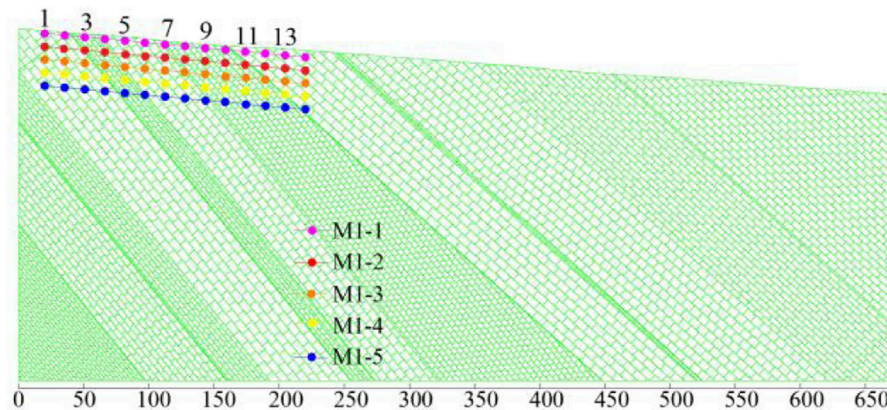


**FIGURE 8**
Layout of each monitoring line.

surface movement (Hao, et al., 2007; Chen and Zhao, 2014; Gui and Fan, 2014; Li and Wan, 2017). The deformation shape and movement angle of overlying strata in goaf could be observed intuitively by the displacement cloud diagram obtained by numerical simulation. In this section, the horizontal displacement, vertical displacement, and combined displacement of overlying strata in the mining area after coal seam mining were comprehensively analyzed and studied.

Figure 7 shows the displacement cloud map of coal seam M1 after mining. From the diagram, it could be seen that after the coal seam M1 excavation reaches equilibrium, the whole calculation model tended to be balanced and stable, and the roof and floor of the coal seam excavation were connected to reach the final rock deformation form.

Figure 7A shows the change of horizontal displacement of overlying strata after the excavation of coal seam M1 rock mass reached stability. As shown in the figure, the maximum horizontal displacement appears at the middle roof of the coal seam M1 mining area, and the maximum displacement was 1.6 m. The rock layer in the excavation area appears obvious bending and collapse.

Figure 7B shows the change of vertical displacement of overlying strata after the mining of coal seam M1 rock mass reached stability. As shown in the figure, the deformation of rock strata in coal seam M1 has reached the surface, and the deformation of overlying strata in goaf was concentrated in the main collapse area. The vertical displacement deformation after excavation was layered, and the displacement variation decreases with the increase of the range. The horizontal displacement at the middle roof of the M1 mining area of the coal seam had the maximum vertical displacement value, and the maximum displacement was 1.2 m.

Figure 7C shows the change of the combined displacement of the overlying strata after the excavation of the coal seam M1 rock mass reached stability. The combined displacement was the result of the calculation of the horizontal displacement and the vertical displacement according to the root number of the Pythagorean Theorem. The combined settlement values in this figure were positive. The change of the combined displacement was roughly the same as that of horizontal displacement and vertical displacement. The combined displacement deformation after
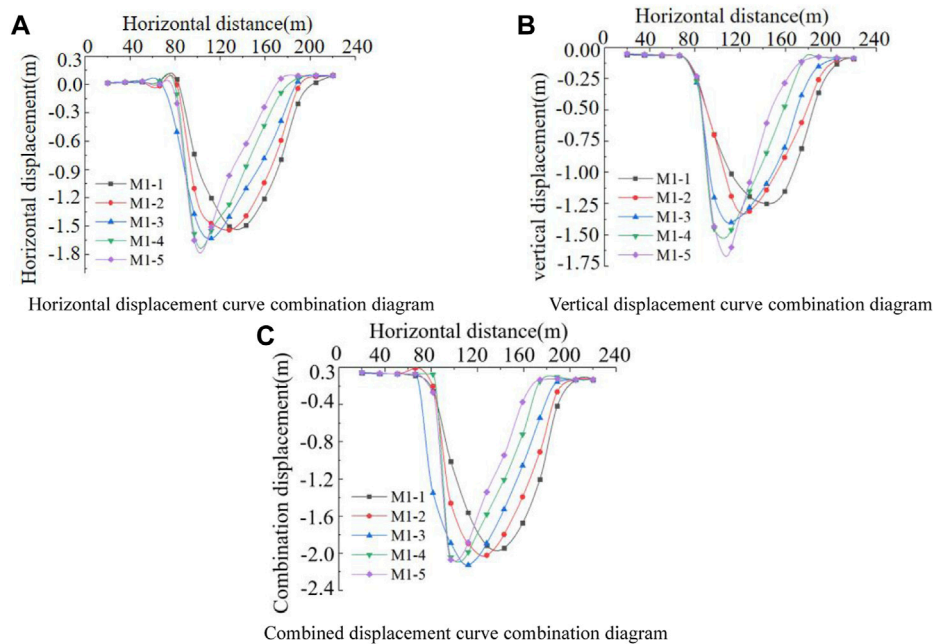
**FIGURE 9**
Sinking displacement curve. **(A)** Horizontal displacement curve combination diagram, **(B)** vertical displacement curve combination diagram, and **(C)** combined displacement curve combination diagram.

excavation was layered, and the displacement change of the roof in coal mine goaf was the largest. The combined displacement value in the large deformation area reached 0.4–2 m, and the displacement change was layered. The displacement change gradually decreased with the increase of range.

In order to analyze the specific subsidence displacement and verify the reliability of the numerical simulation results, we set up five monitoring lines parallel to the surface in the overlying strata of the mining area of coal seam M1, which were M1-1, M1-2, M1-3, M1-4, and M1-5, and each monitoring line was set up with 14 monitoring points. The figure showed monitoring points 1, 3, 5, 7, 9, 11, and 13. The spacing of the measuring points was roughly equal to 15 m, and the spacing of each monitoring line was 10 m. The layout of each monitoring line is shown in Figure 8.

Figure 9A shows a combination of horizontal displacement curves. The abscissa in the figure represents the horizontal distance of the measuring point in the length direction of the numerical model, and the ordinate represents the horizontal displacement monitoring value of the measuring point. According to the change rule of the monitoring line in the figure, it was easy to know that the horizontal displacement change value of monitoring line M1-5 was the largest, and the maximum deformation displacement of the line was 1.8 m. The variation of monitoring line M1-1 was small. The monitoring line was the closest to the surface, and the maximum deformation displacement was 1.5 m. It could be seen from the figure that the horizontal displacement curve combination diagram drawn according to the data of the five monitoring lines showed a "U"-shaped symmetrical distribution change rule. The horizontal displacement deformation of the main subsidence area of the rock stratum within the horizontal distance of 75–180 m was large, and the displacement was roughly in the range of 0.3–1.8 m. On both sides of

the large deformation area, the horizontal displacement deformation of the rock stratum was relatively small, and the displacement was roughly in the range of 0.0–0.1 m.

Figure 9B shows a combination of vertical displacement curves. The abscissa in the figure represents the horizontal distance of the measuring point in the length direction of the numerical model, and the ordinate represents the vertical displacement monitoring value of the measuring point. According to the change rule of the monitoring line in the diagram, it was easy to know that the vertical displacement change value of monitoring line M1-5 was the largest, and the maximum vertical deformation displacement of the monitoring line was about 1.65 m. Because the M1-1 monitoring line was closest to the surface, the deformation of the monitoring line was small, and the maximum deformation displacement was 1.25 m. It could be seen from the figure that the vertical displacement curve combination diagram drawn according to the data of the five monitoring lines showed a "U"-shaped symmetrical distribution change rule. The vertical displacement deformation of the main subsidence area of the rock stratum within the horizontal distance of 80–180 m was large, and the displacement was roughly in the range of 0.25–1.65 m. On both sides outside the large deformation area, the vertical displacement deformation of the rock stratum was small, and the displacement was roughly in the range of 0.0–0.1 m.

Figure 9C shows a combination of displacement change curves. Because the combined displacement was the result of the horizontal displacement and the vertical displacement according to the root number of the Pythagorean Theorem, the combined displacement should be positive. However, in order to compare the three types of curved more intuitively and clearly; the positive values were changed to negative values. The abscissa in the figure represents the horizontal distance of the measuring point in the length direction of the
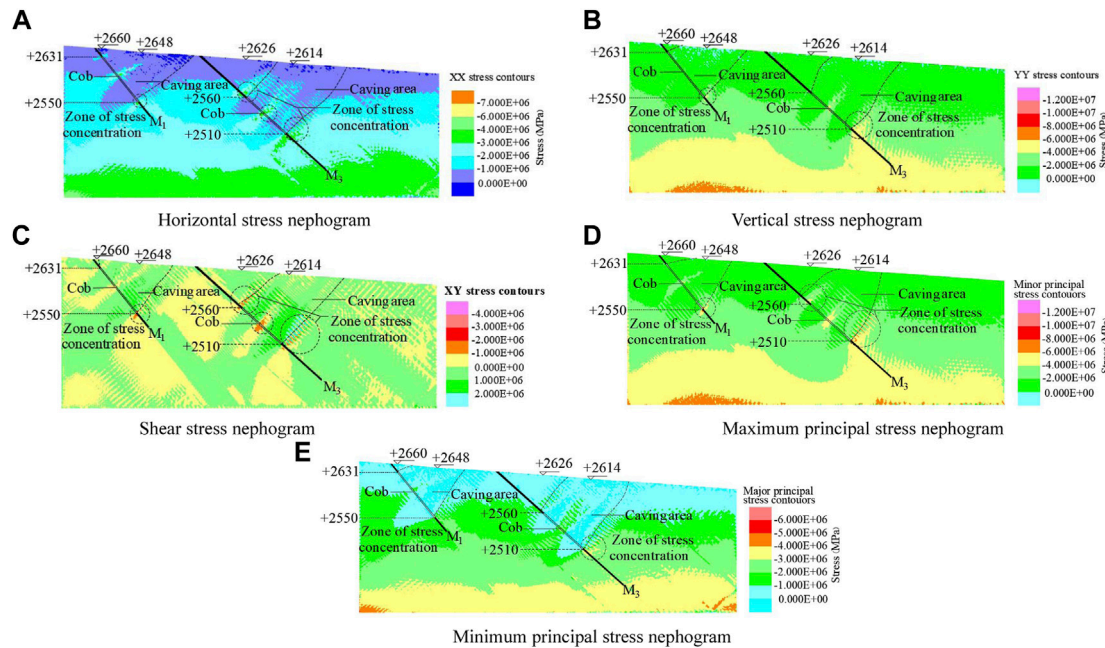
**FIGURE 10**
Stress cloud diagram of coal seams M1 and M3 after simultaneous mining. **(A)** Horizontal stress nephogram, **(B)** vertical stress nephogram, **(C)** shear stress nephogram, **(D)** maximum principal stress nephogram, and **(E)** minimum principal stress nephogram.

numerical model, and the ordinate represents the vertical displacement monitoring value of the measuring point. Similar to the change rule of the aforementioned two monitoring lines, the change value of combined displacement of monitoring line M1-5 was the largest, and the maximum displacement of combined deformation of this line was about 2.1 m because M1-1 monitoring line was the closest to the surface, the deformation of monitoring line was small, and the maximum displacement was 1.9 m. It could be seen from the figure that the combined displacement curve combination diagram drawn according to the data of the five monitoring lines showed a "U"-shaped symmetrical distribution change rule. The combined displacement deformation of the main subsidence area of the rock stratum within the horizontal distance of 80–180 m was large, and the displacement was roughly in the range of 0.3–2.1 m. On both sides of the large deformation area, the combined displacement deformation of the rock stratum was relatively small, and the displacement was roughly in the range of 0.0–0.1 m.

The law of the three displacement monitoring maps was consistent with the law of the horizontal displacement cloud analysis, showing a "U" distribution. Under different depths of rock strata, the closer to the coal seam mining area, the greater the change of horizontal displacement, and the farther away from the main subsidence area, the smaller the change of horizontal displacement of overlying strata. It was proved that the numerical simulation results do have theoretical guidance for mining subsidence control.

## 4.2.3 Stress field analysis of simultaneous excavation of coal seam M1 and M3

Figure 10 shows the stress distribution of coal seams M1 and M3 after simultaneous mining. Among them, Figure 10A shows the distribution of horizontal stress after the balance of coal seams M1 and M3 mining. The horizontal stress cloud map after excavation takes

1 Mpa as the equivalent interval, the minimum was 0 Mpa, the maximum was −6 Mpa (expressed as compressive stress), and the large area in the horizontal stress cloud map was 0–2 Mpa. The stress state gradually decreased with the increase of height, and the bottom stress was larger. As shown in the figure, there were stress concentration areas at the front and back ends of the coal mine goaf, and the horizontal stress was distributed in the range of 3–4 Mpa. The goaf area of the coal mine rock and soil layers was also due to coal seam excavation. The stress release of the goaf area was reduced from the original equilibrium stress of 1–2 Mpa to 0–1 Mpa. It could be seen in the horizontal stress cloud map after this excavation that when the excavated coal seam was again calculated to reach the stress balance, a caving zone would be formed above the goaf, and the stress distribution of the caving zone was 0–2 Mpa.

Figure 10B shows the distribution of vertical stress of coal seams M1 and M3 rock masses. Under the action of self-weight stress, the vertical stress was evenly distributed in layers. The vertical stress state decreased with the increase of height, and the bottom stress was larger. After the excavation of the coal seam, the balance of the original rock stress was destroyed, and the stress field was redistributed. As shown in the diagram, the vertical stress cloud map took 2 Mpa as the equivalent interval, the minimum was 0 Mpa, the maximum was −6 Mpa (expressed as compressive stress), and the large area was 0–2 Mpa. The vertical stress at the bottom of the coal seam mining area was larger, and the stress at the upper roof of the coal seam goaf was smaller. The vertical stress of mining area was reduced from 2–4 Mpa to 0–2 Mpa. There were stress concentration areas at the front and back ends of the coal mine goaf, and the stress concentration areas were distributed in the range of 6–8 Mpa.

Figure 10C shows the distribution of shear stress after the balance of coal seams M1 and M3 mining. From the diagram, it could be seen that the shear stress cloud map took 1 Mpa as the equivalent interval.
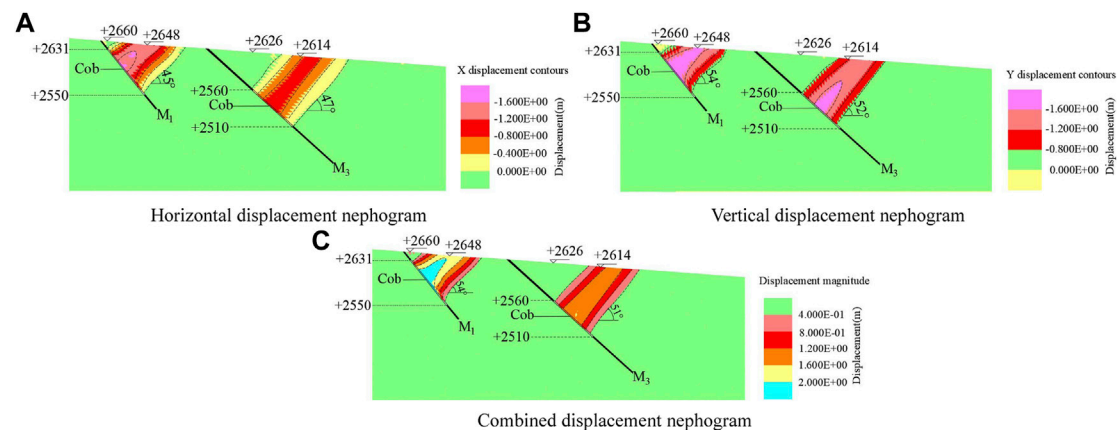
**FIGURE 11**
Coal seams M1 and M3 displacement cloud after mining. **(A)** Horizontal displacement nephogram, **(B)** vertical displacement nephogram, and **(C)** combined displacement nephogram.

When the excavated coal seam reached the stress balance again, the caving zone would be formed above the goaf. The large area of shear stress in the subsidence area was positive, reaching 0–2 Mpa. As shown in the front and back of the coal mine goaf have appeared stress concentration area, and the shear stress was negative, distributed in 1–2 Mpa.

Figures 10D, E show the distribution of the maximum principal stress and the minimum principal stress after the mining of coal seams M1 and M3 rock masses reached equilibrium. It could be seen from the figure that the distribution of the maximum principal stress and the minimum principal stress appeared stress stratification. The stress state gradually decreased with the increase of height, and the stress at the bottom layer was larger. The minimum is 0 Mpa, the maximum was −8 Mpa, and the large area of the caving area was 0–2 Mpa. The minimum principal stress cloud map took 1 Mpa as the equivalent interval, the minimum was 0 Mpa, the maximum was −5 Mpa (expressed as compressive stress), and the large area of the caving zone was within the range of 0–1 Mpa. It could be seen from the diagram that there was a more obvious stress concentration area at the lower end of the excavation area in the maximum principal stress cloud diagram and the minimum principal stress cloud diagram, and the stress concentration area at the upper end was not obvious.

## 4.2.4 Displacement field analysis of simultaneous excavation of coal seams M1 and M3

After the coal seam was mined, the original stress equilibrium state around the mined-out area was destroyed, which caused the redistribution of stress and the deformation, failure, and movement of rock strata. The deformation shape and movement angle of overlying strata in goaf could be observed intuitively by the displacement cloud diagram obtained by numerical simulation. In this section, the horizontal displacement, vertical displacement, and combined displacement of overlying strata in mining area after coal seam mining were comprehensively analyzed and studied.

Figure 11A shows the change of horizontal displacement of overlying strata after the simultaneous excavation of coal seams M1 and M3 reached stability. As shown in the figure, the horizontal displacement at the middle roof of the coal seam

M3 mining area had a maximum value, and the maximum displacement was 1.2 m. The horizontal displacement of the rock strata in the goaf of the coal mine was inclined and layered. The horizontal displacement of the deformation area was relatively large. The displacement of the main subsidence area was the largest, and the range of large deformation area was 0–1.6 m.

Figure 11B shows the change of the vertical displacement of the overlying strata after the simultaneous mining of coal seams M1 and M3. As shown in the figure, the deformation of the rock strata of coal seam M3 had reached the surface, and the deformation of the overlying strata in the goaf was concentrated in the main collapse area. The vertical displacement deformation after excavation was layered, and the displacement variation gradually decreases with the increase of the range. The horizontal displacement at the middle roof of the M3 mining area of the coal seam had the maximum vertical displacement value, and the maximum displacement was 1.6 m; the displacement of the main subsidence area was the largest, the range of large deformation area was 0–1.6 m, and the inclination angle of large deformation area was 52°.

Figure 11C shows the change of the combined displacement of the overlying strata after the simultaneous excavation of coal seams M1 and M3 reached stability. The combined settlement values in this figure were positive. The change of combined displacement was roughly the same as that of horizontal displacement and vertical displacement. The combined displacement deformation after excavation was distributed in layers. The displacement variation of the roof in the coal mine goaf was the largest. The combined displacement value of the large deformation area reached 0.4–1.6 m, and the displacement variation was distributed in layers. The displacement variation decreases with the increase of range, and the inclination angle of large deformation area was 51°.

Figure 12 shows a schematic diagram of the fracture angle and boundary angle after coal mining. After the excavation of the coal seam was balanced, there would be obvious cracks in the rock and soil layers, and the deformation of the rock strata in the upper roof of the mining area was more obvious. Under the condition of full mining or close to full mining, the angle formed by the boundary crack and the horizontal line on the side of the coal pillar was considered to be the crack angle after the balance of coal seam mining. It could be seen from the figure that the crack angle of
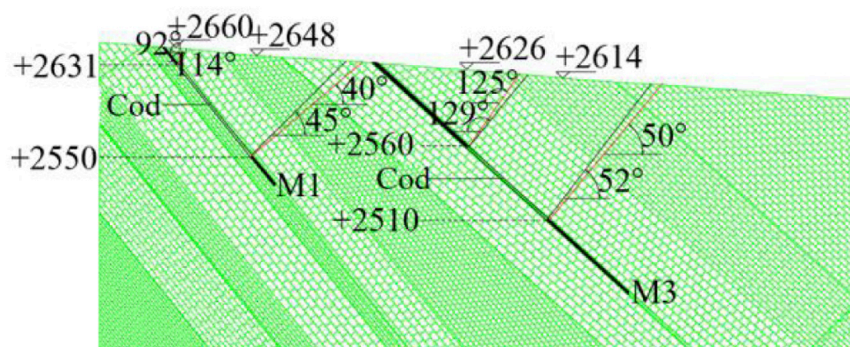
**FIGURE 12**
Fracture angle and boundary angle diagram.

**TABLE 5 Prediction of the fracture angle and boundary angle under sufficient conditions (unit: °).**

| Mining coal seam and direction | Crack angle/° | Rim angle/° |
|---|---|---|
| M1 uphill direction | 114 | 92 |
| M1 downhill direction | 45 | 40 |
| M3 uphill direction | 129 | 125 |
| M3 downhill direction | 52 | 50 |

M1 was 114°, and the crack angle of the downhill was 45°. M3 had an uphill crack angle of 129° and a downhill crack angle of 52°. In the general subsidence area, in fact, we believed that when the rock movement reached a certain value, the small movement of the overlying strata was ignored, that is, the overlying strata are not moving. According to the definition of relevant specifications, under the condition of full mining or near full mining, the measured subsidence curve on the main section of the surface movement basin was used, and the point with a subsidence value of 10 mm was used as the boundary point. The angle between the line connecting the boundary point to the goaf boundary and the horizontal line on the side of the coal pillar was called the boundary angle. It could be seen from the figure that the uphill boundary angle of the overlying strata movement after the excavation of coal seam M1 was 92°, and the downhill boundary angle was 40°. After the excavation of coal seam M3, the uphill boundary angle was 125°, and the downhill boundary angle was 50°. See Table 5 for details.

The cloud map of the displacement change indicates the final overall displacement of the balance after the excavation of coal seam M3. Because the change trend of the rock strata in different strata after the excavation of coal seam M3 was different, the situation of the subsidence of the rock strata was also different. In order to analyze the specific subsidence displacement and the law of the subsidence of the rock strata after the excavation of the coal seam more clearly and intuitively, we set up five monitoring lines parallel to the surface in the overlying strata of the mining area of coal seam M3, which were M3-1, M3-2, M3-3, M3-4, and M3-5, and each monitoring line had 14 monitoring points. The horizontal range of coal seam M3 was 300–520 M, and the distance between measuring points was 16 m. The distance between M3-1

and M3-2, M3-3 and M3-4 was 20 m, and the distance between M3-2 and M3-3, M3-4 and M3-5 was 10 m. The layout of each monitoring line is shown in Figure 13.

Figure 14 shows a combination of displacement curves after simultaneous excavation of coal seams. Figure 14A shows a combination of horizontal displacement curves, which as obtained by comparing five monitoring lines in the same coordinate system. According to the change rule of the monitoring line in the diagram, it was easy to know that the horizontal displacement change value of monitoring line M3-5 was the largest, and the maximum deformation displacement of the monitoring line was 1.0 m. The change of monitoring line M3-1 was small, the monitoring line is closest to the surface, and the maximum deformation displacement was 0.8 m. It could be seen from the figure that the horizontal displacement curve combination diagram drawn according to the data of the five monitoring lines showed a "U"-shaped symmetrical distribution change rule. The horizontal displacement deformation of the main subsidence area of the rock stratum within the horizontal distance of 320–480 m was large, and the displacement was roughly in the range of 0.2–1.0 m. On both sides of the large deformation area, the horizontal displacement deformation of the rock stratum was relatively small, and the displacement was roughly in the range of 0.0–0.1 m.

Figure 14B shows a combination of vertical displacement curves, which was obtained by comparing five monitoring lines in the same coordinate system. According to the change rule of the monitoring line in the diagram, it was easy to know that the vertical displacement change value of monitoring lines M3–5 was the largest, and the maximum vertical deformation displacement of the monitoring line was about 1.3 m. Because the M3-1 monitoring line was the closest to the ground, the deformation of the monitoring line was small, and the maximum displacement was 1.0 m. It could be seen from the figure that the vertical displacement deformation of the main subsidence area of the rock stratum within the horizontal distance of 320–480 m was relatively large, and the displacement was roughly in the range of 0.2–1.3 m. On both sides of the large deformation area, the vertical displacement deformation of the rock stratum was relatively small, and the displacement was roughly in the range of 0–0.1 m.

Figure 14C shows the combined displacement curve combination diagram. Similar to the change rule of the aforementioned two monitoring lines, the change value of combined displacement of monitoring line M3-5 was the largest, and the maximum
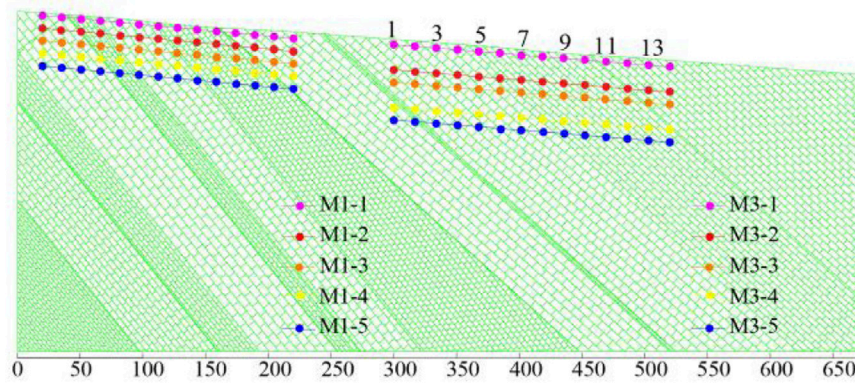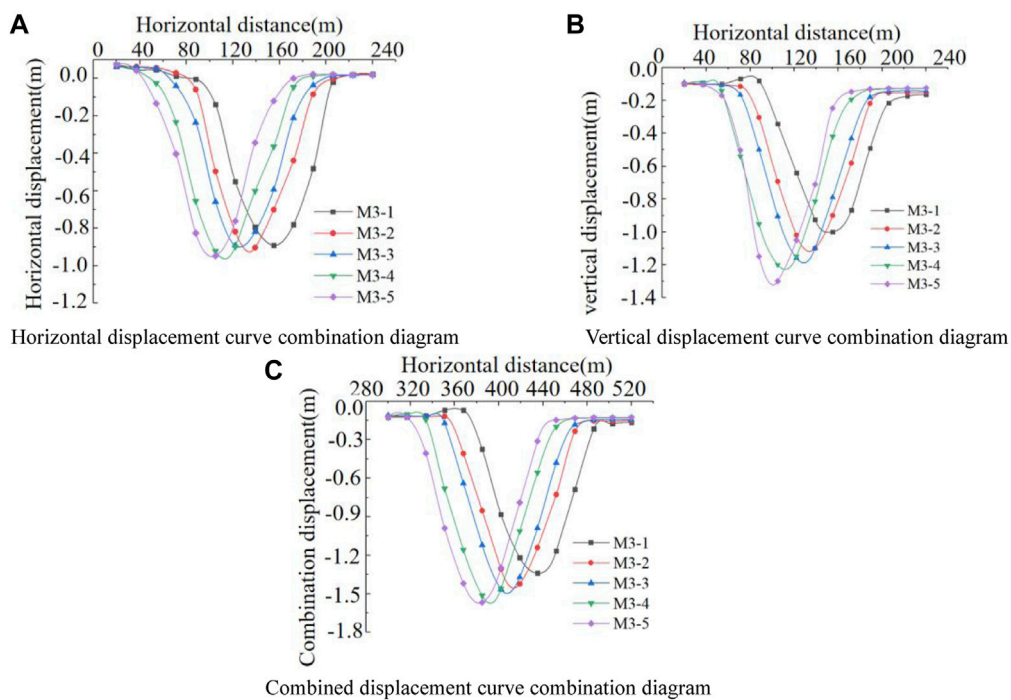
**FIGURE 13**
Layout of each monitoring line.



**FIGURE 14**
Sinking displacement curve. **(A)** Horizontal displacement curve combination diagram, **(B)** vertical displacement curve combination diagram, and **(C)** combined displacement curve combination diagram.

displacement of combined deformation of this line was about 1.6 m because the M3-1 monitoring line was the closest to the surface, the deformation of monitoring line was small, and the maximum displacement was 1.38 m. It could be seen from the figure that the combined displacement curve combination diagram drawn according to the data of the five monitoring lines showed a "U"-shaped symmetrical distribution change rule. The combined displacement deformation of the main subsidence area of the rock stratum in the horizontal distance of 320–480 m was large, and the displacement was roughly in the range of 0.3–1.5 m. On both sides of the large deformation area, the combined displacement deformation of the

rock stratum was relatively small, and the displacement was roughly in the range of 0.0–0.1 m.

The analysis showed that the stress concentration area and the displacement change area were highly coincident, and the displacement monitoring map was consistent with the horizontal displacement cloud analysis, showing a "U"-type distribution. Under different rock depths, the closer to the coal seam mining area, the greater the displacement change, the farther away from the main subsidence area, the smaller the overburden displacement change. It was proved that the numerical simulation results do have theoretical guidance for mining subsidence control.

# 5 Conclusion

According to the special geological conditions, mining conditions, and abundant measured data in the Dameidong mining area, the research idea of "transient electromagnetic detection-numerical simulation" was put forward, that is, using transient electromagnetic to detect the range of coal mine goaf, and combined with numerical simulation to study the settlement law of rock strata and to explore its role in the prevention and control of geological disasters.

1 The transient electromagnetic method was used to explore the hydrogeological conditions of the coal mine site in the study area. According to the geophysical prospecting results, when the apparent resistance was less than 30 Ωm, it was presumed to be the coal mine water-rich area; when the apparent resistance was greater than 30 Ωm and less than 50 Ωm, it was speculated that it was a weak water-rich area of coal mine, which was highly coincident with the mining area of large coal tunnel mining area and can be used as the basic basis for numerical simulation. 2 The numerical simulation results showed that the stress state diagram was layered after coal seam excavation. The stress in the middle roof of the mined-out area was large, and the caving zone would be formed above the mined-out area. The stress concentration area would appear in the front or back of the mined-out area, resulting in the stress release in the mined-out area, and the original equilibrium stress would decrease.
3 Combining the displacement curve drawn by the measured data of the monitoring line with the displacement change law obtained by numerical simulation, it was concluded that the displacement change of the overlying strata in the coal mine goaf was mostly in the 'U′ shape distribution. The displacement on the same horizontal plane increases first and then decreases, and the final deformation not adversely affected the surrounding buildings.
4 Through the combination of transient electromagnetic and numerical simulation, the analysis of the deformation of overlying strata in the old goaf of large coal roadway provided guidance for the prevention of geological disasters in mining area. Finally, it was speculated that the settlement deformation of the overlying strata in the improved coal mine goaf did not cause damage to buildings and residents in Datong County and nearby towns.

# Data availability statement

The original contributions presented in the study are included in the article/supplementary material; further inquiries can be directed to the corresponding author.

# Author contributions

MZ was responsible for the writing of the manuscript. Z-XW was responsible for electromagnetic exploration and numerical simulation. F-HX, J-HD, and Y-DD were responsible for analyzing the data obtained from electromagnetic exploration and numerical simulation.

# Conflict of interest

The authors declare that the research was conducted in the absence of any commercial or financial relationships that could be construed as a potential conflict of interest.

# Publisher's note

All claims expressed in this article are solely those of the authors and do not necessarily represent those of their affiliated organizations, or those of the publisher, the editors, and the reviewers. Any product that may be evaluated in this article, or claim that may be made by its manufacturer, is not guaranteed or endorsed by the publisher.

# References

Che, T., Gong, H., and Bo, J. (2022). Numerical simulation analysis of bedding slope stability of bridge foundation based on UDEC [ J ]. *Sichuan Archit.* 42 (01), 142–145.

Chen, G., and Zhao, F. Numerical simulation and analysis of the movement law of rock strata and surface based on UDEC[J]. *Coal Econ. Inn. Mong* 2014,18(09): 183–184. + 186.

Chen, H., Li, Y., and Zhao, P. (2016). Research on fracture control model of partially filled shallow coal seam based on UDEC simulation[J]. *Shaanxi Coal* 35 (01), 7–10. + 13.

Gao, B., Gao, J., and Yuan, D. (2013). Simulation and analysis of overburden fracture with large mining height based on UDEC[J]. *J. Hunan Univ. Sci. Technol. Sci. Ed.* 28 (02), 1–6.

Guan, K., Dong, T., and Jia, J. (2012). UDEC-based analysis of the coupling effect of topsoil and main key strata on surface subsidence in shallow coal seams[J]. *Coal mine Saf.* 43 (03), 161–163.

Gui, Q., and Fan, S. (2014). Numerical simulation of shallow coal seam in mountainous area based on UDEC[J]. *Mod. coal mine* 31 (01), 80–82.

Guo, C., Li, Y., and Liu, J. (2010). Application of UDEC in numerical simulation of mining subsidence in steeply inclined and extra-thick coal seams[J]. *China Min. Ind.* 19 (04), 71–74.

Hao, Z., Lin, B., and Zhang, J. (2007). Numerical simulation and analysis of overlying strata movement law in protective layer mining based on UDEC[J]. *China Min. Ind.* 16 (07), 81–84.

Li, E., and Wan, X. (2017). Numerical simulation of mine pressure behavior in stope based on UDEC[J]. *Industrial Saf. Environ. Prot.* 43 (11), 18–20. + 48.

Li, L. (2016). Research on the movement law of overlying strata during excavation based on UDEC[J]. *Coal Chem. Industry* 39 (10), 46–47. + 50.

Liang, Y. (2020). UDEC numerical simulation of shallow coal seam working face[J. ]. *Shanxi Coal* 40 (01), 9–12. + 34.

Liiu, Y. (2017). Numerical simulation of close-distance upper protective layer mining based on UDEC[J]. *Energy Environ. Prot.* 39 (09), 179–182. + 187.

Liu, Y., Guangjie, L., and Ma, X. (2010). Genesis analysis and risk prediction of ground fissures in Jingyu County, Jilin Province [J]. *Chin. J. Geol. Hazards Prev.* 21 (1), 136–139.

Pei, X. J., Zhang, S., Huang, R. Q., Wei, K. H., Liu, F. Z., and Duan, Y. X. (2016). Deformation propagation and identification of an impending disaster of a retained high embankment based on monitoring of minor deformation, China. *Landslides Eng. Slopes Exp.* 3, 1583–1590.

Qiang, Y., Wang, X., and Duan, R. (2021). Application of transient electromagnetic method in the exploration of Hancheng mining area[J]. *Shanxi Geol.* 39 (02), 89–95.

Sun, C., Liang, C., and Lu, R. (2021). Feasibility analysis of numerical simulation of high density electrical method applied to the detection of underground water goaf in coal mine [J]. *West. Prospect. Proj.* 33 (03), 148–151.

Wang, H. (2009). Study on the detection method of coal mine Goa. *J. Taiyuan Technol.* (05), 58–59. + 62.

Wang, J., and Liu, X. (2013). Application of high density electrical method in Zhuangzihe coal mine goaf detection. *J. Shanxi coal* 33 (10), 63–64. + 67.

Xia, Y., Lei, T., and Bai, H. (2006). Interaction between overlying strata of coal seam and underground water in mining damage[J]. *Coal Geol. Explor.* 34 (01), 41–45.

Yang, Z., and Guo, K. (2020). Application of high-density electrical method in the detection of concealed goaf in iron mines[J]. *China Min. Ind.* 29 (08), 158–164.

Yin, W. (2022). Magnetotelluric method for detection and prediction of karst collapse area in mining area[J]. *West. Explor. Eng.* 34 (05), 170–172.

Yu, J., and Gui, Q. (2014). UDEC simulation of fracture development in shallow coal seams in mountainous areas[J]. *Mod. coal mines* 27 (02), 57–59.

Zhang, G., and Huang, T. (2010). UDEC numerical simulation of a mine. *J. Coal* 19 (06), 21–23.

Zhang, S., Jiang, T., Pei, X., Huang, R., Xu, Q., Xie, Y., et al. (2022). A new forecasting method for failure time of creep landslide based on nonlinear creep behavior and new prewarning criterion. *Front. Earth Sci.* 10, 1018432. doi:10.3389/feart.2022.1018432

Zhang, S., Pei, X. J., Wang, S. Y., Huang, R. Q., and Zhang, X. C. (2020). Centrifuge model testing of loess landslides induced by excavation in Northwest China. *Int. J. Geomech.* 20. doi:10.1061/(ASCE)GM.1943-5622.0001619

Zhang, S., Pei, X. J., Wang, S. Y., Huang, R. Q., Zhang, X. C., and Chang, Z. L. (2019a). Centrifuge model testing of a loess landslide induced by rising groundwater in Northwest China. *Eng. Geol.* 259, 105170. doi:10.1016/j.enggeo.2019.105170

Zhang, S., Zhang, X. C., Pei, X. J., Wang, S. Y., Huang, R. Q., Xu, Q., et al. (2019b). Model test study on the hydrological mechanisms and early warning thresholds for loess fill slope failure induced by rainfall. *Eng. Geol.* 258, 105135. doi:10.1016/j.enggeo.2019.05.012

# Intelligent identification of pavement cracks based on PSA-Net

Xuan Lin[1], Jian Zhang[2], Daifeng Wu[3], Enhong Meng[4]*, Maoyi Liu[3], Meng Li[2] and Fuliu Gao[2]

[1]School of Mechano-Electronic Engineering, Xidian University, Xi'an, China, [2]Faculty of Geosciences and Environmental Engineering, Southwest Jiaotong University, Chengdu, China, [3]Chongqing Urban Construction Investment (Group) Co., Ltd., Chongqing, China, [4]School of Mechanical Engineering, Southwest Jiaotong University, Chengdu, China

The identification of pavement cracks is critical for ensuring road safety. Currently, manual crack detection is quite time-consuming. To address this issue, automated pavement crack-detecting technology is required. However, automatic pavement crack recognition remains challenging, owing to the intensity heterogeneity of cracks and the complexity of the backdrop, e.g., low contrast of damages and backdrop may have shadows with comparable intensity. Motivated by breakthroughs in deep learning, we present a new network architecture combining the feature pyramid with the attention mechanism (PSA-Net). In a feature pyramid, the network integrates spatial information and underlying features for crack detection. During the training process, it improves the accuracy of automatic road crack recognition by nested sample weighting to equalize the loss caused by simple and complex samples. To verify the effectiveness of the suggested technique, we used a dataset of real road cracks to test it with different crack detection methods.

KEYWORDS

deep learning, pavement crack identification, pyramid pooling, feature fusion, risk assessment

## 1 Introduction

With the continuous development and improvement of China's roads as infrastructure construction, how to carry out scientific and intelligent maintenance management has become a fundamental research problem. The diagnosis of pavement diseases is an important issue in road maintenance, and cracking is the dominant type of pavement disease. The identification of pavement cracks is a critical duty for ensuring road safety. In this work on pavement crack detection, methods based on non-deep learning approaches are referred to as traditional crack-detecting methods. In the past few years, many researchers have been working on the automated detection of cracks. These works can be divided into five categories: 1) crack detection methods based on the wavelet transform: the wavelet transform decomposes the image into different frequency bands, and defect and noise are converted into distinct amplitude wavelet coefficients, which allows them to be applied to pavement crack detection work. Peggy et al. (2006) created a complicated coefficient map by applying a multi-scale 2D wavelet transform (Peggy et al., 2006); the crack region is then determined by scanning for the wavelet coefficients from the most enormous scale to the most miniature scale. However, this method cannot handle cracks with limited continuity or significant curvature characteristics. 2) Image thresholding crack detection method: Scholars use preprocessing algorithms to reduce lighting artifacts and then threshold the image to obtain candidate cracks. The processed crack images are further refined using morphological techniques (Chambon and Jean-Marc, 2011; Huang and Zhang, 2012; Xu et al., 2013; Li et al., 2015). The aforementioned methods were further developed, and new graph-based methods can achieve crack candidate refinement (Zou et al.,

2012; Kelwin and Lucian, 2014; Marcos et al., 2016). 3) Handcrafted features and classification to achieve crack detection: Most conventional crack-detecting algorithms rely on handcrafted features and patch-based classifiers to achieve crack detection. Handcrafted features, such as HOG and LBP, are extracted from the image patches as descriptors. Then, a classifier, such as a support vector machine, is used to achieve crack recognition and classification (Hu and Zhao, 2010; Zakeri et al., 2013; Srivatsan et al., 2014; Rafal et al., 2015). 4) Crack detection is carried out based on edge detection: Yan et al. (2007) introduced a morphological filter in crack detection and used an improved median filter to remove noise to achieve crack detection (Yan et al., 2007). Albert and Nii (2008) applied the Sobel edge detector to detect cracks and used a two-dimensional empirical pattern decomposition algorithm to remove speckle noise (Albert and Nil, 2008). Stochastic structure forest was used by scholars and combined with structural information for crack detection (Piotr and Lawrence, 2013; Shi et al., 2016). 5) Complete crack detection based on the minimal path: The shortest path approach was suggested by Kass et al. (1988) to extract basic open curves from photographs for achieving crack detection (Kass et al., 1988). Vivek et al. (2012) proposed using an improved minimal path method to detect the same type of similar contours in the image structure to achieve crack detection (Vivek et al., 2012). This enhanced method requires less *a priori* knowledge about the topology and endpoints of the required curve. Amhaz et al. (2016) proposed a two-stage approach for crack detection: first, endpoints are selected in the local range, and second, the minimum path is selected in the global range to finally achieve crack detection (Amhaz et al., 2016). Nguyen et al. (2011) proposed a two-stage approach for crack detection by introducing freeform anisotropic features that offered a method that simultaneously considered strength and the shape of cracks to complete the identification and detection of cracks (Nguyen et al., 2011). However, traditional crack detection methods are extremely challenging to identify and detect due to the strong influence of human factors and the low efficiency of detection based on

transformation methods and are not applicable to complex scenes. Their performance is still limited.

For the last several years, deep learning has seen extraordinary progress in the field of computer vision (Alex et al., 2017). Scholars have made several attempts to use deep learning techniques for crack identification. Zhang et al. (2016) developed a patch-based fracture detection neural network comprising four convolutional layers and two fully connected layers (Zhang et al., 2016). In addition, Zhang et al. (2016) compared their approach with handcrafted features to demonstrate the advantages of deep learning methods in feature representation. Pauly et al. (2017) used a deeper neural network to identify the road cracks (Pauly et al., 2017). Feng et al. (2017) proposed a deep active learning system to deal with the problem of limited labeling resources (Feng et al., 2017). Eisenbach et al. (2017) presented a road condition dataset for training a deep learning network and first evaluated and analyzed state-of-the-art methods for pavement distress detection. The approach mentioned previously considers crack detection as a patch-based classification challenge, dividing each picture into tiny patches and then training a deep neural network to determine whether or not each patch is a crack (Eisenbach et al., 2017). However, this approach has a complex operational process and is sensitive to the size of the patches. With the rapid development of semantic segmentation tasks (Jonathan et al., 2017; Vijay et al., 2017; Fan et al., 2018), many algorithms have been applied to different scenarios with good application results. Schmugge et al. (2017) proposed a SegNet-based crack segmentation method to detect cracks by aggregating crack probabilities. In conclusion, deep learning-based techniques show great potential for road crack detection applications (Stephen et al., 2017). Joshi et al. (2022) adopted a segmentation-based deep learning method for surface crack detection. Wang et al. (2022) presented fully convolutional network architecture for crack detection in fast-stitching images. To this end, we propose a new deep learning framework called PSA-Net for the particular task of road crack detection, which focuses on three aspects, namely, multi-scale feature information
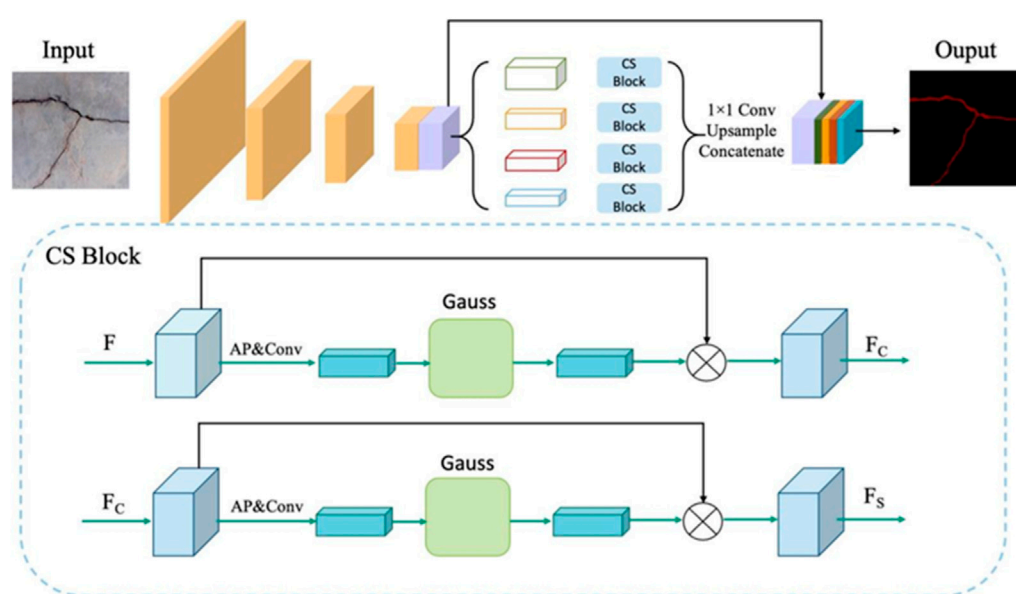


**FIGURE 1**
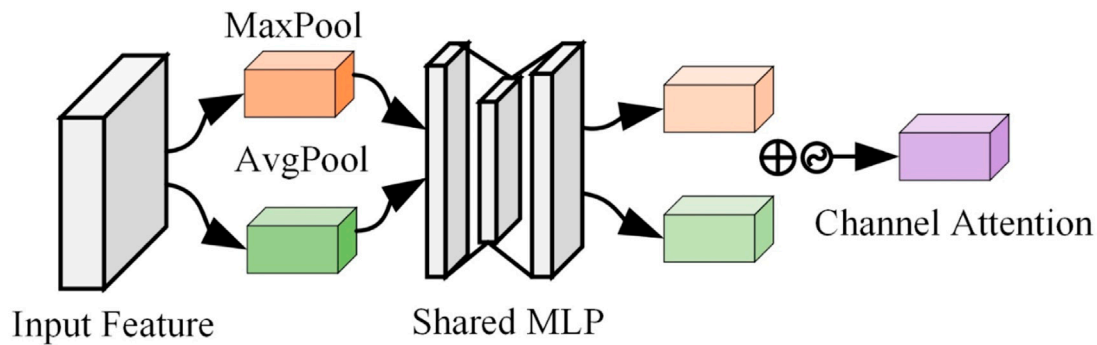Schematic diagram of the network framework.

**FIGURE 2**
Schematic diagram of the channel attention module. MaxPool means maximum pooling, and AvgPool means average pooling.
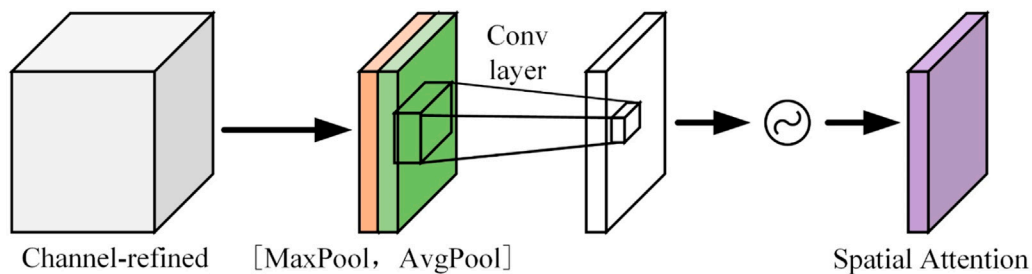


**FIGURE 3**
Schematic diagram of the spatial attention module.

extraction, spatio-temporal attention mechanism, and pyramid pooling, focusing on the contextual semantic information and edge information on crack images to achieve end-to-end pavement crack detection, which aims to improve the accuracy of crack intelligent recognition and detection.

# 2 Methods

For segmentation tasks, contextual information impacts the segmentation's effectiveness. Generally speaking, when we judge the category of an object, besides directly observing its appearance, we sometimes also assist the environment in which it appears, ignoring these to make judgments that sometimes cause problems. The intelligent crack identification and detection of pavement in this paper are similar to the segmentation task, where we can improve the accuracy and precision of crack identification with the help of auxiliary information. First, this subsection describes the composition of the algorithm, and the network used consists of encoder and decoder architecture, as shown in Figure 1. We use ResNet-101 as the backbone in the feature extraction stage (He et al., 2016). The encoder uses the pre-trained model (ResNet-101) and the dilated convolution strategy to achieve the feature map extraction, and the extracted feature map is 1/8 the size of the input. The pyramid pooling module fuses the feature map to get the fused feature with general information, which is upsampled and connected with the feature map before pooling. Finally, the final output is obtained by a convolutional layer.

## 2.1 Dilated convolution

Dilated convolution is a technique for solving picture semantic segmentation issues in which downsampling affects image resolution and results in information loss. By adding holes to expand the perceptual field, the original $3 \times 3$ convolution kernel can have a perceptual area of $5 \times 5$ (dilated rate = 2) or be more significant with the same number of parameters and computation, thus eliminating the need for downsampling. It has the advantage of increasing the field of perception and allowing each convolution output to contain a more extensive range of information. The information is without pooling data or creating loss ambiguity under the same computational conditions. Dilated convolution is often used in real-time image segmentation. Dilated convolution can be used when the network layer requires a bigger perceptual field, but the number or size of convolution kernels cannot be increased, owing to restricted computing resources. The feature extraction module of our network uses dilated convolution to increase the perceptual field and further improve the segmentation efficiency. The mathematical expression of dilated convolution is (Yu and Koltun, 2015)

$$M(i,j) = \sum_{x=1}^{X}\sum_{y=1}^{Y} h(i + atr \times x, j + atr \times y) \times g(x,y), \quad (1)$$

where I and j denote the positions of the image; X and Y represent the length and width of the input image, respectively; h(i,j) denotes the feature value of the input image at (i,j); atr denotes the void rate; $g$ is the convolution kernel function; and M(i,j) denotes the result of the input image after convolution. Dilated convolution is to expand the

size of the convolution kernel by zero-filling in the standard convolution, so that it can better capture the context information on the feature map. The size of the dilated convolution is achieved by adjusting the atrous rate.

## 2.2 Pyramid pooling

The pyramid pooling module aggregates contextual data from several places and enhances the capacity to access global data. Experiments demonstrate that such an *a priori* representation (referring to PSP as a structure) is successful and produces outstanding results on a variety of datasets. The module incorporates four pyramid-scale features. The first row in red is the coarsest feature global pooling, generating a single bin output, and the next three rows are pooling features at different scales (as shown in Figure 1). To ensure the weight of the global features, if the pyramid has a total of N levels, a $1 \times 1$ convolution is used after each class to reduce level channels to the original 1/N. The size before unspooling is then obtained by bilinear interpolation and CONCAT function together. The pooling kernel size for the pyramid levels is settable and related to the input sent to the pyramid. We used four ranks with kernel sizes of $1 \times 1$, $2 \times 2$, $3 \times 3$, and $6 \times 6$.

## 2.3 Feature fusion

Feature fusion is a popular component of current network topologies that merges features from distinct layers or branches. It is often performed using basic operations (such as summation or splicing); however, this is not always the best option. This is a unified general scheme for attentional feature fusion that applies to the most common scenarios, including short-hop and long-hop connections and feature fusion induced in the inception layer. As shown in Figure 1 and Figure 2, we present the multi-scale channel attention module, which solves the challenges of fusing information supplied at distinct scales to better fuse features with inconsistent meanings and scales. We also show that the early integration of feature maps might be a bottleneck, which can be solved by adding another attention level. With fewer parameters or network layers, our model outperforms the latest network on both road crack segmentation datasets, suggesting the more sophisticated attention mechanism used for feature fusion has excellent potential to consistently produce better results than direct feature fusion.

The input feature maps in the channel attention module are pooled and averaged into the shared MLP layer. Then, the output features of the shared MLP layer are summed by sending elementwise and activated by the sigmoid function to obtain the feature map of the channel attention module. The channel attention module (CAM) compresses the feature map in spatial dimensions to get a one-dimensional vector and then operates on it. The channel attention module focuses on what is essential in this graph. Mean pooling has feedback for every pixel point on the feature map. In contrast, maximum pooling has feedback for gradients only where the response is most evident in the feature map when performing gradient backpropagation calculations.

The feature map generated from the channel attention module is utilized as an input in the spatial attention module (as shown in Figure 3). First, execute maximum and average pooling depending on the channel, followed by the CONCAT operation on both layers. The feature map produced from the spatial attention module is then obtained by the sigmoid function after convolution is conducted and reduced to one channel.

The spatial attention module compresses channels and performs mean and maximum pooling in the channel dimension. The final pooling operation is to extract the channel's greatest value, and the number of extractions is H W. The average pooling procedure is used to acquire the channel's average value, and the number of extractions is also H W. As a result, a two-channel feature map is generated.

## 2.4 Loss function

The loss function is the gap between the predicted and actual values of the model. That is to find a standard to help the training mechanism optimize parameters at any time, so as to find the parameters with the highest precision of the network role at all times toameterork proposes to



**FIGURE 4**
Flow chart of algorithm implementation.
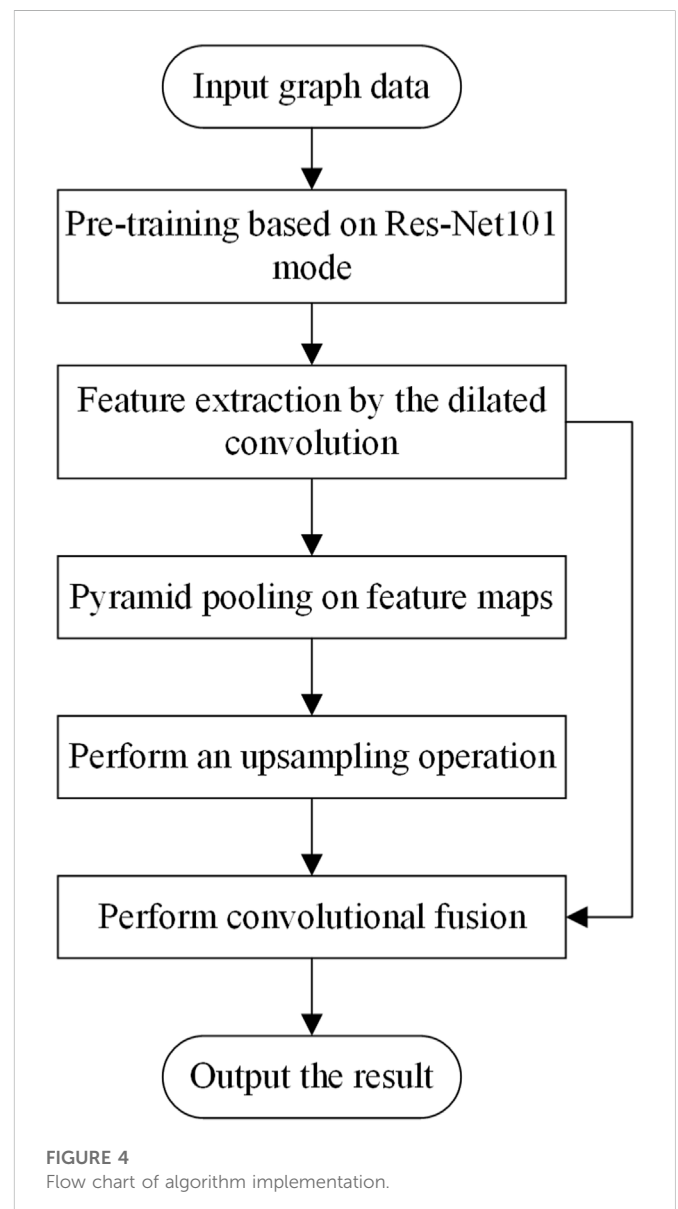
**FIGURE 5**
Road surface crack detection results.

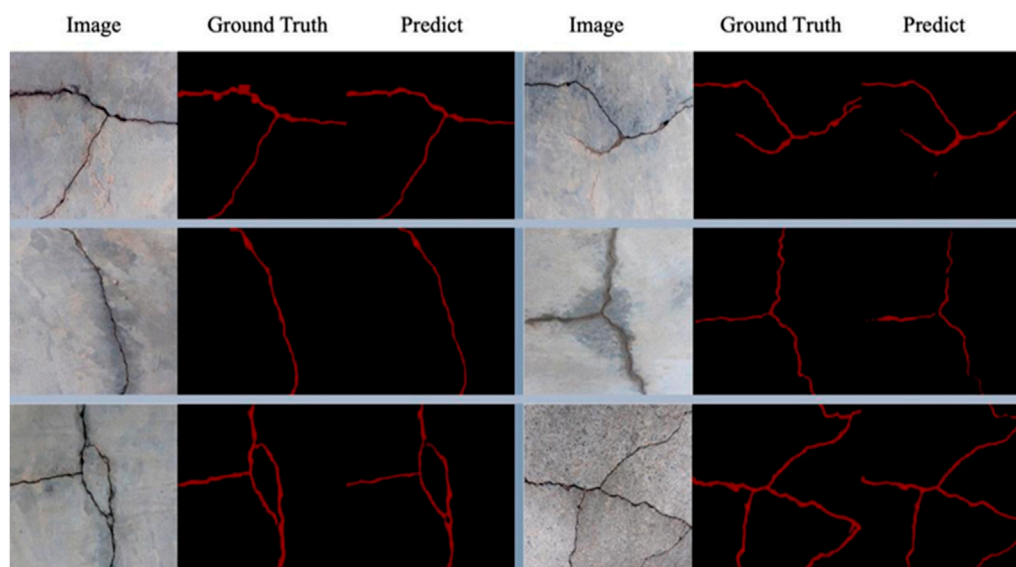**TABLE 1 Comparison of the prediction performance of different methods.**

| Method | Precision | Recall | Accuracy | F1 |
|--------|-----------|--------|----------|-----|
| HED | .9390 | .9025 | .9846 | .9452 |
| RCF | .9451 | .9155 | .9219 | .9392 |
| PCN | .9550 | .9249 | .9412 | .9433 |
| PSPNet | .9652 | .9323 | .9721 | .9534 |
| DeepLabv3 | .9877 | .9432 | .9844 | .9567 |
| PAS-Net (ours) | .9955 | .9450 | .9870 | .9644 |

**TABLE 2 Comparison of the prediction performance of different methods.**

| Method | Dice |
|--------|------|
| CNN + CS | .87 |
| CNN + CS + ASPP | .92 |
| ResNet + CS | .90 |
| ResNet + CS + ASPP | .94 |
| ResNet (pre) + CS + ASPP | .98 |

As the most common loss function, cross-entropy is not optimal for MIS tasks, like road crack image segmentation, in which objects often occupy only a small area, or some medical image processing tasks such as, for example, retinal vascular and eye segmentation. We use the Dice coefficient loss function instead of the common cross loss due to its performance in the presence of ground truth, which is widely used to evaluate segmentation performance. Suppose k is the class label, where k = {1, 2,- - -, K}, and K ∈ N. The ground truth label vector and the predicted probability vector can be expressed as Y = {$y_1(k)$, $y_2(k)$, - -, $y_i(k)$, - -, $y_N(k)$}, where $\hat{y}_i(k) \in [0, 1, 2,...n]$ and $\hat{Y}_i(k) \in [0, 1, 2,...n]$. The Dice loss function can be expressed as follows:

$$L_{Dice} = 1 - \sum_{K=1}^{K} \frac{2\omega_K \sum_i^N \hat{y}_i(k) y_i(k)}{\sum_i^N \hat{y}_i^2(k) + \sum_i^N y_i^2(K)}, \tag{2}$$

where N denotes the number of pixels and k and $\omega_k$ are the number of classes and the category weights, respectively.

Figure 4 shows the flow chart of the algorithm of the proposed method in the paper.

# 3 Numerical experiments

## 3.1 Data set

We collected and labeled a road crack dataset. The dataset contains a total of 600 images. We split the 600 images into a training set, a test set, and a validation set in the ratio of 8:1:1. We also conducted extensive experiments on several public benchmark datasets. The experimental results demonstrate that our method achieves SOTA performance compared to the most common methods.

describe a criterion to help the training mechanism in optimizing the par facilitate finding the network at the greatest accuracy. We want the predicted value to be infinitely close to the actual value, so the difference needs to be minimized (in this process, the loss function needs to be introduced). The choice of the loss function in this process is very critical. In specific projects, some loss functions calculate the gradient of the difference falling fast, while others fall slowly, so choosing the appropriate loss function is also very critical.

## 3.2 Evaluation indicators

We used the PyTorch deep learning framework to build our network. We considered several performance metrics for experimental comparison to better evaluate the experimental results, including accuracy, F1-score, recall, precision, and other evaluation metrics.

$$Accuracy = \frac{TP + TN}{TP + TN + FP + FN}, \quad (3)$$

$$Recall = \frac{TP}{TP + FN}, \quad (4)$$

$$Precision = \frac{TP}{TP + FP}, \quad (5)$$

$$F1 - score = 2 \cdot \frac{precision \cdot recall}{precision + recall}, \quad (6)$$

where TP denotes the true-positive case, FP denotes the false-positive case, FN denotes the false-negative case, and TN denotes the true-negative case.

## 3.3 Experimental details and experimental results

Our proposed network is an end-to-end architecture system that uses a ResNet network that has been pre-trained on ImageNet for four downsampling operations in the encoder phase. We used the PyTorch deep learning framework to build our network. The training and testing platforms were both Ubuntu 18.04, and in terms of hardware configuration, two 3090 graphics cards were used, each with 24G of video memory. In the training process, we used the small batch stochastic gradient descent (SGD) method with a batch size of 8 and a learning rate of .0001. We also used Adam optimization and SGD methods for comparison experiments, and chTor found that SGD usually performs better but that Adam converges in a shorter time. Although Adam converges faster, we carry out a better and more biased performance in terms of performance and time.

The results of our test on the dataset are shown in Figure 5. It is worth noting that these datasets are not exposed to the network in advance to better validate the effectiveness of the proposed method, where image is the original input of an RGB image, ground truth represents our label, and predict is the resulting map predicted by our algorithm. The experimental results show that the results achieved by our algorithm on the crack images have been less different from ground truth, which is enough to prove the effectiveness and accuracy of our algorithm.

The specific performance comparison of different methods is shown in Table 1. The values of the four metrics of the HED (holistically nested edge detection) method such as precision, recall, accuracy, and F1 are .9390, .9025, .9846, and .9452, respectively. The values of the four metrics of the RCF (richer convolutional feature) method such as precision, recall, accuracy, and F1 are .9451, .9155, .9219, and .9392, respectively. The values of the four metrics of the FCN (fully convolutional network) method such as precision, recall, accuracy, and F1 are .9451, .9155, .9219, and .9392, respectively. Our method PAS-Net has values of .9955, .9450, .9870, and .9644 for the

four metrics such as precision, recall, accuracy, and F1, respectively. It can be seen that our method achieves the most advanced performance in all four evaluation metrics compared to these state-of-the-art methods.

To further validate the adequate performance of our method, we disassembled it into multiple parts. We conducted a large number of combinatorial experiments to validate the efficiency of each module fully. As shown in Table 2, the most basic CNN + CS (context spatial) yields a dice metric of .87 on our dataset. CNN + CS + ASPP (atrous spatial pyramid pooling) yields a dice metric of .92 on our dataset. We use ResNet as the backbone; the combination of ResNet + CS gives a dice metric of .90 on our dataset, and ResNet + CS + ASPP provides a dice metric of .94 on our dataset. In addition, the best performance of .98 is achieved when using ResNet that has been pre-trained on ImageNet. Step-by-step tests further validate the effectiveness of the proposed method in this study.

## 4 Conclusion

This study proposes a new deep learning network architecture called PSA-Net for road crack detection. Our algorithm is developed from three aspects, namely, multi-scale feature information extraction, spatio-temporal attention mechanism, and pyramidal pooling, focusing on the contextual semantic information and edge information on crack images, and it is an end-to-end segmentation algorithm. We designed PSA-Net for pavement crack detection without increasing the number of network parameters. We conducted our experiments on our road crack detection datasets. The experimental results show that our PSA-Net offers a significant advantage on various datasets, sufficient to prove the algorithm's effectiveness. In the future, we will continue to contribute to road crack detection and consider combining the detection model with the segmentation model to improve the performance of our algorithm further (H et al., 2013).

## Data availability statement

The raw data supporting the conclusion of this article will be made available by the authors, without undue reservation.

## Author contributions

XL proposed the architecture of the algorithm and wrote the paper. JZ helped write the paper and implement some of the algorithms. DW and MaL provided experimental data. EM gave insight into the implementation process. MeL and FG labeled the images and helped further refine the paper.

## Funding

## Conflict of interest

DW and ML were employed by Chongqing Urban Construction Investment (Group) Co., Ltd.

The remaining authors declare that the research was conducted in the absence of any commercial or financial relationships that could be construed as a potential conflict of interest.

## Publisher's note

## References

Albert, A., and Nii, A. (2008). Evaluating pavement cracks with bidimensional empirical mode decomposition. *EURASIP. J. Adv. Sig. Pr.* 2008, 861701. doi:10.1155/2008/861701

Alex, K., Ilya, S., and Geoffrey E, H. (2017). Imagenet classification with deep convolutional neural networks. *Commun. Acm.* 60 (6), 84–90. doi:10.1145/3065386

Amhaz, R., Chambon, S., Idier, J., and Baltazart, V. (2016). Automatic crack detection on two-dimensional pavement images: An algorithm based on minimal path selection. *Ieee. Trans. Intell. Transp.* 17 (10), 2718–2729. doi:10.1109/TITS.2015.2477675

Chambon, S., and Jean-Marc, M. (2011). Automatic road pavement assessment with image processing: Review and comparison. *Int. J. Geophys.* 2011, 1–20. doi:10.1155/2011/989354

Eisenbach, M., Stricker, R., Seichter, D., Amende, K., Debes, K., Sesselmann, M., et al. (May 2017). "How to get pavement distress detection ready for deep learning? A systematic approach," in Proceedings of the 2017 International Joint Conference on Neural Networks (IEEE), Anchorage, AK, USA 2161–4407.

Fan, H., Mei, X., Danil, P., and Ling, H. (2018). Multi-level contextual rnns with attention model for scene labeling. *Ieee. Trans. Intell. Transp.* 19 (11), 3475–3485. doi:10.1109/TITS.2017.2775628

Feng, C., Liu, M., Kao, C., and Lee, T. (June 2017). "Deep active learning for civil infrastructure defect detection and classification," in Proceedings of the ASCE International Workshop on Computing in Civil Engineering (Seattle, Washington: UnivIWCCE), 298–306.

He, K., Zhang, X., Ren, S., and Sun, J. (June 2016). Deep residual learning for image recognition. Proceedings of the IEEE Conf. Comput. Vis. pattern Recognit, Las Vegas, NV, USA 770–778.

Hu, Y., and Zhao, C. (2010). A novel lbp based methods for pavement crack detection. *J. pattern Recognit. Res.* 5 (1), 140–147. doi:10.13176/11.167

Huang, W., and Zhang, N. (December 2012). "A novel road crack detection and identification method using digital image processing techniques," in Proceedings of the 7th International Conference on Computing and Convergence Technology (Seoul: ICCCT), 397–400.

Jonathan, L., Evan, S., and Trevor, D. (2017). Fully convolutional networks for semantic segmentation. *Ieee. Trans. Pattern Anal.* 39 (4), 640–651. doi:10.1109/TPAMI.2016.2572683

Joshi, D., Singh, T., and Sharma, G. (2022). Automatic surface crack detection using segmentation-based deep-learning approach. *Eng. Fract. Mech.* 268, 108467. doi:10.1016/j.engfracmech.2022.108467

Kass, A., Witkin, A., and Terzopoulos, D. (1988). Snakes: Active contour models. *Int. J. Comput. Vis.* 1, 321–331. doi:10.1007/bf00133570

Kass, M., Witkin, A., and Terzopoulos, D. (1988). Snakes: Active contour models, *International journal of computer vision* 1.4 321-331. doi:10.1007/s11263-022-01685-7

Kelwin, S., and Lucian, C. (October 2014). "Pavement pathologies classification using graph-based features," in Proceedings of the IEEE International Conference on Image Processing (Paris, France: IEEE), 793–797.

Li, P., Wang, C., Li, S., and Feng, B. (September 2015). "Research on crack detection method of airport runway based on twice-threshold segmentation," in Proceedings of the Fifth International Conference on Instrumentation & Measurement, Computer, Communication, and Control (Qinhuangdao, China: IMCCC), 1716–1720.

Marcos, Q., Juan, T., and Jose, M. (2016). A simplified computer vision system for road surface inspection and maintenance. *Ieee. Trans. Intell. Transp.* 17, 608–619. doi:10.1109/TITS.2015.2482222

Nguyen, T. S., Stephane, B., Florent, D., and Manuel, A. (September 2011). "Free-form anisotropy: A new method for crack detection on pavement surface images," in Proceedings of the 18th IEEE International Conference on Image Processing (Brussels, Belgium: ICIP), 1069–1072.

Pauly, L., Peel, H., Luo, S., Hogg, D., and Fuentes, R. (July 2017). "Deeper networks for pavement crack detection," in Proceedings of the 34th International Symposium in Automation and Robotics in Construction (Taipei, Taiwan: IAARC), 479–485.

Peggy, S., Jean, D., Vincent, L., and Dominique, B., (October 2006). "Automation of pavement surface crack detection using the continuous wavelet transform," in Proceedings of the IEEE International Conference on Image Processing. Atlanta, GA, USA: IEEE, 30-37.

Piotr, D., and Lawrence, Z., (December 2013). "Structured forests for fast edge detection," ´ in Proceedings of the IEEE International Conference on Computer Vision. Sydney, NSW, Australia: ICCV, 1841–1848.

Rafal, K., Pawel, S., Adam, T., Andrzej, R., Andrzej, P., Pawel, R., et al. (June 2015). "Asphalt surfaced pavement cracks detection based on histograms of oriented gradients," in Proceedings of the 22nd International Conference on Mixed Design of Integrated Circuits & Systems (Torun, Poland: IEEE), 579–584.

Schmugge, S. J., Rice, L., Lindberg, J., et al. (2017). "Crack segmentation by leveraging multiple frames of varying illumination[C]," in IEEE Winter Conference on Applications of Computer Vision (WACV), IEEE), 1045–1053.

Shi, Y., Cui, L., Qi, Z., Meng, F., and Chen, Z. (2016). Automatic road crack detection using random structured forests. *Ieee. Trans. Intell. Transp.* 17 (12), 3434–3445. doi:10.1109/TITS.2016.2552248

Srivatsan, V., Sobhagya, J., Karan, S., Lars, W., and Christoph, M. (March 2014). "Vision for road inspection," in Proceedings of the IEEE Winter Conference on Applications of Computer Vision (Steamboat Springs, CO, USA: IEEE), 115–122.

Stephen J, S., Lance, R., John, L., Robert, G., Chris, J., and Min C, S. (March 2017). "Crack segmentation by leveraging multiple frames of varying illumination," in Proceedings of the 17th IEEE Winter Conference on Applications of Computer Vision (Santa Rosa, CA, USA: IEEE), 1045–1053.

Vijay, B., Alex, K., and Roberto, C. (2017). Segnet: A deep convolutional encoder-decoder architecture for image segmentation. *Ieee. Trans. Pattern Anal.* 39 (12), 2481–2495. doi:10.1109/TPAMI.2016.2644615

Vivek, K., Anthony, K., and James, T. (2012). Detecting curves with unknown endpoints and arbitrary topology using minimal paths. *Ieee. Trans. Pattern. Anal.* 34 (10), 1952–1965. doi:10.1109/TPAMI.2011.267

Wang, S., Liu, C., and Zhang, Y. (2022). Fully convolution network architecture for steel-beam crack detection in fast-stitching images. *Mech. Syst. Signal Process.* 165, 108377. doi:10.1016/j.ymssp.2021.108377

Xu, W., Tang, Z., Zhou, J., and Ding, J. (September 2013). "Pavement crack detection based on saliency and statistical features," in Proceedings of the 20th IEEE International Conference on Image Processing (Melbourne, VIC, Australia: ICIP), 4093–4097.

Yan, M., Bo, S., Xu, K., and He, Y. (June 2007). "Pavement crack detection and analysis for high-grade highway," in Proceedings of the8th International Conference on Electronic Measurement and Instruments (Xian, China, 548–552.ICEMI

Yu, F., and Koltun, V., (2015). Multi-scale context aggregation by dilated convolutions. https://arxiv.org/abs/1511.07122.doi:10.48550/arXiv.1511.07122

Zakeri, H., Nejad, F. M., Fahimifar, A., and Torshizi, A. D., (June 2013). "A multi-stage expert system for classification of pavement cracking," in Proceedings of the Joint World Congress of the International-Fuzzy-Systems-Association and Annual Meeting of the North-American-Fuzzy-Information-Processing-Society (Edmonton, AB, Canada: IFSA/NAFIPS), 1125–1130.

Zakeri, E., Moezi, S. A., Bazargan-Lari, Y., and Mao, Q. (2013). Control of a ball on sphere system with adaptive feedback linearization method for regulation purpose[J]. *Majlesi J. of Mechatronic Engineering* 2 (3), 23–27.

Zhang, L., Yang, F., Zhang, Y., and Zhu, Y. (September 2016). "Road crack detection using deep convolutional neural network," in Proceedings of the 23rd IEEE International Conference on Image Processing (Phoenix, AZ, USA: ICIP), 3708–3712.

Zou, Q., Cao, Y., Li, Q., Mao, Q., and Wang, S. (2012). Cracktree: Automatic crack detection from pavement images. *Pattern Recogn. Lett.* 33, 227–238. doi:10.1016/j.patrec.2011.11.004

# Deep semantic segmentation of unmanned aerial vehicle remote sensing images based on fully convolutional neural network

Guoxun Zheng[1,2,3], Zhengang Jiang[1]*, Hua Zhang[1,2,3]* and Xuekun Yao[2,3]

[1]School of Computer Science and Technology, Changchun University of Science and Technology, Changchun, China, [2]School of Computer Technology and Engineering, Changchun Institute of Technology, Changchun, China, [3]Jilin Provincial Key Laboratory of Changbai Historical Culture and VR Reconstruction Technology, Changchun Institute of Technology, Changchun, China

In the era of artificial intelligence and big data, semantic segmentation of images plays a vital role in various fields, such as people's livelihoods and the military. The accuracy of semantic segmentation results directly affects the subsequent data analysis and intelligent applications. Presently, semantic segmentation of unmanned aerial vehicle (UAV) remote-sensing images is a research hotspot. Compared with manual segmentation and object-based segmentation methods, semantic segmentation methods based on deep learning are efficient and highly accurate segmentation methods. The author has seriously studied the implementation principle and process of the classical deep semantic segmentation model—the fully convolutional neural network (FCN), including convolution and pooling in the encoding stage, deconvolution and upsampling, etc., in the decoding stage. The author has applied the three structures (i.e., FCN-32s, FCN-16s, and FCN-8s) to the UAV remote sensing image dataset AeroScapes. And the results show that the accuracy of vegetation recognition is stable at about 94%. The accuracy of road recognition can reach up to more than 88%. The mean pixel accuracy rate of the whole test dataset is above 91%. Applying full convolution neural network to semantic segmentation of UAV remote sensing images can improve the efficiency and accuracy of semantic segmentation significantly.

## 1 Introduction

In remote sensing, satellite remote sensing images or UAV remote sensing images can be used for ground object recognition. Satellite remote sensing images have a low resolution for low-altitude targets. They are often affected by weather factors and obscure ground objects, resulting in difficulties in ground object recognition. UAV remote sensing technology takes low-speed unmanned aircraft as the aerial remote sensing platform, captures aerial image data with infrared and camera technology, and processes the image information by computer. Compared with satellite remote sensing platforms, UAVs fly at a lower altitude and can fly close to the ground to improve the resolution of objects (Liu et al., 2021). And their close-range image resolution can reach the centimeter level, which can quickly and economically collect low-altitude high-resolution aerial images. UAV remote

sensing can be applied to environmental monitoring (Green et al., 2019). It can fast update, correct, and upgrade geo-environmental information and outdated GIS databases, providing timely technical assurance for government and related departments' administration, land, and geo-environmental management. In addition, UAV remote sensing can also be applied to electric power inspection (Zhang et al., 2017), agricultural monitoring (Zhang et al., 2021), high-speed patrol (Yang et al., 2021), disaster monitoring and prevention (Kamilaris Prenafeta-Boldú, 2018), meteorological detection (Funk and Stütz, 2017), aerial survey (De Benedetti et al., 2017), etc. In recent years, UAV remote sensing has become a hot topic for global research due to its mobility, speed, and economic advantages. It has gradually developed from research and development to the practical application stage, becoming one of the future leading aerial remote sensing technologies.

With the development of deep learning and the Internet of Things (IoT), the research on the integration of UAV remote sensing and artificial intelligence has become more and more abundant. Many researchers have succeeded in automatic target recognition of UAV remote sensing images based on convolutional neural networks with the help of deep learning methods, such as Region-Convolutional neural network (R-CNN), Fast Region-based Convolutional Network (Fast R-CNN), Faster Region-based Convolutional Network (Faster R-CNN), Single Shot Mutibox Detector (SDD), You Only Look Once (YOLO) and other frameworks (Xu et al., 2017; Li et al.; Liu et al., 2020). Xu et al. (2017) extended the framework of Faster R-CNN for detecting cars from low-altitude UAV images taken over signal intersections and demonstrated that Faster R-CNN has excellent potential for parking lot car detection. Li et al. (2020) proposed a method for UAV monitoring railroad scenes based on SSD detection of small objects. Liu et al. (2020) developed a special detection method for small targets in UAV view based on YOLOv3. All these methods used regular rectangles to frame and identify targets. Still, in many cases, one would like to be able to use the shape of the target itself to locate and precisely segment it, for example, to precisely distinguish the shape of each building, road, river, vehicle, etc., itself, i.e., to achieve semantic segmentation.

Semantic segmentation has been a research hotspot in artificial intelligence. It takes some raw data (e.g., a flat image) as input and converts them into a mask with highlighting by finding the location of all pixels and what they represent, thus understanding the meaning of the image. Semantic segmentation can be used in land monitoring (Mohammadimanesh et al., 2019), autonomous driving (Li et al., 2021), face recognition (Meenpal et al., 2019), precision agriculture (Milioto et al., 2018), etc., and plays a vital role in social development and people's life. This paper discusses applying the fully convolutional neural network in deep learning to semantic segmentation of UAV remote sensing images to accurately extract vegetation, roads, and other targets in the features and improve the segmentation accuracy (Li et al., 2019; Li et al., 2019).

The contributions of this paper are as follows.

(1) The author has conducted an in-depth study on the structure of the fully convolutional neural network and meticulously analyzed the encoder and decoder components. And it forms a network structure image with clear feature map size variation, convolutional kernel size, and fusion ideas.

(2) Under the premise of maintaining the classification balance to the greatest extent, the training set, validation set, and a test set of the AeroScapes dataset are re-divided, and the image files and labels are normalized and label encoded before semantic segmentation, and a complete set of data processing algorithm flow is refined.

(3) The experiments of applying three fully convolutional neural networks (FCN-32s, FCN-16s, and FCN-8s) on the UAV remote sensing image dataset AeroScapes are completed, and the results show that the segmentation effect is good.

The remainder of this paper is organized as follows: Section 2 introduces the work related to UAV remote sensing images, semantic segmentation, and FCN; Section 3 explains the dataset used and the processing method of the dataset, the semantic segmentation method of UAV remote sensing images and the implementation steps; Section 4 shows the experimental results and the related discussion; Section 5 concludes the work of this paper.

# 2 Related works

This section introduces the research related to this paper, which includes semantic segmentation models and fully convolutional neural networks.

## 2.1 Semantic segmentation models

Semantic segmentation is one of the critical tasks in computer vision. It is the process of classifying each pixel in an image and linking each pixel to a category label, which is widely used in medical image analysis (Yang and Yu, 2021), unmanned driving (Feng et al., 2020), geographic information systems (Li et al., 2019), etc., Various models, such as FCN, SegNet, U-Net, DeepLab, etc., can achieve semantic segmentation.

FCN is the cornerstone of deep learning techniques applied to semantic segmentation problems (Shelhamer et al., 2017), building a fully convolutional neural network. The convolutional model with images introduces conditional random fields (CRF) as a post-processing module in the CNN to tune the output of the segmentation architecture and enhance it to capture fine-grained information. The decoder encoder model is divided into encoder structure and decoder structure. SegNet encoder follows the network model of VGG16, which mainly categorizes and analyzes the low-level local pixel values of the image to obtain higher-order semantic information to achieve parsing of object information. Pyramid Scene Parsing Network (PSPN) (Zhao et al., 2017) is a multi-scale and pyramid network-based model that uses ResNet, a covariance network with null convolution, for feature extraction and better learning of global information. The null convolution model can exponentially expand the field of perception without losing resolution. The most typical model of null convolution is DeepLab and its upgraded version. DeepLab V1 (Chen et al., 2014) uses null convolution and CRF to solve the problem of information loss and probabilistic model between labels not being applied due to previous model pooling. DeepLab V2 (Chen et al., 2017a) introduces Atrous Spatial Pyramid Pooling (ASPP), which extracts features using multiple sampling rates of null convolution in parallel, and then fuses the features and changes the base layer from VGG16 to ResNet. DeepLab V3 (Chen et al., 2017b) proposes a more
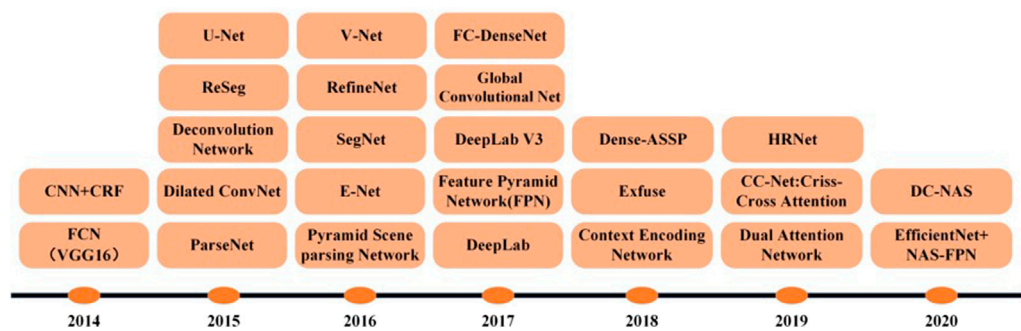
**FIGURE 1**
The timeline of DL-based segmentation model for 2D images.

general framework that applies to any network. DeepLab V3+ (Chen et al., 2018) adds encoder-decoder constructs to achieve accuracy and time balance by changing the Atrous rate. The recurrent neural network-based model RNN successfully models global contextual information and improves segmentation results by linking pixel level with local information. The attention mechanism model (Chen et al., 2016) assigns different weights to different scale images, e.g., large weights to small-scale targets to achieve large scaling and small scaling to closer targets in the image. Learning active contour models ACMs (Chen et al., 2019) propose a new loss function that considers the information of boundary line length and region and a convolutional neural network based on Dense U-Net. In addition, there are segmentation models based on the GAN for semi-supervised semantic segmentation. The semantic segmentation model based on deep learning is shown in Figure 1 (Minaee et al., 2021).

## 2.2 Fully convolutional neural network

FCN is the first neural network applied to image semantic segmentation, which replaces the fully connected layers of VGGNet with convolutional layers to build a deep, fully convolutional neural network. FCN adopts "end-to-end" feature learning, which reveals the non-linear features hidden in the data through multi-layer feature extraction, and can automatically learn global features from a large number of training sets to realize the transformation of feature models from manual to learned features.

In the FCN, the last three layers of the CNN network are all transformed into multi-channel convolutional layers of equivalent vector length corresponding to $1 \times 1$ convolutional kernels (Shelhamer et al., 2017). The network model consists entirely of convolutional layers, and no fully connected layers generate vectors. CNN is an image-level recognition, that is, from image to result. At the same time, FCN is a pixel-level recognition, labeling which category each pixel on the input image is most likely to belong to. FCN changes the classification network into a fully convolutional neural network, specifically transforming the fully connected layers into convolutional layers with up-sampling by deconvolution, fine-tuning using migration learning methods, and using jump structure. Thus, semantic information can be

combined with symbolic information to produce accurate and surprising segmentations. The first half of the FCN network is based on the convolutional layer of VGG, so the weight parameters of the VGG network are directly referenced as the pre-training parameters of the FCN and then fine-tuned. The structure of the FCN and the coding and decoding process are introduced in Section 3.2. Like other segmentation network models, the FCN model loss function is a pixel-level cross-entropy loss function and also uses a stochastic gradient descent optimization algorithm for momentum. Instead of following the previous interpolation of interpolation upsampling, FCN proposes a new upsampling, i.e., deconvolution, which can be understood as the inverse operation of the convolution operation. The deconvolution cannot compound the loss of values due to the convolution operation and simply reverses the steps in the convolution process to transform once, so it is also called transposed convolution. The convolution formula is shown in formula 1, and the deconvolution formula is shown in formula 2:

$$F = \frac{i - k + 2 \times p}{S} + 1 \qquad (1)$$

Where $F$ is the output image size. $i$ is the input image size. $k$ is the convolution kernel size. $p$ is the padding, the complementary zero size. $S$ is the step size.

$$F = (i - 1) \times S + k - 2 \times p \qquad (2)$$

Formula 2 is to exchange the input and output in formula 1 into a sparse state.

FCN training, at least 175 epochs after the algorithm, will perform well. That is, too little will affect the algorithm performance, while too much on the algorithm performance is no more remarkable improvement. And its learning rate can be adjusted after 100 times and is getting smaller. FCN in the upsampling process, only the fusion of pool 5 and pool 4 feature map, pool 3 before the feature map, does not need to be fused. When FCN emerged, it surpassed the most advanced techniques in semantic segmentation. It allows the input of images of arbitrary size, and the output of the same size can be obtained after effective learning, and state-of-the-art results are obtained on the PASCAL VOC, NYUDv2, and SIFT Flow datasets. However, FCN does not have a category-balancing strategy, and the accuracy of semantic
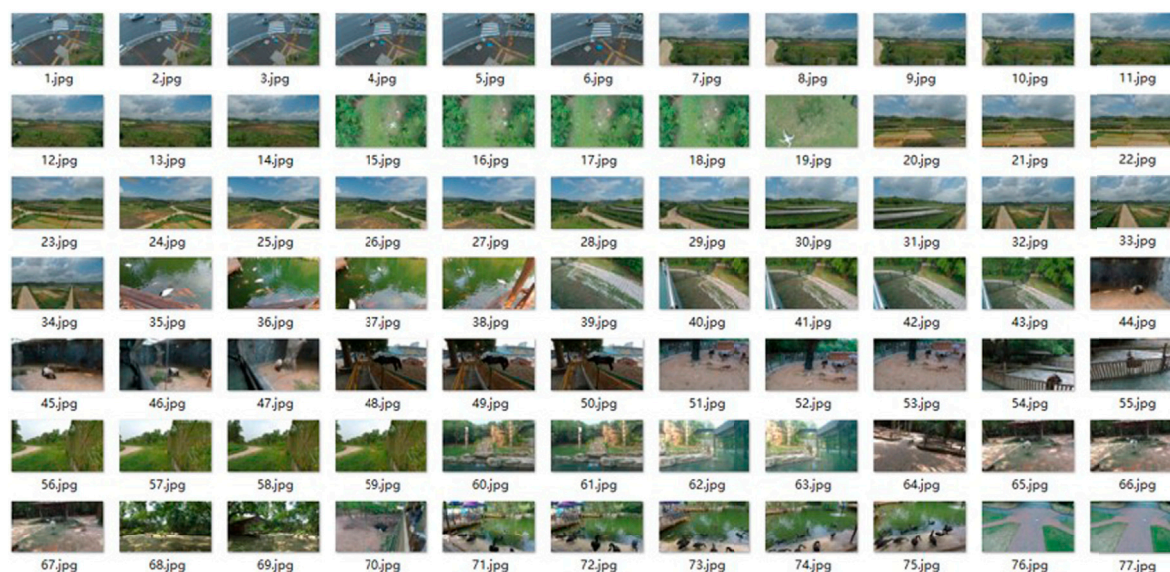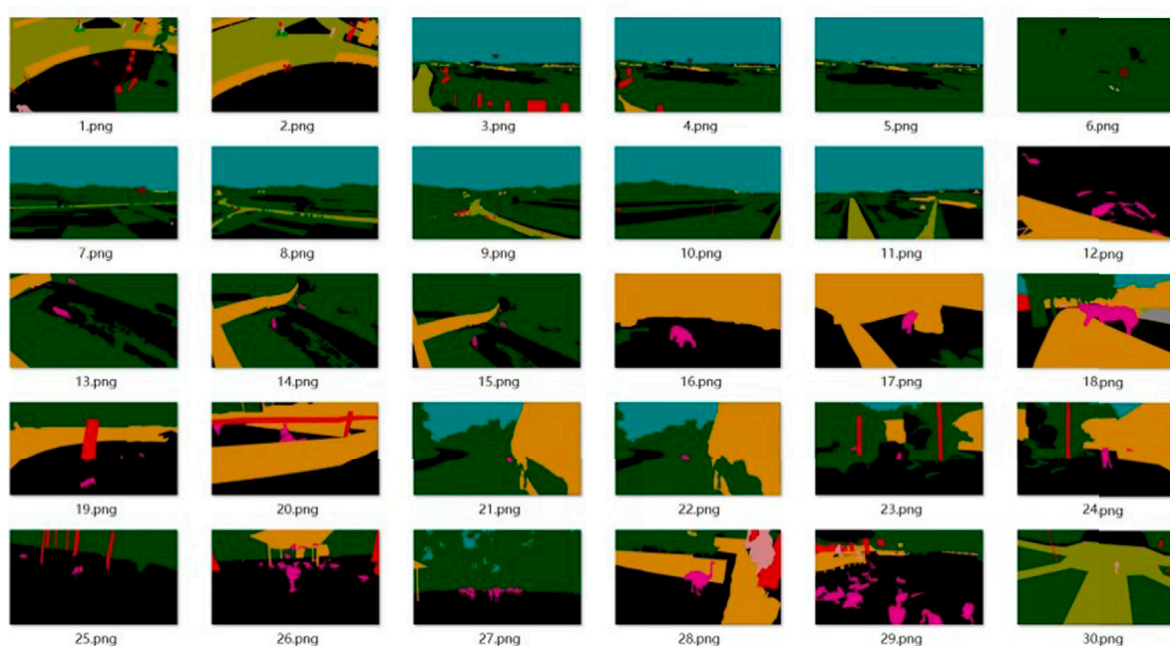
**FIGURE 2**
Dataset of semantic segmentation: **(A)** partial images in the dataset; **(B)** corresponding label data.

segmentation suffers when the categories in a dataset are not balanced.

# 3 Data and methods

## 3.1 Semantic segmentation dataset

The AeroScapes aerial semantic segmentation benchmark includes images captured using commercial UAVs in the altitude range of 5–50 m. The dataset provides 3,269 720p (1,280 × 720) images and 11 categories (excluding background) of ground-truth masks (Figure 2). The dataset offers 3,269 720p (1,280 × 720) images and 11 categories (excluding background) of real masks (Figure 2A), where the 11 categories include Person, Bike, Car, Drone, Boat, Animal, Obstacle, Construction, Vegetation, Road, and Sky. The dataset is provided with a mask map, so no mask map conversion is required. The file structure is as follows.

ImageSets folder: two txt files are stored, dividing the training and test sets.

JPEGImages folder: holds the RGB images.

SegmentationClass folder: holds the mask map of the labels.

Visualizations folder: holds the label images.

This dataset does not divide the training and test sets directly into the corresponding folders, so to use this dataset, it is necessary to read the images according to the divided txt file and distribute each image in the corresponding folder. In addition, the validation set is not provided in this dataset. In this paper, when the original remote sensing images are sent to FCN for training, the author sets the crop to 1,280 × 704 pixels size and divides a part of the images as the validation set under the premise of ensuring the category balance as much as possible in the training set.

It can be seen from Figure 2B that various categories of objects are labeled with different colors, and this is the final output image effect of FCN.

## 3.2 Semantic segmentation of UAV remote sensing images

UAV remote sensing images usually contain a wide range of complex features, and insignificant differences between features, making it challenging to obtain high segmentation accuracy using manual methods. In the early days, most segmentation networks are classified for pixels by finding a piece of the region containing this pixel and using the category of this region as the category of pixel points, which is memory-consuming and inefficient as the areas may overlap. Therefore, this paper uses deep learning to perform semantic segmentation (Minaee et al., 2021).

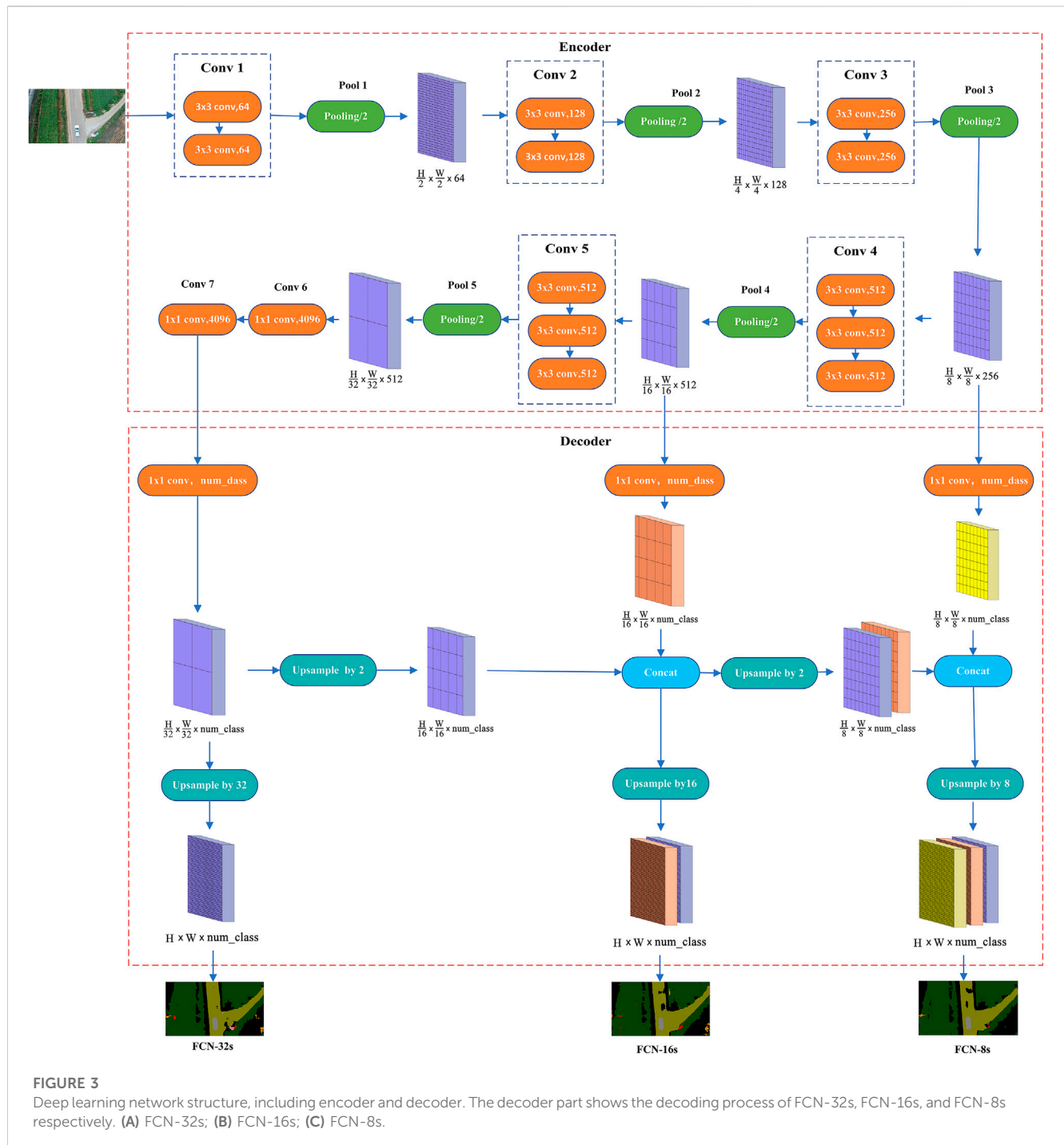### 3.2.1 The principle and implementation of the three structures of the FCN model

Many network models for deep semantic segmentation include fully supervised learning image semantic segmentation methods and weakly supervised image semantic segmentation methods (Huang et al., 2021). However, the performance of most weak supervised methods still lags behind that of fully supervised methods (Tian et al., 2019). This paper uses a fully supervised learning method, FCN, to perform semantic segmentation on the AeroScapes aerial semantic dataset. FCN is the first attempt to classify pixels directly from abstract semantic features, and the pre-training model of VGGNet is used in advance to greatly reduce the training time without affecting the classification accuracy. The pre-training model of VGG16 is used in this paper. After the first five convolutions and pooling, FCN replaces the original fully-connected layer with a fully-convolutional layer. And then completes the deconvolution operation by bilinear interpolation and sums with the corresponding pooled middle layer information to recover the original image resolution finally and achieves end-to-end, pixel-to-pixel semantic segmentation, and the most crucial feature of this network is that it learns features by itself according to the designed algorithm without human intervention (Shelhamer et al., 2017). In this paper, three fully convolutional neural networks, FCN-32s, FCN-16s, and FCN-8s, have been used to carry out the study, and the structures of the three network models are shown in Figure 3.

These three networks, with identical pre-encoding processes, complete the downscaling and feature extraction of the original image, and the good or bad feature extraction directly affects the final prediction results. As shown in Figure 3, after two convolutional layers, called 1 convolutional block (i.e., Conv1), the feature map is obtained, and after the first pooling layer (i.e., Pool1), the feature map is obtained after 1/2. Similarly, after the second convolution block and the second pooling layer, the feature map becomes 1/4 of the original map; after the third convolution block and the third pooling layer, the feature map becomes 1/8 of the original map; after the fourth convolution block and the fourth pooling layer, the feature map becomes 1/16 of the original map; after the fifth convolution block and the fifth pooling layer, the feature map becomes 1/32 of the original map. This process is called downsampling, i.e., the process of feature extraction. FCN uses the five convolutions and five pooling in the VGG16 model, the feature map size becomes 1/32 of the input image size, and the channels change from 3 to 512. FCN replaces the sixth and seventh fully connected layers in VGG16 with fully convolutional layers, and the feature map size does not change, still 1/32 size, but transforms the number of channels to 4,096. After the final transition convolution, the channel number is converted to the number of label categories of the dataset.

The difference between the three networks lies in the post-decoding process, where the decoding is completed to gradually recover the smaller size feature maps into predicted maps of the same size as the image. FCN-32s is to directly up-samples the encoded feature map by 32 times, i.e., to complete the deconvolution. Then, the obtained feature map is passed to the softmax classifier to output a prediction map of the same size as the input image to get the dense prediction result, which does not use the skip architecture. FCN-16s first up-samples the 1/32 sized encoded feature map by a factor of 2 to 1/16 size, and transform the 1/16 sized feature map after the fourth pooling (Pool 4) into the number of label categories of the dataset by transition convolution, then fuses the two 1/16 sized feature maps (i.e., skip architecture). Finally, up-samples them by a factor of 16 to produce a prediction map of the same size as the input image after the softmax classifier. FCN-8s first up-samples the fused feature map from the previous step by a factor of 2 to 1/8 size, transforms the 1/8 sized feature map after the third pooling (Pool 3) to the number of label categories of the dataset by transition convolution, and fuses the two 1/8-sized feature maps, again with skip architecture. Finally, it up-samples them by a factor of 8 to produce a prediction map of the same size as the input image after the softmax classifier. It is worth noting that in FCN-16s and FCN-8s, when multiple feature maps are fused, it must be ensured that each feature map size is the same. The skip architecture of FCN enables the models to ensure both robustness and accuracy, and all three models achieve end-to-end deep semantic segmentation.

### 3.2.2 Data preprocessing

The deep semantic segmentation network needs a lot of time and effort to process the dataset before training, and the processing effect of the dataset directly affects the accuracy of semantic segmentation. Each image in the dataset corresponds to a labeled graph, and each category of targets in the image is identified with different colors, i.e., different labels, and the preprocessing process is shown in Figure 4.

**FIGURE 3**
Deep learning network structure, including encoder and decoder. The decoder part shows the decoding process of FCN-32s, FCN-16s, and FCN-8s respectively. **(A)** FCN-32s; **(B)** FCN-16s; **(C)** FCN-8s.

### 3.2.3 A label processing and encoding

Label encoding is to form a one-to-one correspondence from colors to labels. It needs to store the names and corresponding RGB values of all categories (including background category) in a csv file to form a color map, and hash map each pixel point in the color map to the category it represents using a 256 decimal-like method through a hash function, as shown in formula 3 and formula 4.

$$k = (cm[0] \times 256 + cm[1]) \times 256 + cm[2] \qquad (3)$$

$$cm2lbl[k] = i \qquad (4)$$

$cm[0]$, $cm[20]$, and $cm[10]$ denote the RGB value in a pixel, $k$ denotes the converted integer, $cm2lbl$ is a hash table constructed using the hash function, and $k$ is used as the index of the pixel in the $cm2lbl$ table to query the category $i$ corresponding to the pixel.

### 3.2.4 B initializing the dataset

After completing the corresponding processing, initializing the dataset is to divide the images and labels into the training set, validation set, and test set. Firstly, it is necessary to define the crop size and transformation content. The AeroScapes dataset needs to

**FIGURE 4**
Data preprocessing process: **(A)** label processing and encoding; **(B)** initializing the dataset.
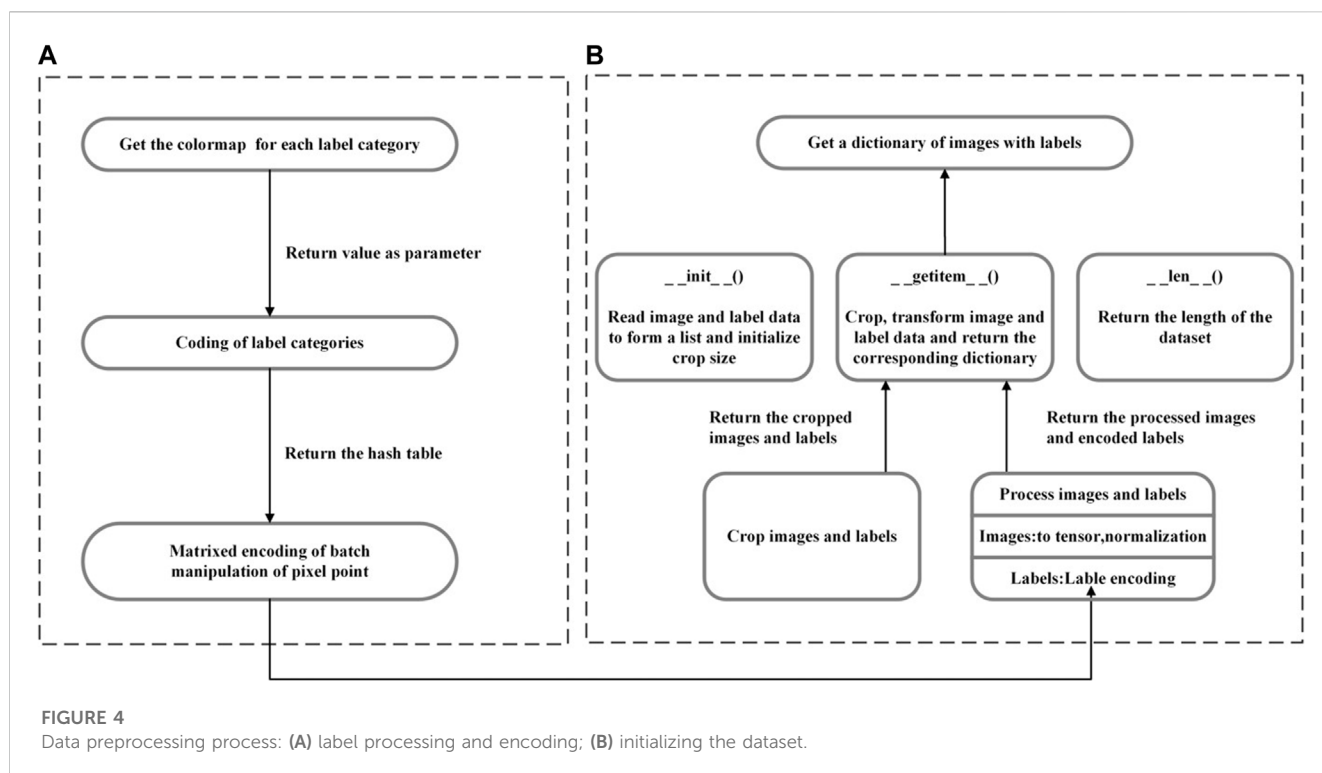
crop each image to 1,280 × 704, transform the image into a tensor and normalize it, and encode the labels using the steps in Figure 3A. In this way, the cropped and correspondingly transformed images and labels can be obtained and combined into a corresponding dictionary for subsequent use.

### 3.2.5 Network training

Semantic segmentation of remote sensing images based on a fully convolutional neural network is trained using PyTorch 1.12 GPU version deep learning framework, Python 3.7, Intel (R) Xeon (R) 12-core processor, NVIDIA Quadro P6000, 24G GDDR5X video memory, and 64G DDR4 memory. In this paper, the training set, validation set, and test set are divided according to the ratio of 6: 2:2, and 1967 training images, 654 validation images, and 648 test images, and the training steps and techniques are shown as follows:

(1) Setting parameters: setting the number of categories, Batch Size, Epoch, initial learning rate value, and image crop size. The AeroScapes dataset contains 11 categories and 1 unlabeled category, 12 in total. In order to improve the training speed and segmentation accuracy, the Batch Size is set to 4; Epoch is set to 175; the learning rate is initialized to $1 \times 10^{-4}$, and every time 50 Epochs are completed, the learning rate is reduced to half of the original one. The training of FCN goes through 5 times of pooling, and after each pooling, the feature map size will change to 1/2 of the original one, and to prevent the image size leads to training failure, the image size is uniformly cropped to 1,280 × 704.

(2) Downloading the pre-training model: in order to speed up the training, migration learning can be performed using some pre-trained models to obtain the weights of the model parameters

quickly. When training FCN, the pre-encoding process uses the backbone of VGG16, and at the beginning of the first training, the model structure of VGG16 is downloaded from the network first according to the URL https://download.pytorch.org/models/vgg16-397923af.pth, and it only needs to be downloaded once and saved locally. None of the subsequent training needs to be downloaded, which dramatically saves training time, obtains reliable parameter weight values, and increases the training speed of the network. In this paper, the pre-training model uses the network structure of VGG16, and subsequent attempts can be made to use the structure such as VGG19.

(3) Randomly disrupting the order of training images: In deep learning, the model is often "biased" in the training process because the dataset is not disrupted, and the trained network model cannot fit the abstract features of the training set well, and the performance is poor. When FCN is trained, the order of the training images is randomly shuffled. And the model can learn different features of the training set better instead of being limited to some features, which not only enhances the generalization ability of the model but also improves the training accuracy.

(4) Selecting Adam optimizer: after the loss function is calculated in the training of the deep neural network, the optimizer needs to be used to obtain the network parameters with the minimum loss function for backpropagation and complete the update of the network parameters, so as to complete the model training as fast as possible and save computer resources. In this paper, the Adam (Kingma and Ba, 2014) optimizer is chosen, which is simple and efficient, requires less memory, makes the convergence speed fast

while making the fluctuation amplitude small, and achieves parameter self-renewal by the newly added two correction terms.

# 4 Results and discussion

The main evaluation metrics of semantic segmentation are execution time, memory usage, and accuracy, where the accuracy metrics include pixel accuracy (PA), mean pixel accuracy (mPA), and mean intersection over union (mIoU) (Feng et al., 2020).

Assuming that there are $k$ categories (including one background category), $p_{ij}$ represents the total number of pixels that are true for category $i$ but predicted for category j. Specifically, $p_{ii}$ represents true positives, $p_{ij}$ represents false positives, and $p_{ji}$ represents false negatives; the pixel accuracy can be calculated with the formula 5.

$$PA = \frac{\sum_{i=1}^{k} p_{ii}}{\sum_{i=1}^{k}\sum_{j=1}^{k} p_{ij}} \qquad (5)$$

The pixel accuracy represents the ratio of the number of correctly classified pixel points to the number of all pixel points.

The mean pixel accuracy can be calculated with the formula 6.

$$mPA = \frac{1}{k}\sum_{i=1}^{k}\frac{p_{ii}}{\sum_{j=1}^{k} p_{ij}} \qquad (6)$$

The mean pixel accuracy represents the average ratio of the number of correctly classified pixel points per category and the number of all pixel points in that category.

The mean intersection over the union can be calculated with the formula 7.

$$mIoU = \frac{1}{k}\sum_{i=1}^{k}\frac{p_{ii}}{\sum_{j=1}^{k} p_{ij} + \sum_{j=1}^{k} p_{ji} - p_{ii}} \qquad (7)$$

The mean intersection over union represents the average intersection ratios for each category.

## 4.1 Experimental results

FCN-32s, FCN-16s, and FCN-8s are trained by 1967 UAV remote sensing images. The model parameters are updated using the validation set during the training process, and the loss functions, PA, and mIoU of training and validation are shown in Table 1. The final trained optimal models are used for semantic segmentation prediction of 648 UAV remote sensing images. The PA, mIoU, and mPA are shown in Table 2; the training, validation, and prediction accuracy of 12 categories are shown in Table 3. The results show that the mPA of all three full convolutional neural network structures can be achieved with a rate above 90%. Among all categories, the segmentation accuracy is higher for vegetation, road, and people and lower for animals and boats. By analyzing the training images of the dataset, it can be found that the image number of animals and boats is extremely small, which is the reason for their poor segmentation results.

**TABLE 1 The accuracy evaluation indicators of the training and validation datasets.**

| Network | Training | | | Validation | | |
|---------|----------|-----|--------|------------|-----|--------|
| | Loss % | PA% | mIoU % | Loss % | PA% | mIoU % |
| FCN-32s | 0.564 | 65.730 | 94.358 | 17.848 | 53.222 | 58.631 |
| FCN-16s | 0.613 | 65.794 | 94.541 | 15.816 | 54.446 | 62.621 |
| FCN-8s | 1.082 | 65.497 | 92.898 | 14.739 | 54.387 | 62.418 |

**TABLE 2 The accuracy evaluation indicators of the test dataset.**

| Network | PA% | mIoU% | mPA% |
|---------|-----|-------|------|
| FCN-32S | 35.271 | 45.509 | 91.562 |
| FCN-16S | 37.853 | 44.521 | 91.607 |
| FCN-8S | 36.313 | 43.120 | 91.200 |

Due to a large number of predicted pictures, they cannot be displayed entirely. The paper selected ten typical scene pictures as sample data and arranged them in the order of original image, labeled image, FCN-8s prediction image, FCN-16s prediction image, and FCN-32s prediction image for display, as shown in Figure 5.

## 4.2 Discussion on experimental results

The semantic segmentation of UAV remote sensing images using deep learning is undoubtedly fast and effective, but some problems still deserve further study.

(1) According to the general experimental conclusion, the segmentation effect of FCN-8s should be significantly higher than that of FCN-32s. Still, from the results of Table 2, this is not the case, which may be related to the resolution of our dataset. The author chooses a crop size closest to the resolution of the original image for this experiment. In future research, the researcher can consider a more optimal crop treatment that makes the number of datasets larger and reflects the differences between various models more obviously.

(2) As shown in Table 2, it can be found that the overall segmentation effect of the categories of animals and boats is poor, which is caused by the imbalance of data categories in the AeroScapes dataset, where there are fewer images in these two categories. The category imbalance problem is especially obvious in the detection and segmentation tasks and often requires special attention. In the future, if continuing to use the public dataset, which is no longer able to change its internal results, the author can consider using weights to control the category balance. Those with more category data should have smaller weights to reduce the impact on the overall

**TABLE 3 The accuracy evaluation indicators for each category in the test dataset.**

| Category | Network | Training accuracy% | Validation accuracy % | Test accuracy % |
|---|---|---|---|---|
| Person | FCN-32s | 97.269 | 76.878 | 52.674 |
| | FCN-16s | 97.433 | 81.793 | 54.686 |
| | FCN-8s | 96.921 | 81.635 | 56.772 |
| Bike | FCN-32s | 82.967 | 46.656 | 10.873 |
| | FCN-16s | 81.844 | 46.369 | 15.369 |
| | FCN-8s | 80.392 | 47.730 | 13.848 |
| Car | FCN-32s | 71.140 | 58.594 | 38.622 |
| | FCN-16s | 73.215 | 59.028 | 47.340 |
| | FCN-8s | 71.138 | 58.795 | 40.827 |
| Drone | FCN-32s | 33.753 | 19.198 | 13.000 |
| | FCN-16s | 32.914 | 21.207 | 18.789 |
| | FCN-8s | 32.770 | 19.484 | 15.954 |
| Boat | FCN-32s | 5.956 | 3.868 | 2.397 |
| | FCN-16s | 5.950 | 5.549 | 2.866 |
| | FCN-8s | 5.921 | 3.994 | 2.760 |
| Animal | FCN-32s | — | — | — |
| | FCN-16s | — | — | — |
| | FCN-8s | — | — | — |
| Obstacle | FCN-32s | 95.337 | 60.213 | 22.732 |
| | FCN-16s | 96.060 | 66.266 | 29.772 |
| | FCN-8s | 95.923 | 65.356 | 20.178 |
| Construction | FCN-32s | 95.010 | 67.319 | 31.460 |
| | FCN-16s | 92.949 | 67.421 | 35.959 |
| | FCN-8s | 94.974 | 69.510 | 35.869 |
| Vegetation | FCN-32s | 99.813 | 96.194 | 95.903 |
| | FCN-16s | 99.789 | 96.102 | 93.882 |
| | FCN-8s | 99.738 | 96.076 | 94.191 |
| Road | FCN-32s | 99.873 | 97.827 | 86.388 |
| | FCN-16s | 99.867 | 98.246 | 85.989 |
| | FCN-8s | 99.634 | 98.156 | 88.054 |
| Sky | FCN-32s | 41.911 | 58.696 | 33.932 |
| | FCN-16s | 43.712 | 56.921 | 31.729 |
| | FCN-8s | 43.059 | 57.520 | 30.989 |
| Background | FCN-32s | 99.486 | 89.135 | 75.615 |
| | FCN-16s | 99.421 | 89.819 | 78.092 |
| | FCN-8s | 99.186 | 90.011 | 77.814 |

model. If the authors use their dataset, it is necessary to ensure the category balance, either trying to control the category balance when collecting data or considering adding algorithms such as adversarial generative networks to solve the small sample data problem and obtain better semantic segmentation results.
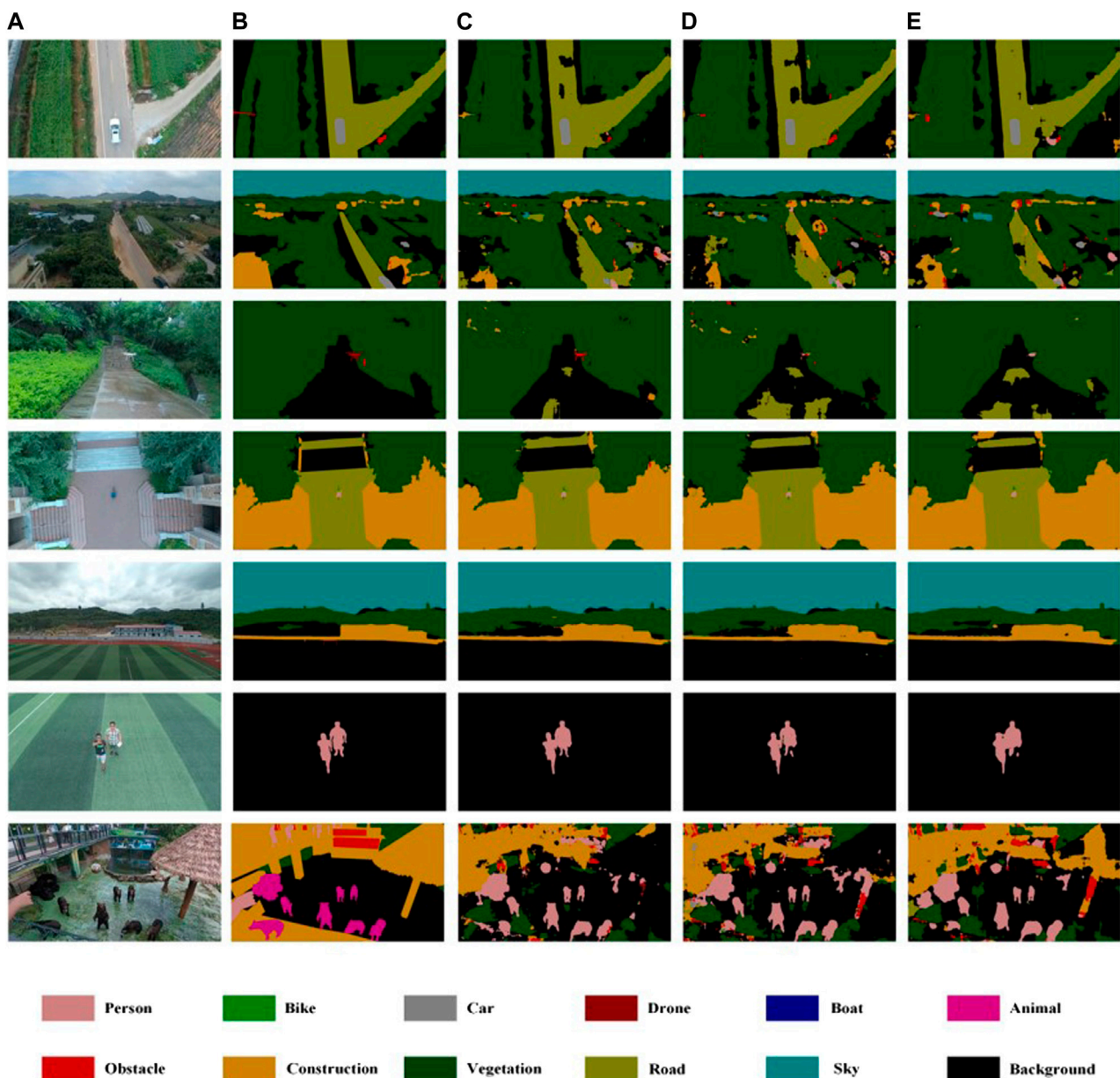
FIGURE 5
Semantic segmentation results in the AeroScapes dataset with FCN-8s, FCN-16s, and FCN-32s, respectively. Different colors represent different labels. **(A)** Image; **(B)** Label; **(C)** FCN-8s; **(D)** FCN-16s; **(E)** FCN-32s.

(3) From the segmentation results of the last two images in Figure 4, it can be easily seen that the animals are not properly labeled, and the same colors are used as persons, which is a common problem of inconsistent scales and small differences between categories in remote sensing images. When the UAV is flying at a low altitude, the images of animals captured are about the same size as the images of persons captured when the UAV is flying at a high altitude. At the same time, the animals standing up have a very high similarity to the appearance of persons, and the differences between the two categories are small, so the

segmentation results are wrong. How to deal with this kind of problem needs further study.

(4) During the experiments, only label coding, center cropping, and normalization were done on the dataset, and the dataset was not expanded by data augmentation. In future studies, geometric enhancements such as horizontal flipping, random cropping and scaling, random mirroring, or texture enhancements such as adjusting brightness and contrast can be considered to expand the dataset to make the trained segmentation model have better robustness and generalization performance.

# 5 Conclusion

This paper has researched the implementation method and process of semantic segmentation of UAV remote sensing images using three fully convolutional neural network structures. And the author has used three models, FCN-32s, FCN-16s, and FCN-8s, respectively, and trained 1,967 images, validated 654 images, and predicted 648 images. The experimental results show that setting the appropriate batch size and initial learning rate value for the fully convolutional neural network and choosing the Adam optimizer can segment the UAV remote sensing images effectively, and the segmentation results of FCN-16s and FCN-8s are better. Compared with traditional semantic segmentation methods such as region-based and SVM methods, deep learning-based segmentation methods do not depend on the quality of features extracted by domain experts, and can solve the problem of automatic feature learning, which is bound to improve the efficiency and accuracy of semantic segmentation significantly. Meanwhile, with the gradual popularization of UAV equipment, it is also easy to obtain high-resolution remote sensing images, which is more beneficial for us to apply deep learning to accomplish more valuable tasks in the image field.

# Data availability statement

The original contributions presented in the study are included in the article/supplementary material, further inquiries can be directed to the corresponding authors.

# Author contributions

GZ was responsible for writing and method. HZ and XY were responsible for data analyzing. ZJ was responsible for review and proofreading.

# Funding

# Conflict of interest

The authors declare that the research was conducted in the absence of any commercial or financial relationships that could be construed as a potential conflict of interest.

# Publisher's note

All claims expressed in this article are solely those of the authors and do not necessarily represent those of their affiliated organizations, or those of the publisher, the editors and the reviewers. Any product that may be evaluated in this article, or claim that may be made by its manufacturer, is not guaranteed or endorsed by the publisher.

# References

Chen, L. C., Papandreou, G., Kokkinos, I., Murphy, K., and Yuille, A. L. (2017a). DeepLab: Semantic image segmentation with deep convolutional nets, atrous convolution, and fully connected CRFs. *IEEE Trans. pattern analysis Mach. Intell.* 40 (4), 834–848. doi:10.1109/tpami.2017.2699184

Chen, L. C., Papandreou, G., and Kokkinos, I. (2014). Semantic image segmentation with deep convolutional nets and fully connected crfs[J]. arXiv preprint arXiv:1412.7062.

Chen, L. C., Papandreou, G., and Schroff, F. (2017b). Rethinking atrous convolution for semantic image segmentation[J]. arXiv preprint arXiv:1706.05587.

Chen, L. C., Yang, Y., and Wang, J. (2016). "Attention to scale: Scale-aware semantic image segmentation[C]," in *Proceedings of the IEEE conference on computer vision and pattern recognition* (Las Vegas, USA: IEEE), 3640–3649.

Chen, L. C., Zhu, Y., and Papandreou, G. (2018). "Encoder-decoder with atrous separable convolution for semantic image segmentation[C]," in *Proceedings of the European conference on computer vision (ECCV)* (Munich, Germany: Spinger), 801–818.

Chen, X., Williams, B. M., and Vallabhaneni, S. R. (2019). "Learning active contour models for medical image segmentation[C]," in Proceedings of the IEEE/CVF conference on computer vision and pattern recognition. Long Beach, CA, USA, 15-20 June 2019 (IEEE) 11632–11640.

De Benedetti, M., D'Urso, F., Fortino, G., Messina, F., Pappalardo, G., and Santoro, C. (2017). A fault-tolerant self-organizing flocking approach for UAV aerial survey. *J. Netw. Comput. Appl.* 96, 14–30. doi:10.1016/j.jnca.2017.08.004

Feng, D., Haase-Schütz, C., Rosenbaum, L., Hertlein, H., Glaser, C., Timm, F., et al. (2020). Deep multi-modal object detection and semantic segmentation for autonomous driving: Datasets, methods, and challenges. *IEEE Trans. Intelligent Transp. Syst.* 22 (3), 1341–1360. doi:10.1109/tits.2020.2972974

Funk, F., and Stütz, P. (2017). "A passive cloud detection system for UAV: Weather situation mapping with imaging sensors[C]," in 2017 IEEE Aerospace Conference. Big Sky, MT, USA, 04-11 March 2017 (IEEE), 1–12.

Green, D. R., Hagon, J. J., and Gómez, C. (2019). "Using low-cost UAVs for environmental monitoring, mapping, and modelling: Examples from the coastal zone[M]," in *Coastal management* (United Stated: Taylor & Franci), p465–p501.

HuangWuPeng, L. X. Q., and Yu, X. (2021). Depth semantic segmentation of tobacco planting areas from unmanned aerial vehicle remote sensing images in plateau mountains. *J. Spectrosc.* 2021, 1–14. doi:10.1155/2021/6687799

Kamilaris, A., and Prenafeta-Boldú, F. X. (2018). Disaster monitoring using unmanned aerial vehicles and deep learning[J]. arXiv preprint arXiv, 1807.

Kingma, D. P., and Ba, J. (2014). Adam: A method for stochastic optimization[J]. arXiv preprint arXiv:1412.6980.

Li, J., Jiang, F., Yang, J., Kong, B., Gogate, M., Dashtipour, K., et al. (2021). Lane-DeepLab: Lane semantic segmentation in automatic driving scenarios for high-definition maps. *Neurocomputing* 465, 15–25. doi:10.1016/j.neucom.2021.08.105

Li, W., He, C., Fang, J., Zheng, J., Fu, H., and Yu, L. (2019a). Semantic segmentation-based building footprint extraction using very high-resolution satellite images and multi-source GIS data. *Remote Sens.* 11 (4), 403. doi:10.3390/rs11040403

Li, Y. D., Dong, H., Li, H. G., Zhang, X., Zhang, B., and Xiao, Z. (2020). Multi-block SSD based on small object detection for UAV railway scene surveillance. *Chin. J. Aeronautics* 33 (6), 1747–1755. doi:10.1016/j.cja.2020.02.024

Li, Y., Peng, B., He, L., Fan, K., and Tong, L. (2019b). Road segmentation of unmanned aerial vehicle remote sensing images using adversarial network with multiscale context aggregation. *IEEE J. Sel. Top. Appl. Earth Observations Remote Sens.* 12 (7), 2279–2287. doi:10.1109/jstars.2019.2909478

Liu, M., Wang, X., Zhou, A., Fu, X., Ma, Y., and Piao, C. (2020). UAV-YOLO: Small object detection on unmanned aerial vehicle perspective. *Sensors* 20 (8), 2238. doi:10.3390/s20082238

Liu, S., Cheng, J., Liang, L., Bai, H., and Dang, W. (2021). Light-weight semantic segmentation network for UAV remote sensing images. *IEEE J. Sel. Top. Appl. Earth Observations Remote Sens.* 14, 8287–8296. doi:10.1109/jstars.2021.3104382

Meenpal, T., Balakrishnan, A., and Verma, A. (2019). "Facial mask detection using semantic segmentation[C]," in 2019 4th International Conference on Computing, Communications and Security (ICCCS). Rome, Italy, 10-12 October 2019 (IEEE), 1–5.

Milioto, A., Lottes, P., and Stachniss, C. (2018). "Real-time semantic segmentation of crop and weed for precision agriculture robots leveraging background knowledge in CNNs[C]," in 2018 IEEE international conference on robotics and automation (ICRA). Brisbane, QLD, Australia, 21-25 May 2018 (IEEE), 2229–2235.

Minaee, S., Boykov, Y., Porikli, F., Plaza, A., Kehtarnavaz, N., and Terzopoulos, D. (2021). "Image segmentation using deep learning: A survey," in IEEE Transactions on Pattern Analysis and Machine Intelligence (IEEE) 44 (7), 3523–3542. doi:10.1109/TPAMI.2021.3059968

Mohammadimanesh, F., Salehi, B., Mahdianpari, M., Gill, E., and Molinier, M. (2019). A new fully convolutional neural network for semantic segmentation of polarimetric SAR imagery in complex land cover ecosystem. *ISPRS J. photogrammetry remote Sens.* 151, 223–236. doi:10.1016/j.isprsjprs.2019.03.015

Shelhamer, E., Long, J., and Darrell, T. (2017). Fully convolutional networks for semantic segmentation. *IEEE Trans. Pattern Analysis Mach. Intell.* 39 (4), 640–651. doi:10.1109/tpami.2016.2572683

Tian, X., Wang, L., and Ding, Q. (2019). Review of image semantic segmentation based on deep learning[J]. *J. Softw.* 30 (2), 440–468. doi:10.13328/j.cnki.jos.005659

Xu, Y., Yu, G., and Wang, Y. (2017). Car detection from low-altitude UAV imagery with the faster R-CNN[J]. *J. Adv. Transp.* 2017, 2823617. doi:10.1155/2017/2823617

Yang, J., Ding, Z., and Wang, L. (2021). The programming model of air-ground cooperative patrol between multi-UAV and police car. *IEEE Access* 9, 134503–134517. doi:10.1109/access.2021.3115950

Yang, R., and Yu, Y. (2021). Artificial convolutional neural network in object detection and semantic segmentation for medical imaging analysis. *Front. Oncol.* 11, 638182. doi:10.3389/fonc.2021.638182

Zhang, H., Wang, L., Tian, T., and Yin, J. (2021). A review of unmanned aerial vehicle low-altitude remote sensing (UAV-LARS) use in agricultural monitoring in China. *Remote Sens.* 13 (6), 1221. doi:10.3390/rs13061221

Zhang, Y., Yuan, X., Li, W., and Chen, S. (2017). Automatic power line inspection using UAV images. *Remote Sens.* 9 (8), 824. doi:10.3390/rs9080824

Zhao, H., Shi, J., and Qi, X. (2017). "Pyramid scene parsing network[C]," in *Proceedings of the IEEE conference on computer vision and pattern recognition* (Hawaii, USA: IEEE), 2881–2890.

# Frontiers in
# Earth Science

**Investigates the processes operating within the major spheres of our planet**

Advances our understanding across the earth sciences, providing a theoretical background for better use of our planet's resources and equipping us to face major environmental challenges.

## Discover the latest Research Topics

See more →

**Frontiers**

Avenue du Tribunal-Fédéral 34
1005 Lausanne, Switzerland
frontiersin.org

**Contact us**

+41 (0)21 510 17 00
frontiersin.org/about/contact



frontiers in
Earth Science

frontiers | Research Topics